

Analytical methods, formation mechanisms and control strategies for endogenous hazardous substances produced during the thermal processing of foods

Edited by

Hongshun Yang, Jie Zheng and Hao Dong

Published in

Frontiers in Nutrition



FRONTIERS EBOOK COPYRIGHT STATEMENT

The copyright in the text of individual articles in this ebook is the property of their respective authors or their respective institutions or funders. The copyright in graphics and images within each article may be subject to copyright of other parties. In both cases this is subject to a license granted to Frontiers.

The compilation of articles constituting this ebook is the property of Frontiers.

Each article within this ebook, and the ebook itself, are published under the most recent version of the Creative Commons CC-BY licence. The version current at the date of publication of this ebook is CC-BY 4.0. If the CC-BY licence is updated, the licence granted by Frontiers is automatically updated to the new version.

When exercising any right under the CC-BY licence, Frontiers must be attributed as the original publisher of the article or ebook, as applicable.

Authors have the responsibility of ensuring that any graphics or other materials which are the property of others may be included in the CC-BY licence, but this should be checked before relying on the CC-BY licence to reproduce those materials. Any copyright notices relating to those materials must be complied with.

Copyright and source acknowledgement notices may not be removed and must be displayed in any copy, derivative work or partial copy which includes the elements in question.

All copyright, and all rights therein, are protected by national and international copyright laws. The above represents a summary only. For further information please read Frontiers' Conditions for Website Use and Copyright Statement, and the applicable CC-BY licence.

ISSN 1664-8714
ISBN 978-2-83251-613-3
DOI 10.3389/978-2-83251-613-3

About Frontiers

Frontiers is more than just an open access publisher of scholarly articles: it is a pioneering approach to the world of academia, radically improving the way scholarly research is managed. The grand vision of Frontiers is a world where all people have an equal opportunity to seek, share and generate knowledge. Frontiers provides immediate and permanent online open access to all its publications, but this alone is not enough to realize our grand goals.

Frontiers journal series

The Frontiers journal series is a multi-tier and interdisciplinary set of open-access, online journals, promising a paradigm shift from the current review, selection and dissemination processes in academic publishing. All Frontiers journals are driven by researchers for researchers; therefore, they constitute a service to the scholarly community. At the same time, the *Frontiers journal series* operates on a revolutionary invention, the tiered publishing system, initially addressing specific communities of scholars, and gradually climbing up to broader public understanding, thus serving the interests of the lay society, too.

Dedication to quality

Each Frontiers article is a landmark of the highest quality, thanks to genuinely collaborative interactions between authors and review editors, who include some of the world's best academicians. Research must be certified by peers before entering a stream of knowledge that may eventually reach the public - and shape society; therefore, Frontiers only applies the most rigorous and unbiased reviews. Frontiers revolutionizes research publishing by freely delivering the most outstanding research, evaluated with no bias from both the academic and social point of view. By applying the most advanced information technologies, Frontiers is catapulting scholarly publishing into a new generation.

What are Frontiers Research Topics?

Frontiers Research Topics are very popular trademarks of the *Frontiers journals series*: they are collections of at least ten articles, all centered on a particular subject. With their unique mix of varied contributions from Original Research to Review Articles, Frontiers Research Topics unify the most influential researchers, the latest key findings and historical advances in a hot research area.

Find out more on how to host your own Frontiers Research Topic or contribute to one as an author by contacting the Frontiers editorial office: frontiersin.org/about/contact

Analytical methods, formation mechanisms and control strategies for endogenous hazardous substances produced during the thermal processing of foods

Topic editors

Hongshun Yang — National University of Singapore, Singapore

Jie Zheng — Jinan University, China

Hao Dong — Zhongkai University of Agriculture and Engineering, China

Citation

Yang, H., Zheng, J., Dong, H., eds. (2023). *Analytical methods, formation mechanisms and control strategies for endogenous hazardous substances produced during the thermal processing of foods*. Lausanne: Frontiers Media SA. doi: 10.3389/978-2-83251-613-3

Table of contents

- 05 **Inhibition of Advanced Glycation End Products in Yogurt by Lotus Seedpod Oligomeric Procyanidin**
Nianjie Feng, Yang Shen, Chuanqin Hu, Jiangying Tan, Zhao Huang, Chao Wang, Zhiqiang Guo, Qian Wu and Juan Xiao
- 19 **Proteomic Analysis of the Protective Effect of Eriodictyol on Benzo(a)pyrene-Induced Caco-2 Cytotoxicity**
Chong Wang, Fan Zhao, Yun Bai, Chunbao Li, Xinglian Xu, Karsten Kristiansen and Guanghong Zhou
- 33 **The Simultaneous Formation of Acrylamide, β -carbolines, and Advanced Glycation End Products in a Chemical Model System: Effect of Multiple Precursor Amino Acids**
Cuyu Chen, Ye Jiao, Maomao Zeng, Zhiyong He, Qingwu Shen, Jie Chen and Wei Quan
- 45 **Sodium Ions Affect Pyrraline Formation in the Maillard Reaction With Lys-Containing Dipeptides and Tripeptides**
Zhili Liang, Xu Chen, Zhao Yang, Yan Liu, Xueying Qiu, Zhenzhen Zeng, Shuidi Lu and Yuehan Liu
- 59 **Formation of N^{ϵ} -Carboxymethyl-Lysine and N^{ϵ} -Carboxyethyl-Lysine in Pacific Oyster (*Crassostrea gigas*) Induced by Thermal Processing Methods**
Pengcheng Zhou, Shiyuan Dong and Mingyong Zeng
- 70 **Effects of Air Frying on French Fries: The Indication Role of Physicochemical Properties on the Formation of Maillard Hazards, and the Changes of Starch Digestibility**
Lu Dong, Cai-yi Qiu, Rui-can Wang, Yan Zhang, Jin Wang, Jing-min Liu, Hua-ning Yu and Shuo Wang
- 82 **Formation and Identification of a 5-(Hydroxymethyl)-2-Furfural-Zingerone Condensate and Its Cytotoxicity in Caco-2 Cells**
Yujing Ke, Zhao Yin, Nenghua Chen, Peifang Chen, Jie Liu, Shiyi Ou and Guoqiang Li
- 92 **Source Tracker Modeling Based on 16S rDNA Sequencing and Analysis of Microbial Contamination Sources for Pasteurized Milk**
Bingyao Du, Lu Meng, Haoming Wu, Huaigu Yang, Huimin Liu, Nan Zheng, Yangdong Zhang, Shengguo Zhao and Jiaqi Wang
- 101 **Formation and Identification of Six Amino Acid - Acrylamide Adducts and Their Cytotoxicity Toward Gastrointestinal Cell Lines**
Dan Li, Fangfang Xian, Juanying Ou, Kaiyu Jiang, Jie Zheng, Shiyi Ou, Fu Liu, Qinchun Rao and Caihuan Huang

- 112 **Exploring Acrylamide and 5-Hydroxymethylfurfural Formation in Glucose-Asparagine-Linoleic Acid System With a Kinetic Model Approach**
Yingjie Ma, You Long, Feng Li, Yan Zhang, Bei Gan, Qiang Yu, Jianhua Xie and Yi Chen
- 122 **Rapid Screening of 22 Polycyclic Aromatic Hydrocarbons Residues in Vegetable Oils by Gas Chromatography-Electrostatic Field Orbitrap High Resolution Mass Spectrometry**
Zhijuan Meng, Sufang Fan, Xiaoxuan Yuan, Qiang Li, Yunxia Huang, Lisha Niu, Guohua Shi and Yan Zhang
- 134 **Formation and metabolism of 6-(1-acetol)-8-(1-acetol)-rutin in foods and *in vivo*, and their cytotoxicity**
Min Chen, Pengzhan Liu, Hua Zhou, Caihuan Huang, Weiye Zhai, Yuantao Xiao, Juanying Ou, Jun He, Hani El-Nezami and Jie Zheng
- 149 **Benzo(a)pyrene and cardiovascular diseases: An overview of pre-clinical studies focused on the underlying molecular mechanism**
Chenghao Fu, Yuemin Li, Hao Xi, Zemiao Niu, Ning Chen, Rong Wang, Yonghuan Yan, Xiaoruo Gan, Mengtian Wang, Wei Zhang, Yan Zhang and Pin Lv
- 162 **Rutin alleviated acrolein-induced cytotoxicity in Caco-2 and GES-1 cells by forming a cyclic hemiacetal product**
Peifang Chen, Shuang Liu, Zhao Yin, Pengjie Liang, Chunhua Wang, Hanyue Zhu, Yang Liu, Shiyi Ou and Guoqiang Li



Inhibition of Advanced Glycation End Products in Yogurt by Lotus Seedpod Oligomeric Procyanidin

Nianjie Feng¹, Yang Shen¹, Chuanqin Hu², Jiangying Tan¹, Zhao Huang¹, Chao Wang¹, Zhiqiang Guo³, Qian Wu^{1*} and Juan Xiao^{3*}

¹ Key Laboratory of Fermentation Engineering (Ministry of Education), Hubei Key Laboratory of Industrial Microbiology, National "111" Center for Cellular Regulation and Molecular Pharmaceutics, Hubei Research Center of Food Fermentation Engineering and Technology, Hubei University of Technology, Wuhan, China, ² Key Laboratory of Cleaner Production and Integrated Resource Utilization of China National Light Industry, Beijing Technology and Business University, Beijing, China, ³ State Key Laboratory of Marine Resource Utilization in South China Sea, Key Laboratory of Food Nutrition and Functional Food of Hainan Province, Ministry of Education, Engineering Research Center of Utilization of Tropical Polysaccharide Resources, School of Food Science and Engineering, Hainan University, Haikou, China

OPEN ACCESS

Edited by:

Hao Dong,
Zhongkai University of Agriculture and
Engineering, China

Reviewed by:

Zhili Liang,
Guangdong Food and Drug
Vocational College, China
Kezhou Cai,
Hefei University of Technology, China
Chunxue Yang,
The University of Hong Kong,
Hong Kong SAR, China

*Correspondence:

Qian Wu
wuqian@hbut.edu.cn
Juan Xiao
xiaojuan209218@163.com

Specialty section:

This article was submitted to
Food Chemistry,
a section of the journal
Frontiers in Nutrition

Received: 23 September 2021

Accepted: 13 October 2021

Published: 04 November 2021

Citation:

Feng N, Shen Y, Hu C, Tan J,
Huang Z, Wang C, Guo Z, Wu Q and
Xiao J (2021) Inhibition of Advanced
Glycation End Products in Yogurt by
Lotus Seedpod Oligomeric
Procyanidin. *Front. Nutr.* 8:781998.
doi: 10.3389/fnut.2021.781998

The basic ingredients of yogurt include lactose and protein. Yogurt undergoes the Maillard reaction easily, producing many advanced glycation end products (AGEs) that cause some chronic diseases. Lotus seedpod oligomeric procyanidin (LSOPC) have demonstrated a strong inhibitory effect on AGE formation in simulated models; however, the inhibition of procyanidin on AGE formation and the subsequent effects on yogurt quality remains unknown. Our study demonstrated that LSOPC had a good inhibitory effect on the formation of fluorescent AGEs and N ϵ -carboxymethyl lysine ($P < 0.05$). The inhibitory capacity on AGEs and antioxidant activity of yogurt were positively correlated with the concentration of LSOPC. The effect of LSOPC on the physicochemical properties of yogurt was also evaluated. Bound water content, viscosity, and flavor of yogurt were significantly increased after LSOPC addition ($P < 0.05$). Therefore, LSOPC may lead to significant benefits for controlling AGE formation and improving the quality of yogurt.

Keywords: yogurt, lotus seedpod oligomeric procyanidin, advanced glycation end products, physicochemical properties, flavor

INTRODUCTION

Yogurt is a fermented dairy food produced by the growth of lactic acid bacteria (LAB). Due to the antioxidant peptides generated during fermentation, yogurt has higher antioxidant properties than ordinary milk (1). Meanwhile, proteins are degraded into small-molecule compounds (2) that are more easily digested and absorbed. In addition, yogurt contains large amounts of amino acids, such as lysine, tryptophan, and methionine, and reducing sugars, such as glucose, galactose, and lactose. Then, free amino groups and reducing sugars interact and undergo non-enzymatic protein glycation, forming Schiff base and Amadori products. Subsequently, various dicarbonyl compounds are produced through the oxidation and dehydration of the Amadori products to react with amino groups to form advanced glycation end products (AGEs) (3). The AGEs content of yogurt (vanilla flavor) is 3.00 kU/100 ml.

AGEs are produced by complex Maillard reactions. AGEs, including N ϵ -carboxymethyl lysine (CML), methylglyoxal (MGO), and pentosidine, are a group of potentially harmful compounds. Humans are exposed to AGEs in two ways, via endogenous AGEs generated from abnormal glucose metabolism or lipid peroxidation or via exogenous AGEs from various foods that they consume daily. Exogenous AGEs can enter the bloodstream and grow in the body (4). The AGEs accumulated in the body can increase oxidative stress, activate nuclear factor- κ B, further inducing various cytokines and growth factors. In any case, AGEs have been proposed to be a risk factor in the pathogenesis of diet-related diseases, such as diabetes, insulin resistance, cardiovascular diseases, kidney injury, and age-related neurodegenerative diseases (5).

Thus, the amount of AGEs in yogurt needs to be controlled. Our previous studies have shown that procyanidin can inhibit AGE formation in simulated food processing (6, 7). Procyanidin, a type of polyphenols, are widely distributed in the plant kingdom (8). Due to their special chemical structures, procyanidin display strong antioxidant properties and free radical scavenging abilities, similar to condensed tannins or oligomeric flavonoids (9–12). Many studies have shown that procyanidin can provide several health benefits, such as preventing cancer and cardiovascular diseases (11–13), reducing acrylamide content in food (14), and resisting neonatal hypoxic-ischemic brain damage (15, 16). Yogurt is a complex system considering its chemical constitution and physical environment. The inhibition of procyanidin on AGE formation and the subsequent effects on yogurt quality remain unclear.

In this study, a B-type procyanidin, named lotus seedpod oligomeric procyanidin (LSOPC), was extracted from lotus seed waste. LSOPC, as a yogurt additive, was found to inhibit AGE formation. The effect of LSOPC on the flavor and physicochemical properties of yogurt was also investigated.

MATERIALS AND METHODS

Materials

Milk (Weidendorf, Germany), caster sugar (Chuan Xiu, Beijing, China), and starter cultures *Lactobacillus plantarum* 21784 (China Industrial Microbial Culture Preservation Management Center) were purchased. Ultrapure water was obtained with a Milli-Q water purification system (Millipore, Microsep, Bellville, USA). All other chemicals (Sinopharm Chemical Reagent Factory, Shanghai, China) were analytical grade. Oligomeric procyanidin were prepared from lotus seedpods (a local supermarket, Wu Zhi 2 hao, China), according to Wu et al. (4).

Yogurt Preparation

Yogurts were prepared as described by Cenobio-Galindo et al. (17). In summary, 100 g milk and 5 g caster sugar were mixed with various concentrations of LSOPC and pasteurized at 85°C for 30 min. 0.2 g of starter culture was inoculated into the mixture, and maintained at 37°C for 12 h.

Counting *Lactobacillus plantarum*

The spread plate method was used to count *L. plantarum* (18). In summary, the sample was diluted with saline to the desired dilution factor and incubated on MRS medium at 37°C for 48 h. Then, the number of colonies are counted.

Titrateable Acidity Determination

A 10-g sample was mixed with 20 mL of water and titrated with 0.1 M NaOH using phenolphthalein as an indicator (19). The control was under the same conditions without the sample. The acidity was calculated as:

$$\text{Acidity } (^{\circ}\text{T}) = \frac{C \times (V_{\text{sample}} - V_{\text{control}}) \times 100}{m \times 0.1} \quad (1)$$

V_{sample} (mL) and V_{control} (mL) were the titration volume of sodium hydroxide for the sample and the control, respectively. C (in M) was the concentration of sodium hydroxide, m (in g) was the dry weight of the sample.

Determination of the Fluorescent AGEs

All the samples were incubated at 50°C for 5 days and diluted 15 times to assess the formation of fluorescent AGEs using an F-4500 luminescence spectrometer (Shimadzu, Japan) at the excitation wavelength of 370 nm and emission wavelength of 440 nm (7). The control was a sample without LSOPC, and the blank was a sample without heating. The inhibition was calculated as:

$$\text{Inhibition } (\%) = \frac{A_{\text{control}} - A_{\text{sample}}}{A_{\text{control}} - A_{\text{blank}}} \times 100 \quad (2)$$

A_{sample} , A_{control} , and A_{blank} were the absorbance of the sample, the control, and the blank, respectively.

N ϵ -Carboxymethyl Lysine Determination

After incubation at 50°C for 5 days, 500 μ L of a sample was added to 500 μ L of 0.2 M sodium borohydride (pH 13, prepared with 0.1 M NaOH), and the mixture was maintained at 4°C for 10 h. The supernatant was collected by centrifugation and passed through a preactivated solid-phase extraction PCX column (20). The eluted compound was resuspended in 1 mL of 0.1% formic acid and filtered through a 0.22- μ m organic membrane before HPLC-MS² analysis. Three parallel experiments were performed.

Next, 15- μ L samples were injected into an Eclipse Plus C₁₈ column (2.1 \times 50 mm, 5- μ m, Agilent Technologies, Germany) at 30°C with 0.2% formic acid (solvent A) and acetonitrile (solvent B) serving as the mobile phases. The chromatographic conditions were optimized to a run time of 25 min and a flow rate of 0.2 mL/min to achieve good separation. The gradient program was as follows: 0–0.5 min, 90% A; 0.5–4.0 min, 90%–60% A; and 4.0–25.0 min, 60% A. The mass spectrometer with multiple reaction monitoring was operated in the positive ion mode. The nitrogen temperature was kept at 300°C and the capillary voltage at 4 kV. With MassHunter Data and MassHunter Qualitative (Agilent Technologies, Germany), the fragments at m/z 84 and 130 were used for the quantitative and qualitative analysis of CML (m/z 205), respectively.

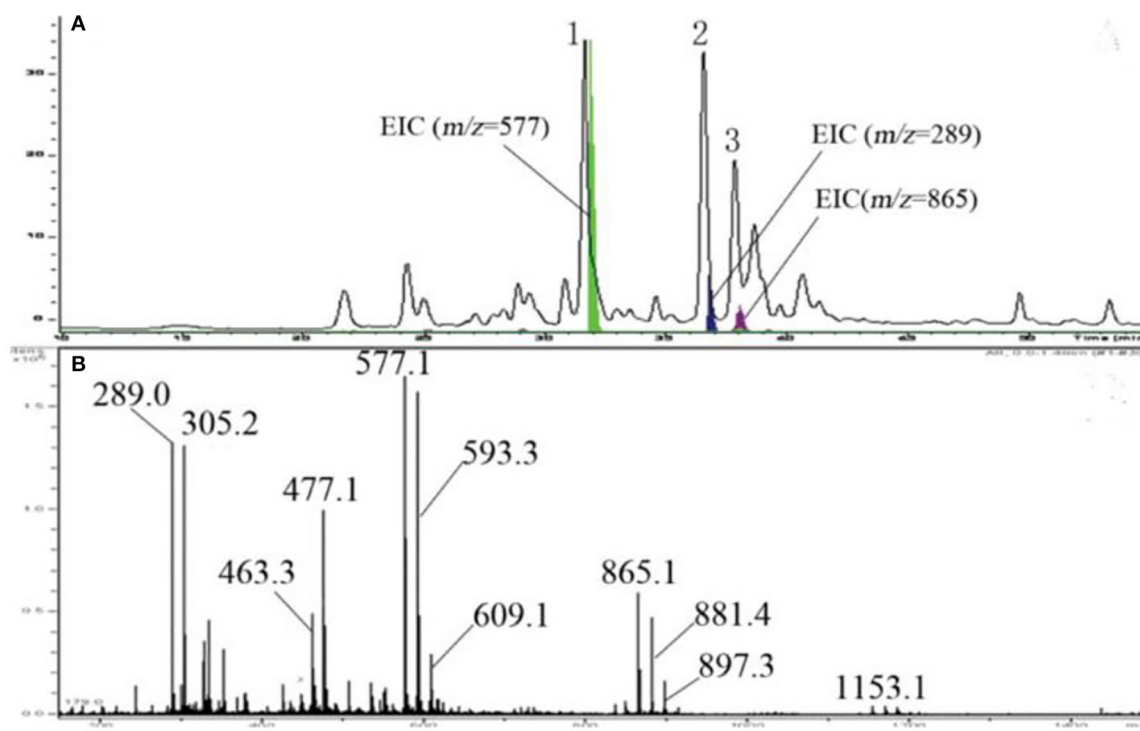


FIGURE 1 | HPLC chromatogram, EICs (A), and mass spectrum (B) of LSOPC using LC-ESI-MS.

LSOPC Degradation Analysis

A UV spectrometer was used to measure the concentration of LSOPC at 546 nm (21). Standard compounds were used under the same conditions to prepare the standard curves. The degradation was calculated as:

$$\text{Degradation (\%)} = \frac{C_a - C_b}{C_b} \times 100 \quad (3)$$

C_a and C_b were the concentration of LSOPC with and without treatment, respectively.

Antioxidant Activity Analysis

A UV spectrometer was used to determine the radical scavenging activity using the 2,2-diphenyl-1-picrylhydrazyl (DPPH) method (22). In summary, 0.2 mL of a sample was added to 3.8 mL of 0.1 mM DPPH in ethanol. The mixture was incubated at room temperature for 30 min and measured at 517 nm. An ethanol solution without DPPH was used as the control group, and the blank group contained water instead of a sample. The DPPH radical scavenging activity was calculated as:

$$\text{DPPH radical scavenging activity (\%)} = \frac{A_{\text{blank}} - (A_{\text{sample}} - A_{\text{control}})}{A_{\text{blank}}} \times 100 \quad (4)$$

A_{sample} , A_{control} , and A_{blank} were the absorbance of the sample, the control and the blank, respectively.

Nuclear Magnetic Resonance

The transverse relaxation time (T_2) of the sample was measured using the Carr-Purcell-Meiboom-Gill pulse sequence (23) and the following parameters: spectral width = 100 kHz, radio frequency delay = 0.16 ms, recycle delay = 3,000 ms, regulate analog gain 1 = 10, regulate digital gain 1 = 3, pre-amplified receiver gain = 1, scanning number = 8, echo number = 4,800, pulse gaps between $\pi/2$ and π = 0.16 ms.

Rheological Property Determination

A DHR-3 rotational rheometer (TA Instruments Inc., United States) was applied to determine the dynamic rheological properties of the samples. The test conditions included the plate diameter of 40 mm, the gap of 0.5 mm, the temperature at 25°C, the scanning strain set to 1%, and the frequency at 0.1–10 Hz. Finally, the spectra of the storage modulus (G') and loss modulus (G'') were obtained.

The viscosity of yogurt was measured by the rotation method. All the samples were tested at $25 \pm 0.5^\circ\text{C}$ using a No. 3 rotor by a Brookfield DV-3T Rheology tester at the rotating speed of 60 rpm.

Texture Determination

A TA.XT Plus texture analyzer with a P50 type probe (Stable Micro System Co., United States) was used to determine the texture of the samples (24) at the pretest, test, and post-test speeds of 1.0 mm/s and the trigger force of 5.0 g. The TPA software was used to analyze the final results.

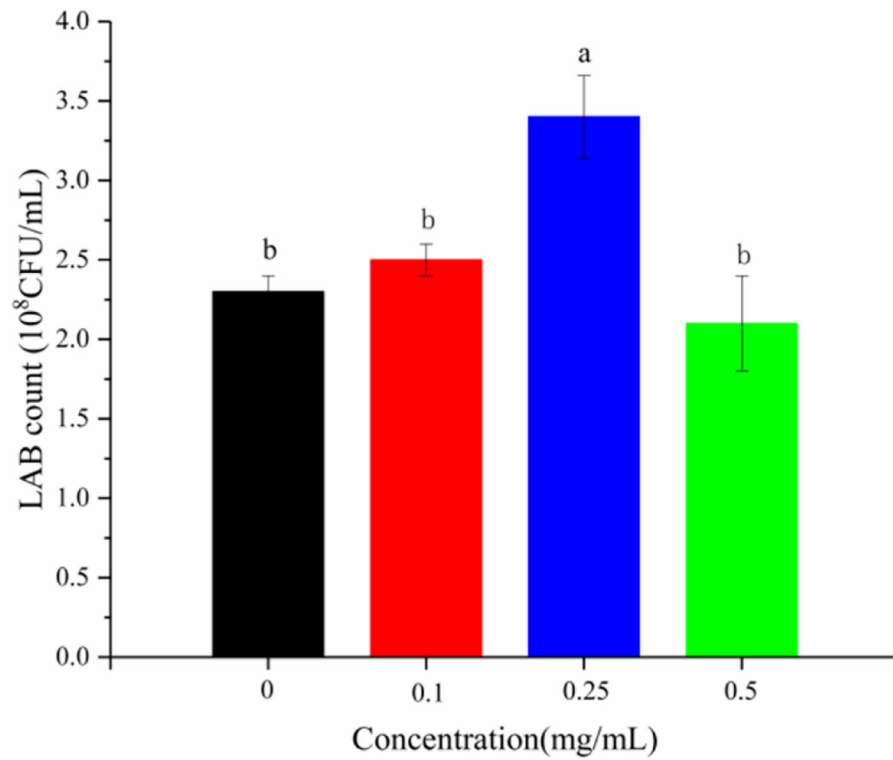


FIGURE 2 | Content of LAB in yogurt with different concentrations of procyanidin. Different letters indicated significant differences ($P < 0.05$).

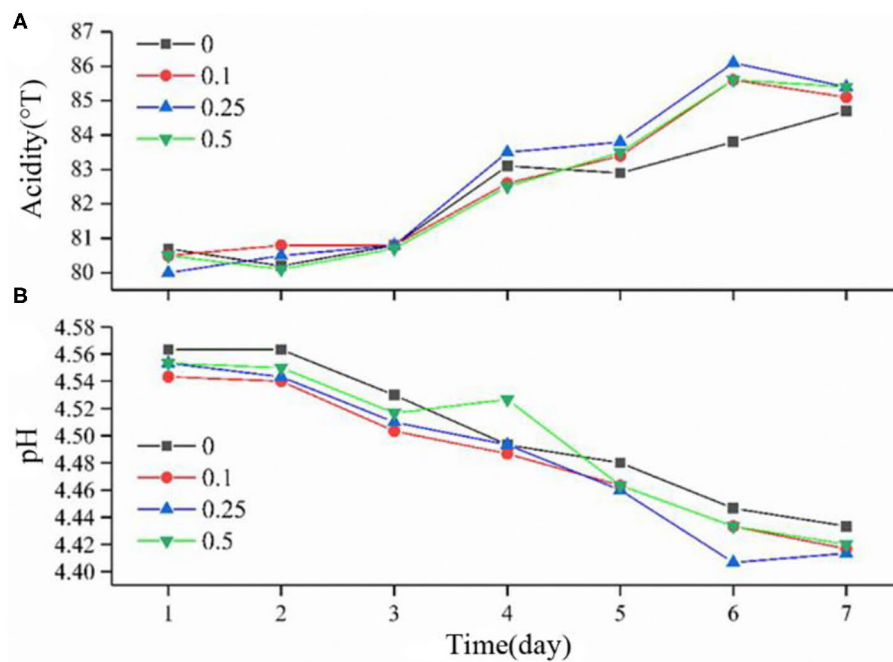


FIGURE 3 | pH (A) and titratable acidity (B) of yogurt during 7 consecutive days.

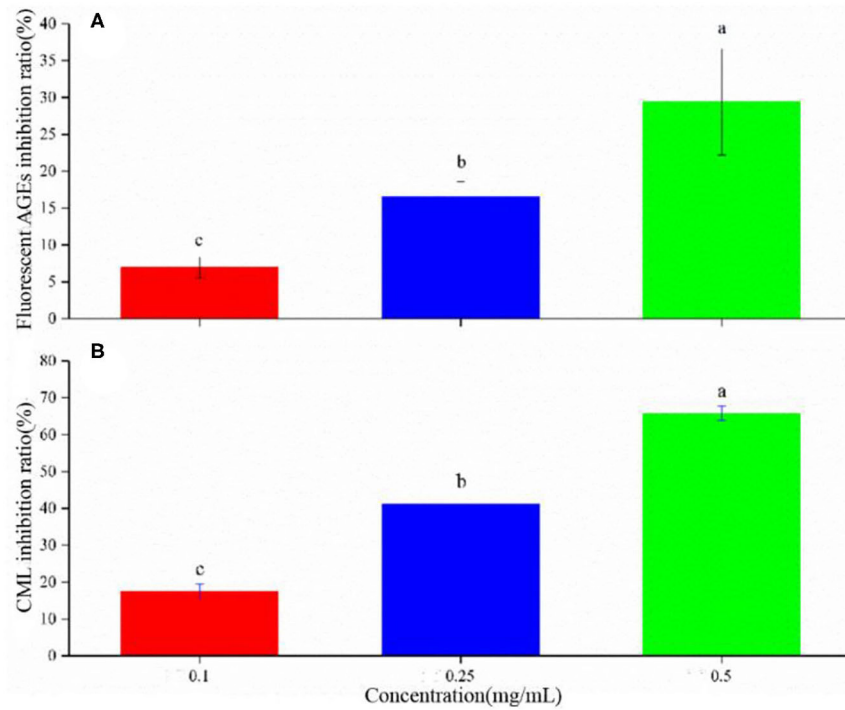


FIGURE 4 | Inhibition rate of AGEs **(A)** and CML **(B)** in yogurt. Different letters indicated significant differences ($P < 0.05$).

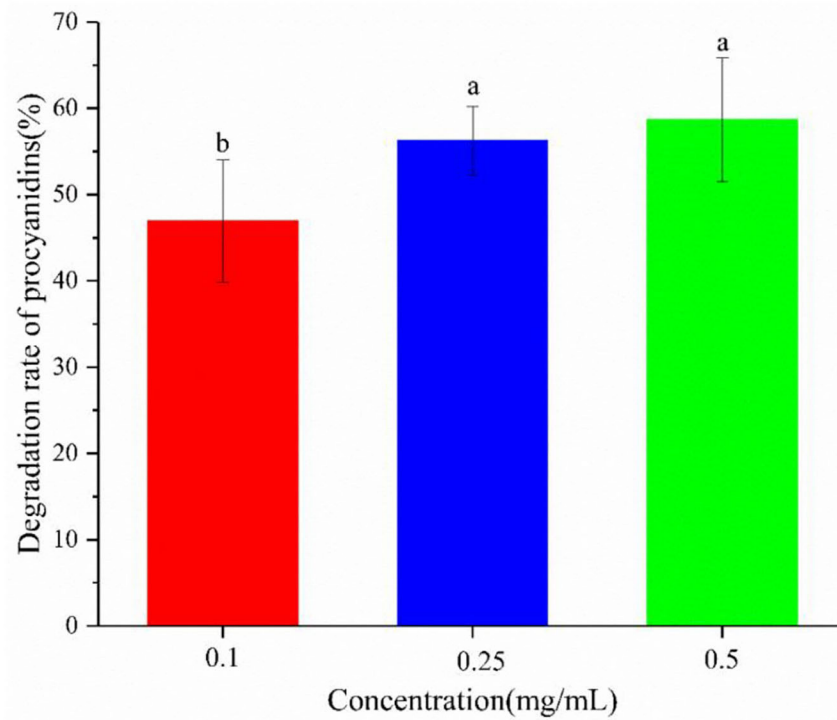


FIGURE 5 | Degradation rate of procyanidin in the yogurt-procyanidin groups. Different letters indicated significant differences ($P < 0.05$).

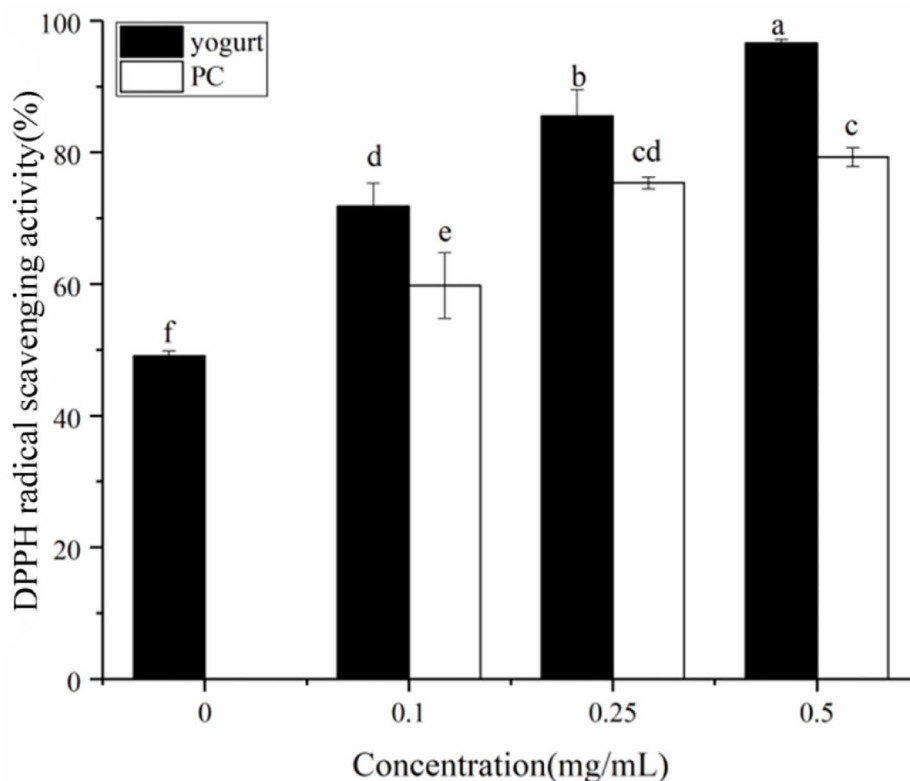


FIGURE 6 | DPPH free radical scavenging by yogurt containing procyanidin and yogurt without procyanidin (solid cylinder). The free radical scavenging rate of procyanidin themselves was also presented as a control (hollow cylinder). Different letters indicated significant differences ($P < 0.05$).

Gas Chromatography-Mass Spectrometry Analysis

A commercial solid-phase microextraction fiber with an 85- μm carbowax/polydimethylsiloxane coating (Supelco, Bellefonte, USA) was fitted into a manual holder and placed into the headspace above the sample to extract the flavor components at 50°C for 30 min (25). The fiber was then inserted into the needle and immediately injected into the GC-MS system. Desorption was performed at 250°C for 5 min.

The subsequent analyses were conducted using an Agilent 6890 GC system coupled to an Agilent 5975 inter quadrupole mass spectrometer. Sample components were separated on an Rtx-WAX capillary column (30 m \times 0.25 mm, 0.25-mm film thickness; Agilent Technologies). The oven temperature program was set at 30°C for 3 min, to increase to 225°C at 15°C/min, and to hold for 5 min. The flow rate of the carrier gas (helium at $\geq 99.999\%$ purity) was set at 1 mL/min. The mass selective detector was operated in the electron ionization mode at 70 eV over a scan range of m/z 30–500. The temperatures of the ion source and quadrupole were 240 and 150°C, respectively. Compound identification was based on mass spectra matching with the standard NIST 2001 MS library and on comparison to the retention indices sourced from the NIST Standard

Reference Database and the authentic reference standards when available.

Electronic-Nose Data Acquisition

A commercial PEN3 E-nose (Airsense Analytics GmbH, Schwerin, Germany) was used (26). A 1-mL sample was kept in a sealed bottle and heated at a selected temperature (70–150°C) for 1 h. Afterward, a 2 mL headspace was drawn off and injected into the e-nose at a flow rate of 300 mL/min. The response values were then recorded at 1-s intervals for 100 s until reaching a stable state. Finally, the probe was cleaned for 120 s, and the baseline was reset in 5 s. All the tests were performed at $25 \pm 0.5^\circ\text{C}$.

Organic Acid Analysis

Two g of sample was extracted by stirring with 25 mL of metaphosphoric acid at 25°C at 150 rpm for 45 min and subsequently centrifuged at 10,000 rpm for 10 min (27). Before analysis by high-performance liquid chromatography (HPLC, Shimadzu, Kyoto, Japan), the sample was passed through a 0.45- μm nylon filter. The fractions were achieved on a reserved-phase eclipse plus C_{18} column (2.1 \times 50 mm, 5- μm ; Agilent Technologies, Germany) and eluted with 100 mM K_2HPO_4 in methanol (v/v,

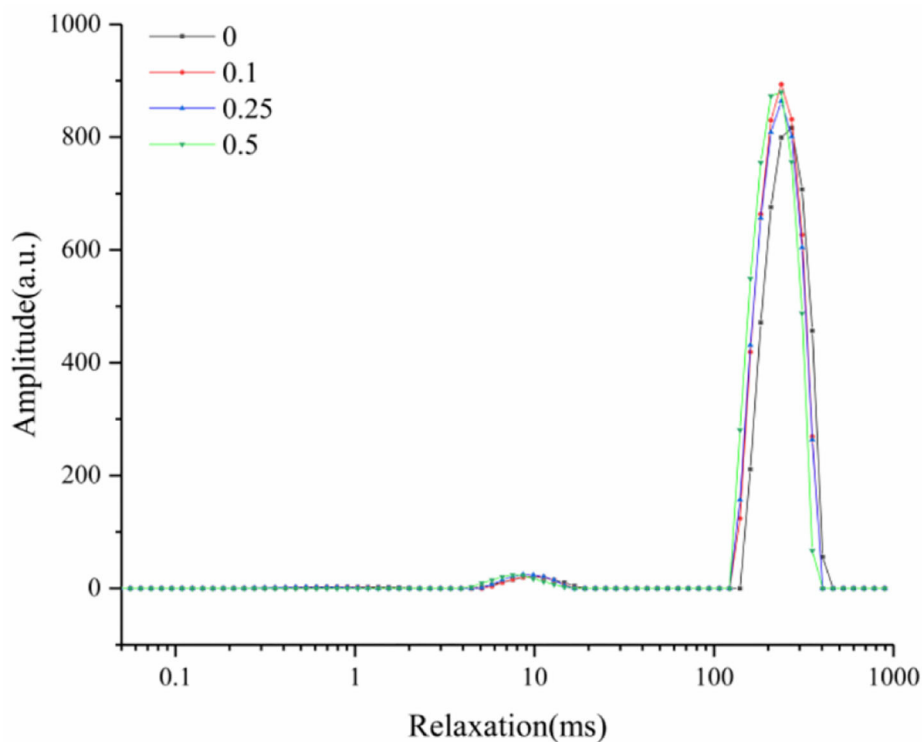


FIGURE 7 | Low-field NMR spectra of yogurt.

97/3) using a flow rate of 1.0 mL/min. Detection was carried out in a PDA using 210 nm as a preferred wavelength.

Statistical Analysis

All the data were presented as means \pm standard deviation (means \pm S.D.) and calculated using one-way ANOVA with SPSS 25.0 followed by the Tukey's multiple-range test. The graphs were drawn with OriginPro 8.0.

RESULTS AND DISCUSSION

Analysis of LSOPC

Using the butanol-HCl assay, we found that LSOPC was rich in procyanidin. The procyanidin content of LSOPC was $106.22 \pm 0.46\%$ compared to that in grape seeds. Grape seed procyanidin with a purity of more than 95% are used as a standard product. Our laboratory has uncovered the structural information of the procyanidin in lotus seedpods (28). The mean degree of polymerization of LSOPC was found to be 3.2. The terminal units in LSOPC were 74% catechin and 26% epicatechin. The extension units in LSOPC were 26% catechin, 43% epicatechin, and 31% epigallocatechin. According to the HPLC chromatogram of LSOPC (**Figure 1A**), peaks 1, 2, and 3 exhibited maximum absorption at 279 nm and corresponded to extracted ion current chromatogram peaks of m/z 577, 289, and 865, respectively, suggesting that peaks 1, 2, and 3 represented

procyanidin dimers, monomers (i.e., catechin or epicatechin), and trimers, respectively.

By coeluting procyanidin B1, B2, and B3, peak 1 was confirmed to be procyanidin B3. From the ESI-MS spectrum of LSOPC (**Figure 1B**), the compounds in LSOPC could be tentatively identified by their m/z ratios as catechin or epicatechin (m/z 289), galocatechin or epigallocatechin (m/z 305), quercetin glycoside (m/z 463), quercetin glucuronide (m/z 477), procyanidin dimers (m/z 577.1), proanthocyanidin dimer gallate (m/z 593.3), prodelfphinidin dimers (m/z 609.1), procyanidin trimers (m/z 865.1), and proanthocyanidin trimers with 1 galocatechin or epigallocatechin unit and 2 catechin units (m/z 881.4), proanthocyanidin trimers with 2 galocatechin or epigallocatechin units and 1 catechin or epicatechin unit (m/z 897.3), and procyanidin tetramers (m/z 1153.1). Thus, LSOPC consists of proanthocyanidin monomers, dimers, trimers, and tetramers.

The Effect of LSOPC on the Growth of *L. plantarum*

Flavonoids inhibit the growth of some bacteria (29) and strictly control their subsequent metabolism (30). LSOPC was added to the medium of *L. plantarum* 21784 to verify this effect. LSOPC was not found to have a growth-inhibiting effect (**Figure 2**). On the contrary, it had a growth-promoting effect at 0.25 mg/mL. Moreover, pH and titratable acidity both correspond to the growth rate of bacteria (31). There was little

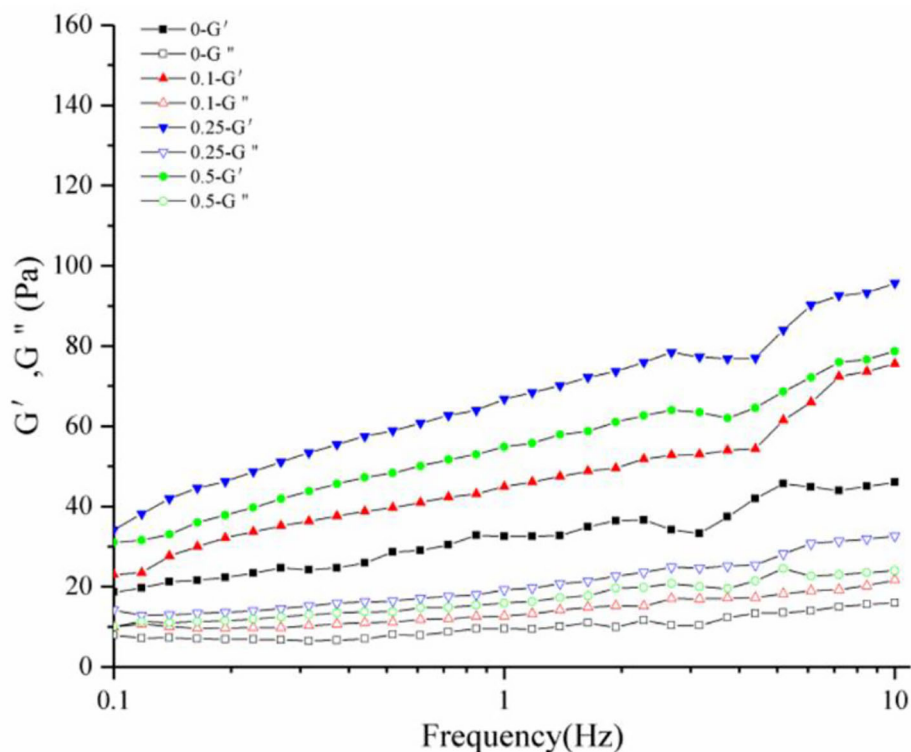


FIGURE 8 | Dynamic rheological diagram of yogurt. G' is the elastic modulus, G'' is the viscous modulus.

increase in the pH and titratable acidity after adding LSOPC (Figure 3).

The Effect of LSOPC on Fluorescent AGEs and CML Formation

Flavonoids can inhibit 2-dicarbonyl production and fluorescent AGE formation (32). The antioxidant activity is dependent on the number and location of hydroxyl groups on the aromatic ring (14, 33, 34). LSOPC could noticeably inhibit the formation of AGEs (Figure 4A). The increasing LSOPC concentrations from 0.1 to 0.5 mg/mL improved the inhibitory effect, increasing the inhibition rate from 7.0 to 29.4%.

CML, formed through a reaction between glyoxal and lysine, is a typically harmful substance and an important index of AGEs (35). Procyanidin can inhibit the formation of CML in a model system and a real food system; however, the inhibitory effect varies with the pH values and heating temperatures (35). Here, LSOPC was observed to have a significant inhibitory effect on the formation of CML in yogurt (Figure 4B). With increasing LSOPC concentrations of 0.1–0.5 mg/mL, the inhibition rate was increased from 17.5 to 65.8%. These data were consistent with the fluorescent AGE content detected in yogurt with different LSOPC concentrations.

The Effect of Yogurt System on Procyanidin Degradation

The inhibitory effect of procyanidin on AGE formation is weakened by yogurt (4, 7, 35). The underlying mechanism was examined by studying the degradation of procyanidin in yogurt (Figure 5). On one hand, the procyanidin degradation rate was high and up to 50%, partly because procyanidin were unstable and degraded by LAB. On the other hand, procyanidin degradation could increase as its concentration increased, especially at lower concentrations of 0.1–0.25 mg/mL. At higher concentrations, procyanidin were more unstable, indicating a greater inhibition of procyanidin. To further explore the weakening of the inhibitory effect of procyanidin by yogurt, the degradation products of procyanidin were analyzing.

Effect of Procyanidin on the Antioxidant Activity of Yogurt

Phenolic compounds have antiglycative activities due to their dicarbonyl-trapping capacity, free radical scavenging activity, and metal-chelating and antioxidant properties (36, 37). The DPPH free radical scavenging rate of yogurt was studied (solid cylinder, Figure 6); the scavenging rate was significantly higher after adding procyanidin. Also, at higher concentrations of added procyanidin, the antioxidant activity the stronger. The antioxidant capacity of flavonoids is closely related to

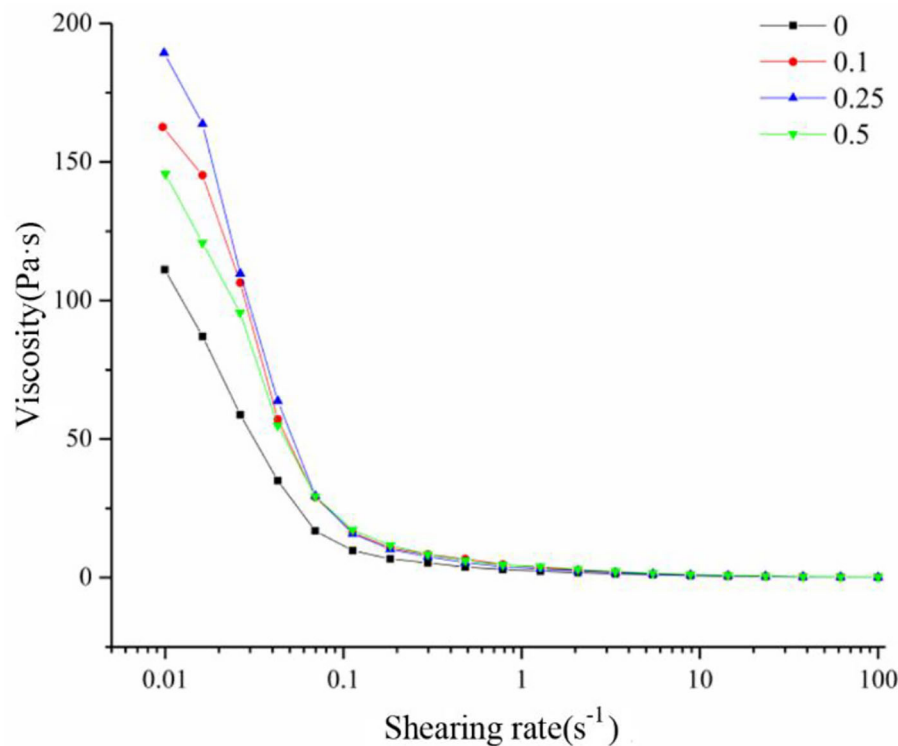


FIGURE 9 | Static rheological diagram of yogurt.

the inhibition rate of the Maillard reaction (38). The effect of procyanidin on the antioxidant activity of yogurt also appeared correlated with its rate of AGE inhibition. Also, interestingly, a synergistic effect of antioxidant activity was found in the yogurt-procyanidin groups, whose scavenging rates were higher than in the procyanidin-only groups (hollow cylinder, Figure 6).

Low-Field NMR Properties

The intermediates of fermented milk and cheese are similar; they are both non-membrane colloidal structures formed by the coagulation of proteins and polysaccharides. Three peaks in the T_2 relaxation curves were ascribed to bound water (1–10 ms), immobile water (10–100 ms), and free water (100–1,000 ms), respectively. The relaxation peak of yogurt slightly shifted to the left with the increasing concentrations of added procyanidin (Figure 7), indicating that the free water in yogurt was more likely to be bound with procyanidin. According to the polyhydroxy structure, procyanidin will provide more hydrogen bonding sites to control the free water in yogurt (3).

Rheological Properties

The rheological properties of a substance can be analyzed by comparing the storage (G') to the loss modulus (G'') master curves (39). The variation of G' and G'' with frequency provides valuable information on the change in the stiffness

and damping capability of a substance, respectively. G' and G'' were measured for the frequency sweep tests (Figure 8). The G' values showed a substantial increase and a comparatively higher frequency dependence. The changes in G'' curves were negligible compared to that in the G' curves, indicating that the yogurt acquired solid-like properties after the addition of procyanidin and had the characteristics of fermented milk.

Shear viscosity was also measured using a rheometer at a shear rate of up to $100 s^{-1}$. The viscosity significantly decreased at a very low shear rate, and then less affected at higher shear rate (Figure 9), consistent with the rheological properties of pseudoplastic fluids.

Texture Properties

The sensory quality of yogurt is very subtle and can be influenced by many factors. General evaluation tools are needed in the industry to meet the global consumer demands for specific sensory attributes. The objective measurement of texture properties may well be far less complex than that of other sensory quality. The texture profile, including parameters like hardness, adhesiveness, springiness, cohesiveness, gumminess, chewiness, and resilience, of the yogurt samples, was analyzed (Table 1). The addition of procyanidin significantly increased the hardness, adhesiveness, gumminess, and chewiness. However, it did not affect the springiness, cohesiveness, or resilience of the yogurt samples,

TABLE 1 | Texture properties of yogurt with different concentrations (0, 0.1, 0.25, and 0.5 mg/ml) of procyanidin.

Samples	Hardness	Adhesiveness	Springiness	Cohesiveness	Gumminess	Chewiness	Resilience
0	7.89 ± 0.9 ^c	28,357 ± 833 ^c	0.97 ± 0.004 ^a	0.729 ± 0.024 ^a	5.53 ± 0.61 ^c	5.37 ± 0.61 ^c	0.052 ± 0.009 ^a
0.1	12.4 ± 1.5 ^b	34,263 ± 318 ^b	0.96 ± 0.002 ^a	0.703 ± 0.007 ^a	8.08 ± 0.92 ^b	7.82 ± 0.90 ^b	0.042 ± 0.003 ^a
0.25	15.7 ± 0.6 ^a	58,267 ± 769 ^a	0.97 ± 0.003 ^a	0.713 ± 0.016 ^a	10.3 ± 0.55 ^a	10.1 ± 0.55 ^a	0.040 ± 0.003 ^a
0.5	13.0 ± 1.7 ^b	34,027 ± 707 ^b	0.96 ± 0.002 ^a	0.712 ± 0.012 ^a	8.66 ± 1.08 ^b	8.39 ± 1.06 ^b	0.041 ± 0.002 ^a

The data are given as mean ± S.D (n = 3). Different letters indicated a significant difference (p < 0.05).

TABLE 2 | Flavor components in yogurt identified by GC-MS analysis.

No.	RT	Component	Relative content (%)			
			0	0.1	0.25	0.5
1	6.242	2-Heptanone	5.09	7.95	9.24	7.08
2	9.603	2-Nonanone	2.4	2.66	3.12	3.07
3	9.144	Heptanoic acid	0.54	0.69	0.74	0.82
4	10.898	Octanoic acid	0.99	1.21	1.76	1.33
5	16.256	n-Hexadecanoic acid	13.88	16.07	18.25	15.54
6	15.687	Tetradecanoic acid	2.05	2.21	1.98	1.72
7	16.404	Hexadecanoic acid	2.17	2.16	1.91	1.73
8	17.996	cis-10-Heptadecenoic acid	ND	1.43	1.47	1.82
9	19.021	(E)-9-Octadecenoic acid	1.33	2.24	2.21	1.98
10	12.093	Pentadecane	0.67	0.76	0.42	0.48
11	14.301	Cyclohexadecane	1.08	ND	ND	ND
12	16.343	Hexadecane	1.21	1.54	0.98	ND
13	15.649	Octadecane	2.16	1.85	1.39	ND
14	11.977	Eicosane	1.6	ND	ND	ND
15	8.691	D-Limonene	ND	0.5	0.45	0.38
16	18.266	1-Octadecene	0.32	0.89	0.75	0.44
17	19.113	1-Heptadecene	ND	0.69	0.88	0.36
18	13.101	Nonacos-1-ene	0.43	0.25	0.36	0.18
19	15.336	13-Methyl-Z-14-nonacosene	1.26	ND	ND	ND

likely due to the increase of bound water content in yogurt. Similar results were observed when grapeseed oil was added to yogurt (40). The improvement of these parameters within a reasonable range should enhance the sensory quality of yogurt.

Volatile Flavor

Nineteen volatile compounds were identified by GC-MS from the yogurt samples, accounting for 37–46% of the absolute dry weight of the samples (Table 2). These compounds included two ketones, seven acids, five alkanes, and five olefins. The ketone content in the yogurt-procyanidin groups was noticeably higher than that in the control group. The content of 2-heptanone increased from 5.09 to 9.24% by adding 0.25 mg/mL

procyanidin. The content of 2-nonanone increased from 2.40 to 3.12% as well. Ketone compounds can promote the degradation of AGE intermediate products (4). Thus, procyanidin likely control the formation of AGEs by increasing the content of ketone compounds.

The principal component analysis was performed by WinMuster software of the e-nose. The contribution rates of the first and the second principal components were 84.89 and 12.21%, respectively, and the total contribution rate was 97.10% (Figure 10A). These data indicated that the principal component could reflect all the characteristics of the volatile odor of yogurt with or without procyanidin. It is generally believed that a data point farther away from the origin has a greater contribution rate (41). Besides, the three yogurt samples with procyanidin displayed some differences and could be completely separated from the yogurt sample without procyanidin.

According to the radar chart (Figure 10B), the four yogurt samples displayed significantly different odor characteristics. All the samples had higher response values at sensors W5S, W1W, and W2W; in addition, the response values of the above sensors differed significantly. In comparison, the samples had similar response values at W6S. The odor characteristics from the analysis of the e-nose data were related to the composition of volatile compounds (GC-MS results).

Organic Acids

Organic acids in fermented dairy products play an important role as natural preservatives and contribute to the characteristic sensory properties of the product (42). Lactic acid content affects, more than other organic acids present in lower amounts, the “sourness” intensity of yogurt, which is disliked by some customers. The mean concentration of lactic acid was increased from 1.3 to 1.6 mg/mL by adding procyanidin (Figure 11 and Table 3); however, the differences were very small in the yogurt-procyanidin groups.

Citric acid is usually present in milk as a product of bovine metabolism. Citric acid is also known to be utilized during the fermentation process, but it is underutilized in the storage process (43). Here, the yogurt-procyanidin groups had a higher concentration of citric acid than the control group. The citric acid concentration was increased from 0.29 to 0.36 mg/mL by the addition of procyanidin. The increase in organic acid concentration in yogurt-procyanidin groups was in agreement with the decrease in pH value.

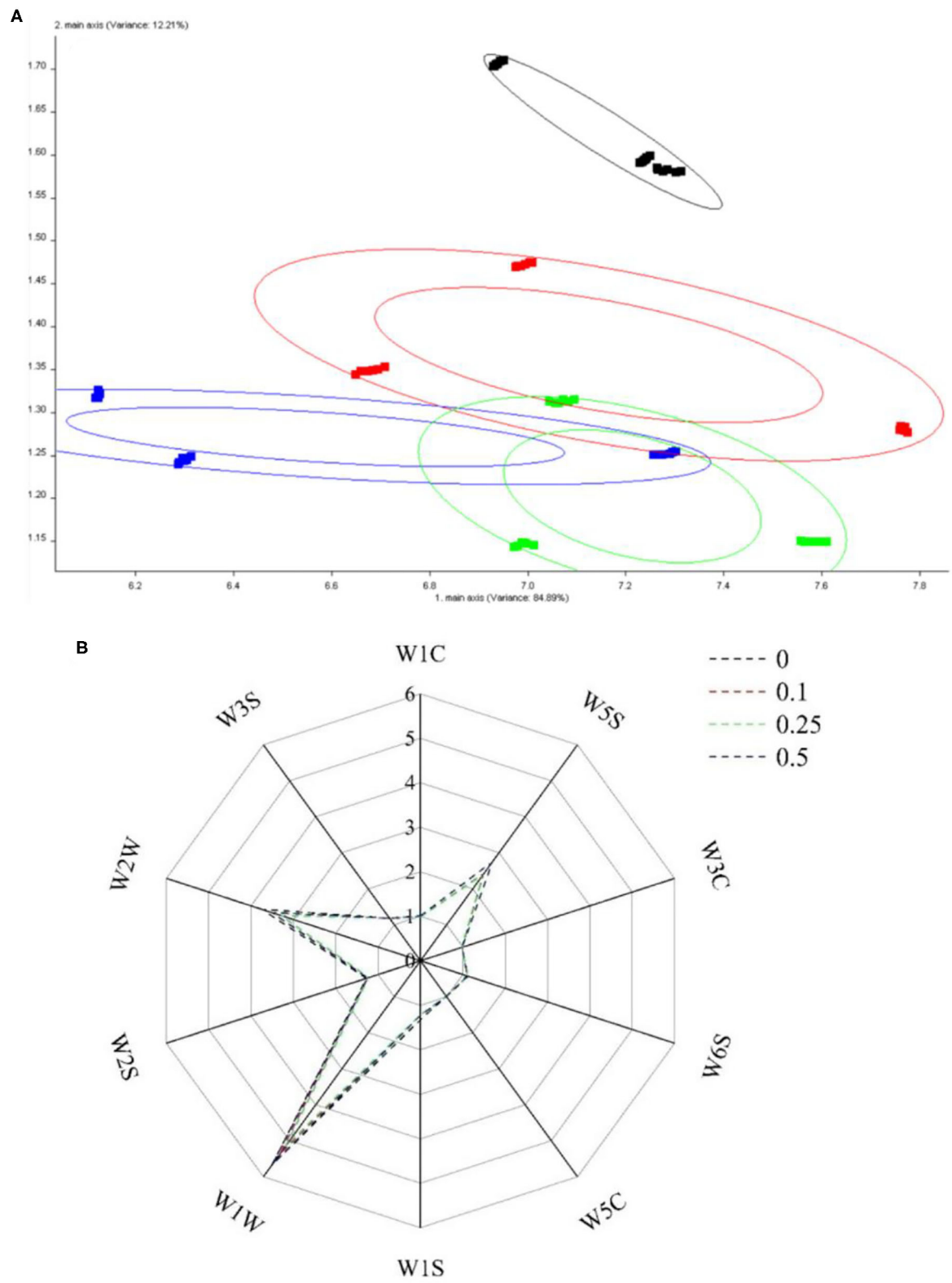


FIGURE 10 | PCA diagram **(A)** and radar chart **(B)** of electronic nose.

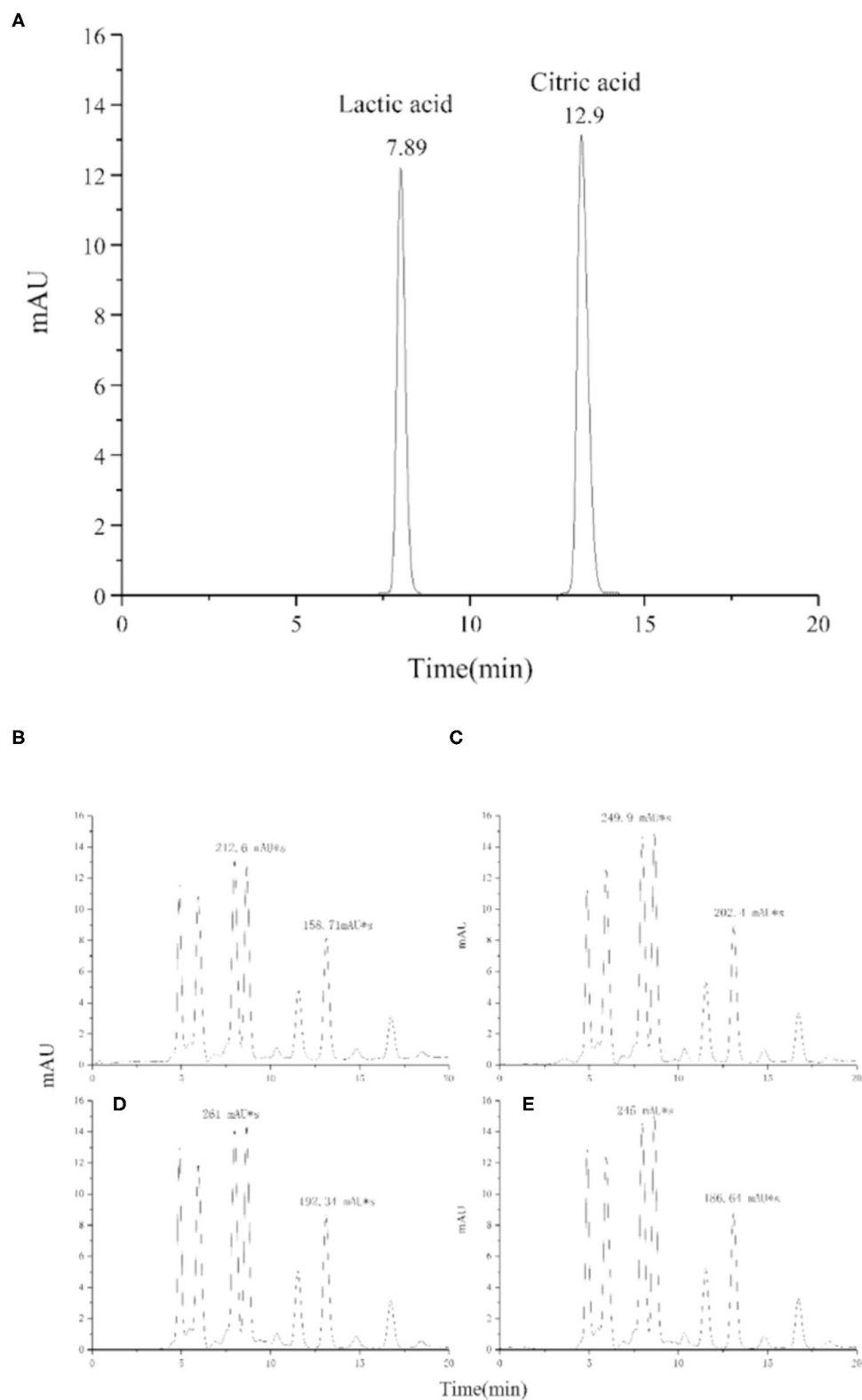


FIGURE 11 | HPLC chromatogram of lactic acid and citric acid in standard sample **(A)** and yogurt samples, 0 mg/mL procyanidin **(B)**, 0.1 mg/mL procyanidin **(C)**, 0.25 mg/mL procyanidin **(D)**, and 0.5 mg/mL procyanidin **(E)**.

TABLE 3 | Content of lactic acid and citric acid in yogurt different concentrations (0, 0.1, 0.25, and 0.5 mg/ml) of procyanidin.

Samples	Lactic acid (mg/mL)	Citric acid (mg/mL)
0	1.34 ± 0.1 ^b	0.29 ± 0.022 ^b
0.1	1.6 ± 0.11 ^a	0.36 ± 0.009 ^a
0.25	1.67 ± 0.07 ^a	0.34 ± 0.009 ^a
0.5	1.56 ± 0.06 ^a	0.33 ± 0.016 ^a

The data are given as mean ± S.D (n = 3). Different letters indicated a significant difference (p < 0.05).

CONCLUSION

Due to the increasing global demand for food function, studying natural additives is necessary. Interestingly, LSOPC demonstrate an inhibitory effect on AGE formation in a simulated system. The increasing LSOPC concentrations from 0.1 to 0.5 mg/mL improved the inhibitory effect, increasing the inhibition rate from 7.0 to 29.4%. At higher concentrations of added procyanidin, the antioxidant activity the stronger. In this study, yogurt with high lactose and protein content was used to evaluate the inhibitory effect of LSOPC. Firstly, LSOPC were found to improve the antioxidant properties of yogurt and reduce the consumption of ketones, thereby displaying an inhibitory effect against AGE formation. Besides, the increase in the bound water content, viscosity, and flavor of yogurt was found in the yogurt-procyanidin groups. These findings likely advance the value-added applications of procyanidin in food additives.

REFERENCES

1. Sabeena-Farvin KH, Baron CP, Nielsen NS, Jacobsen C. Antioxidant activity of yoghurt peptides: Part 1-*in vitro* assays and evaluation in ω -3 enriched milk. *Food Chem.* (2010) 123:1081–9. doi: 10.1016/j.foodchem.2010.05.067
2. Nguyen DD, Busetti F, Johnson SK, Solah VA. Degradation of β -casomorphins and identification of degradation products during yoghurt processing using liquid chromatography coupled with high resolution mass spectrometry. *Food Res Int.* (2018) 106:98–104. doi: 10.1016/j.foodres.2017.12.035
3. Wu Q, Chen H, Lv Z, Hu B, Guan Y, Xie B, et al. Oligomeric procyanidins of lotus seedpod inhibits the formation of advanced glycation end-products by scavenging reactive carbonyls. *Food Chem.* (2013) 138:1493–502. doi: 10.1016/j.foodchem.2012.10.111
4. Wu Q, Min YY, Xiao JS, Feng NJ, Chen YY, Luo Q, et al. Liquid state fermentation vinegar enriched with catechin as an antglycative food product. *Food Funct.* (2019) 10:4877–87. doi: 10.1039/C8FO01892H
5. Cepas V, Collino M, Mayo JC, Sainz RM. Redox signaling and advanced glycation endproducts (AGEs) in diet-related diseases. *Antioxidants.* (2020) 9:142. doi: 10.3390/antiox9020142
6. Chen GJ, Madl RL, Smith JS. Inhibition of advanced glycation endproducts in cooked beef patties by cereal bran addition. *Food Control.* (2017) 73:847–53. doi: 10.1016/j.foodcont.2016.09.037
7. Wu Q, Luo Q, Xiao JS, Tang SM, Chen YY, Shen Y, et al. Catechin-iron as a new inhibitor to control advanced glycation end-products formation during vinegar storage. *LWT-Food Sci Technol.* (2019) 112:108245. doi: 10.1016/j.lwt.2019.06.012
8. Zhang GX, Ma J, Lu HC, Ye ZN, Liu J, Wang CB. Oligomeric Proantho Cyanidins provides neuroprotection against early brain injury

DATA AVAILABILITY STATEMENT

The original contributions presented in the study are included in the article/supplementary material, further inquiries can be directed to the corresponding author/s.

AUTHOR CONTRIBUTIONS

NF: conceptualization, methodology, investigation, and writing-original draft. YS: data curation and writing-original draft. CH: methodology. JT: data curation. ZH and CW: supervision. ZG: conceptualization. QW: writing-review and editing, supervision, and funding acquisition. JX: conceptualization and funding acquisition. All authors contributed to the article and approved the submitted version.

FUNDING

This work was financially supported by National Natural Science Foundation of China (Grant Nos. 32001705 and 21908048), Key Laboratory of Food Nutrition and Functional Food of Hainan Province (No. KF202009), State Key Laboratory of Marine Resource Utilization in South China Sea (Hainan University) (No. MRUKF2021002), and the Collaborative Grant-in-Aid of the HBUT National 111 Center for Cellular Regulation and Molecular Pharmaceuticals (Nos. XBTK-2021003 and XBTK-2020005).

- following subarachnoid hemorrhage possibly via anti-oxidative, anti-inflammatory and anti-apoptotic effects. *J Clin Neurosci.* (2017) 46:148–55. doi: 10.1016/j.jocn.2017.07.011
9. Plumb GW, De Pascual-Teresa S, Santos-Buelga C, Cheynier V, Williamson G. Antioxidant properties of catechins and proanthocyanidins: Effect of polymerisation, galloylation and glycosylation. *Free Radical Res.* (1998) 29:351–8. doi: 10.1080/10715769800300391
10. Bagchi D, Bagchi M, Stohs SJ, Das DK, Ray SD, Kuszynski CA, et al. Free radicals and grape seed proanthocyanidin extract: importance in human health and disease prevention. *Toxicology.* (2000) 148:187–97. doi: 10.1016/S0300-483X(00)00210-9
11. Bagchi D, Swaroop A, Preuss HG, Bagchi M. Free radical scavenging, antioxidant and cancer chemoprevention by grape seed proanthocyanidin: An overview. *Mutat Res Fundamental Mol Mech Mutagenesis.* (2014) 768:69–73. doi: 10.1016/j.mrfmmm.2014.04.004
12. Sherif AA, Abdelhalim SZ, Salim EI. Immunohistochemical and biochemical alterations following administration of proanthocyanidin extract in rats hepatocellular carcinoma. *Biomed Pharmacother.* (2017) 93:1310–9. doi: 10.1016/j.biopha.2017.07.039
13. Liang Y, Wang J, Gao HQ, Wang QZ, Zhang J, Qiu, et al. Beneficial effects of grape seed proanthocyanidin extract on arterial remodeling in spontaneously hypertensive rats via protecting against oxidative stress. *Mol Med Rep.* (2016) 14:3711–8. doi: 10.3892/mmr.2016.5699v
14. Yu SJ, Chen ZJ, Meng HC, Chen MS. Addition of lipophilic grape seed proanthocyanidin effectively reduces acrylamide formation. *J Sci Food Agri.* (2020) 100:1213–9. doi: 10.1002/jsfa.10132
15. Chang P, Mo B, Cauvi DM, Yu Y, Guo ZH, Zhou J, et al. Grape seed proanthocyanidin extract protects lymphocytes against histone-induced apoptosis. *PeerJ.* (2017) 5:e3108. doi: 10.7717/peerj.3108

16. Tu X, Wang MX, Liu YL, Zhao WY, Ren XX, Li YJ, et al. Pretreatment of grape seed proanthocyanidin extract exerts neuroprotective effect in murine model of neonatal hypoxic-ischemic brain injury by its antiapoptotic property. *Cell Mol Neurobiol.* (2019) 39:953–61. doi: 10.1007/s10571-019-00691-7
17. Cenobio-Galindo ADJ, Diaz-Monroy G, Medina-Perez G, Franco-Fernandez MJ, Ludena-Urquiza FE, Vieyra-Alberto R, et al. Multiple emulsions with extracts of cactus pear added in a yogurt: Antioxidant activity, in vitro simulated digestion and shelf life. *Foods.* (2019) 8:429. doi: 10.3390/foods8100429
18. Kwon HC, Bae H, Seo HG, Han SG. Short communication: Chia seed extract enhances physiochemical and antioxidant properties of yogurt. *J Dairy Sci.* (2019) 102:4870–6. doi: 10.3168/jds.2018-16129
19. Xu Y, Li HX, Liang J, Ma J, Yang J, Zhao XJ, et al. High-throughput quantification of eighteen heterocyclic aromatic amines in roasted and pan-fried meat on the basis of high performance liquid chromatography-quadrupole-orbitrap high resolution mass spectrometry. *Food Chem.* (2021) 361:130147. doi: 10.1016/j.foodchem.2021.130147
20. Wei JT, Xiao XJ, Li K, Song YY, Huang SK, Cai ZW, et al. Derivatization strategy for semi-quantitative analysis of medium- and long-chain fatty acids using multiple reaction monitoring. *Talanta.* (2021) 233:122464. doi: 10.1016/j.talanta.2021.122464
21. Olszewska MA, Nowak S, Michel P, Banaszcak P, Kicel A. Assessment of the content of phenolics and antioxidant action of inflorescences and leaves of selected species from the genus *Sorbus* sensu stricto. *Molecules.* (2010) 15:8769–83. doi: 10.3390/molecules15128769
22. Xia YL, Chen C, Liu Y, Ge GB, Dou TY, Wang P. Synthesis and structure-activity relationship of daphnetin derivatives as potent antioxidant agents. *Molecules.* (2018) 23:2476. doi: 10.3390/molecules23102476
23. Stejskal EO, Tanner JE. Spin diffusion measurements: Spin echoes in the presence of a time-dependent field gradient. *J Chem Phys.* (1965) 42:288–92. doi: 10.1063/1.1695690
24. Sandoval-Castilla O, Lobato-Calleros C, Aguirre-Mandujano E, Vernon-Carter EJ. Microstructure and texture of yogurt as influenced by fat replacers. *Int Dairy J.* (2004) 14:151–9. doi: 10.1016/S0958-6946(03)00166-3
25. Sun CX, Wang R, Wang TY, Li Q. Primary evaluation of nine volatile N-nitrosamines in raw red meat from Tianjin, China, by HS-SPME-GC-MS. *Food Chem.* (2020) 310:125945. doi: 10.1016/j.foodchem.2019.125945
26. Benedetti S, Buratti S, Spinardi A, Mannino S, Mignani I. Electronic nose as a non-destructive tool to characterise peach cultivars and to monitor their ripening stage during shelf-life. *Postharvest Biol Technol.* (2008) 47:181–8. doi: 10.1016/j.postharvbio.2007.06.012
27. Fernandez-Garcia E, McGregor JU. Determination of organic acids during the fermentation and cold storage of yogurt. *J Dairy Sci.* (1994) 77:2934–9. doi: 10.3168/jds.S0022-0302(94)77234-9
28. Xiao JS, Xie BJ, Cao YB, Wu H, Sun ZD, Xiao D. Characterization of oligomeric procyanidin and identification of quercetin glucuronide from lotus (*Nelumbo nucifera Gaertn.*) seedpod. *J Agri Food Chem.* (2012) 60:2825–9. doi: 10.1021/jf205331e
29. Yamakoshi J, Tokutake S, Kikuchi M, Kubota Y, Konishi H, Mitsuoka T. Effect of proanthocyanidin-rich extract from grape seeds on human fecal flora and fecal odor. *Microbial Ecol Health Dis.* (2009) 13:25–31. doi: 10.1080/089106001750071672
30. Alvarez-Martinez FJ, Barrajón-Catalán E, Encinar JA, Rodríguez-Díaz JC, Micol V. Antimicrobial capacity of plant polyphenols against gram-positive bacteria: A comprehensive review. *Curr Med Chem.* (2020) 27:2576–606. doi: 10.2174/0929867325666181008115650
31. Solval KM, Chouljenko A, Chotiko A, Sathivel S. Growth kinetics and lactic acid production of *Lactobacillus plantarum* NRRL B-4496, *L. acidophilus* NRRL B-4495, and *L. reuteri* B-14171 in media containing egg white hydrolysates. *LWT-Food Sci Technol.* (2019) 105:393–9. doi: 10.1016/j.lwt.2019.01.058
32. Navarro M, Morales FJ. Effect of hydroxytyrosol and olive leaf extract on 1,2-dicarbonyl compounds, hydroxymethylfurfural and advanced glycation endproducts in a biscuit model. *Food Chem.* (2017) 217:602–9. doi: 10.1016/j.foodchem.2016.09.039
33. Chai WM, Wei QM, Deng WL, Zheng YL, Chen XY, Huang Q, et al. Anti-melanogenesis properties of condensed tannins from *Vigna angularis* seeds with potent antioxidant and DNA damage protection activities. *Food Function.* (2019) 10:99–111. doi: 10.1039/C8FO01979G
34. Chen YS, Zhang RJ, Xie BJ, Sun ZD, McClements DJ. Lotus seedpod proanthocyanidin-whey protein complexes: Impact on physical and chemical stability of β -carotene-nanoemulsions. *Food Res Int.* (2020) 127:108738. doi: 10.1016/j.foodres.2019.108738
35. Wu Q, Zhao KQ, Chen YY, Xiao JS, Zhou MZ, Li DS, et al. Ethanol as an accelerator for the formation of advanced glycation end products in glucose-lysine solution. *LWT-Food Sci Technol.* (2020) 124:109135. doi: 10.1016/j.lwt.2020.109135
36. Srey C, Hull GLJ, Connolly L, Elliott CT, del Castillo MD, Ames JM. Effect of inhibitor compounds on N^ε-(carboxymethyl)lysine (CML) and N^ε-(carboxyethyl)lysine (CEL) formation in model foods. *J Agri Food Chem.* (2010) 58:12036–41. doi: 10.1021/jf103353e
37. Peng XF, Ma JY, Cheng KW, Jiang Y, Chen F, Wang MF. The effects of grape seed extract fortification on the antioxidant activity and quality attributes of bread. *Food Chem.* (2010) 119:49–53. doi: 10.1016/j.foodchem.2009.05.083
38. Peng XF, Ma JY, Chen F, Wang MF. Naturally occurring inhibitors against the formation of advanced glycation end-products. *Food Function.* (2011) 2:289–301. doi: 10.1039/c1fo10034c
39. Urbanśka B, Kowalska H, Szulc K, Ziarno M, Pochitskaya I, Kowalska J. Comparison of the effects of conching parameters on the contents of three dominant flavan-3-ols, rheological properties and sensory quality in chocolate milk mass based on liquor from unroasted cocoa beans. *Molecules.* (2021) 26:2502. doi: 10.3390/molecules26092502
40. Mercan E, Sert D, Karakavuk E, Akin N. Effect of different levels of grape seed (*Vitis vinifera*) oil addition on physicochemical, microbiological and sensory properties of set-type yoghurt. *Int J Technol.* (2018) 71:34–43. doi: 10.1111/1471-0307.12415
41. Zhu WH, Luan HW, Bu Y, Li XP, Li JR, Ji GR. Flavor characteristics of shrimp sauces with different fermentation and storage time. *LWT-Food Sci Technol.* (2019) 110:142–51. doi: 10.1016/j.lwt.2019.04.091
42. Canbulat Z, Ozcan T. Effects of short-chain and long-chain inulin on the quality of probiotic yogurt containing *Lactobacillus rhamnosus*. *J Food Process Preserv.* (2015) 39:1251–60. doi: 10.1111/jfpp.12343
43. Trigueros L, Sayas-Barbera E, Perez-Alvarez JA, Sendra E. Use of date (*Phoenix dactylifera* L.) blanching water for reconstituting milk powder: Yogurt manufacture. *Food Bioprocess Process.* (2012) 90:506–14. doi: 10.1016/j.fbp.2011.10.001

Conflict of Interest: The authors declare that the research was conducted in the absence of any commercial or financial relationships that could be construed as a potential conflict of interest.

Publisher's Note: All claims expressed in this article are solely those of the authors and do not necessarily represent those of their affiliated organizations, or those of the publisher, the editors and the reviewers. Any product that may be evaluated in this article, or claim that may be made by its manufacturer, is not guaranteed or endorsed by the publisher.

Copyright © 2021 Feng, Shen, Hu, Tan, Huang, Wang, Guo, Wu and Xiao. This is an open-access article distributed under the terms of the Creative Commons Attribution License (CC BY). The use, distribution or reproduction in other forums is permitted, provided the original author(s) and the copyright owner(s) are credited and that the original publication in this journal is cited, in accordance with accepted academic practice. No use, distribution or reproduction is permitted which does not comply with these terms.



Proteomic Analysis of the Protective Effect of Eriodictyol on Benzo(a)pyrene-Induced Caco-2 Cytotoxicity

Chong Wang^{1,2}, Fan Zhao², Yun Bai¹, Chunbao Li¹, Xinglian Xu¹, Karsten Kristiansen^{2,3,4*} and Guanghong Zhou^{1*}

¹ College of Food Science and Technology, Nanjing Agricultural University, Key Laboratory of Meat Products Processing, Ministry of Agriculture, Jiangsu Collaborative Innovation Center of Meat Production and Processing, Quality and Safety Control, Nanjing, China, ² Laboratory of Genomics and Molecular Biomedicine, Department of Biology, University of Copenhagen, Copenhagen, Denmark, ³ BGI-Shenzhen, Shenzhen, China, ⁴ Institute of Metagenomics, Qingdao-Europe Advanced Institute for Life Sciences, BGI-Qingdao, Qingdao, China

OPEN ACCESS

Edited by:

Hao Dong,
Zhongkai University of Agriculture and
Engineering, China

Reviewed by:

Yongning Wu,
China National Center for Food Safety
Risk Assessment, China
Kezhou Cai,
Hefei University of Technology, China
Guoliang Li,
Shaanxi University of Science and
Technology, China

*Correspondence:

Guanghong Zhou
guanghong.zhou@hotmail.com
Karsten Kristiansen
kk@bio.ku.dk

Specialty section:

This article was submitted to
Food Chemistry,
a section of the journal
Frontiers in Nutrition

Received: 19 December 2021

Accepted: 08 February 2022

Published: 03 March 2022

Citation:

Wang C, Zhao F, Bai Y, Li C, Xu X,
Kristiansen K and Zhou G (2022)
Proteomic Analysis of the Protective
Effect of Eriodictyol on
Benzo(a)pyrene-Induced Caco-2
Cytotoxicity. *Front. Nutr.* 9:839364.
doi: 10.3389/fnut.2022.839364

We evaluated the possible protective effects of six polyphenols on benzo(a)pyrene (BaP)-induced cytotoxicity in Caco-2 cells. We show that treatment with quinic acid, ferulic acid, homovanillic acid, trolox and BaP decreased cell viability, whereas naringenin and eriodictyol affected viability in a bi-phasic manner with low concentrations decreasing viability whereas higher concentrations increase viability. Co-treatment with 20 μ M eriodictyol or naringenin reduced BaP-induced cytotoxicity, including cell apoptosis, cell cycle progression, and oxidative stress. Our results show that the protective effect of eriodictyol was superior to that of naringenin. The potential protective mechanisms of eriodictyol on BaP-induced toxicity were investigated by proteomics. We identified 80 differentially expressed proteins (DEPs) with proteins associated with genetic information processing pathway representing the highest proportion and number of proteins responding to eriodictyol treatment, including key proteins such as RPA2, SNRPA, RAD23B, NUP155 and AARS. Our results provide new knowledge on how polyphenols may prevent BaP-induced carcinogenesis.

Keywords: benzo(a)pyrene, eriodictyol, Caco-2 cells, cytotoxicity, proteomics

INTRODUCTION

Benzo(a)pyrene (BaP), a well-known genotoxic polycyclic aromatic hydrocarbon (PAH), is a ubiquitous environmental chemical carcinogen, mainly present in cigarette smoke, incompletely combusted crude oils, coal tars, and certain types of processed foods. Humans are exposed to BaP by inhalation and intake, particularly *via* food which contributes with 97% of the intake. Long-term exposure to BaP can elicit genotoxic, neurotoxic, mutagenic and carcinogenic responses in various organs and tissues (1). As part of its carcinogenic mechanism, BaP is activated by phase I and II metabolizing enzymes generating 7, 8-diol-9, 10-epoxide (BPDE), which may interfere with cellular processes by covalently binding to DNA, eventually linked to carcinogenesis (2). In addition, BaP is associated with formation of reactive oxygen species (ROS) that may induce the generation of the highly reactive genotoxic BaP-quinone component, 8-hydroxy-2-deoxyguanosine, 8-oxo-dG (3).

BaP is generated during the preparation of food such as grilling, frying, and roasting. These processes significantly increase the content and accumulation of BaP in the food. The use of herb and dietary supplements such as polyphenols to protect against the detrimental effects of BaP has gained support worldwide. Many studies have shown that polyphenols hold promises for reducing DNA damage, oxidative stress, and carcinogenesis induced by BaP *in vitro* and *in vivo* (4, 5). In *in vitro* studies, primary cultured neurons (6), HepG2 cells (7) and Bhas 42 cells (8) have been used to investigate how polyphenols may counteract the detrimental effects of BaP exposure. In addition, several animal studies have reported that oral administration of polyphenols such as quercetin (9), curcumin (10), and galangin (11) elicited protection against BaP-induced damage of the lung and other organs.

Reducing the production of BaP is another important way to prevent exposure. Zhao et al. (12) reported on a 71.75 and 74.80% reduction in PAHs and oxygenated PAHs (OPAHs), respectively, when tert-butylhydroquinone (TBHQ) was added to the frying oil. This reduction in the formation of PAHs and OPAHs can be attributed to the antioxidant properties of TBHQ (12). Analysis of the effect of synthetic [e.g., butylated hydroxyanisole (BHA) and 3,5-di-tert-4-butylhydroxytoluene (BHT)] and natural (e.g., epigallocatechin gallate (EGCG), α -tocopherol, and sesamol) antioxidants on PAH generation in heated meat model systems revealed that total PAHs decreased upon addition of antioxidants (13). Our previous studies have shown that polyphenols such as eriodictyol, naringenin, quinic acid, ferulic acid, homovanillic acid, and trolox in tea and beer effectively can inhibit the production of BaP in chicken wings during grilling (14, 15). However, whether these polyphenols can also reduce the toxicity of BaP at the cellular level, and the mechanisms behind such a possible action have not yet been studied.

High-throughput, proteomics has become a powerful approach for understanding the mechanisms of toxicity and for the development of specific biomarkers for BaP exposure. Proteome profiles comparing BaP-transformed and normal 16HBE cells have revealed that FOXA1 is a key protein in BaP-induced lung cancer *via* its ability to increase colony formation and migration *in vitro*, and promote tumor growth and metastasis *in vivo* (16). Proteomics studies have identified a substantial number of candidate proteins associated with BaP toxicity. However, few of these proteins have been investigated in order to decipher their biological functions in BaP-induced colonic cancer. Therefore, studies to identify key proteins understanding their biological role in BaP-induced carcinogenesis, and determine how polyphenols may prevent or alleviate the detrimental effects of BaP are still warranted.

The intestine plays a critical role in the primary defense against carcinogens and toxic compounds, and the human colon carcinoma cell line Caco-2 has been widely used in studies of the actions of xenobiotics (17). In this study, we evaluated whether polyphenols (eriodictyol, naringenin, quinic acid, ferulic acid, homovanillic acid and trolox) are critical for reducing BaP-induced cell damage. We used proteomics to investigate possible mechanisms by which eriodictyol might alleviate BaP toxicity in Caco-2 cells.

MATERIALS AND METHODS

Benzo(a)pyrene (BaP, $\geq 96\%$ HPLC), eriodictyol ($\geq 95\%$ HPLC), naringenin ($\geq 95\%$ HPLC), quinic acid ($\geq 98\%$ HPLC), ferulic acid ($\geq 99\%$ HPLC), homovanillic acid ($\geq 95\%$ HPLC), trolox ($\geq 98\%$ HPLC), dimethyl sulfoxide (DMSO), glacial acetic acid, thiobarbituric acid (TBA), Tris-HCl, dithiothreitol (DTT), iodoacetamide, ammonium bicarbonate, formic acid, acetonitrile, urea were obtained from Sigma-Aldrich Chemical (St. Louis, MO, USA). Protease inhibitor cocktail, phosphatase inhibitor cocktail, BCA protein assay kit, RIPA lysis and extraction buffer, Dulbecco modified Eagle medium (DMEM), fetal bovine serum (FBS), penicillin-streptomycin, trypsin, phosphate-buffered saline (PBS), cell apoptosis kit, cell cycle assay kit were obtained from Thermo Fisher Scientific (Waltham, MA, USA). Sequencing-grade trypsin was obtained from Promega (Madison, WA, USA). Superoxide dismutase (SOD) assay kit and malondialdehyde (MDA) assay kit were obtained from JianCheng Bioengineering Institute (Nanjing, China). Antibodies (RPA2, SNRPA, RAD23B, NUP155 and AARS) and HRP-conjugated anti-rabbit immunoglobulin G (IgG), were purchased from Sigma-Aldrich Chemical (St. Louis, MO, USA).

Cell Culture and Treatments

The human colon carcinoma cell line Caco-2 was obtained from Jiangsu KeyGen BioTech (Nanjing, China). Caco-2 cells were grown in DMEM containing 10% FBS and 1% penicillin-streptomycin. The incubator was kept at 37°C with 5% CO₂ and the medium was replaced every 2 days until confluence reached 80%.

The trial was set up including the following three parts. In the first part, cells were treated with BaP (1, 2, 5, 10, 20, 50 and 100 μ M) for different times (3, 6, 12, 24 and 48 h) and 6 types of polyphenols (1, 2, 5, 10 and 20 μ M) for 24 h to evaluate the cytotoxicity of BaP and polyphenols. In the second part, cells were Pre-treated or co-treated with eriodictyol (5, 10 and 20 μ M), naringenin (20 μ M) and BaP (50 μ M) for 24 h to assess the protective effects of the polyphenols on BaP-induced cytotoxicity. In the third part, cells were co-treated with eriodictyol (20 μ M) and BaP (50 μ M) to elucidate the possible mechanism by which eriodictyol may counteract the detrimental effects of BaP using proteomics. The doses of BaP used to treat the cells were selected according to previous *in vitro* studies and do not reflect the amounts attainable by oral intake.

Cell Viability Assay

Cell viability was measured as previously described with slight modifications (18). MTT was dissolved in dilution buffer at a final concentration of 5 mg/mL. After experimental treatments, MTT solution (10 μ L) was added to each well. After incubation at 37°C for 4 h, the formed formazan crystals were dissolved in 1 mL of DMSO and the absorbance was measured at 570 nm. The results were calculated as following:

$$\text{Cell viability (\%)} = \frac{\text{average OD of treatment}}{\text{average OD of control}} \times 100\%$$

Cell Apoptosis and Cycle Assay by Flow Cytometry

Cell apoptosis was assessed using annexin as the marker according to the manufacturer's recommendations. Briefly, the cells were washed with PBS and harvested with trypsin. After centrifugation at 800 rpm for 5 min, cells were resuspended in 0.5 mL binding buffer. 5 μ L Annexin-V EGFP and 5 μ L propidium iodide (PI) were added. The tubes were incubated for 20 min in the dark at room temperature. Cells were measured by flow cytometry within 1 h. For cell cycle analysis, cells were collected and fixed in 70% ethanol overnight at 4°C. Cells were washed with PBS three times, and 25 μ L PI and 10 μ L RNase A (50 μ g/mL) were added. The tubes were incubated at 37°C for 30 min. The excitation and emission wavelengths were 488 nm and 530 nm, respectively. The Annexin-V EGFP and PI channel was set as FL1-A and FL2-A, respectively.

ROS, SOD Activity and MDA Content

Intracellular ROS was measured using the DCFH-DA method (19). After treatments, cells were washed with PBS and then treated with DCFH-DA (10 μ M) for 30 min. Subsequently, cells were collected and washed with PBS two times. ROS-dependent fluorescence was detected using a Leica DMI 6000B (Wetzlar, Germany), and then the cells were transferred into a black 96-well plate to detect fluorescence intensity using a Multimode Reader (TECAN, Switzerland). The excitation and emission wavelengths were 485 and 535 nm, respectively. SOD activity and MDA content were assessed according to the manufacturer's protocol. In addition, the protein content was measured using the BCA protein assay kit. The enzyme activity and MDA content were expressed as units per mg of protein (U/mg protein) and μ M per mg of protein (μ M/mg protein).

Protein Digestion

Protein samples (200 μ g) were digested using the filter-aided sample preparation (FASP) method (20). In brief, protein was reduced with 10 mM DTT for 1 h at 60°C, alkylated in the presence of 55 mM of iodoacetamide for 45 min at 25°C in the dark. Subsequently, the buffer was exchanged with 100 mM ammonium bicarbonate (pH 8.5) using a 10 kDa molecular weight cut-off ultrafiltration tube (Millipore, Billerica, MA, USA). After that, 4 μ g of trypsin were added to each sample for protein digestion overnight at 37°C (trypsin: protein, 1: 50 w/w). The digested peptides were desalted using Sep-Pak C18 cartridges (Waters, Milford, USA) and quantified using a NanoDrop spectrophotometer at 280 nm.

Proteomics Analysis by LC-MS

A Nano-LC tandem with a linear trap quadrupole mass spectrometer (Thermo Fisher Scientific, USA) was applied to analyze the protein profiles. The resulting peptides (1.5 μ g) were acidified with 0.1% formic acid and subsequently loaded onto the C18 column (75 μ m \times 15 cm, 3 μ m, 100 Å; Thermo-Fisher Scientific). Chromatographic separation was carried out with a linear gradient of 3–55% buffer B (80% acetonitrile and 0.1% FA) at a flow rate of 0.25 μ L/min over 112 min. Due to loading and washing steps, the total time for an LC-MS/MS

run was \sim 160 min. Electrospray ionization (ESI) was applied in the positive mode with the following parameters: MS data were acquired using a data-dependent top 10 method dynamically exclusion to screen the most abundant precursor ions from the survey scan (300–1800 m/z) for HCD fragmentation. Dynamic exclusion duration was 25 s. Survey scans were acquired at a resolution of 70,000 at m/z 200 and the resolution for HCD spectra was set to 17,500 at m/z 200.

A label-free method was applied for protein quantification. The MS data were analyzed using the MaxQuant software (version 1.3.0.5) and searched against the corresponding UniProt *Homo sapiens* database. The precursor mass and MS/MS tolerance of peptides were set to 6 and 20 ppm, respectively. The maximum number of missed cleavages was two. The carbamidomethylation of cysteine was set as a fixed modification, with protein N-terminal oxidation of methionine as a variable modification. The false discovery rate (FDR) was set to 1%. Protein abundance was calculated on the basis of the normalized spectral protein intensity (LFQ intensity). Differentially expressed proteins (DEPs) were characterized as proteins with a fold change in intensity > 1.5 or < 0.67 and $p < 0.05$. The Kyoto Encyclopedia of Genes and Genomes (KEGG) and protein-protein interaction analysis were performed using Omicsbean (<http://www.omicsbean.cn>). The strengths of the PPI network relationships were visualized by assigning line weights to the compiled scores. PPI analysis was done with minimum required interaction score set to medium confidence 0.400.

Western Blotting

The protein sample was mixed with loading buffer and heated at 95°C for 5 min. 20 μ g samples and standard protein (Bio-Rad, Hercules, CA, USA) were loaded on a gradient polyacrylamide gel (4–10%, Genscript, Piscataway, USA). The gel was run at 110 V for 120 min (4°C) and then the proteins were transferred onto a polyvinylidene difluoride membrane. After transfer at 120 V for 90 min, the membrane was blocked in 5% bovine serum albumin for 60 min at room temperature. Subsequently, the membrane was incubated with the primary antibodies overnight at 4°C and then incubated with anti-rabbit IgG for 60 min. The detection was preformed using a chemiluminescence system (Thermo Fisher Scientific, Rockford, IL, USA), and the bands were analyzed using the Quantity One system (Version 4.6.2).

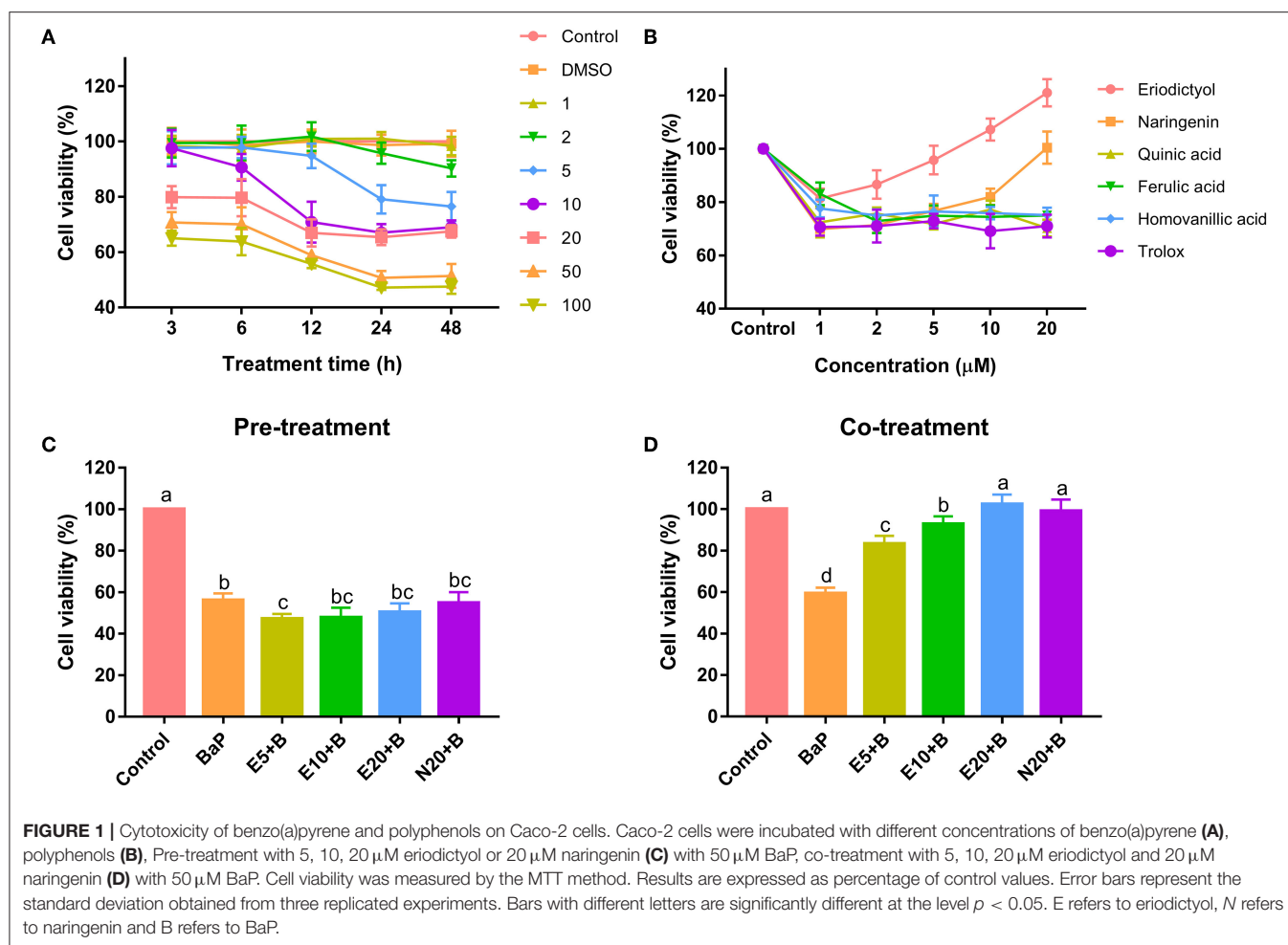
Statistical Analysis

All results were calculated as the means with standard deviations. The results were statistically analyzed by ANOVA ($p < 0.05$). Comparison of mean values was performed using Duncan's test. Statistical analyses were performed with SPSS for Windows version 20 (SPSS Inc., Chicago, IL).

RESULTS AND DISCUSSION

Cytotoxicity of BaP and Polyphenols on Caco-2 Cells

Caco-2 cells were treated with different doses for different period of time with BaP and polyphenols to define the most suitable conditions for the exposure to BaP and polyphenols.

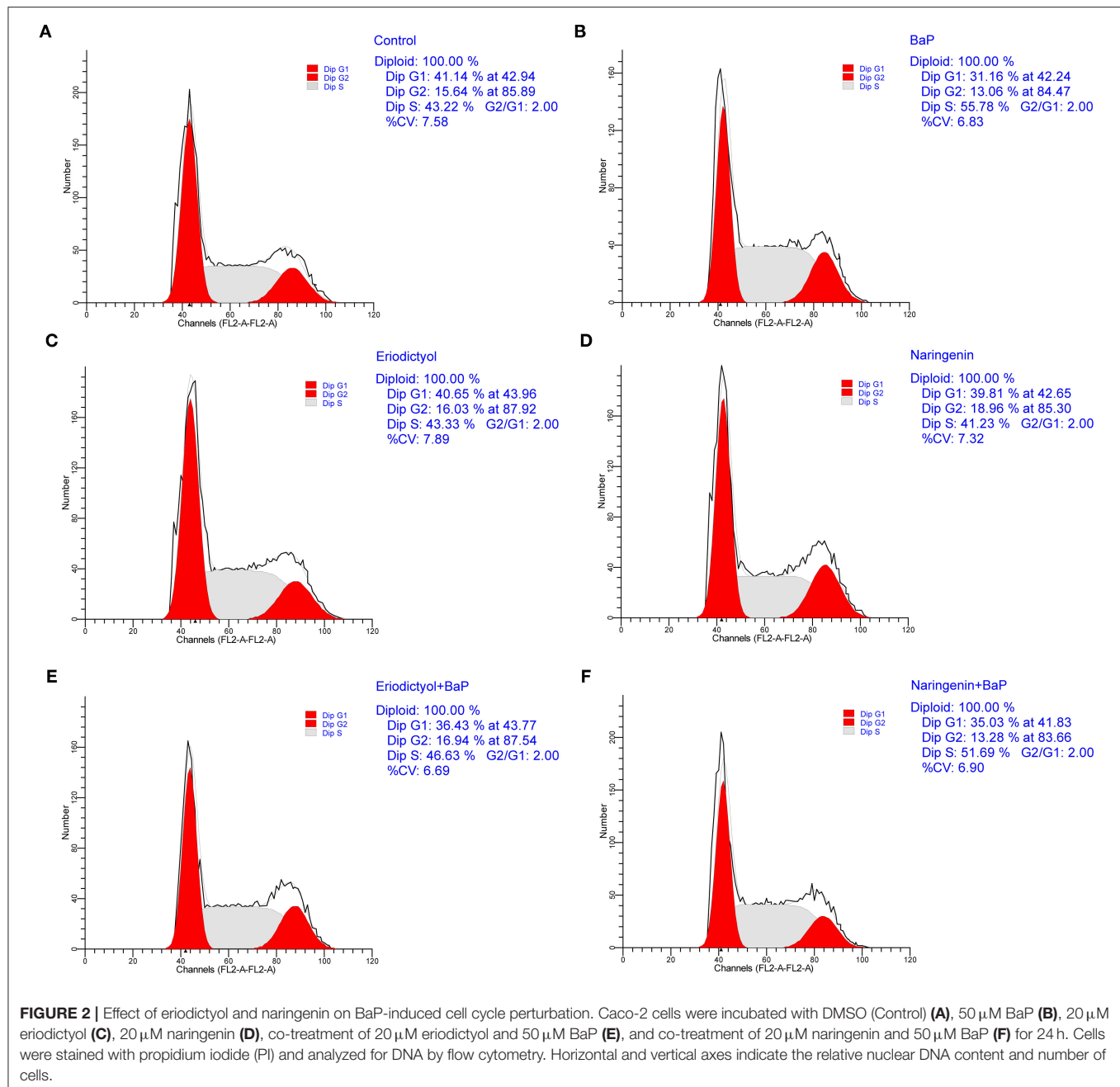


BaP significantly decreased cell viability in a dose- and time-dependent manner in concentrations ranging from 2 to 100 μM (Figure 1A). Treatments with 50 μM BaP for 24 and 48 h significantly decreased cell viability by 50.7 and 51.4%, respectively. At any treatment time, there was no significant difference in cell viability between the 50 and 100 μM treatment groups. As shown in previous studies, BaP significantly inhibited cell viability of HepG2 cells (7), HL-7702 cells (21) and HELF cells (22). The concentrations of BaP that caused a decrease in cell viability are within the range reported in other studies (21, 23).

The cells were treated with different concentrations of polyphenols to investigate possible effects on viability or cytotoxicity. A decrease in viability was observed when Caco-2 cells were treated with quinic acid, ferulic acid, homovanillic acid and trolox at any concentration for 24 h (Figure 1B). This result is in accordance with previous studies showing that cell viability is reduced in a concentration-dependent manner when cells were treated with quinic acid, ferulic acid, or homovanillic acid (24, 25). Interestingly, treatment with eriodictyol and naringenin resulted in a reduction in cell viability at low

concentrations, for naringenin from 1 to 10 μM, for eriodictyol at concentrations of 1 and 2 μM. However, treatment with eriodictyol at concentrations of 5, 10 and 20 μM for 24 h or treatment with naringenin at 20 μM revealed no toxicity, and for eriodictyol, treatment even appeared to increase the apparent cell viability at high concentrations (10 and 20 μM), suggesting increased cell proliferation. Based on the results, we used 50 μM BaP and Non-toxic concentration eriodictyol (5, 10 and 20 μM) and naringenin (20 μM) for the following exposure experiments with mixtures of the compounds.

To evaluate the protective effect of eriodictyol and naringenin on BaP-induced cytotoxicity, cells were co-treated with the polyphenols or pre-treated with the polyphenols prior to administration of BaP. Pre-treatment with eriodictyol and naringenin was unable to alleviate the toxicity of BaP in the cell viability assay (Figure 1C). However, co-treatment with 20 μM eriodictyol or naringenin completely restored viability (Figure 1D). It is known that BaP displays its toxicity after modification by P450 monooxygenase to generate a series of metabolites which react with DNA. Polyphenols can form adducts with BaP and its metabolites, which reduces the



bioavailability of BaP (26). In the co-treatment group, we speculate that both eriodictyol and naringenin formed complexes with BaP and its metabolites. However, in the pre-treatment group, most of the polyphenols may have been completely metabolized after treatment for 24 h abolishing their effect on BaP. A similar observation was reported for fresh cashew apple juice where co- and post-treatment showed a reduced mutagenic effect of BaP, while pre-treatment had no effect (27). Based on the cell viability data, 20 μ M of eriodictyol and naringenin were used for further experiments.

Effect of Eriodictyol and Naringenin on BaP-Induced Cell Cycle Perturbation and Cell Apoptosis

To ascertain whether BaP inhibited growth of Caco-2 cells *via* perturbation of the cell cycle, DNA contents were determined using flow cytometry (Figure 2; the statistical analyses are shown in Supplementary Figure 1). Compared to control cells, there were no significant differences in cell cycle parameters when cells were exposed to eriodictyol and naringenin alone. Treatment with BaP for 24 h significantly decreased the percentage of cells

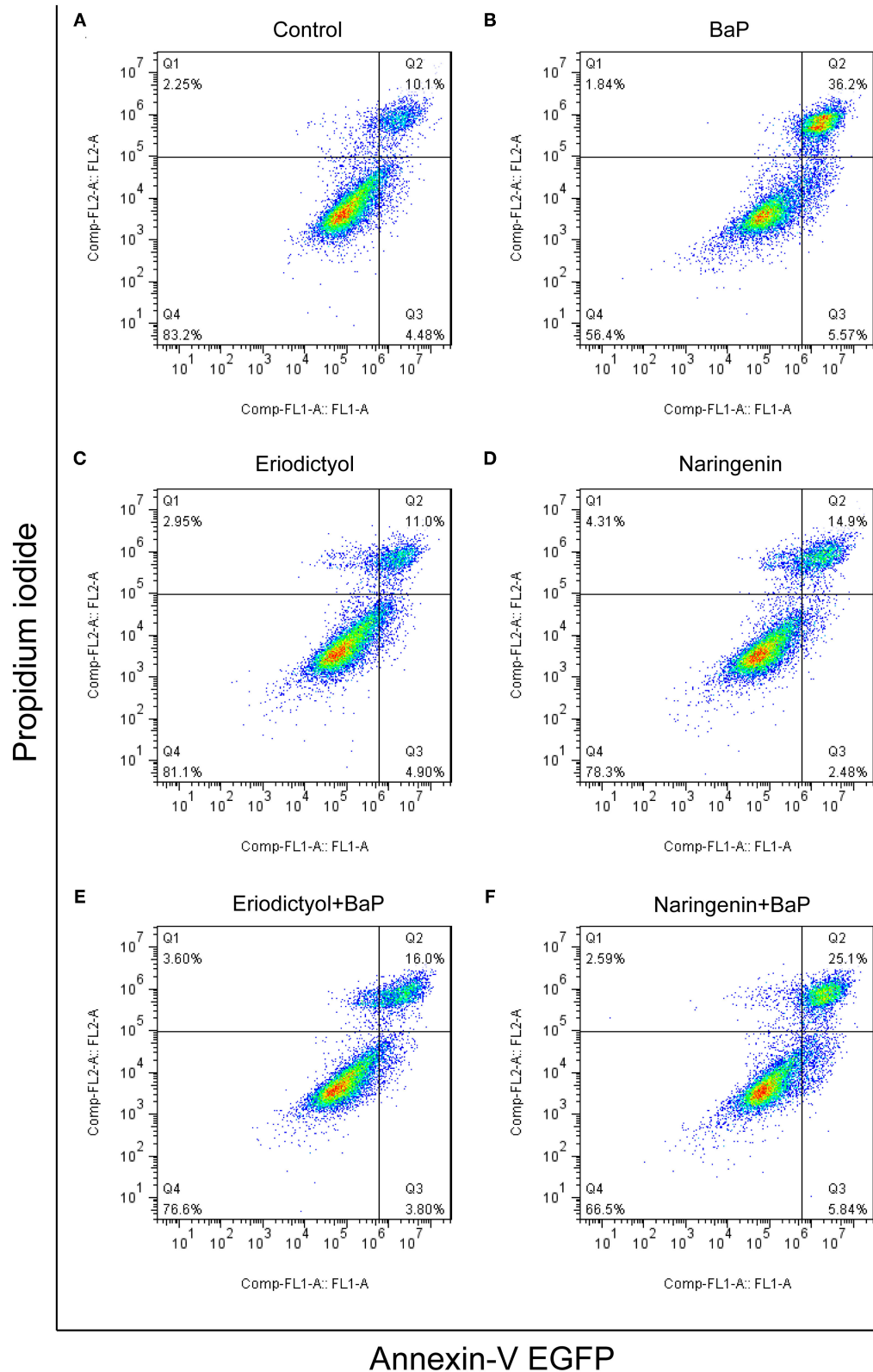


FIGURE 3 | Effect of eriodictyol and naringenin on BaP-induced cell apoptosis. Caco-2 cells were incubated with DMSO (Control) **(A)**, 50 μ M BaP **(B)**, 20 μ M eriodictyol **(C)**, 20 μ M naringenin **(D)**, co-treatment of 20 μ M eriodictyol and 50 μ M BaP **(E)**, and co-treatment of 20 μ M naringenin and 50 μ M BaP **(F)** for 24 h. Cell apoptosis was determined by the Annexin-V EGFP/PI assay and flow cytometry.

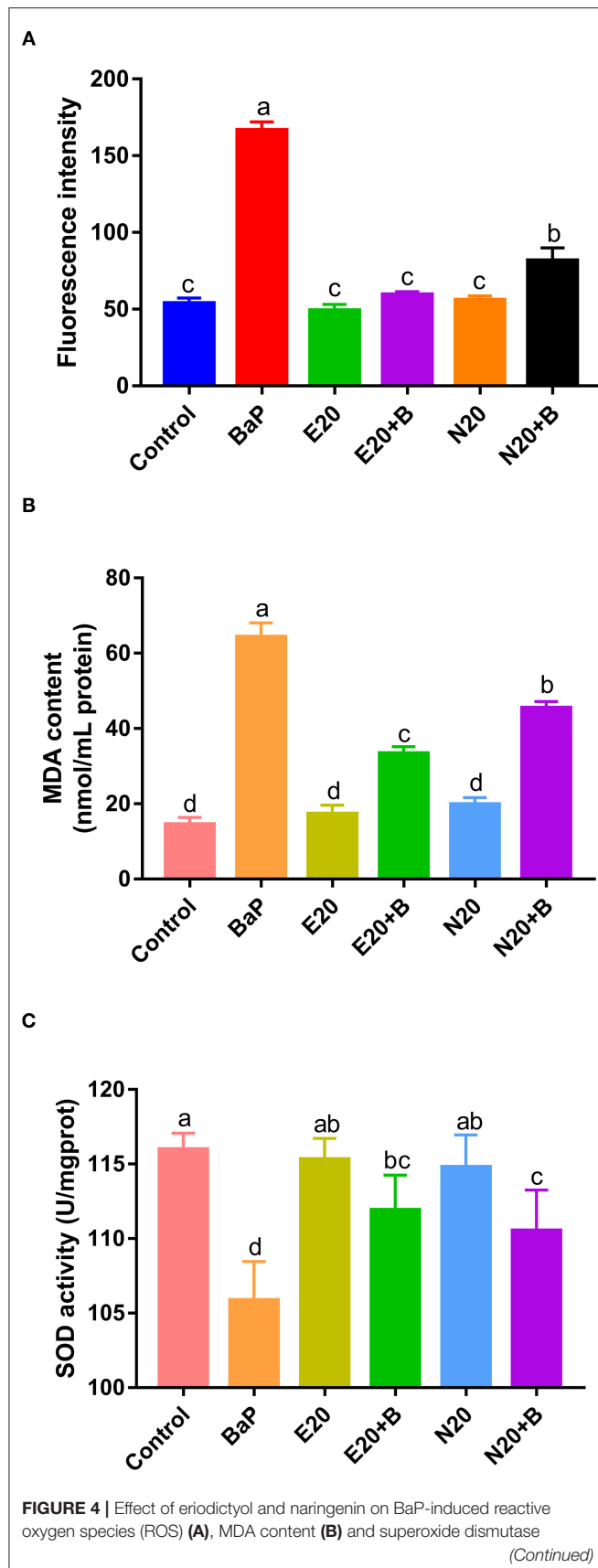


FIGURE 4 | (SOD) activity (C). Caco-2 cells were incubated with DMSO (Control), 50 μ M BaP, 20 μ M eriodictyol, 20 μ M naringenin, co-treatment of 20 μ M eriodictyol and 50 μ M BaP, and co-treatment of 20 μ M naringenin and 50 μ M BaP for 24 h. ROS was detected by fluorescence microscopy. Error bars represent the standard deviation obtained from three replicated experiments. Bars with different letters are significantly different at the level $p < 0.05$. E refers to eriodictyol, N refers to naringenin and B refers to BaP.

in the G1 phase (31.16%) when compared to the control group (41.14%). The percentage of cells in the G2 phase of cells treated with BaP did not differ from that of control cells. However, the percentage of cells in the G2 phase in cells treated with BaP was lower than that of cells treated with naringenin alone or BaP co-treated with eriodictyol, but overall the changes in the percentage of cells in the G2 phase were modest. Noteworthy, treatment with BaP significantly increased the percentage of cells in the S-phase from 43.22 to 55.78%, and this increase was counteracted by co-treatment with naringenin or eriodictyol. These results indicated that treatment with BaP impaired progression through the S-phase and this inhibition was prevented by the co-treatment with the polyphenols. These results are consistent with other studies. Thus, upon treatment of HT-29 cells with 25 μ M BaP, the number of cells in the S-phase increased, concomitantly with a decline in the number of cells in the G1 phase (28). When administrated together with BaP, eriodictyol and naringenin at least partly counteracted the changes of the cell cycle caused by BaP. Thus, the percentage of cells arrested in G1 and S-phase decreased from 46.63% in cell treated with BaP to 36.43% in cell co-treated with eriodictyol, whereas co-treatment with naringenin did not significantly reduce the number of cell in the S-phase. These results are consistent with the study by Liu et al. (29) showing that eriodictyol inhibited epidermal growth factor-induced cell S-phase accumulation and increased the percentage of G1-phase cells.

BaP has been shown to induce apoptosis in primary cultured neurons (6), HL-7702 human normal liver cells (21), and rat lung epithelial cells (30). Metabolism of BaP leads to the formation of BPDE, which can bind to DNA to form BPDE-DNA adducts that may lead to cell apoptosis (31). To assess to what extent BaP induced apoptosis of Caco-2 cells, Annexin-V EGFP and PI staining assay and flow cytometry were used. The results are displayed in Figure 3 (the statistical analyses are shown in Supplementary Figure 2). Based on the report by Wang et al. (32), the cell populations were divided into four regions: the necrotic cells in the Q1 region, cells in the later stage of apoptosis in the Q2 region, cells in the early stage of apoptosis in the Q3 region, and viable cells in the Q4 region. The percentage of cells in the later stage of apoptosis was significantly increased after BaP treatment (36.2%) compared to control cells (10.1%), while eriodictyol treatment alone did not significantly affect the percentage of cells in the stage of later apoptosis.

Of note, co-treatment with eriodictyol or naringenin significantly reduced the percentage of cells in the later stage of apoptosis cells (from 36.2 to 16.0% and 25.1% for eriodictyol

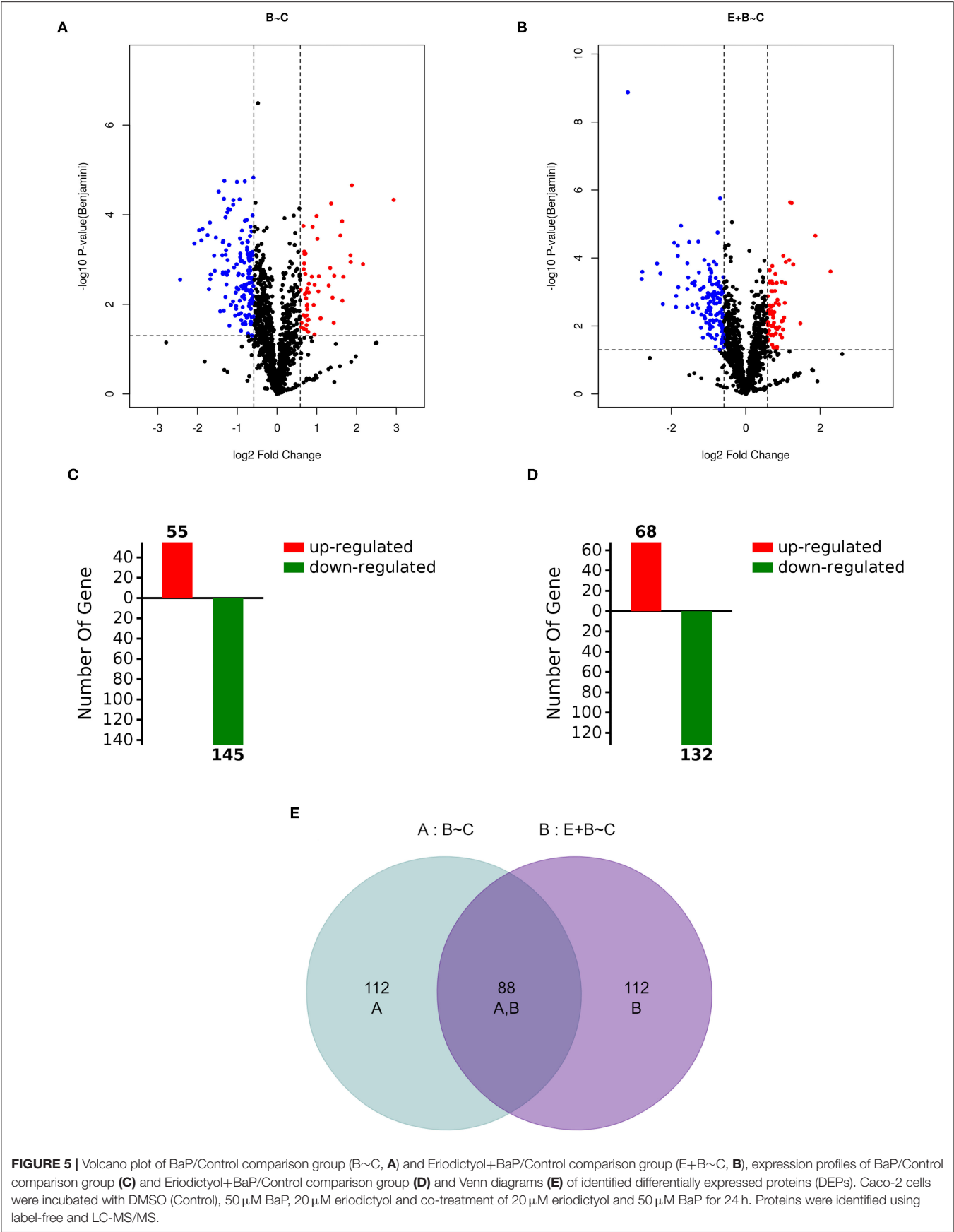


FIGURE 5 | Volcano plot of BaP/Control comparison group (B~C, **A**) and Eriodictyol+BAP/Control comparison group (E+B~C, **B**), expression profiles of BaP/Control comparison group (**C**) and Eriodictyol+BAP/Control comparison group (**D**) and Venn diagrams (**E**) of identified differentially expressed proteins (DEPs). Caco-2 cells were incubated with DMSO (Control), 50 μ M BaP, 20 μ M eriodictyol and co-treatment of 20 μ M eriodictyol and 50 μ M BaP for 24 h. Proteins were identified using label-free and LC-MS/MS.

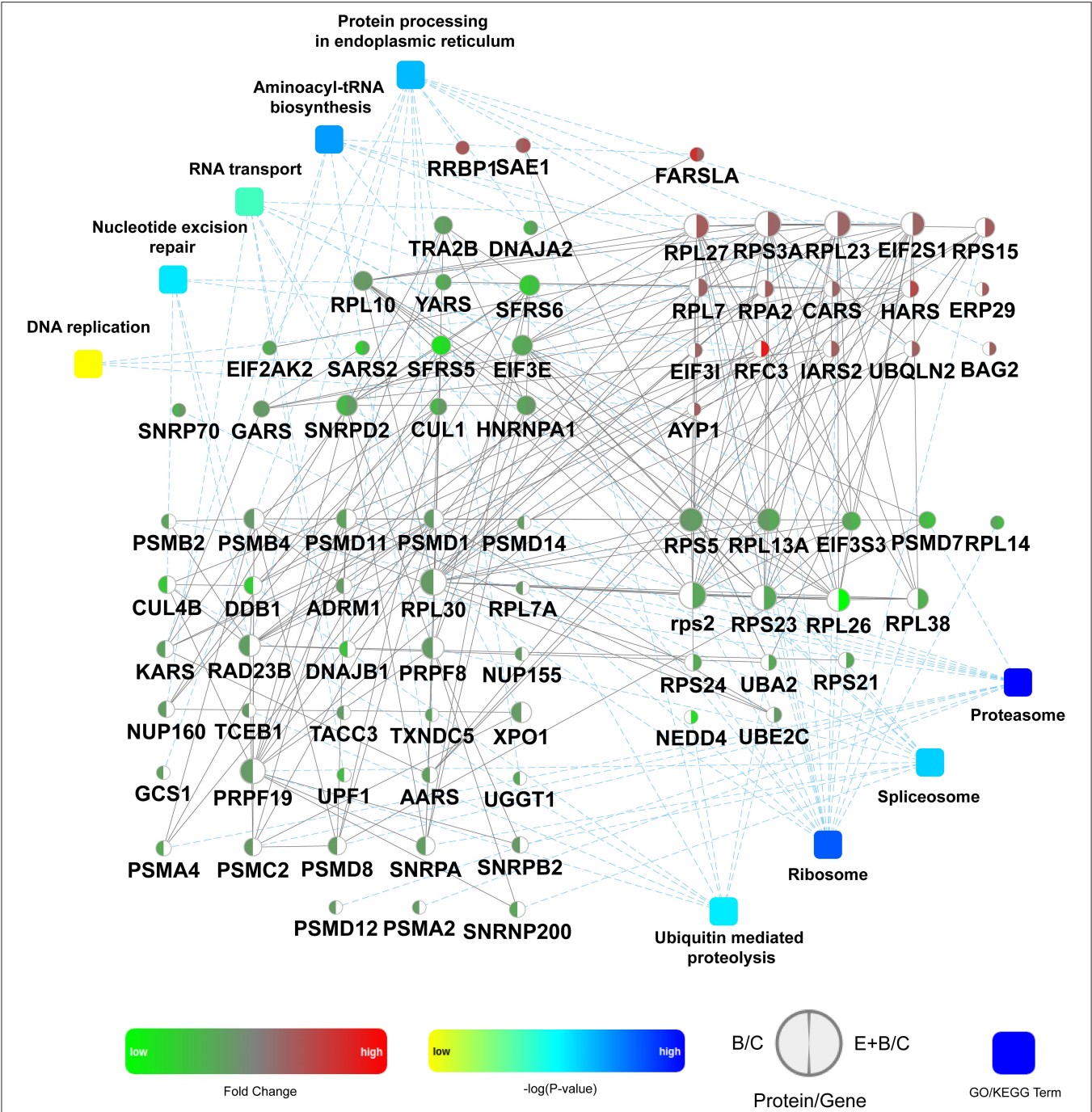


FIGURE 6 | Protein-protein interactions analysis of 80 differentially expressed proteins (DEPs) involved in genetic information processing. The network model was generated by Omicsbean. Circle nodes for genes/proteins, rectangle for KEGG pathway or biological process. Pathways were colored with gradient color from yellow to blue, yellow for smaller P -value, and blue for larger P -value. In case of fold change analysis, genes/proteins exhibiting significant changes in expression are colored in red (up-regulation) and green (down-regulation) and no significant expression genes/proteins are colored in white. A default confidence cutoff of 400 was used: interactions with bigger confident scores are show as solid lines between genes/proteins, otherwise as dashed lines.

and naringenin, respectively). These results were consistent with a previous report showing that eriodictyol was able to protect retinal ganglion cells from high glucose induced oxidative stress and cell apoptosis (33). Another study demonstrated that naringenin reduced apoptosis and oxidative stress in cortical neuron cells (34). The protective effect of eriodictyol seemed superior to that of naringenin. This may be associated with the structure-activity relationship of polyphenols. A previous study

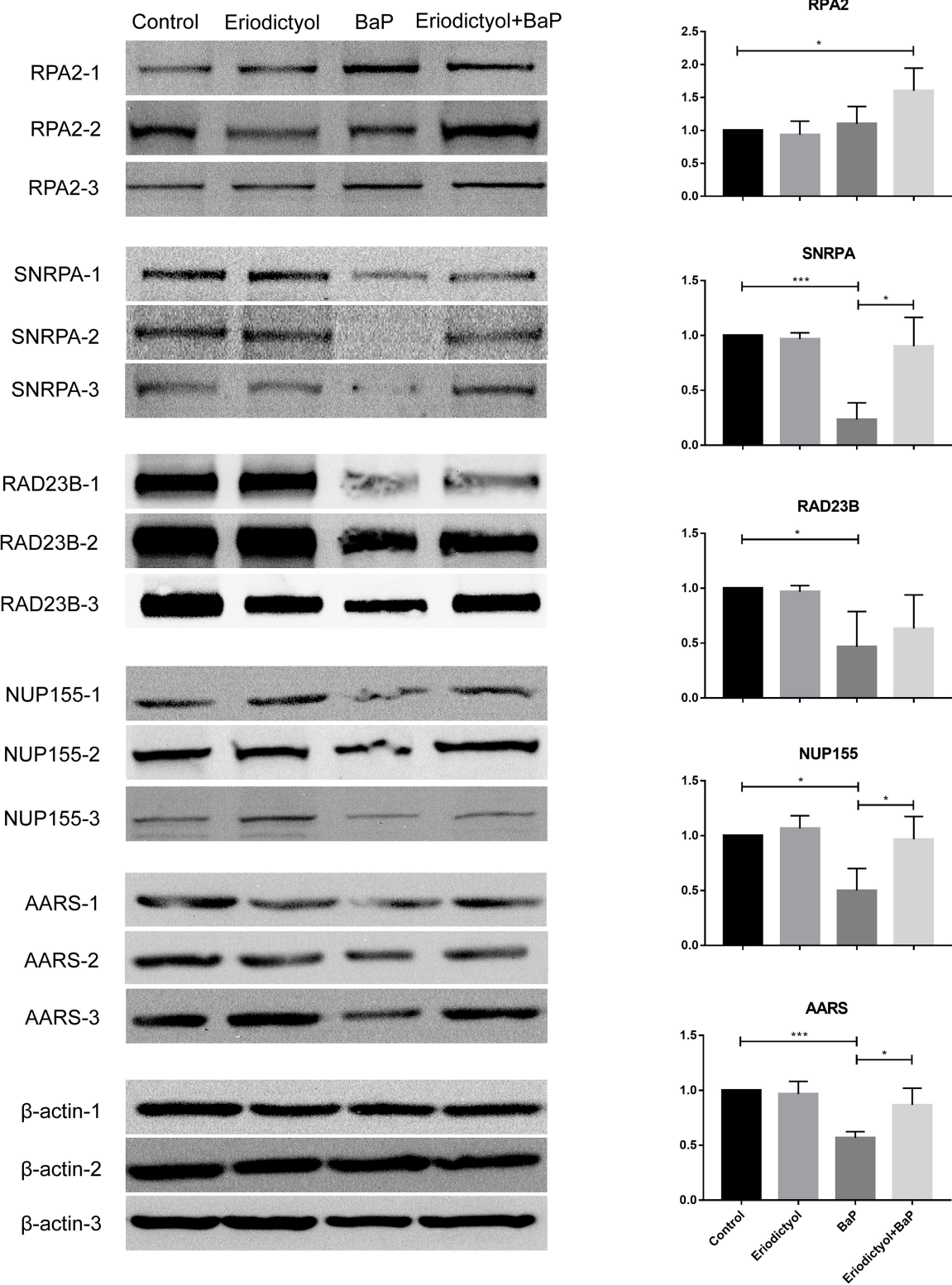
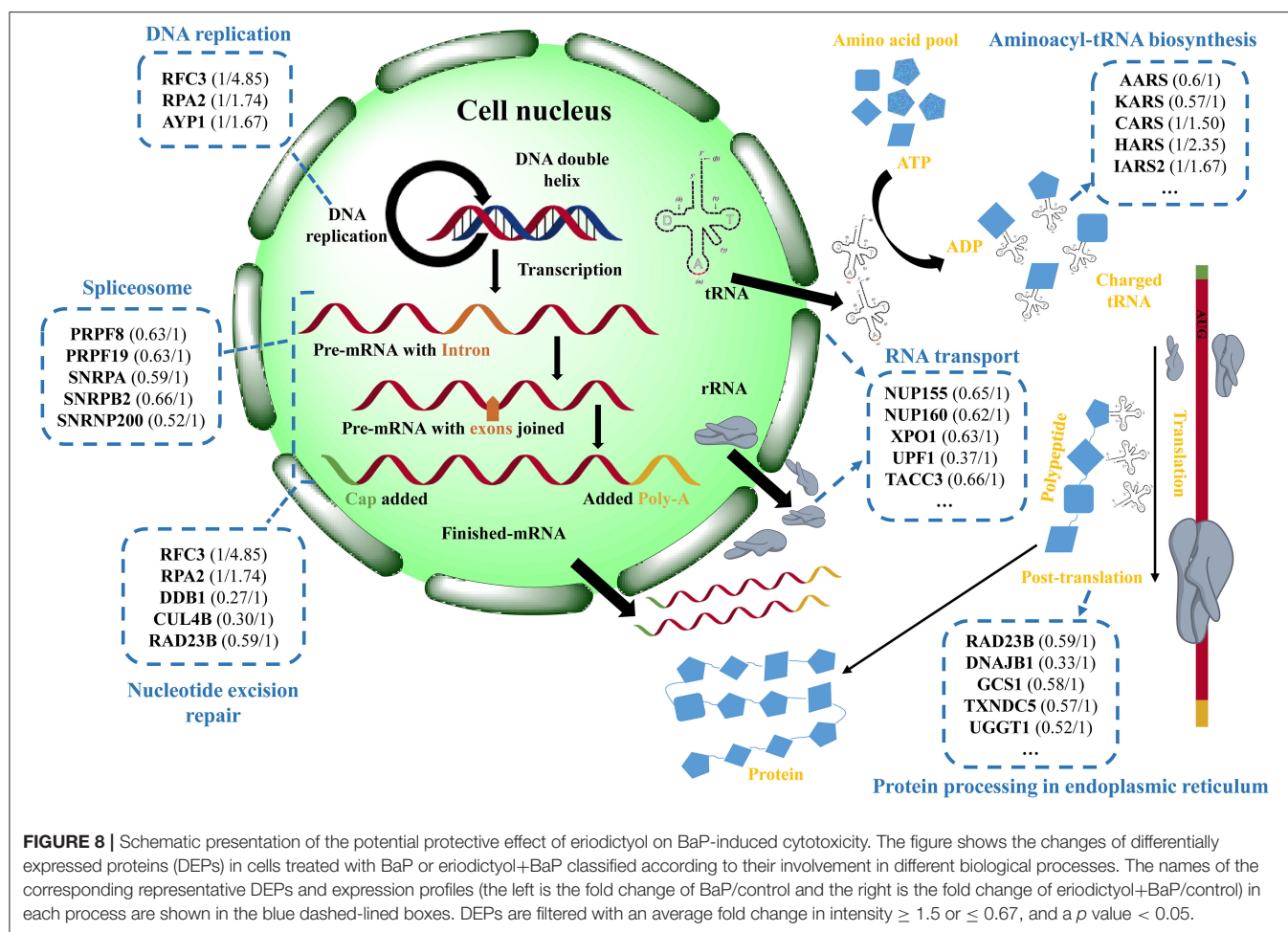


FIGURE 7 | Analysis of expression of selected proteins by western blotting. Caco-2 cells were treated with DMSO (control), 50 μ M BaP, 20 μ M eriodictyol and co-treatment of 20 μ M eriodictyol and 50 μ M BaP for 24 h. * p < 0.05, ** p < 0.01, and *** p < 0.001.



demonstrated that catechins and tannins are highly effective in inhibiting BPDE-DNA adduct formation due to direct interaction *via* adjacent hydroxyl groups in their structures and that the activity increases with an increasing number of functional hydroxyl groups (35). In the molecular structure of eriodictyol, there is one more functional hydroxyl group in the B ring than in naringenin.

Effect of Eriodictyol and Naringenin on BaP-Induced ROS, MDA and SOD Activity

BaP has previously been reported to induce oxidative stress *in vivo* and in cultured cells (6, 8). To assess BaP-induced oxidative stress in Caco-2 cells, the induction of oxidative stress markers including intracellular ROS, MDA and SOD was monitored. We used 2'-7'-dichlorofluorescein for estimating the level of ROS in Caco-2 cells exposed to BaP and co-treated or not with eriodictyol or naringenin (Figure 4A; Supplementary Figure 3). 2'-7'-dichlorofluorescein (DCF) derivatives are relatively nonselective probes that react with many oxidants such as peroxynitrite, hydroxyl radicals, lipid peroxides, nitric oxide, and hypochloride, but not directly with H_2O_2 (19, 36). DCF fluorescence is thus a measure of generalized oxidant production

rather than that of any particular reactive species. In our study, we aimed to detect BaP-induced generalized oxidation products. In addition, studies have reported that intracellular ROS of cells treated with BaP might be the cause of 8-OHdG formation (37). Here, the aim was to monitor possible signs of ROS production in cells in response to BaP exposure. Therefore, in keeping with a vast number of studies we chose to use the 2'-7'-dichlorofluorescein protocol in our study. Thus, we observed an increase in the number of fluorescent cells and fluorescence intensity upon treatment with BaP compared to the control group. Co-treatment with eriodictyol or naringenin significantly reduced the number of fluorescent cells and the fluorescence intensity (Figure 4A; Supplementary Figure 3). The cellular content of MDA was significantly increased when cells were treated with BaP (Figure 4B), whereas the SOD activity markedly decreased (Figure 4C). For both MDA and SOD, co-treatment with eriodictyol or naringenin partly restored the level toward that of the control cells. In BaP-treated Caco-2 cells, the cell viability was significantly reduced compared with control cells, possibly reflecting an imbalance between oxidation and antioxidant systems caused by the massive ROS accumulation and impaired ROS-scavenging capacity (22).

A previous study similarly demonstrated that eriodictyol and naringenin suppressed oxidative stress and apoptosis in cells (33), and that treatment with naringenin up-regulated SOD activity and reduced the levels of MDA and ROS (34). These results further supported the protective effects of eriodictyol and naringenin on alleviation of BaP-induced cell damage. Again we observed that the protective effect of eriodictyol was superior to that of naringenin. Therefore, in order to further investigate possible mechanisms, we used the simultaneous treatment of eriodictyol and BaP, coupled with proteomics analyses for follow-up studies.

Comparative Proteomic Analysis of the Effect of Eriodictyol on BaP-Induced Cytotoxicity

Mass spectrometry-based label-free quantitative techniques were applied to determine the proteomic profiles of Caco-2 cells treated with DMSO (control, C), BaP alone (B) and co-treated with eriodictyol and BaP (E+B). A total of 1571 proteins were identified in the treatment groups including 200 differentially expressed proteins (DEPs) with an average fold change in intensity [BaP/Control (B/C) or Eriodictyol+BaP/Control (E+B/C)] ≥ 1.5 or ≤ 0.67 , and a p value < 0.05 (Figure 5; Supplementary Table 1). Among these DEPs, 55 and 68 of the DEPs were up-regulated, and 145 and 132 of DEPs were down-regulated in the B/C and the E+B/C groups, respectively (Figures 5C,D). Of these, 88 DEPs were shared between the two groups (Figure 5E).

Subsequently, the identified DEPs were distributed into 4 categories based on KEGG annotation comprising metabolism, genetic information processing, cellular processes, and organismal systems (Supplementary Figure 4). Of note, 80 DEPs associated with genetic information processing were identified, representing the highest proportion and number of identified DEPs. The expression of these 80 DEPs in the B/C and the E+B/C treatment groups based on protein-protein interactions (PPI) was further analyzed (Figure 6). Some proteins are involved in more than one pathway. For instance, RFC3 participates in the processes of DNA replication and nucleotide excision repair (NER) explaining why there are 88 DEPs involved in genetic information processing in Supplementary Figure 4, while only 80 were displayed in the PPI network.

DNA replication was enriched into the genetic information processing category (Figure 6). A previous study reported that BaP metabolites bound to DNA may interfere with the vital cellular process of DNA replication, leading to an accumulation of mutations and eventually carcinogenesis (11). It has been reported that RPA may control DNA repair and damage checkpoint activation in this pathway (38). Our results showed that RPA2 was up-regulated in the E+B/C group, with no significant change in the B/C group, indicating that eriodictyol prevents BaP-induced cytotoxicity by activating the expression

of RPA2 to repair damaged DNA. Moreover, BaP-DNA adducts can be removed by NER (39). In this study, the expression of CUL4B, DDB1, RAD23B involved in NER was down-regulated after BaP treatment, which may result in a deficiency of these proteins. Of note, the expression of these three proteins was recovered in the E+B/C group. Furthermore, since the expression of RPA2 and RFC3 involved in NER was up-regulated after co-treatment, we speculate that they may play a central role in restoring the NER process. SNRPA is a component of the spliceosomal U1 small nuclear ribonucleoprotein (snRNP), which is essential for recognition of the pre-mRNA 5' splice-site and the subsequent assembly of the spliceosome (40). Export of mRNAs through the nuclear pore complex (NPC) from the nucleus to the cytoplasm is a key regulatory step in the expression of proteins (41). In our study, SNRPA and NUP155 were down-regulated after BaP treatment, indicating that BaP may affect mRNA processing and export impairing central cell biological processes. In addition, a possibly impairment of aminoacyl-tRNA biosynthesis was observed as indicated by down-regulation of AARS, KARS, YARS, GARS and SARS2 in the B/C group.

Proteasomes are large protein complexes and play roles in apoptosis and cell cycle regulation (42). We observed that the level of all identified proteins involved in proteasomes was down-regulated in the B/C group, indicating that they might be associated with the significant changes in apoptosis and cell cycle progression after BaP treatment. The expression of the proteins involved in aminoacyl-tRNA biosynthesis and proteasomes did not significantly differ between co-treated and control cells.

Confirmation of Altered Expression of Selected Proteins

To confirm the expression of selected proteins based on proteomics, Western blotting and statistical analyses were performed (Figure 7). The expression of SNRPA, RAD23B, NUP155 and AARS was down-regulated in cells treated with BaP, whereas eriodictyol treatment at least partly restored the expression of these proteins, implying that eriodictyol may play a protective role. In addition, the expression of RPA2 was up-regulated after co-treatment treatment, while its expression did not be changed in the BaP treatment group. These results were in agreement with the proteomics data. In addition, previous studies have reported similar results, with similar expression trends of RPA2, SNRP31 and RAD23B observed after BaP exposure (43, 44). Interestingly, the proteins reported in previous studies are all involved in the process of transcription, while in the present study, we found that specific proteins involved in the translation process also presented significant changes, which indicates that BaP might affect several central biological processes.

Based on the above results and analyses, a possible protective mechanism of eriodictyol alleviating cytotoxicity induced by BaP is summarized in Figure 8, i.e., eriodictyol plays a protective role by regulating the expression of key proteins in transcription and translation. Other identified proteins may

also make an important contribution in the cellular response to BaP, and further studies of these proteins may provide a better understanding of the mechanisms of BaP-induced Caco-2 cytotoxicity.

CONCLUSION

In this study, our results showed that eriodictyol and naringenin have a protective effect on BaP induced cell apoptosis, cell cycle progression, and oxidative stress, especially for eriodictyol. A total of 80 differentially expressed proteins (DEPs) were identified in response to treatment with eriodictyol. Proteins associated with genetic information processing pathways represented the highest proportion amongst the DEPs and included key proteins such as RPA2, SNRPA, RAD23B, NUP155 and AARS. These results provided new insights into the role of polyphenol in inhibiting BaP-induced cell damage, not only through the DNA replication pathway. In addition, treatment with quinic acid, ferulic acid, homovanillic acid and trolox decreased cell viability, indicating that a potential adverse effect of polyphenols should be considered when choosing suitable chemical protective agents.

All claims expressed in this article are solely those of the authors and do not necessarily represent those of their affiliated organizations, or those of the publisher, the editors and the reviewers. Any product that may be evaluated in this article, or claim that may be made by its manufacturer, is not guaranteed or endorsed by the publisher.

DATA AVAILABILITY STATEMENT

The datasets presented in this study can be found in online repositories. The names of the repository/repositories and accession number(s) can be found below: <http://www.proteomexchange.org/>, PXD030049.

REFERENCES

- Hattemer-Frey HA, Travis CC. Benzo-a-pyrene: environmental partitioning and human exposure. *Toxicol Ind Health*. (1991) 7:141–57. doi: 10.1177/074823379100700303
- Gelboin HV. Benzo[alpha]pyrene metabolism, activation and carcinogenesis: role and regulation of mixed-function oxidases and related enzymes. *Physiol Rev*. (1980) 60:1107–66. doi: 10.1152/physrev.1980.60.4.1107
- Lobo V, Patil A, Phatak A, Chandra N. Free radicals, antioxidants and functional foods: Impact on human health. *Pharma Rev*. (2010) 4:118. doi: 10.4103/0973-7847.70902
- Khattab SA, Hussien WF, Raafat N, Ahmed Alaa El-Din E. Effects of catechin hydrate in benzo[a]pyrene-induced lung toxicity: roles of oxidative stress, apoptosis, and DNA damage. *Toxicol Mech Methods*. (2021):1–9. doi: 10.1080/15376516.2021.1916667
- Jee S-C, Kim M, Kim KS, Kim H-S, Sung J-S. Protective effects of myricetin on benzo[a]pyrene-induced 8-hydroxy-2'-deoxyguanosine and BPDE-DNA adduct. *Antioxidants*. (2020) 9:446. doi: 10.3390/antiox9050446
- Kang R-R, Sun Q, Chen K-G, Cao Q-T, Liu C, Liu K, et al. Resveratrol prevents benzo(a)pyrene-induced disruption of mitochondrial homeostasis via the AMPK signaling pathway in primary cultured neurons. *Environ Pollut*. (2020) 261:114207. doi: 10.1016/j.envpol.2020.114207
- Lee S-C, Jee S-C, Kim M, Kim S, Shin MK, Kim Y, et al. Curcumin suppresses the lipid accumulation and oxidative stress induced by Benzo[a]pyrene toxicity in HepG2 cells. *Antioxidants*. (2021) 10:1314. doi: 10.3390/antiox10081314
- Omidian K, Rafiei H, Bandy B. Polyphenol inhibition of benzo[a]pyrene-induced oxidative stress and neoplastic transformation in an *in vitro* model of carcinogenesis. *Food Chem Toxicol*. (2017) 106:165–74. doi: 10.1016/j.fct.2017.05.037
- Liu Y, Wu Y, Zhang P. Protective effects of curcumin and quercetin during benzo(a)pyrene induced lung carcinogenesis in mice. *Eur Rev Med Pharmacol Sci*. (2015) 19:17361743.
- Kim KS, Kim NY, Son JY, Park JH, Lee SH, Kim HR, et al. Curcumin ameliorates benzo[a]pyrene-induced DNA damages in stomach tissues of Sprague-Dawley rats. *Int J Mol Sci*. (2019) 20:5533. doi: 10.3390/ijms20225533
- Wang L, Xue J, Wei F, Zheng G, Cheng M, Liu S. Chemopreventive effect of galangin against benzo(a)pyrene-induced stomach tumorigenesis through modulating aryl hydrocarbon receptor in Swiss albino mice. *Hum Exp Toxicol*. (2021) 40:1434–44. doi: 10.1177/0960327121997979
- Zhao X, Wu S, Gong G, Li G, Zhuang L. TBHQ and peanut skin inhibit accumulation of PAHs and oxygenated PAHs in peanuts during frying. *Food Control*. (2017) 75:99–107. doi: 10.1016/j.foodcont.2016.12.029

AUTHOR CONTRIBUTIONS

CW and GZ designed and conceived the research. CW and FZ drafted the manuscript. CW, FZ, YB, and XX analyzed the data and interpreted the results. CL and KK reviewed and extensively edited the final manuscript. All authors contributed to the article and approved the submitted version.

FUNDING

This research was supported by the National Natural Science Foundation of China (32001721) and Priority Academic Program Development of Jiangsu Higher Education Institutions (RAPD).

SUPPLEMENTARY MATERIAL

The Supplementary Material for this article can be found online at: <https://www.frontiersin.org/articles/10.3389/fnut.2022.839364/full#supplementary-material>

Supplementary Figure 1 | Statistical analyses of cell cycle perturbation. Bars with different letters are significantly different at the level $p < 0.05$.

Supplementary Figure 2 | Statistical analyses of cell apoptosis. Bars with different letters are significantly different at the level $p < 0.05$.

Supplementary Figure 3 | Fluorescent images of intracellular ROS in Caco-2 cells co-treated with eriodictyol/naringenin and BaP.

Supplementary Figure 4 | Classes of enriched KEGG Pathways. The general information of the enrichment includes pathway name, p value (calculated with Fisher's exact test with Hypergeometric algorithm), count (number of genes/proteins in the query that are involved in this term).

Supplementary Figure 5 | The QC analysis for the label-free method. Basepeak of chromatograms of Caco-2 cells treated with BaP (A), DMSO (B), and BaP and eriodictyol (C). Correlation analysis (D) and normal distribution diagrams (E) of protein intensity in different samples.

Supplementary Table 1 | Summary information of the identified differentially expressed proteins (DEPs).

13. Min S, Patra JK, Shin H-S. Factors influencing inhibition of eight polycyclic aromatic hydrocarbons in heated meat model system. *Food Chem.* (2018) 239:993–1000. doi: 10.1016/j.foodchem.2017.07.020
14. Wang C, Xie Y, Wang H, Bai Y, Dai C, Li C, et al. The influence of natural antioxidants on polycyclic aromatic hydrocarbon formation in charcoal-grilled chicken wings. *Food Control.* (2019) 98:34–41. doi: 10.1016/j.foodcont.2018.11.012
15. Wang C, Xie Y, Wang H, Bai Y, Dai C, Li C, et al. Phenolic compounds in beer inhibit formation of polycyclic aromatic hydrocarbons from charcoal-grilled chicken wings. *Food Chem.* (2019) 294:578–86. doi: 10.1016/j.foodchem.2019.05.094
16. Wang Y, Li L, Hao M, Fu D, Chen J, Zhou C, et al. Label-free quantitative proteomic analysis identifies the oncogenic role of FOXA1 in BaP-transformed 16HBE cells. *Toxicol Appl Pharmacol.* (2020) 403:115160. doi: 10.1016/j.taap.2020.115160
17. Niestroy J, Barbara A, Herbst K, Rode S, van Liempt M, Roos PH. Single and concerted effects of benzo[a]pyrene and flavonoids on the AhR and Nrf2-pathway in the human colon carcinoma cell line Caco-2. *Toxicol In Vitro.* (2011) 25:671–83. doi: 10.1016/j.tiv.2011.01.008
18. Marks DC, Belov L, Davey MW, Davey RA, Kidman AD. The MTT cell viability assay for cytotoxicity testing in multidrug-resistant human leukemic cells. *Leuk Res.* (1992) 16:1165–73. doi: 10.1016/0145-2126(92)90114-M
19. Sudhakar S, Nazeer RA. Structural characterization of an Indian squid antioxidant peptide and its protective effect against cellular reactive oxygen species. *J Funct Foods.* (2015) 14:502–12. doi: 10.1016/j.jff.2015.02.028
20. Wang C, Wang J, Wang X, Xia Y, Chen C, Shen Z, et al. Proteomic analysis on roots of *Oenothera glazioviana* under copper-stress conditions. *Sci Rep.* (2017) 7:1–12. doi: 10.1038/s41598-017-10370-6
21. Yuan L, Liu J, Deng H, Gao C. Benzo[a]pyrene induces autophagic and pyroptotic death simultaneously in HL-7702 human normal liver cells. *J Agric Food Chem.* (2017) 65:9763–73. doi: 10.1021/acs.jafc.7b03248
22. Jiang J, Xu H, Wang H, Zhang Y, Ya P, Yang C, et al. Protective effects of lemongrass essential oil against benzo (a) pyrene-induced oxidative stress and DNA damage in human embryonic lung fibroblast cells. *Toxicol Mech Methods.* (2017) 27:121–7. doi: 10.1080/15376516.2016.1266541
23. Huang M-C, Chen F-Y, Chou M-T, Su J-GJ. Fluoranthene enhances p53 expression and decreases mutagenesis induced by benzo[a]pyrene. *Toxicol Lett.* (2012) 208:214–24. doi: 10.1016/j.toxlet.2011.11.011
24. Rosa LdS, Jordão NA, da Costa Pereira Soares N, DeMesquita JF, Monteiro M, Teodoro AJ. Pharmacokinetic, antiproliferative and apoptotic effects of phenolic acids in human colon adenocarcinoma cells using *in vitro* and *in silico* approaches. *Molecules.* (2018) 23:2569. doi: 10.3390/molecules23102569
25. Kang H, Ling F, Xin X, Ping L. (-)-4-O-(4-O-β-D-glucopyranosylcaffeoyl) quinic acid exerts anti-tumour effects against uveal melanoma through PI3K/AKT pathway. *Cutaneous Ocul Toxicol.* (2021):1–6. doi: 10.1080/15569527.2021.1914074
26. Chen H-Y, Yen G-C. Possible mechanisms of antimutagens by various teas as judged by their effects on mutagenesis by 2-amino-3-methylimidazo[4, 5-f]quinoline and benzo[a]pyrene. *Mutat Res Toxicol Environ Mutagen.* (1997) 393:115–22. doi: 10.1016/S1383-5718(97)00092-2
27. Melo-Cavalcante AA, Picada JN, Rubensan G, Henriques JA. Antimutagenic activity of cashew apple (*Anacardium occidentale* Sapindales, Anacardiaceae) fresh juice and processed juice (*cajuína*) against methyl methanesulfonate, 4-nitroquinoline N-oxide and benzo[a]pyrene. *Genet Mol Biol.* (2008) 31:759–66. doi: 10.1590/S1415-47572008000400024
28. Myers JN, Harris KL, Rekhadevi PV, Pratap S, Ramesh A. Benzo(a)pyrene-induced cytotoxicity, cell proliferation, DNA damage, and altered gene expression profiles in HT-29 human colon cancer cells. *Cell Biol Toxicol.* (2021):1–23. doi: 10.1007/s10565-020-09579-5
29. Liu K, Cho Y-Y, Yao K, Nadas J, Kim DJ, Cho E-J, et al. Eriodictyol inhibits RSK2-ATF1 signaling and suppresses EGF-induced neoplastic cell transformation. *J Biol Chem.* (2011) 286:2057–66. doi: 10.1074/jbc.M110.147306
30. Almatroodi SA, Alrumaihi F, Alsahli MA, Alhomrani MF, Khan A, Rahmani AH. Curcumin, an active constituent of turmeric spice: implication in the prevention of lung injury induced by benzo(a)pyrene (BaP) in rats. *Molecules.* (2020) 25:724. doi: 10.3390/molecules25030724
31. Vijayaraman KP, Muruganatham S, Subramanian M, Shunmugiah KP, Kasi PD. Silymarin attenuates benzo(a)pyrene induced toxicity by mitigating ROS production, DNA damage and calcium mediated apoptosis in peripheral blood mononuclear cells (PBMC). *Ecotoxicol Environ Saf.* (2012) 86:79–85. doi: 10.1016/j.ecoenv.2012.08.031
32. Wang W, Wang R, Zhang Q, Mor G, Zhang H. Benzo(a)pyrene-7, 8-dihydrodiol-9, 10-epoxide induces human trophoblast Swan 71 cell dysfunctions due to cell apoptosis through disorder of mitochondrial fission/fusion. *Environ Pollut.* (2018) 233:820–32. doi: 10.1016/j.envpol.2017.11.022
33. Lv P, Yu J, Xu X, Lu T, Xu F. Eriodictyol inhibits high glucose-induced oxidative stress and inflammation in retinal ganglial cells. *J Cell Biochem.* (2019) 120:5644–51. doi: 10.1002/jcb.27848
34. Wang K, Chen Z, Huang J, Huang L, Luo N, Liang X, et al. Naringenin prevents ischaemic stroke damage via anti-apoptotic and anti-oxidant effects. *Clin Exp Pharmacol Physiol.* (2017) 44:862–71. doi: 10.1111/1440-1681.12775
35. Cao P, Cai J, Gupta RC. Effect of green tea catechins and hydrolyzable tannins on Benzo[a]pyrene-Induced DNA adducts and structure-activity relationship. *Chem Res Toxicol.* (2010) 23:771–7. doi: 10.1021/tx900412a
36. Kalyanaraman B, Darley-Usmar V, Davies KJ, Dennery PA, Forman HJ, Grisham MB, et al. Measuring reactive oxygen and nitrogen species with fluorescent probes: challenges and limitations. *Free Radic Biol Med.* (2012) 52:1–6. doi: 10.1016/j.freeradbiomed.2011.09.030
37. Zhang X, Wu RS, Fu W, Xu L, Lam PK. Production of reactive oxygen species and 8-hydroxy-2'-deoxyguanosine in KB cells co-exposed to benzo[a]pyrene and UV-A radiation. *Chemosphere.* (2004) 55:1303–8. doi: 10.1016/j.chemosphere.2003.12.004
38. He Z, Henricksen LA, Wold MS, Ingles CJ. RPA involvement in the damage-recognition and incision steps of nucleotide excision repair. *Nature.* (1995) 374:566–9. doi: 10.1038/374566a0
39. Pavanello S, Pulliero A, Siwinska E, Mielzynska D, Clonfero E. Reduced nucleotide excision repair and GSTM1-null genotypes influence anti-B[a]PDE-DNA adduct levels in mononuclear white blood cells of highly PAH-exposed coke oven workers. *Carcinogenesis.* (2005) 26:169–75. doi: 10.1093/carcin/bgh303
40. Reed R. Mechanisms of fidelity in pre-mRNA splicing. *Curr Opin Cell Biol.* (2000) 12:340–5. doi: 10.1016/S0955-0674(00)00097-1
41. Borden KL. The nuclear pore complex and mRNA export in cancer. *Cancers.* (2021) 13:42. doi: 10.3390/cancers13010042
42. Adams J. The proteasome: structure, function, and role in the cell. *Cancer Treat Rev.* (2003) 29:3–9. doi: 10.1016/S0305-7372(03)00081-1
43. Yan C, Wu W, Li H, Zhang G, Duerksen-Hughes PJ, Zhu X, et al. Benzo[a]pyrene treatment leads to changes in nuclear protein expression and alternative splicing. *Mutat Res Toxicol Environ Mutagen.* (2010) 686:47–56. doi: 10.1016/j.mrfmmm.2010.01.015
44. Lu X, Shao J, Li H, Yu Y. Temporal gene expression changes induced by a low concentration of benzo[a]pyrene diol epoxide in a normal human cell line. *Mutat Res Toxicol Environ Mutagen.* (2010) 684:74–80. doi: 10.1016/j.mrfmmm.2009.12.002

Conflict of Interest: The authors declare that the research was conducted in the absence of any commercial or financial relationships that could be construed as a potential conflict of interest.

Publisher's Note: All claims expressed in this article are solely those of the authors and do not necessarily represent those of their affiliated organizations, or those of the publisher, the editors and the reviewers. Any product that may be evaluated in this article, or claim that may be made by its manufacturer, is not guaranteed or endorsed by the publisher.

Copyright © 2022 Wang, Zhao, Bai, Li, Xu, Kristiansen and Zhou. This is an open-access article distributed under the terms of the Creative Commons Attribution License (CC BY). The use, distribution or reproduction in other forums is permitted, provided the original author(s) and the copyright owner(s) are credited and that the original publication in this journal is cited, in accordance with accepted academic practice. No use, distribution or reproduction is permitted which does not comply with these terms.



The Simultaneous Formation of Acrylamide, β -carboline, and Advanced Glycation End Products in a Chemical Model System: Effect of Multiple Precursor Amino Acids

Cuyu Chen¹, Ye Jiao², Maomao Zeng³, Zhiyong He³, Qingwu Shen¹, Jie Chen^{3,4*} and Wei Quan^{1,3*}

¹ College of Food Science and Technology, Hunan Agricultural University, Changsha, China, ² School of Chemistry and Food Engineering, Changsha University of Science and Technology, Changsha, China, ³ State Key Laboratory of Food Science and Technology, Jiangnan University, Wuxi, China, ⁴ International Joint Laboratory on Food Safety, Jiangnan University, Wuxi, China

OPEN ACCESS

Edited by:

Hao Dong,
Zhongkai University of Agriculture and
Engineering, China

Reviewed by:

Bing Li,
South China University of
Technology, China
Zhili Liang,
Guangdong Food and Drug
Vocational College, China

*Correspondence:

Wei Quan
reus_quan@hunau.edu.cn
Jie Chen
chenjie@jiangnan.edu.cn

Specialty section:

This article was submitted to
Food Chemistry,
a section of the journal
Frontiers in Nutrition

Received: 11 January 2022

Accepted: 14 February 2022

Published: 09 March 2022

Citation:

Chen C, Jiao Y, Zeng M, He Z,
Shen Q, Chen J and Quan W (2022)
The Simultaneous Formation of
Acrylamide, β -carboline, and
Advanced Glycation End Products in a
Chemical Model System: Effect of
Multiple Precursor Amino Acids.
Front. Nutr. 9:852717.
doi: 10.3389/fnut.2022.852717

This study investigated the effect of multiple precursor amino acids on the simultaneous formation of acrylamide, β -carboline (i.e., harmane and norharmane), and advanced glycation end products (AGEs) [i.e., N^ε-(carboxymethyl)lysine and N^ε-(carboxyethyl)lysine] via a chemical model system. This model system was established with single or multiple precursor amino acids, including lysine–glucose (Lys/Glu), asparagine–glucose (Asn/Glu), tryptophan–glucose (Trp/Glu), and a combination of these amino acids (Com/Glu). Kinetic parameters were calculated by multiresponse non-linear regression models. We found that the *k* values of the AGEs and of acrylamide decreased, while those of harmane increased in the Com/Glu model when heated to 170 and 200°C. Our results indicated that the precursor amino acid of acrylamide and AGEs compete for α -dicarbonyl compounds, leading to a decrease in the formation of AGEs and acrylamide. Moreover, compared with asparagine, the precursor amino acid of β -carboline was more likely to react with acetaldehyde by Pictet–Spengler condensation, which increased the formation of harmane and decreased the formation of acrylamide via the acrolein pathway.

Keywords: precursor amino acids, acrylamide, N^ε-(carboxymethyl)lysine, N^ε-(carboxyethyl)lysine, β -carboline heterocyclic amines

INTRODUCTION

The Maillard reaction (MR) refers to the interaction between protein's free amine groups and carbohydrate's carbonyl groups (1, 2) and is often used in food processing to imbue food products with appealing flavors and colors. Incidentally, MR also produces some undesirable and harmful products that can have a negative impact on human's health (1), such as heterocyclic amines, advanced glycation end products, and acrylamide. These products, produced in heat-processed foods, have aroused widespread concern because of their carcinogenic, mutagenic, and other health risks.

Acrylamide is major harmful products of MR, which was first identified in high-temperature-processed, starch-rich food including french fries, potato chips, coffee, and bakery products (3). Currently, enough evidence has led acrylamide to be classified as a human carcinogen and a neurotoxic compound that exerts toxic effects on the nervous system, liver, and kidneys (4). In general, according to the literature, the formation of acrylamide has been reported to proceed in a step-wise manner: A Schiff base is first formed in the MR's early stages, and then it rearranges to produce an Amadori/Heyns product that can be decarboxylated to form acrylamide directly or reacted with asparagine (Asn) to form acrylamide via a Strecker degradation (5–7). In addition, the acrolein pathway is another important way to produce acrylamide, and acrolein is usually generated by the oxidation of ethanal during the MR (7, 8).

Advanced glycation end products (AGEs) refer to a group of structurally complex and chemically stable Maillard reaction harmful products (MRHPs) generated in the last stage of the MR (9). *N*^ε-(carboxymethyl)lysine (CML) and *N*^ε-(carboxyethyl)lysine (CEL) are typical AGEs found in food including tea, milk, meat, and bread (10, 11). In brief, CML is formed by the reaction of a reactive α -dicarbonyl, including glyoxal (GO), and CEL is produced by the reaction of methylglyoxal (MGO) with lysine (Lys) in the MR (12, 13). Diets rich in AGEs may increase the potential risk for several chronic kidney and liver diseases, diabetes, cardiovascular disease, and Alzheimer's disease (9, 12).

β -carboline heterocyclic amines (HAs) including harmane and norharmane are a series of complex food carcinogens and mutagens, which can form at lower temperatures without the presence of creatine and creatinine (14, 15). Toxicology studies have indicated that harmane and norharmane display comutagenic activity in the presence of other carcinogens, and they also show neurotoxic characteristics, which may lead to the development of some nervous system disorders (16). As studies have shown (17), except for the dehydration and β -elimination of AP (15), the oxidation of tetrahydro- β -carbolines (TH β Cs) is also an important way to produce β -carboline HAs, although TH β Cs are usually generated through the Pictet–Spengler condensation between tryptophan (Trp) and acetaldehyde during the MR (14, 15, 17).

Until now, although a large number of studies have focused on formation pathways, the influencing factors and inhibition methods for the individual harmful compounds or homologs with similar structure. The formation mechanisms of the above-mentioned MRHPs have only been investigated using MR chemical model systems with a single substrate amino acid and a single reducing sugar (18, 19). These chemical model systems ignore the fact that some precursors for the formation of these MRHPs, including Lys, Asn, and Trp, exist together in certain foods such as potatoes, cookies, and bread (20). Studies that have focused on the effect of multiple precursor amino acids on the simultaneous generation of these MRHPs in heat-processed food are few. Although some studies have indicated that the addition of amino acids including lysine and tryptophan were effective at inhibiting the formation of acrylamide in MR chemical model systems, the formation of AGEs and β -carboline HAs was not

considered (21, 22). Moreover, in cereals and potato-based food, the amount of reducing sugars is relatively lower than the amount of free amino acids, and the ratio of each amino acid is different (20). Because of the limitations of reducing sugars, lysine, asparagine, and tryptophan may have to compete to participate in the MR, and there are some similar intermediate compounds in the formation of MRHPs. The effect of multiple precursor amino acids on the formation of the previously mentioned MRHPs remains unclear.

Based on an aqueous MR chemical model system, the effect of multiple precursor amino acids including Lys, Asn, and Trp on the simultaneous formation of acrylamide, β -carboline HAs, and AGEs was investigated. The present study offers insight into the reaction mechanism and provides mathematical evidence for predicting the simultaneous formation of acrylamide, β -carboline HAs (harmane and norharmane), and AGEs (CML and CEL) in high-temperature-processed cereals and potato-based foods.

MATERIALS AND METHODS

Chemicals

The standards of tryptophan, and asparagine, acetaldehyde, acrolein, glyoxal and methylglyoxal, and nonafluoropentanoic acid were purchased from J&K Scientific Co, Ltd. (Beijing, China). harmane, norharman, *N*^ε-(carboxymethyl)lysine (CML), *d*₄-CML, *N*^ε-(carboxyethyl)lysine (CEL), and *d*₄-CEL were obtained by Santa Cruz Biotechnology Co. (Paso Robles, CA). Glucose and ¹³C₆-glucose, lysine and *d*₄-lysine, acrylamide and ¹³C₃-acrylamide were purchased from Sigma-Aldrich (Darmstadt, Germany). Other analytical grade chemicals were purchased from Sinopharm Chemical Reagent Co, Ltd. (Shanghai, China).

Preparation of Maillard Reaction Model Systems and Thermal Reaction

According to previous studies with some modifications (23, 24), aqueous Maillard reaction model systems were prepared in phosphate buffer (0.1 M, pH 6.8). Four amino acid–glucose reaction solutions containing Lys–glucose (Lys/Glu; 30/100 mmol), Asn–glucose (Asn/Glu; 200/100 mmol), Trp–glucose (Trp/Glu; 5/100 mmol), or a combination of Lys–Asn–Trp–glucose (Com/Glu; 100/200/5/100 mmol). The ratios and concentrations of amino acids and glucose in the chemical model system (Lys 30, Asn 200, Trp 5, glucose 100 mmol) were selected based on their actual proportions in real cereal and potato-based food (20, 25, 26), and their concentrations were appropriately magnified to better evaluate the intermediates and final products.

Next, 20 ml reaction solutions were added to glass reaction vials with Teflon caps. The reaction vials were fully sealed as much as possible to avoid water evaporation and oil absorption. The reaction vials were heated at 170 and 200°C for 0–21 min using a Jintan thermostat-controlled oil bath (Zhejiang, China). Each glass reaction vial was preheated for 5 min before sealing and inserting it into the oil bath. The reaction vials were taken out of the oil bath at predetermined heating times (3, 6, 9, 12, 15,

18, and 21 min), cooled in an ice bath to stop any further reaction, and stored at -80°C for further analysis.

Determination of Reactants

After centrifugation and dilution, the 300 μL reaction sample were added to 300 μL of an internal standard containing 100 $\mu\text{g}/\text{mL}$ d_4 -lysine, and 200 $\mu\text{g}/\text{mL}$ $^{13}\text{C}_6$ -glucose.

The identification and quantification of lysine, asparagine, tryptophan, and glucose were conducted on an Acquity UHPLC system equipped with a triple quadrupole MS (Waters, Milford, MA, USA). The separation of analytes was performed on a Waters Atlantis dC18 column (250×4.6 mm i.d., $3.0 \mu\text{m}$) using a gradient elution with 0.1% formic acid (pH 6.8) (solvent A) and acetonitrile (solvent B). The solvent composition was 0–0.1 min, 5% A; 0.1–10 min, 5–100% A; 10–10.5 min, 100–5% A; and 10.5–15 min, 5% A. The flow rate was 0.3 mL/min, the column temperature was 30°C and the injection volume was 10 μL . The capillary voltage was 3.5 kV. The temperature of the ion source and that of the desolvation gas were 130 and 350°C , respectively. The fragment used for quantification were m/z 133 \rightarrow 74 (asparagine); m/z 147 \rightarrow 84 (lysine); m/z 151 \rightarrow 88 (d_4 -lysine); m/z 151 \rightarrow 88 (d_4 -lysine); m/z 383 \rightarrow 203 (glucose); and m/z 395 \rightarrow 209 ($^{13}\text{C}_6$ -glucose).

Determination of Intermediate MRPs

Glyoxal and Methylglyoxal

Analysis of α -dicarbonyl compounds including glyoxal (GO) and methylglyoxal (MGO) was carried out as described previously (27). Reaction samples were centrifuged at 12,000 g for 5 min, then 300 μL supernatant was collected used for derivatization. Derivatization of α -dicarbonyl compounds was carried out with 150 μL of 5 μM *o*-phenylenediamine. In addition, 100 μL of 2,3-hexanedione (4 μM) was added as an internal standard. Then the mixture was kept at 4°C in the dark for 12 h.

The derivatives of α -dicarbonyl compounds were determined by using a Waters 2695 LC system with a Micromass Quattro Micro triple quadrupole MS and Waters X-Bridge C18 column (2.1×100 mm, $3.5 \mu\text{m}$, Milford, MA, USA) at a flow rate of 0.3 mL/min. The gradient mixture was started from 30% A and increased to 90% and 100% A in 5 and 3 min, respectively. Then it decreased to 30% A in 2 min and the 30% A remained for 5 min, mobile phase A was 1% formic acid and B was methanol. The α -dicarbonyl compounds were identified with the same MS parameters used in the analysis for CML and CEL. The fragments used of the α -dicarbonyl derivatives were m/z 131 \rightarrow 77 (GO), 145 \rightarrow 77 (MGO), and 187 \rightarrow 77 (internal standard).

Acetaldehyde and Acrolein

According to the method reported by Uchiyama et al. (28) with some modification, 3 mL samples or standard solutions of acetaldehyde or acrolein were mixed with 1.5 mL 2% NaCl–0.8 mol/L HCl solution, 1.0 mL 15% Na_2HPO_4 , and 1.0 mL 0.2% 2,4-dinitrophenylhydrazine, added sequentially. Then the mixed solution was heated in a water bath at 65°C for 20 min. After cooling to room temperature, 5 mL hexane was added twice for extraction of acrolein. Then 2 mL hexane was filtered through a $0.22\text{-}\mu\text{m}$ organic microporous membrane for HPLC analysis.

Lichrospher C18 (4.6×250 mm, $5.0 \mu\text{m}$) column was selected for HPLC separation. For each sample, 10 μL was injected onto the column and allowed to elute isocratically at 30°C with 62% acetonitrile in water at a flow rate of 1.0 mL/min. The detection wavelength was 365 nm. A run time of 20 min was enough for complete elution of sample components.

Determination of Final MRPs

Melanoidins

The concentrations of melanoidins were determined at 470 nm on a spectrophotometer (UV-1601, Shimadzu, Kyoto, Japan). The concentrations of melanoidins were calculated from the Lambert–Beer equation with an extinction coefficient of 282 L/mol·cm, a value derived for melanoidins formed from glucose and asparagine (24, 29).

CML and CEL

According to Jiao et al. (10) and Yu et al. (11), 150- μL reaction sample was spiked with 150 μL of internal standard solution which containing 71.2 ng of d_4 -CML and 66.0 ng of d_4 -CEL. Chromatographic separation was performed on a Waters 2695 liquid chromatograph (LC) module coupled with a Waters X-Bridge C18 column (2.1×100 mm, $3.5 \mu\text{m}$, Milford, MA, USA). The mobile phase A was acetonitrile and mobile phase B was NFPA (5 mM). The flow rate was 0.3 mL/min, the injection volume was 5 μL and the column temperature was set to 40°C . The gradient elution was performed as follows: 0–0.1 min, 5% A; 0.1–5 min, 5–60% A; 5–8 min, 60%–100% A; 8–10 min, 100% A; 10–12 min, 100–5% A; 12–20 min, 5% A.

The LC was interfaced with a Micromass Quattro Micro triple quadrupole mass spectrometer (Manchester, UK). The mass spectrometer (MS) was operated in an electrospray ionization (ESI) positive mode with multiple reaction monitoring (MRM). The capillary voltage was 3.6 kV. Temperatures of the ionization source and the desolvation gas were 110 and 400°C , respectively. The flow rates of the cone gas and desolvation were 50 and 600 L/h, respectively. Argon gas was used as the collision gas in the collision cell. For CML, d_4 -CM, CEL, and d_4 -CEL, the fragments m/z 205 \rightarrow 84, m/z 209 \rightarrow 88, m/z 219 \rightarrow 84, and m/z 223 \rightarrow 88, respectively, were used for quantification.

Acrylamide, Harmane, and Norharmane

After centrifugation and dilution, the 300 μL reaction sample were added to 300 μL of an internal standard containing 100 $\mu\text{g}/\text{mL}$ $^{13}\text{C}_3$ -acrylamide. The identification and quantification of acrylamide, harman, and norharman were also conducted on an Acquity UHPLC system equipped with a triple quadrupole MS (Waters, Milford, MA, USA). The parameters of UHPLC-MS were same as section 2.3. The fragment used for quantification were m/z 72 \rightarrow 55 (acrylamide); m/z 75 \rightarrow 58 ($^{13}\text{C}_3$ -acrylamide); m/z 169 \rightarrow 115 (norharman).

Kinetic Modeling

In the present study, only GO, MGO, and acrolein was detected and taken into consideration during the kinetic modeling. The kinetic model for the MR model system was developed based on the proposed reaction pathways as shown in **Figure 1A**.

Equations for the reaction rates of each compound are expressed in **Supplementary Figure 1**. For modeling purposes, the average concentrations of analysis were used (measured in triplicate), and data were normalized and expressed in millimoles per liter. All experiment data were made to fit the proposed kinetic model, and the kinetic parameters (k) were estimated based on the non-linear curve fitting function of the Origin 8.5 software (OriginLab, USA) and SAS 9.0 software (SAS Institute Inc, China). Moreover, the R-squared (R^2) values were calculated to determine the fitting performance of the non-linear fitted models (29, 30).

Statistical Analysis

Analysis of all components was conducted in triplicate, with values reported as the mean \pm standard deviation of three independent experiments. Statistical analysis was carried out using the general linear model procedure of Statistix software 9.0 (Analytical Software, Tallahassee, FL, USA). Significant differences ($p < 0.05$) between means were identified by the least significance difference procedure.

RESULTS AND DISCUSSION

The Concentration Changes of Reaction Substrates in the MR Model System

As shown in **Figure 2**, the concentrations of lysine, asparagine, tryptophan, and glucose declined with increased heating time; the degradation rates of amino acids and glucose also decreased over time, which is consistent with previously reported results (7). The degradation rates of the majority of the amino acids as well as glucose underwent a steep decline during the initial 9 min of heating. When heated to 170°C (**Figures 2A–D**), the concentration of Trp in Trp/Glu model decreased by 96.9% at 9 min compared with the initial Trp concentration. Lys showed results similar to those for Trp, with a reduction of 83.1% at 9 min in the Lys/Glu model, followed by a gradual reduction in the decrease rate. At the final stage of the reaction, the concentrations of both Trp and Lys in the control group were nearly 0 after 21 min of applied heat, as expected. However, Trp and Lys levels in the Com/Glu model remained at 58.4 and 21.5% of their initial concentrations, respectively. Unlike Trp and Lys, Asn was reduced by 80.3 and 77.3% in the Asn/Glu and Com/Glu models, respectively, indicating that the degradation rates were the same in both the Asn/Glu and Com/Glu models. **Figures 2E–H** shows the concentration change of the amino acids at 200°C, which was similar to their kinetics at 170°C. The reduction of the amino acids in the Com/Glu model was also significantly less than that of the single amino acid/Glu model.

The concentration of another important MR precursor, glucose, was also monitored (**Figures 2D,H**). When heated at 170°C for 9 min (**Figure 2D**), the glucose concentration in the Asn/Glu, Trp/Glu, Lys/Glu, and Com/Glu models decreased by 95.1, 86.8, 91.1, and 97.6%, respectively, and the gradually lessening reduction rate of glucose eventually decreased by 98.3, 94.0, 96.1, and 98.5%, respectively. Meanwhile, similar results were obtained at 200°C (**Figure 2H**). At 200°C, the concentration of glucose in the Asn/Glu, Trp/Glu, Lys/Glu, and Com/Glu

models decreased by 88.9, 83.2, 74.6, and 94.6%, respectively, by 9 min, and had decreased by 94.7, 90.4, 97.7, and 83.8%, respectively, at the end of heating. Comparing the different model systems, the reduction of glucose in the Trp/Glu and Lys/Glu models was less than the reduction of glucose in the Asn/Glu and Com/Glu models.

The Concentration Changes of Reaction Intermediates in the MR Model System

In order to further analyze the generation mechanism of related MRHPs in the model system, several intermediate compounds were selected by reference to the literature (5, 6, 13). Changes in the concentration of these compounds during the reactions were determined.

α -Dicarbonyl compounds are important intermediates formed in MRs. They are mainly produced by the thermal degradation of glucose and the decarboxylation of a Schiff base that reacts with amino acids to form a series of MR products (31). As **Figures 3A,B** shows, all of the model systems produced a large amount of GO at the initial stage of the reaction (after 3 min), but as the reaction progressed, the concentration of GO decreased. In addition, a higher GO content was observed at 170°C rather than at 200°C. Comparing the different model systems, the content of GO in the Trp/Glu model was significantly lower than in the other models, especially for the Lys/Glu model. Despite this, there was no significant difference in the GO content in the different model systems at the end of the reaction.

The changes in MGO concentration are shown in **Figures 3C,D**. The content of MGO reached a relatively high value at 9–15 min and then either remained at a stable level or decreased. Similar to the effects seen with the GO content, higher temperatures efficiently induced the formation of MGO. The generation of MGO in the different model systems was different than what was observed for GO, however. When heated to 170°C, the amount of MGO produced in the Asn/Glu model was higher than in the other systems. When heated to 200°C, the Lys/Glu model showed the highest content of MGO.

Aldehydes are also important MR intermediates and are degradation products of glucose at high temperatures (19). As shown in **Figures 3E,F**, the formation of ethanal was significantly different ($p < 0.05$) in the different model systems. The Asn/Glu model had a higher reactivity, which generated more ethanal than in the other models. The content of ethanal in the Asn/Glu model was $97.25 \pm 8.91 \mu\text{g/ml}$ at 170°C and $62.97 \pm 7.97 \mu\text{g/ml}$ at 200°C, which was 51.92–73.98% and 24.01–34.20% higher, respectively, than in the other model systems.

Acrolein is produced by the oxidation of ethanal, so it is an important intermediate compound that can make acrylamide through the acrolein pathway (7, 8, 32). The content of acrolein was significantly different ($p < 0.05$) in each of the model systems. At the two heating temperatures (**Figures 3G,H**), the concentration of acrolein formed in the Asn/Glu model system was the highest, while it was the lowest in the Trp/Glu and Com/Glu models.

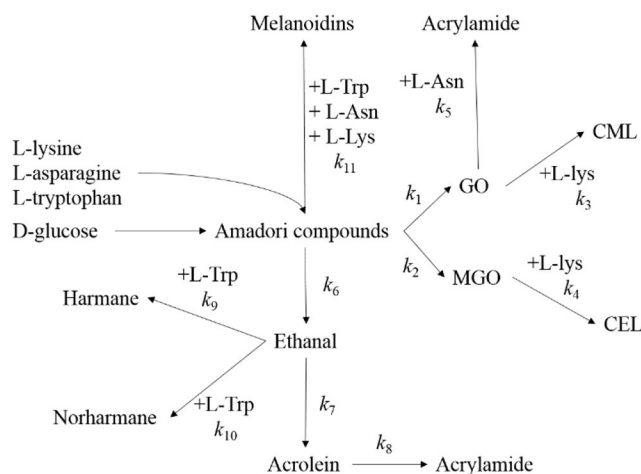
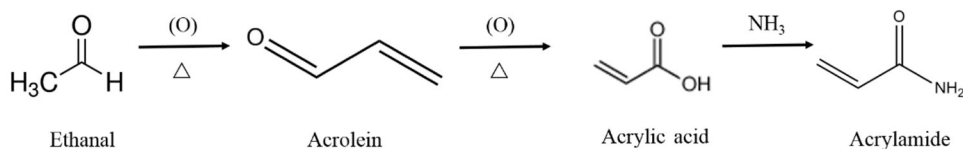
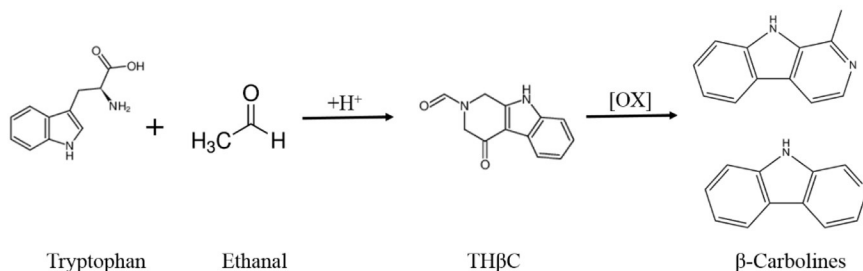
A Proposed reaction scheme:**B** Proposed acrolein pathway for acrylamide:**C** Proposed TH β Cs pathway for β -carbolines:

FIGURE 1 | Proposed reaction scheme for the simultaneous formation of acrylamide, CML, CEL, harman and norharman in multiple precursors amino acids/ glucose chemical model system **(A)**. Proposed acrolein pathway for the production of acrylamide **(B)** and Proposed TH β C pathway for the generation of β -carbolines **(C)**.

The Concentration Changes of MRHPs in the MR Model System

Acrylamide

The kinetics of acrylamide in the different models are shown in **Figures 4A,B**. Acrylamide concentrations in all the models underwent a stage during the initial 12 min of heating in which the generation of acrylamide was dominant. After prolonged heating, a decrease in the acrylamide content was observed, which can be attributed to acrylamide's elimination becoming dominant over acrylamide's formation (33). Since acrylamide is mainly reactive through its double bond and can react as an electrophile by a 1,4-addition to nucleophiles, the elimination of acrylamide is ascribed to acrylamide degradation,

polymerization, or reactions with various other components present or formed in the model system (33). The content of acrylamide formed at 200°C was significantly higher than that at 170°C, which is similar to the results found by Bråthen et al. (32) and Rydberg et al. (34) who showed that the a maximum amount of acrylamide was formed at approximately 200°C. The acrylamide content in the Asn/Glu model reached a maximum of $43.12 \pm 0.62 \mu\text{g/ml}$ and $82.28 \pm 4.01 \mu\text{g/ml}$ and then was reduced by 34.7 and 13.5% at 170 and 200°C, respectively. Trp and Lys may reduce the concentration of acrylamide as Koutsidis et al. (22) reported. The maximum content of acrylamide in the Com/Glu model reached only $25.51 \pm 3.42 \mu\text{g/ml}$ at 170°C and $38.05 \pm 3.71 \mu\text{g/ml}$ at 200°C, which

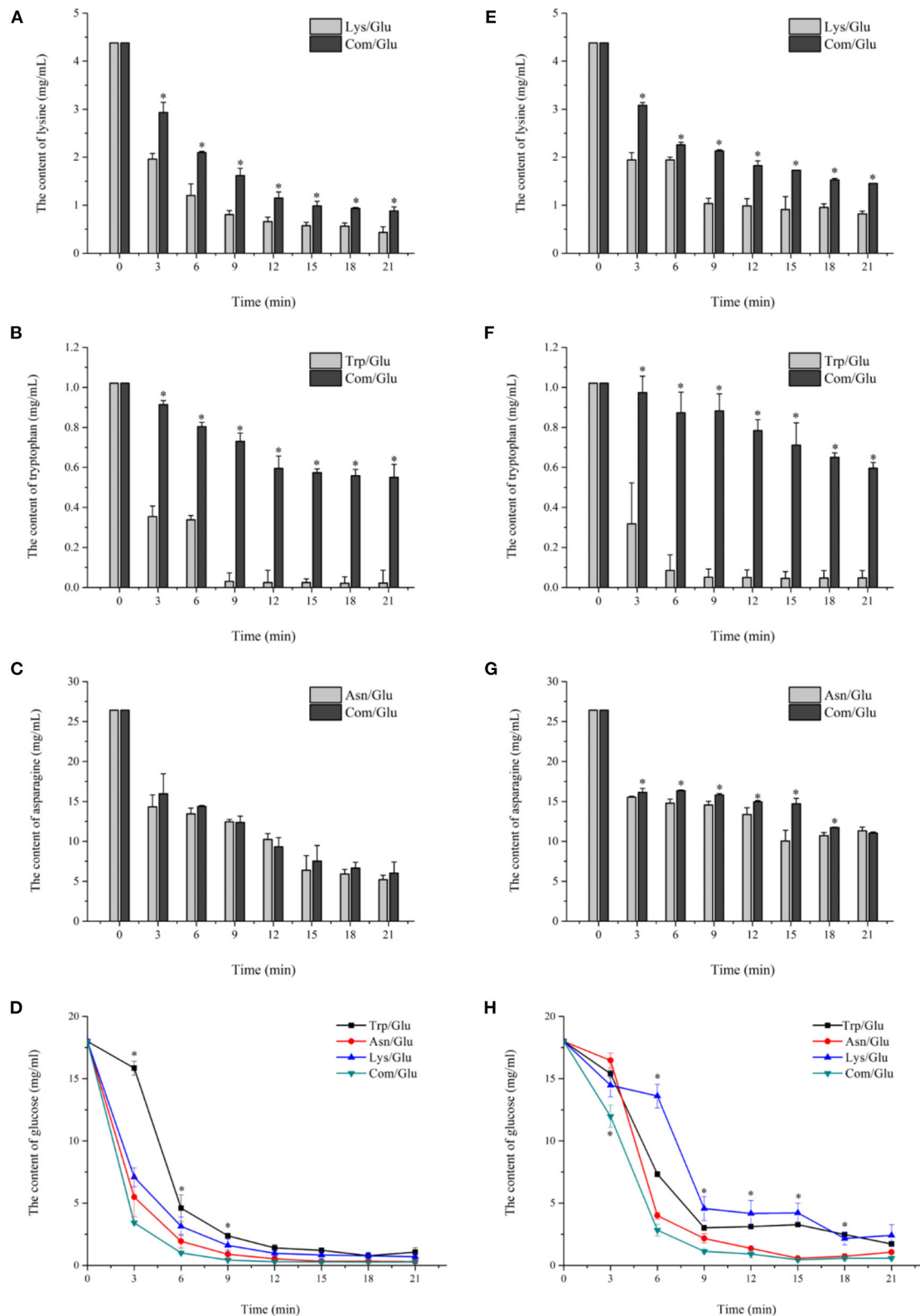


FIGURE 2 | Kinetic profiles of Lys (A,E), Trp (B,F), Asn (C,G), and glucose (D,H) in the different amino acid/glucose model system heated at 170 °C (A–D) and 200 °C (E–H). Data were expressed as mean ± SD in triplicates ($n = 3$), *, ($P < 0.05$).

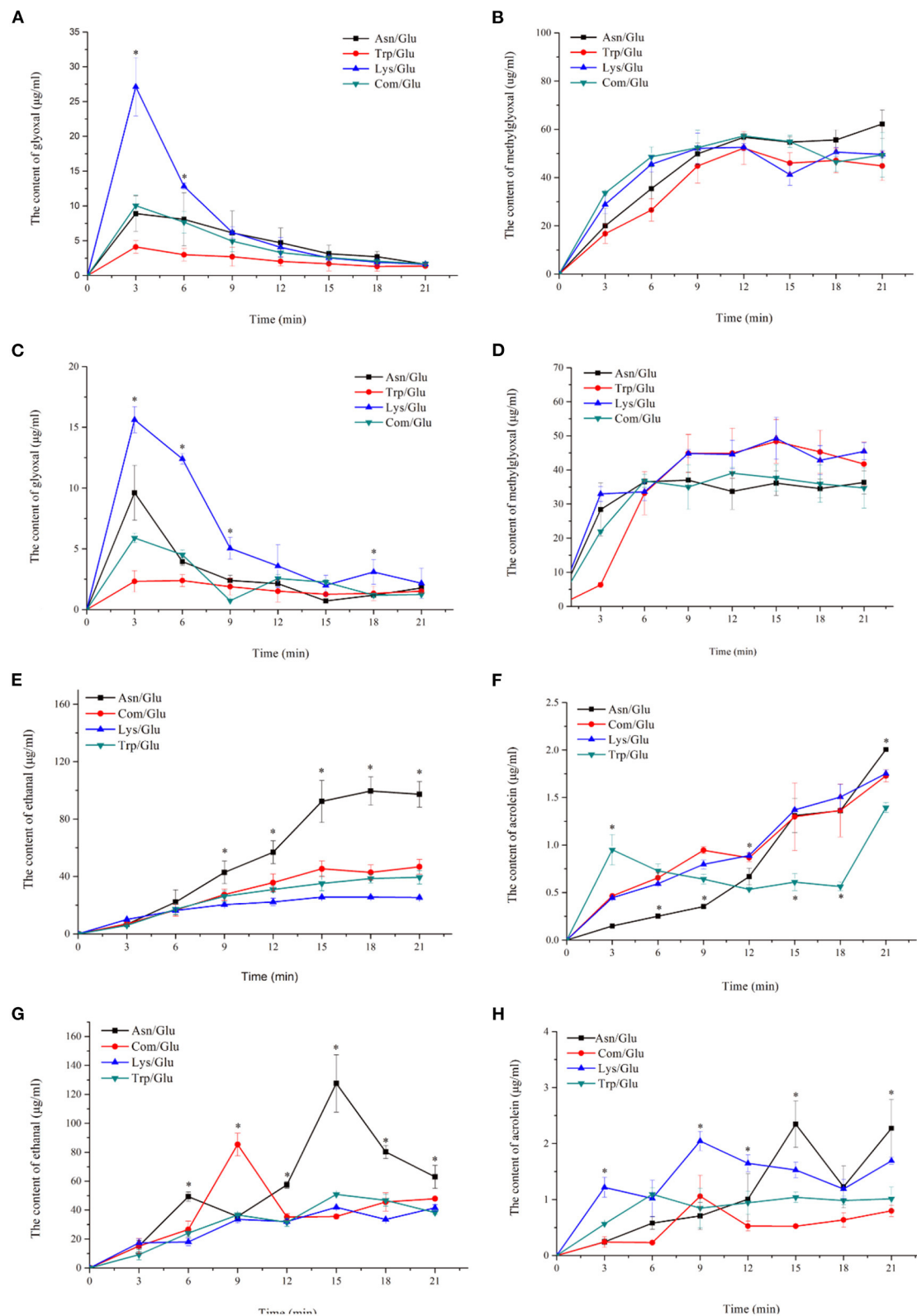


FIGURE 3 | Kinetic profiles of major ketone and aldehyde intermediate compounds: glyoxal (A,B), methylglyoxal (C,D), acetaldehyde (E,F) and acrolein (G,H) in the different amino acid/glucose model system heated at 170°C (A,C,E,G) and 200°C (B,D,F,H). Data were expressed as mean \pm SD in triplicates ($n = 3$), *, ($P < 0.05$).

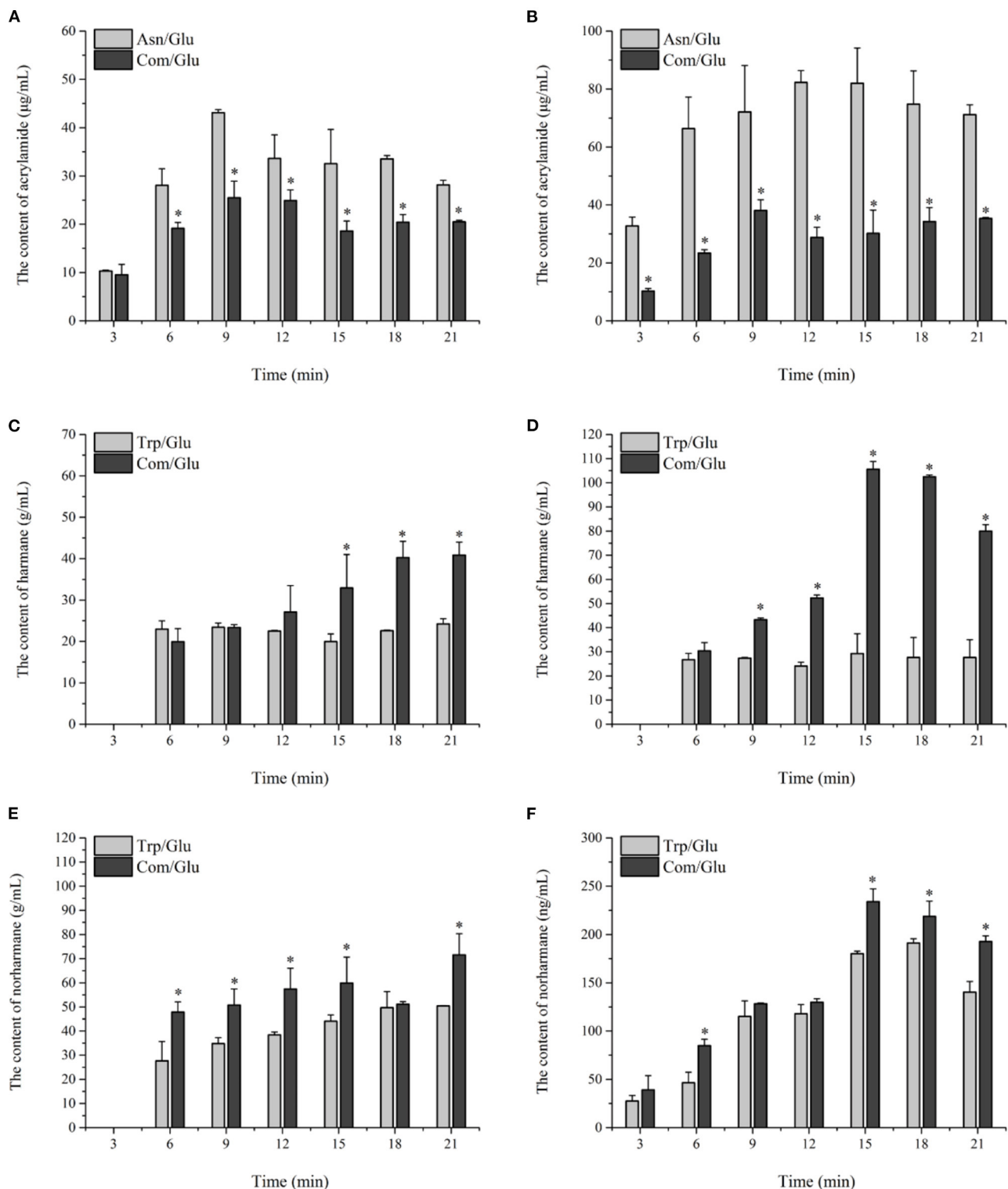


FIGURE 4 | Kinetic profiles of Maillard reaction products includes Acrylamide (A,B), harman (C,D), and norharman (E,F) in the different amino acid/glucose model system heated at 170°C (A,C,E) and 200°C (B,D,F). Data were expressed as mean \pm SD in triplicates ($n = 3$), * ($P < 0.05$).

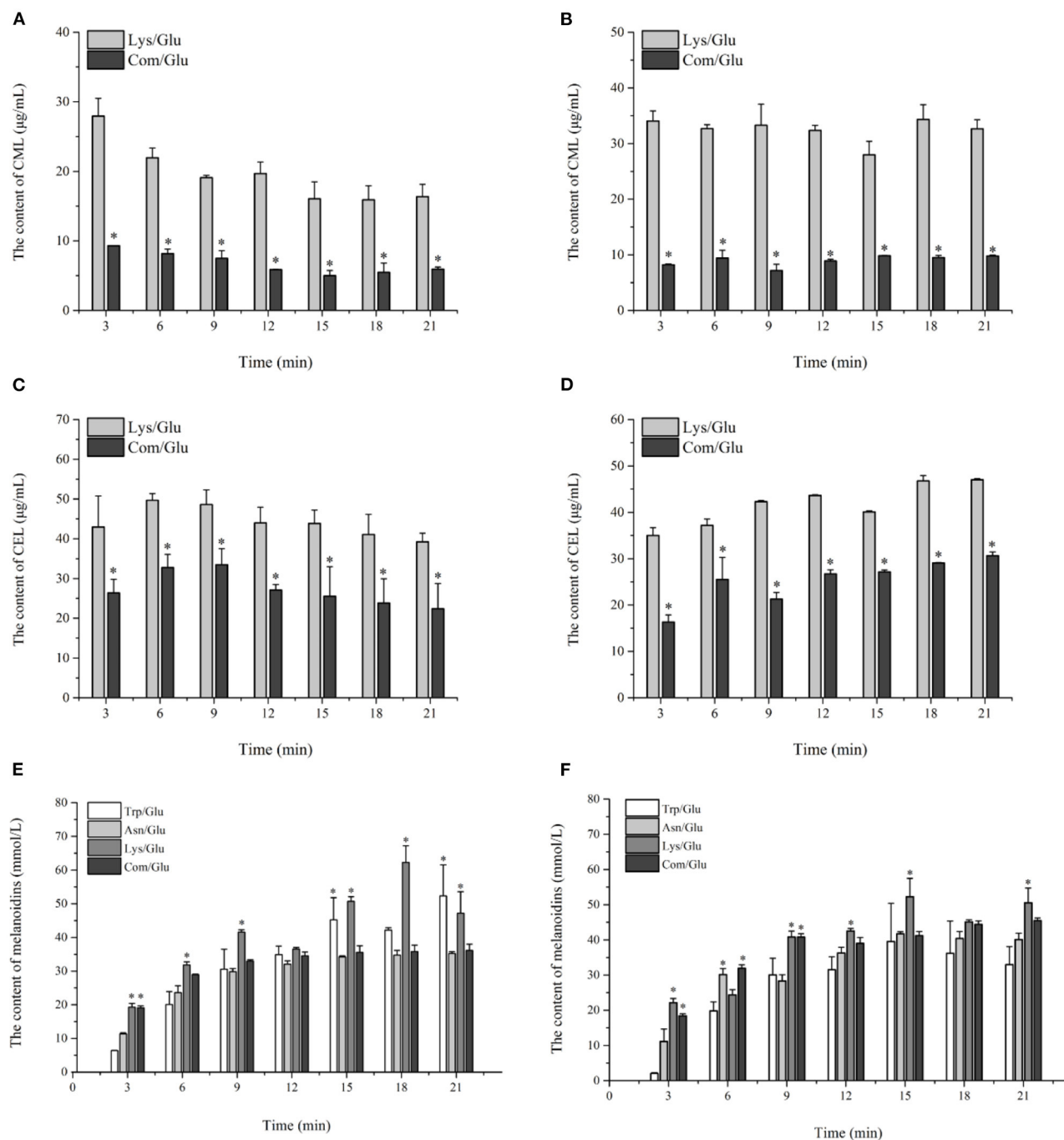


FIGURE 5 | Kinetic profiles of Maillard reaction products includes CML (A,B), CEL (C,D), and melanoidins (E,F) in the different amino acid/glucose model system heated at 170°C (A,C,E) and 200°C (B,D,F). Data were expressed as mean \pm SD in triplicates ($n = 3$), *, ($P < 0.05$).

was significantly lower ($p < 0.05$) than the results seen in the Asn/Glu model.

Harmane and Norharmane

In general, the contents of harmane and norharmane increased with time when heated to 170°C (Figures 4C,E). The highest concentration of harmane and norharmane in the Trp/Glu and

Com/Glu models was obvious at 21 min. When heated to 200°C (Figures 4D,F), the concentrations of harmane and norharmane were significantly reduced after reaching a maximum value. Furthermore, samples heated to 200°C showed a higher content of harmane and norharmane than the samples heated to 170°C, which is consistent with previous results (15). However, it should be noted that when comparing the content of harmane in the

TABLE 1 | Estimation of kinetic parameters among different amino acid model systems.

Group/T (°C)	Kinetics parameters ^a										
	k ₁ [*]	k ₂ [*]	k ₃ ^{**}	k ₄ ^{**}	k ₅ [*]	k ₆ [*]	k ₇ [*]	k ₈ [*]	k ₉ ^{***}	k ₁₀ ^{***}	k ₁₁ [*]
Lys-Glu/170°C	0.135	0.030	0.042	0.721	–	0.041	0.012	–	–	–	2.198
Trp-Glu/170°C	0.172	0.029	–	–	–	0.049	0.006	–	0.006	0.019	1.833
Asn-Glu/170°C	0.257	0.015	–	–	0.062	0.197	0.105	0.103	–	–	1.579
Com-Glu/170°C	0.199	0.023	0.015	0.523	0.050	0.114	0.072	0.071	0.012	0.015	1.420
Lys-Glu/200°C	0.178	0.029	0.072	0.441	–	0.027	0.014	–	–	–	2.369
Trp-Glu/200°C	0.199	0.029	–	–	–	0.045	0.005	–	0.007	0.063	2.480
Asn-Glu/200°C	0.143	0.037	–	–	0.095	0.237	0.114	0.112	–	–	1.864
Com-Glu/200°C	0.160	0.026	0.022	0.211	0.089	0.155	0.101	0.099	0.028	0.052	1.882

^aData were expressed as mean ± SD in triplicates (n = 3) and fit by the Marquardt non-linear least squares regression method. *, min⁻¹; **, 10⁻² min⁻¹; ***, 10⁻³ min⁻¹.

Trp/Glu and Com/Glu models, the amount of harmane produced in the Com/Glu model was significantly higher ($p < 0.05$) than that in the Trp/Glu model.

AGEs and Melanoidins

The trends for the two AGEs, CML and CEL, are shown in **Figures 5A–D**. Contrary to the results already presented for acrylamide and HAs, the amount of CML and CEL formed at the two reaction temperatures reached a maximum level in the initial reaction stage, and remained stable or decreased during the remainder of the reaction. The content range of CML produced in the Com/Glu and Lys/Glu models when heated to 170°C was from 5.01 ± 0.75 to 9.31 ± 0.02 μg/ml and from 16.35 ± 1.79 to 27.95 ± 2.54 μg/ml, respectively. When the heating temperature was 200°C, the content range of CML generated in the Com/Glu and Lys/Glu models was from 7.15 ± 0.14 to 9.80 ± 0.07 μg/ml and from 27.96 ± 2.42 to 34.34 ± 2.61 μg/ml, respectively. The content of CML formed in the Com/Glu model was significantly lower ($p < 0.05$) than that in the Lys/Glu model. In addition, the content of CEL produced in the Com/Glu model was also significantly lower than the content of CEL in the Lys/Glu model. The content range of CEL was from 22.40 ± 6.36 to 33.48 ± 4.02 μg/ml (for the Com/Glu model) and from 39.25 ± 2.17 to 49.67 ± 1.70 μg/ml (for Lys/Glu) at 170°C, while the ranges were from 16.31 ± 1.54 to 30.66 ± 0.79 μg/ml (for the Com/Glu model) and from 35.01 ± 1.66 to 46.99 ± 0.30 μg/ml (for the Lys/Glu model) at 200°C.

In addition to the already discussed MRHPs, melanoidins are generated via aldol condensations and the polymerization of carbonyl compounds and are considered as the main indicator of the browning state (35). The kinetic changes of melanoidins were also investigated in this study (**Figures 5E,F**). In general, the generation of melanoidins in all model systems exhibited a steep growth rate during the initial 9 min of heating, followed by a gentle increase during the remaining heating time. Specifically, the concentration of melanoids in the Lys/Glu and Trp/Glu models at 170°C (**Figure 5E**) were 47.20 ± 6.36 and 52.34 ± 9.23 mmol/L, respectively, which were significantly higher than the concentration of melanoids in the Asn/Glu and Com/Glu models. However, results differed when heating to 200°C (**Figure 5F**), as the concentration of melanoidins in the

Trp/Glu model was significantly lower than that in the other model systems.

Reaction Kinetic Modeling and Kinetic Parameters

According to available experimental data, and the reaction scheme proposed in **Figure 1A**. The kinetic data were fitted, and related kinetic parameters (k_1 – k_{18}) were calculated by the Marquardt non-linear least squares regression.

A comparison of the kinetic parameter estimation among the four model systems is shown in **Table 1**. In general, the reaction rate of each time point increased with an increase in the reaction temperature, which is consistent with the general rule of kinetics (19). The formation of melanoids in all the model systems was the fastest. The formation of CML, CEL, and acrylamide (k_3 , k_4 , and k_5) in the Com/Glu model system was significantly reduced when compared with the kinetics in the Lys/Glu and Asn/Glu model systems ($p < 0.05$). Previous studies also found that the addition of Lys to the Asn/Glu model can significantly reduce the production of acrylamide, but those studies did not consider the formation of CML and CEL (22, 36). These studies stated that the high activity of Lys in the MR was responsible for Asn's competition for the reducing sugar (22, 36). From **Table 1**, it can be seen that k_5 was significantly higher than k_3 and k_4 , thus indicating that acrylamide was formed more rapidly than CML and CEL in the simulation systems. According to previous research (18, 37), after the rapid formation of acrylamide, the presence of Lys could lower the acrylamide yield via adduct formation; this is because the electrophilic double bond of acrylamide can participate in nucleophilic reactions with hydrogen-bearing groups, such as the -NH₂ group of Lys. This addition reaction not only causes a decrease in acrylamide, but may also reduce the generation of CML and CEL by consuming Lys. When Asn and Lys participate in the MR together, the reason for the significant decrease in the formation of acrylamide, CML, and CEL may be the competition for α-dicarbonyl compounds (especially GO), as Amrein et al. (18) reported that α-dicarbonyl compounds play a key role in the formation of acrylamide.

In addition, previous studies have reported that the addition of Trp to the Asn/Glu model can significantly reduce the production

of acrylamide (22), but research in this area indicates that the main cause of acrylamide's significant decrease was due to Trp competing with Asn for reducing sugars, and a non-covalent interaction occurred between acrylamide and Trp (22).

According to the results of this study, the formation of acetaldehyde and acrolein (k_6 and k_7) in the Com/Glu model was significantly reduced compared with their formation in the Asn/Glu model. As a result, acrylamide (k_8) produced by the acrolein oxidation pathway was also significantly reduced. In contrast, a significant increase in the content of harmane generated in the Com/Glu model was observed. As shown in **Table 1**, the formation of acetaldehyde and acrolein (k_6 and k_7) in the Com/Glu model increased significantly compared with its formation in the Trp/Glu model. According to Herraiz et al. (17), acetaldehyde is an important intermediate for the formation of β -carboline HAs. In the presence of Trp, acetaldehyde can be used to form TH β C by Pictet–Spengler condensation, and then this will further generate harmane by the oxidation of TH β C (**Figures 1B,C**). Therefore, Trp's and Asn's competition for acetaldehyde and thus the decrease in the production of acrolein may be an important reason for the higher content of harmane and lower content of acrylamide observed in the Com/Glu model compared with the Trp/Glu model.

CONCLUSION

In order to illustrate the effect of multiple precursor amino acids on the simultaneous formation of multiple MRHPs in real heat-processed food systems, aqueous MR chemical model systems were established according to the concentrations and proportions of Lys, Asn, Trp present in real cereal and potato-based food. Changes in the content of precursors, MRHPs, key intermediates, and kinetic parameters in the MR model systems were determined. Our findings indicated significant interaction effects of Lys, Trp, and Asn in the MR model system. The competitive effect between Lys and Asn led to a significant reduction in CML, CEL, and acrylamide. Additionally, it could be explained that the formation of harmane is carried

out through Pictet–Spengler condensation and the oxidation of TH β C, which significantly increased the content of harmane, although the formation of acrylamide from the acrolein oxidation pathway decreased. Our results revealed the influence of multiple precursor amino acids on the formation of their MRHPs. These findings will be invaluable for understanding the simultaneous formation and interaction of multiple MRHPs in heat-processed food, will aid in the development of new processes for simultaneous control pathways, and help to improve the safety and quality of heat-processed food.

DATA AVAILABILITY STATEMENT

The original contributions presented in the study are included in the article/**Supplementary Material**, further inquiries can be directed to the corresponding authors.

AUTHOR CONTRIBUTIONS

YJ: formal analysis. CC and WQ: investigation. MZ: methodology. JC: project administration. ZH and QS: resources. WQ: writing—original draft. All authors contributed to the article and approved the submitted version.

FUNDING

This work has been supported by the National Natural Science Foundation of China (Grant No. 3217160166), the Key Research and Development Plan of Guangdong Province, China (Grant No. 2019B020212011), and the National First-class Discipline Program of Food Science and Technology (No. JUFSTR20180201).

SUPPLEMENTARY MATERIAL

The Supplementary Material for this article can be found online at: <https://www.frontiersin.org/articles/10.3389/fnut.2022.852717/full#supplementary-material>

REFERENCES

- Aljahdali N, Carbonero F. Impact of maillard reaction products on nutrition and health: current knowledge and need to understand their fate in the human digestive system. *Crit Rev Food Sci Nutr*. (2019) 59:474–87. doi: 10.1080/10408398.2017.1378865
- Stadler RH, Blank I, Varga N, Robert F, Hau J, Guy PA, et al. Acrylamide from Maillard reaction products. *Nature*. (2002) 419:449–50. doi: 10.1038/419449a
- Zhang Y, Ren Y, Zhang Y. New research developments on acrylamide: analytical chemistry, formation mechanism, and mitigation recipes. *Chem Rev*. (2009) 109:4375–97. doi: 10.1021/cr800318s
- Zamani E, Shokrzadeh M, Fallah M, Shaki F. A review of acrylamide toxicity and its mechanism. *Pharm Biomed Res*. (2017) 3:1–7. doi: 10.18869/acadpub.pbr.3.1.1
- Manzocco L, Calligaris S, Mastrocola D, Nicoli MC, Lerici CR. Review of non-enzymatic browning and antioxidant capacity in processed foods. *Trend Food Sci Technol*. (2000) 11:340–6. doi: 10.1016/S0924-2244(01)00014-0
- Yaylayan VA, Wnorowski A, Perez Locas C. Why asparagine needs carbohydrates to generate acrylamide. *J Agric Food Chem*. (2003) 51:1753–7. doi: 10.1021/jf0261506
- Zyzak DV, Sanders RA, Stojanovic M, Tallmadge DH, Eberhart BL, Ewald DK, et al. Acrylamide formation mechanism in heated foods. *J Agric Food Chem*. (2003) 51:4782–7. doi: 10.1021/jf034180i
- Becalski A, Lau BPY, Lewis D, Seaman SW. Acrylamide in foods: occurrence, sources, and modeling. *J Agric Food Chem*. (2003) 51:802–8. doi: 10.1021/jf020889y
- Poulsen MW, Hedegaard RV, Andersen JM, de Courten B, Bugel S, Nielsen J, et al. Advanced glycation endproducts in food and their effects on health. *Food Chem Toxicol*. (2013) 60:10–37. doi: 10.1016/j.fct.2013.06.052
- Jiao Y, He J, Li F, Tao G, Zhang S, Zhang S, et al. N-epsilon-(carboxymethyl)lysine and N-epsilon-(carboxyethyl)lysine in tea and the factors affecting their formation. *Food Chem*. (2017) 232:683–8. doi: 10.1016/j.foodchem.2017.04.059

11. Yu L, Chai M, Zeng M, He Z, Chen J. Effect of lipid oxidation on the formation of N-epsilon-carboxymethyl-lysine and N-epsilon-carboxyethyl-lysine in Chinese-style sausage during storage. *Food Chem.* (2018) 269:466–72. doi: 10.1016/j.foodchem.2018.07.051
12. Singh R, Barden A, Mori T, Beilin L. Advanced glycation end-products: a review. *Diabetologia.* (2001) 44:129–46. doi: 10.1007/s001250051591
13. Srey C, Hull GLJ, Connolly L, Elliott CT, Dolores del Castillo M, Ames JM. Effect of Inhibitor Compounds on N-epsilon-(Carboxymethyl)lysine (CML) and N-epsilon-(Carboxyethyl)lysine (CEL) Formation in Model Foods. *J Agric Food Chem.* (2010) 58:12036–41. doi: 10.1021/jf103353e
14. Chen J, He Z, Qin F, Chen J, Zeng M. Formation of free and protein-bound heterocyclic amines in roast beef patties assessed by UPLC-MS/MS. *J Agric Food Chem.* (2017) 65:4493–9. doi: 10.1021/acs.jafc.7b01828
15. Gibis M. Heterocyclic aromatic amines in cooked meat products: causes, formation, occurrence, and risk assessment. *Compr Rev Food Sci Food Saf.* (2016) 15:269–302. doi: 10.1111/1541-4337.12186
16. Totsuka Y, Ushiyama H, Ishihara J, Sinha R, Goto S, Sugimura T, et al. Quantification of the co-mutagenic beta-carbolines, norharman and harman, in cigarette smoke condensates and cooked foods. *Cancer Lett.* (1999) 143:139–43. doi: 10.1016/S0304-3835(99)00143-3
17. Herraiz T. Analysis of the bioactive alkaloids tetrahydro-beta-carboline and beta-carboline in food. *J Chromatogr A.* (2000) 881:483–99. doi: 10.1016/S0021-9673(99)01313-8
18. Amrein TM, Andres L, Manzardo GGG, Amado R. Investigations on the promoting effect of ammonium hydrogencarbonate on the formation of acrylamide in model systems. *J Agric Food Chem.* (2006) 54:10253–61. doi: 10.1021/jf0625860
19. Martins SI, Jongen WM, Van Boekel MA. A review of Maillard reaction in food and implications to kinetic modelling. *Trend Food Sci Technol.* (2000) 11:364–73. doi: 10.1016/S0924-2244(01)00022-X
20. Choi S-H, Kozukue N, Kim H-J, Friedman M. Analysis of protein amino acids, non-protein amino acids and metabolites, dietary protein, glucose, fructose, sucrose, phenolic, and flavonoid content and antioxidative properties of potato tubers, peels, and cortexes (pulp). *J Food Compos Anal.* (2016) 50:77–87. doi: 10.1016/j.jfca.2016.05.011
21. Kim CT, Hwang ES, Lee HJ. Reducing acrylamide in fried snack products by adding amino acids. *J Food Sci.* (2005) 70:C354–8. doi: 10.1111/j.1365-2621.2005.tb09966.x
22. Koutsidis G, Simons SPJ, Thong YH, Haldoupis Y, Mojica-Lazaro J, Wedzicha BL, et al. Investigations on the effect of amino acids on acrylamide, pyrazines, and michael addition products in model systems. *J Agric Food Chem.* (2009) 57:9011–5. doi: 10.1021/jf9014763
23. Claeys WL, De Vleeschouwer K, Hendrickx ME. Kinetics of acrylamide formation and elimination during heating of an asparagine-sugar model system. *J Agric Food Chem.* (2005) 53:9999–10005. doi: 10.1021/jf051197n
24. Knol JJ, van Loon WAM, Linssen JPH, Ruck A-L, van Boekel MAJS, Voragen AGJ. Toward a kinetic model for acrylamide formation in a glucose-asparagine reaction system. *J Agric Food Chem.* (2005) 53:6133–9. doi: 10.1021/jf050504m
25. Halford NG, Muttucumaru N, Powers SJ, Gillatt PN, Hartley L, Elmore JS, et al. Concentrations of Free Amino Acids and Sugars in Nine Potato Varieties: Effects of Storage and Relationship with Acrylamide Formation. *J Agric Food Chem.* (2012) 60:12044–55. doi: 10.1021/jf3037566
26. Viklund GAI, Olsson KM, Sjöholm NM, Skog KI. Impact of harvest year on amino acids and sugars in potatoes and effect on acrylamide formation during frying. *J Agric Food Chem.* (2008) 56:6180–4. doi: 10.1021/jf073053+
27. Scheijen JLM, Schalkwijk CG. Quantification of glyoxal, methylglyoxal and 3-deoxyglucosone in blood and plasma by ultra performance liquid chromatography tandem mass spectrometry: evaluation of blood specimen. *Clin Chem Lab Med.* (2014) 52:85–91. doi: 10.1515/cclm-2012-0878
28. Uchiyama S, Inaba Y, Kunugita N. Derivatization of carbonyl compounds with 2, 4-dinitrophenylhydrazine and their subsequent determination by high-performance liquid chromatography. *J Chromatogr B.* (2011) 879:1282–9. doi: 10.1016/j.jchromb.2010.09.028
29. Zhang Y, Wang Q, Huang M, Chen X. Unravelling the effect of flavonoids on the kinetic profiles of acrylamide in the Maillard reaction. *RSC Adv.* (2015) 5:84084–92. doi: 10.1039/C5RA14692E
30. Yu H, Zhong Q, Xie Y, Guo Y, Cheng Y, Yao W. Kinetic study on the generation of furosine and pyrrolidine in a maillard reaction model system of D-glucose and L-lysine. *Food Chem.* (2020) 317. doi: 10.1016/j.foodchem.2020.126458
31. Chen X-M, Kitts DD. Identification and quantification of alpha-dicarbonyl compounds produced in different sugar-amino acid Maillard reaction model systems. *Food Res Int.* (2011) 44:2775–82. doi: 10.1016/j.foodres.2011.06.002
32. Brathen E, Kita A, Knutsen SH, Wicklund T. Addition of glycine reduces the content of acrylamide in cereal and potato products. *J Agric Food Chem.* (2005) 53:3259–64. doi: 10.1021/jf048082o
33. Furrer A, Cladis DP, Kurilich A, Manoharan R, Ferruzzi MG. Changes in phenolic content of commercial potato varieties through industrial processing and fresh preparation. *Food Chem.* (2017) 218:47–55. doi: 10.1016/j.foodchem.2016.08.126
34. Rydberg P, Eriksson S, Tareke E, Karlsson P, Ehrenberg L, Tornqvist M. Investigations of factors that influence the acrylamide content of heated foodstuffs. *J Agric Food Chem.* (2003) 51:7012–8. doi: 10.1021/jf034649+
35. Wang HY, Qian H, Yao WR. Melanoidins produced by the mail lard reaction: structure and biological activity. *Food Chem.* (2011) 128:573–84. doi: 10.1016/j.foodchem.2011.03.075
36. Mestdagh F, Maertens J, Cucu T, Delporte K, Van Peteghem C, De Meulenaer B. Impact of additives to lower the formation of acrylamide in a potato model system through pH reduction and other mechanisms. *Food Chem.* (2008) 107:26–31. doi: 10.1016/j.foodchem.2007.07.013
37. Friedman M. Chemistry, biochemistry, and safety of acrylamide. a review. *J Agric Food Chem.* (2003) 51:4504–26. doi: 10.1021/jf030204%2B

Conflict of Interest: The authors declare that the research was conducted in the absence of any commercial or financial relationships that could be construed as a potential conflict of interest.

Publisher's Note: All claims expressed in this article are solely those of the authors and do not necessarily represent those of their affiliated organizations, or those of the publisher, the editors and the reviewers. Any product that may be evaluated in this article, or claim that may be made by its manufacturer, is not guaranteed or endorsed by the publisher.

Copyright © 2022 Chen, Jiao, Zeng, He, Shen, Chen and Quan. This is an open-access article distributed under the terms of the Creative Commons Attribution License (CC BY). The use, distribution or reproduction in other forums is permitted, provided the original author(s) and the copyright owner(s) are credited and that the original publication in this journal is cited, in accordance with accepted academic practice. No use, distribution or reproduction is permitted which does not comply with these terms.



Sodium Ions Affect Pyrraline Formation in the Maillard Reaction With Lys-Containing Dipeptides and Tripeptides

Zhili Liang^{1*}, Xu Chen², Zhao Yang¹, Yan Liu¹, Xueying Qiu¹, Zhenzhen Zeng¹, Shuidi Lu¹ and Yuehan Liu¹

¹ School of Food Science, Guangdong Food and Drug Vocational College, Guangzhou, China, ² Engineering Research Center of Health Food Design and Nutrition Regulation, School of Chemical Engineering and Energy Technology, Dongguan University of Technology, Dongguan, China

OPEN ACCESS

Edited by:

Hao Dong,
Zhongkai University of Agriculture and
Engineering, China

Reviewed by:

Xia Zhang,
South China University of
Technology, China
Di Zhao,
Nanjing Agricultural University, China
Yueliang Zhao,
Shanghai Ocean University, China

*Correspondence:

Zhili Liang
liangzl@gdzy.edu.cn

Specialty section:

This article was submitted to
Food Chemistry,
a section of the journal
Frontiers in Nutrition

Received: 12 February 2022

Accepted: 25 February 2022

Published: 25 March 2022

Citation:

Liang Z, Chen X, Yang Z, Liu Y, Qiu X,
Zeng Z, Lu S and Liu Y (2022) Sodium
Ions Affect Pyrraline Formation in the
Maillard Reaction With Lys-Containing
Dipeptides and Tripeptides.
Front. Nutr. 9:874650.
doi: 10.3389/fnut.2022.874650

Advanced glycation end products (AGEs) are potentially-hazardous chemical compounds, produced by the Maillard reaction between reducing sugars and Lysine side-chain amino groups in proteins. AGEs are strongly associated with diabetes, Alzheimer's disease and atherosclerosis. Pyrraline, a sugar derivative of Lysine, is a major AGE and an established marker for the presence of dietary AGEs. In this study, the effects of NaCl and different dipeptide and tripeptide structures were compared on the formation of pyrraline-containing peptides and the glucose derivative 3-deoxyglucosone in the presence of glucose and at different NaCl concentrations. The physicochemical properties (polarizability, dipole moment, molecular volume and dissociation constant) and the thermodynamic properties of the peptides were determined. The amount of the pyrraline decreased significantly in the following order of peptides (at the same concentrations): Lys-Phe > Lys-Ala > Lys-Gly; Lys-Gly-Phe > Lys-Gly-Ala > Lys-Gly-Gly. The highest levels of both pyrraline and 3-deoxyglucosone occurred at 0.2 mol/L Na⁺. Sodium ions appear to alter the intramolecular electron density and charge distribution of the peptides and facilitate the reaction by stabilizing some of the intermediates in the reaction sequence.

Keywords: advanced glycation end products, Maillard reaction, pyrraline, salt, peptides

INTRODUCTION

The Maillard reaction (MR) is a complex series of reactions, first proposed by Louis Camille Maillard in 1912, which occurs during cooking of any food that contains both sugars and protein. It is a non-enzymatic condensation reaction between the carbonyl group of a reducing sugar and the primary amine of the Lysine side-chain in protein. The MR is very useful to the food industry because it contributes desirable brown colors, aromas and flavors during thermal food processing (1). However, thermal processing accompanied by the MR can also lead to the formation of potentially-harmful reaction products, such as advanced glycation end products (AGEs). Dietary AGEs can accumulate in the body and have a harmful effect on human health (2). Pyrraline is a

major AGE, arising from a MR of the Lysine side-chain amino group, which is commonly detected in food products and is often used as an indicator of the degree of damage caused by heat treatment of foods (3). Pyrraline is easily absorbed from the human digestive system into the body (4, 5) and contributes to chronic diseases, such as diabetes, Alzheimer's disease and atherosclerosis (6, 7).

Pyrraline is commonly found in a wide range of foods. Pyrraline in milk and whey protein powders can reach 3.1 g/kg protein, and is easily transferred to processed foods made from these ingredients (8). Pyrraline can reach 3.7 g/kg protein in bakery products, especially in the outer crust of bread and cookies, 20–140 mg/kg protein in pasta (9, 10), up to 378 mg/kg protein in processed carrots and up to 382 mg/kg protein in roasted peanuts (11). The pyrraline content in processed carrots and roasted peanuts is much higher than those of other AGEs (12), indicating that pyrraline is the major AGE in many foods, and therefore, a good representation of influences on AGE formation in general.

In addition to amino acids, peptides, proteins and sugars, inorganic salts are also an important factor influencing the MR pathway. The presence of metal ions (especially Fe^{2+} and Cu^{2+}) in foods accelerates the MR and increases browning, whereas the presence of high concentrations of NaCl inhibits browning (13). Addition of Ca^{2+} to an asparagine/glucose model system inhibited acrylamide formation, but promoted the production of 5-hydroxymethyl furfural and furan (14, 15). Increasing the concentration of NaCl in a wheat-dough cooking-model reduced acrylamide production (16), but NaCl only decreased acrylamide formation at concentrations of 1–2% w/w, above 2% w/v, it increased acrylamide formation (17). These findings suggest that inorganic salts are an important factor influencing the rate and mechanism of the MR, but there are no systematic studies on the influence of inorganic salts on AGE formation.

In most foods, the content of free amino acids is much lower than that of peptides and proteins (18), therefore, the content of protein-pyrraline and peptide-pyrraline conjugates in foods would be much higher than that of free pyrraline. However, the complexity of protein structure is a serious impediment to studying the effect of protein structure on pyrraline formation. After protein digestion and hydrolysis in the intestine, proteins, are absorbed in the form of free amino acids and short peptides containing 2–4 amino acid residues. Peptide-pyrraline is produced by a MR between the side chain amino group of a lysine residue in a protein or peptide and 3-deoxyglucosone (3-DG), a derivative of glucose, or glucose itself. The spatial structure and charge distribution of lysine can be influenced by adjacent amino acids (19, 20), thus affecting the rate of pyrraline formation. Therefore, this study investigated the influence of sodium ions on the formation of peptide-AGEs by the MR. The effects of different di- and tri-peptide structures on the production of their corresponding peptide-AGEs were compared at various sodium ion concentrations. The physicochemical properties (polarizability, dipole moment, molecular volume and dissociation constant) and thermodynamic properties of the peptides were calculated, to characterize the resulting peptide-AGEs.

MATERIALS AND METHODS

Chemicals and Reagents

The three dipeptides (Lys-Gly, Lys-Ala, Lys-Phe) and three tripeptides (Lys-Gly-Gly, Lys-Gly-Ala, Lys-Gly-Phe) were from LifeTein LLC. (Beijing, China). Standards of 3-Deoxyglucosone (3-DG, purity > 99.99%) and pyrraline (purity > 99.99%) were from Toronto Research Chemicals (Toronto, ON, Canada). Formic acid (for LC-MS, 99%) was from Aladdin Biochemical Technology Co., Ltd. (Shanghai, China). Solid-phase extraction (SPE) cartridges (Cleanert PEP-2, 200 mg/6 ml) for purification were from Bonna-Agela Technologies Co., Ltd. (Tianjin, China). Chromatographic grade acetonitrile was from Merck (Darmstadt, Germany). Pepsin, pronase E, and prolidase were from Sigma-Aldrich (Shanghai, China). All other reagents were of analytical grade from Macklin Inc. (Shanghai, China).

Glucose–Peptide–NaCl Model Systems

Six sodium chloride solutions of concentration 0.0, 0.1, 0.2, 0.3, 0.4, and 0.5 mol/L were prepared. Peptide solution (50 mM, 0.3 ml) and glucose solution (50 mM, 0.3 ml) were added to a 25-ml polytetrafluoroethylene (PTFE)-lined hydrothermal autoclave reactor (Tefic Biotech Co., Xi'an, China), then, the mixture was diluted to 15 ml with one of the sodium chloride solutions. The final concentrations of each peptide (Lys-Gly, Lys-Ala, Lys-Phe; Lys-Gly-Gly, Lys-Gly-Ala, Lys-Gly-Phe) and glucose were 1 mM. The autoclave reactor was sealed, then heated in an oil bath at 140°C for 20 min. All reactions were performed in triplicate.

After the heat treatment, the autoclave reactor was immediately cooled to room temperature in an ice/water bath, unsealed, then *o*-Phenylenediamine solution (OPD, 5 mol/L, 0.1 ml) was added to terminate the reaction, by combining with any remaining reducing sugars.

To facilitate the determination of the pyrraline content of peptides, enzymatic digestion of the peptides was performed as described previously (21). Briefly, an aliquot (~2 mg protein equivalent) of the reaction solution was removed, the pH adjusted to two and the peptide digested with pepsin solution (1 FIP-U/sample) at 37°C for 24 h. Next, the pH was adjusted to 7.5 and the peptide further digested with pronase E (400 PU/sample) at 37°C for 24 h, followed by addition of aminopeptidase (0.4 U/sample) and prolidase (1 U/sample) and the digestion continued at 37°C for 24 h. After complete enzymatic digestion, the solution was centrifuged ($7,840 \times g$, 25 min) and the supernatant retained for solid phase extraction, as described previously (22).

Instrumental Analysis Methods

The concentrations of pyrraline, 3-DG and lysine were determined using LC-MS in multiple ion monitoring mode, as described previously (22, 23). The pyrraline concentration was determined at M/z 255.13, 3-DG quinoxaline at M/z 235.10, and lysine at M/z 147.11. Quantitative calibration curves were constructed by comparison with an external standard mixture of pyrraline, 3-DG and lysine.

Peptide Content Determination

Since the six peptides selected had only one lysine residue in their structures, the molar concentration of lysine in each sample after complete hydrolysis was equal to the concentration of the remaining peptide in the system after the MR.

Calculation of Physico-Chemical and Thermodynamic Parameters

The four physicochemical parameters used to characterize the peptides were polarizability, dipole moment, volume and pK_a . The volume was calculated by Multiwfn software, using the Marching Tetrahedron algorithm (24). The polarizability and dipole moment calculations were performed using ORCA version 4.2.1 software (25) at the B3LYP-D3/def2-TZVP level of theory, and the energy-related parameter calculations at the B3LYP/6-311++G(d,p) level in the SMD water solvent model.

For a deprotonation reaction, $AH \rightleftharpoons A^- + H^+$, the pK_a was calculated as follows:

$$pK_a = \frac{\Delta G_{aq}^{1M}}{2.303RT}$$

where R is the gas constant, T is the temperature (298.15 K), and ΔG_{aq}^{1M} is the aqueous phase free energy change for the deprotonation reaction.

For the proposed reaction of peptide-sodium complex formation, $\text{peptide} + Na^+ \rightleftharpoons \text{peptide} \sim Na^+$, the change in energy after the reaction was calculated as follows:

$$\Delta G = G_{\text{peptide} \sim Na^+} - (G_{\text{peptide}} + G_{Na^+})$$

Statistical Analysis

Analysis of variance (ANOVA) of data was calculated using Origin 9.0 program (OriginLab Co., Northampton, MA, USA); comparison of means was performed by ANOVA and Duncan's multiple range test ($p < 0.05$).

RESULTS

Calculated Physico-Chemical and Thermodynamic Properties of the Peptides

The peptides all had an N-terminal Lys and a C-terminal Gly, Ala, or Phe, with the tripeptides having an additional Gly in the middle position (Figure 1); these different sequences were chosen to maximize the differences in their influence on pyrroline formation during the MR. The polarizability, dipole moment and molecular volume of the three dipeptides increased in the order, Lys-Gly, Lys-Ala and Lys-Phe, as did those of the three tripeptides, Lys-Gly-Gly, Lys-Gly-Ala and Lys-Gly-Phe and the values for the tripeptides were all higher than the corresponding dipeptide (Table 1). In contrast, the pK_a values had the opposite trend and the tripeptides had lower values.

The dipole moment is the product of the distance between the positive and negative charge centers and the charge carried by each charge center, so it is a vector quantity with the direction specified as pointing from the positive to the negative charge. The calculated dipole moment values and vector orientations of

the peptides are shown in Figure 2 and those of the proposed peptide-sodium complexes in Figure 3.

For the proposed sodium complex formation, $\text{peptide} + Na^+ \rightleftharpoons \text{peptide} \sim Na^+$, the ease with which each peptide forms a transition-state, or intermediate with Na^+ was determined by calculating the enthalpy change of the complex. The descending order of enthalpy changes was: Lys-Gly-Phe (−79.31 KJ/mol) > Lys-Gly-Ala (−61.45 KJ/mol) > Lys-Gly-Gly (−57.07 KJ/mol); Lys-Phe (−76.25 KJ/mol) > Lys-Ala (−65.08 KJ/mol) > Lys-Gly (−58.30 KJ/mol). 76.25 KJ/mol > Lys-Ala (−65.08 KJ/mol) > Lys-Gly (−58.30 KJ/mol) (Figure 4). However, comparing each dipeptide and its corresponding tripeptide, the enthalpy changes were small and did not show a consistent trend: Lys-Gly-Gly (−57.07 KJ/mol) > Lys-Gly (−58.30 KJ/mol), Lys-Gly-Ala (−61.45 KJ/mol) < Lys-Ala (−65.08 KJ/mol), Lys-Gly-Phe (−79.31 KJ/mol) > Lys-Phe (−76.25 KJ/mol).

Pyrroline Formation

The extent of pyrroline formation was determined analytically after the reaction between the peptides and glucose in the presence of 0.0 to 0.5 mol/L (Figure 5). Very little pyrroline (0.060 ± 0.002 mmol/mol lysine) was produced in the absence of Na^+ , but the pyrroline content increased markedly with Na^+ present, with a maximum at 0.2 mol/L.

Comparing the different peptides, the pyrroline content was markedly higher in the Phe-containing peptides than the others (Supplementary Table S1 in the Supplementary Information) and very significantly higher in the dipeptide reactions than the tripeptide reactions at a given Na^+ concentration (except for 0.0 mol/L Na^+) (Figure 5). A study of pyrazine formation during the MR found, similarly, that reaction mixtures containing dipeptides produced more pyrazine compared with those containing tripeptides (26).

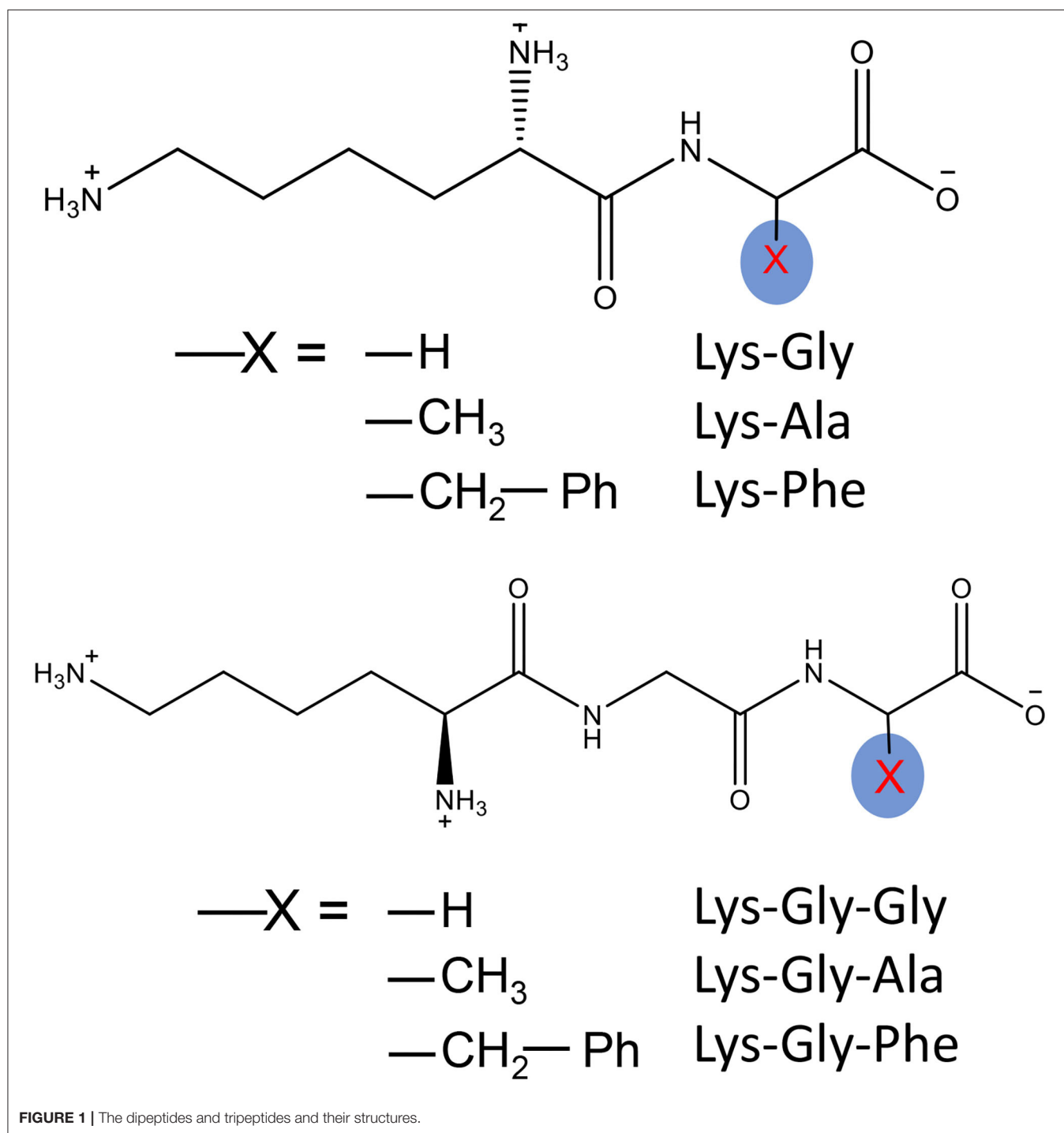
The findings from this study suggest that the C-terminal amino acid of the peptide has a major influence on pyrroline formation. Although the N atom in the pyrrole ring in pyrroline is derived from the ϵ -NH₂ of lysine, the reactivity of the ϵ -NH₂ appears to be strongly influenced by the physicochemical properties of the adjacent amino acid residues.

3-Deoxyglucosone Formation

3-DG is a dicarbonyl compound derived from glucose and is thought to be an important intermediate in the formation of pyrroline and browning during the MR.

3-DG formation during reactions of peptides with glucose, with and without Na^+ was determined (Figure 6). Very little 3-DG (0.060 ± 0.012 mmol/mol glucose) was produced in the absence of Na^+ , but the 3-DG content increased markedly with Na^+ present, with a maximum at 0.2 mol/L.

Comparing the different peptides, the 3-DG content was very significantly higher in the dipeptide reactions than the tripeptide reactions, at a given Na^+ concentration (except for 0.0 mol/L Na^+). The 3-DG content was strongly influenced in the following order of the amino acid residues adjacent to lysine: Phe > Ala > Gly (Supplementary Table S2 in the Supplementary Information), however, the differences in 3-DG



content between Phe and the others were smaller than the corresponding differences in pyrraline content (**Figure 5**).

There are two main mechanisms of 3-DG formation during the MR; one is the direct degradative rearrangement reaction of sugar, without involvement of amino groups (27). The other is Schiff's base formation between amino groups and glucose, followed by Amadori rearrangement to a 3-DG residue,

containing a keto-amine group *via* the 1,2-enol pathway (28). However, the occurrence of sugar cleavage reactions is very limited in the absence of amine groups, so 3-DG formation by the Amadori rearrangement predominates. In the initial stages of MR, the Schiff bases are formed from an aldose and an amine group. If the activity of the amine groups involved in the MR is expressed in terms of the conversion rate of glucose involved

TABLE 1 | Calculated physicochemical properties of the peptides.

Peptide	Polarizability (α) ($\times 10^{-25}$ esu)	Dipole Moment (Debye)	Volume (\AA^3)	pK _a
Lys-Gly	257.89	45.90	316.57	7.64
Lys-Ala	283.46	55.42	322.70	7.29
Lys-Phe	431.95	57.59	453.34	7.26
Lys-Gly-Gly	326.49	59.43	389.94	6.92
Lys-Gly-Ala	350.68	51.57	417.16	6.91
Lys-Gly-Phe	501.96	69.72	526.29	6.90

in Schiff's base formation, the order of reactivity of glucose with various glycine polymers is: glycine dimer > glycine trimer > glycine (27).

It appears that the pathway by which glucose reacts with the peptide to form a Schiff's base and subsequently 3-DG, is influenced by the peptide structure. Thus, the amount of 3-DG formed in the various peptide-glucose mixtures may be influenced by the amino acid residues close to lysine in the peptide and their effects on the Amadori rearrangement of the Schiff base to 3-DG.

Consumption of Peptides During the MR

Consumption of peptide by the MR should be related to the formation of pyrraline and 3-DG. In the absence of Na⁺, low peptide consumption was observed (mean $6.2 \pm 0.5\%$) (Figure 7) and there was no significant difference between the six peptides. Peptide consumption increased markedly in the presence of Na⁺, reaching a maximum at 0.2 mol/L Na⁺, then plateauing at higher concentrations with all peptides. Lys-Phe consumption (~72%) was markedly higher than that of the other dipeptides (~23%), whereas Lys-Gly-Phe consumption was considerably higher (~97%), but not greatly different from that of the other tripeptides (~80%).

A comparison of peptide consumption with pyrraline-peptide formation (Figures 5A vs. 7A; Figures 5B vs. 7B) revealed a weak correlation, i.e., high consumption of non-Phe peptides resulted in relatively much lower pyrraline-peptide formation than from Phe peptides. Although the reaction between amine groups and glucose can produce pyrraline, it can also produce many other compounds by aldol-amine condensation at the later stages of the MR and the diversity and structural complexity of these other MR products (29) makes their quantification, relative to pyrraline, impractical.

DISCUSSION

Effect of Peptide Structures on the Maillard Reaction

Chemically, pyrraline is the 2-formyl-5-(hydroxymethyl)pyrrole derivative of lysine. It is generally formed in the late stages of the MR by the reaction of the ϵ -NH₂ amino group of lysine with glucose, followed by structural rearrangement, or 1, 2-dicarbonyl

compounds generated by structural rearrangement of glucose, in particular by the reaction with 3-DG (21, 30, 31).

In summary, the formation of peptide-pyrralines was mainly influenced by and correlated with the polarizability of the starting peptide (Figure 5 and Table 1). There is a positive correlation between the polarizability and the flexibility of the peptide (32–35). In addition, polarizability is an important quantitative indicator of the tendency of nucleophilic reagents to participate in reactions; nucleophilic reactions usually follow the “decreasing polarizability” rule, i.e., they tend to proceed in the direction of decreasing polarizability (36).

During the early stages of the MR, the carbonyl group of the reducing sugar undergoes a condensation reaction with the nucleophilic ϵ -NH₂ amino group of Lys, to form a Schiff's base, followed by an Amadori rearrangement to form a keto-amine. Therefore, the polarizability of the amino acid close to the lysine has a strong influence on the rate of Schiff's base formation because it influences the nucleophilicity of the Lysine ϵ -NH₂ amino group (37–39). According to Pearson's hard and soft acids and bases (HSAB) principle (40), peptides with high polarizability (e.g., Lys-Phe and Lys-Gly-Phe) have higher reactivity with polarizable substrates (e.g., carbonyl groups of glucose), whereas peptides with low polarizability (e.g., Lys-Gly, Lys-Gly-Gly) are less reactive. Polarizability also correlated with the ease of formation of the peptide-sodium complexes (Figure 3). Therefore, Schiff's base formation and rearrangement to produce 3-DG during the early stages of the MR are accelerated by increased peptide polarizability. In addition, the reaction of 3-DG with a peptide to form peptide-pyrralines, during the later stages of the MR is similarly accelerated, because differences in peptide structure affect the electron cloud density and distribution of the whole peptide molecule.

There was a strong positive correlation between the size of the C-terminal amino acid (Phe \gg Ala > Gly) and the molecular volume of the peptide (Figure 1 and Table 1). Molecular volume is an indicator of potential steric hindrance, or blockage of a reactive center, which can result in a reduction in its reactivity (41). Although both the Lysine α -NH₂ and ϵ -NH₂ can be involved in the MR, and the reactivity of the α -NH₂ is higher than that of ϵ -NH₂ (31), the pyrraline structure can only be derived from the reaction of 3-DG with the ϵ -NH₂. In Lys-Phe and Lys-Gly-Phe, the large volume of the phenyl side-chain sterically hinders the reactivity of the α -NH₂ of lysine, whereas the more distant ϵ -NH₂ is much less affected by steric hindrance. The probability of α -NH₂ being involved in the MR is reduced, while the probability of ϵ -NH₂ is not affected. There is an increased probability that the MR will proceed along the pyrraline formation pathway. Therefore, the Phe-containing dipeptides and tripeptides are more likely to form peptide-pyrralines. In addition, the peptide may undergo degradation under high temperature conditions, but the large Phe side chain in Lys-Phe and Lys-Gly-Phe help to stabilize the peptide by cation- π interaction (42). It appears that peptides with Phe side chain are more conducive to peptide-pyrraline formation.

The acid dissociation constant represents the ability of a substance to dissociate from hydrogen ions or protons. For the deprotonation reaction $\text{AH} \rightleftharpoons \text{A}^- + \text{H}^+$, the pK_a value

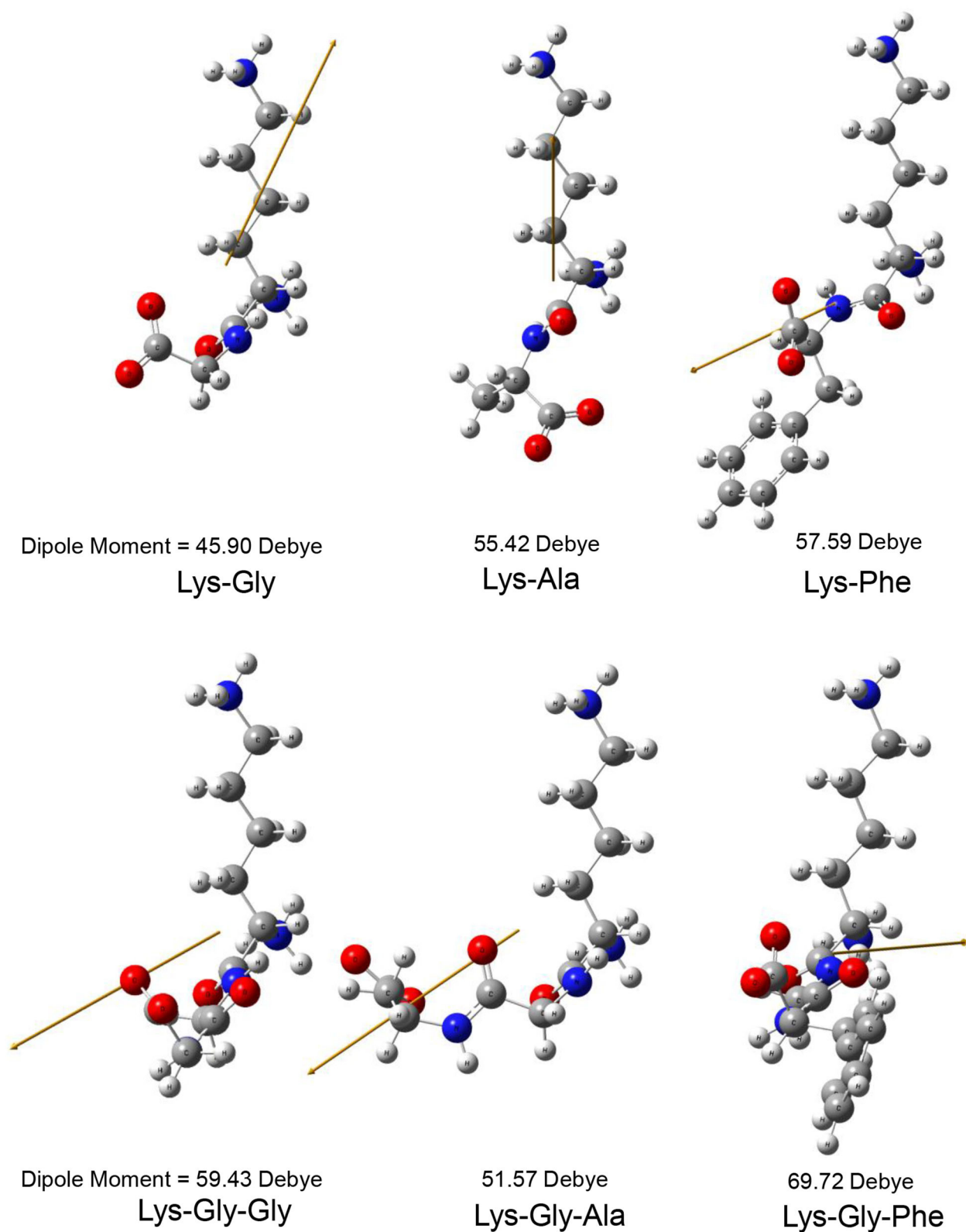


FIGURE 2 | Steric structure of peptides and their dipole moments (the yellow arrow represents the dipole derivative unit vector).

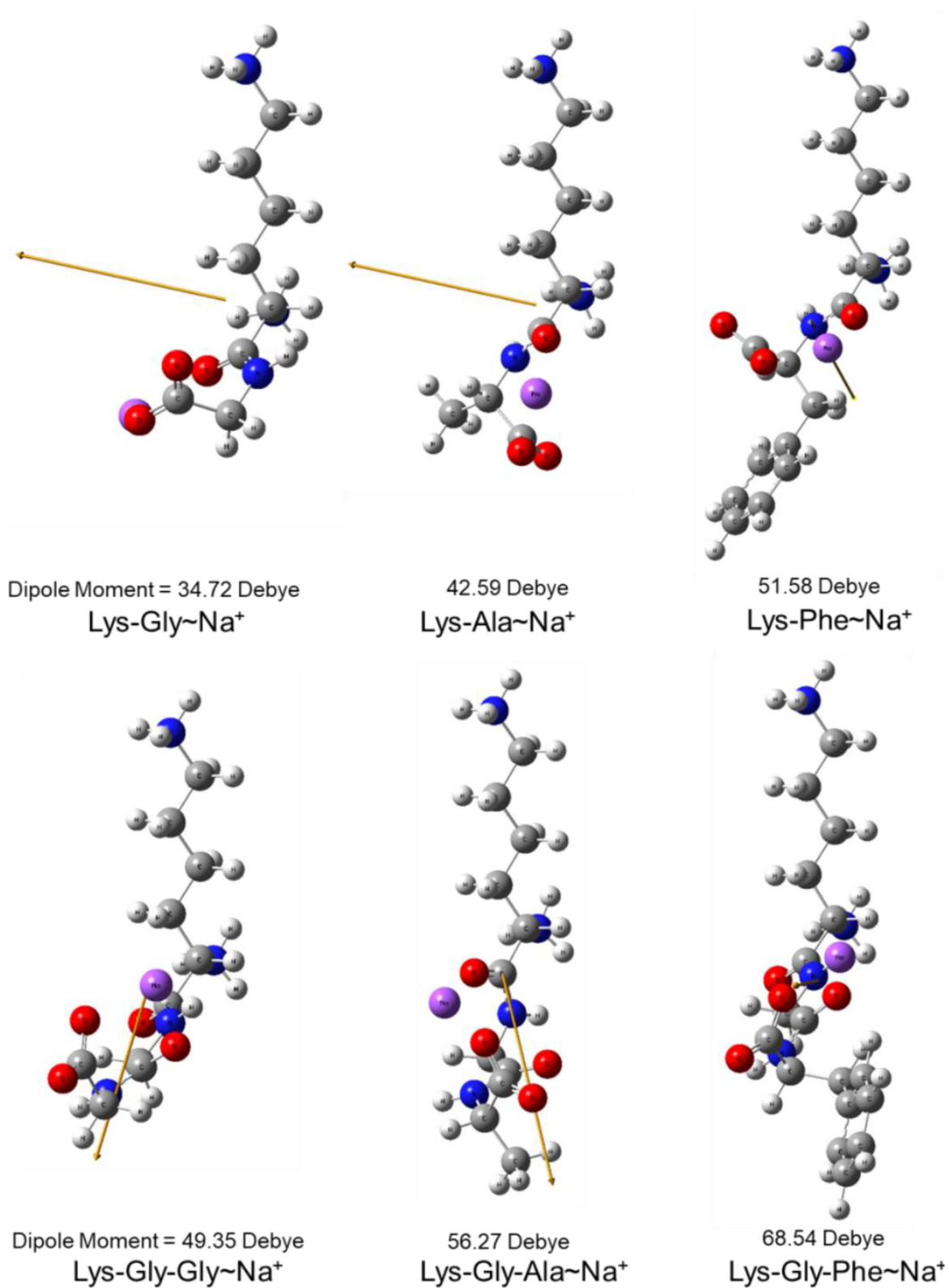
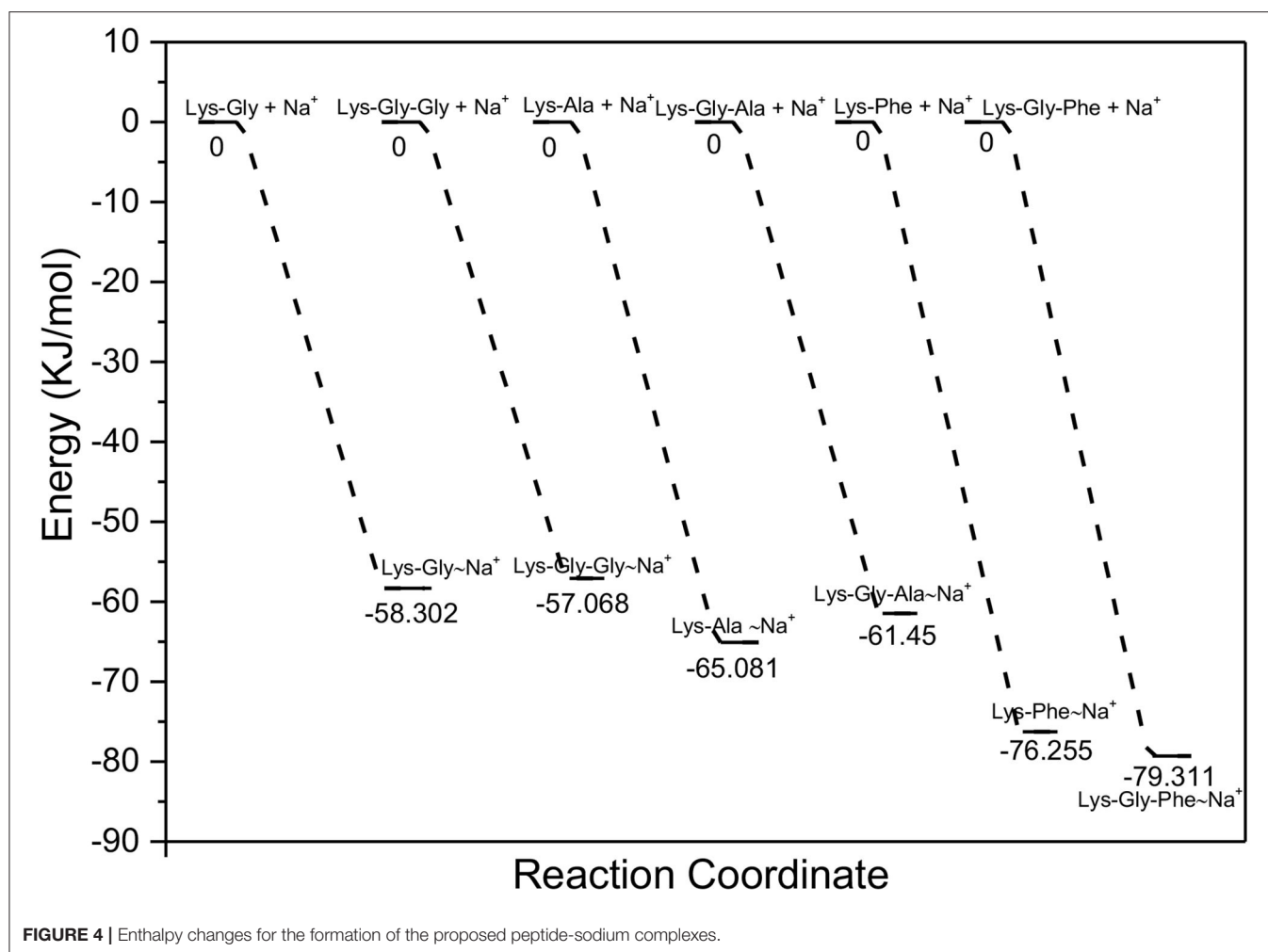


FIGURE 3 | Steric structure of proposed peptide-sodium complexes and their dipole moments (the yellow arrow represents the dipole derivative unit vector and the Na⁺ ion is highlighted in purple).



is reduced when the interaction of molecules is biased toward the deprotonated state (A^-) ($[A^-]$ to $[AH]$ ratio increases). Conversely, the pK_a value is raised when the molecular interaction is biased toward the protonated state (AH). For the three dipeptides and tripeptides, the order of their pK_a values is: Lys-Gly > Lys-Ala > Lys-Phe \gg Lys-Gly-Gly > Lys-Gly-Ala > Lys-Gly-Phe. This order also represents their ability to be deprotonated, i.e., the probability of presenting a deprotonated state under the same conditions. In neutral solutions, the α -NH₂ and ϵ -NH₂ on the lysine residues in the various peptide structures are in the positive ionic form. They are present in non-positive ionic form only after a deprotonation reaction has occurred. Therefore, peptides with high pK_a values under the same conditions also have a higher number of non-ionic N in their structure. Yamaguchi's findings show that the reaction of amino acids with glucose is difficult to occur when the amino acid residues are in positive ionic form (43). The reaction in the early stages of the MR is the nucleophilic addition of N to the carbonyl group, which must be in the non-ionic form (i.e., protonated state) at the N terminus. The rate of the amino-carbonyl reaction

in the MR depends on the lone pair of electrons, whereas non-ionic amino acids have a lone pair of electrons on N, which is more conducive to the MR. These are also important factors in explaining the formation of pyrroline (Figure 5) and 3-DG (Figure 6).

Differences in hydrophobicity may also contribute to the differences in pyrroline and 3-DG formation between the different peptides. Hydrophobic interactions between apolar molecules or apolar parts of molecules in aqueous solutions can accelerate organic chemical reactions, probably because they destabilize the initial state of the reaction and promote the formation of the reaction transition state, which accelerates the reaction (44).

As is apparent from Figure 1, the hydrophobicity of the peptides is in the following order: Lys-Phe > Lys-Ala > Lys-Gly; Lys-Gly-Phe > Lys-Gly-Ala > Lys-Gly-Gly. Peptides containing Ala and Phe, especially those containing Phe, produced more peptide-pyrroline, therefore, peptides with higher hydrophobicity may contribute to enhanced peptide-pyrroline formation.

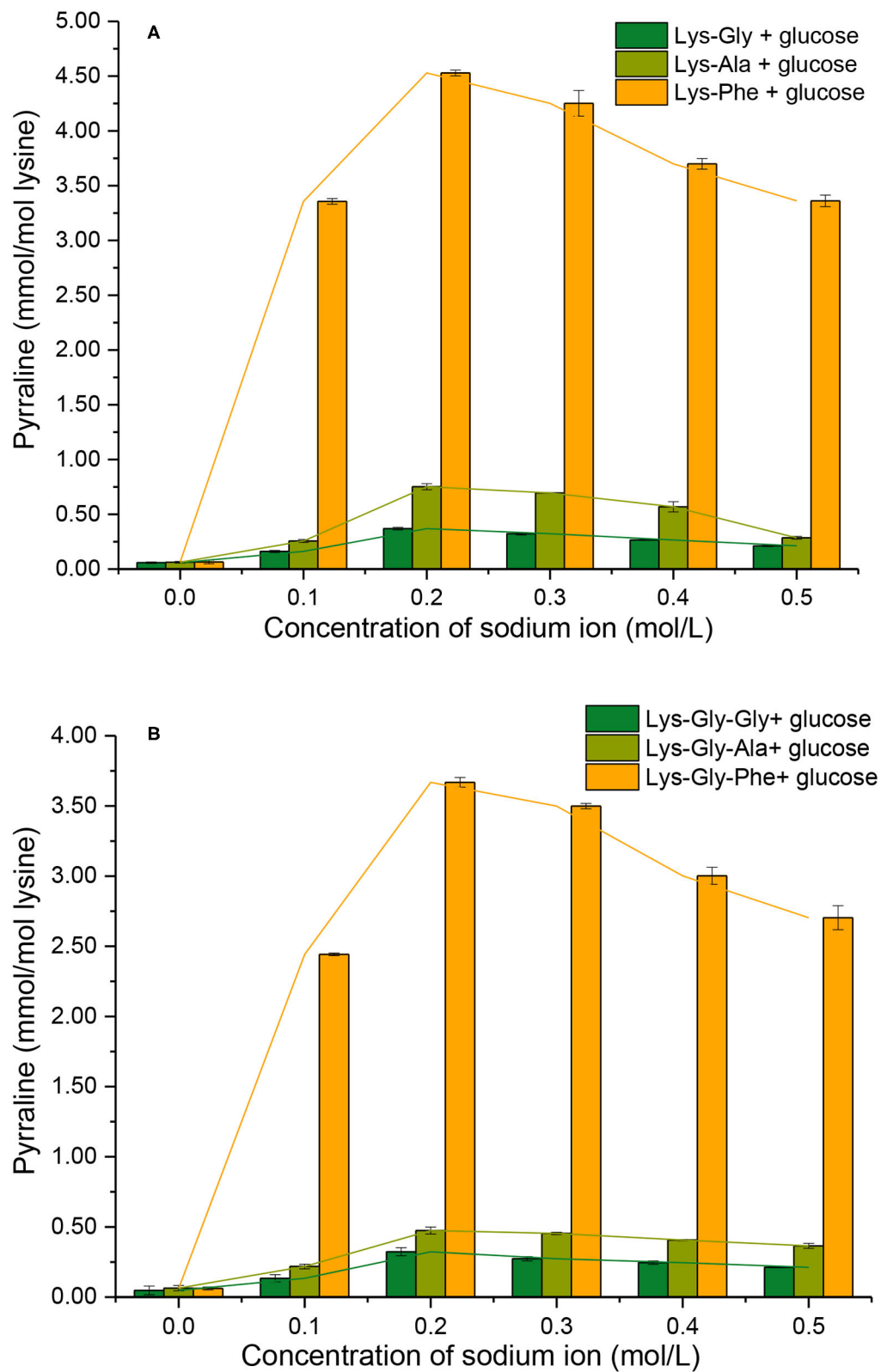


FIGURE 5 | Pyrroline formation during the Maillard reaction of peptides with glucose at different sodium ion concentrations [(A): in the mixtures containing dipeptides; (B): in the mixtures containing tripeptides].

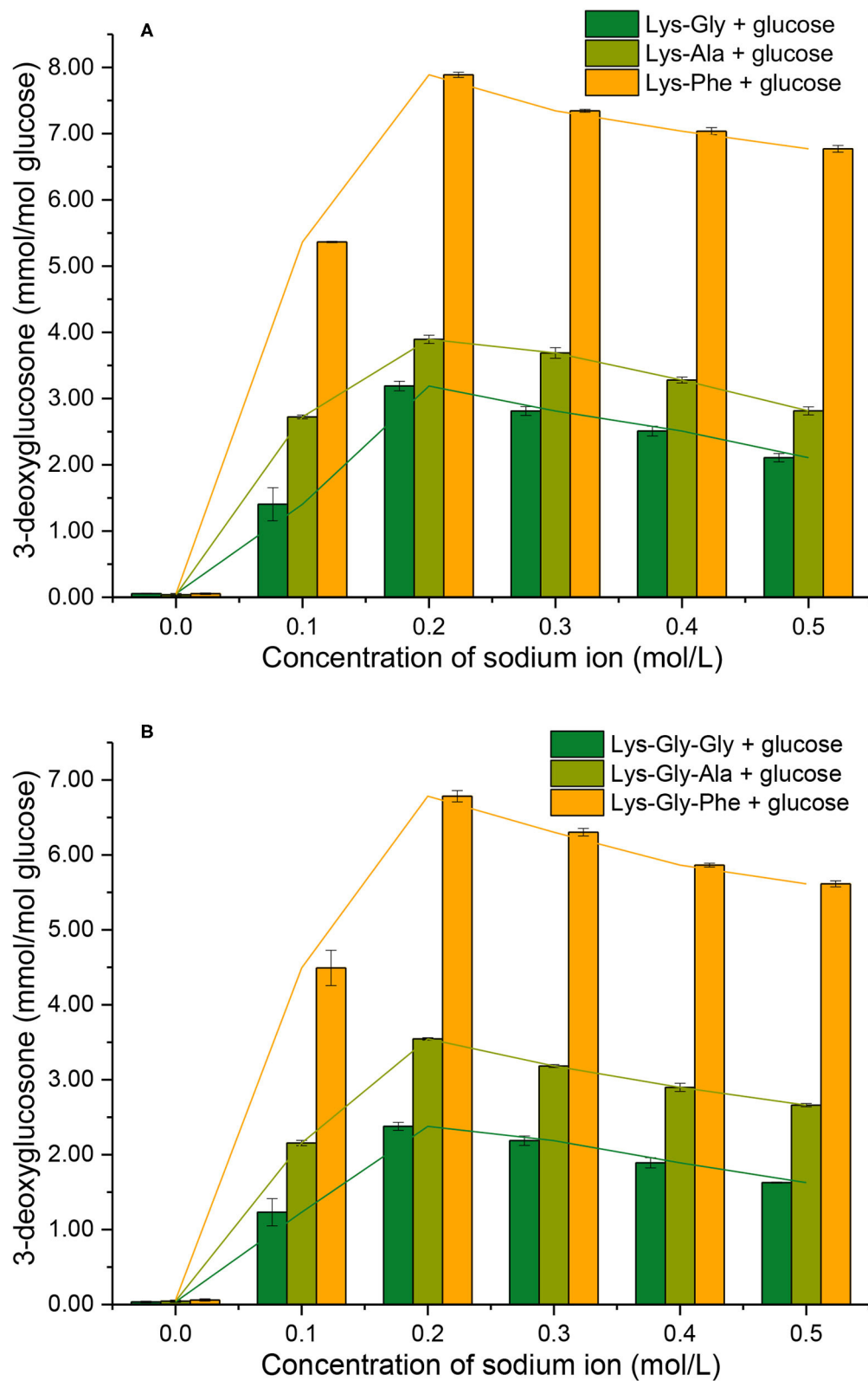


FIGURE 6 | 3-deoxyglucosone formation from the Maillard reaction of peptides with glucose at different sodium ion concentrations [(A): in the mixtures containing dipeptides; (B): in the mixtures containing tripeptides].

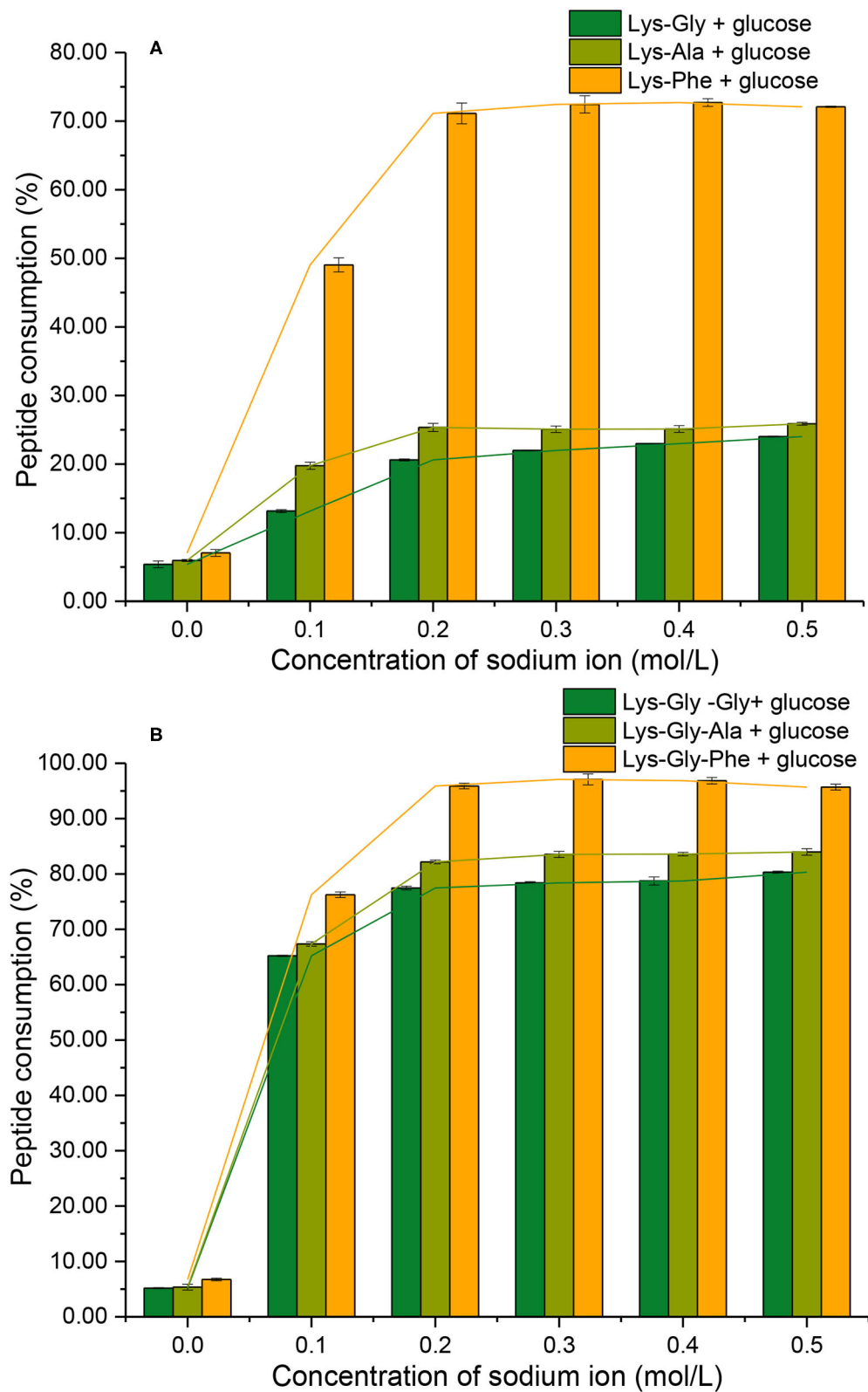


FIGURE 7 | Peptide consumption after the Maillard reaction of peptides with glucose at different sodium ion concentrations [(A): in the mixtures containing dipeptides; (B): in the mixtures containing tripeptides].

Effect of NaCl Concentration on the Reaction

In this study, pyrraline and 3-DG formation, as well as peptide consumption, were markedly accelerated in the presence of Na^+ ions, with the greatest acceleration at 0.2 mol/L Na^+ . Higher Na^+ concentrations produced no further increase, or a small decrease. Nucleophilic and electrophilic organic reactions are influenced by changes in intramolecular electron density distribution and the main mode of action of metal ion catalysts is to initiate such electron density changes. Metal ions induce major electron density changes when coordinated with organic substrates, so that reactions dependent on electron rearrangement may be promoted by metal ions (45). Even in concerted reactions, metal ions can perturb the rate coefficients by more than an order of magnitude, through interactions with charge-separated transition states (46–49) and may accelerate, or inhibit the reaction. The rate of most of reaction steps of glucose pyrolysis increased, which is consistent with the experimental observation that the rate of reaction increases in the presence of inorganic salts (50, 51). The reason why high concentrations of NaCl (> 0.2 mol/L) in this study reduced pyrraline and 3-DG formation is not clear. The effectiveness of metal ion catalysis depends not only on the type of reaction, but also on the stereochemistry in and around the reaction center (52). The electric dipole moment measures the separation of the positive and negative charge distribution in the molecular structure, that is, the overall polarity of the molecule and the orientation of the dipole moment is from negative to positive charge. When an Na^+ ion interacted with the peptide structures, the calculated dipole moment values for each peptide changed to varying degrees, and the orientation of the dipole moment also changed markedly (compare **Figures 2, 3**), i.e., the presence of Na^+ markedly altered the charge distributions of the peptides. In addition, there is a greater extent of perturbation of the electronic structure of α -glucose by Na^+ than that of β -glucose. The effect of inorganic salts on glucose cleavage products may cause a shift in the equilibrium ratio of glucose between α - and β -glucose isomers or cause a selective redistribution of electron density in the reaction process (53).

Many reactions require the presence of an “electron sink” in the molecule to absorb the electron density generated by the reaction transition state, or an intermediate species. The reaction between glucose/3-DG and an amino group requires neutralization of the negative charge to reduce electrostatic repulsion (45) and the addition of metal ions may serve this purpose.

It is possible for metal ions to interact electrostatically with both components of a bimolecular reaction, thereby holding them in close proximity and facilitating transition state formation, and may also assist the reaction through an increase in entropy. In addition, nucleophilic substitutions will be accelerated by the presence of a metal ion if both molecules contain a whole or partial negative charge because the electrostatic repulsion between the molecules is reduced. Metal ions can also facilitate the reaction by stabilizing a transition state, or intermediate. In the reaction between glucose/3-DG and an amino group, the Na^+ ion does not interact with the ground

state, but may facilitate the formation and stabilization of an intermediate or a transition state in the reaction sequence (45). This effect, of stabilizing a reaction intermediate or a transition state, is consistent with the negative enthalpy changes calculated for binding of sodium to the peptides (**Figure 4**).

CONCLUSION

This study aimed to increase knowledge of the mechanism of the Maillard reaction (MR), between protein (Lysine) amino groups and reducing sugars, which can produce potentially toxic advanced glycation end products (AGE), such as pyrraline. Comparison of pyrraline and 3-deoxyglucosone (3-DG) yields from different model peptides, in the presence of glucose and various concentrations of NaCl, showed that a highly polarizable amino acid residue (e.g., Phe) close to the reactive Lys residue strongly accelerated the reactions that produce pyrraline and 3-DG, compared with less-polarizable Ala or Gly. However, the dominant influence on these reactions was the presence of NaCl, i.e., sodium ions, which strongly catalyzed the reaction; in the absence of NaCl, there was negligible pyrraline, or 3-DG formed from any model peptide reaction.

The MR mainly occurs during cooking, or other heat treatment of food products containing both sugar and protein, during industrial processing and initially produces both an attractive brown color and desirable flavors, but can also produce undesirable AGEs after extended heating. The findings of this study have two implications for minimizing AGE formation during food processing, thereby minimizing the content of potential toxins. The main one is that the salt concentration in the food should be minimized as much as possible before heat treatment and any salt in the final formulation should be added later. In addition, where practical, proteins with amino acid sequences containing multiple Lys residues, close to a polarizable residue such as Phe, should not be heated in the presence of sugar. These findings may have great utility to the food industry and form the basis for further studies on minimizing AGE formation in processed foods.

DATA AVAILABILITY STATEMENT

The original contributions presented in the study are included in the article/**Supplementary Material**, further inquiries can be directed to the corresponding author/s.

AUTHOR CONTRIBUTIONS

ZL: funding acquisition, investigation, methodology, writing—original draft, and writing—review and editing. XC: conceptualization, funding acquisition, and methodology. ZY: writing—review and editing. XQ, ZZ, SL, YaL, and YuL: investigation and methodology. All authors contributed to manuscript revision, read, and approved the submitted version.

FUNDING

This work was financially supported by the National Natural Science Foundation of China (No. 31801667), Natural Science Foundation of Guangdong Province (No. 2020A1515011341), Dongguan Social Science and Technology Development Key Project in 2021 (20211800904672), the Foundation for Innovation Team in Higher Education of Guangdong, China

REFERENCES

- Xu Y, Li H, Liang J, Ma J, Yang J, Zhao X, et al. High-throughput quantification of eighteen heterocyclic aromatic amines in roasted and pan-fried meat on the basis of high performance liquid chromatography-quadrupole-orbitrap high resolution mass spectrometry. *Food Chem.* (2021) 361:130147. doi: 10.1016/j.foodchem.2021.130147
- Sergi D, Boulestin H, Campbell FM, Williams LM. The role of dietary advanced glycation end products in metabolic dysfunction. *Mol Nutr Food Res.* (2021) 65:1900934. doi: 10.1002/mnfr.201900934
- Hegele J, Parisod V, Richoz J, Förster A, Maurer S, Krause R, et al. Evaluating the extent of protein damage in dairy products. *Ann N Y Acad Sci.* (2008) 1126:300–6. doi: 10.1196/annals.1433.016
- Odani H, Shinzato T, Matsumoto Y, Takai I, Nakai S, Miwa M, et al. First evidence for accumulation of protein-bound and protein-free pyrraline in human uremic plasma by mass spectrometry. *Biochem Biophys Res Commun.* (1996) 224:237–41. doi: 10.1006/bbrc.1996.1013
- Miyata S, Liu B-F, Shoda H, Ohara T, Yamada H, Suzuki K, et al. Accumulation of pyrraline-modified albumin in phagocytes due to reduced degradation by lysosomal enzymes *. *J Biol Chem.* (1997) 272:4037–42. doi: 10.1074/jbc.272.7.4037
- Miyata S, Monnier V. Immunohistochemical detection of advanced glycosylation end products in diabetic tissues using monoclonal antibody to pyrraline. *J Clin Invest.* (1992) 89:1102–12. doi: 10.1172/JCI115690
- Ruiz HH, Ramasamy R, Schmidt AM. Advanced glycation end products: building on the concept of the “common soil” in metabolic disease. *Endocrinology.* (2019) 161:bqz006. doi: 10.1210/endo/bqz006
- Hellwig M, Henle T. Quantification of the maillard reaction product 6-(2-formyl-1-pyrrolyl)-L-norleucine (formyllysine) in food. *Eur Food Res Technol.* (2012) 235:99–106. doi: 10.1007/s00217-012-1738-3
- Henle T, Walter AW, Klostermeyer H. Simultaneous determination of protein-bound maillard products by ion exchange chromatography and photodiode array detection. In: Labuza TP, Reineccius GA, Monnier VM, O'Brien J, Baynes JW, editors. *Maillard Reactions in Chemistry, Food and Health.* Cambridge: Woodhead Publishing (2005). p. 195–200. doi: 10.1533/9781845698393.3.195
- Resmini P, Pellegrino L. Occurrence of protein-bound lysylpyrrolaldehyde in dried pasta. *Cereal Chem.* (1994) 71:254–62.
- Wellner A, Huettl C, Henle T. Formation of maillard reaction products during heat treatment of carrots. *J Agric Food Chem.* (2011) 59:7992–8. doi: 10.1021/jf2013293
- Wellner A, Nußpöckl L, Henle T. Glycation compounds in peanuts. *Eur Food Res Technol.* (2012) 234:423–9. doi: 10.1007/s00217-011-1649-8
- Kwak EJ, Lim SI. The effect of sugar, amino acid, metal ion, and NaCl on model maillard reaction under pH control. *Amino Acids.* (2004) 27:85–90. doi: 10.1007/s00726-004-0067-7
- Gökmen V, Senyuva HZ. Acrylamide formation is prevented by divalent cations during the maillard reaction. *Food Chem.* (2007) 103:196–203. doi: 10.1016/j.foodchem.2006.08.011
- Gökmen V, Senyuva HZ. Effects of some cations on the formation of acrylamide and furfurals in glucose-asparagine model system. *Eur Food Res Technol.* (2007) 225:815–20. doi: 10.1007/s00217-006-0486-7
- Levine RA, Ryan SM. Determining the effect of calcium cations on acrylamide formation in cooked wheat products using a model system. *J Agric Food Chem.* (2009) 57:6823–9. doi: 10.1021/jf901120m
- Claus A, Mongili M, Weisz G, Schieber A, Carle R. Impact of formulation and technological factors on the acrylamide content of wheat bread and bread rolls. *J Cereal Sci.* (2008) 47:546–54. doi: 10.1016/j.jcs.2007.06.011
- Arnoldi A. Thermal processing and nutritional quality. In: Henry CJK, Chapman C, editors. *The Nutrition Handbook for Food Processors.* Cambridge, UK: Woodhead Publishing Ltd (2002). p. 265–92. doi: 10.1533/9781855736658.2.265
- Bukharov MS, Shtyrin VG, Mamin GV, Stapf S, Mattea C, Mukhtarov AS, et al. Structure and dynamics of solvation shells of copper(II) complexes with N,O-containing ligands. *Inorg Chem.* (2015) 54:9777–84. doi: 10.1021/acs.inorgchem.5b01467
- Farkas E, Sóvágó I. Metal complexes of amino acids and peptides. *Amino Acids, Peptides and Proteins, Vol. 41.* Cambridge, UK: The Royal Society of Chemistry (2017). p. 100–51. doi: 10.1039/9781782626619-00100
- Hellwig M, Henle T. Release of pyrraline in absorbable peptides during simulated digestion of casein glycated by 3-deoxyglucosone. *Eur Food Res Technol.* (2013) 237:47–55. doi: 10.1007/s00217-013-2027-5
- Liang Z, Li L, Fu Q, Zhang X, Xu Z, Li B. Formation and elimination of pyrraline in the maillard reaction in a saccharide-lysine model system. *J Sci Food Agric.* (2016) 96:2555–64. doi: 10.1002/jsfa.7376
- Liang Z, Li L, Qi H, Xu Z, Zhang X, Li B. Kinetic study on peptide-bound pyrraline formation and elimination in the maillard reaction using single- and multiple-response models. *J Food Sci.* (2016) 81:C2405–C24. doi: 10.1111/1750-3841.13428
- Lu T, Chen F. Multiwfn: a multifunctional wavefunction analyzer. *J Comput Chem.* (2012) 33:580–92. doi: 10.1002/jcc.22885
- Neese F. The Orca program system. *WIREs Computational Molecular Science.* (2012) 2:73–8. doi: 10.1002/wcms.81
- Van Lancker E, Adams A, De Kimpe N. Impact of the N-terminal amino acid on the formation of pyrazines from peptides in maillard model systems. *J Agric Food Chem.* (2012) 60:4697–708. doi: 10.1021/jf301315b
- de Kok PMT, Rosing EAE. Reactivity of peptides in the maillard reaction. In: Parliment TH, Morello MJ, Mc Gorrin RJ, editors. *Thermally Generated Flavors.* ACS Symposium Series, Vol. 543. Washington, D.C: American Chemical Society (1993). p. 158–79. doi: 10.1021/bk-1994-0543.ch013
- Tressl R, Rewicki D. Heat generated flavors and precursors. In: Teranishi R, Wick EL, Hornstein I, editors. *Flavor Chemistry: Thirty Years of Progress.* Boston, MA: Springer US (1999). p. 305–25. doi: 10.1007/978-1-4615-4693-1_26
- Nursten HE. *The Maillard Reaction: Chemistry, Biochemistry, and Implications.* Cambridge, UK: Royal Society of Chemistry (2005).
- Nakayama T, Hayase F, Kato H. Formation of epsilon-(2-formyl-5-hydroxy-methyl-pyrrol-1-yl)-L-norleucine in the maillard reaction between D-glucose and L-lysine. *Agric Biol Chem.* (1980) 44:1201–2. doi: 10.1080/00021369.1980.10864104
- Henle T, Bachmann A. Synthesis of pyrraline reference material. *Zeitschrift für Lebensmittel-Untersuchung und Forschung.* (1996) 202:72–4. doi: 10.1007/BF01229689
- Politzer P. A relationship between the charge capacity and the hardness of neutral atoms and groups. *J Chem Phys.* (1987) 86:1072–3. doi: 10.1063/1.452296

(No. 2021KCXTD035), and the Institute of Science and Technology Innovation of DGUT, China (KCYCXPT2017007).

SUPPLEMENTARY MATERIAL

The Supplementary Material for this article can be found online at: <https://www.frontiersin.org/articles/10.3389/fnut.2022.874650/full#supplementary-material>

33. Ghanty TK, Ghosh SK. Correlation between hardness, polarizability, and size of atoms, molecules, and clusters. *J Phys Chem.* (1993) 97:4951–3. doi: 10.1021/j100121a015
34. Fuentealba P, Reyes O. Atomic softness and the electric dipole polarizability. *J Mol Struct.* (1993) 282:65–70. doi: 10.1016/0166-1280(93)85035-W
35. Simón-Manso Y, Fuentealba P. On the density functional relationship between static dipole polarizability and global softness. *J Phys Chem A.* (1998) 102:2029–32. doi: 10.1021/jp972733k
36. Chattaraj PK, Sengupta S. Popular electronic structure principles in a dynamical context. *J Phys Chem.* (1996) 100:16126–30. doi: 10.1021/jp961096f
37. Edwards JO, Pearson RG. The factors determining nucleophilic reactivities. *J Am Chem Soc.* (1962) 84:16–24. doi: 10.1021/ja00860a005
38. Bartoli G, Todesco PE. Nucleophilic substitution. Linear free energy relations between reactivity and physical properties of leaving groups and substrates. *Acc Chem Res.* (1977) 10:125–32. doi: 10.1021/ar50112a004
39. Ho T-L. *Hard and Soft Acids and Bases Principle in Organic Chemistry*. In: Ho T-L, editor. New York, USA: Academic Press (1977). doi: 10.1016/B978-0-12-350050-2.50009-8
40. Pearson RG. Hard and soft acids and bases. *J Am Chem Soc.* (1963) 85:3533–9. doi: 10.1021/ja00905a001
41. Taft RW. Separation of polar, steric and resonance effects in reactivity. In: Newman MS, editor. *Steric Effects in Organic Chemistry*. New York, USA: John Wiley (1956). p. 556–675.
42. Tsou LK, Tatko CD, Waters ML. Simple cation- π interaction between a phenyl ring and a protonated amine stabilizes an α -helix in water. *J Am Chem Soc.* (2002) 124:14917–21. doi: 10.1021/ja026721a
43. Yamaguchi K, Noumi Y, Nakajima K, Nagatsuka C, Aizawa H, Nakawaki R, et al. Effects of salt concentration on the reaction rate of Glc with amino acids, peptides, and proteins. *Biosci Biotechnol Biochem.* (2009) 73:2379–83. doi: 10.1271/bbb.90252
44. Otto S, Engberts JBFN. Hydrophobic interactions and chemical reactivity. *Org Biomol Chem.* (2003) 1:2809–20. doi: 10.1039/b305672d
45. Bender ML. Metal ion catalysis of nucleophilic organic reactions in solution. In: Busch DH, editor. *Reactions of Coordinated Ligands*. Advances in Chemistry, Vol. 37. Washington, DC, USA: American Chemical Society (1962). p. 19–36. doi: 10.1021/ba-1963-0037.ch002
46. Pauling L. Molecular architecture and biological reactions. *Chem Eng News.* (1946) 24:1375–7. doi: 10.1021/cen-v024n010.p1375
47. Herschlag D, Jencks WP. The effects of magnesium²⁺, hydrogen bonding, and steric factors on rate and equilibrium constants for phosphoryl transfer between carboxylate ions and pyridines. *J Am Chem Soc.* (1990) 112:1942–50. doi: 10.1021/ja00161a046
48. Pregel MJ, Dunn EJ, Nagelkerke R, Thatcher GRJ, Buncel E. Alkali-metal ion catalysis and inhibition in nucleophilic displacement reaction of phosphorus-sulfur- and carbon-based esters. *Chem Soc Rev.* (1995) 24:449–55. doi: 10.1039/CS9952400449
49. Mayes HB, Nolte MW, Beckham GT, Shanks BH, Broadbelt LJ. The α -bet(a) of salty glucose pyrolysis: computational investigations reveal carbohydrate pyrolysis catalytic action by sodium ions. *ACS Catal.* (2015) 5:192–202. doi: 10.1021/cs501125n
50. Sekiguchi Y, Shafizadeh F. The effect of inorganic additives on the formation, composition, and combustion of cellulosic char. *J Appl Polym Sci.* (1984) 29:1267–86. doi: 10.1002/app.1984.070290421
51. Sanders EB, Goldsmith AI, Seeman JJ. A model that distinguishes the pyrolysis of D-glucose, D-fructose, and sucrose from that of cellulose. Application to the understanding of cigarette smoke formation. *J Anal Appl Pyrolysis.* (2003) 66:29–50. doi: 10.1016/S0165-2370(02)00104-3
52. Nimlos MR, Blanksby SJ, Ellison GB, Evans RJ. Enhancement of 1,2-dehydration of alcohols by alkali cations and protons: a model for dehydration of carbohydrates. *J Anal Appl Pyrolysis.* (2003) 66:3–27. doi: 10.1016/S0165-2370(02)00103-1
53. Mayes HB, Tian J, Nolte MW, Shanks BH, Beckham GT, Gnanakaran S, et al. Sodium ion interactions with aqueous glucose: insights from quantum mechanics, molecular dynamics, and experiment. *J Phys Chem.* (2014) 118:1990–2000. doi: 10.1021/jp409481f

Conflict of Interest: The authors declare that the research was conducted in the absence of any commercial or financial relationships that could be construed as a potential conflict of interest.

Publisher's Note: All claims expressed in this article are solely those of the authors and do not necessarily represent those of their affiliated organizations, or those of the publisher, the editors and the reviewers. Any product that may be evaluated in this article, or claim that may be made by its manufacturer, is not guaranteed or endorsed by the publisher.

Copyright © 2022 Liang, Chen, Yang, Liu, Qiu, Zeng, Lu and Liu. This is an open-access article distributed under the terms of the Creative Commons Attribution License (CC BY). The use, distribution or reproduction in other forums is permitted, provided the original author(s) and the copyright owner(s) are credited and that the original publication in this journal is cited, in accordance with accepted academic practice. No use, distribution or reproduction is permitted which does not comply with these terms.



Formation of N^{ϵ} -Carboxymethyl-Lysine and N^{ϵ} -Carboxyethyl-Lysine in Pacific Oyster (*Crassostrea gigas*) Induced by Thermal Processing Methods

Pengcheng Zhou, Shiyuan Dong* and Mingyong Zeng*

College of Food Science and Engineering, Ocean University of China, Qingdao, China

OPEN ACCESS

Edited by:

Jie Zheng,
Jinan University, China

Reviewed by:

Bingcan Chen,
North Dakota State University,
United States
Ru Song,
Zhejiang Ocean University, China

*Correspondence:

Mingyong Zeng
mingyz@ouc.edu.cn
Shiyuan Dong
dongshiyuan@ouc.edu.cn

Specialty section:

This article was submitted to
Food Chemistry,
a section of the journal
Frontiers in Nutrition

Received: 25 February 2022

Accepted: 15 March 2022

Published: 15 April 2022

Citation:

Zhou P, Dong S and Zeng M (2022)
Formation of
 N^{ϵ} -Carboxymethyl-Lysine and
 N^{ϵ} -Carboxyethyl-Lysine in Pacific
Oyster (*Crassostrea gigas*) Induced by
Thermal Processing Methods.
Front. Nutr. 9:883789.
doi: 10.3389/fnut.2022.883789

Advanced glycation end products (AGEs) are important endogenous hazardous substances produced during the thermal processing of foods, which have attracted much attention due to the potential health risks. The current research first investigated the effect of different thermal processing methods (steaming, boiling, sous vide (SV), and sterilizing) on the formation of two typical markers of AGEs, including N^{ϵ} -carboxymethyl-lysine (CML) and N^{ϵ} -carboxyethyl-lysine (CEL), in Pacific oyster (*Crassostrea gigas*). The compositions, lipid oxidation, di-carbonyl compounds, and AGEs in 12 kinds of processed oysters were detected, and the Index values (total Z-score) were calculated. The SV treatment at 70°C caused higher processing yield and lower CEL level while sterilizing in oil at 121°C greatly resulted in the formation of CML. The Index value of SV-treated oysters was much lower than steamed, boiled, and sterilized ones. Correlation analysis showed that the CML and CEL levels were positively correlated with fat content, a^* and b^* value ($p < 0.05$), and negatively correlated with moisture content and L^* value ($p < 0.05$). Besides, thiobarbituric acid reactive substances had a negative correlation with CML ($r = -0.63, p < 0.05$) while no significant correlation with CEL ($p > 0.05$), suggesting that lipid oxidation had a greater effect on the formation of CML but less on the formation of CEL. In summary, SV treatment at 70°C within 15 min was a recommended thermal processing method to reduce the formation of AGEs in oysters.

Keywords: advanced glycation end products, N^{ϵ} -carboxymethyl-lysine, N^{ϵ} -carboxyethyl-lysine, thermal processing, pacific oyster, sous vide

INTRODUCTION

Many physical and chemical changes affect the quality of food during thermal processing. Proper thermal processing could eliminate the harm of pathogenic microorganisms and improve food's flavor, texture, color, and nutritional value (1). The Maillard reaction is one of the critical reactions in the thermal processing of food, which produces tantalizing aroma and color. It generates a series of complex chemicals at the advanced stage named advanced glycation end products (AGEs) (2). High levels of AGEs in the daily diet led to the retention and accumulation in the human blood, which were reported to induce diabetes (3), kidney disease (4), cardiovascular diseases (5), and inflammation (6). In addition, long-term consumption of food with high di-carbonyl

compounds could also elevate the level of di-carbonyl compounds in human plasma and lead to severe endothelial dysfunction (7). *N*^ε-carboxymethyl-lysine (CML) and *N*^ε-carboxyethyl-lysine (CEL) are typically two kinds of AGEs biomarkers in food (8). The Amadori rearrangement products generated in the early stage of the Maillard reaction are dehydrated and rearranged to produce highly reactive di-carbonyl compounds, such as glyoxal (GO) and methylglyoxal (MGO), which react with lysine residues to form CML and CEL (9). Besides, GO, and MGO could also be generated by the oxidation pathways of lipids and reducing sugars, eventually forming CML and CEL (10).

To the best of our knowledge, the formation of CML and CEL depends on food composition, processing time, and temperature. Some studies have determined the contents of CML and CEL in hundreds of food products by ultra-performance liquid chromatography-tandem mass spectrometry (UPLC-MS/MS) and established a reliable dietary AGE database (11, 12). The results showed that foods with high protein or fat content, such as milk, cheese, biscuits, and chocolates, had relatively high AGEs. In contrast, foods with high moisture content, such as apple, mushroom, and tomato soup, had relatively low AGEs. Recently, more and more studies have focused on the effects of different thermal processing on the formation of AGEs. For instance, Sun et al. (13) found that (121°C for 10 min) led to about 0.6- to 3.6-fold increase of CML and CEL in beef, pork, or chicken. Yu et al. (14) showed that the content of CML in pasteurized meat products was 1.5-fold higher than that in sterilized ones, but the content of CEL in sterilized meat products was 2.5-fold higher than that in pasteurized ones. Our previous study found that the CML levels in fried hairtail filets were higher than boiled and baked ones, regardless of the cooking time (15).

Oysters are one of the largest marine bivalves for global human consumption. The global production of oysters has reached >5,000,000 t, and China produces about 82% of the total output (16). Pacific oysters (*Crassostrea gigas*) are the main cultured oyster species in North China (Shandong and Liaoning provinces), with an annual production of >1,200,000 t (17). In China and other Asian countries, steaming and boiling are the most common home cooking methods of oysters, and commercial sterilization is used in the industrial production of canned oysters (18). In addition, sous vide (SV) treatment is an emerging method of low-temperature and long-time heating in a thermostable vacuum bag, which reduces moisture loss and oxidation of asparagus spears (19), beef (20), and fish burgers (21). However, there is little information about the profiles of CML and CEL in the thermally processed oyster.

The objective of this study was primarily to compare the generation of CML and CEL at four thermal processing methods (steaming, broiling, sous vide, and sterilizing) of Pacific oysters (*Crassostrea gigas*). Particularly, the compositions, lipid oxidation products, di-carbonyl compounds, and AGEs were investigated, and the correlation between these parameters was analyzed. Index value (total Z-score) of the processed oysters was also calculated to elucidate the effect of different methods on the formation of CML and CEL.

The findings of this study could help optimize the thermal processing conditions of oysters to minimize CML and CEL formation.

MATERIALS AND METHODS

Materials

Fresh Pacific oyster (*Crassostrea gigas*) was purchased in October from Qingdao (Shandong province, China) aquatic product market and transported to the laboratory immediately on ice. CML, CEL, *N*^ε-carboxymethyl-lysine-d4 (CML-d4) and *N*^ε-carboxyethyl-lysine-d4 (CEL-d4) were obtained from Toronto Research Chemicals Inc. (Toronto, Canada). GO, MGO, and o-Phenylenediamine (OPD) were bought from Sigma-Aldrich (St. Louis, MO, USA). Acetonitrile and methanol of HPLC grade were purchased from Merck (Darmstadt, Germany). All other chemical reagents used in this study were of analytical grade.

Sample Preparation

Oysters were treated in various ways, reflecting the traditional and emerging thermal treatments of shellfish. The 12 treatments included the following: raw sample (Control); steaming at 98°C for 5 min (ST5), 10 min (ST10), and 15 min (ST15) (mimicking steaming of shelled oyster); boiling at 98°C for 5 min (BO5), 10 min (BO10), and 15 min (BO15) (mimicking boiling of oyster meat); sous vide processing at 70°C for a time when the internal temperature reached 70°C and stayed at this temperature for 5 min (SV5), 10 min (SV10), and 15 min (SV15) (used as a new method for cooking seafood at French restaurants) (22); sterilizing in water (SW30) or oil (SO30) at 121°C for 30 min (mimicking sterilization of canned oyster). Photos of raw and processed oyster meats are shown in **Supplementary Table 1**. Oysters processed at 70 and 121°C were vacuum-packed in retort pouches (20 cm × 15 cm, PA/PE, Leadpacks Environmental Protection Packing Co., Ltd, Fujian, China). A digital probe thermometer (NAPUI thermocouple, Mod.TR230X-8, Guangdong, China) was used to measure the internal temperature of oysters during heating. The above preparation of samples was triplicate. After thermal processing, the steamed and sous vide treated oysters were shucked, packed, and plunged into iced water to cool below 20°C within 5 min. Oyster meats were mixed with deionized water at a ratio of 1:3 (w/v) and then freeze-dried. Freeze-dried samples were kept at −25°C within 3 months for further analyses.

Processing Yield, Moisture, Protein, Lipids, and Lysine Measurement

The processing yield was calculated following the USDA (2012) formula:

$$\text{Yield (\%)} = \frac{\text{Processed sample weight}}{\text{Raw sample weight}} \times 100 \quad (1)$$

The content of moisture, protein, and lipids in oyster meats was analyzed by the AOAC official methods (23). The content of lysine was determined using an amino acid analyzer (L-8500A, Hitachi Co., Tokyo, Japan) according to Cao et al. (24).

Color Measurement

According to the method slightly modified by Tavares et al. (15), the surface color of raw and processed oysters was measured by the chroma meter (3nh, NR60CP, Guangdong, China) with a viewing angle of 10° and an illuminant D-65. Before testing, the equipment was calibrated against a standard whiteboard. Measurement for each sample after calibration, where L^* refers to the lightness component, a^* red (+a) to green (-a) component, and b^* yellow (+b) to blue (-b) component. ΔE (the total color difference) was determined by the following equation. The final result was the mean value of reading three times on the visceral mass of each sample.

$$\Delta E = [(L_s - L_0)^2 + (a_s - a_0)^2 + (b_s - b_0)^2]^{\frac{1}{2}} \quad (2)$$

Where “s” defines values of processed samples and “0” denotes values of raw samples.

Lipid Oxidation Products Measurement

To evaluate the level of lipid oxidation in processed oysters, thiobarbituric acid-reactive substances (TBARS) were determined using UV-VIS spectrophotometer (UV-2550, Shimadzu, Japan). TBARS analysis was performed according to Wang et al. (25), and the absorbance of the resulting solution was measured at 532 nm against a blank containing only extraction and TBA solutions. The results of TBARS content were expressed as malondialdehyde (MAD) (mg MAD/kg dry sample).

Analysis of di-Carbonyl Compounds

Glyoxal and MGO were determined as described by Kocadagli et al. (26, 27) with some modifications. The analyses were performed using an Agilent Series 1200 binary pump LC system (Agilent Technologies, Santa Clara, CA, USA), coupled to an Agilent triple quadrupole mass spectrometer (6410B) equipped with electrospray ionization. A Waters Symmetry C18 column (2.1 × 100 mm, 3.5 μm) was used.

Analysis of CML and CEL

Sample Preparation

A modified acid hydrolysis method was employed to prepare CML and CEL analysis (28, 29). First, 0.02 g of raw or processed freeze-dried samples were incubated with 0.4 mL borate buffer (0.2 M, pH 9.2) and 0.08 mL sodium borohydride (2 M in 0.1 M NaOH) at 4°C for 8 h and then hydrolyzed with 0.8 mL 6 M HCl at 110°C for 24 h. Next, the protein hydrolysate was dried in a vacuum oven (DZF-6050; Shanghai Jinghong Laboratory Instrument Co., Ltd, Shanghai, China) at 60°C and diluted with water to 4 mL, from which 1 mL were withdrawn and spiked with 20 μL CML-d4, CEL-d4 (5 μg/mL, internal standard). Following this, the sample solution was purified by a pre-activated MCX column (60 mg/3 mL; Shanghai ANPEL Scientific Instrument Co., Ltd, Shanghai, China) and eluted with 3 mL methanol containing 5% ammonia water. Finally, the eluent was dried in nitrogen with a nitrogen evaporator (DC12H; Shanghai ANPEL Scientific Instrument Co., Ltd, Shanghai, China), reconstituted with 2 mL deionized water, and filtered through a 0.22 μm filter before LC-MS/MS analysis.

LC-MS/MS Analysis

The analysis of CML and CEL in the sample extracts was performed with a Waters 2695 HPLC system (Waters Inc., Milford, USA) and a Waters Quattro Micro triple-quadrupole tandem mass spectrometer (MS/MS) operated in positive electrospray ionization (ESI) mode. A Waters ACQUITY BEH Amide column (2.1 × 100 mm, 1.7 μm) was used. The sample injection volume was 3 μL, and the column temperature was set at 35°C. The binary mobile phase used was (A) water containing 10 mM ammonium formate and 0.1% formic acid, and (B) acetonitrile. The instrument settings for the mass spectrometer were the same as those described in the study of Sun et al. (28).

Calculation of Z-Score and Index

According to the method of Guseman et al. (30), Z-score and Index value (total Z-score) were measured with a slight modification. In brief, the average concentration of the three repeats was used to calculate each sample's Z-score following Equation A and an Index value was created by following Equation B.

$$A: Z = \frac{x - \bar{x}}{s} \quad (3)$$

$$B: \text{Index} = Z_{GO} + Z_{MGO} + Z_{CML} + Z_{CEL} \quad (4)$$

Where A: \bar{x} = the average level of each sample, x = the mean of the 12 processed samples, and s = the standard deviation of the 12 processed samples. B: Z_{GO} = the sample's Z-score of GO, Z_{MGO} = the sample's Z-score of MGO, Z_{CML} = the sample's Z-score of CML, Z_{CEL} = the sample's Z-score of CEL.

Statistical Analysis

The experiments were performed in triplicate, and results were expressed in means ± SD. The statistical analysis was performed using SPSS 22 software (SPSS Inc., Chicago, IL, USA). Significant differences in the means of treatments were identified at a level of $p < 0.05$ by one-way ANOVA and the Duncan test. Pearson's correlation test was analyzed by OriginPro 2021b software (OriginLab Inc., Northampton, MA, USA). Z-score analysis was conducted using Microsoft Excel 2016 software (Microsoft corp., Redmond, WA, USA).

RESULTS AND DISCUSSION

Processing Yield and Composition

The internal temperature of all processed oysters was higher than the safe minimum internal temperature of 62.8°C (31), and the microbial safety could be guaranteed. The processing yield, moisture, protein, and fat contents of raw and processed oyster meats are shown in **Table 1**. Compared with raw oysters, the processing yield and moisture level decreased. Sterilizing in water (SW30) or oil (SO30) resulted in a processing yield of 52.35 and 48.3%, respectively. Conversely, the processing yield of SV-treated samples was above 86%, which was related to the processing temperature maintained at 70°C. The fat content in all processed oysters increased compared to the raw ones, and a significant difference was observed, especially in SO30 ($p < 0.05$). The fact was probably related that the moisture lost during

TABLE 1 | Processing yield (%) and composition of raw and processed oysters (per 100 g of dry matter).

Treatments	Time (min)	Processing yield (%)	Moisture (%)	Fat (% dry sample)	Protein (% dry sample)
Raw	—	100.00	80.55 ± 0.07 ^a	8.68 ± 0.34 ^g	57.22 ± 1.01 ^e
Steamed	5	75.60 ± 0.75	76.54 ± 0.63 ^{cd}	9.81 ± 0.97 ^{def}	60.78 ± 0.36 ^c
	10	70.70 ± 0.50	75.25 ± 0.78 ^{de}	10.30 ± 0.20 ^{de}	64.25 ± 0.19 ^a
	15	67.41 ± 0.35	72.46 ± 1.51 ^f	10.85 ± 0.43 ^{cd}	65.02 ± 0.66 ^a
Boiled	5	73.62 ± 1.51	77.08 ± 0.31 ^c	10.70 ± 0.00 ^{cd}	60.78 ± 0.47 ^c
	10	63.11 ± 1.59	76.25 ± 0.35 ^{cd}	11.60 ± 0.35 ^c	61.80 ± 0.71 ^b
	15	58.69 ± 1.57	74.05 ± 0.64 ^e	10.37 ± 0.56 ^{de}	61.87 ± 0.73 ^b
Sous vide ¹	5	92.10 ± 1.27	79.50 ± 0.57 ^{ab}	9.91 ± 0.10 ^{def}	58.56 ± 0.05 ^d
	10	88.65 ± 0.92	79.05 ± 0.92 ^b	8.98 ± 0.09 ^g	57.22 ± 0.02 ^e
	15	86.00 ± 0.99	78.83 ± 0.46 ^b	9.67 ± 0.48 ^{efg}	58.12 ± 0.48 ^d
Sterilized (in water)	30	52.35 ± 1.20	72.26 ± 0.78 ^f	12.65 ± 0.31 ^b	60.47 ± 0.06 ^c
Sterilized (in oil)	30	48.30 ± 0.57	66.01 ± 1.84 ^g	21.63 ± 1.45 ^a	52.61 ± 0.09 ^f

Value are means ± SD (n = 3). Different lowercase letters in the same column indicate the significant difference (p < 0.05).

¹ Time indicates the internal temperature of the oyster reached 70°C and stayed at this temperature for 5, 10, and 15 min.

TABLE 2 | Instruments color of raw and processed oyster meat according to the CIE Lab color scale.

Treatments	Time (min)	L*	a*	b*	ΔE
Raw	—	66.36 ± 0.52 ^e	0.12 ± 0.01 ^h	7.86 ± 1.20 ^g	—
Steamed	5	73.11 ± 0.11 ^{ab}	2.17 ± 0.13 ^e	13.35 ± 0.32 ^{cd}	9.04 ± 0.27 ^{bc}
	10	74.23 ± 1.51 ^a	2.54 ± 0.36 ^e	13.62 ± 1.12 ^{cd}	10.13 ± 0.63 ^b
	15	70.31 ± 0.12 ^d	4.45 ± 0.53 ^{bc}	16.89 ± 0.88 ^b	10.76 ± 1.00 ^b
Boiled	5	73.98 ± 0.11 ^a	3.83 ± 0.24 ^{cd}	14.59 ± 0.21 ^{bc}	10.83 ± 0.29 ^b
	10	71.73 ± 0.69 ^c	3.29 ± 0.28 ^d	15.66 ± 0.41 ^{bc}	10.01 ± 0.04 ^b
	15	70.35 ± 0.66 ^d	3.42 ± 0.53 ^d	13.06 ± 0.56 ^{cde}	7.34 ± 0.99 ^{cd}
Sous vide ¹	5	74.31 ± 0.42 ^a	1.34 ± 0.76 ^{fg}	10.60 ± 0.30 ^{fg}	8.52 ± 0.19 ^{bcd}
	10	71.85 ± 0.71 ^{bc}	0.92 ± 0.06 ^g	10.47 ± 0.56 ^{fg}	6.16 ± 0.39 ^d
	15	71.46 ± 0.10 ^{cd}	1.93 ± 0.03 ^{ef}	11.63 ± 0.46 ^{def}	6.60 ± 0.19 ^{cd}
Sterilized (in water)	30	65.35 ± 0.57 ^e	4.80 ± 0.01 ^b	16.78 ± 3.43 ^b	10.19 ± 3.05 ^b
Sterilized (in oil)	30	50.35 ± 0.25 ^f	11.24 ± 0.33 ^a	26.45 ± 1.97 ^a	26.96 ± 1.08 ^a

L* = lightness; a* = redness; b* = yellowness. Different uppercase letters in the same column indicate significant differences (p < 0.05).

¹ Time indicates the internal temperature of the oyster reached 70°C and stayed at this temperature for 5, 10, and 15 min.

sterilizing was replaced by oil uptake through capillary pores formed by water evaporation, which increased fat content (32). Besides, protein content is an important indicator to evaluate the quality of nutrition and safety in thermally processed oysters (33). Compared to the raw oysters, protein content in processed ones increased due to internal water losses (15). Interestingly, the protein content significantly decreased from 57.22% of raw oysters to 52.61% of SO30 (p < 0.05). According to Ismail et al. (34), the thermal processing method and duration greatly influenced the content of moisture, fat, and protein. Therefore, we suspect that the decrease of protein content may be due to the protein degradation during sterilizing in oil at 121°C for 30 min.

Color Values

The color values of oyster meat under different thermal processing conditions are illustrated in **Table 2**. The steamed, boiled, and SV-treated oysters indicated higher L*, a*, or b* value than the raw ones regardless of processing time. The a* or b* value of sterilized oysters was higher than the raw ones, while

L* value of raw oysters was lower than the sterilized ones. The a* or b* value in steamed and SV-treated oysters increased with processing time, while the opposite trend was observed in the boiled ones. The ΔE of SV-treated oysters from 6.16 to 8.52 was the lowest value in all four methods. Conversely, the ΔE value of SO30 (26.96) was much higher than the other processed samples. The reason behind this phenomenon was most likely due to oil infiltration and some colored substances formed on the surface of oyster meats through the Maillard reaction pathway (35). Therefore, the color of oyster meat was obviously changed by sterilizing in oil at 121°C for 30 min (**Supplementary Table 1**).

Thiobarbituric Acid-Reactive Substances (TBARS)

Thiobarbituric acid-reactive substances value is commonly used as an indicator to assess the extent of lipid oxidation in food by measuring the content of MAD (36). TBARS values of oysters under different thermal processing conditions are shown in **Figure 1**. In the present study, the values of all processed

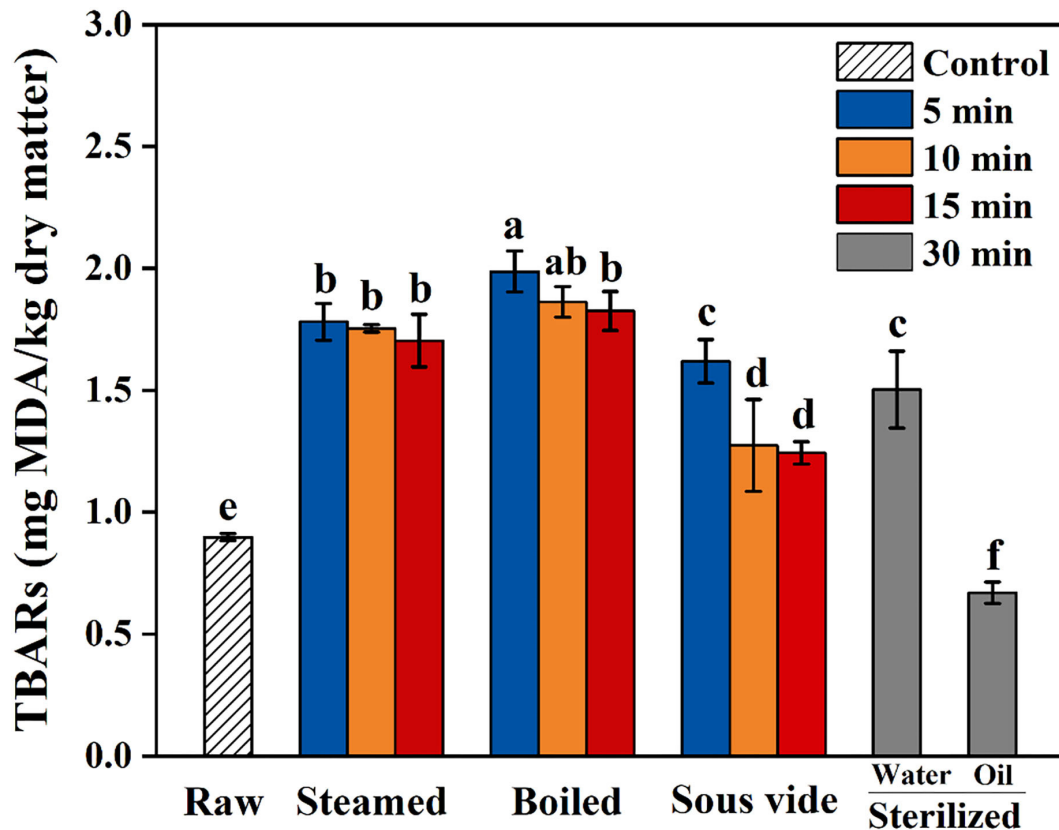


FIGURE 1 | Thiobarbituric acid reactive substances (TBARS) of raw and processed oysters under different thermal processing conditions. Error bars indicate standard deviation ($n = 3$). Samples designated with different lowercase letters were significantly different ($p < 0.05$).

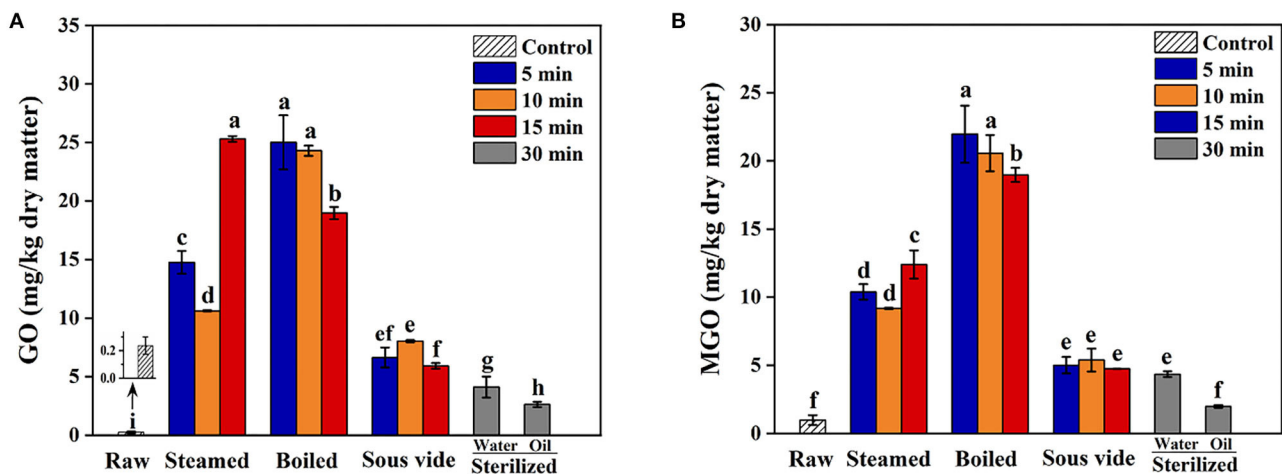


FIGURE 2 | Effect of steamed, boiled, sous vide, and sterilized treatments on the levels of (A) glyoxal (GO) and (B) methylglyoxal (MGO) in raw and processed oysters. Error bars indicate standard deviation ($n = 3$). Samples designated with different lowercase letters were significantly different ($p < 0.05$).

samples were below 2.5 mg MDA/kg dry sample. The values of steamed, boiled, and SV-treated samples were higher than the raw ones and showed similar trends, which gradually decreased with processing time. Compared with raw samples, the value

of SW30 increased by 67%, while the value of SO30 decreased by 26%. To the best of our knowledge, the reason for the decrease in SO30 is still unclear. The finding of Tavares et al. (15) was similar to the present study, which reported that the

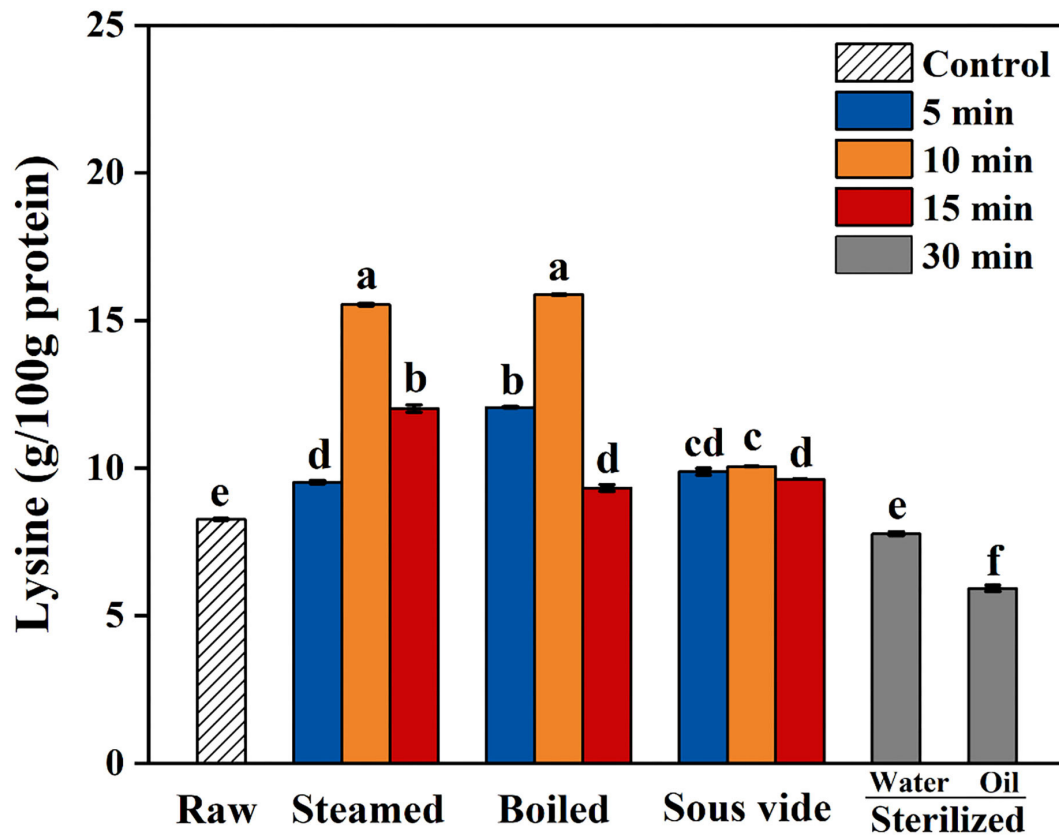


FIGURE 3 | Content of lysine in raw and processed oysters under different thermal processing conditions. Error bars indicate standard deviation ($n = 3$). Samples designated with different lowercase letters were significantly different ($p < 0.05$).

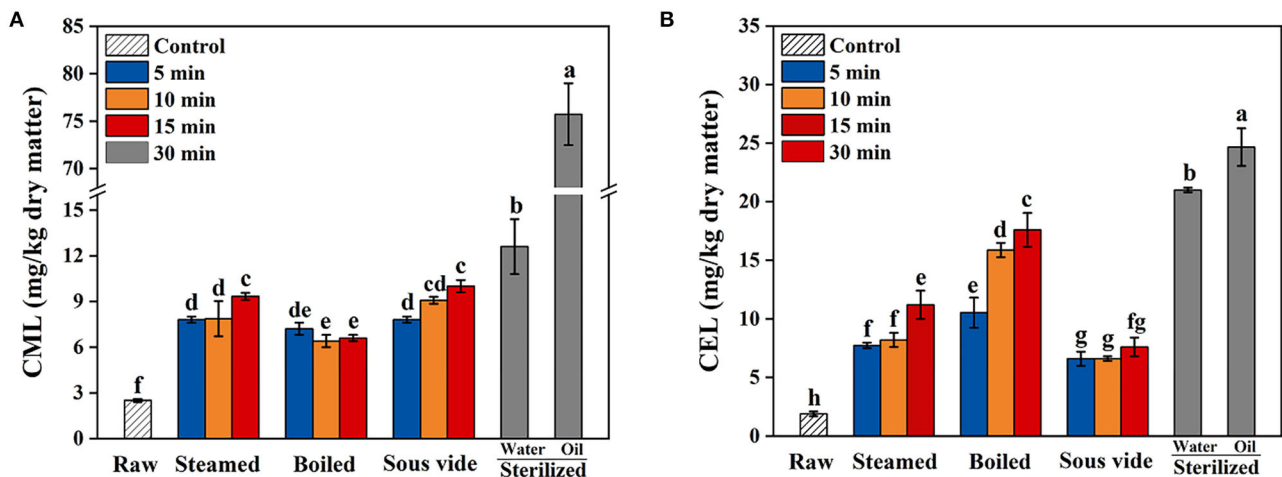


FIGURE 4 | Effects of steamed, boiled, sous vide, and sterilized treatments on the levels of (A) *N*^ε-carboxymethyl-lysine (CML) and (B) *N*^ε-carboxyethyl-lysine (CEL) in raw and processed oysters. Error bars indicate standard deviation ($n = 3$). Samples designated with different lowercase letters were significantly different ($p < 0.05$).

TBARS value of fried filets was about one-half of the boiled ones. We hypothesized that the decrease of TBARS value of oysters processed with a longer time and higher temperature might be

caused by the reaction of some aldehydes produced by lipid oxidation with free amino groups of protein *via* Maillard reaction pathways (37).

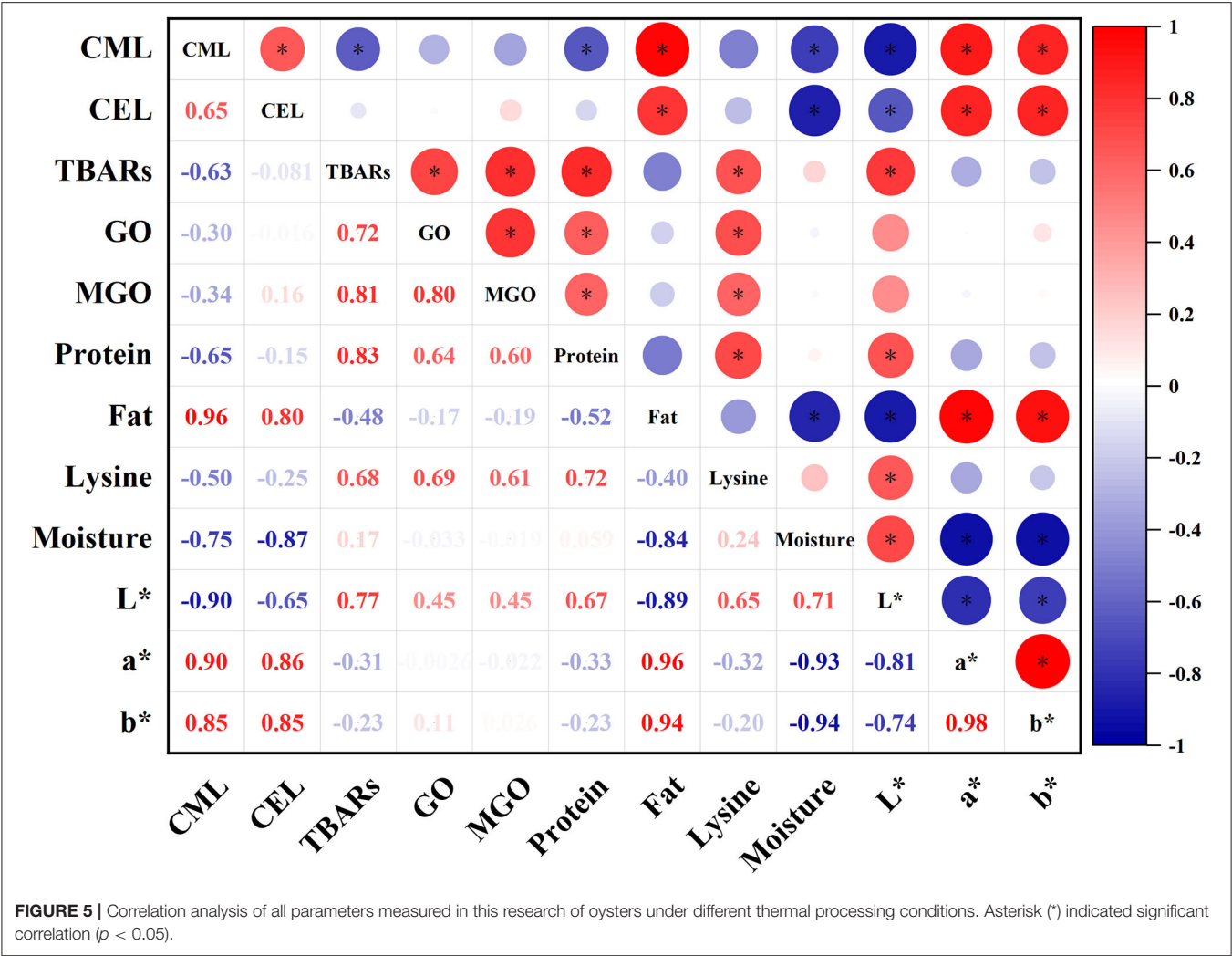


FIGURE 5 | Correlation analysis of all parameters measured in this research of oysters under different thermal processing conditions. Asterisk (*) indicated significant correlation ($p < 0.05$).

GO and MGO Levels

Glyoxal and MGO levels in oysters under different thermal processing conditions are shown in **Figures 2A,B**, respectively. All thermal processing methods increased GO and MGO levels of oysters compared to the raw ones, in which the contents of GO and MGO ranged from 2.62 to 25.31 mg/kg dry sample and 1.98 to 21.97 mg/kg dry sample, respectively. The GO and MGO levels of steamed samples increased with processing time, while the boiled ones observed the opposite trend. The SV-treated samples showed relatively lower GO and MGO than the steamed and boiled ones. The phenomenon was probably that mild reaction conditions were not favorable for the production and accumulation of GO and MGO (38). Furthermore, the GO and MGO levels of SO30 were significantly lower than the other processed samples ($p < 0.05$). The research results of Zhu et al. (33) also found that the content of MGO in braised chicken decreased with the increase of sterilization time. Since GO and MGO were the vital substrates in Maillard reactions, we speculated that the substantial reduction of GO and MGO levels in sterilized oysters might be due to the reaction with amino acids to form many Maillard reaction products (38, 39).

The mechanisms behind this phenomenon still need to be further investigated.

Lysine Levels

Maillard reaction in food during thermal processing leads to the loss of essential amino acids (especially lysine) and decreased bioavailability (40). The levels of lysine in oysters under different thermal processing conditions are shown in **Figure 3**. During the first 10 min of steaming and boiling, the lysine levels gradually increased with cooking time. When steaming and boiling for 15 min, the decline of lysine levels were 23 and 41% more than that of 10 min, respectively. Furthermore, the oysters sterilized in water or oil for 30 min had 6 and 28% lower lysine levels than the raw ones, respectively. The decrease of lysine levels could be attributed to the combination of lysine and di-carbonyl compounds, one of the main reactions for CML and CEL formation (33). Regardless of processing time, the levels of lysine in SV-treated oysters were close to that in raw ones. From the present results, the SV treatment could effectively reduce the loss of lysine in oysters than the other processed methods.

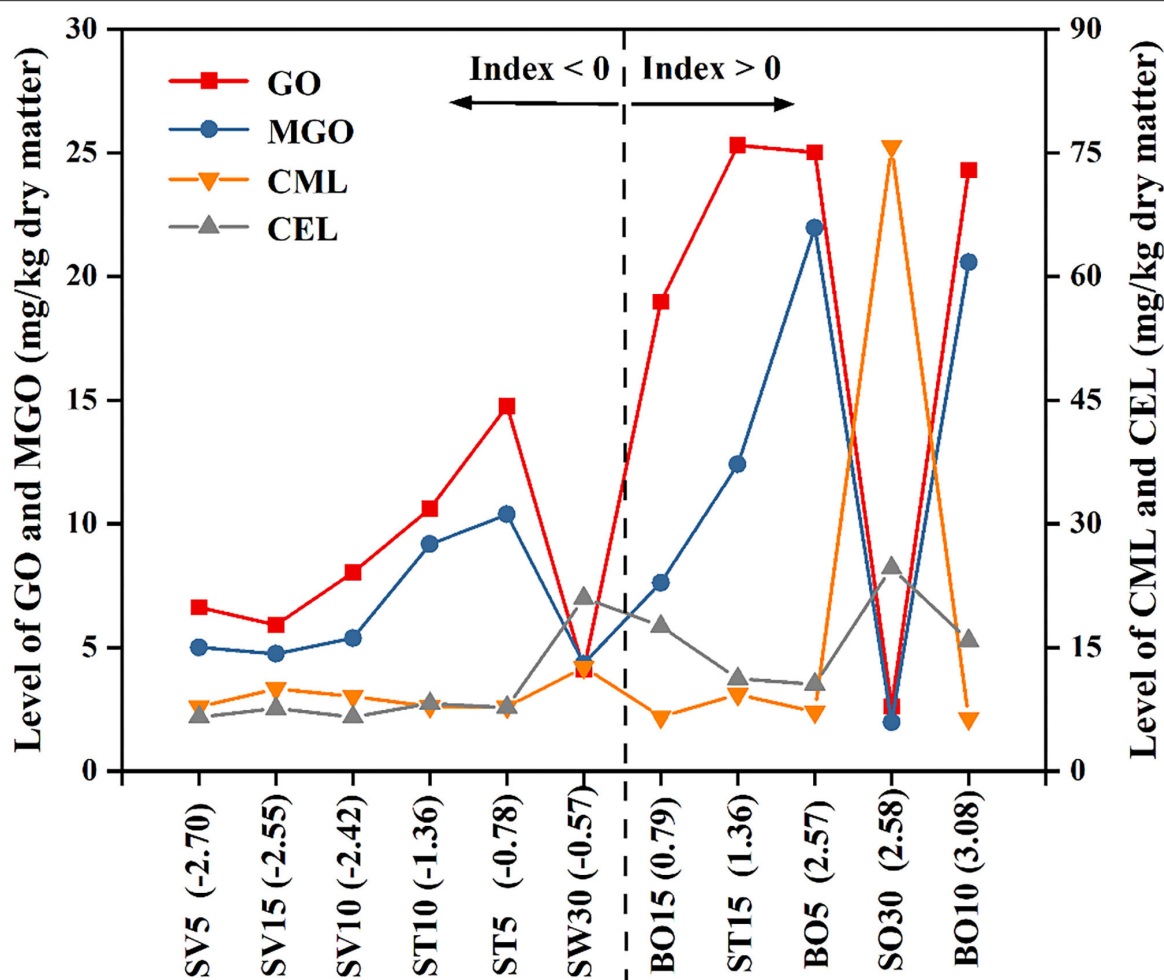


FIGURE 6 | The distribution of various processed oysters based on Z-score analysis.

CML and CEL Levels

The levels of CML and CEL in oysters under different thermal processing conditions are shown in **Figure 4**. In general, the levels of CML and CEL in all processed oysters were increased with processing time. As shown in **Figure 4A**, the levels of CML in steamed, boiled, and SV-treated oysters for 15 min increased by 3.7, 2.6, and 3.6 times that in the raw ones, respectively. Sterilizing in water or oil for 30 min compared to 0 min, the levels of CML increased by 5.0 and 30.3 times, respectively. Therefore, it was summarized that the formation of CML during sterilizing was larger than that in the other three processes. As shown in **Figure 4B**, the levels of CEL in steamed, boiled, and SV-treated oysters for 15 min increased by 5.9, 9.3, and 3.5 times that in the raw ones, respectively. Sterilizing in water or oil for 30 min compared to 0 min, the levels of CEL increased by 11.1 and 13 times, respectively. The CEL level in oysters processed by SV is the lowest among all methods. Based on the above results, SV treatment could better control CEL increase during thermal processing. To the best

of our knowledge, few studies were available on the effect of SV treatment on the formation of AGEs in oysters. So the mechanism behind this phenomenon was not precise, which should be further investigated.

In addition, the CML level in processed oysters was lower than that of CEL except sterilized (in oil) and SV-treated ones. Similar results were found in Sun et al. (13) and Yu et al. (14), which reported that the CEL level in commercial sterilized beef and sterilized meat products was higher than that of CML. However, Zhu et al. (33) found that the content of CML (1.97–27.57 mg/kg) in braised chicken was higher than that of CEL (0.08–0.72 mg/kg). This difference may be caused by different types of food and processing methods, as well as different reaction rates of lysine with GO or MGO (41).

Correlation Analysis

To further understand the relationship between composition, oxidation, precursor, and AGEs of oysters during thermal processing, the correlation between them was analyzed

(Figure 5). It was observed that the generation of CML and CEL were positively correlated with fat content, a^* and b^* value ($p < 0.05$), and negatively correlated with moisture content and L^* value ($p < 0.05$). Besides, CML was negatively correlated with TBARS and protein content ($p < 0.05$). Interestingly, CML and CEL levels were weakly associated with GO, MGO, and lysine content ($p > 0.05$).

The formation of AGEs is strictly linked with the later steps of the Maillard reaction and is affected by food composition (8, 15). In the present study, high CML and CEL levels in oysters were closely related to the high fat and low moisture content. Similar results were found in evaporated milk, canned salmon, and peanut sauce (11), suggesting that the formation of CML and CEL can be promoted under low-moisture and high-fat conditions (9). Besides, high CML and CEL levels were also closely related to the high a^* , b^* , and low L^* values. The more severely the oyster meats were processed, the darker it would be. In fact, several studies have shown that many known Maillard reaction products, such as CML and CEL, have distinctive yellow to brown colors (42, 43).

In addition, the influence of lipid oxidation on the formation of AGEs is very complex, and some pathways are still unclear. Our results showed that the TBARS was negatively correlated with the CML level ($r = -0.63$, $p < 0.05$), which indicated that the formation of CML was closely related to the consumption of lipid oxidation productions. Besides, the TBARS was positively correlated with GO level ($r = 0.72$, $p < 0.05$), suggesting that the lipid oxidation caused the formation of some aldehyde compounds, such as GO. However, CML level had weak correlation with GO and lysine content ($r = -0.3$, $p > 0.05$ and $r = -0.5$, $p > 0.05$, respectively). The reason behind this interesting finding might be that some aldehyde compounds generated from lipid oxidation were the vital substrates in Maillard reactions and spontaneously reacted with amino acids under high-temperature conditions (38, 44). Furthermore, CEL level was insignificantly correlated with TBARS, MGO, and lysine content. Based on the results above, it was summarized that the combined effect of lipid oxidation and Maillard reactions during thermal processing of oysters had a greater effect on the formation of CML but less on the formation of CEL.

Z-Score Analysis

To make a comprehensive comparison of different processed oysters based on their levels of aforementioned di-carbonyl compounds (Figure 2) and AGEs (Figure 4). The Z-score and Index value (total Z-score) of each processed oyster were calculated, and a graph was drawn to show the level of GO, MGO, CML, and CEL based on the order of Index value (Figure 6). Z-score indicates the value of how many standard deviations from the mean, while Index value is the sum of Z-scores representing the full derivations in terms of the GO, MGO, CML, and CEL. Therefore, Index < 0 means less than average value, and the less of Index, the better, and vice versa (45). In the present study, the SV-treated oysters (SV5, SV10, and SV15) had lower Index values (-2.7 , -2.42 , and -2.55 , respectively), probably owing to the relatively mild thermal processing conditions which restricted the formation of AGEs and di-carbonyl compounds.

However, the Index values of boiled oysters (BO5, BO10, and BO15) were 2.57, 3.08, and 0.79, respectively. During high-temperature sterilization, the Index value of SW30 was -0.57 , whereas the Index value of SO30 was 2.58. Based on the above results, endogenous hazardous substances were formed in boiled oysters (BO5, BO10, and BO15) and SO30, with GO or MGO as the major endogenous hazardous substances in boiled oysters and CML or CEL being the predominant one in SO30. In summary, the SV processing (SV5, SV15, and SV10) with the lowest Index value of the four methods mentioned in this study were recommended to consumers.

CONCLUSION

In summary, the effect of four thermal processing methods [steaming, boiling, sous vide (SV), and sterilizing] on CML and CEL formation of oysters was first investigated in the present study. The formation of CML and CEL was closely related to high-fat content, a^* , and b^* values as well as low moisture content and L^* value. Besides, lipid oxidation during thermal processing promoted the formation of CML but had less effect on the formation of CEL. According to the Z-score of processed oysters, SV treatment at 70°C within 15 min might be an effective thermal processing method to control the formation of CML and CEL. This study could provide some valuable references and guidelines for the safety of home-cooked and commercial sterilized oysters based on the control of AGEs levels.

DATA AVAILABILITY STATEMENT

The original contributions presented in the study are included in the article/Supplementary Material, further inquiries can be directed to the corresponding author/s.

AUTHOR CONTRIBUTIONS

PZ, SD, and MZ involved in conceptualization, involved in writing, and reviewing, and editing. PZ involved in analysis, performed methodology, conducted the investigation, and wrote the original draft. MZ and SD performed funding acquisition and supervised the study. All authors contributed to the article and approved the submitted version.

ACKNOWLEDGMENTS

We gratefully acknowledged financial support for this investigation from National Key R&D Program of China (2018YFD0901005).

SUPPLEMENTARY MATERIAL

The Supplementary Material for this article can be found online at: <https://www.frontiersin.org/articles/10.3389/fnut.2022.883789/full#supplementary-material>

REFERENCES

- Lund MN, Ray CA. Control of maillard reactions in foods: strategies and chemical mechanisms. *J Agric Food Chem.* (2017) 65:4537–52. doi: 10.1021/acs.jafc.7b00882
- Brownlee M, Vlassara H, Cerami A. Nonenzymatic glycosylation and the pathogenesis of diabetic complications. *Ann Intern Med.* (1984) 101:527–37. doi: 10.7326/0003-4819-101-4-527
- Vlassara H, Uribarri J. Advanced Glycation End products (AGE) and diabetes: cause, effect, or both? *Curr Diab Rep.* (2014) 14:453. doi: 10.1007/s11892-013-0453-1
- Feng Z, He C, Cai W, Hattori M, Steffes M, Vlassara H. Prevention of diabetic nephropathy in mice by a diet low in glycoxidation products. *Diabetes Metab Res Rev.* (2010) 18:224–37. doi: 10.1002/dmrr.283
- Inès B, Giselle S, Tessier FJ, Anne G, Lamia AA, Florence L, et al. A diet based on high-heat-treated foods promotes risk factors for diabetes mellitus and cardiovascular diseases. *Am J Clin Nutr.* (2010) 91:1220–6. doi: 10.3945/ajcn.2009.28737
- Vlassara H, Cai W, Crandall J, Goldberg T, Oberstein R, Dardaine V, et al. Inflammatory mediators are induced by dietary glycotoxins, a major risk factor for diabetic angiopathy. *Proc Nat Acad Sci.* (2002) 99:15596–601. doi: 10.1073/pnas.242407999
- Sena CM, Matafome P, Crisóstomo J, Rodrigues L, Fernandes R, Pereira P, et al. Methylglyoxal promotes oxidative stress and endothelial dysfunction. *Pharmacol Res.* (2012) 65:497–506. doi: 10.1016/j.phrs.2012.03.004
- Wei Q, Liu T, Sun DW. Advanced Glycation End-products (AGEs) in foods and their detecting techniques and methods: a review. *Trends Food Sci Technol.* (2018) 82:32–45. doi: 10.1016/j.tifs.2018.09.020
- Zhu Z, Huang M, Cheng Y, Khan IA, Huang J, A. comprehensive review of Nε-carboxymethyllysine and Nε-carboxyethyllysine in thermal processed meat products. *Trends Food Sci Technol.* (2020) 98:30–40. doi: 10.1016/j.tifs.2020.01.021
- Poulsen MW, Hedegaard RV, Andersen JM, de Courten B, Bügel S, Nielsen J, et al. Advanced glycation endproducts in food and their effects on health. *Food Chem Toxicol.* (2013) 60:10–37. doi: 10.1016/j.fct.2013.06.052
- Scheijen J, Clevers E, Engelen L, Dagnelie PC, Brouns F, Stehouwer CDA, et al. Analysis of advanced glycation endproducts in selected food items by ultra-performance liquid chromatography tandem mass spectrometry: Presentation of a dietary AGE database. *Food Chem.* (2016) 190:1145–50. doi: 10.1016/j.foodchem.2015.06.049
- Hull GLJ, Woodside JV, Ames JM, Cuskelly GJ. Nε-(carboxymethyl)lysine content of foods commonly consumed in a Western style diet. *Food Chem.* (2012) 131:170–4. doi: 10.1016/j.foodchem.2011.08.055
- Sun X, Tang J, Wang J, Rasco BA, Lai K, Huang Y. Formation of free and protein-bound carboxymethyllysine and carboxyethyllysine in meats during commercial sterilization. *Meat Sci.* (2016) 116:1–7. doi: 10.1016/j.meatsci.2016.01.009
- Yu L, Gao C, Zeng M, He Z, Wang L, Zhang S, et al. Effects of raw meat and process procedure on Nε-carboxymethyllysine and Nε-carboxyethyllysine formation in meat products. *Food Sci Biotechnol.* (2016) 25:1163–8. doi: 10.1007/s10068-016-0185-5
- Tavares W, Dong S, Jin W, Yang Y, Han K, Zha F, et al. Effect of different cooking conditions on the profiles of Maillard reaction products and nutrient composition of hairtail (*Thichiurus lepturus*) filets. *Food Res Int.* (2018) 103:390–7. doi: 10.1016/j.foodres.2017.10.063
- FAO. *Fisheries and Aquaculture Information and Statistics Service.* (2017). Available online at: <http://www.fao.org/fishery/statistics/en>.
- CSY. *China Statistical Yearbook.* Beijing: China Statistical Publishing House (2020).
- Liu C, Ji W, Jiang H, Shi Y, He L, Gu Z, et al. Comparison of biochemical composition and non-volatile taste active compounds in raw, high hydrostatic pressure-treated and steamed oysters *Crassostrea hongkongensis*. *Food Chem.* (2021) 344:128632. doi: 10.1016/j.foodchem.2020.128632
- Gonnella M, Durante M, Caretto S, D'Imperio M, Renna M. Quality assessment of ready-to-eat asparagus spears as affected by conventional and sous-vide cooking methods. *LWT Food Sci Technol.* (2018) 92:161–8. doi: 10.1016/j.lwt.2018.02.017
- Botinestean C, Keenan D, Kerry JP, Hamill RM. The effect of thermal treatments including sous-vide, blast freezing and their combinations on beef tenderness of Msemiteminosus steaks targeted at elderly consumers. *LWT Food Sci Technol.* (2016) 74:154–9. doi: 10.1016/j.lwt.2016.07.026
- Zhou P, Feng Q, Yang X, Gao R, Li Y, Bai F, et al. Sous vide pretreatment in cooking sturgeon fish burger: effects on physicochemical properties and sensory characteristics. *Int J Food Sci Technol.* (2021) 56:2973–82. doi: 10.1111/ijfs.14938
- Rodgers S, Young NWG. The potential role of latest technological developments including industrial gastronomy in functional meal design. *J Culinary Sci Technol.* (2008) 6:170–87. doi: 10.1080/15428050802338977
- AOAC. *Association of Official Analytical Chemists. "Official Methods of Analysis of AOAC".* 18 ed. AOAC International, Gaithersburg (2005).
- Cao W, Zhang C, Hong P, Ji H, Hao J, Zhang J. Autolysis of shrimp head by gradual temperature and nutritional quality of the resulting hydrolysate. *LWT Food Sci Technol.* (2009) 42:244–9. doi: 10.1016/j.lwt.2008.05.026
- Wang LL, Xiong YL. Inhibition of lipid oxidation in cooked beef patties by hydrolyzed potato protein is related to its reducing and radical scavenging ability. *J Agric Food Chem.* (2005) 53:9186–92. doi: 10.1021/jf051213g
- Kocadagli T, Gökmen V. Investigation of α-dicarbonyl compounds in baby foods by high-performance liquid chromatography coupled with electrospray ionization mass spectrometry. *J Agric Food Chem.* (2014) 62:7714–20. doi: 10.1021/jf502418n
- Kocadagli T, Žilić S, Taş NG, Vančetošević J, Dodig D, Gökmen V. Formation of α-dicarbonyl compounds in cookies made from wheat, hull-less barley and colored corn and its relation with phenolic compounds, free amino acids and sugars. *Eur Food Res Technol.* (2015) 242:51–60. doi: 10.1007/s00217-015-2517-8
- Sun X, Tang J, Wang J, Rasco BA, Lai K, Huang Y. Formation of advanced glycation endproducts in ground beef under pasteurisation conditions. *Food Chem.* (2015) 172:802–7. doi: 10.1016/j.foodchem.2014.09.129
- Niu L, Sun X, Tang J, Wang J, Rasco BA, Lai K, et al. Free and protein-bound N-carboxymethyllysine and N-carboxyethyllysine in fish muscle: biological variation and effects of heat treatment. *J Food Compos Anal.* (2017) 57:56–63. doi: 10.1016/j.jfca.2016.12.017
- Guseman EH, Eisenmann JC, Laurson K, Cook SR, Stratbucker W. Calculating a continuous metabolic syndrome score using nationally representative reference values. *Acad Pediatr.* (2018) 18:589–92. doi: 10.1016/j.acap.2018.02.011
- United States Department of Agriculture's Food Safety and Inspection Service (USDA-FSIS). *Safe Minimum Internal Temperature Chart.* (2020). Available online at: <https://www.fsis.usda.gov/food-safety/safe-food-handling-and-preparation/food-safety-basics/safe-temperature-chart> (accessed May 11, 2020).
- Ngadi M, Li Y, Oluka S. Quality changes in chicken nuggets fried in oils with different degrees of hydrogenation. *LWT Food Sci Technol.* (2007) 40:1784–91. doi: 10.1016/j.lwt.2007.01.004
- Zhu Z, Fang R, Huang M, Wei Y, Zhou G. Oxidation combined with Maillard reaction induced free and protein-bound Nε-carboxymethyllysine and Nε-carboxyethyllysine formation during braised chicken processing. *Food Sci Hum Wellness.* (2020) 9:383–93. doi: 10.1016/j.fshw.2020.05.013
- Ismail A, Emmy H. Effects of cooking practices (boiling and frying) on the protein and amino acids contents of four selected fishes. *Nutr Food Sci.* (2004) 34:54–9. doi: 10.1108/00346650410529005
- Starowicz M, Zieliński H. How Maillard reaction influences sensorial properties (color, flavor and texture) of food products? *Food Rev Int.* (2019) 35:707–25. doi: 10.1080/87559129.2019.1600538
- Salih AM, Smith DM, Price JF, Dawson LE. Modified extraction 2-thiobarbituric acid method for measuring lipid oxidation in poultry. *Poult Sci.* (1987) 66:1483–8. doi: 10.3382/ps.0661483
- Andreo A, Doval M, Romero A, Judis MA. Influence of heating time and oxygen availability on lipid oxidation in meat emulsions. *Eur J Lipid Sci Technol.* (2003) 105:207–13. doi: 10.1002/ejlt.200390042
- Zheng J, Guo H, Ou J, Liu P, Huang C, Wang M, et al. Benefits, deleterious effects and mitigation of methylglyoxal in foods: a critical review. *Trends Food Sci Technol.* (2021) 107:201–12. doi: 10.1016/j.tifs.2020.10.031

39. Chen G, Smith JS. Determination of advanced glycation endproducts in cooked meat products. *Food Chem.* (2015) 168:190–5. doi: 10.1016/j.foodchem.2014.06.081
40. Rufian-Henares JA, Delgado-Andrade C, Jimenez-Perez S, Morales FJ. Assessing nutritional quality of milk-based sport supplements as determined by furosine. *Food Chem.* (2007) 101:573–8. doi: 10.1016/j.foodchem.2006.02.016
41. Srey C, Hull G, Connolly L, Elliott CT, Castillo D, Ames JM. Effect of Inhibitor Compounds on N ϵ -(Carboxymethyl)lysine (CML) and N ϵ -(Carboxyethyl)lysine (CEL) formation in model foods. *J Agric Food Chem.* (2010) 58:12036–41. doi: 10.1021/jf103353e
42. John WG, Lamb EJ. The Maillard or Browning reaction in diabetes. *Eye.* (1993) 7:230–7. doi: 10.1038/eye.1993.55
43. Raj DSC, Choudhury D, Welbourne TC, Levi M. Advanced glycation end products: a nephrologist's perspective. *Am J Kidney Dis.* (2000) 35:365–80. doi: 10.1016/S0272-6386(00)70189-2
44. Sharma SD, Barone M. Deleterious consequences of dietary advanced glycation end products on human health due to oxidative stress and inflammation. In: Sharma SD, Barone M, editors. *Dietary Patterns, Food Chemistry and Human Health*. Cham: Springer International Publishing (2019). p. 1–13.
45. Liu D, He Y, Xiao J, Zhou Q, Wang M. The occurrence and stability of Maillard reaction products in various traditional Chinese sauces. *Food Chem.* (2020) 342:128319. doi: 10.1016/j.foodchem.2020.128319

Conflict of Interest: The authors declare that the research was conducted in the absence of any commercial or financial relationships that could be construed as a potential conflict of interest.

Publisher's Note: All claims expressed in this article are solely those of the authors and do not necessarily represent those of their affiliated organizations, or those of the publisher, the editors and the reviewers. Any product that may be evaluated in this article, or claim that may be made by its manufacturer, is not guaranteed or endorsed by the publisher.

Copyright © 2022 Zhou, Dong and Zeng. This is an open-access article distributed under the terms of the Creative Commons Attribution License (CC BY). The use, distribution or reproduction in other forums is permitted, provided the original author(s) and the copyright owner(s) are credited and that the original publication in this journal is cited, in accordance with accepted academic practice. No use, distribution or reproduction is permitted which does not comply with these terms.



Effects of Air Frying on French Fries: The Indication Role of Physicochemical Properties on the Formation of Maillard Hazards, and the Changes of Starch Digestibility

Lu Dong^{1†}, Cai-yi Qiu^{1†}, Rui-can Wang¹, Yan Zhang¹, Jin Wang¹, Jing-min Liu¹, Hua-ning Yu^{2*} and Shuo Wang^{1*}

OPEN ACCESS

Edited by:

Hongshun Yang,
National University of
Singapore, Singapore

Reviewed by:

Shaojuan Lai,
Guizhou University of Traditional
Chinese Medicine, China
Yun Deng,
Shanghai Jiao Tong University, China

*Correspondence:

Hua-ning Yu
yuhuaning1981@126.com
Shuo Wang
wangshuo@nankai.edu.cn

[†]These authors have contributed
equally to this work and share first
authorship

Specialty section:

This article was submitted to
Food Chemistry,
a section of the journal
Frontiers in Nutrition

Received: 04 March 2022

Accepted: 06 April 2022

Published: 27 April 2022

Citation:

Dong L, Qiu C-y, Wang R-c, Zhang Y,
Wang J, Liu J-m, Yu H-n and Wang S
(2022) Effects of Air Frying on French
Fries: The Indication Role of
Physicochemical Properties on the
Formation of Maillard Hazards, and
the Changes of Starch Digestibility.
Front. Nutr. 9:889901.
doi: 10.3389/fnut.2022.889901

¹ Tianjin Key Laboratory of Food Science and Health, School of Medicine, Nankai University, Tianjin, China, ² MideaGroup
Guangdong Midea Kitchen Appliances Manufacturing Co., Ltd., Foshan, China

This study focused on the formation of Maillard hazards in air fried fries, highlighting the correlation between the resultant physical properties of the fries and the formation of Maillard hazards. In the meantime, the effects of air frying on the *in vitro* starch digestibility of fries were explored. Potato strips were fried at various temperatures (180–200°C) and time (12–24 min). Results indicated that the extent of browning, hardness, and the contents of Maillard hazards (acrylamide, 5-hydroxymethylfurfural, methylglyoxal, and glyoxal) all increased steadily with air frying temperature and time. Moisture content were negatively correlated ($p < 0.001$) with Maillard hazards content and physicochemical properties except for L^* with the correlation coefficients range from -0.53 to 0.94 , and positively correlated with L^* value with correlation coefficient was 0.91 , hence, reducing the Maillard hazard exposure while maintaining the desired product quality can be achieved by controlling the moisture content of the air fried French fries. Compared with deep frying (180°C–6 min), air frying decreased acrylamide and 5-hydroxymethylfurfural content with the maximum reduction rate were 47.31 and 57.04%, respectively. In addition, the *in vitro* digestion results suggested that air frying resulted in higher levels of slowly digestible starch (48.54–58.42%) and lower levels of resistant starch (20.08–29.34%) as compared to those from deep frying (45.59 ± 4.89 and $35.22 \pm 0.65\%$, respectively), which might contribute to more balanced blood sugar levels after consumption. Based on the above results, it was concluded that air frying can reduce the formation of food hazards and was relatively healthier.

Keywords: air frying, French fries, Maillard hazards, physicochemical properties, starch digestibility

INTRODUCTION

Potatoes are one of the most consumed foods globally, and deep frying is the most common method of cooking (1). Deep frying gives rise to a variety of pigments and volatiles to fries through Maillard reaction, resulting in characteristic colors and aroma of fries. However, deep fried fries tend to have a higher oil content (about 40%), which is considered unhealthy due to potentially

excessive fat intake (2). Moreover, it can lead to the production of a variety of Maillard hazards, such as acrylamide (AM), 5-hydroxymethylfurfural (5-HMF), heterocyclic amines, polycyclic aromatic hydrocarbon, and advanced glycation end products (3). In addition, some frying oils derived from plant seeds may contain lipophilic aflatoxin B₁, and these aflatoxin B₁ may be immersed into food along with the oil, which brings food safety hazards (4). French fries are the most widely acknowledge dietary source of AM (5), which has been classified as a probable carcinogen (Group 2A) by the International Agency for Research on Cancer (6, 7). In 2017, the European commission set a “benchmark level” for AM in French fries at 500 ng/g (8). 5-HMF is formed via Maillard reaction or caramelization reaction of hexose after hydrolysis. Moreover, it has been reported that 5-HMF can form AM by reacting with asparagine during heating (9). To date, the human health risks of 5-HMF are still controversial, but it can be metabolized into 5-sulfoxymethylfurfural and 5-chloromethylfurfural in human body, which has potential genotoxicity and carcinogenicity (10). In addition, α -dicarbonyl compounds (α DCs) are important intermediates in Maillard reaction, such as glyoxal (GO), methylglyoxal (MGO), and 3-deoxyglucosone (3-DG), which arise from the degradation of Amadori compounds or the caramelization of sugars (11). They can react with the amino in dietary proteins, yielding advanced glycation end products, which associated with various chronic diseases, such as diabetes, aging and atherosclerosis (12, 13). For the sake of healthier foods, many attempts have been made to find inhibitors of the formation of Maillard hazards (14). For processed potatoes, it was suggested that using potato cultivars that are low in reducing sugars or asparagine, or treating potatoes with acids, flavonoids, or glutathione effectively reduced AM content in products (5, 15, 16). However, such pretreatments can cause deteriorated eating quality, limiting their practical application.

Air frying is an emerging processing technology that has been widely accepted by consumers. Instead of immersing food materials in oil, hot air is used as the heat transfer medium, by which it not only imparts comparably palatable products to deep frying products, but also shows health and environmental advantages, such as reduced oil consumption and zero effluent discharge (17–19). However, the physical properties of air fried food also have certain shortcomings. Gouyo et al. (20) reported that deep fried products are crispier than air fried ones because of more effective water loss that contributed to greater crispness and hardness. There have been studied the microstructure and sensory analysis in air fried fries (18), but information on the effects of air frying on the formation of Maillard hazards remains scarce. Water is a key factor for fried food products (fries, chips, etc.). Moisture content not only determines the crispiness and hardness of the products, but also relates to the formation of Maillard hazards. Yuan et al. (21) reported the relationships between moisture content, lipid oxidation, and the production of AM and MGO, which suggested that extended frying and accelerated temperature led to reduced moisture content and intensified lipid oxidation. Considering the impacts of water on texture and the Maillard reaction, and that the latter plays a key role in color, there should be certain correlation between

the physical (texture and color) and chemical (Maillard hazards) properties of the products. In other words, for a certain heat-processed food system like French fries, a predictive model could be established between sensory/physical properties and potential food hazards. Previous studies suggested that α DCs are involved in the subsequent formation of AM and 5-HMF. For example, in the fructose/asparagine model system, the correlation coefficient between MGO consumption and AM formation was 0.931 (22). It has found that the production of 5-HMF has a positive correlation with the content of 3-DG in wheat-flour biscuits (23). Nevertheless, the effect of α DCs on AM and 5-HMF formation in air frying process has not been fully studied.

Furthermore, potatoes contain 70–80% starch, which may potentially lead to high blood glucose levels after meals. Based on *in vitro* methods, starch can be divided into rapidly digestible starch (RDS), slowly digestible starch (SDS) and resistant starch (RS) (24). It has been reported that different cooking methods alter the microstructure and the nutritional value of food, and the microstructure might strongly link with the starch digestibility (25). RDS refers to the amount of starch hydrolyzed by α -amylase within 20 min, causing a rapid rise in blood sugar levels. SDS takes a long time (20–120 min) to digest and thus not making a great contribution to increase blood sugar. RS, unhydrolyzed after 120 min, is classified as dietary fiber, is not digestible, but can be fermented by bacteria in human colon to produce short-chain fatty acids, which plays an important role in preventing colon cancer, diverticulitis, and hemorrhoids (26, 27). Thus, *in vitro* starch digestibility provides an indicator of the glycemic index (GI) and potential health benefits/hazards of starchy foods. Cooked potatoes contain significant amounts of RS, and the digestibility of potatoes is related to cooking method, time, and temperature (28). However, the effects of air frying on the digestibility of potato starch by new technology had not been well-reported.

This study focused on the formation of Maillard hazards (AM, 5-HMF, α DCs) in air fried fries, highlighting the correlation between the resultant physicochemical properties (moisture content, texture, and color) of the fries and the formation of Maillard hazards. The effects of air frying on starch digestibility and RS content of French fries were also studied. Furthermore, based on the similar sensory score, the Maillard hazards, physicochemical properties, and starch digestibility of air fried French fried was compared with the deep fried French fried, which will provide a theoretical basis for the application of air frying technology in food processing.

MATERIALS AND METHODS

Material and Reagents

AM, ¹³C-Acrylamide, 5-HMF, formic acid, methanol, and acetonitrile (HPLC grade) were obtained from Sigma-Aldrich (St. Louis, Mo., U.S.A.). 3-DG was supplied by Toronto Research Chemicals (Toronto, Canada). MGO (40% aqueous solution), GO (40% aqueous solution), *o*-phenylenediamine (OPA), *n*-hexane, potassium ferrocyanide trihydrate, zinc acetate dihydrate were purchased from Aladdin Bio-Chem Technology Co. Ltd. (Shanghai, China). Oasis HLB (6 mL, 200 mg) and Oasis MCX

(3 mL, 60 mg) cartridges were supplied by Waters Corp. (Milford, MA, USA). French fries (9 × 9 mm) were obtained from Metro Chef[®] frozen French fries. Sunflower oil was bought from the local supermarket. Milli-Q System was used for preparing the ultrapure water (Millipore, St. Louis, MO, USA). Potassium hexacyanoferrate (3.6 g) and zinc acetate (7.2 g) were dissolved in 100 mL of water to prepared Carrez I and II solutions, respectively.

Preparation of French Fries

Deep frying process was conducted in an electric fryer (HENG ZHI, GuangZhou, China) filled with 5 kg sunflower oil. Frozen French fries (300 g) were carefully poured into the oil when the center temperature reached 180°C and cooked for 6 min according to previous method (5). The center temperature of oil was measured with a TESTO 905T1 Probe Thermometer (Testo SE & Co. KGaA, Shanghai, China) with temperature measurement range is from −50 to 350°C.

Air frying was conducted in air fryer equipment (Toshiba ET-VD7250, Foshan, Guangdong, China). Frozen French fries (300 g) were put in the cooking basket, making sure that the stripes make little contact with each other. The air frying program was set for different temperatures (180, 190, 200°C) and times (12, 15, 18, 21, 24 min).

Three independent repetitions of each treatment condition were performed. All samples were cooled to room temperature. Each sample was ground to coarse powders for analyses except for texture analysis.

Determination of Moisture Content

Moisture content was determined in an oven (BAO-80A, STIK instrument equipment Co., Ltd., Shanghai, China) heated at 102 ± 3°C until constant weight.

Determination of Color Parameters

The color measurements of French fries were measured in a colorimeter (model CM-5; Konica Minolta Sensing, Inc., Osaka, Japan). L^* (lightness/darkness), a^* (greenness/redness), and b^* (blueness/yellowness) were used to express the color of French fries (29). The total color difference (ΔE) was calculated as follows:

$$\Delta E = \sqrt{(L^* - L)^2 + (a^* - a)^2 + (b^* - b)^2}$$

where L , a , and b refer to the color values of the fresh potato strips.

Determination of Texture

A TA-XT plus texture analyzer (Stable Micro Systems Co. Ltd., Surrey, UK) was used for the texture profile analysis (TPA) of French fries. French fries were cut into 9 × 9 × 20 mm cubes and placed on the center of the fixture with the rectangle size exposing to the probe. A P/36R probe was used to compress the sample, according to following settings: pre-test speed, 4.0 mm/s; test speed, 2.0 mm/s; post-test speed, 4.0 mm/s; Interval between two compressions, 5 s; strain: 40%; trigger force, 5 g. The textural parameters, hardness, and chewiness, were calculated from the TPA curve (30). Six cubes were used to measure the

TABLE 1 | Score criteria on the sensory evaluation of French fries.

Dimensionality Deduct fraction (Basic points 100)	Color	Texture
0	<5% of the fries are black on both ends	Thin layer of brittle skin, soft inside, one end of the hand is straight and not bent
5	5–10% of the fries are black on both ends	More than 95% have a thin layer of brittle skin, soft inside, one end of the hand is straight and not bent
10	/	More than 90% have a thin layer of brittle skin, soft inside, one end of the hand is straight and not bent
Disqualification	Dark brown and white	Soft and burnt

texture indices and the average reading of it was calculated for one independent experiment.

Sensory Analysis

Ten postgraduates (age: 21–30, 5 males, 5 females) with food sensory evaluation experience were invited as panelists to score the samples in terms of color and texture, the score criteria of French fries were presented in Table 1. The panelists were trained according to national standard method (GB/T 16291) and were required to clean their mouth with water before the first taste and between samples.

Determination of Maillard Hazards

Sample Pretreatment

A multiple stage extraction protocol was applied for pretreatment as described in Gökmen et al. (31). 1.00 g well-ground sample was weighted in a 50 mL centrifuge tube, and vortexed for 3 min in each step after extracting with 20 mL of water (10, 10 mL), then centrifugation at 8,000 × g for 10 min, and transfer the clear supernatant into a test tube. Then, 5 mL of *n*-hexane, 0.5 mL of Carrez I and 0.5 mL of Carrez II solutions were added to the supernatant, vortexed for 5 min, and centrifuged at 10,000 × g for 10 min to remove the fat and protein. This procedure was repeated twice. Subsequently, the resultant aqueous extract was used to analyze AM, 5-HMF, and α DCs.

Analysis of AM

The extract samples purified and quantitated protocols of AM refer to our previous report (32). Briefly, the extract was purified through an Oasis MCX column and filtered through a 0.22 μ m filter membrane for analyze. Waters Acquity I Class UPLC System coupled to a TQ detector with electrospray ionization operated in positive mode was used for AM analysis. The product ions of AM were 54.8 and 44 with 8 V and 12 V collision energy; the product ions of ¹³C-acrylamide were 45 and 58

TABLE 2 | Changes in moisture content, color, texture, and sensory score of French fries during the production process.

Samples	Moisture content	L*	a*	b*	ΔE	Hardness/g	Chewiness	Sensory score
18°C 12 min	60.52 ± 0.07% ^o	76.45 ± 0.33 ^{gh}	−0.39 ± 0.14 ^a	32.21 ± 0.97 ^a	6.46 ± 0.29 ^{ab}	648.29 ± 121.88 ^a	247.84 ± 17.53 ^a	0
15 min	54.02 ± 0.36% ^m	76.14 ± 0.13 ^g	0.65 ± 0.18 ^{bc}	35.32 ± 0.55 ^{bc}	8.96 ± 0.48 ^c	783.42 ± 117.60 ^a	306.86 ± 30.75 ^a	91.5 ± 2.42
18 min	51.58 ± 0.19% ^k	74.95 ± 0.40 ^f	1.35 ± 0.29 ^d	36.49 ± 0.31 ^{ce}	10.75 ± 0.06 ^d	1029.42 ± 67.47 ^{ab}	465.22 ± 71.23 ^{bc}	92.5 ± 2.63
21 min	43.82 ± 0.16% ^g	71.97 ± 0.46 ^d	3.07 ± 0.21 ^f	38.14 ± 0.52 ^{ef}	14.33 ± 0.10 ^{gh}	1434.93 ± 47.87 ^c	621.13 ± 109.18 ^{de}	98 ± 2.58
24 min	35.11 ± 0.32% ^d	69.38 ± 0.97 ^b	5.74 ± 0.20 ^h	40.79 ± 0.37 ^g	18.74 ± 0.35 ^j	1950.58 ± 51.85 ^{de}	736.70 ± 129.97 ^{ef}	93 ± 2.58
190°C 12 min	59.22 ± 0.25% ⁿ	76.20 ± 0.20 ^g	−0.02 ± 0.18 ^{ab}	32.40 ± 0.85 ^a	6.79 ± 0.58 ^b	697.75 ± 219.68 ^a	263.34 ± 18.52 ^a	0
15 min	52.86 ± 0.39% ^l	75.68 ± 0.38 ^{fg}	1.03 ± 0.30 ^{cd}	36.70 ± 0.72 ^{ce}	10.42 ± 0.29 ^d	1031.41 ± 264.23 ^{ab}	350.42 ± 45.63 ^{ab}	92 ± 2.59
18 min	46.21 ± 0.08% ⁱ	73.60 ± 0.77 ^e	2.62 ± 0.62 ^{ef}	37.65 ± 1.54 ^{df}	12.85 ± 1.17 ^{ef}	1354.81 ± 105.82 ^{bc}	553.31 ± 32.01 ^{cd}	97.5 ± 2.64
21 min	40.87 ± 0.08% ^e	71.15 ± 0.26 ^{cd}	4.62 ± 0.37 ^g	38.70 ± 0.71 ^f	15.78 ± 0.39 ^j	1680.86 ± 78.07 ^{cd}	720.57 ± 99.54 ^{ef}	96 ± 3.94
24 min	32.98 ± 0.48% ^b	69.19 ± 0.64 ^b	6.13 ± 0.37 ^h	40.61 ± 1.56 ^g	18.88 ± 1.55 ^j	2606.59 ± 385.64 ^f	1317.02 ± 6.57 ^h	0
200°C 12 min	59.50 ± 0.21% ⁿ	77.39 ± 0.33 ^h	0.02 ± 0.16 ^{ab}	31.49 ± 0.63 ^a	5.35 ± 0.42 ^a	681.00 ± 80.66 ^a	295.00 ± 13.60 ^a	91 ± 2.11
15 min	49.92 ± 0.45% ^j	76.09 ± 0.24 ^g	1.39 ± 0.43 ^d	34.48 ± 0.26 ^b	8.58 ± 0.33 ^c	875.99 ± 39.76 ^a	305.57 ± 35.56 ^a	95 ± 4.08
18 min	45.19 ± 0.95% ^h	73.87 ± 0.25 ^e	3.03 ± 0.45 ^f	35.85 ± 0.48 ^{bd}	11.52 ± 0.62 ^{de}	1691.04 ± 55.27 ^{cd}	629.37 ± 57.16 ^{df}	97 ± 3.49
21 min	33.79 ± 0.27% ^c	70.60 ± 0.41 ^c	4.39 ± 0.12 ^g	36.88 ± 0.08 ^{cf}	14.95 ± 0.31 ^{hi}	2244.77 ± 194.28 ^{ef}	960.82 ± 57.84 ^g	95 ± 4.09
24 min	31.80 ± 0.11% ^a	64.70 ± 0.31 ^a	7.79 ± 0.12 ⁱ	41.96 ± 1.50 ^g	23.46 ± 1.03 ^k	4218.56 ± 389.62 ^g	1399.97 ± 54.97 ^h	0

Different lowercase letters indicate significant differences ($p < 0.05$) between different production process.

with 9 V collision energy. AM concentration in samples was quantified by internal standard calibration curve established in the range between 1.0 and 100 ng/mL spiked with 50 ng/mL ¹³C-acrylamide. The limit of detection (LOD) and the limit of the quantitation (LOQ) were 5.19, 17.33 ng/g, respectively. The recoveries ranged between 87.84 and 96.72%.

Analysis of 5-HMF

One milliliter of the extract was filtered through 0.22 μm filter membrane and analyzed by Waters Acquity I Class UPLC System in positive mode. Chromatographic separations were performed on an Symmertry C18 (4.6 × 150 mm, 5 μm) column at 30°C. The injection volume was 10 μL. 5% Methanol (A) and 95% (v/v) 0.1% formic acid (B) were used as the mobile phase (0–2 min, 5–20% A; 2–4 min, 20% A; 4–6 min, 20–5% A; 6–8 min, 5% A) at a flow rate of 0.5 mL/min. 5-HMF was eluted in 6.41 min. The electrospray source settings were the same as AM. The product ions of 5-HMF were 109 and 81 with 13 V and 17 V collision energy. The concentration of 5-HMF was quantified by the external calibration curve established in the range between 1 and 100 ng/mL. The LOD and LOQ were set at 1.26, 4.23 ng/g, respectively. The recoveries ranged between 73.82 and 80.44%.

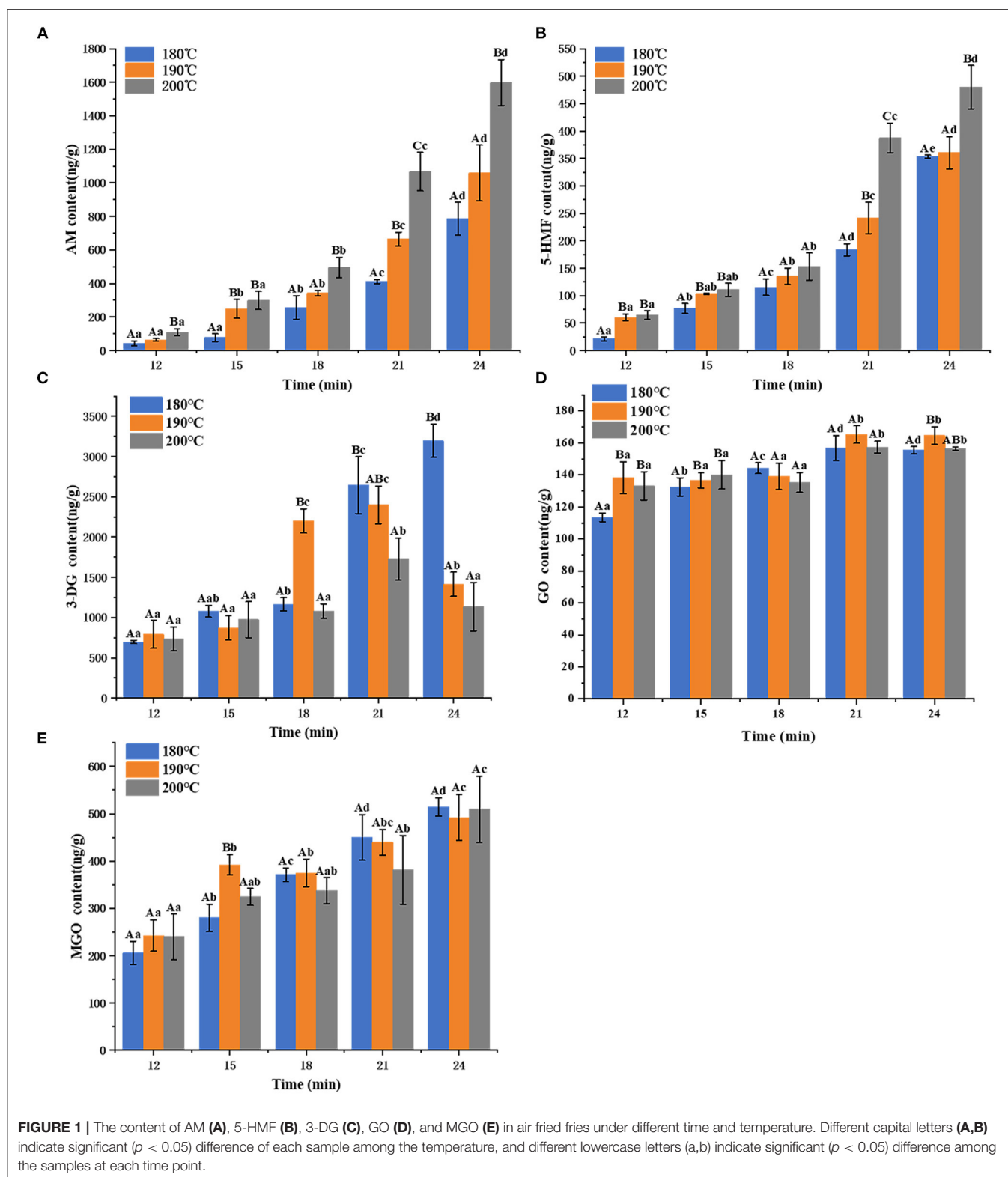
Analysis of αDCs

Three milliliter of the extract was mixed with 100 μL of OPA solution (20 mg/mL) and shaken (100 rpm) for 20 min at 60°C and protected against exposure to light for the derivatization. Then the mixture was loaded onto the Oasis-HLB column (pre-balanced with 5 mL of methanol and 5 mL of water), and eluent was discharged. Next, 5 mL water was loaded and the eluent was discharged. Finally, 3 mL of the mixture of acetonitrile: water (1:1, v/v) was passed through the cartridge, the eluent was collected and filtered through 0.22 μm organic filter membrane

and analyzed by Waters Acquity I Class UPLC System in positive ionization mode. Chromatographic separation was performed in Symmertry C18 (4.6 × 150 mm, 5 μm) at 40°C. 5% Methanol (A) and 95% (v/v) 0.1% formic acid (B) were used as the mobile phase (0–10 min, 30–60% A; 10–12 min, 60–30% A; 12–15 min, 30% A) at a flow rate of 0.4 mL/min. 3-DG, GO and MGO were eluted in 7.61, 10.76, and 12.49 min, respectively. The electrospray source settings were the same as AM. The fragment ions of m/z 235 → 199 (collision energy of 30 V), m/z 131 → 77 (collision energy of 11 V) and m/z 145 → 77 (collision energy of 14 V) were used to quantify quinoxaline derivatives of 3-DG, GO, and MGO, respectively. The levels of quinoxaline derivatives of 3-DG, GO and MGO were calculated using the external standard calibration curve established in the range between 1 and 100 ng/mL. The LOD of αDCs were 0.089–0.670 ng/g; LOQ were 0.297–2.235 ng/g; The recoveries ranged between 78.28 and 104.88%.

In vitro Starch Digestibility

In vitro starch digestion method was conducted based on the protocol of Englyst et al. (1992) with slight modifications (33). The starch content of each fried sample was determined with the Megazyme Total Starch method. French fries containing 100 mg of starch were added to 4.0 mL of acetate buffer (0.2 M, pH 5.2) in a 50 mL centrifuge tube with 2 magnetic beads. Starch digestion was then initiated by adding 1.0 mL of the enzyme mixture, which was prepared by dissolving 0.738 g of α-Amylase in 12.0 mL of water, stirring at 37°C for 10 min, centrifuging at 5,000 × g for 10 min, then adding 50 μL of amyloglucosidase (3,300 U/mL) to the supernatant. The samples were digested at 37°C for 2 h under magnetic stirrer. During digestion, 50 μL aliquots were taken and mixed with



950 μ L of absolute ethanol at 20, 40, 60, 80, 100, and 120 min, respectively. After that the samples were centrifuged at 13,000 \times g for 5 min, the D-glucose (GOPOD Format) assay was

used to determine the glucose content in the supernatant (34). The RDS, SDS, and RS amounts were calculated using the following equations:

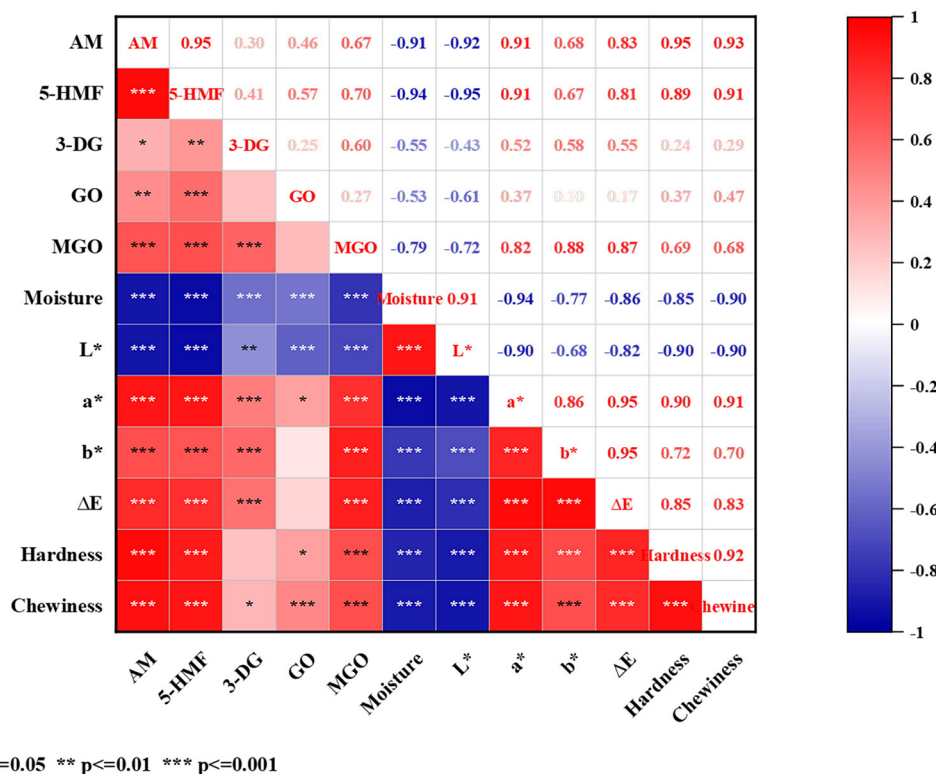


FIGURE 2 | Heat map of correlation based on the concentration of AM, 5-HMF, α DCs, moisture content, color, and texture. Red and blue colors represented the correlation coefficients from 1 to -1. * $p = 0.05$; ** $p = 0.01$; *** $p = 0.001$.

$$\text{RDS} = (\text{G}_{20} \times \text{F} \times 0.9 \times 100) / \text{TS}$$

$$\text{SDS} = (\text{G}_{120} - \text{G}_{20}) \times \text{F} \times 0.9 \times 100 / \text{TS}$$

$$\text{RS} = \text{TS} - (\text{RDS} + \text{SDS})$$

G_{20} : Absorbance value for glucose at 20 min incubation.

G_{120} : Absorbance value for glucose at 120 min incubation.

F: 100/GPOD absorbance

TS: total starch weight (mg).

Statistical Analysis

The data were drawn with Origin 8.0 software (OriginLab Corporation, Northampton, MA, USA) and expressed as mean \pm standard deviation (SD). One-way ANOVA ($n = 3$ for all treatments) analysis was done using SPSS statistical software (Chicago, USA). Statistical significance was determined for p -value of <0.05 . The correlation between thermal processing hazards and sensory characteristics was evaluated by Pearson's correlation test of SPSS.

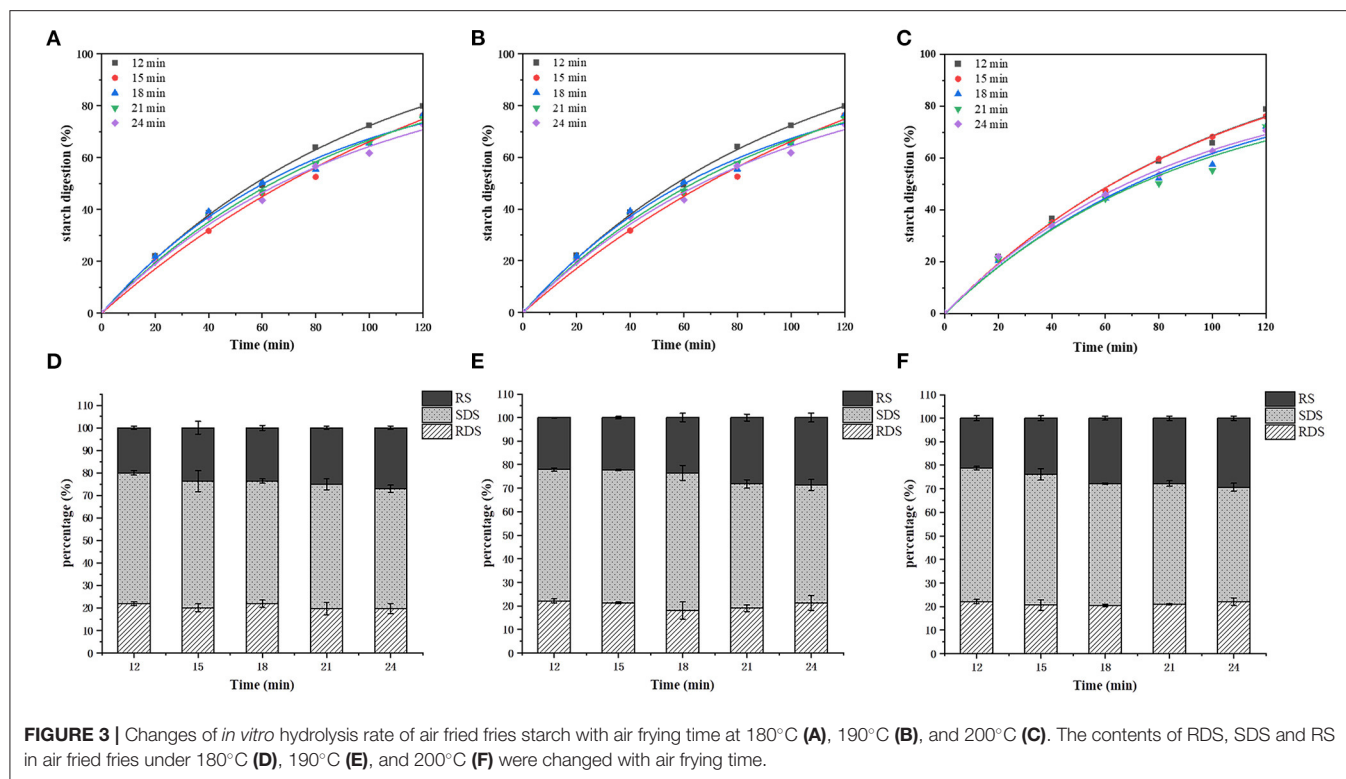
RESULTS

The Physical Characteristics of Air Fried French Fries

The physical results (moisture content, color, texture, and sensory scores) of air fried French fries from different treatments are shown in **Table 2**. The moisture content decreased significantly with both the temperature and duration of the air frying treatment ($p < 0.05$). The L^* , a^* , b^* values of raw potatoes were 81.51 ± 0.27 , -1.37 ± 0.15 , and 28.44 ± 0.14 , respectively. L^* decreased, while a^* , b^* , and ΔE increased with the air frying time and temperature. The texture attributes, including hardness and chewiness, showed the same trend as that of ΔE . The sensory score results indicated that air frying process at 180°C –21 min, 190°C –18 min, and 200°C –18 min obtained the best physical attributes.

AM, 5-HMF and α DCs Content in Air Fried French Fries

The levels of Maillard hazards after the air frying processes are shown in **Figure 1**. The AM content of air fried French fries increased from 42.12 ± 14.46 ng/g to 1598.41 ± 136.62 ng/g as the increase of temperature and time. Likewise, the 5-HMF content of air fried French fries increased from 20.86 ± 3.55 to 479.88 ± 39.63 ng/g. For intermediate α DCs, the GO (from 113.42 ± 2.66 to 165.25 ± 5.45 ng/g) and MGO (from $205.81 \pm$



24.42 to 514.34 ± 19.29 ng/g) exhibited increasing trend with the time at the same air frying temperature. However, there was no significant difference in the content of GO and MGO in air fried French fries with different temperatures under the same time. The change of 3-DG (from 697.07 ± 18.44 to 3195.25 ± 207.48 ng/g) was not linear when the air frying temperature were 190 and 200°C, it exhibited increment before showing subsequent decline afterwards, whereas 3-DG content increased with the time when air fried at 180°C.

Correlations Between Maillard Hazards and Physicochemical Properties of Air Fried French Fries

A heat map (Figure 2) was constructed to present the Pearson correlations between Maillard hazards (AM, 5-HMF, and α DCs) and physicochemical properties (moisture content, color, and texture). The contents of AM and 5-HMF were significantly ($p < 0.001$) negatively correlated with moisture and L^* value, and positively ($p < 0.001$) correlated with a^* and b^* value, ΔE , hardness and chewiness. For intermediates α DCs, the correlations between MGO and the physicochemical properties were similar to AM and 5-HMF, but the correlation coefficients between 3-DG/GO and the physicochemical properties comparatively lower.

Starch Digestibility Characteristics of Air Fried French Fries

The *in vitro* starch digestion results are shown in Figure 3. The *in vitro* digestibility of all samples increased as the

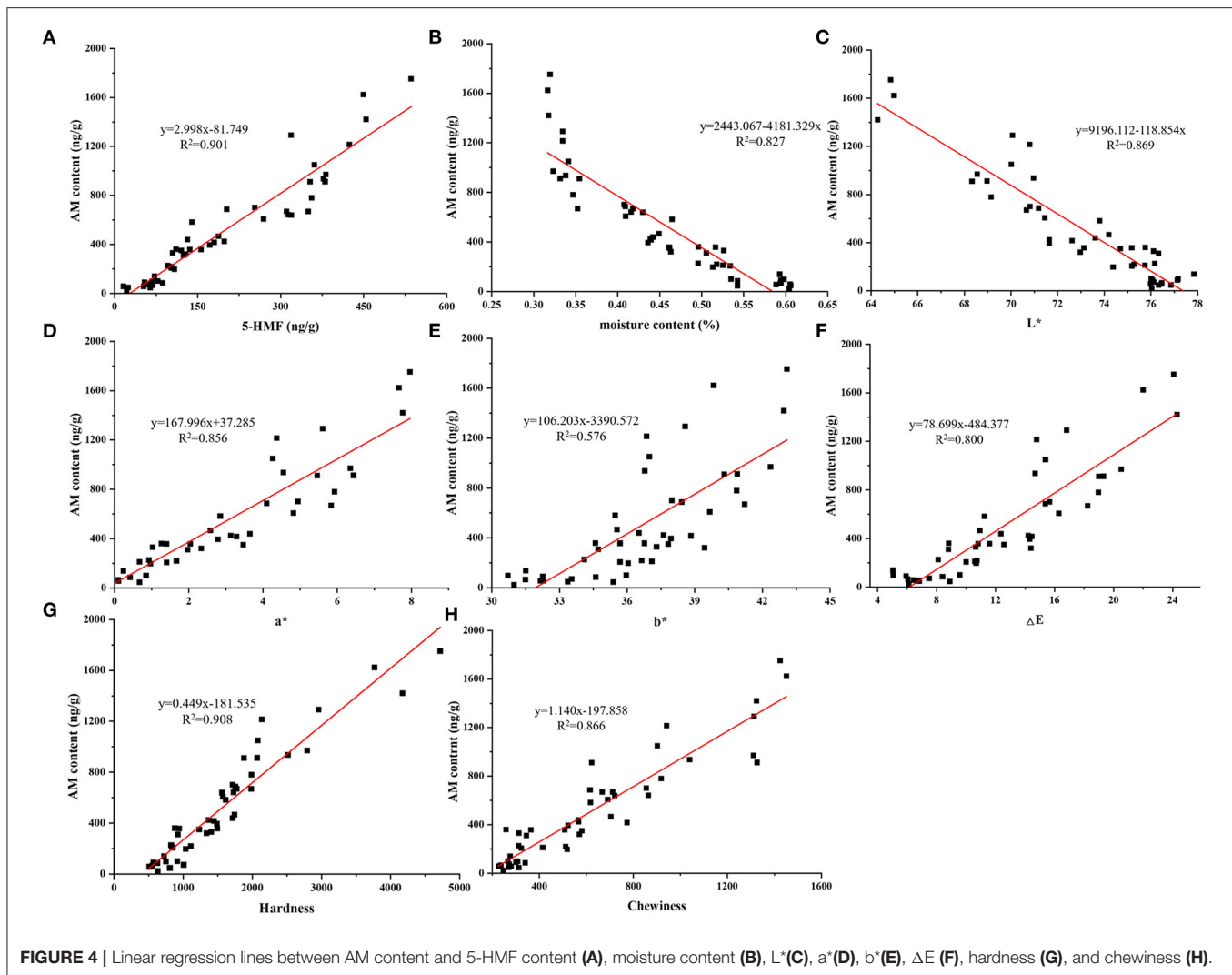
enzymatic hydrolysis proceeded, and all the samples followed similar digestion trend but variations were obvious during the 40–120 min digestion. In general, the digestibility of the starch decreased with the air frying temperature and time (Figures 4A–C). The RDS, SDS and RS values of the air frying samples were $18.04\% \pm 3.63$ – $22.12\% \pm 0.86\%$, $48.54\% \pm 1.74$ – $58.42\% \pm 3.19\%$, $20.08\% \pm 0.65$ – $29.34\% \pm 0.89\%$, respectively. No significant differences were observed for RDS among the treatments, SDS content decreased and RS content increased gradually with the air frying temperature and time.

Maillard Hazards Content, Physicochemical Properties, Sensory Score, and Starch Digestibility of Deep Fried French Fried

The content of Maillard hazards, including AM, 5-HMF, MG, GO and 3-DG, physical characteristics, including moisture, texture, and color, and sensory score are shown in Table 3.

DISCUSSION

At sufficiently high temperatures can reduce some of hazards in food matrix and thus decrease the residues of it (35), but also accompany Maillard reaction, especially in carbohydrate-rich foods (such as fried potato products), resulting in the production of Maillard hazards (active intermediates α DCs, AM, 5-HMF, and polycyclic aromatic hydrocarbons) (36). The concentration



of 3-DG was the highest among the α DCs compared to GO and MGO. 3-DG content showed a cumulative trend when air fired at 180°C, whereas 3-DG concentration firstly increased and subsequently declined when air frying at 190 and 200°C. This may be attributed to the promotion of the degradation of 3-DG with the increase of air frying temperature, making it more involved in the subsequent reactions (10). The correlation coefficients of MGO with 3-DG was 0.60 ($p < 0.001$), showing that MGO formed in air fried French fries may be mainly derived from 3-DG. This result is consistent with the previous study found that 3-DG can through the retroaldolization path to form MGO (37). There is no significantly correlation between 3-DG and GO, it may be due to that GO is mainly a product of autooxidation of glucose (38). A significant increase ($p < 0.05$) in AM formation as the air frying temperature and time increased, and the trend of 5-HMF was consistent with that of AM. AM was positively correlated with 5-HMF ($r = 0.95$, $p < 0.01$) of air fried French fries. This may be attributed to 5-HMF with a low melting point makes it thermodynamically favorable in the conversion

of asparagine into acrylamide (39). Several studies have shown that α DCs were involved in the subsequent generation of AM and 5-HMF in thermal processed foods (10). The trend in the change of AM and 5-HMF content of air fried French fries was consistent with that of MG and GO with the time under the same air fried temperature. AM and 5-HMF were positively correlated with the three α DCs with correlation coefficient in the following order: MGO > GO > 3-DG. α DCs can through the pathway of Strecker degradation to promote the formation of AM (10), and 80% of MGO as the precursor involved in the formation of AM in the Maillard reaction simulation system of glucose and asparagine (40). 3-DG can also be transferred into 5-HMF (10). The Maillard reaction is a series of chain reactions, the results in the present study and the previous reports proved that the three α DCs directly or indirectly participate in AM and 5-HMF formation.

Moisture content was certainly related to the formation of Maillard hazards (21). The moisture content of air fried French fries was decreased with the air firing temperature and time.

TABLE 3 | The Maillard hazards content and physical characteristics of deep fried French fries.

AM (ng/g)	HMF (ng/g)	MG (ng/g)	GO (ng/g)	3-DG (ng/g)	Moisture content (%)	L*	a*	b*	ΔE	Hardness/g	Chewiness	Sensory score
649.75 \pm 16.86	314.73 \pm 4.38	301.41 \pm 5.79	231.76 \pm 5.27	1164.90 \pm 29.01	42.13% \pm 0.61%	69.15 \pm 0.57	2.17 \pm 0.41	32.10 \pm 0.93	13.39 \pm 0.68	1687.89 \pm 91.83	765.99 \pm 69.67	98.5 \pm 2.42

We found that moisture content was negatively related to the content of α DCs, AM and 5-HMF of air fried French fries with the correlation coefficient order was 5-HMF (-0.94) > AM (-0.91) > MGO (-0.79) > 3-DG (-0.55) > GO (-0.53). The reason of the correlation coefficient of α DCs was lower than AM and 5-HMF may be due to α DCs were the active intermediates of AM and 5-HMF, a certain of α DCs were consumed. The decrease of moisture content results in the increase in the activation energy of AM formation (21). This suggest that control the moisture content of foods can furtherly reduce the Maillard hazards formation. The accumulation of Maillard hazard is inseparable from the degree of Maillard reaction, which is visualized by the change in the color of the food surface. Color properties containing L*, a*, and b* has been widely used to establish the correlations with the Maillard hazards in different foods (41, 42). According to the Pearson analysis, a negatively correlation ($p < 0.01$) between L* value with the five Maillard hazards content, but a*, b*, and ΔE value was positively correlation ($p < 0.001$) with AM, 5-HMF, MGO, and 3-DG contents of air fried French fries. Correlation of L*, a*, b* and ΔE value with AM and 5-HMF contents were higher than that of α DCs. The changes of the surface color of foods reflects the degree of Maillard reaction, which is closely related to the moisture content of food matrix. Therefore, the correlations of L*, a*, and b* value with AM, 5-HMF content and moisture content were consistent. For texture, hardness and chewiness instrumentally indicate the sensory attributes during biting and chewing, and are often used to evaluate the quality of French fries. The textural properties of food are mainly affected by the spatial structure of food components and moisture (43). The trend in the change of hardness and chewiness were consistent with moisture content with the positively correlation coefficient was -0.85 and -0.90 , respectively. Importantly, we found a significant correlation ($p < 0.001$) between moisture content and both Maillard hazards and physicochemical properties. Except for GO and 3-DG, the correlation coefficients are all > -0.77 . This suggests that reducing the Maillard hazard exposure while maintaining the desired product quality can be achieved by controlling the moisture content of the air fried French fries.

Additionally, we evaluated the influence of air frying process on the *vitro* starch digestibility. More and more non-digestible polysaccharides in human gastrointestinal tracts are used in food processing to develop healthy foods such as low GI. They can be fermented by intestinal bacteria to generate short chain fatty acids that are beneficial to intestinal health (44). Potatoes contain a plenty of starch, and the effect of heat treatment on starch structure determines its GI. With the increase of air frying temperature and time, starch hydrolysis rate decreased and RS content increased. The temperature increase reduced the moisture content and increased the probability of the amylose molecules approaching each other in the aging recovery process, which was conducive to the formation of double helix structure and promoted the generation of RS. Air fried fries contain higher SDS content, which took long time for digestion, and was degraded to glucose after 120 min of enzymatic digestion. It has been proved that SDS does not cause

a sudden increase of blood sugar, which benefits in balance blood sugar levels (27).

The deep fried fries and air fry fries were compared from the four aspects of Maillard hazards formation, starch digestibility, physicochemical properties and sensory scores to explore whether air frying can reduce Maillard hazards exposure while maintaining the expected product quality for the consumer. The optimal air frying process were 180°C–21 min, 190°C–18 min, and 200°C–18 min, with the sensory scores were 98 ± 2.58 , 97.5 ± 2.64 , and 97 ± 3.49 , respectively, which were similar to sensory score of deep fried French fries (98.5 ± 2.42). Air fried samples had higher moisture content than deep fried fries. Deep frying is an immersive cooking process where a material remains in direct contact with hot oil at a temperature above the boiling point of water, which indicates greater heat and mass transfer, causing substantial water loss and high oil absorption (45), therefore, deep frying has lower moisture content. Nevertheless, due to lower heat and mass transfer, air frying process require longer cooking time and are often less crisp (20). Consumers are more satisfied with French fries with high lightness (L^*), yellowness (b^*) and lower redness (a^*) (46). Compared with deep fried fries, the appropriately air fried fries with a longer heat treatment time, have higher L^* , a^* , and b^* values, characterized by higher lightness, higher brownness, and stronger golden yellow color. For texture, there was no significant difference in hardness compared with air fried fries and deep fried fries, but the chewiness was lower. Researches showed that an increase in water loss increased the hardness and chewiness of products (20). In terms of Maillard hazards content, 190°C–18 min showed the lowest production of AM (342.37 ng/g), which meant a reduction of 47.31% compared with deep frying (649.75 ng/g). Such a disparity in AM content between the two processes may be related to the factors such as oil content and oxygen. Previous reports confirmed that there was a significant ($p < 0.01$) correlation between oil content and AM formation ($p < 0.01$) (47). During deep frying process, AM can be formed not only through the Maillard reaction, but also from oil oxidation. Under high temperature conditions, the lipid oxidation promotes the formation of acrolein, and then acrolein further oxidized to acrylic acid, which can react with asparagine to generate appreciable amounts of AM (48), and the reduction rate of 5-HMF reached 57.04% at 190°C–18 min. In the model system, lipid oxidation products were reported to facilitate the formation of 5-HMF, then it can further generate AM, and some factors that promotes 5-HMF formation are therefore expected to promote AM formation (3). Moreover, there was no significant difference in RDS content between air fried and deep fried French fries, while air frying French fries had higher SDS content, lower RS content, and higher starch hydrolysis rate compared with deep-fried French fries. Due to the longer time required for air frying, a higher degree of gelatinization occurs, which makes it more easily available for enzymatic attack during digestion,

thus increasing the starch hydrolysis rate (28). A dense crust was formed during deep frying that acted as a physical barrier to prevent digestive enzymes from penetrating into the starch granules and prevented starch from diffusing out of the disrupted starch granules, this may slow down starch hydrolysis in French fries (25). Studies have found that the RS content of French fries can be increased by adding fat or oil, ultimately reducing the process of starch digestion, thus it does not cause a sudden spike in blood sugar (27).

In this study, we clarified that Maillard hazards content increased with air frying temperature and time. Moisture content was significantly correlated with Maillard hazards content and physicochemical properties of air fried French fries, hence, reducing the Maillard hazard exposure while maintaining the desired product quality can be achieved by controlling the moisture content of the air fried French fries. Moreover, we found that although the physicochemical properties of optimal air fried and deep fried fries are slightly different, there is no difference in sensory evaluation; and the optimal air frying process can significantly reduce the formation of Maillard hazards; and air frying causes the starch digestibility change but couldn't cause a sudden spike in blood sugar. As a result, air frying can be used as an alternative process to fry potato strips, which is healthier and more attractive to customers.

DATA AVAILABILITY STATEMENT

The original contributions presented in the study are included in the article/supplementary material, further inquiries can be directed to the corresponding authors.

AUTHOR CONTRIBUTIONS

SW and H-nY: conceptualization and validation. LD and C-yQ: methodology, formal analysis, writing—original draft, and data curation. J-mL and JW: investigation and visualization. R-cW and YZ: writing—review and editing. All authors contributed to the article and approved the submitted version.

FUNDING

This research was funded by the National Key R&D Program of China (2019YFC1606202).

ACKNOWLEDGMENTS

Thank to the teachers of the instrument platform of Nankai University for their technical assistance in the use of the instrument.

REFERENCES

- Sadeghi R, Lin YL, Price WJ, Thornton MK, Lin AHM. Instrumental indicators of desirable texture attributes of French fries. *LWT Food Sci Technol.* (2021) 142:110968. doi: 10.1016/j.lwt.2021.110968
- Quan XJ, Zhang M, Fang ZX, Liu HH, Shen QS, Gao ZX. Low oil French fries produced by combined pre-frying and pulsed-spouted microwave vacuum drying method. *Food Bioprocess Process.* (2016) 99:109–15. doi: 10.1016/j.fbp.2016.04.008
- Wang YT, Hu HY, McClements DJ, Nie SP, Shen MY, Li C, et al. pH and lipid unsaturation impact the formation of acrylamide and 5-hydroxymethylfurfural in model system at frying temperature. *Food Res Int.* (2019) 123:403–13. doi: 10.1016/j.foodres.2019.05.001
- Yu X, Li Z, Zhao M, Lau SCS, Tan HR, Teh WJ, et al. Quantification of aflatoxin B1 in vegetable oils using low temperature clean-up followed by immuno-magnetic solid phase extraction. *Food Chem.* (2019) 275:390–6. doi: 10.1016/j.foodchem.2018.09.132
- Cerit I, Demirkol O. Application of thiol compounds to reduce acrylamide levels and increase antioxidant activity of French fries. *LWT Food Sci Technol.* (2021) 143:111165. doi: 10.1016/j.lwt.2021.111165
- Pedreschi F, Ferrera A, Bunger A, Alvarez F, Huaman N, Mariotti-Celis MS. Ultrasonic-assisted leaching of glucose and fructose as an alternative mitigation technology of acrylamide and 5-hydroxymethylfurfural in potato chips. *Innov Food Sci Emerg.* (2021) 73:102752. doi: 10.1016/j.ifset.2021.102752
- Wang YM, Wu H, Zhang WL, Xu W, Mu WM. Efficient control of acrylamide in French fries by an extraordinarily active and thermo-stable L-asparaginase: a lab-scale study. *Food Chem.* (2021) 360:100046. doi: 10.1016/j.foodchem.2021.130046
- Pérez-López AJ, Noguera-Artiaga L, González SLM, Miguel PGS, Ferrández B, Carbonell-Barrachina NA. Acrylamide content in French fries prepared with vegetable oils enriched with β -cyclodextrin or β -cyclodextrin-carvacrol complexes. *LWT Food Sci Technol.* (2021) 148:111765. doi: 10.1016/j.lwt.2021.111765
- Ciesarová Z, Kukurová K, Torbica A, Belović M, Horvathová J, Daško L, et al. Acrylamide and 5-hydroxymethylfurfural in thermally treated non-wheat flours and respective breads. *Food Chem.* (2021) 365:130491. doi: 10.1016/j.foodchem.2021.130491
- Huang YS, Lu JN, Li MY, Li C, Wang YT, Shen MY, et al. Effect of acidity regulators on acrylamide and 5-hydroxymethylfurfural formation in french fries: the dual role of pH and acid radical ion. *Food Chem.* (2022) 371:131154. doi: 10.1016/j.foodchem.2021.131154
- Degen J, Hellwig M, Henle T. 1,2-dicarbonyl compounds in commonly consumed foods. *J Agric Food Chem.* (2012) 60:7071–9. doi: 10.1021/jf301306g
- Maasen K, Scheijen JLM, Opperhuizen A, Stehouwer CDA, Van Greevenbroek MM, Schalkwijk CG. Quantification of dicarbonyl compounds in commonly consumed foods and drinks; presentation of a food composition database for dicarbonyls. *Food Chem.* (2020) 339:128063. doi: 10.1016/j.foodchem.2020.128063
- Hyoung S, Chu M, Park H, Park J, Lee KG. Analysis of α -dicarbonyl compounds and 4-methylimidazole in coffee made with various roasting and brewing conditions. *LWT.* (2021) 151:112231. doi: 10.1016/j.lwt.2021.112231
- Nematollahi A, Meybodi NM, Khaneghah AM. An overview of the combination of emerging technologies with conventional methods to reduce acrylamide in different food products: perspectives and future challenges. *Food Control.* (2021) 127:108144. doi: 10.1016/j.foodcont.2021.108144
- Schouten MA, Genovese J, Tappi S, Francesco AD, Baraldi E, Cortese M, et al. Effect of innovative pre-treatments on the mitigation of acrylamide formation in potato chips. *Innov Food Sci Emerg.* (2020) 64:102397. doi: 10.1016/j.ifset.2020.102397
- Ledbetter M, Bartlett L, Fiore A, Montague G, Sturrock K, McNamara G. Acrylamide in industrial potato crisp manufacturing: a potential tool for its reduction. *LWT Food Sci Technol.* (2020) 123:109111. doi: 10.1016/j.lwt.2020.109111
- Ghaitaranpour A, Mohebbi M, Koocheki A. An innovative model for describing oil penetration into the doughnut crust during hot air frying. *Food Res Int.* (2021) 147:110458. doi: 10.1016/j.foodres.2021.110458
- Gouyo T, Rondet E, Mestres C, Hofleitner C, Bohuon P. Microstructure analysis of crust during deep-fat or hot-air frying to understand French fry texture. *J Food Eng.* (2021) 298:110484. doi: 10.1016/j.jfoodeng.2021.110484
- Yu XN, Li LQ, Xue J, Wang J, Song GS, Zhang YQ, et al. Effect of air-frying conditions on the quality attributes and lipidomic characteristics of surimi during processing. *Innov Food Sci Emerg.* (2020) 60:102305. doi: 10.1016/j.ifset.2020.102305
- Gouyo T, Mestres C, Maraval I, Fontez B, Hofleitner C, Bohuon P. Assessment of acoustic-mechanical measurements for texture of French fries: comparison of deep-fat frying and air frying. *Food Res Int.* (2020) 131:108947. doi: 10.1016/j.foodres.2019.108947
- Yuan Y, Zhang HJ, Deng J, Miao YT, Chen F, Hu XS. A predictive model of acrylamide formation influenced by moisture content, lipid oxidation, and methylglyoxal in fried potato slices. *RSC Adv.* (2014) 4:6608–15. doi: 10.1039/c3ra45622f
- Yuan Y, Zhao GH, Chen F, Liu J, Wu JH, Hu XS. Correlation of methylglyoxal with acrylamide formation in fructose/asparagine maillard reaction model system. *Food Chem.* (2008) 108:885–90. doi: 10.1016/j.foodchem.2007.11.054
- Navarro M, Morales FJ. Effect of hydroxytyrosol and olive leaf extract on 1,2-dicarbonyl compounds, hydroxymethylfurfural and advanced glycation endproducts in a biscuit model. *Food Chem.* (2017) 217:602–9. doi: 10.1016/j.foodchem.2016.09.039
- Li M, George J, Hunter S, Hamaker BR, Mattes R, Ferruzzi MG. Potato product form impacts *in vitro* starch digestibility and glucose transport but only modestly impacts 24 h blood glucose response in humans. *Food Funct.* (2019) 10:1846–55. doi: 10.1039/C8FO02530D
- Tian JH, Chen SG, Shi J, Chen JC, Liu DH, Cai YD, et al. Microstructure and digestibility of potato strips produced by conventional frying and air-frying: an *in vitro* study. *Food Struct.* (2017) 14:30–5. doi: 10.1016/j.foostr.2017.06.001
- Pinhero RG, Liu Q, Sullivan JA, Marcone M, Yada RY. The effect of potato varieties and processing methods on glycemic response. *Am J Plant Sci.* (2020) 11:1144–62. doi: 10.4236/ajps.2020.117081
- Singh A, Raigond P, Lal MK, Singh B, Thakur N, Changan SS, et al. Effect of cooking methods on glycemic index and *in vitro* bioaccessibility of potato (*Solanum Tuberosum* L.) carbohydrates. *LWT Food Sci Technol.* (2020) 127:109363. doi: 10.1016/j.lwt.2020.109363
- Yang YL, Achaerandio I, Pujola M. Effect of the intensity of cooking methods on the nutritional and physical properties of potato tubers. *Food Chem.* (2016) 197:1301–10. doi: 10.1016/j.foodchem.2015.11.028
- Jia B, Fan DM, Li JW, Duan ZH, Fan LP. Effect of guar gum with sorbitol coating on the properties and oil absorption of French fries. *Int J Mol Sci.* (2017) 18:2700. doi: 10.3390/ijms18122700
- Zhang C, Lyu XM, Zhao W, Yan WX, Wang MM, Rei NGK, et al. Effects of combined pulsed electric field and blanching pretreatment on the physicochemical properties of French fries. *Innov Food Sci Emerg.* (2021) 67:102561. doi: 10.1016/j.ifset.2020.102561
- Gokmen V, Morales FJ, Atac B, Serpen A, Arribas-Lorenzo G. Multiple-stage extraction strategy for the determination of acrylamide in foods. *J Food Compos Anal.* (2009) 22:142–7. doi: 10.1016/j.jfca.2008.09.007
- Dong L, Qiu C, Wei F, Yu Z, Zhang Y, Wang S. The effect of microwave baking conditions on the quality of biscuits and the control of thermal processing hazards in the maillard reaction. *Front Nutr.* (2022) 9:825365. doi: 10.3389/fnut.2022.825365
- Mbogo D, Muzhingi T, Janaswamy S. Starch digestibility and β -arotene bioaccessibility in the orange-fleshed sweet potato puree heat bread. *J Food Sci.* (2021) 86:901–6. doi: 10.1111/1750-3841.15620
- Huang M, Zhao X, Mao Y, Chen L, Yang H. Metabolite release and rheological properties of sponge cake after *in vitro* digestion and the influence of a flour replacer rich in dietary fibre. *Food Res Int.* (2021) 144:110355. doi: 10.1016/j.foodres.2021.110355
- Wongmaneepratip W, Gao X, Yang H. Effect of food processing on reduction and degradation pathway of pyrethroid pesticides in mackerel fillet (*Scomberomorus commerson*). *Food Chem.* (2022) 384:132523. doi: 10.1016/j.foodchem.2022.132523
- Yang Y, Achaerandio I, Pujola M. Influence of the frying process and potato cultivar on acrylamide formation in French fries. *Food Control.* (2016) 62:216–23. doi: 10.1016/j.foodcont.2015.10.028

37. Weenen H. Reactive intermediates and carbohydrate fragmentation in Maillard chemistry. *Food Chem.* (1998) 62:393–401. doi: 10.1016/S0308-8146(98)00074-0
38. Wells-Knecht KJ, Zyzak DV, Litchfield JE, Thorpe SR, Baynes JW. Mechanism of autoxidative glycosylation: identification of glyoxal and arabinose as intermediates in the autoxidative modification of proteins by glucose. *Biochemistry.* (1995) 34:3702–9. doi: 10.1021/bi00011a027
39. Gökmen V, Kocadagli T, Goncuoglu N, Mogol BA. Model studies on the role of 5-hydroxymethyl-2-furfural in acrylamide formation from asparagine. *Food Chem.* (2012) 132:168–74. doi: 10.1016/j.foodchem.2011.10.048
40. Yuan Y, Zhao GH, Hu XS, Wu JH, Liu J, Chen F. High correlation of methylglyoxal with acrylamide formation in glucose/asparagine Maillard reaction model. *Eur Food Res Technol.* (2008) 226:1301–7. doi: 10.1007/s00217-007-0658-0
41. Amrein TM, Schonbachler B, Escher F, Amado R. Acrylamide in gingerbread: critical factors for formation and possible ways for reduction. *J Agric Food Chem.* (2004) 52:4282–8. doi: 10.1021/jf049648b
42. Pedreschi F, Moyano P, Kaack K, Granby K. Color changes and acrylamide formation in fried potato slices. *Food Res Int.* (2005) 38:1–9. doi: 10.1016/j.foodres.2004.07.002
43. Leiva-Valenzuela GA, Quilaqueo M, Lagos D, Estay D, Pedreschi F. Effect of formulation and baking conditions on the structure and development of non-enzymatic browning in biscuit models using images. *J Food Sci Technol.* (2018) 55:1234–43. doi: 10.1007/s13197-017-3008-7
44. Ran X, Yang Z, Chen Y, Yang H. Konjac glucomannan decreases metabolite release of a plant-based fishball analogue during *in vitro* digestion by affecting amino acid and carbohydrate metabolic pathways. *Food Hydrocolloid.* (2022) 129:107623. doi: 10.1016/j.foodhyd.2022.107623
45. Mellema M. Mechanism and reduction of fat uptake in deep-fat fried foods. *Trends Food Sci Tech.* (2003) 14:364–73. doi: 10.1016/S0924-2244(03)00050-5
46. Li PY, Wu GC, Yang D, Zhang H, Qi XG, Jin QZ, et al. Effect of multistage process on the quality, water and oil distribution and microstructure of French fries. *Food Res Int.* (2020) 137:109229. doi: 10.1016/j.foodres.2020.109229
47. Basaran B, Turk H. The influence of consecutive use of different oil types and frying oil in French fries on the acrylamide level. *J Food Compos Anal.* (2021) 104:104177. doi: 10.1016/j.jfca.2021.104177
48. Haddarah A, Naim E, Dankar I, Sepulcre F, Pujolà M, Chkeir M. The effect of borage, ginger and fennel extracts on acrylamide formation in French fries in deep and electric air frying. *Food Chem.* (2021) 350:129060. doi: 10.1016/j.foodchem.2021.129060

Conflict of Interest: H-nY was employed by MideaGroup Guangdong Midea Kitchen Appliances Manufacturing Co., Ltd.

The remaining authors declare that the research was conducted in the absence of any commercial or financial relationships that could be construed as a potential conflict of interest.

Publisher's Note: All claims expressed in this article are solely those of the authors and do not necessarily represent those of their affiliated organizations, or those of the publisher, the editors and the reviewers. Any product that may be evaluated in this article, or claim that may be made by its manufacturer, is not guaranteed or endorsed by the publisher.

Copyright © 2022 Dong, Qiu, Wang, Zhang, Wang, Liu, Yu and Wang. This is an open-access article distributed under the terms of the Creative Commons Attribution License (CC BY). The use, distribution or reproduction in other forums is permitted, provided the original author(s) and the copyright owner(s) are credited and that the original publication in this journal is cited, in accordance with accepted academic practice. No use, distribution or reproduction is permitted which does not comply with these terms.



Formation and Identification of a 5-(Hydroxymethyl)-2-Furfural-Zingerone Condensate and Its Cytotoxicity in Caco-2 Cells

Yujing Ke^{1†}, Zhao Yin^{2†}, Nenghua Chen³, Peifang Chen¹, Jie Liu⁴, Shiyi Ou³ and Guoqiang Li^{1,5*}

¹ Department of Food Science, Foshan University, Foshan, China, ² Department of Hematology, Guangdong Second Provincial General Hospital, Guangzhou, China, ³ Department of Food Science and Engineering, Jinan University, Guangzhou, China, ⁴ School of Medicine, Shenzhen University, Shenzhen, China, ⁵ South China National Center for Food Safety Research and Development, Foshan, China

OPEN ACCESS

Edited by:

Hongshun Yang,
National University of
Singapore, Singapore

Reviewed by:

Yueliang Zhao,
Shanghai Ocean University, China
Yanbo Wang,
Zhejiang Gongshang University, China
Shaojuan Lai,
Guizhou University of Traditional
Chinese Medicine, China

*Correspondence:

Guoqiang Li
liguoqiang@fosu.edu.cn

[†]These authors have contributed
equally to this work and share first
authorship

Specialty section:

This article was submitted to
Food Chemistry,
a section of the journal
Frontiers in Nutrition

Received: 11 March 2022

Accepted: 06 April 2022

Published: 28 April 2022

Citation:

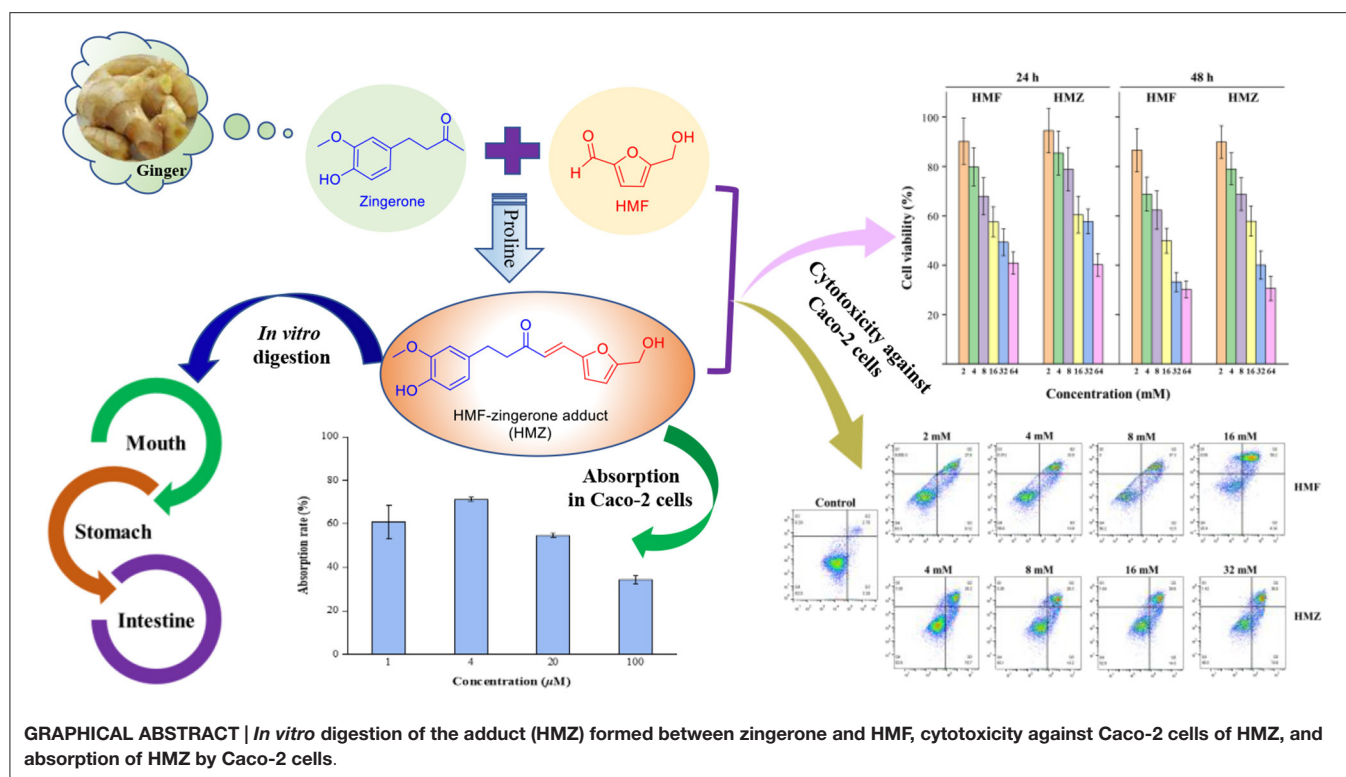
Ke Y, Yin Z, Chen N, Chen P, Liu J,
Ou S and Li G (2022) Formation and
Identification of a 5-(Hydroxymethyl)-
2-Furfural-Zingerone Condensate and
Its Cytotoxicity in Caco-2 Cells.
Front. Nutr. 9:893991.
doi: 10.3389/fnut.2022.893991

5-(Hydroxymethyl)-2-furfural (HMF), an active furfural, widely exists in various food products and has potential safety risks. It can be eliminated by occurring aldol condensation with α -unsubstituted ketones in the presence of catalysts. However, the elimination process between HMF and ketones from food is rarely studied. In this study, the adduct formation between HMF and zingerone (ZGR) catalyzed by proline was investigated. It revealed that the adduct formation led to 99.75% of HMF being trapped under the optimized reaction condition. Moreover, the *in vitro* digestion stability of HMF-ZGR adduct (HMZ) and its cytotoxicity against Caco-2 cells were evaluated. The results indicated that more than 75% of HMZ was remained after a three-stage simulated digestion. Following 24 and 48 h of incubation, HMZ exhibited cytotoxicity against Caco-2 cells with IC₅₀ values of 41.47 ± 5.33 and 25.39 ± 3.12 mM, respectively, versus 35.39 ± 4.03 and 19.17 ± 2.10 mM by HMF.

Keywords: 5-(hydroxymethyl)-2-furfural, zingerone, adduct, aldol condensation, cytotoxicity

INTRODUCTION

5-(Hydroxymethyl)-2-furfural (HMF), a common heat-induced endogenous compound, is formed as an intermediary product of Maillard reaction or carbohydrate dehydration in a low pH environment (1). It exists in a wide range of food products, such as honey (e.g., mean HMF concentration in Malaysian honey at 4–5°C to be 35.98 mg/kg after 2 months storage while that at 25–30°C to be 118.47–1139.95 mg/kg after 1 year storage) (2), coffee (e.g., 213.02–238.99 and 336.03–362.05 mg/kg HMF in traditionally and instant Turkish coffee before brewing, respectively) (3), cereal or cereal products (e.g., breakfast cereals, 6.91–240.51 mg/kg) (4), dried fruits (e.g., dried plum, 1,600–2,200 mg/kg) (5), and dairy products (e.g., infant milk powder, mean 2.3 mg/kg) (6). However, it is found that HMF could exert negative effects on human beings. For example, high HMF concentration can irritate eyes, upper respiratory tract, skin, and mucous membranes (7). On the other hand, HMF can also metabolize into toxic 5-sulfo-oxymethylfurfural (SMF) *in vivo*, of which mutagenicity has been recognized by the European Food Safety Authority (EFSA) (8, 9). Additionally, Bakhiya et al. confirmed that SMF could induce nephrotoxicity after the uptake by



cells (10). Besides, SMF also caused hepatic lesions in a study carried out on FVB/N mice, in which the mice were administrated with SMF at dosages of 31.25, 62.5, 125, and 250 mg SMF/kg (11). Concerning the potentially harmful impact, an intake threshold of 0.54 mg/day for furan derivatives used as flavoring agents is established in Europe (12, 13). In this case, exploring effective methods to control the content of dietary HMF is of necessity.

Currently, a number of researches on adducting HMF have been conducted to find effective methods to control or reduce the HMF content in foods. For instance, Wang et al. found that Lysine could adduct HMF to form a Schiff base (HML) and 74.70% of HMF was eliminated under the optimized condition (14), and Hamzalioglu et al. reported that the reaction of HMF with amino as well as sulfhydryl groups to form Michael adducts was another potential strategy for HMF elimination (8). Additionally, it is also found that polyphenols [e.g., (+)-catechin, (–)-epicatechin, and malvidin 3-O-glucoside] can behave as possible HMF scavengers by forming condensates with HMF (15). However, the adducts formation between HMF and ketones from food has not been reported in any literature.

Ginger, also known as ginger root, belongs to the Zingiberaceae family, and is commonly used as a flavoring agent in Asia because of its aromatic odor and pungent taste (16). Zingerone (ZGR) is one of the key active ketone compounds

in ginger that possesses various biological activities, including anti-oxidant (17), anti-inflammatory (18), anti-cancer (19), anti-hyperlipidemic (20), anti-bacterial (21), and liver protection (22) effects. Proline, an amino acid commonly distributed in plants, is also widely used as an effective catalyst for the aldol reaction between ketones and aldehydes (23–25). Hence, in the present study, the adduct formation between HMF and ZGR was investigated, with proline as a catalyst. Herein, we report the investigation of different reaction conditions on the elimination of HMF and the formation of HMF-ZGR adduct (HMZ), the structural characterization of HMZ, and the evaluation of the stability of HMZ in simulated *in vitro* digestion as well as the cytotoxicity of HMZ against Caco-2 cell lines.

MATERIALS AND METHODS

Materials

HMF (99%), ZGR (98%), proline (99%), and phosphate-buffered saline (PBS, 0.1 M, pH 7.4) were purchased from Sigma-Aldrich (Shanghai, China). High-performance liquid chromatography (HPLC)-grade methanol was acquired from Merck (Darmstadt, Germany). All other reagents were of analytical grade and sourced from Guangdong Guanghua Sci-Tech Co., Ltd. (Shantou, China). Simulated salivary fluid (SSF), simulated gastric fluid (SGF), and simulated intestinal fluid (SIF) were obtained from Phygene Biotechnology Co., Ltd. (Fuzhou, China). Minimum essential medium alpha (α -MEM) was purchased from Thermo Fisher Scientific, Inc. (Waltham, MA). Fetal bovine serum (FBS), non-essential

Abbreviations: HMF, 5-(hydroxymethyl)-2-furfural; ZGR, zingerone; SMF, 5-sulfo-oxymethylfurfural; α -MEM, minimum essential medium ALPHA; FBS, fetal bovine serum; NEAA, non-essential amino acids; CCK-8, cell counting kit-8; PI, propidium iodide; NMR, nuclear magnetic resonance.

amino acid (NEAA), penicillin, streptomycin, 0.25% trypsin-EDTA, Hank's balanced salt solution (HBSS), cell counting kit-8 (CCK-8) and Annexin V-fluorescein isothiocyanate (FITC) apoptosis detection kit were purchased from Lubio Science (Bern, Switzerland). Filters were from Jinteng Experimental Equipment Co., Ltd. (Tianjin, China). Sample solutions (HMF and HMZ) were dissolved with DMSO, diluted with PBS to different concentrations, and filtered through a 0.22 μm filter for cell experiments.

Preparation of HMZ

The proline-catalyzed aldol reaction between acetone and several aldehydes was reported previously (26), while that between HMF and ZGR has not been described yet. Here, the preparation of the adduct between HMF and ZGR was performed as follows: ZGR (1.1 mmol), proline (0.1 mmol), HMF (1.0 mmol), and PBS (5 mL) was mixed and reacted in a three-necked flask at 37°C for 2 h. At the end of the reaction, the mixture was extracted with ethyl acetate and purified by silica column chromatography using petroleum ether/ethyl acetate (60/1, v/v) as eluent to obtain the product, HMZ.

Determination and Characterization of HMZ

The reaction mixture and purified product were subjected to HPLC analysis (Shimadzu, Japan; with diode array detector). The sample (0.5 mg/mL, 10 μL) was dissolved with HPLC-grade methanol, filtered through a 0.45 μm filter, and analyzed by a Zorbax SB-C18 column (4.6 mm \times 150 mm, 5 μm , Agilent, USA) with a gradient elution composed of eluents A (0.01% acetic acid in water) and B (100% methanol) at a flow rate of 1.0 mL/min. The mobile phase started with 90% A and 10% B, then linearly increased to 100% B from 0.01 min to 30 min, and was maintained at 100% B for 10 min. The wavelength for UV detection was set in the range of 200–400 nm.

Nuclear magnetic resonance (NMR) spectroscopy was an efficient and accurate technique for characterization, which was also applied in metabolomic analysis (27). In the present study, the chemical structure of HMZ was elucidated by collecting its 1D and 2D NMR data. HMZ (20 mg) was dissolved in 0.5 mL of CDCl_3 at 25°C to record the ^1H NMR, ^{13}C NMR, distortionless enhancement by polarization transfer 135 (DEPT-135), 2D ^1H correlation spectroscopy (^1H - ^1H COSY), ^1H -detected heteronuclear single-quantum coherence (HSQC), and ^1H -detected heteronuclear multiple-bond correlation (HMBC) spectra on a Bruker 400 MHz NMR apparatus (Bruker Corp, Fallanden, Switzerland). Chemical shifts were expressed in parts per million (ppm).

The mass spectrometric (MS) data of HMZ was acquired using the LCMS-8045 triple quadrupole mass spectrometer (Shimadzu Corporation, Tokyo, Japan) equipped with an electrospray ionization (ESI) source in negative ionization mode. The scan range was from m/z 50 to m/z 1000. For MS/MS measurement, the collision energy was 19.5 eV. Data analysis was performed in the LabSolutions workstation for LCMS-8045.

Effects of Different Reaction Parameters on HMF Elimination and HMZ Formation

A one-factor-at-a-time design was applied to estimate the effects of different reaction parameters on HMF elimination by ZGR, as well as the adduct formation between HMF and ZGR. ZGR/HMF in the molar ratio of 2: 1 was mixed in a three-necked flask and incubated at 40°C for different durations (0.5, 1.0, 1.5, 2.0, 2.5, and 3.0 h) to investigate the effect of reaction time. ZGR/HMF in the molar ratio of 2: 1 was mixed and reacted for 3 h at different temperature levels (20, 30, 40, 50, 60, and 70°C) to study the effect of temperature. In addition, temperature and reaction duration were kept constant at 40°C and 3 h, respectively, to evaluate the effect of different ZGR/HMF molar ratios (4: 1, 3: 1, 2: 1, 1: 1, and 1: 2). At the end of each reaction, 30 μL of the aqueous reaction mixture was diluted with methanol to a final volume of 500 μL for HPLC analysis. HMF and HMZ were quantified by comparing their peak areas to each standard curve.

In vitro Simulation Digestion of HMZ

The adduct was subjected to *in vitro* simulated digestion at three stages, namely, the mouth, gastric, and intestinal stages, to evaluate its stability (28, 29). Briefly, HMZ (2 mg) was dissolved in DMSO (200 μL), diluted with ultra-pure water to the final concentration of 0.5 mg/mL, and then mixed with 6 mL of SSF in a flask. The mixture was magnetically stirred at 100 r/min for 2 min at 37°C to mimic saliva digestion. Afterward, 10 mL of SGF was added to simulate the gastric phase, and the mixture was reacted for 2 h under the same condition. Subsequently, 20 mL of SIF was added for the simulation of intestinal digestion for another 2 h. Samples (100 μL) were withdrawn at the end of each stage of the digestion process for HPLC analysis. Each digestion process was repeated in triplicate, and the content of HMZ was calculated by referring to the calibration curve.

Caco-2 Cell Culture

The Caco-2 cell line (ATCC HTB-37) was obtained from the American Type Culture Collection (Rockville, MD, USA). Cells were cultivated by the method of Kosińska-Cagnazzo et al. (30) with slight modifications. Specifically, α -MEM medium supplemented with 10% FBS, 1% penicillin/streptomycin, and 1% NEAA was used to cultivate Caco-2 cells at 37°C and 5% (v/v) CO_2 atmosphere. When the cells reached 80–90% confluence, they were detached with 0.25% trypsin-EDTA and further sub-cultured on fresh growth medium. Cells between passages 30 and 35 were used.

Cell Viability Assay

Cell viability was measured by the CCK-8 method as described by Zhao et al. (31) with modifications. Briefly, Caco-2 cells at a density of 2.5×10^4 cells/well were seeded into 96-well plates and maintained at 37°C under a humidified atmosphere containing 5% CO_2 and 95% air for 24 h. Subsequently, the origin culture medium was removed, and different concentrations (2, 4, 8, 16, 32, and 64 mM) of HMZ and HMF were added. Three duplicate wells were set for each concentration. The cells were further incubated for 24 and 48 h, respectively. Then, 10 μL of CCK-8 solution was added into each well for 2 h,

and the absorbance was read at 450 nm on a microplate reader (Multiskan, Thermo, USA).

Annexin V and Propidium Iodide (PI) Double-Staining Assay

The Annexin V-FITC apoptosis detection kit was used to measure the percentage of apoptotic cells in flow cytometry (FACS Calibur Becton Dickinson, USA) (14). Two milliliters of each cell suspension (9×10^5 cells/well) were cultured in 6-well plates. When the confluence reached 90%, the cells were treated with HMF (0, 2, 4, 8, and 16 mM) and HMZ (0, 4, 8, 16, and 32 mM) for 48 h and then harvested with trypsin (without EDTA). Subsequently, each cell suspension was centrifuged and washed with cold PBS twice. Then, the cells were suspended with 400 μ L of binding buffer to a final density of 1×10^6 cells/well, incubated with 5 μ L of Annexin V and 1 μ L of PI for 5 min in the dark, and subjected to flow cytometry assay.

Effect of Concentration on the Absorption of HMZ in Caco-2 Cells

HMZ absorption was evaluated according to de Oliveira et al. with slight modifications (32). Briefly, Caco-2 cells were inoculated in 6-well plates at the density of 2×10^4 cells/well (2 mL) and cultured until 90% confluence at 37°C with 5% CO₂. Then, the cells were washed thrice with 1 mL of HBSS. Another 1 mL of HBSS was added for further culture for 30 min. Ten microliters of HMZ solution (pH 7.4) at concentrations of 1–100 μ M were added separately and cultivated for 2 h to allow the adduct solution to be absorbed by cells under certain condition (37°C, 5% CO₂/95% air). The treated solution was transferred into Eppendorf tubes for HPLC analysis. The control of each

sample under different concentrations was the respective sample without incubation, and each of the absorption rate of the adduct by Caco-2 cells was calculated as follows:

$$\text{Absorption rate (\%)} = \frac{S_1 - S_2}{S_1} \times 100\% \quad (1)$$

where S_1 is the peak area of the control, and S_2 is the peak area of the sample incubated for 2 h.

Statistical Analysis

All experiments were repeated thrice. Data analysis was performed using Microsoft Excel, SPSS 22.0.0.1 (SPSS, Inc., Chicago, IL), and MestReNova software (version 12.0). The results were expressed as means \pm standard deviation.

RESULTS AND DISCUSSION

Structural Elucidation of HMZ

The retention time (R_t) of HMZ was 19.54 min with purity over 95% according to the HPLC chromatogram (Supplementary Figure 1A). The UV spectrum displayed the absorption maxima at 334 nm, which exhibited a bathochromic shift compared with those of ZGR (276 nm) and HMF (284 nm) (Supplementary Figure 1B).

Based on the structural characteristic of HMF and ZGR, an aldol condensation reaction was supposed to occur between HMF and ZGR with proline as a catalyst to generate HMZ (Figure 1A). In the MS spectrum (data not shown), the adduct exhibited a deprotonated molecular ion at m/z 301 [$M - H$][−] (calculated for C₁₇H₁₇O₅, 301.1), which was consistent with that of the suggested structure (C₁₇H₁₈O₅). This molecular

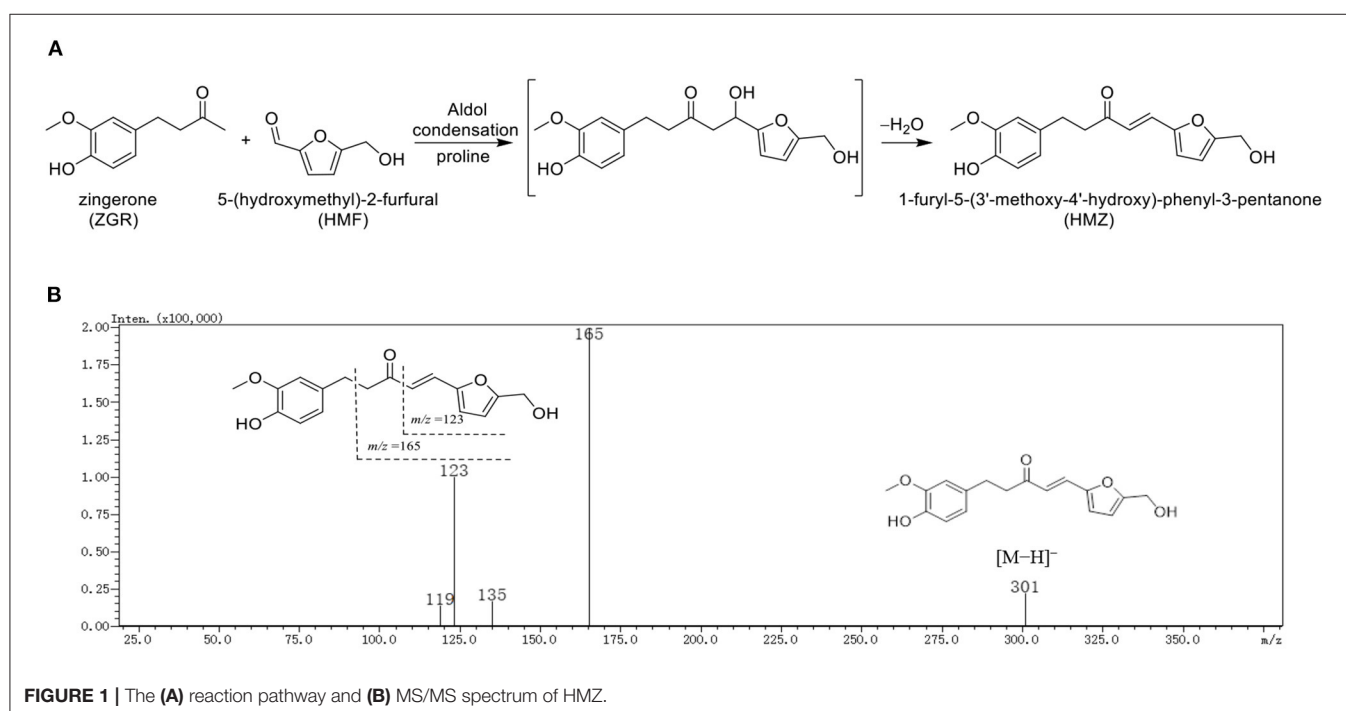


FIGURE 1 | The (A) reaction pathway and (B) MS/MS spectrum of HMZ.

TABLE 1 | ^1H and ^{13}C NMR data of HMZ, ZGR, and HMF (δ in ppm, J in Hz).

Position	HMZ ^a		ZGR ^b		HMF ^c	
	^1H	^{13}C	^1H	^{13}C	^1H	^{13}C
1	7.24 d (15.8)	128.8			9.33 s	180.5
2	6.63 d (15.8)	123.2	2.12 s	29.5		
3	–	199.4	–	207.8		
4	2.89	30.1	2.80–2.83 t (6.6)	30.0		
5	2.89	43.5	2.70–2.74 t (6.9)	44.9		
1'	–	133.2	–	137.9		
2'	6.71 s	111.3	6.64–6.66 dd (2,8)	112.6		
3'	–	146.6	–	150.8		
4'	–	144.0	–	140.0		
5'	6.81 d (8.0)	114.5	6.80 d (8.0)	122.5		
6'	6.68 d (8.0)	120.9	6.69 d (2.0)	120.2		
7'	3.85 s	56.0	3.84 s	55.7		
2''	–	151.0			–	151.8
3''	6.58 d (3.3)	116.9			7.40 d (3.6)	126.8
4''	6.36 d (3.3)	110.6			6.55 d (3.1)	110.9
5''	–	157.0				161.3
6''	4.63 s	57.7			4.57 s	56.0

^aMeasured at 400 (^1H) and 100 (^{13}C) MHz in CDCl_3 .

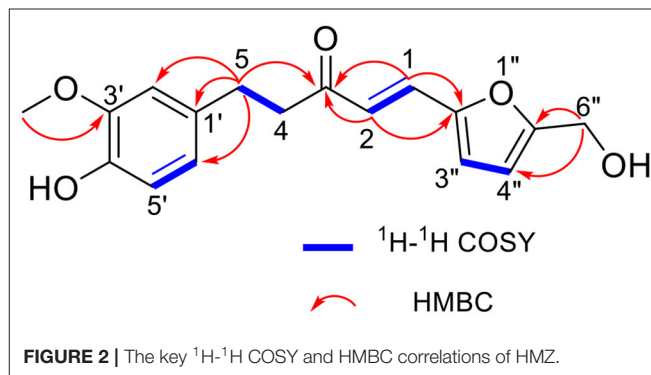
^bReferred to Agarwal et al. (33), ^cReferred to Chen et al. (34).

Overlapped signals were reported without designating multiplicity.

ion yielded two prominent peaks at m/z 165 and 123 in the MS/MS spectrum (**Figure 1B**). Specifically, the fragment ion at m/z 165 $[\text{M} - \text{C}_8\text{H}_9\text{O}_2]^-$ indicated the mass loss of 3-methoxy-4-hydroxybenzyl moiety, then subsequent α -scission of ketone yielded the ion at m/z 123 $[\text{M} - \text{C}_8\text{H}_9\text{O}_2 - \text{C}_2\text{H}_2\text{O}]^-$. Thus, the structure of HMZ was tentatively identified.

Subsequently, the structure of HMZ was entirely determined by the 1D and 2D NMR data, and the detailed assignment of H and C signals was listed in **Table 1**. The ^1H NMR spectrum (**Supplementary Figure 2**) showed the signals of 7 olefinic protons (δ_{H} 7.24, 6.63 [each 1H, d, $J = 15.8$ Hz]; δ_{H} 6.81, 6.68 [each 1H, d, $J = 8.0$ Hz]; 6.71 (1H, s); 6.58, 6.36 [each 1H, d, $J = 3.0$ Hz]), one methoxy group (δ_{H} 3.85, 3H, s), and one oxygenated methylene (δ_{H} 4.63, 2H, s). The ^{13}C NMR spectrum (**Supplementary Figure 3**) displayed 17 carbon signals, including one carbonyl (δ_{C} 199.4) and 12 unsaturated carbons (δ_{C} 157.0, 151.0, 146.6, 144.0, 133.2, 128.8, 123.2, 120.9, 116.9, 114.5, 111.3, 110.6). A detailed analysis of the 1D NMR data (**Table 1**) showed high similarities to those of HMF and ZGR. These results suggested that HMZ was an adduct between HMF and ZGR.

A further comparison of the data of HMZ with those of HMF and ZGR showed the following differences: the signal of a methyl connected with carbonyl and that of an aldehyde group were absent, two additional olefinic carbons (δ_{C} 128.8, 123.2) appeared, and some chemical shift changes (δ_{C} 199.4 in HMZ vs. δ_{C} 208.5 in ZGR; δ_{C} 157.0, 151.0, 116.9 in HMZ vs. δ_{C} 161.6, 152.3, 123.3 in HMF) occurred. These differences implied that the methyl, which was connected with the carbonyl (C-3) in ZGR, reacted with the aldehyde group of HMF to

**FIGURE 2** | The key ^1H - ^1H COSY and HMBC correlations of HMZ.

generate a double bond (C-1/C-2) to link the two residues. In the HMBC spectrum (**Supplementary Figure 7**), the observed correlations between H-1 (δ_{H} 7.26)/H-2 (δ_{H} 6.63) and C-3 (δ_{C} 199.4) confirmed that the double bond was directly connected with the carbonyl (C-3). The large coupling constant of H-1 and H-2 ($J = 15.8$ Hz) indicated the *E* geometry of C-1 and C-2. Thus, the exact structure of the adduct was determined as shown in **Figure 2**. The adduct was determined as a new compound with the systematic name of 1-furyl-5-(3'-methoxy-4'-hydroxy)-phenyl-3-pentanone.

Effects of Different Reaction Parameters on HMF Elimination and HMZ Formation

Here, the reduction of HMF by ZGR and the formation of their adduct were investigated at different conditions, including

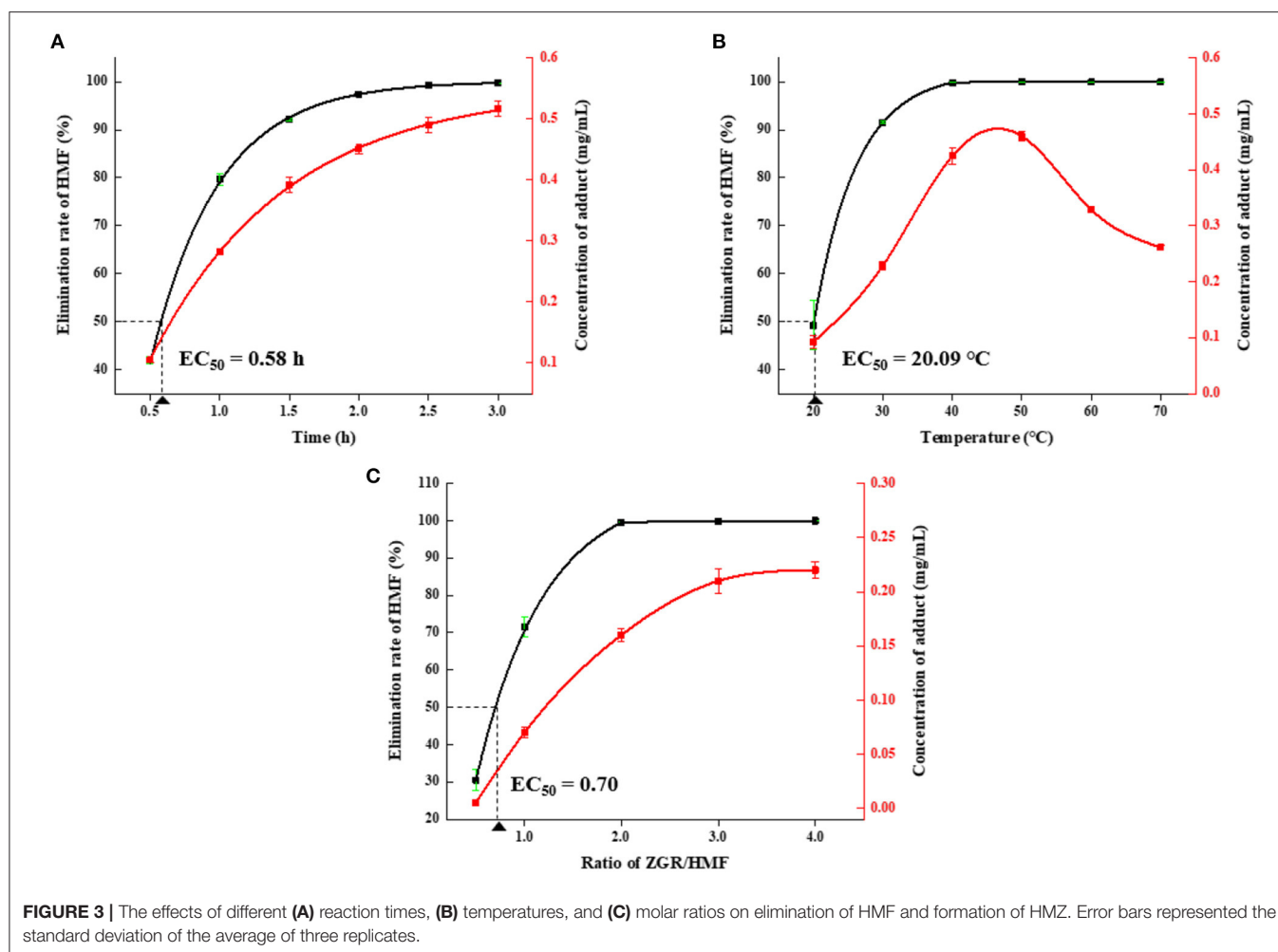


FIGURE 3 | The effects of different (A) reaction times, (B) temperatures, and (C) molar ratios on elimination of HMF and formation of HMZ. Error bars represented the standard deviation of the average of three replicates.

reaction time, temperature, and molar ratio. Standard curves for the quantitative analyses of HMF (50–450 $\mu\text{g/mL}$, $r^2 = 0.9999$, $n = 3$) and HMZ (50–500 $\mu\text{g/mL}$, $r^2 = 0.9999$, $n = 3$) were established.

As depicted in **Figure 3A**, the amount of HMF decreased and the concentration of HMZ increased with the prolongation of reaction time. Over 99% of HMF was depleted, and HMZ concentration reached 0.52 mg/mL after incubation for 3 h. **Figure 3B** showed the effect of reaction temperature on HMF reduction and HMZ formation. The remaining proportion of HMF dramatically decreased with the increase in temperature. In comparison, the amount of HMZ initially increased as the temperature increased but then decreased when the temperature was over 50°C. It was concluded that HMF elimination and HMZ formation were remarkably affected by temperature, and HMZ appeared to degrade when the temperature was over 50°C (**Supplementary Figure 8**). Thermal treatment-induced degradation could be also found in other substances, such as pyrethroid, which underwent hydrolysis, reduction or oxidation to yield lower molecular weight compounds (35). **Figure 3C** showed the influence of the molar ratio on the

reduction of HMF. HMF could be remarkably trapped by ZGR when the ZGR/HMF ratio increased (1:2 to 2:1), and the elimination rate could reach as high as 99% when the ratio was $\geq 2:1$. Additionally, a higher molar ratio promoted the accumulation of HMZ. Hence, based on the above results, the optimized condition for HMF elimination was the reaction time of 3 h, the temperature of 40°C, and the ZGR/HMF ratio of 2:1.

Stability of HMZ in Simulated *in vitro* Digestion

Adduct formation might be accompanied by adduct ingestion, while the stability of HMZ during the digestion process was not clear. Thus, the amount of HMZ was measured after mimic digestion in the oral, gastric, and intestinal phases to evaluate its stability in *in vitro* digestion process. The content of HMZ decreased by 7.14, 14.19, and 24.06% after digestion in SSE, SGE, and SIF (**Supplementary Figure 9**), respectively. In addition, three new peaks with small peak areas ($R_t = 12.49, 12.82, \text{ and } 13.56 \text{ min}$) in the HPLC chromatograph could

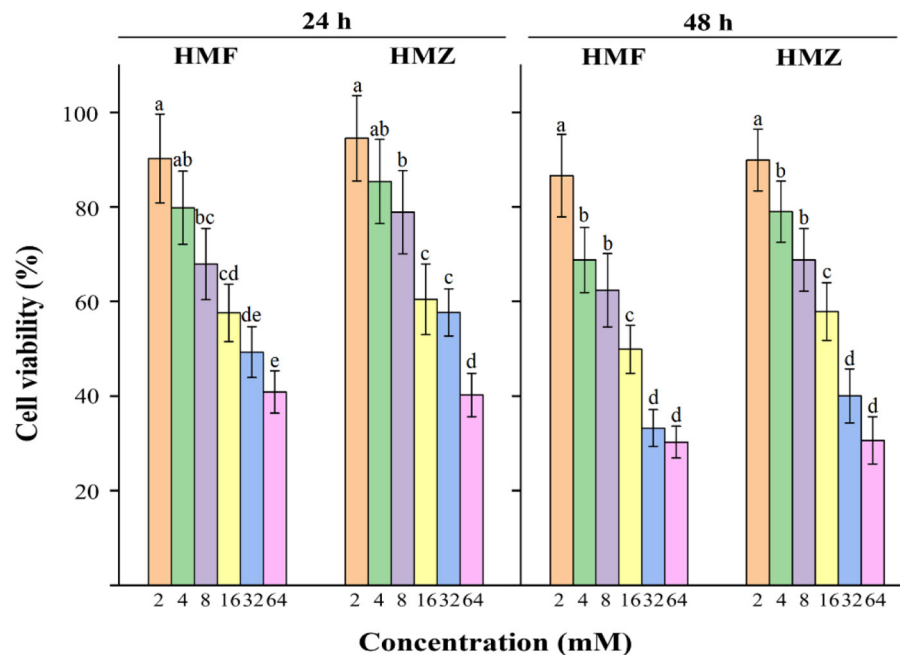


FIGURE 4 | Effects of HMF and HMZ at different concentrations on cell viability after 24 and 48 h. Different letters indicated significant differences ($P < 0.05$).

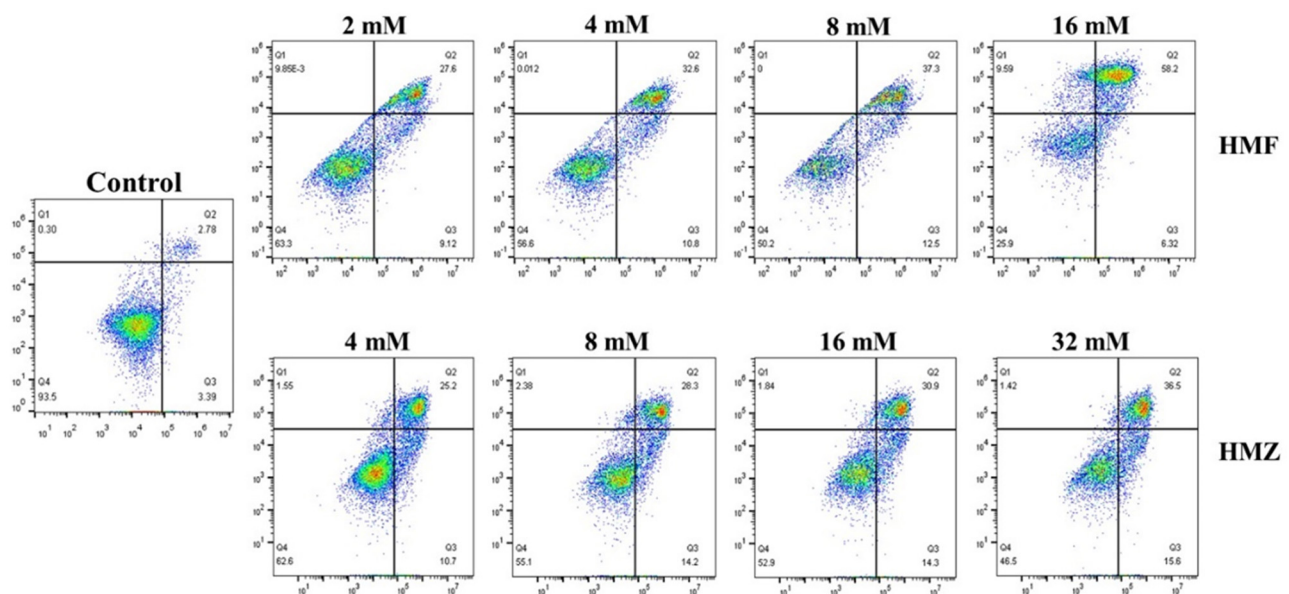


FIGURE 5 | Effects of HMF and HMZ at different concentrations on apoptosis in Caco-2 cells after 48 h.

be observed in the intestinal stage as digestion progressed (Supplementary Figure 10). But regrettably, these new peaks could not be characterized with current data. While, few peaks could be observed in the other two digestive environments. The reason might be that the content of decomposition

products in the oral and gastric phases was below the detection limit of HPLC. The results indicated that the stability of HMZ was of moderate level because 75.94% of the adduct was remained after undergoing three different digestion conditions.

Effects of HMF and HMZ on the Viability and Apoptosis of Caco-2 Cells

In order to evaluate the cytotoxicity of HMF and HMZ against Caco-2 cells, a combination of the CCK-8 method and Annexin V/PI staining assay was applied and the results were shown below.

In general, cells incubated with HMF and HMZ for 24 and 48 h displayed decreased viability in concentration- and time-dependent manners (**Figure 4**). The viability of Caco-2 cells decreased from 90.24 to 40.89% after exposure to 2–64 mM HMF for 24 h, while that of Caco-2 cells decreased from 94.54 to 40.22% in the HMZ treated group under the same condition. Similar results could be observed when the incubation time was prolonged to 48 h: the percentages of viable cells were from 86.65 to 30.27% in the HMF group and from 89.95 to 30.64% in the HMZ group. The IC_{50} values of HMZ were 41.47 ± 5.33 and 25.39 ± 3.12 mM after incubation for 24 and 48 h, respectively, whereas those of HMF were 35.39 ± 4.03 and 19.17 ± 2.10 mM. This CCK-8 analysis demonstrated that HMZ did not display obvious lower cytotoxicity to Caco-2 cells than that of HMF.

Apoptosis was commonly accompanied by some characteristic biochemical changes, such as the exposure of phosphatidylserine (Annexin V positive) on the cell membrane and the increase in cell membrane permeability that allowed the nucleic acid to be stained by PI (36). Therefore, Annexin V/PI double-staining assay was applied to measure apoptosis, and the apoptotic effects of HMF and HMZ on Caco-2 cells were determined by flow cytometry. As seen in **Figure 5**, HMF and HMZ induced apoptosis in Caco-2 cells dose-dependently, which manifested as an increase in the number of apoptotic cells (Annexin V+/PI– and Annexin V+/PI+). It was noticed that exposure to HMF at 2–16 mM for 48 h induced 64.52% of normal Caco-2 cells apoptosis, whereas exposure to HMZ at 4–32 mM resulted in ~52.10% of cell apoptosis. Meanwhile, compared with the control (8.54%), both HMF (43.40–64.52%) and HMZ (35.90–45.20%) displayed obvious cytotoxicity to Caco-2 cells after exposure at 4–16 mM for 48 h. Consistent with the analysis of the CCK-8 assay, the reduction of viable cells induced by HMZ was observed. In this sense, the cytotoxicity of HMZ toward Caco-2 cells should be noted, and that of HMZ to other cells was also worth studying.

Effect of Concentration on HMZ Absorption in Caco-2 Cells

According to the HPLC analysis (**Supplementary Table 1**), a positive correlation was observed between the concentration of HMZ and its absorption by Caco-2 cells. While, the HMZ absorption rate by Caco-2 cells initially increased when the HMZ concentration increased from 1 to 4 μ M, but declined at higher HMZ concentrations. The percentages of absorption rate were 60.74, 71.38, 56.11, and 34.71% for 1, 4, 20, and 100 μ M, respectively. Although the uptake of HMZ by Caco-2 cells increased with the increase in concentration, it was observed that the absorptivity decreased at higher molar concentrations. It had been well-elucidated that compounds either lipophilic or hydrophilic could be absorbed via active and passive transport routes (37). Moreover, several intestinal efflux and

uptake transporters expressed in Caco-2 cells were found to be responsible for regulating the permeation of the substrate during absorption, which would be also some factors to affect the absorption process (38).

CONCLUSION

In summary, HMF could be eliminated by ZGR through the formation of an adduct via aldol condensation with proline as a catalyst. This process was not reported previously. In this work, the structural elucidation of the adduct by HPLC, MS, and NMR data, along with the investigation of the effects of different reaction conditions, namely, reaction time, temperature, and molar ratio, on HMF elimination and HMZ formation, were carried out. Besides, the stability of the adduct (HMZ) after *in vitro* digestion, as well as its absorption and cytotoxicity in Caco-2 cells, were evaluated. The results demonstrated that HMZ was stable at a moderate level. Although compared with HMF, HMZ did show a certain toxic effect against Caco-2 cells, its effect on other cells remained to be studied. Overall, this study provided new data on ketones in food materials that could contribute to the elimination of HMF.

DATA AVAILABILITY STATEMENT

The original contributions presented in the study are included in the article/**Supplementary Materials**, further inquiries can be directed to the corresponding author.

AUTHOR CONTRIBUTIONS

YK: conceptualization, methodology, and writing—original draft. ZY: methodology, investigation, and writing—original draft. NC: methodology. PC: data curation, writing, and editing. JL: supervision. SO: conceptualization. GL: conceptualization and funding acquisition. All authors contributed to the article and approved the submitted version.

FUNDING

This work was supported by grants from Natural Science Foundation of China (82003609), Natural Science Foundations of Guangdong Province (2021A1515010110 and 2020A1515110453), China Postdoctoral Science Foundation (2019M663403), Graduate Education Innovation Program Project of Guangdong Province (2020JGXM107), Foundation of Guangdong Second Provincial General Hospital (TJGC-2021011), Doctoral Workstation Foundation of Guangdong Second Provincial General Hospital (2021BSGZ017), and Guangdong Basic and Applied Basic Research Foundation (2021A1515110430).

SUPPLEMENTARY MATERIAL

The Supplementary Material for this article can be found online at: <https://www.frontiersin.org/articles/10.3389/fnut.2022.893991/full#supplementary-material>

REFERENCES

- Farag MR, Alagawany M, Bin-Jumah M, Othman SI, Khafaga AF, Shaheen HM, et al. The toxicological aspects of the heat-borne toxicant 5-hydroxymethylfurfural in animals: a review. *Molecules*. (2020) 25:1941. doi: 10.3390/molecules25081941
- Shapla UM, Solayman M, Alam N, Khalil MI, Gan SH. 5-Hydroxymethylfurfural (HMF) levels in honey and other food products: effects on bees and human health. *Chem Cent J*. (2018) 12:35. doi: 10.1186/s13065-018-0408-3
- Mortas M, Gul O, Yazici F, Dervisoglu M. Effect of brewing process and sugar content on 5-hydroxymethylfurfural and related substances from Turkish coffee. *Int J Food Prop*. (2016) 20:1866–75. doi: 10.1080/10942912.2016.1222587
- Rufián-Henares JA, Delgado-Andrade C, Morales FJ. Analysis of heat-damage indices in breakfast cereals: influence of composition. *J Cereal Sci*. (2006) 43:63–9. doi: 10.1016/j.jcs.2005.05.001
- Murkovic M, Pichler N. Analysis of 5-hydroxymethylfurfural in coffee, dried fruits and urine. *Mol Nutr Food Res*. (2006) 50:842–6. doi: 10.1002/mnfr.200500262
- Czerwonka M, Pietrzak-Sajjad R, Bobrowska-Korczak B. Evaluation of 5-hydroxymethylfurfural content in market milk products. *Food Addit Contam Part A Chem Anal Control Expo Risk Assess*. (2020) 37:1135–44. doi: 10.1080/19440049.2020.1757162
- Janzowski C, Glaab V, Samimi E, Schlatter J, Eisenbrand G. 5-hydroxymethylfurfural: assessment of mutagenicity, dna-damaging potential and reactivity towards cellular glutathione. *Food Chem Toxicol*. (2000) 38:801–9. doi: 10.1016/S0278-6915(00)00070-3
- Hamzalioglu A, Gokmen V. Formation and elimination reactions of 5-hydroxymethylfurfural during *in vitro* digestion of biscuits. *Food Res Int*. (2017) 99:308–14. doi: 10.1016/j.foodres.2017.05.034
- Kavousi P, Mirhosseini H, Ghazali H, Ariffin AA. Formation and reduction of 5-hydroxymethylfurfural at frying temperature in model system as a function of amino acid and sugar composition. *Food Chem*. (2015) 182:164–70. doi: 10.1016/j.foodchem.2015.02.135
- Bakhiya N, Monien B, Frank H, Seidel A, Glatt H. Renal organic anion transporters OAT1 and OAT3 mediate the cellular accumulation of 5-sulphoxymethylfurfural, a reactive, nephrotoxic metabolite of the Maillard product 5-hydroxymethylfurfural. *Biochem Pharmacol*. (2009) 78:414–19. doi: 10.1016/j.bcp.2009.04.017
- Bauer-Marinovic M, Taugner F, Florian S, Glatt H. Toxicity studies with 5-hydroxymethylfurfural and its metabolite 5-sulphoxymethylfurfural in wild-type mice and transgenic mice expressing human sulphotransferases 1A1 and 1A2. *Arch Toxicol*. (2012) 86:701–11. doi: 10.1007/s00204-012-0807-5
- European Food Safety Authority. Consideration of furfuryl alcohol and related flavouring substances evaluated by JECFA (55th meeting) structurally related to furfuryl and furan derivatives with and without additional side chain substituents and heteroatoms. *EFSA J*. (2009) 752:1–39. doi: 10.2903/j.efsa.2009.752
- Yang N, Qiu R, Yang S, Zhou K, Wang C, Ou S, et al. Influences of stir-frying and baking on flavonoid profile, antioxidant property, and hydroxymethylfurfural formation during preparation of blueberry-filled pastries. *Food Chem*. (2019) 287:167–75. doi: 10.1016/j.foodchem.2019.02.053
- Wang G, Liu P, He J, Yin Z, Yang S, Zhang G, et al. Identification of a 5-hydroxymethylfurfural-lysine Schiff base and its cytotoxicity in three cell lines. *J Agric Food Chem*. (2019) 67:10214–21. doi: 10.1021/acs.jafc.9b04539
- Es-Safi NE, Cheynier V, Moutounet M. Role of aldehydic derivatives in the condensation of phenolic compounds with emphasis on the sensorial properties of fruit-derived foods. *J Agric Food Chem*. (2002) 50:5571–85. doi: 10.1021/jf025503y
- Mahomoodally MF, Aumeeruddy MZ, Rengasamy KRR, Roshan S, Hammad S, Pandohee J, et al. Ginger and its active compounds in cancer therapy: from folk uses to nano-therapeutic applications. *Semin Cancer Biol*. (2021) 69:140–49. doi: 10.1016/j.semcancer.2019.08.009
- Shin SG, Kim JY, Chung HY, Jeong JC. Zingerone as an antioxidant against peroxynitrite. *J Agric Food Chem*. (2005) 53:7617–22. doi: 10.1021/jf051014x
- Mehrzadi S, Khalili H, Fatemi I, Malayeri A, Siahpoosh A, Goudarzi M. Zingerone mitigates carrageenan-induced inflammation through antioxidant and anti-inflammatory activities. *J Inflamm*. (2021) 44:186–93. doi: 10.1007/s10753-020-01320-y
- Gan H, Zhang Y, Zhou Q, Zheng L, Xie X, Veeraraghavan VP, et al. Zingerone induced caspase-dependent apoptosis in MCF-7 cells and prevents 7,12-dimethylbenz(a)anthracene-induced mammary carcinogenesis in experimental rats. *J Biochem Mol Toxicol*. (2019) 33:e22387. doi: 10.1002/jbt.22387
- Hemalatha KL, Stanely Mainzen Prince P. Antihyperlipidaemic, antihypertrophic, and reducing effects of zingerone on experimentally induced myocardial infarcted rats. *J Biochem Mol Toxicol*. (2015) 29:182–8. doi: 10.1002/jbt.21683
- Manjunatha JR, Bettadaiah BK, Negi PS, Srinivas P. Synthesis of quinoline derivatives of tetrahydrocurcumin and zingerone and evaluation of their antioxidant and antibacterial attributes. *Food Chem*. (2013) 136:650–8. doi: 10.1016/j.foodchem.2012.08.052
- Mani V, Arivalagan S, Siddique AI, Namasivayam N. Antioxidant and anti-inflammatory role of zingerone in ethanol-induced hepatotoxicity. *Mol Cell Biochem*. (2016) 421:169–81. doi: 10.1007/s11010-016-2798-7
- List B, Pojarliev P, Castello C. Proline-catalyzed asymmetric aldol reactions between ketones and α -unsubstituted aldehydes. *Org Lett*. (2001) 3:573–5. doi: 10.1021/ol006976y
- Mandal S, Mandal S, Ghosh SK, Ghosh A, Saha R, Banerjee S, et al. Review of the aldol reaction. *Synth Commun*. (2016) 46:1327–42. doi: 10.1080/00397911.2016.1206938
- List B, Hoang L, Martin HJ. New mechanistic studies on the proline-catalyzed aldol reaction. *Proc Natl Acad Sci USA*. (2004) 101:5839–42. doi: 10.1073/pnas.0307979101
- List B, Lerner RA, Barbas CF. Proline-catalyzed direct asymmetric aldol reactions. *J Am Chem Soc*. (2000) 122:2395–6. doi: 10.1021/ja994280y
- Chen L, Wu JE, Li ZM, Liu Q, Zhao X, Yang HS. Metabolomic analysis of energy regulated germination and sprouting of organic mung bean (*Vigna radiata*) using NMR spectroscopy. *Food Chem*. (2019) 286:87–97. doi: 10.1016/j.foodchem.2019.01.183
- Ran XL, Yang ZX, Chen YE, Yang HS. Konjac glucomannan decreases metabolite release of a plant-based fishball analogue during *in vitro* digestion by affecting amino acid and carbohydrate metabolic pathways. *Food Hydrocoll*. (2022) 129:107623. doi: 10.1016/j.foodhyd.2022.107623
- Huang M, Zhao X, Mao YH, Chen L, Yang HS. Metabolite release and rheological properties of sponge cake after *in vitro* digestion and the influence of a flour replacer rich in dietary fibre. *Food Res Int*. (2021) 144:110355. doi: 10.1016/j.foodres.2021.110355
- Kosińska-Cagnazzo A, Diering S, Prim D, Andlauer W. Identification of bioaccessible and uptaken phenolic compounds from strawberry fruits in *in vitro* digestion/Caco-2 absorption model. *Food Chem*. (2015) 170:288–94. doi: 10.1016/j.foodchem.2014.08.070
- Zhao Q, Zou Y, Huang C, Lan P, Zheng J, Ou S. Formation of a hydroxymethylfurfural-cysteine adduct and its absorption and cytotoxicity in Caco-2 cells. *J Agric Food Chem*. (2017) 65:9902–8. doi: 10.1021/acs.jafc.7b03938
- de Oliveira CL, Brychkova G, Esteves-Ferreira AA, McKeown P, de Souza Gomes M, Maluf WR, et al. Thermal disruption of the food matrix of biofortified lettuce varieties modifies absorption of carotenoids by Caco-2 cells. *Food Chem*. (2019) 308:125443. doi: 10.1016/j.foodchem.2019.125443
- Agarwal M, Walia S, Dhingra S, Khambay BP. Insect growth inhibition, antifungal and antifungal activity of compounds isolated/derived from *Zingiber officinale* Roscoe (ginger) rhizomes. *Pest Manag Sci*. (2001) 57:289–300. doi: 10.1002/ps.263
- Chen J, Zhao G, Chen L. Efficient production of 5-hydroxymethylfurfural and alkyl levulinate from biomass carbohydrate using ionic liquid-based polyoxometalate salts. *RSC Adv*. (2014) 4:4194–202. doi: 10.1039/C3RA45632C
- Wongmaneepratap W, Gao XF, Yang HS. Effect of food processing on reduction and degradation pathway of pyrethroid pesticides in mackerel fillet (*Scomberomorus commerson*). *Food Chem*. (2022) 384:132523. doi: 10.1016/j.foodchem.2022.132523

36. Riccardi C, Nicoletti I. Analysis of apoptosis by propidium iodide staining and flow cytometry. *Nat Protoc.* (2006) 1:1458–61. doi: 10.1038/nprot.2006.238
37. Press B, Di Grandi D. Permeability for intestinal absorption: caco-2 assay and related issues. *Curr Drug Metab.* (2008) 9:893–900. doi: 10.2174/138920008786485119
38. Iftikhar M, Iftikhar A, Zhang H, Gong L, Wang J. Transport, metabolism and remedial potential of functional food extracts (FFE) in Caco-2 cells monolayer: a review. *Food Res Int.* (2020) 136:109240. doi: 10.1016/j.foodres.2020.109240

Conflict of Interest: The authors declare that the research was conducted in the absence of any commercial or financial relationships that could be construed as a potential conflict of interest.

Publisher's Note: All claims expressed in this article are solely those of the authors and do not necessarily represent those of their affiliated organizations, or those of the publisher, the editors and the reviewers. Any product that may be evaluated in this article, or claim that may be made by its manufacturer, is not guaranteed or endorsed by the publisher.

Copyright © 2022 Ke, Yin, Chen, Chen, Liu, Ou and Li. This is an open-access article distributed under the terms of the Creative Commons Attribution License (CC BY). The use, distribution or reproduction in other forums is permitted, provided the original author(s) and the copyright owner(s) are credited and that the original publication in this journal is cited, in accordance with accepted academic practice. No use, distribution or reproduction is permitted which does not comply with these terms.



Source Tracker Modeling Based on 16S rDNA Sequencing and Analysis of Microbial Contamination Sources for Pasteurized Milk

Bingyao Du^{1,2,3}, Lu Meng^{1,3}, Haoming Wu^{1,3}, Huaigu Yang⁴, Huimin Liu^{1,3}, Nan Zheng^{1,3}, Yangdong Zhang^{1,3}, Shengguo Zhao^{1,3} and Jiaqi Wang^{1,3*}

¹ Key Laboratory of Quality and Safety Control for Milk and Dairy Products of Ministry of Agriculture and Rural Affairs, Institute of Animal Sciences, Chinese Academy of Agricultural Sciences, Beijing, China, ² State Key Laboratory of Grassland Agro-Ecosystems, Key Laboratory of Grassland Livestock Industry Innovation, Ministry of Agriculture and Rural Affairs, College of Pastoral Agriculture Science and Technology, Lanzhou University, Lanzhou, China, ³ Laboratory of Quality and Safety Risk Assessment for Dairy Products of Ministry of Agriculture and Rural Affairs, Institute of Animal Sciences, Chinese Academy of Agricultural Sciences, Beijing, China, ⁴ Sericultural and Agri-Food Research Institute, Guangdong Academy of Agricultural Sciences, Key Laboratory of Functional Foods, Ministry of Agriculture and Rural Affairs, Guangdong Key Laboratory of Agricultural Products Processing, Guangzhou, China

OPEN ACCESS

Edited by:

Hao Dong,
Zhongkai University of Agriculture and
Engineering, China

Reviewed by:

Xin Yi Lan,
Hunan Agricultural University, China
Hongbo Li,
Shaanxi University of Science and
Technology, China

*Correspondence:

Jiaqi Wang
jiaqi.wang@vip.163.com

Specialty section:

This article was submitted to
Food Chemistry,
a section of the journal
Frontiers in Nutrition

Received: 29 December 2021

Accepted: 31 March 2022

Published: 28 April 2022

Citation:

Du B, Meng L, Wu H, Yang H, Liu H,
Zheng N, Zhang Y, Zhao S and
Wang J (2022) Source Tracker
Modeling Based on 16S rDNA
Sequencing and Analysis of Microbial
Contamination Sources for
Pasteurized Milk.
Front. Nutr. 9:845150.
doi: 10.3389/fnut.2022.845150

Milk is rich in fat, protein, minerals, vitamins, peptides, immunologically active substances, and other nutrients, and it plays an important role in satisfying human nutrition and health. However, dairy product safety incidents caused by microbial contamination have occurred. We found that the total bacterial numbers in the pasteurized product were low and far below the limit requirements of the food safety standards of the European Union, the United States, and China. At the genus level, the primary microbial groups found in milk samples were *Acinetobacter*, *Macroccoccus*, *Pseudomonas*, and *Lactococcus*, while in the equipment rinse water and air samples there was contamination by *Stenotrophomonas* and *Acinetobacter*. The Source Tracker model analysis indicated that the microorganisms in the final milk products were significantly related to the contamination in product tanks and raw milk. Therefore, it is the hope that this work can provide guidance to pinpoint contamination problems using the proper quality control sampling at specific stages in the pasteurization process.

Keywords: milk, microbial, contamination, 16s rDNA sequencing, Source Tracker

INTRODUCTION

Milk, which is a nutrient source for protein, minerals, vitamins, and immunologically active substances, is considered a perfect food and plays an important role in meeting human nutritional needs (1–3). However, it is a good growth media for microorganisms because of the rich nutrients.

Contaminated milk may rapidly deteriorate and pose a potential health threat (4–8). According to reports, the detection rate of pathogens in pasteurized milk in Brazil is 4.7%, and pasteurized milk in China is often reported to be contaminated with pathogens (9–11). These bacteria are not naturally present in the mammary glands of healthy cows, and therefore, it is necessary to track the source of the microorganisms in milk, as they may find their way into milk as a result of poor milking and farming practices (12).

Spanu et al. used polymerase chain reaction (PCR) and pulsed-field gel electrophoresis technology to analyze the contamination sources of *Listeria monocytogenes* in cheese, and found that the processing environment of the cheese factory was the main source of microbial contamination (13). Maya analyzed the source of contamination of methicillin-resistant *Staphylococcus aureus* in pasteurized milk through multilocus sequence typing and pulsed-field gel electrophoresis technology, and found that cross-contamination after processing was one of the main sources of contamination (14). Wang et al. used 16S rRNA-PacBio Single Molecule Real-Time sequencing method to trace the microbes in milk powder and found that raw milk or processing equipment was one of the main sources of contamination (15). These studies are based on the typing and identification of strains based on the culture method or single sequencing technology, which has certain limitations.

In recent years, the Source Tracker modeling based on 16S rDNA sequencing and analysis of microbial contamination sources for raw milk have been widely used. Du et al. used Source Tracker modeling based on 16S rDNA sequencing to analyze the sources of microbial contamination in raw milk and found that the teat liner and teat dip cup were the main sources of contamination (16). Wu et al. used Source Tracker modeling based on 16S rDNA sequencing to analyze the source of microbial contamination in farm milk using automatic milking systems and found that airborne dust was the most important source of contamination (17).

Traceability analysis or determination of the presence of a particular substance or microorganism along a sample processing chain has been widely applied in microbiological studies. However, there have been few studies on the traceability of microorganisms in pasteurized milk and finding the particular processing step in which the contamination most likely occurs. The objective of the current study was to evaluate the traceability of microorganisms in pasteurized milk and analyze the individual processing steps, utilizing the Source Tracker model based on 16S rDNA sequencing, and find the potential sources of microbial contamination, which will help us formulate reasonable disinfection and cleaning procedures to improve the quality of dairy products.

MATERIALS AND METHODS

Sampling

Milk samples were collected at 8 critical control points along the milk processing pathway at the dairy processors in Zhengzhou City, Henan province in May 2019. The ambient temperature was 25°C. The control points included milk tanker (30 tons, raw milk, M1), storage tank (30 tons, raw milk, M2), storage tank for processing (30 tons, raw milk, M3), milk in balance tank (72°C/15 s, M4), milk in balance tank (75°C/15 s, M5), milk in balance tank (80°C/15 s, M6), milk in product tank (72°C/15 s, M7), milk in product tank (75°C/15 s, M8), milk in product tank (80°C/15 s, M9), pasteurized milk (72°C/15 s, M10), pasteurized milk (75°C/15 s, M11), pasteurized milk (80°C/15 s, M12), equipment water rinses (W), and processing factory air (A). The cleaning frequency of the tank was once a day. The milk

was stored in the tank for 2 h before processing. A quantity of 200 ml of clean in place (CIP) water from the dairy factory was collected every day, and stored in sterile sampling bottles. For the collection method of air samples, referring to Du et al. (16), milk samples (50 ml) were collected in triplicate each day at each sampling point for 4 consecutive days and immediately stored at −20°C until analysis.

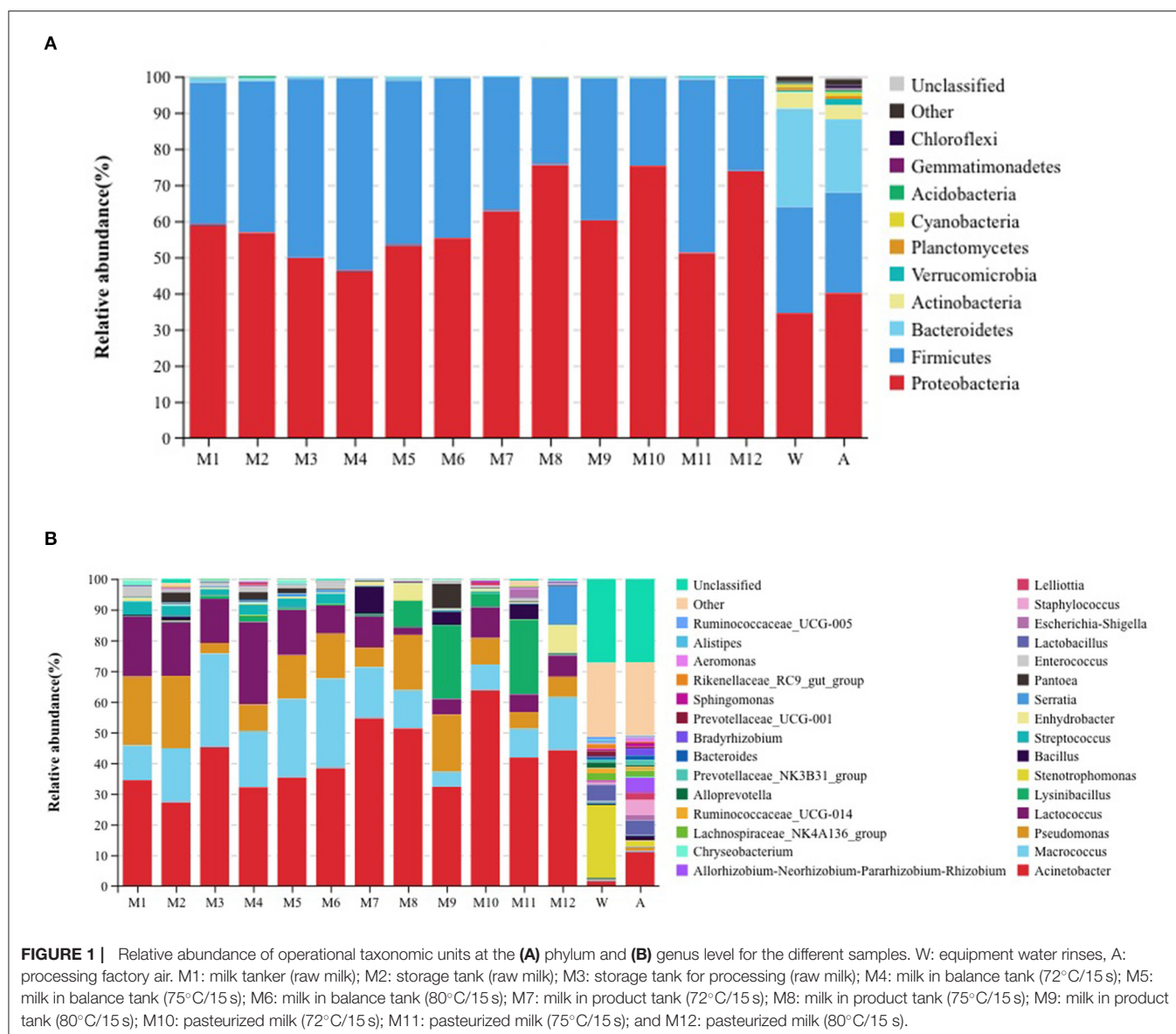
Detection of Total Viable Bacterial Counts, Alkaline Phosphatase, and Lactoperoxidase

The counts of total viable bacteria (TBC) was determined following the National Standards of the Republic of China (GB 4789.2-2016) (18), alkaline phosphatase was detected following the International Dairy Federation (IDF) procedure (IDF, method 209, 2007) (19), and lactoperoxidase was determined following the Tianjin Dairy Science and Technology Innovation Association Group Standard (T/TDSTIA, method 001, 2021) (20).

16S RDNA Sequencing

Milk samples (10 ml each) were centrifuged at 14,000 × g for 5 min, and the precipitate was used for DNA extraction using the HiPure Stool DNA Kits (Magen, Guangzhou, China) according to the manufacturer's instructions. Extracted DNA was amplified using the following PCR cycling program: 94°C for 2 min, followed by 30 cycles at 98°C for 10 s, 62°C for 30 s, and 68°C for 30 s, and a final extension at 68°C for 5 min. The PCR primers were specific for the 16S rDNA V3-V4 region: (5'-3') 341F: CCTACGGGNGGCWGCAG, 806R: GGACTACHVGGGTATCTAAT (21). PCR reactions utilized KOD Polymerase (Millipore Sigma, Rockville, MD, USA). Reagents were provided with the commercial enzyme kit. DNA recovery of amplicons was obtained following agarose gel electrophoresis using an AxyPrep DNA gel extraction kit (Axygen Biosciences, Union City, AZ, USA). FASTP was used to filter the original data, and reads containing >10% of unknown nucleotides (nt) were deleted as were strings of 20 nt with a mass <50% of the Q value (22, 23). Pairs of clean reads were combined into the original tag with a minimum overlap of 10 nt and a mismatch error of 2%. The original tag sequences were then filtered through QIIME (version 1.9.1) (24) using the reference database v.r20110519 (http://drive5.com/uchime/uchime_download.html) (25) to obtain high quality clean labels. Noise reduction, chimera detection, and aggregation into operational taxonomic units (OTU) containing 97% identities were performed using UPARSE (v. 9.2.64) (26).

The SILVA database (v. 132) (27) was used to classify representative sequences as biological using the naive Bayes model using confidence threshold ranges from 0.8 to 1. Krona (v.2.6) was used to visualize the abundance of each taxonomic group (28). Stacked bar charts were visualized using R project ggplot2 (v.2.2.1) (17, 29) and Omicsmart (<http://www.omicsmart.com>). Pheatmap software (v. 1.0.12) from Omicsmart was used to indicate species richness.



Statistical Analyses

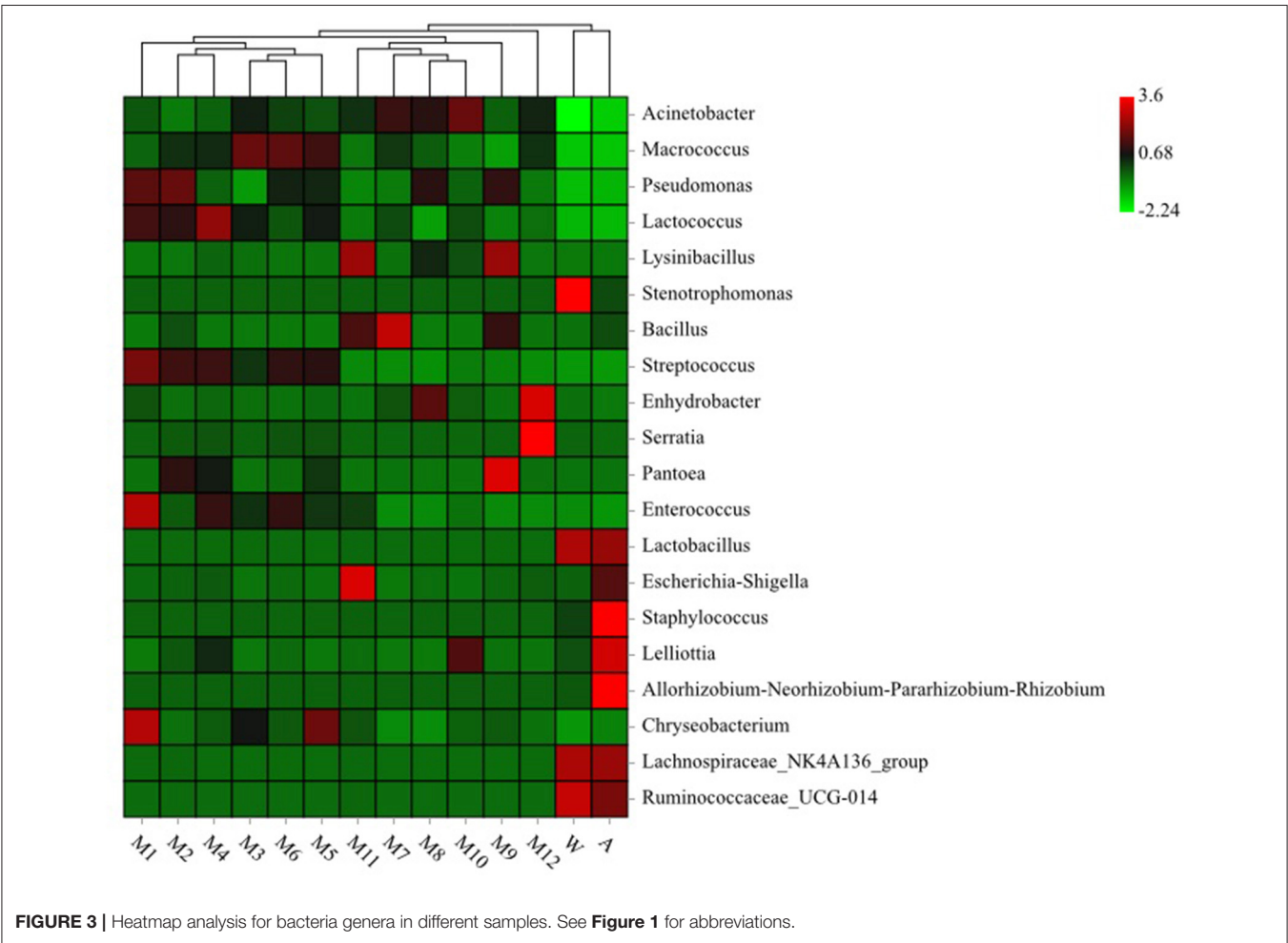
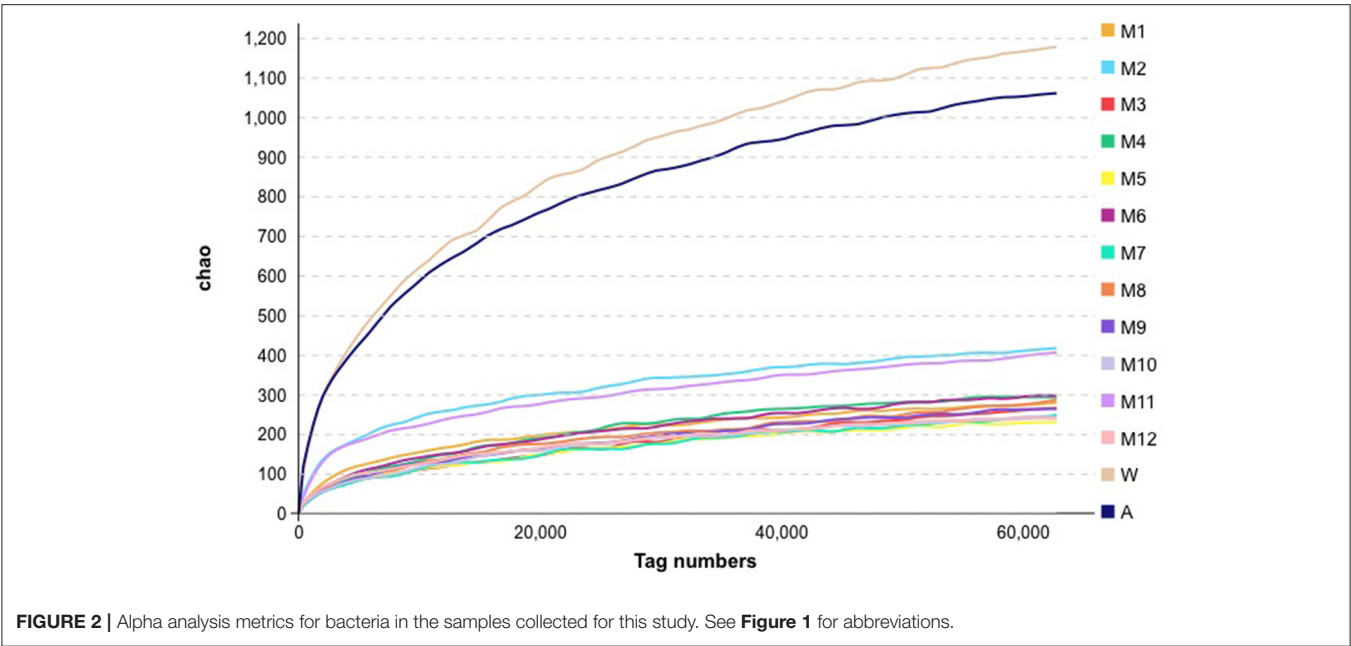
The principal coordinate (CAP) graphs were visualized using ggplot2 (30, 31). Pearson correlation coefficient >0.7 was considered significant. Similarly, hierarchical clustering and heat map construction were completed. The Source Tracker modeling based on 16S rDNA sequencing can be used for the analysis of microbial contamination sources for raw milk and pasteurized milk, and can calculate the similarities between different bacterial communities (32). The Source Tracker model was based on the Bayesian algorithm (<https://github.com/danknights/sourcetracker>, accessed as of July 2021) to predict the composition ratio of the target samples from each source sample, according to the microbial community structure distribution of the target samples and the source samples. The colored sector area indicated the proportion of each source in the samples, and explored the analysis

of the source of microbial contamination in the target sample (32–34).

RESULTS

Overall Microbiome Analysis

We tested the total number of colony counts in raw milk and pasteurized product for 4 consecutive days. The average total number of colonies in raw milk was 2.1×10^3 CFU/ml, and the average total number of colonies in the pasteurized products was 2.1×10^2 CFU/ml (72°C for 15 s), 18 CFU/ml (75°C for 15 s), and 2 CFU/ml (80°C for 15 s). The alkaline phosphatase in all pasteurized products was negative (<350 mU/L), and the average lactoperoxidase of the pasteurized products were 6,278.7 U/L (72°C for 15 s), 3,644.2 U/L (75°C for 15 s), and 0 U/L (80°C for 15 s).



An analysis of the microbiota of all samples indicated the presence of 10 phyla that were considered as abundant. These included Chloroflexi, Gemmatimonadetes, Actinobacteria, Cyanobacteria, Planctomycetes, Verrucomicrobia, Acidobacteria, Bacteroidetes, Firmicutes, and Proteobacteria. All milk samples had the two major phyla groups of Proteobacteria and Firmicutes. Air and water samples had the largest number of OTUs present, comprising primarily of the three major phyla groups of Proteobacteria, Firmicutes, and Bacteroidetes. A comparison with the raw milk samples indicated that Firmicutes abundance in pasteurized samples gradually decreased while Bacteroidetes almost disappeared, even though Firmicutes and Proteobacteria remained the primary phyla. In addition, the relative abundance of Bacteroidetes in the water and air samples was higher than in the milk samples (Figure 1A). We also found 30 genera that were considered as abundant, of which, *Acinetobacter*, *Macrococcus*, *Pseudomonas*, and *Lactococcus* were the most abundant genera found in samples from the milk tanker, storage tanks, storage tank for processing, and milk in balance tank. *Lysinibacillus* was a relatively abundant genus in milk samples from the product tank. *Acinetobacter* was the most abundant genera in pasteurized samples. *Stenotrophomonas* and *Acinetobacter* were the most abundant genera in water and air samples, respectively (Figure 1B). Among the water samples, the relative abundance of *Stenotrophomonas* was higher than in other samples, but the relative abundance of *Acinetobacter* was lower than in other samples.

Microbiota Diversity Based on Alpha Analysis

The diversity within samples and between samples was evaluated using alpha diversity analyses. We found differences in microbiota richness between raw milk in the farm milk tanks and the air samples, when compared with all of the other samples, using the Chao1 index (Figure 2). Compared with raw milk, the Chao1 indices for the samples following pasteurization decreased, indicating a reduction in bacterial abundance.

Clustering Heat Map Analysis

We used clustering heat map analysis to further explore the differences in the community structure (the top 20 relative abundances) of microorganisms in different samples at the genus level (Figure 3), and found that milk tanker sample (raw milk), storage tank sample (raw milk), storage tank for processing sample (raw milk), milk in balance tank sample (72°C/15s), milk in balance tank sample (75°C/15s), and milk in balance tank sample (80°C/15s) were apparently clustered together due to *Pseudomonas*, *Lactococcus*, *Streptococcus*, and *Enterococcus*. Equipment water rinses sample and processing factory air sample were apparently clustered together due to *Ruminococcaceae*_UCG-014, *Lachnospiraceae*_NK4A136_group, and *Lactobacillus*.

Canonical Analysis of Principal Coordinates

Canonical analysis of principal coordinates (CAP) indicated the top 10 most abundant genera (*Acinetobacter*, *Macrococcus*,

Pseudomonas, *Lactococcus*, *Lysinibacillus*, *Stenotrophomonas*, *Bacillus*, *Streptococcus*, and *Enhydrobacter*) associated with milk, which were clustered in contrast to the rinse water and the processing factory air represented by *Stenotrophomonas*, which was considered as an independent group with a 70% similarity (Figure 4). *Acinetobacter*, *Macrococcus*, *Pseudomonas*, *Lactococcus*, and *Streptococcus*, which are regarded as typical bacterial taxa of other samples, were not abundant in the processing factory air.

The Source Tracker Analysis

Sources of environmental contamination in milk were assessed using the Source Tracker model. The sources included all factory environmental samples, raw milk sample, and processed samples, while the sinks were represented by including pasteurized milk samples. The Source Tracker model considered each individual community as a mixed community deposited from other known or unknown environmental sources. The Source Tracker model analysis indicated that the microorganisms in the products were significantly correlated to those in the product tank, followed by milk tanker, which was the second most important source of contaminants (Figure 5).

DISCUSSION

This study utilized high-throughput sequencing technology to analyze the microbial communities of milk from the delivery tanks to the final stage of pasteurization at a milk processing facility. The primary phyla found in raw milk were *Proteobacteria* and *Firmicutes*, while *Proteobacteria*, *Firmicutes*, and *Bacteroidetes* predominated the air and equipment rinse water. The *Proteobacteria* was the most dominant phylum in the pasteurized milk samples, followed by *Firmicutes*. After pasteurization of 15 s at 72, 75, and 80°C, the *Proteobacteria* and *Firmicutes* population remained constant. Previous studies have shown that the primary bacterial phyla were *Proteobacteria* and *Firmicutes* (35), while *Pseudomonas*, *Acinetobacter*, *Lactococcus*, *Corynebacterium*, and *Streptococcus* were the most abundant genera in raw milk (36). At the same time, the researchers compared the community structure of microbes in the raw milk collected from two dairy farms and found that *Moraxellaceae*, *Streptococcaceae*, *Pseudomonadaceae*, *Staphylococcaceae*, and *Enterobacteriaceae* were the main microorganisms, but the relative abundance was different. The most obvious were *Enterobacteriaceae* and *Moraxellaceae*. The relative abundances of *Enterobacteriaceae* in the raw milk from the two dairy farms were 82.8 and 0.6%, respectively, and the relative abundances of *Moraxellaceae* in the raw milk of the two dairy farms were 35.7 and 5.4%, respectively (16). The relative abundance of microorganisms in raw milk was different, which may be related to the cleanliness of farm production management, milk tankers, and transport vehicles. *Enterobacteriaceae* and *Pseudomonadaceae* are mainly derived from the environment. Comparing the microbial community structure of the same pasture in summer and winter, the microorganisms with relatively high abundance in summer milk were *Staphylococcaceae*, *Ruminococcaceae*, *Aerococcaceae*,

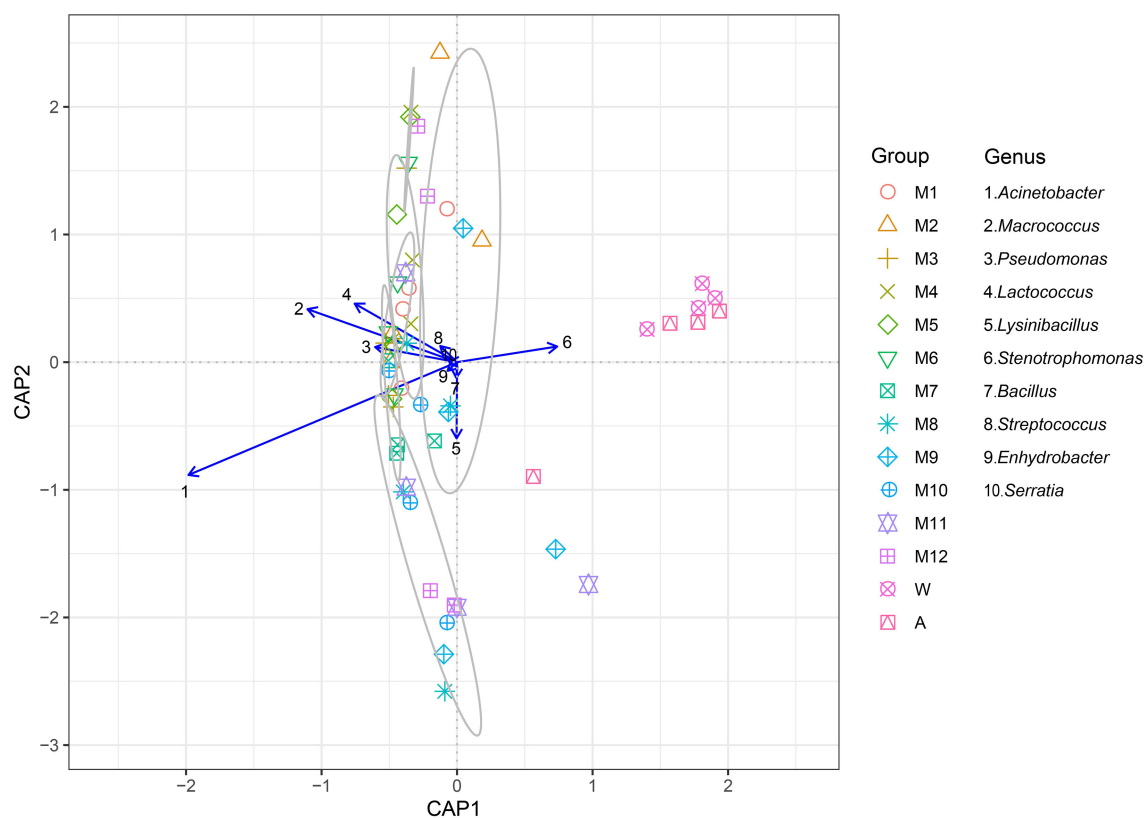
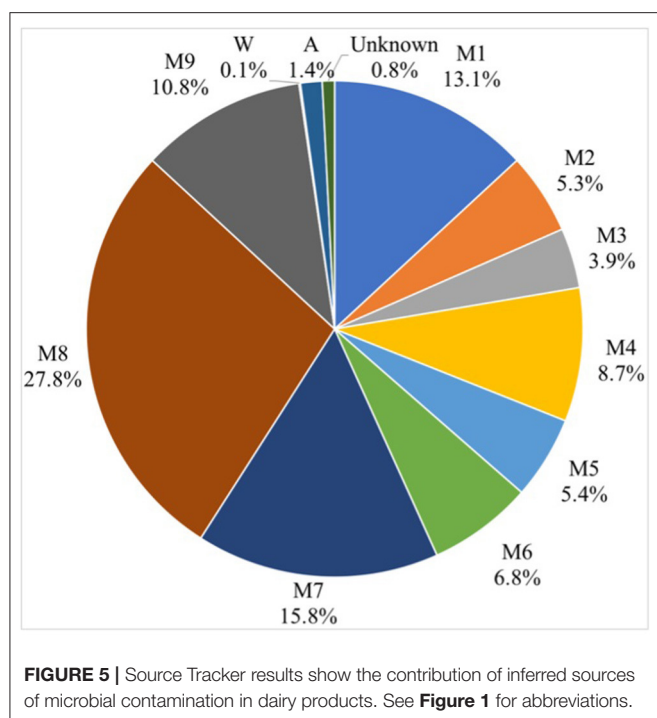


FIGURE 4 | The canonical analysis of principal coordinates (CAP) explained the correlation of the level of the 10 primary bacterial genera (*Acinetobacter*, *Macroccoccus*, *Pseudomonas*, *Lactococcus*, *Lysinibacillus*, *Stenotrophomonas*, *Bacillus*, *Streptococcus*, *Enhydrobacter*, and *Serratia*) in different samples. The samples in the gray circle are regarded as a group because the similarity was >70%. See **Figure 1** for abbreviations.

Lachnospiraceae, and *Corynebacteriaceae*, while in winter the microorganisms were *Staphylococcaceae*, *Ruminococcaceae*, *Aerococcaceae*, and *Lactonospirillaceae*. The microorganisms in raw milk were relatively stable (30). In addition, researchers investigated the microbial community structure from the dairy farm to the final cheese products. Phylum Firmicutes was found as a main phylum, and the ratio between dairy farms and finished cheeses were 31% and 92%, respectively. The relative proportions of *Lactococcus*, *Lactobacillus*, *Streptococcus*, and *Leuconostoc* in cheese products accounts for 69–98% (37). Our results were consistent with another study, in which it was also reported that Gram-negative bacteria were more abundant than Gram-positive bacteria in all samples. Microorganisms in raw milk are mainly *Proteobacteria*, *Firmicutes*, *Cyanobacteria*, *Actinobacteria*, *Bacteroidetes*, and *Verrucomicrobia*, while *Proteobacteria* and *Firmicutes* are still the dominant phyla in pasteurized milk samples (38). Another study found that the primary bacterial communities in raw milk were *Firmicutes*, *Actinobacteria*, *Bacteroidetes*, *Proteobacteria*, and *Tenericutes* (39). Our study found that similar bacteria dominated the microbial communities of raw milk and pasteurized milk. Therefore, it is necessary to formulate good farm management practices, good production practices, and food safety systems to ensure the safety of dairy products.

Studies of the microorganisms of dairy products have also been reported. For example, Kamimura et al. used 16S rDNA sequencing to analyze the importance of microbial diversity in the processing environment, raw materials and final cheese to the characteristics and quality of cheese. They found that the microbial community structure of raw milk, whey, and environmental samples were significantly different. Both cheese and mature cheese showed a more stable and similar microbial community structure. *Streptococcus* and *Lactococcus* had high relative abundance throughout the cheese processing process (40). Zheng et al. used 16S rDNA sequencing to analyze the diversity of bacterial and fungal communities related to the quality and flavor during cheese maturation, and they found that *Lactobacillus*, *Streptococcus*, and *Kluyveromyces* were the main microorganisms in cheese (41). Schoen et al. used 16S rDNA sequencing to analyze the microbial community structure of the floor drain and biofilm samples of the Austrian cheese processing plant, and it was found that the microbial community was mainly composed of related bacteria in cheese such as *Lactobacillus* and *Streptococcus thermophilus* (42). Porcellato et al. used 16S rDNA sequencing to analyze the changes in the microbial community structure in raw milk and pasteurized milk, and demonstrated that *Bacillus cereus* was the dominant one in pasteurized milk, compared with pasteurized milk stored at 4°C. In comparison,



the diversity of microorganisms was higher in pasteurized milk stored at 8°C (43). In this study, the predominant genera found in the milk sample were *Acinetobacter*, *Macroccoccus*, *Pseudomonas*, and *Lactococcus*, while *Stenotrophomonas* and *Acinetobacter* were the most abundant genera in air and rinse water. *Macroccoccus* are Gram-positive cocci belonging to the *Staphylococcaceae* family and are closely related to *Staphylococcus* but are not considered human pathogens. *Pseudomonas*, *Lactococcus*, and *Acinetobacter* are known psychrophilic bacteria and are relatively abundant in raw milk (44, 45). In the latter, there are also many species of *Pseudomonas* that produce heat-stable proteolytic and lipolytic enzymes and are responsible for milk quality defects including increased viscosity, sedimentation, aging gelation, fat separation, and increased bitterness. These are the most common reasons for milk spoilage and shortened shelf-life of milk products (46). In addition, *Pseudomonas* are dominant in the microflora of raw milk (38). In our study, *Acinetobacter*, *Macroccoccus*, *Pseudomonas*, and *Lactococcus* were the most abundant in the microflora of raw milk and products. However, compared with raw milk, the relative abundance of *Pseudomonas* and *Lactococcus* were significantly reduced.

Viazis et al. analyzed the inactivation of specific microorganisms (*Escherichia coli*, *Listeria monocytogenes*, *Staphylococcus aureus*, and *Streptococcus agalactiae*) in milk for human consumption through traditional pasteurization, and found that pasteurization of the microorganisms inoculated milk (62.5°C for 30 min) can kill all microorganisms (47). Gabriel et al. analyzed the inactivation of specific microorganisms by pasteurization. The inactivation rate of *Salmonella enterica*, *Escherichia coli* O157:H7, *Listeria monocytogenes*, *Pseudomonas*

aeruginosa, and *Staphylococcus aureus* after heating of heavily contaminated milk at 62.5°C for 30 min was 90.8–99.9% (48). Stabel and Lambertz through different pasteurization intensities (i.e., 62.7°C for 30 min, 65.5°C for 16 s, 71.7°C for 15 s, 71.7°C for 20 s, and 74.4°C for 15 s, respectively). Analysis of the inactivation of specific microorganisms (e.g., *Mycobacterium avium* subsp. *paratuberculosis*) found that pasteurization can significantly reduce the survival rate of the organisms, but the inactivation is not complete (49). Heat treatment of milk samples heavily contaminated by pathogenic bacteria shows that traditional pasteurization processes cannot completely eliminate biological hazards. The total number of bacteria in the dairy products in our study was very low and far below the limit requirements of the food safety standards established by the European Union, the United States, and China. We did not detect the presence of any pathogenic bacteria, such as *Salmonella*, *Staphylococcus aureus*, and *Cronobacter*. This may be related to the improved management methods developed by the dairy farm and processing factory management personnel. For example, the pasture uses sandy bedding, which does not allow bacteria to breed easily. In addition, the cleaning and disinfection procedures during milking also effectively control the raw milk.

The Source Tracker modeling indicated that the microorganisms in the products were significantly correlated to that in the product tank. The product tank becomes a source of microbial contamination due to defects in the management program, e.g., the cleaning-in-place procedures were not followed, the time was too short, rendering these practices ineffective, or the product tank had a secondary contamination source. Our results were consistent with a previous study of bacterial source tracking analysis for milk powder based on 16S rDNA-based single-molecule real-time sequencing technology, indicating that the primary microbes in milk powder originated in the raw milk (15). The Source Tracker model based on 16S rDNA sequencing technology was previously used to analyze potential contamination sources in pasteurized raw milk, and the contributions of cow pasture environmental samples to microbial contamination in raw milk were traced. The teat liners and the teat dip cups were found to be the most important sources of contamination, and this is most likely related to farm cleaning procedures or management practices (16). Source Tracker was also used to analyze the potential sources of microbial contamination in raw milk using an automatic milking system, and the effects of rumen fluid, drinking water, feed, bedding, air, and feces were analyzed. Air was found to be the most important source of contamination. If the cleaning measures of the automatic milking system were complete, the microbial impact on raw milk was relatively small (17).

CONCLUSIONS

In this study, we evaluated the traceability of microorganisms in pasteurized milk, and traced the influence of different steps in the processing lines on the microorganisms in pasteurized

milk, using the Source Tracker model based on 16S rDNA sequencing technology. We observed significant differences in richness of microbiota in the samples between the raw milk and the processing factory air samples, even though the uniformity and coverage of bacteria in raw milk and the final products were similar. The Source Tracker model analysis indicated that the microorganisms in the products were significantly related to the product tank. Our analysis can assist in localizing potential sources of microbial contamination and act as guidance for quality control sampling to avoid food quality problems.

DATA AVAILABILITY STATEMENT

The original contributions presented in the study are publicly available. This data can be found here: Genome Sequence Archive in BIG Data Center, CRA005796.

REFERENCES

- Loss G, Depner M, Ulfman LH, van Neerven RJJ, Hose AJ, Genuneit J, et al. Consumption of unprocessed cow's milk protects infants from common respiratory infections. *J Allergy Clin Immunol.* (2015) 135:56–62. doi: 10.1016/j.jaci.2014.08.044
- Waser M, Michels KB, Bieli C, Floistrup H, Pershagen G, von Mutius E, et al. Inverse association of farm milk consumption with asthma and allergy in rural and suburban populations across Europe. *Clin Exp Allergy.* (2007) 37:661–70. doi: 10.1111/j.1365-2222.2006.02640.x
- Zhan J-w, Shen Y-y, Li X, Zhang H, Niu H, Fang L-y, et al. Microbiome and metabolic changes of milk in response to dietary supplementation with bamboo leaf extract in dairy cows. *Front Nutr.* (2021) 8:e723446. doi: 10.3389/fnut.2021.723446
- UN News. *Deadly E. coli Outbreak Caused by Rare Strain of Bacterium, UN Confirms.* (2011). Available online at: <https://news.un.org/en/story/2011/06/377302> (accessed June 3, 2011).
- UN News. *Children Under Five Account for One Third of Deaths from Foodborne Diseases.* (2015). Available online at: <https://news.un.org/en/story/2015/12/517172> (accessed December 3, 2015).
- He Y, Ren Y, Guo B, Yang Y, Ji Y, Zhang D, et al. Development of a specific nanobody and its application in rapid and selective determination of *Salmonella enteritidis* in milk. *Food Chem.* (2020) 310:125942. doi: 10.1016/j.foodchem.2019.125942
- Kuehn B. Drug-resistant infections from raw milk. *J Am Med Assoc.* (2018) 319:1191. doi: 10.1001/jama.2018.2363
- Costard S, Espejo L, Groenendaal H, Zagmutt FJ. Outbreak-related disease burden associated with consumption of unpasteurized cow's milk and cheese, United States, 2009–2014. *Emerg Infect Dis.* (2017) 23:957–64. doi: 10.3201/eid2306.151603
- Montanini MTM, Bersot LdS. Evaluation of psychrotrophic behavior and lipolytic and proteolytic activity of *Bacillus cereus* isolated from refrigerated dairy products. *Acta Scientiarum-Technol.* (2013) 35:163–7. doi: 10.4025/actascitechnol.v35i1.13752
- Gao T, Ding Y, Wu Q, Wang J, Zhang J, Yu S, et al. Prevalence, virulence genes, antimicrobial susceptibility, and genetic diversity of *Bacillus cereus* isolated from pasteurized milk in China. *Front Microbiol.* (2018) 9:e00533. doi: 10.3389/fmicb.2018.00533
- Zhou G, Liu H, He J, Yuan Y, Yuan Z. The occurrence of *Bacillus cereus*, *B. thuringiensis* and *B. mycoides* in Chinese pasteurized full fat milk. *Int J Food Microbiol.* (2008) 121:195–200. doi: 10.1016/j.ijfoodmicro.2007.11.028
- Quigley L, O'Sullivan O, Stanton C, Beresford TP, Ross RP, Fitzgerald GF, et al. The complex microbiota of raw milk. *FEMS Microbiol Rev.* (2013) 37:664–98. doi: 10.1111/1574-6976.12030

AUTHOR CONTRIBUTIONS

BD: conceptualization, methodology, investigation, and writing—original draft. LM: methodology. HL: data curation. HW and HY: supervision. NZ: conceptualization. YZ and SZ: writing—review, supervision, and funding acquisition. JW: conceptualization and funding acquisition. All authors contributed to the article and approved the submitted version.

FUNDING

This study was funded by the Scientific Research Project for Major Achievements of Agricultural Science and Technology Innovation Program (CAAS-ZDXT2019004), the Agricultural Science and Technology Innovation Program (ASTIP-IAS12), and the Modern Agro-Industry Technology Research System of the PR China (CARS-36).

- Spanu C, Scarano C, Ibba M, Spanu V, De Santis EPL. Occurrence and traceability of *Listeria monocytogenes* strains isolated from sheep's milk cheese-making plants environment. *Food Control.* (2015) 47:318–25. doi: 10.1016/j.foodcont.2014.07.027
- El-Mokdad MM. *Implementing a Traceability System in a Small to Medium Dairy Plant in Lebanon with Isolation and Characterization of Staphylococcus aureus.* Beirut: American University of Beirut (2014).
- Wang J, Zheng Y, Xi X, Hou Q, Xu H, Zhao J, et al. Application of PacBio Single Molecule Real-Time (SMRT) sequencing in bacterial source tracking analysis during milk powder production. *Food Control.* (2018) 93:226–34. doi: 10.1016/j.foodcont.2018.05.044
- Du B, Meng L, Liu H, Zheng N, Zhang Y, Guo X, et al. Impacts of milking and housing environment on milk microbiota. *Animals.* (2020) 10:2339. doi: 10.3390/ani10122339
- Wu H, Nguyen QD, Tran TTM, Tang MT, Tsuruta T, Nishino N. Rumen fluid, feces, milk, water, feed, airborne dust, and bedding microbiota in dairy farms managed by automatic milking systems. *Animal Sci J.* (2019) 90:445–52. doi: 10.1111/asj.13175
- National Standards of the Republic of China. *GB 4789.2: Determination of Microbiological Properties (Total Bacterial Count).* Beijing: National Standards of the Republic of China (2016).
- International Dairy Federation, IDF. *209:2007, Milk and Milk-based Drinks- Determination of Alkaline Phosphatase Activity-Enzymatic Photo-activated System (EPAS) Method.* Brussels: International Dairy Federation. (2007).
- Tianjin Dairy Science and Technology Innovation Association, T/TDSTIA. *001: Determination of Lactoperoxidase in Milk and Dairy Products.* Tianjin: Tianjin Dairy Science and Technology Innovation Association (2021).
- Guo M, Wu F, Hao G, Qi Q, Li R, Li N, et al. *Bacillus subtilis* improves immunity and disease resistance in rabbits. *Front Immunol.* (2017) 8:e00354. doi: 10.3389/fimmu.2017.00354
- Chen S, Zhou Y, Chen Y, Gu J. Fastp: an ultra-fast all-in-one FASTQ preprocessor. *Bioinformatics.* (2018) 34:884–90. doi: 10.1093/bioinformatics/bty560
- Magoc T, Salzberg SL. FLASH fast length adjustment of short reads to improve genome assemblies. *Bioinformatics.* (2011) 27:2957–63. doi: 10.1093/bioinformatics/btr507
- Caporaso JG, Kuczynski J, Stombaugh J, Bittinger K, Bushman FD, Costello EK, et al. QIIME allows analysis of high-throughput community sequencing data. *Nat Methods.* (2010) 7:335–6. doi: 10.1038/nmeth.f.303
- Edgar RC, Haas BJ, Clemente JC, Quince C, Knight R, UCHIME. improves sensitivity and speed of chimera detection. *Bioinformatics.* (2011) 27:2194–200. doi: 10.1093/bioinformatics/btr381
- Edgar RC. UPARSE highly accurate OTU sequences from microbial amplicon reads. *Nat Methods.* (2013) 10:996–1000. doi: 10.1038/nmeth.2604

27. Pruesse E, Quast C, Knittel K, Fuchs BM, Ludwig W, Peplies J, et al. SILVA: a comprehensive online resource for quality checked and aligned ribosomal RNA sequence data compatible with ARB. *Nucleic Acids Res.* (2007) 35:7188–96. doi: 10.1093/nar/gkm864
28. Ondov BD, Bergman NH, Phillippy AM. Interactive metagenomic visualization in a Web browser. *BMC Bioinformatics.* (2011) 12:85. doi: 10.1186/1471-2105-12-385
29. ggplot2 (2013). Available online at: <http://ggplot2.org/> (accessed 2013).
30. Nguyen TT, Wu H, Nishino N. An investigation of seasonal variations in the microbiota of milk, feces, bedding, and airborne dust. *Asian-Australas J Anim Sci.* (2019) 33:1858–65. doi: 10.5713/ajas.19.0506
31. Wickham H. *Ggplot2: Elegant Graphics for Data Analysis*. New York, NY: Springer (2009).
32. Knights D, Kuczynski J, Charlson ES, Zaneveld J, Mozer MC, Collman RG, et al. Bayesian community-wide culture-independent microbial source tracking. *Nature Methods.* (2011) 8:761–5. doi: 10.1038/nmeth.1650
33. Dominguez-Bello MG, De Jesus-Laboy KM, Shen N, Cox LM, Amir A, Gonzalez A, et al. Partial restoration of the microbiota of cesarean-born infants via vaginal microbial transfer. *Nat Med.* (2016) 22:250–3. doi: 10.1038/nm.4039
34. Metcalf JL, Xu ZZ, Weiss S, Lax S, Van Treuren W, Hyde ER, et al. Microbial community assembly and metabolic function during mammalian corpse decomposition. *Science.* (2016) 351:158–62. doi: 10.1126/science.aad2646
35. Li N, Wang Y, You C, Ren J, Chen W, Zheng H, et al. Variation in raw milk microbiota throughout 12 months and the impact of weather conditions. *Sci Rep.* (2018) 8:1–10. doi: 10.1038/s41598-018-20862-8
36. McHugh AJ, Feehily C, Fenelon MA, Gleeson D, Hill C, Cotter PD. Tracking the dairy microbiota from farm bulk tank to skimmed milk powder. *mSystems.* (2020) 5:1–16. doi: 10.1128/mSystems.00226-20
37. Falardeau J, Keeney K, Trmcic A, Kitts D, Wang S. Farm-to-fork profiling of bacterial communities associated with an artisan cheese production facility. *Food Microbiol.* (2019) 83:48–58. doi: 10.1016/j.fm.2019.04.002
38. Ding R, Liu Y, Yang S, Liu Y, Shi H, Yue X, et al. High-throughput sequencing provides new insights into the roles and implications of core microbiota present in pasteurized milk. *Food Res Int.* (2020) 137:109586. doi: 10.1016/j.foodres.2020.109586
39. Kable ME, Srisengfa Y, Laird M, Zaragoza J, McLeod J, Heidenreich J, et al. The core and seasonal microbiota of raw bovine milk in tanker trucks and the impact of transfer to a milk processing facility. *MBio.* (2016) 7:e00836–16. doi: 10.1128/mBio.00836-16
40. Kamimura BA, Cabral L, Noronha MF, Baptista RC, Nascimento HM, Sant'Ana AS. Amplicon sequencing reveals the bacterial diversity in milk, dairy premises and Serra da Canastra artisanal cheeses produced by three different farms. *Food Microbiol.* (2020) 89:103453. doi: 10.1016/j.fm.2020.103453
41. Zheng X, Liu F, Shi X, Wang B, Li K, Li B, et al. Dynamic correlations between microbiota succession and flavor development involved in the ripening of Kazak artisanal cheese. *Food Res Int.* (2018) 105:733–42. doi: 10.1016/j.foodres.2017.12.007
42. Schoen K, Schornsteiner E, Dzieciol M, Wagner M, Mueller M, Schmitz-Esser S. Microbial communities in dairy processing environment floor-drains are dominated by product-associated bacteria and yeasts. *Food Control.* (2016) 70:210–5. doi: 10.1016/j.foodcont.2016.05.057
43. Porcellato D, Aspholm M, Skeie SB, Mellegard H. Application of a novel amplicon-based sequencing approach reveals the diversity of the *Bacillus cereus* group in stored raw and pasteurized milk. *Food Microbiol.* (2019) 81:32–9. doi: 10.1016/j.fm.2018.01.014
44. Meng Y, Chen X, Sun Z, Li Y, Chen D, Fang S, et al. Exploring core microbiota responsible for the production of volatile flavor compounds during the traditional fermentation of Koumiss. *LWT-Food Sci Technol.* (2021) 135:49. doi: 10.1016/j.lwt.2020.110049
45. Zheng X, Ge Z, Lin K, Zhang D, Chen Y, Xiao J, et al. Dynamic changes in bacterial microbiota succession and flavour development during milk fermentation of Kazak artisanal cheese. *Int Dairy J.* (2021) 113:878. doi: 10.1016/j.idairyj.2020.104878
46. Zhang C, Bijl E, Svensson B, Hettinga K. The extracellular protease AprX from *Pseudomonas* and its spoilage potential for UHT milk: a review. *Compreh Rev Food Sci Food Safety.* (2019) 18:834–52. doi: 10.1111/1541-4337.12452
47. Viazis S, Farkas BE, Jaykus LA. Inactivation of bacterial pathogens in human milk by high-pressure processing. *J Food Prot.* (2008) 71:109–18. doi: 10.4315/0362-028X-71.1.109
48. Gabriel AA, Bayaga CLT, Magallanes EA, Aba RPM, Tanguilig KMN. Fates of pathogenic bacteria in time-temperature-abused and Holder-pasteurized human donor, infant formula and full cream cow's milk. *Food Microbiol.* (2020) 89:103450. doi: 10.1016/j.fm.2020.103450
49. Stabel JR, Lambert A. Efficacy of pasteurization conditions for the inactivation of *Mycobacterium avium* subsp *paratuberculosis* in milk. *J Food Prot.* (2004) 67:2719–26. doi: 10.4315/0362-028X-67.12.2719

Conflict of Interest: The authors declare that the research was conducted in the absence of any commercial or financial relationships that could be construed as a potential conflict of interest.

Publisher's Note: All claims expressed in this article are solely those of the authors and do not necessarily represent those of their affiliated organizations, or those of the publisher, the editors and the reviewers. Any product that may be evaluated in this article, or claim that may be made by its manufacturer, is not guaranteed or endorsed by the publisher.

Copyright © 2022 Du, Meng, Wu, Yang, Liu, Zheng, Zhang, Zhao and Wang. This is an open-access article distributed under the terms of the Creative Commons Attribution License (CC BY). The use, distribution or reproduction in other forums is permitted, provided the original author(s) and the copyright owner(s) are credited and that the original publication in this journal is cited, in accordance with accepted academic practice. No use, distribution or reproduction is permitted which does not comply with these terms.



Formation and Identification of Six Amino Acid - Acrylamide Adducts and Their Cytotoxicity Toward Gastrointestinal Cell Lines

Dan Li^{1†}, Fangfang Xian^{1†}, Juanying Ou^{2,3}, Kaiyu Jiang¹, Jie Zheng^{1,3}, Shiyi Ou^{1,3}, Fu Liu^{1,3}, Qinchun Rao⁴ and Caihuan Huang^{1,3*}

¹ Department of Food Science and Engineering, Jinan University, Guangzhou, China, ² Institute of Food Safety & Nutrition, Jinan University, Guangzhou, China, ³ Guangdong-Hong Kong Joint Innovation Platform for the Safety of Bakery Products, Guangzhou, China, ⁴ Department of Nutrition and Integrative Physiology, Florida State University, Tallahassee, FL, United States

OPEN ACCESS

Edited by:

Liguang Xu,
Jiangnan University, China

Reviewed by:

Yueliang Zhao,
Shanghai Ocean University, China
Marco Iammarino,
Experimental Zooprophyllactic Institute
of Puglia and Basilicata (IZSPB), Italy

*Correspondence:

Caihuan Huang
thamy@jnu.edu.cn

Specialty section:

This article was submitted to
Food Chemistry,
a section of the journal
Frontiers in Nutrition

Received: 22 March 2022

Accepted: 28 April 2022

Published: 20 May 2022

Citation:

Li D, Xian F, Ou J, Jiang K, Zheng J, Ou S, Liu F, Rao Q and Huang C (2022) Formation and Identification of Six Amino Acid - Acrylamide Adducts and Their Cytotoxicity Toward Gastrointestinal Cell Lines. *Front. Nutr.* 9:902040. doi: 10.3389/fnut.2022.902040

Acrylamide (AA) is a food contaminant, and amino acids are suggested to mitigate its toxicity by forming adducts. The emergence of acrylamide adducts may cause underestimation of acrylamide exposure level as well as trigger new safety problems. Based on the acrylamide elimination capability of four amino acids, this study chemically synthesized six amino acid-acrylamide adducts. Their structures were analyzed, followed by content determination in 10 commercially baking foods. The Michael adduct formed by one molecule of γ -aminobutyric acid (GABA) and acrylamide was most abundant in foods among six adducts. Furthermore, it markedly decreased the cytotoxicity of acrylamide in Caco-2 cells and GES-1 cells. This finding suggests that amino acids can be used to reduce acrylamide level in processed foods and mitigate its hazardous effects after intake.

Keywords: acrylamide, amino acid, adduct, elimination mechanism, cytotoxicity

INTRODUCTION

Acrylamide (AA) is a contaminant present widely in thermally processed foods. It has been classified as a probable human carcinogen by the International Agency for Research on Cancer (IARC) (1) and raises health concerns with detrimental effects. As an undesirable product of Maillard reaction, it is produced at high temperatures from amino acid asparagine and reducing sugars, such as glucose and fructose (2). Therefore, high content of acrylamide is often detected in carbohydrate-rich foods, such as potato chips (12–3,241 $\mu\text{g/kg}$), breakfast cereals (167–726 $\mu\text{g/kg}$), and coffee (7.5–1190.2 $\mu\text{g/kg}$) (3, 4). According to the European regulation (Commission Regulation (EU) 2017/2,158), the benchmark of acrylamide in the above foods is 750, 300, and 850 $\mu\text{g/kg}$, respectively, which are far less than the actual levels of acrylamide. In this case, long term intake of foods with high acrylamide content will increase the risk of prostate cancer, breast cancer and ovarian cancer (5).

After ingestion, acrylamide can be metabolized to glycidamide, which, like acrylamide, can covalently bind to the N-terminal valine of hemoglobin (Hb) and form adducts. Hb adduct levels are associated with increased breast cancer risk, adverse peripheral nervous system symptoms, reduced serum insulin, etc (6, 7). Besides, acrylamide and glycidamide can also react with the $-\text{NH}_2$

and -NH groups of purine and pyrimidine bases in DNA, inducing DNA damage and mutagenic consequences (7). In addition, acrylamide has been reported to present neurotoxic effects in the human workplace environment and reproductive toxicity as well as immunotoxicity in laboratory animals (8).

Considering the health risks associated with acrylamide ingestion, reducing acrylamide content in foods has become one of the most important issues in food safety. A number of strategies have been proposed to control acrylamide levels in processed foods, including replacing food materials with those has low acrylamide precursor content, such as selecting potato cultivars with low concentrations of reducing sugars or changing harvest time and storage conditions (9, 10); reducing the amount of acrylamide precursor, such as application of *L*-asparaginase in foods (11); pretreatment of food materials, such as washing olives with water at 25°C before lye and thermal treatment, or immersing potato slices in different solutions before frying (12, 13); regulation of food processing conditions, such as lower temperature and shorter processing time (14); and applying functional food ingredients to prevent acrylamide formation, such as amino acids. Kobayashi et al. (15) found lysine and cysteine mediated acrylamide content reduction in aqueous solution below 120°C. Koutsidis and his colleagues (16) reported that proline, tryptophan, glycine, and cysteine suppressed acrylamide formation by 45–80% after heating at 160°C for 60 min in the asparagine-glucose model system. Our previous studies found that cysteine, glycine and lysine could directly eliminate 69.6–94.6% of acrylamide in 15 min in the amino acid-acrylamide systems at 160°C (17). In the food system, soaking potato slices with 0.5% glycine decreased more than 70% acrylamide content in fried potato chips (18). These researches indicate that amino acids are ideal acrylamide eliminators and may be potent agents to reduce the negative effects of acrylamide.

The high elimination rate of amino acids was related to the formation of the amino acid-acrylamide adduct (16, 17, 19). The structures of adducts, however, have not been confirmed yet. Also, there is a need to find out the formation mechanism of acrylamide adducts, their presence in real food systems, and whether they are hazardous in foods. The present work aims to answer the above questions by synthesizing amino acid-acrylamide adducts and building relevant determination methods. Four amino acids were selected to react with acrylamide. γ -Aminobutyric acid (GABA) is a non-proteinogenic amino acid with high content in potatoes (6,460 $\mu\text{mol/kg}$), which plays an important role in preventing sleeplessness, promoting neuron growth, and controlling anxiety and depression (20). Glycine is the lowest molecular weight amino acid, required for various metabolic pathways, including glutathione synthesis and one-carbon metabolism (21). Lysine and tryptophan are essential amino acids in human nutrition involved in several physiological processes, including growth performance and regulation of the immune systems (22, 23). Their elimination capability to acrylamide, the structure and level of main products in foods, and cytotoxicity were investigated in the current study.

MATERIALS AND METHODS

Materials

Acrylamide (AA, $\geq 99\%$), lysine (Lys, $\geq 98\%$), tryptophan (Trp, $\geq 99\%$), GABA ($\geq 98\%$), glycine (Gly, $\geq 99.5\%$) and n-hexane were purchased from J&K Scientific Co., Ltd (Beijing, China). Methanol (HPLC), D₂O and DMSO were purchased from Energy Chemical Reagent Co., Ltd (Shanghai, China). A-HG type octadecyl bonded 1 silica gel was purchased from YMC Co., Ltd (Tokyo, Japan). Dextran gel Sephadex LH-20 was purchased from Extrasynthese Co., Ltd (Lyon, France). 3-(4,5-Dimethylthiazol-2-yl)-2,5-diphenyltetrazolium bromide (MTT), RPMI-1640 medium, fetal bovine serum (FBS) and penicillin-streptomycin were purchased from Shanghai Zhongqiao Xinzhou Biotechnology Co., Ltd, (China). Ten food products (Potato chips A, Potato chips B, Potato chips C, brown rice cake, egg biscuit, cereal bars, dough twist, walnut cake and rice crust) were purchased from Utilize modern supermarkets (Guangzhou, China).

Scavenging Capacity of Amino Acids for Acrylamide

The scavenging ability of four amino acids for acrylamide was studied in a model system. Four milliliters of reaction solution containing 50 mM amino acids (Lys, Trp, GABA, Gly) and 5 mM AA aqueous solutions were placed in a 10 mL stopper colorimeter and heated in a water bath at 80°C for 5 h. The samples were then cooled in an ice bath and analyzed with high performance liquid chromatography-diode array detector (HPLC-DAD) systems (UltiMate 3000, Thermo Fisher, Germany). The residual content of AA was determined using our previously reported method (13). Briefly, 5 μL of the filtered sample was injected into an Atlantis T3 column (4.6 mm \times 250 mm, 5 μm , Waters Corporation, Milford, US) and isocratically eluted by methanol/water (2:98, v/v) solution at a flow rate of 0.4 mL min⁻¹ and 40.0°C. AA residue was measured at 205 nm and quantified using an external standard curve.

The reaction products were further identified through HPLC-MS/MS analysis (LCMS-8045, Shimadzu Corporation, Kyoto, Japan) based on Hu et al. (21). The injection volume was 10 μL . HPLC procedure was applied as described above. MS/MS spectrum was acquired in positive ion mode with mass spectra over a range of m/z 50–800, source temperature of 300°C, desolvation temperature of 250°C and capillary voltage of 4.0 kV. The collision energy was set at 20.0 eV for product ion scans.

Optimization of Reaction Conditions Between Acrylamide and Amino Acids

Forty milliliters of reaction solutions containing 50 mM amino acids and different levels of AA (6.25, 12.5, 25, 50 mM) were, respectively reacted in a 50 mL sealed conical flask at 95°C for 5 h. The samples were then cooled down in an ice bath and filtered through a 0.45 μm membrane (Jinteng Equipment Co. Ltd, Tianjin, China) for HPLC analysis as described above. The injection volume was 10 μL . Acrylamide and the adducts

TABLE 1 | Condition of column chromatography and semi-preparative LC.

Reaction	Column chromatography		Semi-preparative LC elution solution
	Column packing	Elution solution (methanol:water)	
Lys-AA	ODS	2: 98	methanol: 0.1% ammonia water = 9:91
Trp-AA	Sephadex LH-20	15:85	methanol: water = 2:98
GABA-AA	Sephadex LH-20	2: 98	methanol: water = 2:98
Gly-AA	ODS	2: 98	methanol: water = 2:98

were detected at 205 nm and confirmed with LC-MS/MS as described above.

Synthesis and Purification of Amino Acid-Acrylamide Adducts

Amino acids-acrylamide adducts were synthesized by mixing amino acids and acrylamide according to the method of Zhao et al. (24) with little modifications and the optimized reaction conditions were obtained from 2.3. Briefly, 100 mL of the aqueous solution containing a different ratio of acrylamide and amino acids were incubated at 80°C under constant stirring for 300 min. The ratio of amino acids to acrylamide (50 mM) was set as follows: Lys:AA = 1:1, Gly:AA = 1:2, GABA/Trp:AA = 1:4. At the end of the reaction, the products were concentrated with a vacuum rotary evaporator (Eyela N-1300, Tokyo, Japan), and the adducts in the concentrate were purified with an ODS C18 reverse silica gel column (Gly-AA and Lys-AA) or Sephadex LH-20 (Trp-AA and GABA-AA) monitored by HPLC (UltiMate 3000, Thermo Fisher, Germany). Elution solutions for different adducts were listed in **Table 1**, and the fractions containing more than 80% of the target adducts were collected and further purified with semi-preparative liquid chromatography (25). Separation was performed with a Pntulips QC-C18 column (250 × 10 mm, 5 μm, Puning Analytical Technology Co. Ltd, Shanghai, China) using a five-peak series liquid chromatography system (Wufeng Scientific Instrument Co., Ltd, Shanghai, China) consisting of a reciprocating double-plunger parallel pump and AN LC 100 ultraviolet detector. The elution solutions were presented in **Table 1**, and the purified adducts were evaporated using a rotary vacuum evaporator at 55°C, followed by freeze-drying with a scientZ-10N vacuum freeze-dryer (Xinzhi Biotechnology Co., Ltd, Ningbo, China).

Structural Analysis of Purified Amino Acid-Acrylamide Adducts

The structures of purified adducts were identified with mass spectrometry (MS) analysis and nuclear magnetic resonance (NMR). An X500R QTOF high-resolution mass spectrometer (HRMS; AB Sciex, MA, United States) was operated at 500°C, with a capillary voltage of 5.5 kV, drying gas and nebulizer gas pressure of 50 and 55 psi, respectively. The sample was separated on an Atlantis T3 C18 column (4.6 × 150 mm, 5 μm, Waters Corporation, Milford, US). The spectrum was scanned in positive ion mode and obtained over a mass range from 50 to 1,000 Da.

TABLE 2 | Qualitative ion pair, quantitative ion pair and optimized voltage.

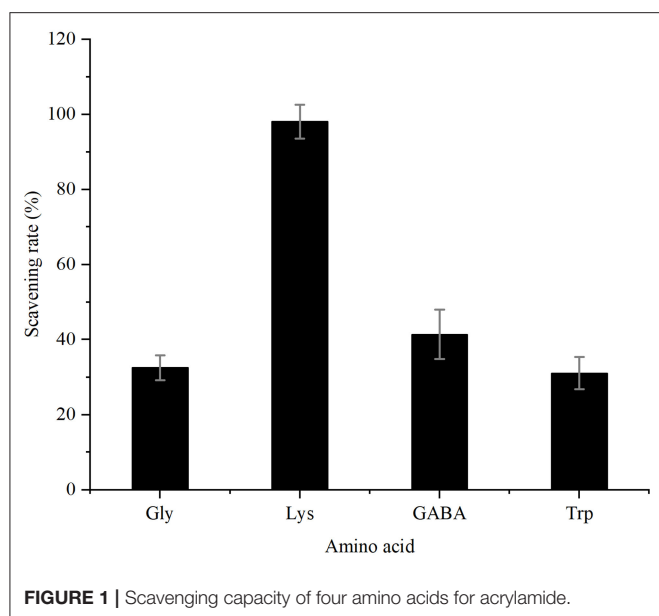
Compounds	Ion pairs	Q1 voltage (V)	Collision voltage (V)	Q3 voltage (V)
AA	72/55*	−14	−15	−22
	72/27	−12	−26	−29
	72/44	−13	−25	−19
Gly-AA 1	147/88*	−10	−14	−16
	147/101	−15	−13	−18
	147/60	−10	−18	−24
Gly-AA 2	218/159*	−24	−13	−29
	218/88	−11	−22	−16
	218/130	−24	−18	−22
Lys-AA	218/142*	−11	−16	−14
	218/114	−11	−24	−21
	218/84	−11	−22	−15
Trp-AA	276/188*	−30	−16	−20
	276/144	−29	−26	−14
	276/230	−30	−13	−25
GABA-AA 1	175/98*	−19	−19	−18
	175/116	−21	−15	−20
	175/140	−19	−13	−14
GABA-AA 2	246/187*	−12	−15	−19
	246/84	−12	−27	−15
	246/101	−29	−22	−10

*: Quantitative ion.

For NMR analysis, 10 mg of the purified adducts were dissolved in 0.55 mL of D₂O (Lys-AA, GABA-AA 1, Gly-AA 1 and Gly-AA 2) or DMSO-d₆ (Trp-AA and GABA-AA 2) (20). ¹H, ¹³C, Dept 135 and two-dimensional NMR spectra were obtained using a Bruker 600 MHz Avance III NMR spectrometer.

Detection of the Adduct in Ten Commercially Available Baking Foods

Fifteen grams of crushed samples were defatted with n-hexane using vortex at 25°C. Four grams of defatted samples were ultrasonically extracted three times in a 50 mL centrifuge tube for 10 min with 10 mL of 30% methanol solution at 25°C and frequencies of 100 kHz, followed by centrifugation at 4,481 ×g for 10 min at 25°C. The supernatants were combined and filtered through a 0.45 μm membrane for HPLC-MS/MS analysis (LC-MS 8045, Shimadzu Corp., Kyoto, Japan). Ten microliters of the sample were injected into the LC-MS system and separated on an Atlantis T3 C18 column with a flow rate of 0.4 mL/min at 40 °C. Elution was carried out with methanol (A) and water (B), and gradient flow was as followed: A = 2% at 0 ~ 6 min; A = 50% at 6.01 ~ 16 min; A = 2% at 16.01 ~ 23 min. A multiple reaction monitoring (MRM) method was applied to detect the adducts with mass spectrometry, which was operated in positive ion mode with the source temperature of 300°C, the de-solvation temperature of 250°C, the capillary voltage of 4,000 V, and the scanning rate of 1,000 Da/sec. The parent ions and daughter ions of each adduct were obtained by the first-stage full scan and the second-stage fragment ion analysis of mass spectrometry, followed by optimizing the collision voltage. Qualitative ion pair, quantitative ion pair and optimized voltage are shown in **Table 2**.



Cell Viability Assay

Human colon cancer epithelial cell line Caco-2 and Human gastric mucosal epithelial cell line GES-1 cell lines were applied to investigate the cytotoxicity of the adduct GABA-AA 1. Cells were cultivated with RPMI-1640 medium containing 10% FBS and 1% penicillin-streptomycin in an incubator with 5% CO₂ at 37 °C. The MTT assay was performed for cell viability analysis. Briefly, cells were seeded in a 96-well-plate at a density of 5×10^3 /well overnight to allow sufficient attachment, and then treated with AA or GABA-AA 1 at 0.5, 1.0, 1.5, 2.0, 2.5, 3.0, 3.5, 4.0, 4.5 and 5.0 mM for 24 h. Cell viability was determined by the MTT assay described by Zou et al. (26).

Statistical Analysis

All experiments were repeated at least three times. The data were presented as mean \pm standard deviation (SD) and were analyzed with one-way ANOVA using SPSS statistical software (version 25.0, SPSS, Inc., Chicago, IL, USA). $P < 0.05$ was considered to be statistically significant.

RESULTS AND DISCUSSION

Amino Acid Scavenges Acrylamide via Adduct Formation

Model reactions containing acrylamide and different amino acids were performed at 80 °C for 5 h. The remaining acrylamide content was quantified using calibration curves obtained from HPLC-DAD and the scavenging rates were calculated as shown in **Figure 1**. Among the four amino acids, lysine had the highest elimination rate of acrylamide (98%), which was much higher than our previous results of 69.6% (17), since the reaction time was more sufficient. The other three amino acids showed lower elimination capability that 41, 32, and 31% of

acrylamide was reduced by γ -aminobutyric acid, glycine and tryptophan, respectively.

As displayed by the HPLC chromatograms in **Figure 2**, the decreased intensity of the acrylamide peak was accompanied by the emergence of new peaks, indicating the formation of new compounds. Zamora et al. (27) reported that acrylamide could react with nucleophilic amino groups on amino acid side chains to produce the corresponding Michael adducts. Therefore, these new substances were further analyzed with HPLC-MS/MS and were confirmed as acrylamide adducts (**Supplementary Figures S1, S2**).

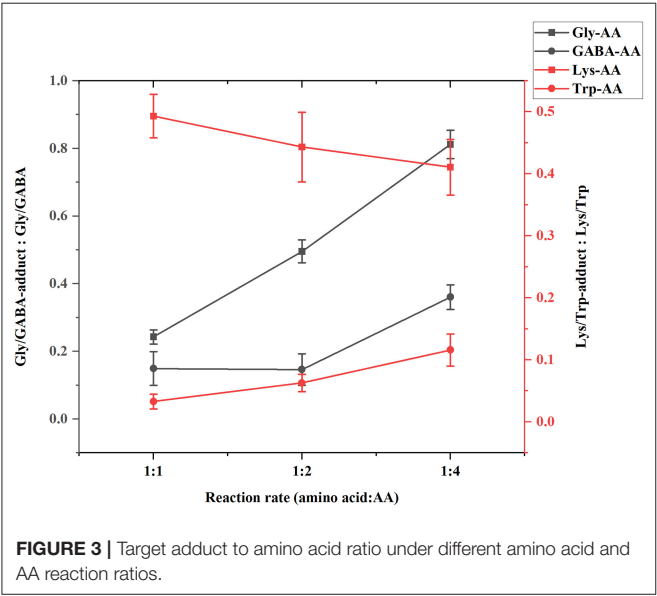
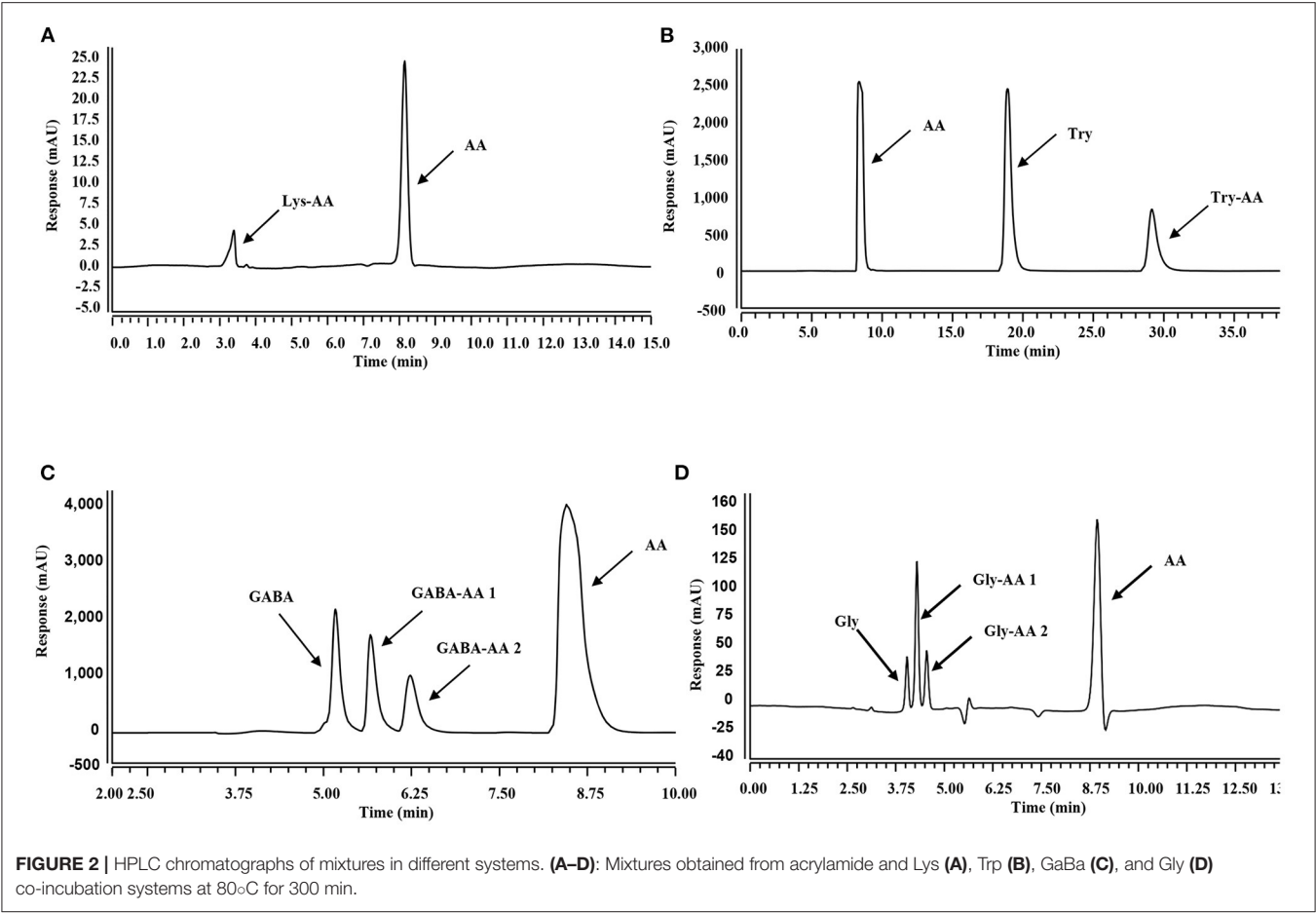
Optimization of Reaction Conditions for Amino Acid-Acrylamide Adducts Synthesis

To obtain abundant adducts for further investigation, reaction conditions were studied for adducts synthesis. Three reaction ratios of amino acids to acrylamide (1:1, 1:2, 1:4) were performed to obtain more adducts and fewer remaining amino acids for isolation and purification. The optimum reaction ratio was determined by the peak area ratio of the adduct and remaining amino acids in HPLC chromatograms. As shown in **Figure 3**, with the increase of acrylamide concentration, the content of lysine adducts decreased, so the ratio of 1:1 was selected for lysine adduct synthesis. For GABA and tryptophan, 1:4 was chosen for reaction since the higher acrylamide concentration, the higher the adducts concentrations. In the glycine reaction system, although the adduct levels were in proportion to the remaining amino acids concentration, excessive acrylamide formed gel with glycine in the reaction solution. Therefore, the reaction ratio was 1:2 for glycine and acrylamide.

Structural Analysis of the Amino Acid-Acrylamide Adducts

Six purified adducts were obtained since GABA and glycine formed two adducts with acrylamide. HRMS and NMR were subsequently performed to confirm the structures of these adducts. The wavelength, molecular weight and chemical formula of the adducts in the four reaction systems was shown in **Table 3**.

In the lysine-acrylamide system, Lys-AA (MW = 146 + 71 = 217) with $[M+H]^+$ at m/z 218.1499 was identified. HRMS result showed that the formula was C₉H₁₉N₃O₃, with the signal at m/z 142 indicating losing of $[-CH_2CH_2CONH_2]$ and $[-NH_2]$ (**Table 4**). ¹H NMR spectrum showed one set of lysine protons (δ_H = 3.23, 1.67, 1.38, 2.97 and 2.53 ppm) and two methylene protons (δ_H = 2.88 and 2.94 ppm, δ_H = 1.67 ppm). The ¹³C NMR spectrum displayed two carbonyl signals (δ_C = 176.77 and 179.51 ppm), six methylene signals (δ_C = 31.19, 21.91, 39.16, 33.64, 43.14, and 26.61 ppm), and one methine (δ_C = 63.04 ppm). In addition, the heteronuclear multiple bond correlation (HMBC) from H-2 to C-3, C-4 and C-7, from H-4 to C-5, and from H-7 to C-2 and C-8 suggested that this adduct was formed by nucleophilic addition of amine group of lysine and double bond of acrylamide. Adams et al. (28) also detected the substance with a molecular weight of 217 in the lysine-acrylamide reacting



system at pH 11.75 and 180°C for 2 h, but they did not share the spectrum.

Trp-AA (MW = 204 + 71 = 275) was detected as [M+H]⁺ m/z 276.1337 with formula of C₁₄H₁₇N₃O₃ by HRMS. The ion

TABLE 3 Wavelength, m/z, and molecular formula of adducts.			
Adducts	Wavelength (nm)	m/z	Molecular formula
Lys-AA	198.4	217.1490	C ₉ H ₁₉ N ₃ O ₃
Trp-AA	217.9	275.1337	C ₁₄ H ₁₇ N ₃ O ₃
GABA-AA 1	193.1	174.1077	C ₇ H ₁₄ N ₂ O ₃
GABA-AA 2	193.4	246.1443	C ₁₀ H ₁₉ N ₃ O ₄
Gly-AA 1	194.9	146.0764	C ₅ H ₁₀ N ₂ O ₃
Gly-AA 2	192.9	217.1135	C ₈ H ₁₅ N ₃ O ₄

at m/z 230 and m/z 188 suggested the loss of [–COOH] and [–NHCH₂CH₂CONH₂] (Table 5). The ¹H NMR spectrum showed one set of tryptophan protons (3.41, 3.01, 3.19, 7.20, 7.32, 7.05, 6.96 and 7.56 ppm), and two methylene protons (δ_H = 2.73 and 2.91 ppm, δ_H = 2.31 ppm). The ¹³C NMR spectrum displayed two carbonyl signals (δ_C = 172.03 and 173.14 ppm), eight signals of C=C carbon (δ_C = 110.25, 124.26, 136.66, 111.75, 121.35, 118.74, 118.93 and 127.78 ppm), three methylene signals (δ_C = 43.64, 32.91 and 27.51 ppm), and one methine (δ_C = 62.78 ppm). Moreover, the HMBC correlations from H-2 to C-3, C-6 and C-7, from H-3 to C-4 and C-5, and from H-6 to C-8, which suggested this adduct was formed by nucleophilic addition between amine group of tryptophan and double bond of acrylamide (29).

TABLE 4 | NMR spectra data of Lys-AA measured in D₂O.

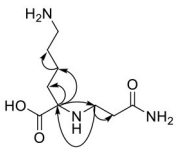
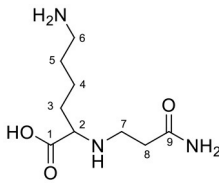
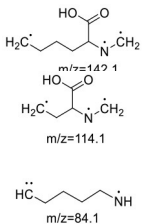
HMBC Correlations	No.	δ _C (ppm)	δ _H (ppm)	Structural formula	Fragment ion structure
	1	176.77		 MW=217.1490 Lys-AA	
	2	63.04	3.23(dd, <i>J</i> = 7.7, 5.4 Hz, 1H)		
	3	31.19	1.67 (m, 2H)		
	4	21.91	1.38 (m, 2H)		
	5	39.16	2.97(m, 2H)		
	6	26.61	1.67 (m, 2H)		
	7	43.14	2.94, 2.88(m, 2H)		
	8	33.64	2.53(td, <i>J</i> = 6.8, 3.3 Hz, 2H)		
	9	179.51			

TABLE 5 | NMR spectra data of Trp-AA measured in DMSO-*d*₆.

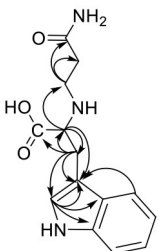
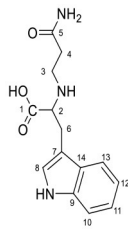
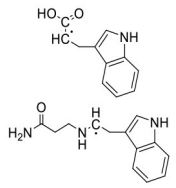

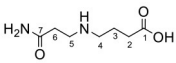
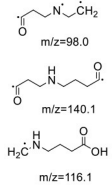
HMBC correlations	No.	δ _C (ppm)	δ _H (ppm) (multiplicity)	Structural formula	Fragment ion structure
	1	172.03		 MW=275.1337 Trp-AA	
	2	62.78	3.41(t, <i>J</i> = 12.9 Hz, 1H)		
	2 -NH-		7.49(s,1H)		
	3	43.64	2.73(dt, <i>J</i> = 12.4, 6.8 Hz, 1H) 2.91(dt, <i>J</i> = 13.0, 6.8 Hz, 1H)		
	4	32.91	2.31(td, <i>J</i> = 6.9, 3.7 Hz, 2H)		
	5	173.14			
	6	27.51	3.01(dd, <i>J</i> = 15.0, 7.4 Hz, 1H) 3.19(dd, <i>J</i> = 15.0, 5.3 Hz, 1H)		
	7	110.25			
	8	124.26	7.20(d, <i>J</i> = 2.3 Hz, 1H)		
	8 -NH-		10.86(s,1H)		
	9	136.66			
	10	111.75	7.32(d, <i>J</i> = 8.1 Hz, 1H)		
	11	121.35	7.05(m,1H)		
	12	118.74	6.96(t, <i>J</i> = 7.4 Hz, 1H)		
	13	118.93	7.56(d, <i>J</i> = 7.9 Hz, 1H)		
	14	127.78			

TABLE 6 | NMR spectra data of GABA-AA 1 measured in D₂O.

HMBC correlations	No.	δ _C (ppm)	δ _H (ppm)	Structural formula	Fragment ion structure
	1	181.34		 MW=174.1077 GABA-AA 1	
	2	34.47	2.31 t, (<i>J</i> = 7.0Hz,2H)		
	3	22.26	1.92 (m, <i>J</i> = 7.4Hz,2H)		
	4	47.56	3.09 (t, <i>J</i> = 7.6Hz,2H)		
	5	43.21	3.32 (t, <i>J</i> = 6.8Hz,2H)		
	6	30.58	2.74 (t, <i>J</i> = 6.8Hz,2H)		
	7	174.58			

For the GABA-AA reaction system, two adducts, namely, GABA-AA 1 and GABA-AA 2, were separated and analyzed. GABA-AA 1 was determined as C₇H₁₄N₂O₃ with [M+H]⁺ m/z 175.1077, which was the total of molecular weight of γ-aminobutyric acid (MW = 103) and acrylamide (MW = 71).

After losing [-CH₂COOH] and [-NH₂], the fragment ion m/z 98 was detected (Table 6). The ¹H NMR spectrum showed one set of γ-aminobutyric acid protons (δ_H = 2.31, 1.92 and 3.09 ppm) and two methylene protons (δ_H = 3.32 and 2.74 ppm). The ¹³C NMR spectrum displayed two carbonyl signals (δ_C = 181.34 and 174.58

ppm) and five methylene signals ($\delta_C = 34.47, 22.26, 47.56, 43.21$ and 30.58 ppm). In addition, the HMBC correlations from H-4 to C-2, C-3 and C-5, from H-5 to C-4, C-6 and C-7, and from H-3 to C-2 and C-4, which suggested that GABA-AA 1 was formed by nucleophilic addition between amine group of γ -aminobutyric acid and double bond of acrylamide.

The HRMS of GABA-AA 2 exhibited a peak at m/z 246.1443 $[M+H]^+$ indicating a molecular formula of $C_{10}H_{19}N_3O_4$, which

just had one more molecular weight of acrylamide than GABA-AA 1 ($174 + 71 = 245$), indicating that GABA-AA 2 was a di-AA adduct of GABA. The base peak at m/z 187 was referred to as the loss of $[-CH_2CONH_2]$ from the molecular ion (Table 7). Comparison of the 1H and ^{13}C NMR spectral data of GABA-AA 2 (Table 7) with that of GABA-AA 1 (Table 6) showed a close structural relationship between these two compounds, except for the integral of two methylene protons ($\delta_H = 2.19$

TABLE 7 | NMR spectra data of GABA-AA 2 measured in DMSO- d_6 .

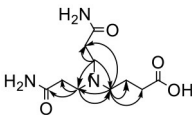
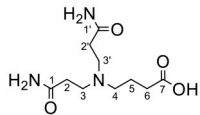
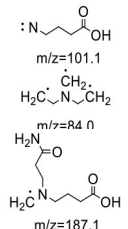
HMBC correlations	No.	δ_C (ppm)	δ_H (ppm)	Structural formula	Fragment ion structure
	1/1'	173.93		 MW=246.1443 GABA-AA 2	
	1/1' -NH ₂		6.82 (s, 1H) 7.42 (s, 1H)		
	2/2'	32.65	2.19 (t, $J = 7.4$ Hz, 2H)		
	3/3'	49.38	2.66 (t, $J = 7.1$ Hz, 2H)		
	4	52.42	2.41 (t, $J = 7.1$ Hz, 2H)		
	5	22.20	1.58 (m, $J = 7.1$ Hz, 2H)		
	6	32.65	2.16 (t, 1H)		
	7	175.52			

TABLE 8 | NMR spectra data of Gly-AA 1 measured in D₂O.

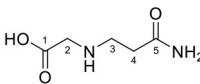
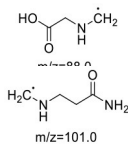
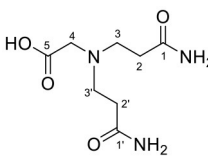
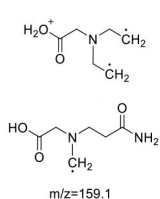
No.	δ_C (ppm)	δ_H (ppm)	Structural formula	Fragment ions structure
1	171.12		 MW=146.0764 Gly-AA 1	
2	49.27	3.66 (d, 2H)		
3	43.35	3.35 (t, $J = 6.7$ Hz, 2H)		
4	30.40	2.77 (t, $J = 6.7$ Hz, 2H)		
5	174.75			

TABLE 9 | NMR spectra data of Gly-AA 2 measured in D₂O.

No.	δ_C (ppm)	δ_H (ppm)	Structural formula	Fragment ions structure
1/1'	174.36		 MW=217.1135 Gly-AA 2	
2/2'	28.78	2.84 (t, $J = 6.8$ Hz, 2H)		
3/3'	51.31	3.55 (t, $J = 7.2$ Hz, 2H)		
4	56.14	3.81 (s, 2H)		
5	170.14			

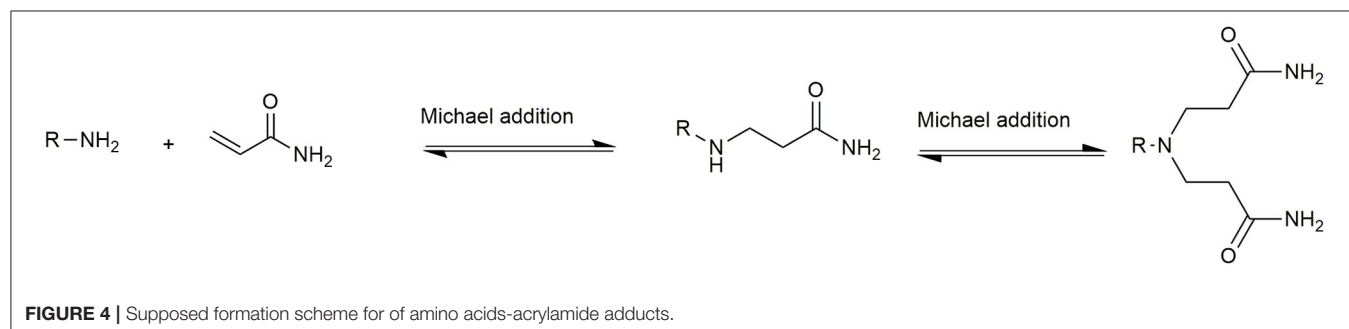


TABLE 10 | Standard curves of AA and six adducts.

Additive species	Linear equation	Determination coefficients (R^2)	LOD($\mu\text{g/L}$)	LOQ($\mu\text{g/L}$)	Linear range ($\mu\text{g/L}$)
AA	$Y = 405467X + 5042.57$	0.996	2	5	2~400
Lys-AA	$Y = 729807X - 90291.9$	0.996	5	20	5~200
Trp-AA	$Y = 3708160X - 3860.05$	0.997	1	3	1~50
GABA-AA 1	$Y = 15504500X - 76457.0$	0.997	3	10	3~400
GABA-AA 2	$Y = 13956800X + 41748.8$	0.999	0.5	1	0.5~100
Gly-AA 1	$Y = 2950500X + 11684.9$	0.998	5	20	5~250
Gly-AA 2	$Y = 2526290X + 11086.8$	0.997	1	4	1~50

LOD, Limit of Detection.
LOQ, Limit of Quantitation.

TABLE 11 | The content of acrylamide and adducts in foods.

Snake food*	Main composition	AA ($\mu\text{g/kg}$)	Lys-AA ($\mu\text{g/kg}$)	Trp-AA ($\mu\text{g/kg}$)	GABA-AA 1 ($\mu\text{g/kg}$)	GABA-AA 2 ($\mu\text{g/kg}$)	Gly-AA 1 ($\mu\text{g/kg}$)	Gly-AA 2 ($\mu\text{g/kg}$)
Potato chips A	potato	2620.3 ± 474.6	ND	ND	1997.5 ± 155.6	ND	804.5 ± 55.2	225.6 ± 68.7
Potato chips B	potato	1178.2 ± 173.5	104.3 ± 3.3	ND	1695.0 ± 153.9	ND	482.2 ± 49.8	45.5 ± 4.2
Potato chips C	potato	1357.9 ± 21.6	120.4 ± 0.4	ND	1777.5 ± 149.8	10.0 ± 2.2	645.7 ± 14.8	16.7 ± 9.2
Brown rice Cake	brown rice	76.2 ± 13.6	53.6 ± 4.8	ND	25.0 ± 4.3	ND	231.3 ± 86.6	9.6 ± 5.3
Egg biscuit	wheat flour	42.2 ± 36.6	58.5 ± 2.1	ND	40.5 ± 4.3	ND	ND	9.8 ± 1.8
Cereal bars	oatmeal, corn flour	29.6 ± 21.1	53.3 ± 1.2	22.6 ± 12.7	78.7 ± 18.8	ND	206.8 ± 26.2	ND
Fried dough twist	wheat flour	331.4 ± 102.9	64.3 ± 9.7	7.3 ± 2.4	56.2 ± 6.5	ND	ND	15.4 ± 6.1
Cracker	wheat flour	528.0 ± 166.2	53.5 ± 1.7	ND	21.2 ± 4.3	ND	ND	1.1 ± 1
Walnut cake	wheat flour	388.4 ± 25.3	52.3 ± 2.2	ND	ND	ND	ND	ND
Millet rice crust	millet rice flour	336.4 ± 145.4	50.3 ± 2.9	ND	57.5 ± 2.2	ND	ND	ND

ND, Not detected; the content was below the LOD presented in Table 10.
*: Store at room temperature and belong to ready-to-eat food.

and 2.66 ppm) is twice as many as that of GABA-AA 1. Under the condition of slow rotation, the chemical shifts of the two hydrogen atoms combined with nitrogen atoms differed by 0.5–1 ppm, respectively $\delta_{\text{H}} = 6.82$ and 7.41 ppm. ^{13}C MNR indicated that substructure of two propionamide groups to be a symmetric framework. In addition, the HMBC correlations from H-3 to C-1, C-2 and C-4, from H-4 to C-3, C-5, C-6 and C-2'; and from H-3' to C-3, C-4 and C-2'. It was speculated that GABA-AA 2 was formed by one molecular of γ -aminobutyric acid and two molecular of acrylamide.

The formation mechanism of two GABA-AA adducts was identical to Gly-AA adducts. For Gly-AA 1, the appearance of fragment ions m/z 101 and m/z 88 indicated the loss of $[-\text{COOH}]$, $[-\text{CONH}_2]$ and $[-\text{CH}_2]$. For Gly-AA 2, the fragment m/z 159 indicated the loss of $[-\text{CH}_2\text{CONH}_2]$ and m/z 130 for losing two molecules of $[-\text{CH}_2\text{CONH}_2]$ (Tables 8, 9). The ^1H MNR spectrum of Gly-AA 1 showed three methylene protons ($\delta_{\text{H}} = 3.66$, 3.35 and 2.77 ppm). The ^{13}C NMR spectrum displayed two carbonyl signals ($\delta_{\text{C}} = 171.12$ and 174.75 ppm), and three methylene signals ($\delta_{\text{C}} = 49.27$, 43.35 and 30.40 ppm). Comparison of the ^1H and ^{13}C NMR spectral data of Gly-AA 2 (Table 9) with that of Gly-AA 1 (Table 8) showed a close structural relationship between these two compounds, except for the integral of two methylene protons ($\delta_{\text{H}} = 3.55$ and 2.84 ppm) is twice as many as that of Gly-AA 1. On the basis of the above

analysis, Gly-AA 2 could be proposed to be a di-AA adduct of Glycine. This structure is consistent with the results reported by Liu et al. (25).

The above information confirmed that acrylamide reacts with the nucleophilic amino groups on amino acid side chains (27). Olefinic double bond and amide group are the two reactive sites of acrylamide. The double bond of acrylamide firstly reacts with the amino group in amino acids to form a Michael addition adduct (Figure 4). Since this adduct still has a nucleophilic group ($-\text{NH}$), it might attack another molecule of acrylamide to produce the dimer. Lysine and tryptophan, however, only had one major adduct with acrylamide, possibly owing to serious steric hindrance of the adduct generated in the first step, which was difficult to further react with acrylamide.

The levels of six adducts formed in baking foods were evaluated with multiple reaction monitoring (MRM) mode by mass spectrometry. Linear equation, determination coefficients, and linear range are listed in Table 10. The standards of six adducts had good linearity in a specific concentration range, and the determination coefficients were all >0.996 .

Ten food samples were made from potatoes or cereals. Different raw materials contributed to various adduct distribution (Table 11). High levels of AA (1178.2 – 2260.3 $\mu\text{g/kg}$) and GABA-AA 1 ($1,685$ – $1,995$ $\mu\text{g/kg}$) were detected in three brands of potato chips because uncooked potato flake was

rich in free asparagine and GABA (30). GABA-AA 2 content, however, was much lower than GABA-AA1 since the acrylamide content to form a dimer in foods was less than that in model system (27). Similarly, the dimer of glycine was also far less than Gly-AA 1. Lysine adducts were found in most of food samples while the contents were below 120 $\mu\text{g/kg}$, for its content was limited in both potato and cereals. Tryptophan adduct was only found in cereal bars (22.6 $\mu\text{g/kg}$) and fried dough twists (7.3 $\mu\text{g/kg}$), which are made from oat, corn or added with sesame.

Therefore, although tryptophan is thermally unstable, its adduct was found in these two food samples (31–33).

GABA-AA 1 Adduct Attenuates the Cytotoxicity of Acrylamide

Acrylamide is an unavoidable food contaminant in thermal processed foods. Although the appearance of adducts decreased acrylamide content in processed foods, the adducts were also inevitably exposed to humans. Whether they will pose new health

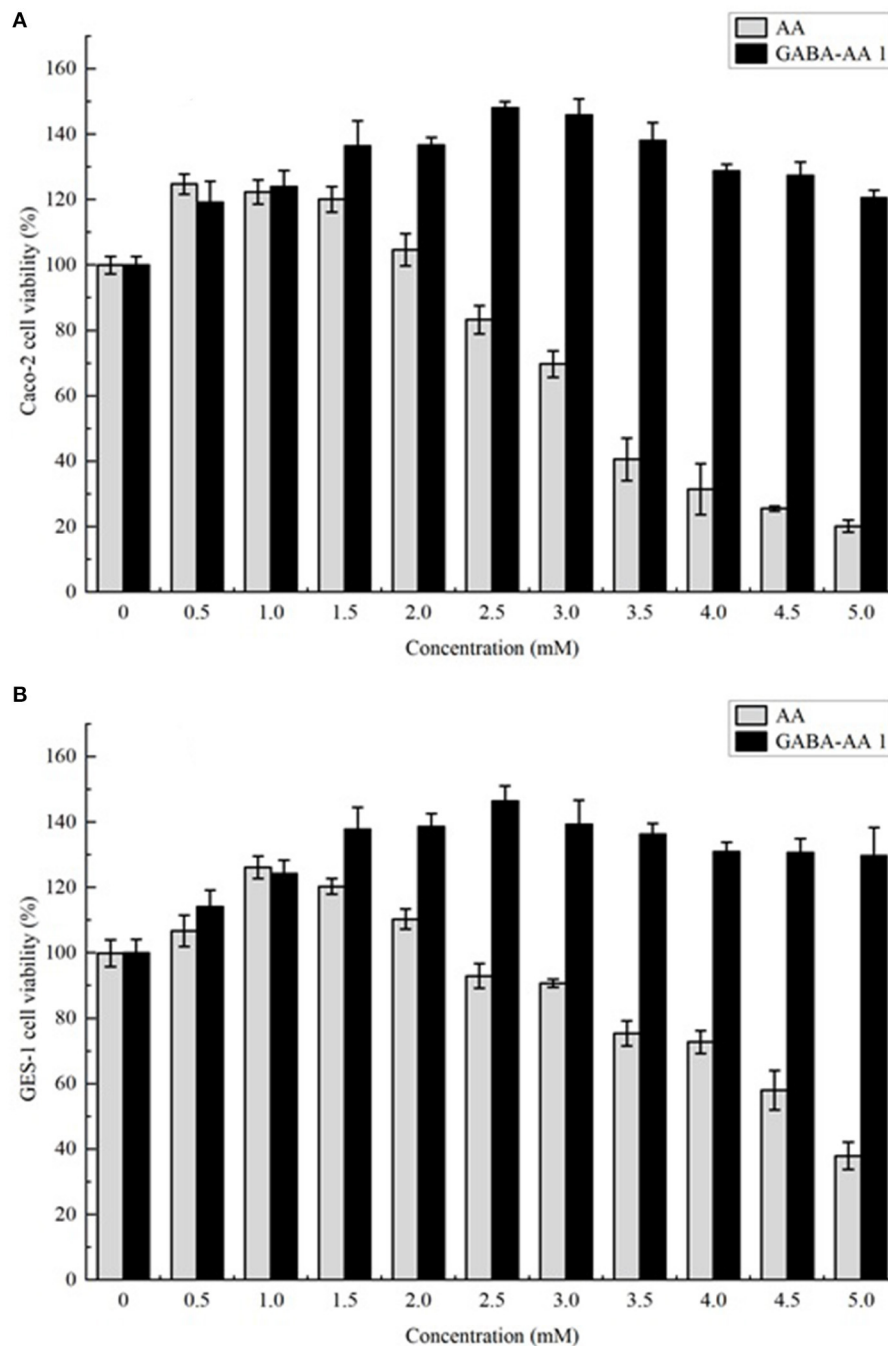


FIGURE 5 | The cytotoxicity of AA and its adduct GABA-AA 1 towards Caco-2 (A) and GES-1 (B) cells.

risks after ingestion remains unknown. Therefore, two cell lines from gastrointestinal tract (Caco-2 cells and GES-1 cells) were applied for cytotoxicity analysis. Since the content of GABA-AA 1 was far more than other adducts, it was chosen for cell viability evaluation. As shown in **Figure 5**, at low concentrations, AA showed no toxic effect on cell viability in both cell lines. However, it reduced the cell viability at a concentration dependent manner over 1 mM, with IC₅₀ values of 3.48 mM and 4.66 mM in GES-1 cells and Caco-2 cells, respectively. In contrast, GABA-AA 1 kept cell viability over 100% at all treated concentrations and even prompted cell growth to maximum 140%. These findings indicated that formation of GABA-AA 1 significantly decrease the cytotoxicity of AA without new health risks. As an intrinsic component of many foods, GABA may has reduced the final content of acrylamide in food processing. However, due to the limited content of GABA in food materials, acrylamide generated during food processing cannot be completely removed. Therefore, as a safe and efficient agent, GABA has the potential to be applied in food processing as additive or pretreatment, so as to mitigate the risks caused by food-derived AA.

CONCLUSION

Acrylamide, a food contaminant with harmful effects on humans, can be mitigated by amino acids through forming adducts. This work analyzed the elimination rate of four amino acids and obtained six related amino acid-acrylamide adducts through chemical synthesis. Their structures were analyzed, and the formation mechanism was confirmed as Michael addition. A quantification method of these adducts was established with LC-MS/MS, and their levels in 10 commercially baking foods were determined. GABA-AA 1, the adduct formed from one

molecular GABA and acrylamide, was identified at the highest levels in foods. In addition, its formation significantly reduced the cytotoxicity of acrylamide in Caco-2 cells and Ges-1 cells. This study provides the basic knowledge that amino acids may decrease acrylamide level in processed foods and lessen its deleterious effects on the body.

DATA AVAILABILITY STATEMENT

The raw data supporting the conclusions of this article will be made available by the authors, without undue reservation.

AUTHOR CONTRIBUTIONS

DL, FX, and KJ carried out experiments and drafted the manuscript. JZ, FL, and SO edited the manuscript. QR reviewed the submitted version. CH and JO conceived and designed this study. All authors proofread and approved the final manuscript.

FUNDING

This work was financially supported by the Guangdong Natural Science Fund (no. 2018A030313064), National Natural Science Fund of China (no. 32102097), and Zhongshan Torch Modern Industrial Engineering Technology Research Institute Innovation Center (no. 2019CYY01002).

SUPPLEMENTARY MATERIAL

The Supplementary Material for this article can be found online at: <https://www.frontiersin.org/articles/10.3389/fnut.2022.902040/full#supplementary-material>

REFERENCES

- Lyon F. Iarc monographs on the evaluation of carcinogenic risks to humans: *Some Ind Chem*. (1994) 60:389–433 p.
- Zyzak DV, Sanders RA, Stojanovic M, Tallmadge DH, Eberhart BL, Ewald DK, et al. Acrylamide formation mechanism in heated foods. *J Agric Food Chem*. (2003) 51:4782–7. doi: 10.1021/jf034180i
- Mousavi Khaneghah A, Fakhri Y, Nematollahi A, Seilani F. The concentration of acrylamide in different food products: a global systematic review, meta-analysis, and meta-regression. *Food Rev International*. (2020):1–19. doi: 10.1080/87559129.2020.1791175. [Epub ahead of print].
- Koh BK. Determination of acrylamide content of food products in Korea. *J Sci Food Agric*. (2006) 86:2587–91. doi: 10.1002/jsfa.2652
- Riboldi BP, Vinhas on of acrylamide content of food products in Korea. : a systematic review. *Food Chem*. (2014) 157:310–22. doi: 10.1016/j.foodchem.2014.02.046
- Pedersen M, Vryonidis E, Joensen A, Törnqvist M. Hemoglobin adducts of acrylamide in human blood—what has been done and what is next? *Food Chem Toxicol*. (2022) 161:112799. doi: 10.1016/j.fct.2021.112799
- Ou J, Zheng J, Huang J, Ho CT, Ou S. Interaction of acrylamide, acrolein, and 5-hydroxymethylfurfural with amino acids and DNA. *J Agric Food Chem*. (2020) 68:5039–48. doi: 10.1021/acs.jafc.0c01345
- Zamani E, Shokrzadeh M, Fallah M., Shaki F. A review of acrylamide toxicity and its mechanism. *Pharm Biomed Res*. (2017) 3:1–7. doi: 10.18869/acadpub.pbr.3.1.1
- Hanley A, Offen C, Clarke M, Roberts M, Burch R. Acrylamide reduction in processed foods. *ChemSafety Acrylamide Food*. Boston, MA: Springer (2005) 387–92 p.
- Amrein TM, Bachmann S, Noti A, Biedermann M, Barbosa MF, Biedermann-Brem S, et al. Potential of acrylamide formation, sugars, and free asparagine in potatoes: a comparison of cultivars and farming systems. *J Agric Food Chem*. (2003) 51:5556–60. doi: 10.1021/jf034344v
- Munir N, Zia MA, Sharif S, Tahir IM, Jahangeer M, Javed I, et al. L-asparaginase potential in acrylamide mitigation from foodstuff: a mini-review. *Prog Nutr*. (2019) 21:498–506. doi: 10.23751/pn.v21i3.6771
- Mart3.6771w. ase potential in acrylamide mitigation from foodstuff potatoescessed foods. hylfurfural with amino acids and DNA. next? n californian-style green ripe olives. *Foods*. (2020) 9:1202. doi: 10.3390/foods9091202
- Pedreschi F, Kaack K, Granby K. Reduction of acrylamide formation in potato slices during frying. *LWT-Food Sci Technol*. (2004) 37:679–85. doi: 10.1016/j.lwt.2004.03.001
- Esposito F, Fasano E, De Vivo A, Velotto S, Sarghini F, Cirillo T. Processing effects on acrylamide content in roasted coffee production. *Food Chem*. (2020) 319:126550. doi: 10.1016/j.foodchem.2020.126550
- Kobayashi A, Gomikawa S, Yamazaki A, Sato S, Konishi T. Elimination of acrylamide by moderate heat treatment below 120°C. Elimination of acrylamid. *Food Sci Technol Res*. (2014) 20:979–85. doi: 10.3136/fstr.20.979
- Koutsidis G, Simons SP, Thong YH, Haldoupis Y, Mojica-Lazaro J, Wedzicha BL, et al. Investigations on the effect of amino acids on acrylamide, pyrazines,

- and michael addition products in model systems. *J Agri Food Chem.* (2009) 57:9011–5. doi: 10.1021/jf9014763
17. Yu M, Ou S, Liumengzi D, Huang C, Zhang G. Effect of ten amino acids on elimination of acrylamide in a model reaction system. *African J Food Science.* (2013) 7:329–33. doi: 10.5897/AJFS2013.1031
 18. Kim CT, Hwang ES, Lee HJ. Reducing acrylamide in fried snack products by adding amino acids. *J Food Sci.* (2005) 70:354–8. doi: 10.1111/j.1365-2621.2005.tb09966.x
 19. Friedman M, Levin C. Review of methods for the reduction of dietary content and toxicity of acrylamide. *J Agri Food Chem.* (2008) 56:6113–113:6113–40. doi: 10.1021/jf0730486
 20. Jiang K, Yin Z, Zhou P, Guo H, Huang C, Zhang G, et al. The scavenging capacity of γ -aminobutyric acid for acrolein and the cytotoxicity of the formed adduct. *Food Func.* (2020) 11:7736–47. doi: 10.1039/C9FO02518A
 21. Hu J, Jiang K, Huang C, Zheng J, Zhou H, Ou J, et al. Glycine and serine markedly eliminate methylglyoxal in the presence of formaldehyde via the formation of imidazole salts. *Food Chem.* (2022) 369:130952. doi: 10.1016/j.foodchem.2021.130952
 22. Yang QQ, Suen PK, Zhang CQ, Wan SM, Gu MH, Liu QQ, et al. Improved growth performance, food efficiency, and lysine availability in growing rats fed with lysine-biofortified rice. *Sci Rep.* (2017) 7:1–11. doi: 10.1038/s41598-017-01555-0
 23. Hoseini SM, Powth performance, food efficiency, and lysine availability in growing rats fed with lysine-: current knowledge and perspectives for future studies. *Rev Aquacult.* (2019) 11:3–24. doi: 10.1111/raq.12223
 24. Zhao Q, Zou Y, Huang C, Lan P, Zheng J, Ou S. Formation of a hydroxymethylfurfural rats fed with lysine-biofortified rice. NA. next? in caco-2 cells. *J Agri Food Chem.* (2017) 65:9902–8. doi: 10.1021/acs.jafc.7b03938
 25. Liu J, Chen F, Man Y, Dong J, Hu X. The pathways for the removal of acrylamide in model systems using glycine based on the identification of reaction products. *Food Chem.* (2011) 128:442–9. doi: 10.1016/j.foodchem.2011.03.051
 26. Zou Z, Yin Z, Ou J, Zheng J, Liu F, Huang C, et al. Identification of adducts formed between acrolein and alanine or serine in fried potato crisps and the cytotoxicity-lowering effect of acrolein in three cell lines. *Food Chem.* (2021) 361:130164. doi: 10.1016/j.foodchem.2021.130164
 27. Zamora R, Delgado RM, Hidalgo FJ. Model reactions of acrylamide with selected amino compounds. *J Agri Food Chem.* (2010) 58:1708–13. doi: 10.1021/jf903378x
 28. Adams A, Hamdani S, Lancker FV, MS, L S, De Kimpe N. Stability of acrylamide in model systems and its reactivity with selected nucleophiles. *Food Res Int.* (2010) 43:1517–22. doi: 10.1016/j.foodres.2010.04.033
 29. Xing Z, Wu X, Zhao J, Zhao X, Zhu X, Wang Y, et al. Isolation and identification of induced systemic resistance determinants from bacillus simplex sneb545 against heterodera glycines. *Sci Rep.* (2020) 10:1–15. doi: 10.1038/s41598-020-68548-4
 30. Elmore JS, Koutsidis G, Dodson AT, Mottram DS, Wedzicha BL. Measurement of acrylamide and its precursors in potato, wheat, and rye model systems. *J Agric Food Chem.* (2005) 53:1286–93. doi: 10.1021/jf048557b
 31. Friedman M, Cuq JL. Chemistry, analysis, nutritional value, and toxicology of tryptophan in food. *A Rev J Agr Food Chem.* (1988) 36:1079–93. doi: 10.1021/jf00083a042
 32. Friedman M. Analysis, nutrition, and health benefits of tryptophan. *Int J Tryptophan Res.* (2018) 11:1178646918802282. doi: 10.1177%2F1178646918802282
 33. Martinchik AN. Nutritional value of sesame seeds. *Vopr Pitan.* (2011) 80:41–3.

Conflict of Interest: The authors declare that the research was conducted in the absence of any commercial or financial relationships that could be construed as a potential conflict of interest.

Publisher's Note: All claims expressed in this article are solely those of the authors and do not necessarily represent those of their affiliated organizations, or those of the publisher, the editors and the reviewers. Any product that may be evaluated in this article, or claim that may be made by its manufacturer, is not guaranteed or endorsed by the publisher.

Copyright © 2022 Li, Xian, Ou, Jiang, Zheng, Ou, Liu, Rao and Huang. This is an open-access article distributed under the terms of the Creative Commons Attribution License (CC BY). The use, distribution or reproduction in other forums is permitted, provided the original author(s) and the copyright owner(s) are credited and that the original publication in this journal is cited, in accordance with accepted academic practice. No use, distribution or reproduction is permitted which does not comply with these terms.



Exploring Acrylamide and 5-Hydroxymethylfurfural Formation in Glucose-Asparagine-Linoleic Acid System With a Kinetic Model Approach

Yingjie Ma¹, You Long¹, Feng Li¹, Yan Zhang¹, Bei Gan², Qiang Yu¹, Jianhua Xie¹ and Yi Chen^{1*}

¹ State Key Laboratory of Food Science and Technology, Nanchang University, Nanchang, China, ² Jiangxi Provincial Product Quality Supervision Testing College, Nanchang, China

OPEN ACCESS

Edited by:

Jie Zheng,
Jinan University, China

Reviewed by:

Bing Hu,
Nanjing Agricultural University, China
Maomao Zeng,
Jiangnan University, China

*Correspondence:

Yi Chen
chenyi-417@163.com

Specialty section:

This article was submitted to
Food Chemistry,
a section of the journal
Frontiers in Nutrition

Received: 10 May 2022

Accepted: 23 May 2022

Published: 23 June 2022

Citation:

Ma Y, Long Y, Li F, Zhang Y, Gan B,
Yu Q, Xie J and Chen Y (2022)
Exploring Acrylamide and
5-Hydroxymethylfurfural Formation in
Glucose-Asparagine-Linoleic Acid
System With a Kinetic Model
Approach. *Front. Nutr.* 9:940202.
doi: 10.3389/fnut.2022.940202

In the “glucose-asparagine-linoleic acid” ternary system, a kinetic model approach was used to explore formation and elimination law of target hazards, including acrylamide (AA) and 5-hydroxymethylfurfural (5-HMF), and their related precursors and intermediate products. The results showed that the elimination of glucose and asparagine and the formation of fructose (generated from glucose isomerization), 3-deoxyglucosone (3-DG), methylglyoxal (MGO), and glyoxal (GO), AA and 5-HMF followed first-order reaction kinetics with high fit coefficients ($R^2 > 0.9$). In addition, the kinetic reaction rate constants increased as the increasing temperature, and all models followed the Arrhenius law. Results of statistical correlations analysis suggested that at lower temperature, the generic amino acid route and the specific amino acid route may play crucial roles for the formation of AA and 5-HMF, while at high temperature a linoleic acid pathway may be predominantly involved.

Keywords: acrylamide, 5-hydroxymethylfurfural, kinetics, Maillard reaction, glucose-asparagine-linoleic acid

INTRODUCTION

During the thermal processing of foods rich in sugar, amino acids and oil, parallel and consecutive reactions take place, including Maillard reaction, caramelization, and lipid oxidation. In Maillard reaction, aldoses (e.g., glucose) or ketoses (e.g., fructose) have been reported to condense with amine groups to form Schiff bases, which are very unstable and can be cyclized into N-substituted aldoglycamine or N-substituted ketosylamine. They were then rearranged to Amadori products (1-amino-1-deoxy-ketose) or Heyns products (2-amino-2-deoxy-aldose) (1). Besides, it has been reported that fructofuranosyl cations react with amino compounds to form fructofuranosyl amines and rearrange to form Heyns products (2). Meanwhile, the degradation of Amadori or Heyns products is an important step in the reaction, resulting in α -dicarbonyl compounds formation (3, 4). For the caramelization reaction, it is the process by which aldoses or ketoses degrade at high temperature in the absence of amino compounds to form brown substances, and α -dicarbonyl compounds can be formed from sugar molecules during dehydration and degradation. In addition, some studies demonstrated that lipids can also produce many low molecular weight carbonyl compounds including α -dicarbonyl compounds via oxidative degradation or heat treatment (5).

α -Dicarbonyl compounds are important reactive intermediates in carbohydrate degradation. 3-deoxyglucosone (3-DG), methylglyoxal (MGO), and glyoxal (GO) as the main α -Dicarbonyl compounds can react with asparagine to form acrylamide (AA) via Strecker degradation (6). Additionally, the removal of two water molecules by 3-DG has been reported to lead to the formation of 5-hydroxymethylfurfural (5-HMF) (7, 8). The IARC has classed AA as a “probable human carcinogen” since it possesses genotoxic and carcinogenic characteristics, as well as neurotoxic properties at high doses (9). Studies have shown that 5-HMF has mutagenic effect on DNA, and cytotoxic effects on eyes, skin, upper respiratory tract and mucous membranes (10, 11).

More and more studies have been done to explore the involvement of Maillard and caramelization reaction in the formation mechanism of AA or 5-HMF in the model system. De Vleeschouwer et al. (12, 13) reported the formation/elimination kinetics of acrylamide in asparagine-glucose systems by changing the initial reactant concentration and ratio and sugar types. Kocadagli et al. (14) explored the kinetics of the formation and degradation of α -dicarbonyl compounds in glucose/wheat flour system heated under low moisture conditions. These results have also been confirmed in real food systems. Berk et al. (15) explored the AA and 5-HMF formation mechanism during roasting of sesame seeds. Hamzalioglu et al. (16) reported that 5-HMF was a key intermediate during AA formation in the coffee system. However, these studies are focused on the Maillard reaction and caramelization, and the synergistic effect of lipid oxidation pathways has not been explored. In addition, kinetic modeling has received increasing attention in food research fields. It can reflect chemical changes in food, such as changes in color over time and temperature. If the rate and temperature dependence of the reaction is known, the occurrence of the reaction can in principle be predicted and controlled. Furthermore, it helps to understand the chemical nature and mechanism of the reaction (17).

Thus, in this study, the “glucose-asparagine-linoleic acid” ternary model system was applied to explore the simultaneous involvement of lipid oxidation and Maillard reaction in the formation of target hazards (AA and 5-HMF) through kinetic studies. It will give insights to evaluate the levels of α -dicarbonyl compounds including 3-DG, MGO, GO and hazards including AA and 5-HMF from food rich in carbohydrate, amino acids and unsaturated fatty acids. It also concerned about the relation of 5-HMF conversion into AA during thermal processing.

MATERIALS AND METHODS

Chemicals

Standards for AA, 5-HMF, $^{13}\text{C}_3$ -AA, $^{13}\text{C}_6$ -HMF, 3-deoxyglucosone, quinoxaline, 2-methylquinoxaline, *o*-phenylenediamine (OPD), glucose and fructose were purchased from Sigma-Aldrich (St. Louis, MO, USA.). L-asparagine analytical standard was purchased from Beijing Solarbio Technology Co., Ltd (Beijing, China). HPLC-grade methanol and acetonitrile were obtained from Merck Company (Darmstadt, Germany). HPLC-grade formic acid was obtained from Shanghai

Anpel Technology Co., Ltd (Shanghai, China). Distilled water was purchased from Watsons Water Co., Ltd. (Guangzhou, China). HPLC-grade *n*-heptane, D-glucose, asparagine and linoleic acid were obtained from Aladdin Biochemical Technology Co. Ltd. (Shanghai, China). *O*-phthalaldehyde (OPA) and 2-mercaptoethanol (2-ME) were purchased from Macklin Biochemical Technology Co., Ltd (Shanghai, China).

Preparation of Model System

The model systems were prepared in 15 mL thick-walled pressure-resistant glass tubes (Beijing Synthware Glass Instrument Co. LTD, Beijing, China) with a sugar, asparagine, and oil mass ratio of about 15:13:4 to simulate the mass ratio used in biscuit manufacture (18), which contained 60 mg of glucose, 50 mg of asparagine, 16 mg of linoleic acid, and 2 mL of 0.1 M phosphate buffer (pH 7.4). The tubes were sealed with a polytetrafluoroethylene screwcap with a sealing ring and heated for 1, 3, 5, 7, 10, and 15 min in an oil bath (HH-SJ, Changzhou Jintan Youlian Instrument Research Institute, Changzhou, China) at 160, 180, and 200°C, respectively, then rapidly cooled in an ice bath.

Analysis of Sugars

The analysis was conducted using an Agilent 1260 high performance liquid chromatography (HPLC) connected to a refractive index detector condition (RID). Separation of the analytes was performed on a CNW Athena NH₂-RP column (4.6 × 250 mm, 5 μm , Shanghai Anpel Technology Co., Ltd, Shanghai, China) at 40 °C using an isocratic elution with a mobile phase consisting acetonitrile and distilled water (v/v = 70:30) at a flow rate of 1 mL/min and the injection volume was 20 μL .

Analysis of Asparagine

Asparagine was analyzed by an Agilent 1290 HPLC system equipped with a diode array detector (DAD). OPA-2-ME reagent was prepared by a method described in a previous study (19). For precolumn derivatization, 20 μL of sample or 20 μL of asparagine standard was mixed with 30 μL of OPA-2-ME reagent and 150 μL of 0.1 M Na₂B₄O₇ at room temperature for 3 min and passed through a 0.45 μm filter membrane waiting for analysis. The mobile phase consists of 0.01 M sodium phosphate buffer (pH 6.85) (A) and methanol (B) following a gradient elution procedure as previously reported by Yuan et al. (20). Samples were injected (20 μL) at 30 °C onto a Kromasil C₁₈ column (250 × 4.6 mm, 5 μm ; Akzo Nobel Pulp and Performance Chemicals, Bohus, Sweden) with the flow rate of 0.8 mL/min and the detection wavelength was 340 nm.

Analysis of Linoleic Acid

The oil samples in the model system were extracted with petroleum ether and placed in a centrifuge tube. Then 2 mL of *n*-heptane and 0.1 mL of 2 M potassium hydroxide-methanol solution were added respectively. After mixing with a vortex mixer for 30 s, centrifuge at 4,800 rpm for 5 min, and take 1 mL of supernatant through a 0.22 μm filter for injection.

Analysis of linoleic acid was carried out using Agilent 8860 gas chromatography (GC) equipped with a flame ionization detector

(FID) and a DB-FATWAX UI column (0.25 mm × 3 m, 0.25 μm; Agilent Technologies Inc., Santa Clara, CA, USA). The oven temperature program was as follows: 60°C held for 3 min, then increased to 170°C at 35 °C/min, held for 5 min, followed by heating up to 180°C at 5°C/min, held for 15 min, and finally increased at a rate of 5°C/min to 200°C. The helium flow rate was maintained constant at a flow rate of 1 mL/min and shunt ratio was 10:1.

Analysis of AA and 5-HMF

The determination of AA and 5-HMF was performed according to the method described in a previous study (21). An Agilent ultra-high performance liquid chromatography system conjunction with triple-quadrupole mass spectrometer (LC-QqQ-MS/MS) coupled with electrospray ionization (ESI) source was used to conduct the analysis (Agilent Technologies Inc., Santa Clara, CA, USA). Separation of the analytes was performed on a Phenomenex Synergi Hydro-RP column (150 × 2.0 mm, 4 μm; Phenomenex, Torrance, CA, USA) with temperature of the column thermostat maintained at 30 °C. As mobile phase, methanol (A)/0.1% (V/V) formic acid in distilled water (B) were used at a flow rate of 0.3 mL min⁻¹. The gradient elution was achieved under the following conditions: the program began at 95% B and was reduced to 80% B from 0 to 3 min; returned to 95% B over 5 min; and it was held at 95% B for 2 min. The injection volume was 1 μL. AA and 5-HMF were identified and quantified by means of multiple reaction monitoring (MRM) mode set to record the transitions m/z 72 → 55 and 72 → 27 for AA, m/z 75 → 58 and 75 → 29 for ¹³C₃-AA, m/z 127 → 109 and 127 → 81 for 5-HMF and 133 → 115 and 133 → 86 for ¹³C₆-HMF.

Analysis of α-Dicarbonyl Compounds Derivatization Procedure

200 μL of supernatant were combined with 400 μL of potassium phosphate buffer (pH 7.0) and 400 μL of 10 mg/mL OPD (in water), then filtered through 0.22 μm filters into an autosampler vial and stored at 25 °C for 3 h before determination.

LC-QqQ-MS/MS Analysis

The α-dicarbonyl compounds were analyzed using an Agilent LC-QqQ-MS/MS with ESI source. 3-DG, MGO and GO quinoxaline derivatives were chromatographically separated on a Phenomenex Synergi Hydro-RP column (150 × 2.0 mm, 4 μm; Phenomenex, Torrance, CA, USA) at 30 °C. The mobile phase consisted of methanol/0.1% (V/V) formic acid in distilled water [60/40 (v/v)] at a flow rate was 0.25 mL/min with time of 10 min. The injection volume was 1 μL. Analytes were obtained using MRM mode with the ions monitored in the sample: m/z 235 → 199 and 235 → 171 for 3-DG, m/z 145 → 77 and 145 → 92 for MGO and m/z 131 → 77 and 131 → 51 for GO.

Kinetic Modeling

The kinetic models were conducted using Origin 2019 (Microcal Software, Inc., Northampton, MA, USA)

The temperature dependence of the reaction is described by the activation energy E_a (kJ/mol) by establishing the

Arrhenius equation:

$$k(T) = A \times \exp\left(\frac{E_a}{RT}\right),$$

where k is the reaction rate constant, A is the pre-exponential factor, E_a is the activation energy (J mol⁻¹), R is the universal gas constant (8.3145 kJ/mol K), and T is the temperature concerned.

Statistical Analysis

All the experiments were performed at least triplicate and data was statistically analyzed using IBM SPSS statistical software (version 26.0, SPSS Inc., Chicago, IL, USA) and present as mean value ± SD (standard deviation) to determine the statistical significance. Analysis of variance (ANOVA) and Duncan's test were used to determine the differences between means, with a significance level of $P < 0.05$.

RESULTS AND DISCUSSION

Kinetic Changes of Glucose, Fructose, Asparagine and Linoleic Acid Concentrations in Model System

During the heating process, the concentration of glucose and asparagine, as the main precursors, decreased gradually with the increase of temperature and time, showing a trend of elimination kinetics (Figures 1A,B). Glucose decreased to the lowest concentration after heating for 15 min at 160, 180, and 200°C, respectively. Especially, the glucose was almost depleted when heated for 15 min at 200°C. The loss of glucose was not only a result of its reaction with asparagine, but also partly due to its participation in the isomerization reaction to form fructose in the heated sample (Figure 1C). By comparison, during the heating process, fructose was continuously formed. Furthermore, we found that fructose appeared to be the only detectable product of glucose isomerization under the applied reaction conditions, which was consistent with observations by other researchers (22, 23). At 160 and 180°C, the fructose concentration gradually increased with the increase of time and temperature, and reached the highest concentration at 15 min. While at 200°C, the concentration of fructose in the early stage of the reaction was more than three times higher than that of low temperature, but after 7 min, the reaction rate began to flatten out, which may be due to the further reaction of fructose with other compounds at higher temperature. It's been found that asparagine decreased slowly at 160°C, while decreased sharply at 180 and 200°C. It is reported that the concentration change of amino compounds was actually the result of at least three reactions: the reaction with sugar in the initial stage of the Maillard reaction; the regeneration of the amino compounds in the intermediate stage and the participation of the amino group in the browning reaction in the final stage (24). As shown in Figure 1B, a clear continuous loss of asparagine was observed when high temperature was applied. Meanwhile, it was found that the rate of asparagine loss was slower than that of glucose, which was consistent with the results of a glucose-asparagine system by Knol et al. (23). It can be explained by the regeneration

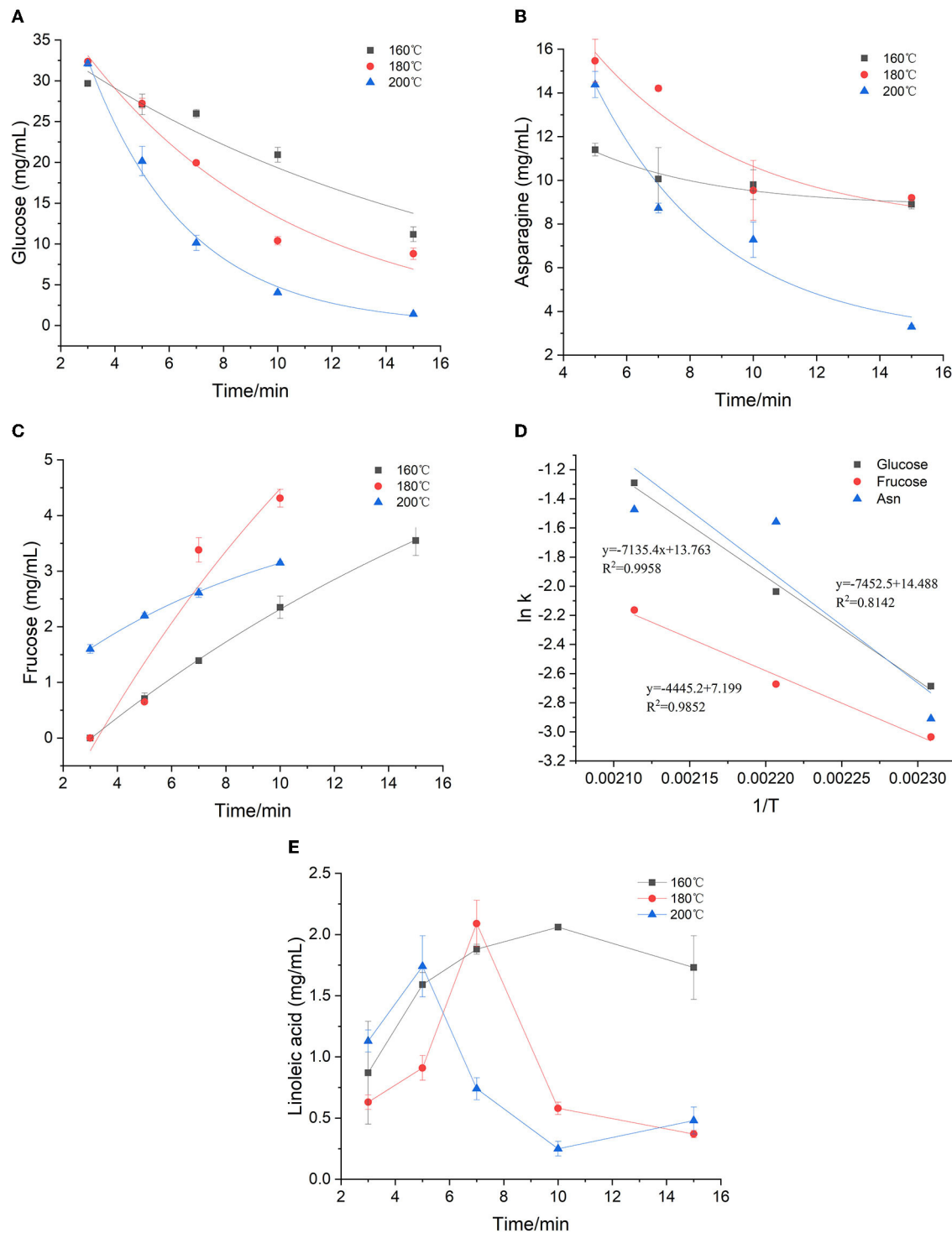


FIGURE 1 | Kinetic changes of precursors in heated model system **(A)** glucose, **(B)** asparagine, **(C)** fructose, **(D)** Arrhenius plot and **(E)** Effect of time and temperature on linoleic acid concentration.

of asparagine from the initial condensation product (such as the Amadori rearrangement product) and the possible formation of diglucosamine (22).

The first-order kinetic equation (Exp2PMod1) was used to fit the data of glucose in the model system. As for fructose and

asparagine, their formation rates conformed to the first-order kinetic equation (Exponential). As shown in **Figures 1A–C**, the coincidence of the kinetic model curve with the actual data points showed that the model can accurately describe the glucose concentration at the three temperatures. Kinetic

TABLE 1 | Parameter of kinetics of glucose, fructose, and asparagine in heated model system.

	Temperature (°C)	k	R ²	E _a (kJ/mol)
Glucose	160	0.068	0.897	59.32
	180	0.130	0.951	
	200	0.275	0.993	
Fructose	160	0.048	0.999	36.96
	180	0.069	0.771	
	200	0.115	0.998	
Asparagine	160	0.054	0.844	61.96
	180	0.211	0.734	
	200	0.229	0.875	

parameters were calculated by fitting the measured glucose values, as shown in **Table 1**. The fitting model of glucose obtained $R^2 > 0.897$, indicating that the first-order kinetic model can be well described its concentration changes. Except that R^2 at 180 °C was slightly lower (0.771 and 0.734) for fructose and asparagine, and $R^2 > 0.998$ and 0.844 at 160 and 200°C, which could accurately describe the reaction process. As the baking temperature increased, the degradation rate constants of glucose and asparagine increased from 0.068 min⁻¹ to 0.275 min⁻¹ and from 0.054 to 0.229 min⁻¹, indicating that the higher the temperature, the faster the reaction rate. In a previous study on a glucose/wheat flour system, the reaction rate constants for glucose at 160–200 °C ranged from 0.048 to 0.204 min⁻¹ (14), in an order of magnitude with our results. The formation rate constants of fructose at three temperatures were 0.045, 0.069 and 0.115 min⁻¹, respectively, which were slower than glucose and asparagine. The Arrhenius plot was plotted with the natural logarithm of the rate constant (ln k) vs. the inverse of the absolute temperature (1/T) (**Figure 1D**), which showed that ln k increased linearly as a function of 1/T. According to the slope of the linear equation, the calculated E_a of glucose and asparagine was 59.32 kJ/mol and 61.96 kJ/mol, while E_a of fructose was 36.96 kJ/mol, indicating that fructose formation was easier to be achieved compared to glucose and asparagine.

As shown in **Figure 1E**, the concentration of linoleic acid increased at the beginning and then decreased at three temperatures. Meanwhile, the higher the temperature, the earlier the drop point arrived, the faster the concentration decreased. At 160, 180, and 200 °C, the lowest concentrations of linoleic acid were obtained after 1 min, 15 min and 10 min with 0.87, 0.37, and 0.25 mg/mL, respectively. We presumed that polyunsaturated fatty acids may be converted to linoleic acid at the initial stage of the reaction, and then linoleic acid continues to oxidize to form saturated fatty acids at sustained high temperatures. Because the concentration of linoleic acid was unstable, and the temperature dependence of the reaction was complicated, the Arrhenius equation was not suitable for this case.

Kinetic Changes of α -Dicarbonyl Compounds Concentrations in Model System

α -Dicarbonyl compounds such as 3-DG, MGO, GO are key reaction intermediates formed during caramelization and

Maillard reactions in food processing. The concentrations of three main α -dicarbonyl compounds (3-DG, MGO and GO) in the model system at three temperatures were detected and then the kinetic fit plots were drawn (**Figures 2A–C**). They reached their maximum concentration at a corresponding time points under three heating temperatures, and the maximum concentration increased with increasing temperature. In general, their maximum concentration was in the order as MGO > 3-DG > GO (except for MGO at 160°C). Similar results were previously reported for the α -dicarbonyl compounds formation of coffee during roasting at 220 and 240 °C, which was indicated that formation of MGO predominantly through 3-DG (16).

The degradation of Amadori products and Heyns products leads to the formation of 3-DG (25). In addition, 3-DG can also be formed by removing one molecule of water from glucose during caramelization (3). As shown in **Figure 2A**, at the three heating temperatures, 3-DG increased instantly with the extension of heating time, and appeared to be flat at the later stage of reaction at 200°C, and then gradually decreased. 3-DG reached the highest concentration when heated at 160°C for 15 min, 180 °C for 10 min and 200°C for 7 min, which were 24.7 μ M, 25.5 μ M and 26.4 μ M, respectively. The formation of MGO could be a result of the cleavage of Schiff base into C2 and C3 compounds (26). In addition, it has been reported that MGO formation occurs due to the cleavage of the C3-C4 bond in 1-deoxyglucosone (1-DG) (3). Besides, Thornalley et al. (25) also reported that MGO can be formed from 3-DG by retroaldol cleavage. As shown in **Figure 2B**, with the increase of heating temperature and time, the increasing rate of MGO was gradually accelerated, which was faster than that of 3-DG. In the early stage of the reaction at the three temperatures, the concentrations of 3-DG (0.3, 1.9, 7.1 μ M) were higher than that of MGO (0.1, 0.8, 1.4 μ M). But as the reaction progressed, the maximum concentrations of MGO were about 1.5 times higher than 3-DG at the late reaction stage. GO was one of the α -dicarbonyl compounds observed in the samples, but its content was lower than that of 3-DG and MGO. It is formed due to the degradation of Amadori products or deoxyglycosides (27). In addition, it can also be directly formed from glucose or imine via retroacetalization followed by oxidation (25). As shown in **Figure 2C**, only at high temperature of 200°C the reaction rate of GO increased sharply at the beginning of the reaction and then leveled off. Its concentration at later stages of the reaction was lower than that of 3-DG and MGO.

The kinetic changes of α -dicarbonyl compounds during the heating process could be expressed by the first-order reaction kinetic model, which were all in line with the Exponential equation. The model parameters fitted according to the measured concentrations of the reaction were shown in **Table 2**. It is observed that $R^2 > 0.915$ for the fitted curves of 3-DG, $R^2 > 0.819$ for MGO and $R^2 > 0.922$ for GO, indicating that the models can describe the concentration changes of the reaction well. The kinetic rate constants k of each substance was gradually increasing with the temperatures, which indicated that high temperature promoted the reaction. The Arrhenius plots of 3-DG, MGO and GO were shown in **Figure 2D**. According to the slope of the linear equation, the activation energy E_a of the

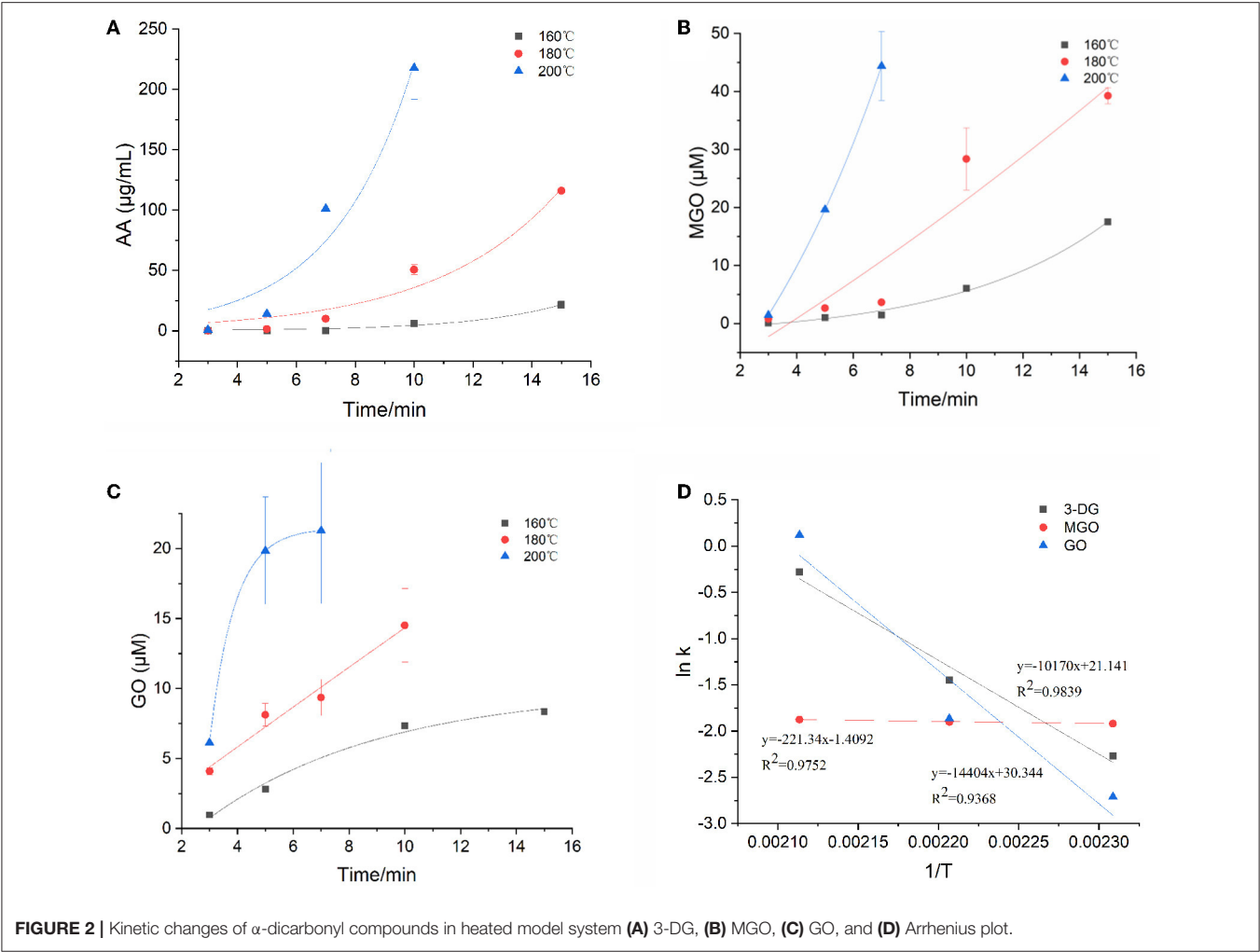
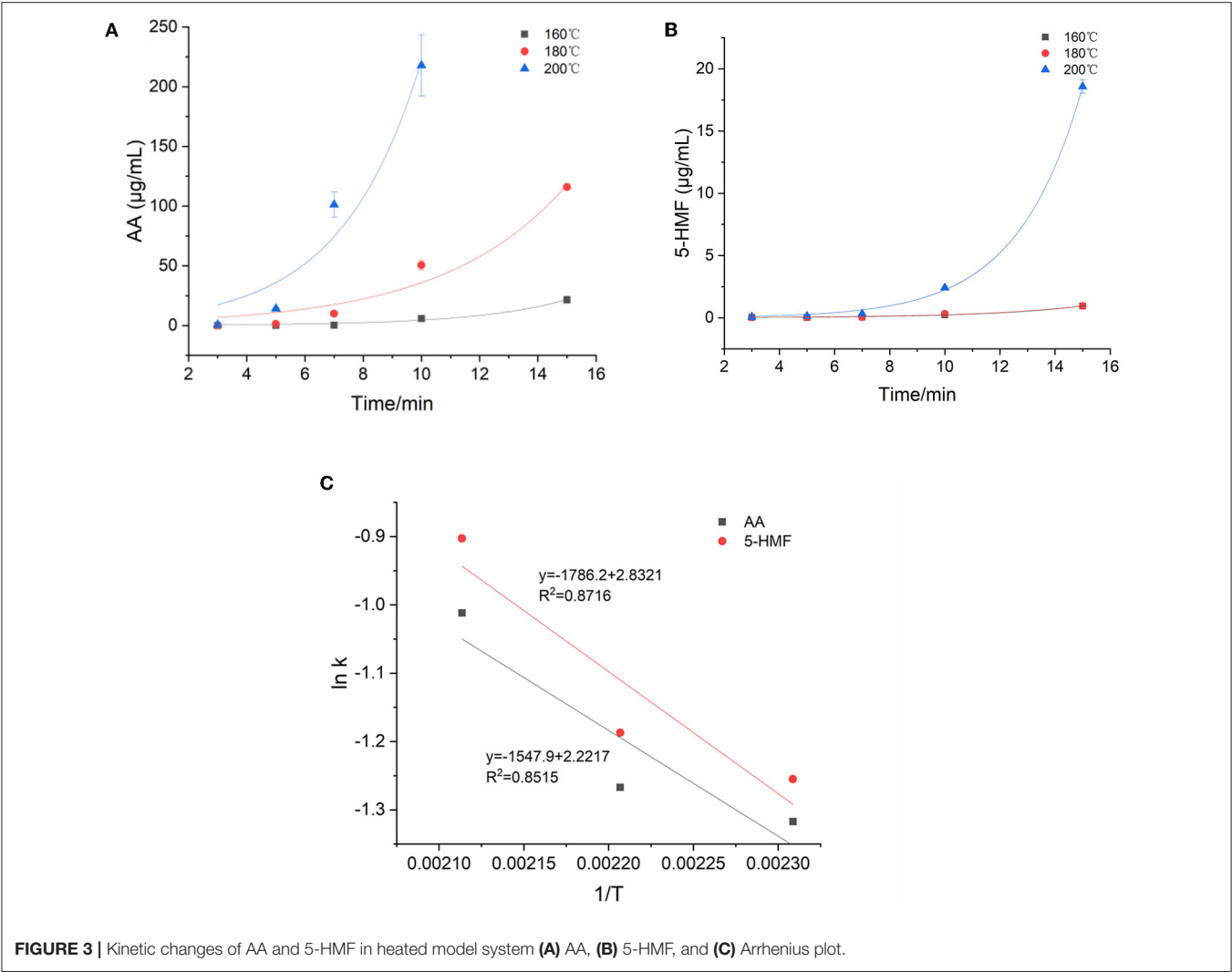


TABLE 2 Parameter of kinetics of α -dicarbonyl compounds in heated model system.				
	Temperature ($^{\circ}\text{C}$)	k	R ²	E _a (kJ/mol)
3-DG	160	0.103	0.915	84.55
	180	0.235	0.917	
	200	0.758	0.917	
MGO	160	0.147	0.991	1.84
	180	0.149	0.819	
	200	0.153	0.819	
GO	160	0.067	0.961	119.75
	180	0.155	0.922	
	200	1.128	0.922	

reaction can be calculated, and E_a of 3-DG, MGO and GO were 84.55, 1.84, and 119.75 kJ/mol, respectively. According to the E_a values, MGO is more sensitive to temperature than 3-DG and GO.

Kinetic Changes of AA and 5-HMF Concentrations in Model System

Figure 3A showed the kinetic fitting diagram of AA. Throughout the reaction process, AA showed an upward trend with the heating time, and at 160°C, the AA concentration gradually increased after a longer lag period of 10–15 min, but increased sharply at 180 and 200°C, indicating that the concentration of AA was greatly affected by time and temperature. The concentration increased by >276–2,000 times from the start of the reaction to the highest point of the reaction. Parker et al. (28) called the direct reaction of asparagine with reducing sugar to generate AA as the specific amino acid pathway. In addition to specific amino acid pathways, α -dicarbonyl or hydroxycarbonyl compounds formed from the dehydration of Amadori products of reducing sugars and amino acids may also react with asparagine to form AA. They called these AA formation pathways the universal amino acid pathway. By monitoring the concentration changes of 5-HMF during the reaction process, the reaction kinetic diagram was fitted based on the measured value of the concentration (Figure 3B). Although the dynamic change of 5-HMF was similar to that of AA, the concentration increased to the

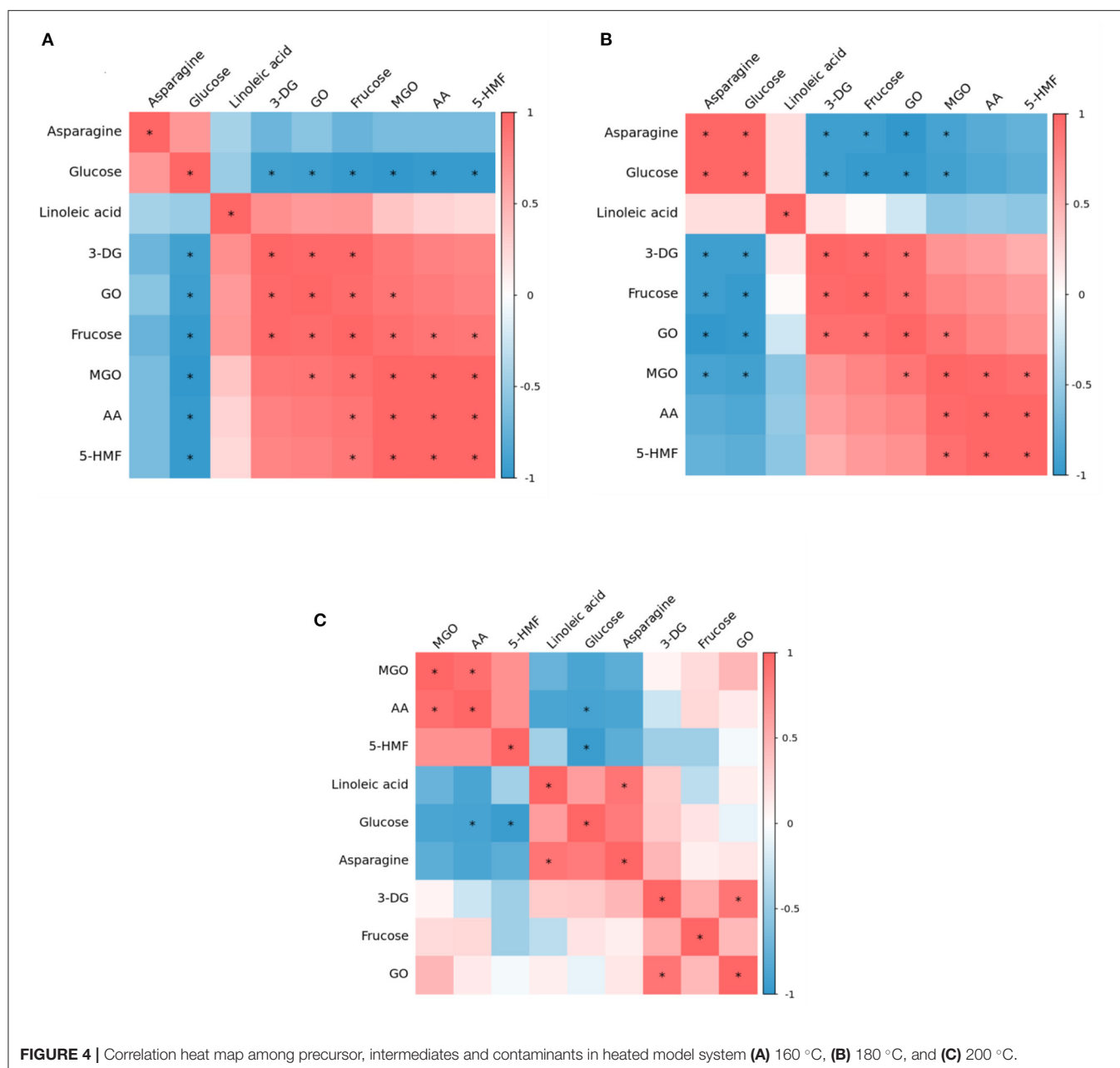


maximum value with the increasing temperature and time, the temperature and heating time had no significant effects on the concentration of 5-HMF when heated below 200°C. Moreover, at 200°C, 5-HMF increased sharply in the late reaction phase, and the maximum concentration was nearly 20 times higher than that at 160 and 180°C, which suggested that 5-HMF was easier to form at temperature higher than 200°C. In this model, the concentration of AA is 10–100 times higher than that of 5-HMF. Gokmen et al. (29) reported that 5-HMF with a carbonyl function was able to form AA in a low-moisture model system by reacting with asparagine. This may explain the above difference of concentration between AA and 5-HMF.

The kinetic changes of AA and 5-HMF during the heating process were both described by the first-order reaction kinetic model (Exp2PMod1). The kinetic parameters were shown in Table 3. Unsurprisingly, the kinetic rate constants (k) of the two target hazards increased with increasing temperature, with k values ranging from 0.268 to 0.364 and 0.285–0.405min^{−1} for AA and 5-HMF. Obviously, the reaction rate of 5-HMF

TABLE 3 Parameter of kinetics of AA and 5-HMF in heated model system.				
	Temperature (°C)	k	R ²	E _a (kJ/mol)
AA	160	0.268	0.980	12.87
	180	0.282	0.944	
	200	0.364	0.926	
5-HMF	160	0.285	0.996	14.85
	180	0.305	0.974	
	200	0.405	0.999	

was higher than that of AA. It was observed from Table 3 that the concentration changes of AA and 5-HMF fitted the curve with $R^2 > 0.926$, indicating that the model could accurately describe the concentration changes of the reaction, confirming that their generation followed a first-order reaction. The temperature dependence of AA and 5-HMF was estimated using the Arrhenius equation and shown in Figure 3C. The activation energy E_a of the reaction was calculated according to



the slope of the linear equation, and the E_a of AA and 5-HMF were calculated to be 12.87 and 14.85 kJ/mol, respectively, which indicated that the formation reaction of hazardous substances was more likely to occur at high temperature. In contrast to the previous overview of AA formation in various model systems and corresponding E_a (48.5–277 kJ/mol) by De Vleeschouwer et al. (30), much lower E_a was obtained for our study, which probably resulted from the lower concentration of reactants we used. Meanwhile, a study about coffee showed that the E_a values for the formation 5-HMF was calculated to be 47.31–117.38 kJ mol⁻¹ (31), which can be explained by the matrix effect of the coffee system.

Correlation Analysis Between Precursors, α -Dicarbonyl Compound and Target Hazards

Maillard, caramelization and lipid oxidation almost simultaneously exist in food systems, thus they may interact with each other. Therefore, heat maps of correlation analysis (Figure 4) were constructed based on the concentrations of precursors (glucose, fructose, asparagine, linoleic acid), α -dicarbonyl compounds (3-DG, GO, MGO) and hazardous substances (AA and 5-HMF) at three heating temperature to identify possible correlations between various parameters in the glucose-asparagine-linoleic acid model system. This

analysis was carried out using a Pearson's correlation test for the significance assessment.

At 160°C, glucose and asparagine were positively correlated with each other, but negatively correlated with other substances, among which glucose had a significant negative correlation with all detected intermediates and hazardous substances, which proved that in the model system, glucose should be the main precursor for the formation of intermediates and hazardous substances. Nguyen et al. have found glucose can produce the highest AA and 5-HMF concentration compared to other sugars (6). Interestingly, linoleic acid and fructose were observed to have positive correlations with each intermediate and two hazards. Meanwhile, there were significant positive correlations between 3-DG and GO, GO and MGO, MGO and AA, MGO and 5-HMF, and AA and 5-HMF. It was reported that both of glucose and fructose can generate 5-HMF through the formation of a dicarbonyl intermediate, 3-DG, from the Maillard reaction and caramelization. Thus, we presumed that the formation of AA and 5-HMF from a generic amino acid route with glucose and fructose simultaneously involved (but glucose as the main precursor) played a crucial role at this stage of lower temperature.

Whereas at 180°C, it is clear from **Figure 4B** that the correlation between the various substances was weakened. Besides, at 180°C glucose and asparagine became significantly positively correlated with each other, and the negative correlation between asparagine and 3-DG, fructose, GO, MGO became significant. However, glucose still negatively correlated with AA and 5-HMF, but not significantly. The correlations between 3-DG, fructose, GO, MGO, AA and 5-HMF were the same as at 160°C, but the positive correlations of fructose with MGO, AA and 5-HMF became insignificant. It was reported that in the specific amino acid route, reducing sugars react with asparagine to form the Schiff base that is thereafter decarboxylated to form acrylamide, without rearrangement of the Amadori products and fragmentation of sugar (28). Thus it was possible that at this stage the specific amino acid route may play a dominant role in the AA and 5-HMF formation.

As shown in **Figure 4C**, at 200°C, the correlations between various parameters gradually weakened, among which, the correlations of 3-DG, fructose and GO concentration with other substances were not significant. It is worth mentioning that at 180 and 200°C, the relationship of linoleic acid with AA and 5-HMF changed from a positive correlation at 160°C to a negative correlation, and the negative correlation with AA was stronger in comparison, indicating that under such high temperature conditions, in addition to the glucose and asparagine pathways, the linoleic acid pathway may be crucially involved for the formation of AA and 5-HMF.

CONCLUSION

This study systematically studies kinetic changes of the precursors (glucose, fructose, asparagine, linoleic acid), α -dicarbonyl compound intermediates (3-DG, MGO, GO) and target hazards (AA and 5-HMF) in the “glucose-asparagine-linoleic acid” ternary system. The kinetics analysis suggested that MGO was more likely to be formed during the reaction. The formation of AA and 5-HMF both obeyed first-order kinetics. In addition, the kinetic reaction rate constants under different heating temperatures suggested the formation of AA and 5-HMF were temperature dependent. Furthermore, the correlation analysis between precursors, intermediates and target hazardous substances indicated that at lower temperature, the generic amino acid route and the specific amino acid route may play crucial roles for the formation of AA and 5-HMF. With the temperature increased, the relationship between linoleic acid and AA and 5-HMF changed from a positive correlation at low temperature to a negative correlation, indicating that at this high temperature, except for glucose and asparagine pathways, there may also be a linoleic acid pathway for the generation of AA and 5-HMF.

DATA AVAILABILITY STATEMENT

The original contributions presented in the study are included in the article/supplementary material, further inquiries can be directed to the corresponding authors.

AUTHOR CONTRIBUTIONS

YM: methodology, investigation, data curation, software, and writing—original draft. YL: software and investigation. YZ: investigation. FL: data curation. BG: validation. QY: project administration, validation, and formal analysis. JX: resources and supervision. YC: conceptualization, writing—review and editing, visualization, project administration, and funding acquisition. All authors contributed to the article and approved the submitted version.

FUNDING

The financial supports from the National Key Research and Development Program of China (2019YFE0106000 and 2017YFC1600405), the Technology Innovation Leading Program of Jiangxi (20212BDH80001), and the Open Project Program of State Key Laboratory of Food Science and Technology, Nanchang University (No. SKLF-KF-202011) are gratefully acknowledged.

REFERENCES

1. Yaylayan VA, Huyghues-Despointes A. Chemistry of amadori rearrangement products - analysis, synthesis, kinetics, reactions, and spectroscopic properties. *Crit Rev Food Sci Nutr.* (1994) 34:321–69. doi: 10.1080/10408399409527667
2. Locas CP, Yaylayan VA. Isotope labeling studies on the formation of 5-(hydroxymethyl)-2-furaldehyde (HMF) from sucrose by pyrolysis-GC/MS. *J Agric Food Chem.* (2008) 56:6717–23. doi: 10.1021/jf8010245
3. Hollnagel A, Kroh LW. Formation of α -dicarbonyl fragments from mono- and disaccharides under caramelization and Maillard reaction conditions. *Zeitschrift Fur Lebensmittel-Untersuchung Und-Forschung a-Food Research and Technology.* (1998) 207:50–4. doi: 10.1007/s002170050294

4. Kroh LW, Fiedler T, Wagner J. α -dicarbonyl compounds - Key intermediates for the formation of carbohydrate-based melanoidins. *Maillard React.* (2008) 1126:210–5. doi: 10.1196/annals.1433.058
5. Jiang YP, Hengel M, Pan CP, Seiber JN, Shibamoto T. Determination of toxic α -dicarbonyl compounds, glyoxal, methylglyoxal, and diacetyl, released to the headspace of lipid commodities upon heat treatment. *J Agric Food Chem.* (2013) 61:1067–71. doi: 10.1021/jf3047303
6. Nguyen HT, Van Der Fels-Klerx H, Peters RJB, Van Boekel Ma JS. Acrylamide and 5-hydroxymethylfurfural formation during baking of biscuits: Part I: Effects of sugar type. *Food Chemistry.* (2016) 192:575–85. doi: 10.1016/j.foodchem.2015.07.016
7. Belitz HD, Grosch W, Schieberle P. *Food Chemistry.* Berlin: Springer Science and Business Media (2008).
8. Kroh LW. Caramelisation in food and beverages. *Food Chem.* (1994) 51:373–9. doi: 10.1016/0308-8146(94)90188-0
9. International Agency for Research on Cancer (IARC). *Acrylamide. IARC Monographs on the Evaluation of Carcinogenic Risks to Humans, Vol. 60.* Lyon, France: Some industrial chemicals. (1994) p. 389–433.
10. Svendsen C, Husoy T, Glatt H, Paulsen JE, Alexander J. 5-Hydroxymethylfurfural and 5-Sulfooxymethylfurfural Increase Adenoma and Flat ACF Number in the Intestine of Min/ plus Mice. *Anticancer Res.* (2009) 29:1921–6.
11. Morales FJ. Hydroxymethylfurfural (HMF) and related compounds. In: *Process-Induced Food Toxicants: Occurrence, Formation, Mitigation and Health Risks.* (2008) p. 135–174. doi: 10.1002/9780470430101.ch2e
12. De Vleeschouwer K, Van Der Plancken I, Van Loey A, Hendrickx ME. The kinetics of acrylamide formation/elimination in asparagine-glucose systems at different initial reactant concentrations and ratios. *Food Chem.* (2008) 111:719–29. doi: 10.1016/j.foodchem.2008.04.045
13. De Vleeschouwer K, Van Der Plancken I, Van Loey A, Hendrickx ME. Role of precursors on the kinetics of acrylamide formation and elimination under low moisture conditions using a multiresponse approach - Part I: Effect of the type of sugar. *Food Chem.* (2009) 114:116–26. doi: 10.1016/j.foodchem.2008.09.024
14. Kocadagli T, Gokmen V. Multiresponse kinetic modelling of Maillard reaction and caramelisation in a heated glucose/wheat flour system. *Food Chem.* (2016) 211:892–902. doi: 10.1016/j.foodchem.2016.05.150
15. Berk E, Hamzalioglu A, Gokmen V. Multiresponse kinetic modelling of 5-hydroxymethylfurfural and acrylamide formation in sesame (*Sesamum indicum*L) seeds during roasting. *Eur Food Res Technol.* (2020) 246:2399–410. doi: 10.1007/s00217-020-03583-z
16. Hamzalioglu A, Gokmen V. 5-Hydroxymethylfurfural accumulation plays a critical role on acrylamide formation in coffee during roasting as confirmed by multiresponse kinetic modelling. *Food Chem.* (2020) 318:126467. doi: 10.1016/j.foodchem.2020.126467
17. Martins SIF, Jongen WMF, Van Boekel Ma JS. A review of Maillard reaction in food and implications to kinetic modelling. *Trends Food Sci Technol.* (2000) 11:364–73. doi: 10.1016/S0924-2244(01)00022-X
18. Liu H, Chen X, Zhang D, Wang J, Wang S, Sun B. Effects of highland barley bran extract rich in phenolic acids on the formation of ϵ (ϵ -silo)-carboxymethyllysine in a biscuit model. *J Agric Food Chem.* (2018) 66:1916–22. doi: 10.1021/acs.jafc.7b04957
19. Tcherkas YV, Kartsova LA, Krasnova IN. Analysis of amino acids in human serum by isocratic reverse-phase high-performance liquid chromatography with electrochemical detection. *J Chromatography A.* (2001) 913:303–8. doi: 10.1016/S0021-9673(00)01206-1
20. Yuan Y, Zhao GH, Chen F, Liu J, Wu JH, Hu XS. Correlation of methylglyoxal with acrylamide formation in fructose/asparagine Maillard reaction model system. *Food Chem.* (2008) 108:885–90. doi: 10.1016/j.foodchem.2007.11.054
21. Wang Y T, Hu H Y, McClements D J, Nie S P, Shen M Y, Li C, et al. pH and lipid unsaturation impact the formation of acrylamide and 5-hydroxymethylfurfural in model system at frying temperature. *Food Res Int.* (2019) 123:403–13. doi: 10.1016/j.foodres.2019.05.001
22. Martins S, Van Boekel M, A. kinetic model for the glucose/glycine Maillard reaction pathways. *Food Chem.* (2005) 90:257–69. doi: 10.1016/j.foodchem.2004.04.006
23. Knol JJ, Van Loon WM, Linssen JH, Ruck AL, Van Boekel M, Voragen AGJ. Toward a kinetic model for acrylamide formation in a glucose-asparagine reaction system. *J Agric Food Chem.* (2005) 53:6133–9. doi: 10.1021/jf050504m
24. Van Boekel M. Kinetic aspects of the Maillard reaction: a critical review. *Nahrung-Food.* (2001) 45:150–9. doi: 10.1002/1521-3803(20010601)45:3<150::AID-FOOD150>3.0.CO;2-9
25. Thornalley PJ, Langborg A, Minhas HS. Formation of glyoxal, methylglyoxal and 3-deoxyglucosone in the glycation of proteins by glucose. *Biochemical J.* (1999) 344:109–16. doi: 10.1042/bj3440109
26. Hayashi T, Mase S, Namiki M. Formation of three-carbon sugar fragment at an early stage of the browning reaction of sugar with amines or amino acids. *Agric Biol Chem.* (1986) 50:1959–64. doi: 10.1080/00021369.1986.10867691
27. Weenen H. Reactive intermediates and carbohydrate fragmentation in Maillard chemistry. *Food Chem.* (1998) 62:393–401. doi: 10.1016/S0308-8146(98)00074-0
28. Parker JK, Balagiannis DP, Higley J, Smith G, Wedzicha BL, Mottram DS. Kinetic model for the formation of acrylamide during the finish-frying of commercial french fries. *J Agric Food Chem.* (2012) 60:9321–31. doi: 10.1021/jf302415n
29. Gokmen V, Kocadagli T, Goncuoglu N, Mogol B A. Model studies on the role of 5-hydroxymethyl-2-furfural in acrylamide formation from asparagine. *Food Chem.* (2012) 132:168–74. doi: 10.1016/j.foodchem.2011.10.048
30. De Vleeschouwer K, Van Der Plancken I, Van Loey A, Hendrickx M E. Modelling acrylamide changes in foods: from single-response empirical to multiresponse mechanistic approaches. *Trends Food Sci Technol.* (2009) 20:155–67. doi: 10.1016/j.tifs.2009.01.060
31. Zhu M T, Long Y, Ma Y J, Huang Y S, Wan Y, Yu Q, et al. Investigation of thermal contaminants in coffee beans induced by roasting: a kinetic modeling. *Food Chem.* (2022) 378:132063. doi: 10.1016/j.foodchem.2022.132063

Conflict of Interest: The authors declare that the research was conducted in the absence of any commercial or financial relationships that could be construed as a potential conflict of interest.

Publisher's Note: All claims expressed in this article are solely those of the authors and do not necessarily represent those of their affiliated organizations, or those of the publisher, the editors and the reviewers. Any product that may be evaluated in this article, or claim that may be made by its manufacturer, is not guaranteed or endorsed by the publisher.

Copyright © 2022 Ma, Long, Li, Zhang, Gan, Yu, Xie and Chen. This is an open-access article distributed under the terms of the Creative Commons Attribution License (CC BY). The use, distribution or reproduction in other forums is permitted, provided the original author(s) and the copyright owner(s) are credited and that the original publication in this journal is cited, in accordance with accepted academic practice. No use, distribution or reproduction is permitted which does not comply with these terms.



Rapid Screening of 22 Polycyclic Aromatic Hydrocarbons Residues in Vegetable Oils by Gas Chromatography-Electrostatic Field Orbitrap High Resolution Mass Spectrometry

OPEN ACCESS

Edited by:

Jie Zheng,
Jinan University, China

Reviewed by:

Feng Chen,
Clemson University, United States
Jin Cao,
National Institutes for Food and Drug
Control, China

*Correspondence:

Guohua Shi
shiguohua@nepp.com.cn
Yan Zhang
snowwinglv@126.com

[†]These authors have contributed
equally to this work and share first
authorship

Specialty section:

This article was submitted to
Food Chemistry,
a section of the journal
Frontiers in Nutrition

Received: 20 May 2022

Accepted: 10 June 2022

Published: 30 June 2022

Citation:

Meng Z, Fan S, Yuan X, Li Q, Huang Y,
Niu L, Shi G and Zhang Y (2022)
Rapid Screening of 22 Polycyclic
Aromatic Hydrocarbons Residues in
Vegetable Oils by Gas
Chromatography-Electrostatic Field
Orbitrap High Resolution Mass
Spectrometry. *Front. Nutr.* 9:949025.
doi: 10.3389/fnut.2022.949025

Zhijuan Meng^{1†}, Sufang Fan^{1†}, Xiaoxuan Yuan¹, Qiang Li¹, Yunxia Huang¹, Lisha Niu¹,
Guohua Shi^{1*} and Yan Zhang^{1,2*}

¹ Hebei Food Safety Key Laboratory, Key Laboratory of Special Food Supervision Technology for State Market Regulation, Hebei Engineering Research Center for Special Food Safety and Health, Hebei Food Inspection and Research Institute, Shijiazhuang, China, ² Hebei Key Laboratory of Forensic Medicine, College of Forensic Medicine, Hebei Medical University, Shijiazhuang, China

A method for simultaneous determination of 22 polycyclic aromatic hydrocarbons (PAHs) residues in vegetable oils by gas chromatography-electrostatic field orbitrap high resolution mass spectrometry (Orbitrap GC-MS) was established. The samples were vortexed with acetonitrile, centrifuged at 8,000 r/min for 5 min, and frozen at -70°C for 10 min. The extracts of upper layer were poured out, dried with nitrogen at 40°C , redissolved in dichloromethane, and measured by Orbitrap GC-MS. The matrix interference in vegetable oil could be effectively removed by determining the accurate mass number of target compounds under the full scan mode. Six typical vegetable oil samples (soybean oil, sesame oil, peanut oil, olive oil, rapeseed oil, sunflower oil) were used for method validation. The calibration curve displayed good linearity in the range of 1–100 ng/mL, with correlation coefficients > 0.9950 . The limits of detection (LODs) were in the range of 0.10–0.60 $\mu\text{g/kg}$, and the limits of quantification (LOQs) were in the range of 0.35–2.00 $\mu\text{g/kg}$. The average spiked recoveries of 22 PAHs in 6 matrices at 5, 50 and 100 $\mu\text{g/kg}$ levels were 76.4–115.4%, and the average relative standard deviations (RSDs) were 1.8–10.8%. The results showed that 22 PAHs were detected in 6 types of 90 edible vegetable oil samples in the Chinese market by this method. Meanwhile, the abundance of light PAHs (LPAHs) was higher than that of heavy PAHs (HPAHs), and its relative contribution of LPAHs to the total PAHs was higher. All levels of BaP conformed to the Chinese requirement of upper limit, 10 $\mu\text{g/kg}$. However, 13.3 and 11.1% of the samples exceeded the maximum limits of BaP and PAH4 set by EU, 2 and 10 $\mu\text{g/kg}$, respectively. The total concentrations of 22 PAHs (defined as PAH22) varies greatly among different oil species, and the average PAH22 contents were listed

in descending order as follows: peanut oil > sesame oil > olive oil > rapeseed oil > soybean oil > sunflower seed oil. The established method effectively avoided interference from large amounts of lipids and pigments. Therefore, the method is simple, sensitive and suitable for rapid screening and confirmation of PAHs in vegetable oil.

Keywords: gas chromatography-electrostatic field orbitrap high resolution mass spectrometry (Orbitrap GC-MS), polycyclic aromatic hydrocarbons, vegetable oils, frozen in addition to fat, real sample determination

INTRODUCTION

Polycyclic aromatic hydrocarbons (PAHs) are compounds containing more than two benzene rings in the molecule, which include more than 150 compounds such as naphthalene, anthracene, phenanthrene, and pyrene. Benzo[a]pyrene (BaP) was one of the earliest discovered environmental chemical carcinogen, which had strong carcinogenicity hence was often used as the representative of PAHs (1). Meanwhile, some of them were considered to be possible or probable human carcinogens (2–6). Edible oil, as an indispensable cooking material in people's daily life, played a pivotal role in life (7, 8). However, it has been reported that edible oils are more susceptible to PAHs contamination, and the absorption of PAHs contained in oils will increase in the intestinal tract, which can seriously harm human health. PAHs pollution in edible oil mainly came from the migration of pollutants in raw materials, processing and packaging materials (9–11). At present, the upper residue level for BaP was set at 10 mg/kg in edible oils according to the China national standard (12). Meanwhile, the European Food Safety Authority Panel on Contaminants in the Food Chain demonstrated that BaP was not a sufficient surrogate of PAHs existence in food and recommended the sum of four PAHs (PAH4) (BaP, benzo[a]anthracene, chrysene and benzo[b]fluoranthene) as evaluation indicators. Recently, Commission Regulation of European Union No 835/2011 established the maximum legislation levels of BaP and PAH4 for edible oils, which were 2 and 10 µg/kg, respectively (13). And the detection method of PAH in edible oil under China national standard only involved 16 species (14). PAHs can be divided into light polycyclic aromatic hydrocarbons (LPAHs) containing 2–4 aromatic rings, and heavy polycyclic aromatic hydrocarbons (HPAHs) containing five or more aromatic rings. The carcinogenicity of PAHs increased with the number of benzene rings (13–16). Therefore, it is of great significance to study a variety of efficient PAH detection methods to more comprehensively monitor and evaluate the PAHs pollution in edible oils, and ensure the quality and safety of edible oils.

Lipophilic compounds in vegetable oils are easily co-extracted with the target PAHs, which affects the accurate qualitative and quantitative analysis of PAHs. PAHs in vegetable oils usually needed to be extracted with solvent, and then purified by gel-permeation chromatography (17, 18), solid-phase extraction (SPE) (19–21), solid-phase microextraction (22). The methods are relatively cumbersome and expensive, and they are impossible to achieve efficient and rapid detection

of PAHs in vegetable oil. Freeze-defatting is a simple and low-cost method which can effectively remove fat and other macromolecular interfering substances in the sample. The detection of PAHs mainly included high performance liquid chromatography (HPLC) (23, 24), gas chromatography-mass spectrometry (GC-MS) (9, 25), liquid chromatography-tandem mass spectrometry (LC-MS/MS) (26) and gas chromatography-tandem mass spectrometry (GC-MS/MS) (27). HPLC and GC-MS are more commonly used, and they are also adopted in China national standard. The practical application of capillary electrophoresis is relatively rare. LC-MS/MS and GC-MS/MS provide new and effective methods for the detection of PAH due to their better selectivity and detection ability. The use of ordinary mass spectrometry has limitations on account of the complex matrix and high interference of vegetable oil. And it is prone to produce false positives and misjudgments. High resolution mass spectrometry, such as gas chromatography-electrostatic field orbitrap high resolution mass spectrometry (Orbitrap GC-MS) has the characteristics of high resolution and high sensitivity. Moreover, it is not limited by the number of compounds. It also could collect more comprehensive compound information, and could quickly and accurately screen and quantify target compounds at low levels in complex matrices (28). Its high resolution enables better separation of target compounds from interfering impurities. What is more, its high sensitivity ensures effective detection of low-concentration compounds. At present, Orbitrap GC-MS technology had been used in pharmaceutical research (29), environmental analysis (30) and pesticide residues in fruits and vegetables (31). However, the use of Orbitrap GC-MS to determine PAHs in vegetable oils is rarely reported.

In this study, a new method was developed for the determination of 22 PAHs in edible vegetable oils by Orbitrap GC-MS after removing major lipophilic interfering compounds through freezing at ultra-low temperature. It was proven that this method could be used as an accurate and quantitative technique for routine analysis. The collection mode allows non-target analysis using databases and/or libraries, as well as retrospective analysis. The data collection has no relationship with the number of compounds in the database so that the data can be reviewed and reanalyzed to expand the target range. At the same time, satisfactory results were also obtained in the verification of actual samples. The method has the characteristics of fast detection speed, high throughput, accurate and reliable detection results, and provides a scientific basis and a new method for national supervision.

MATERIALS AND METHODS

Materials and Reagents

Soybean oil, peanut oil, olive oil, rapeseed oil, sesame oil, sunflower seed oil and vegetable oil samples were purchased from China local supermarkets and sealed at room temperature for use later.

Acetonitrile and dichloromethane (both chromatographically pure) was purchased from Merck (Darmstadt, Germany). The standard substances of twenty-two PAEs (mixed standard solutions with mass concentration of 1,000 µg/mL, and dichloromethane as the solvent) were purchased from Alta Scientific Co., Ltd. Stock solutions (Tianjin, China): Naphthalene (Nap), Acenaphthylene (Acy), Acenaphthene (Ace), Fluorene (Fl), Phenanthrene (Phe), Anthracene (Ant), Fluoranthene (Flu), Pyrene (Pyr), Benz[a]anthracene (BaA), Chrysene (Chr), 5-Methylchrysene (5-Mchr), Benzo[b]fluoranthene (BbFlu), Benzo[k]fluoranthene (BkFlu), Benzo[e]pyrene (BeP), Benzo[a]pyrene (BaP), Benzo[g,h,i]perylene (BgHiP), Indeno[1,2,3-cd]pyrene (IP), Dibenz[a,h]anthracene (DBaH), Dibenz[a,l]pyrene (DBaL), Dibenz[a,e]pyrene (DBaE), Dibenz[a,i]pyrene (DBaI), Dibenz[a,h]pyrene (DBaH).

Instruments and Equipment

Orbitrap GC-MS (Thermo Fisher Scientific, USA), 3K15 high-speed refrigerated centrifuge (Sigma, Germany), Vortex mixer (IKA, Germany), Refrigerator (Qingdao Haier Co., Ltd., China) were used in our experiment.

Orbitrap GC-MS Analytical Conditions

A Orbitrap GC-MS consisting of an AI/AS 1310 autosampler, a TRACE 1300 Series GC with a hot split/splitless injector, an electron impact ion source (EI), and a hybrid quadrupole Orbitrap mass spectrometer with an HCD (higher energy collision-induced dissociation) cell, was used. The column was set at a constant flow rate of 1.0 mL/min using helium as carrier gas (purity $\geq 99.999\%$). GC separation was performed on a 30 m \times 0.25 mm ID, 0.25 µm HP-5MS column (5% phenyl-95% methylpolysiloxane, Agilent Scientific, USA). The column temperature program started from 80°C (hold 2 min), increased to 260°C at the rate of 8°C/min (hold 5 min), then increased to 310°C at the rate of 8°C/min, and held at this final temperature for 10 min. The temperature of the injector port was 280°C, and an aliquot of 1 µL of the sample was injected in the splitless mode. The flow rate of helium carrier gas was 1.0 mL/min. EI was performed at 70 eV, with the ion source and transfer line temperature at 280°C.

All data with m/z range of 50–500 were acquired in full scan mode. The nitrogen gas supply for the C-trap and HCD cell was 5.0 grade (99.999%, Linde gas). In the method, the Orbitrap resolving power was set at 60,000 FWHM (200 m/z) and the automatic gain control (AGC) target was set at $3e6$. The actual scan speed under these conditions was ~ 4 scans/s. External mass calibration was performed before each sequence using perfluorotributylamine (68.9945, 99.9928, 130.9911, 196.9827, 218.9846, 263.9860, 413.9760, and 501.9694) with a mass error tolerance of ± 1 ppm (± 0.2 mDa), and internal mass calibration

was carried out in the instrument using three background ions from the column bleed as lock mass ($C_5H_{15}O_3Si_3^+$, 207.03236; $C_7H_{21}O_4Si_4^+$, 281.05115; $C_9H_{27}O_5Si_5^+$, 355.06994) with a search window of ± 2 ppm (± 1 mDa) during the measurement. If none of the three specified background ions were found within their exact mass ± 2 ppm in a certain scan, no internal locking was applied for that scan. The instrument was controlled using Tune 2.8 and Trace Finder 4.1 (Thermo Scientific).

Preparation of Standard Solutions

One milliliter of the mixed standard solution was pipetted. Each mixed standard solution was placed into a 100-mL volumetric flask and diluted with dichloromethane, and then stored as a stock solution in a brown storage bottle at -20°C . It could be used after being placed at room temperature for 30 min. The stock solution was diluted with dichloromethane to prepare intermediate working solutions with mass concentrations of 1 and 0.1 µg/mL, respectively, which were used for addition and recovery experiments and preparation of standard working solutions. The mixed standard intermediate working solution was diluted with dichloromethane to obtain mass concentrations of 1, 5, 10, 20, 50, and 100 ng/mL, respectively. Then they were stored in the refrigerator at 4°C until use.

Sample Pretreatment

A total of 0.5 g of vegetable oil sample (± 0.001 g) were weighted accurately and placed into a 15 mL centrifuge tube, then 3 mL of acetonitrile were accurately added, vortex was carried out for 2 min, and then this solution centrifuge at 8,000 r/min for 3 min. The extraction processes were repeated twice, and the supernatants from the two extractions were combined and placed in a -70°C ultra-low temperature freezer for 10 min. The supernatant was purified under nitrogen blowing to nearly dry in a water bath at 40°C , and 1 mL of dichloromethane was added, vortexed for 5 s, transferred to a sample vial, and sent to Orbitrap GC-MS for analysis. For the reagent blank, the operations were the same except that no sample was added.

Database Creation

In this experiment, 22 PAHs compounds were selected and prepared into 1.0 µg/mL mixed standard solutions. The retention time of the corresponding compound, the accurate molecular weight, and the chemical formula of the fragment ions were obtained under the full scan mode. Three fragment ions of each compound were selected to obtain ion information (accurate mass and chemical formula). The data were inputted into Trace Finder (4.1) software to establish the relevant database. The Trace Finder software could not only realize the rapid batch and automatic processing of data, but also set the functions of qualitative, quantitative and method establishment. According to the established database, it could realize the rapid screening of target substances. The database mainly contains the compounds name, CAS registration number, fragment ion information, retention time, rings and other information (Table 1).

TABLE 1 | Formula, Retention time and Mass spectrometric of the 22 PAHs.

PAH	CAS number	Chemical formula	Molecular weigh	Rings	Retention time/min	Quantitative ion (m/z)	Qualitative ion (m/z)	Qualitative ion (m/z)
Nap	91-20-3	C10H8	128	2	7.46	128.06205	129.06541	102.04640
Acy	208-96-8	C12H8	152	3	11.93	152.06205	153.06541	126.04640
Ace	83-32-9	C12H10	154	3	12.48	154.07770	152.06205	153.06988
Fl	86-73-7	C13H10	166	3	13.97	166.07770	165.06988	139.05423
Phe	85-01-8	C14H10	178	3	16.75	178.07770	152.06205	179.08106
Ant	120-12-7	C14H10	178	3	16.89	178.07770	176.06205	152.06205
Flu	206-44-0	C16H10	202	4	20.28	202.07770	200.06205	101.03858
Pyr	129-00-0	C16H10	202	4	20.90	202.07770	200.06205	203.08106
BaA	56-55-3	C18H12	228	4	24.51	228.09325	226.07770	209.09669
Chr	218-01-9	C18H12	228	4	24.62	228.09335	226.07770	113.03858
5-Mchr	3697-24-3	C19H14	242	4	26.14	242.10900	241.10118	226.07770
BbFlu	205-99-2	C20H12	252	5	28.54	252.09335	250.07770	125.03858
BkFlu	207-08-9	C20H12	252	5	28.57	252.09335	250.07770	126.04640
BeP	192-97-2	C20H12	252	5	29.79	252.09335	250.07770	113.03858
BaP	50-32-8	C20H12	252	5	30.03	252.09335	250.07770	125.03864
BghiP	191-24-2	C22H12	276	6	34.34	276.09335	274.07770	138.04640
IP	193-39-5	C22H12	276	6	34.49	278.10895	276.09335	274.07770
DBahA	53-70-3	C22H14	278	5	35.05	276.09335	274.07770	138.04640
DBaIP	191-30-0	C24H14	302	6	38.57	302.10886	300.09332	150.04643
DBaeP	192-65-4	C24H14	302	6	39.82	302.10886	300.09332	225.04292
DBaIP	189-55-9	C24H14	302	6	40.35	302.10886	300.09332	281.05121
DBahP	189-64-0	C24H14	302	6	40.37	302.10886	300.09332	253.01678

Validation of the Analytical Procedure

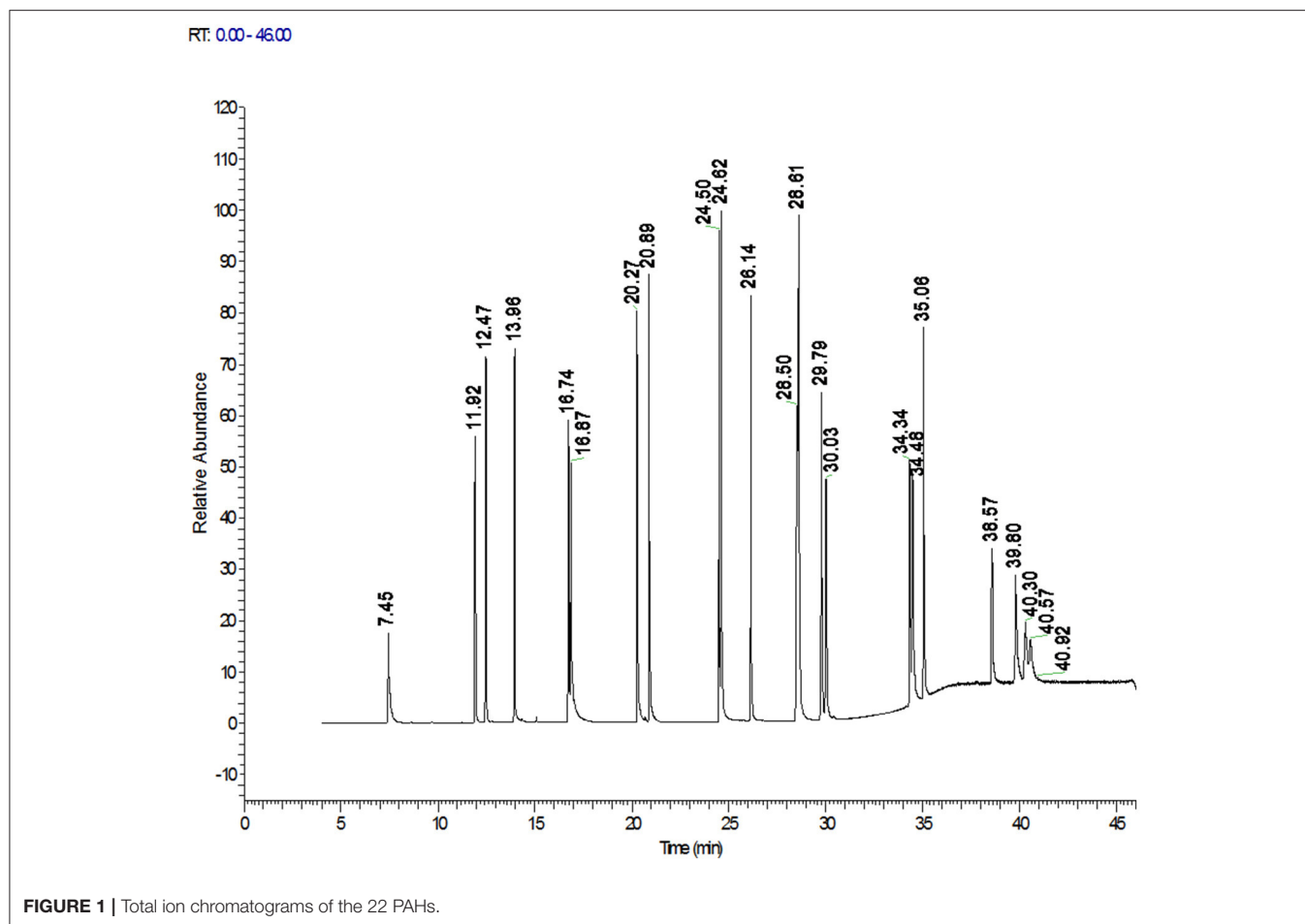
A validation study was performed in terms of matrix effects, linearity, LODs, LODs, recovery, as well as intra-day and inter-day precision. The recoveries and precision of the method were determined by analyzing the average of six replicates of spiked blank matrix at concentration levels of 5, 50, and 100 µg/kg. The multi-standard working solution with concentration of 0.18–100 ng/mL were used to evaluate the linearity of the method. Spiked samples were used to test the LODs and LOQs, the levels of spiked analytes with signal-to-noise ratio of 3 and 10 were defined as the LOD and LOQ of the method. To determine the matrix effects, the slopes of the calibration curves obtained in matrix matched standards were compared with those acquired from the solvent-based standards. The intra-day and inter-day precision of the method were tested using the soybean oil and sesame oil samples at vial concentrations of 5 and 50 µg/kg, which were used as the repeatability and reproducibility of the method, respectively. More specifically, the repeatability analysis was performed by preparing and analyzing six identical samples in 1 day, and the reproducibility analysis was performed by preparing and analyzing one sample on six different days.

RESULTS AND DISCUSSION

Selection of Extraction Conditions

PAHs are insoluble in water, but soluble in most organic solvents. According to the method in Section Sample Pretreatment. Dichloromethane, n-hexane, acetonitrile and n-hexane +

acetonitrile were used for extraction, and the effects of different extraction solvents on the recovery rate of 22 PAHs (addition amount of 10 µg/kg) were compared. The results showed that there were many co-extraction substances in dichloromethane, which had an impact on the result. The matrix effect was serious, and the recovery rate was low. Meanwhile, fat has high solubility in n-hexane, and its interference effect is serious. Acetonitrile could precipitate proteins and has a good degreasing effect. Moreover, some lipophilic compounds, such as triglycerides, diglycerides, fatty acids and other substances could still be extracted by acetonitrile from the vegetable oil although the solubility of fat in acetonitrile is low, which might bring trouble to the subsequent purification. In this study, an ultra-low temperature freezer at –70°C was used for freezing. It was found that organic extraction solvent and oil were both liquid when the freezing time was <5 min and the organic extraction solvent and oil were solid when the freezing time was longer than 15 min. The oil of lower layer remained solid and the extract of upper layer was still liquid when the freezing time was about 10 min. Therefore, the freezing time was determined to be 10 min. After freezing, the extract of upper layer can be easily separated and poured into a centrifuge tube to achieve full separation from oil. The remaining part after the nitrogen blowing is also an important factor affecting the detection of PAH. The losses of Nap and BaA are more serious, while the Acy, Ace and Flu also have certain losses when the temperature is too high. The above losses can be effectively avoided at temperature of 40°C. Therefore, the oil samples were extract by acetonitrile, then the



supernatant was frozen at -70°C for 10 min. After the solidified oil of lower layer was removed, the supernatant was taken to be purified, which could effectively avoid the interference of oil on the sample. In this way, the spiked recoveries of the 22 PAHs in the samples were all higher than 75%.

Comparison of Sample Pretreatment Between This Method and the China National Standard Method

At present, the detection of polycyclic aromatic hydrocarbons in food is mainly based on the China national standard GB 5009.265-2021 (14), which includes two types, HPLC fluorescence and GC-MS method. The former one has high sensitivity but not suitable for the detection of acenaphthene because of its weak fluorescence absorption. Moreover, the target peak is easily interfered by impurity peaks, and the vegetable oil sample matrix is more complex, making it difficult to guarantee the accuracy of qualitative and quantitative analysis. In contrast, the latter one is generally more complicated and has lower recovery rate. The procedure of GC-MS method includes saponification with potassium hydroxide ethanol solution, purified by SPE column, diluting to volume with acetone-iso-octane after nitrogen blowing, and sample injection

on the machine. During the experimental process, there is need to activate the SPE purification column with a lot of reagents, and this operation is complicated and time-consuming. The determination method in this experiment combined freeze-defatting purification and Orbitrap GC-MS, specifically using acetonitrile vortex extraction, freeze defatting purification, nitrogen blowing for concentration, and on-machine measurement. This method shortens the time of pretreatment, and utilizes the qualitative and quantitative accuracy of Orbitrap GC-MS to achieve the purpose of high-throughput detection. Its ability to resist matrix interference is higher than that of single quadrupole, and it can accurately qualitatively and quantitatively analyze PAHs, which is suitable for rapid screening and analysis of PAHs in vegetable oil.

Optimization of Mass Spectrometry Conditions

The high-resolution mass spectrometer is different from the triple quadrupole quantification method. The Orbitrap GC-MS used in this study adopts the full scan mode, which simplifies the optimization of gas chromatography-mass spectrometry parameters, saves the sample preparation time of the pretreatment, makes the screening and accurate quantitative

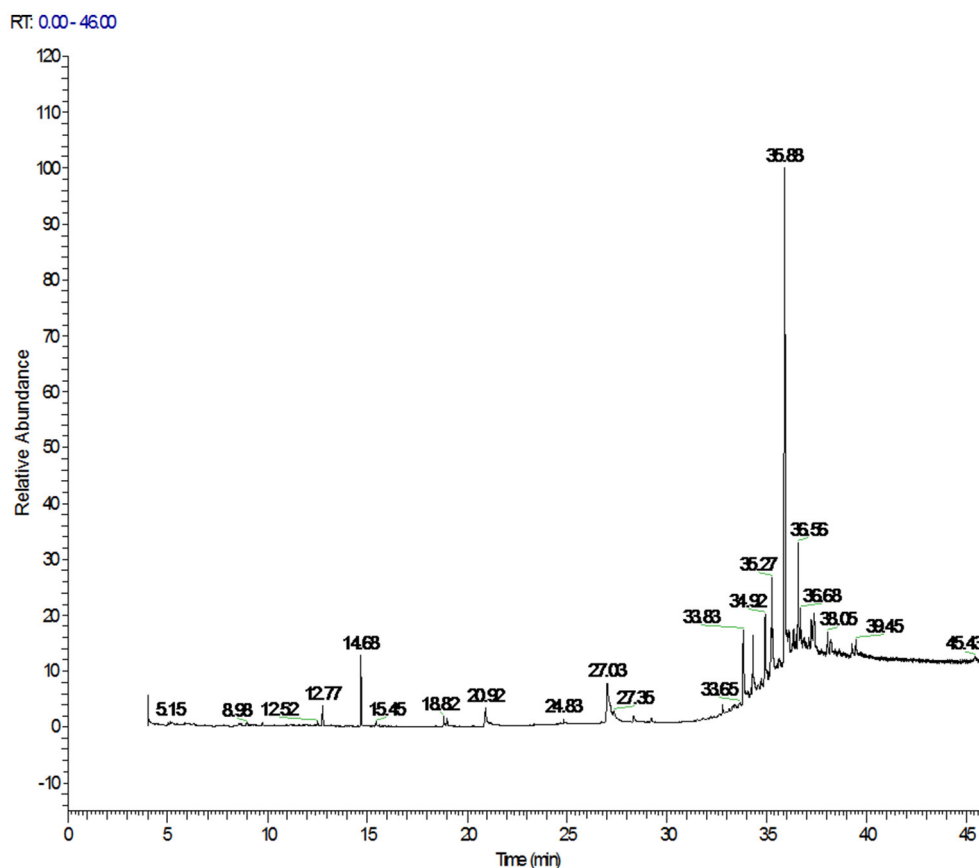


FIGURE 2 | Total ion chromatograms of PAHs in positive soybean oil sample.

analysis more convenient, and improves the work efficiency and accuracy. Accurate mass of the target compound was obtained by full scan. The exact mass of 3 fragment ions of 22 PAHs are listed in **Table 1**, which can be kept to 5 decimal places and can be effectively and accurately distinguished from interfering substances. One was used as the quantification ion, and the other two were used as the qualitative ions. This study found that matrix interference was significantly reduced and the screening accuracy was also improved when the resolution of $R \geq 60,000$ was used in sample detection. All the analyte targets could be clearly distinguished from the interferences in the matrix, and PAHs could be quickly determined and accurately quantified to improve the reliability of test results. The total ion chromatograms of 22 PAHs were shown in **Figure 1**.

Qualitative Screening Confirmation and Retrospective Analysis

The main factors affecting the qualitative determination included the exact mass deviation, retention time deviation, isotope distribution and isotope abundance ratio of the compounds when searching with the spectral library established in **Table 1**. According to EU SANTE/11945/2015 (32), at least 1 accurate

mass ion and 1 fragment ion were required for confirmation using high-resolution mass spectrometry.

The PAHs target compounds could be accurately identified using the spectral library established in this paper. The total ion chromatograms of PAHs in positive soybean oil sample were shown in **Figure 2** which contained rich chemical information. However, the chromatographic peak of the target could not be seen. This information was inputted into the qualitative and quantitative analysis software for analysis so as to achieve the purpose of confirming the target and accurate quantification. **Figure 3** showed the mass spectrogram of reference materials and positive soybean oil sample. The qualitative and quantitative ions in the positive sample were consistent with those in the standard, and the presence of the compound could be determined. This demonstrates that Orbitrap GC-MS can extract useful information from the experiment of complex matrices, highlighting its advantages in high-throughput screening.

Orbitrap GC-MS often collects the full spectrum and can collect data more comprehensively. The data collection is independent of the number of compounds in the database so that the data can be reviewed and re-analyzed after collection to expand the target range. For the analysis of samples of new compounds, such as Cyclopenta[cd]pyrene (CPcdP), the

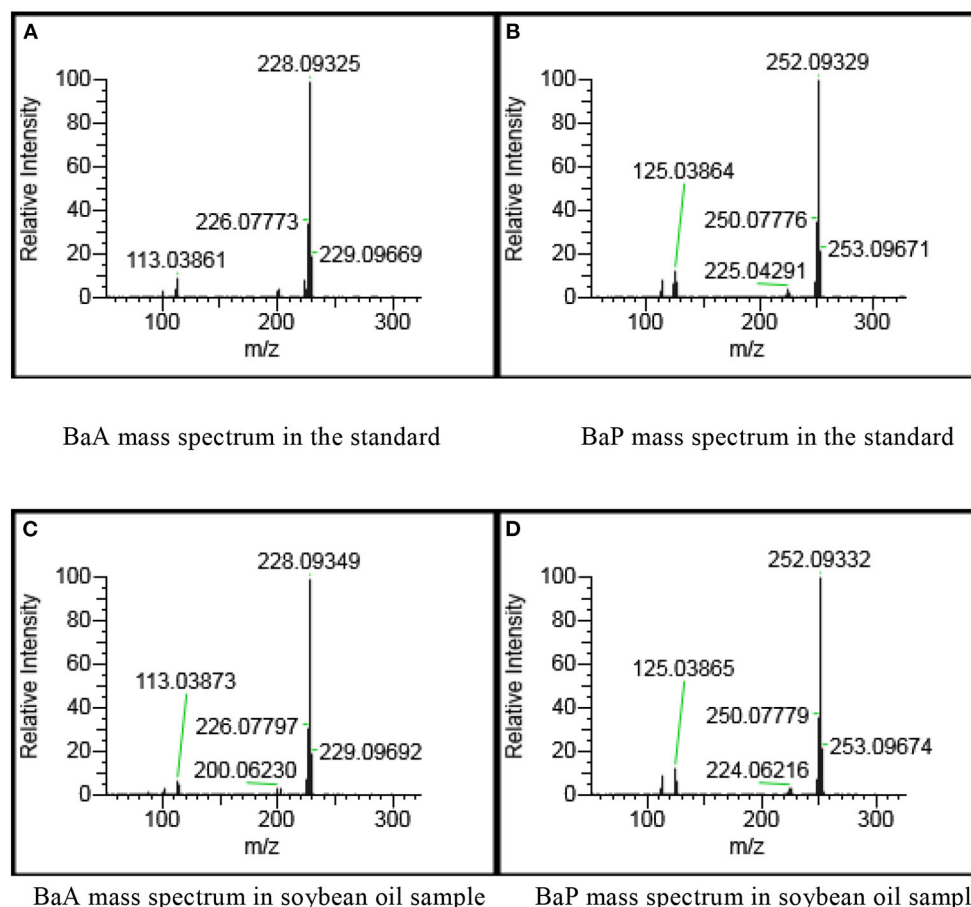


FIGURE 3 | Mass spectrogram of reference materials and positive soybean oil sample at 50 $\mu\text{g/kg}$. **(A)** BaA mass spectrum in the standard. **(B)** BaP mass spectrum in the standard. **(C)** BaA mass spectrum in soybean oil sample. **(D)** BaP mass spectrum in soybean oil sample.

retention time, molecular formula, exact molecular mass and CAS number of CPCdP were added to the 22 PAHs database. This method can expand and analyze target compounds without re-collecting real-time data. It has flexibility, which is convenient for high-throughput screening and quantitative analysis of PAHs. This method could be adopted in vegetable oil risk monitoring technology.

Methodological Validation

Matrix Effect

As we all know, the co-elution of matrix constituents can interfere with the ionization of the target compounds, causing ion enhancement or suppression. The presence of matrix effects was perceived as a signal enhancement or suppression of the analytes, which plays an important role in the quality of the quantitative data obtained from the method. In the present study, the matrix effect was considered to be ignored if the slope ratios of matrix/solvent were in the range of 0.9–1.1, while it would be regarded as matrix suppression effect if the value was lower than 0.9, and it would be regarded as a matrix enhancement effect when the value was larger than 1.1. The experimental results showed that the effects of 22 PAHs in 6 kinds of vegetable oil

samples were different, and the range of variation was 0.91–1.08. The target to be tested has a certain matrix effect in six kinds of matrix, however the effect is not obvious. Therefore, in this method dichloromethane is used to prepare a series of standard working solutions for quantitative analysis.

Linear Range, LODs, LOQs, and Intra-Day and Inter-day Precision for the Method

Orbitrap GC-MS was used for qualitative and quantitative analysis of 22 kinds of PAHs. The curve was plotted with peak area (y-axis) against the concentration (x-axis). The results of mass spectrometry demonstrated that the R-squared of 22 PAHs were no < 0.9950 . The LODs and LOQs of the method were determined by the addition of blank samples. The LODs and LOQs for the 22 PAHs were found to be 0.10–0.60 $\mu\text{g/kg}$ and 0.35–2.0 $\mu\text{g/kg}$. It is superior to the national standard method (22) and can meet the testing requirements. The related parameters are listed in **Table 2**. Information of **Table 3** in which precision values were expressed as intra-day ($n = 6$) and inter-day (6 days) precision for the chromatographic method was included in the data. The RSDs of repeatability and reproducibility were

TABLE 2 | Linear equations, correlation coefficients, linear ranges, LODs and LOQs of the 22 PAHs.

PAH	Linear equation	R ²	Linear range/ (ng/mL)	LOD/(μg/kg)	LOQ/(μg/kg)
Nap	$Y = 3.482 \times 10^3 X - 4.320 \times 10^6$	0.9998	1.40–100	0.40	1.40
Acy	$Y = 4.037 \times 10^3 X - 5.528 \times 10^6$	0.9993	0.35–100	0.10	0.35
Ace	$Y = 3.259 \times 10^3 X - 2.456 \times 10^6$	0.9996	0.35–100	0.10	0.35
Fl	$Y = 4.612 \times 10^3 X - 2.094 \times 10^7$	0.9991	0.35–100	0.10	0.35
Phe	$Y = 6.313 \times 10^3 X - 6.452 \times 10^6$	0.9995	0.70–100	0.20	0.70
Ant	$Y = 3.953 \times 10^3 X - 8.159 \times 10^5$	0.9977	0.70–100	0.20	0.70
Flu	$Y = 4.538 \times 10^3 X - 1.437 \times 10^7$	0.9995	0.35–100	0.10	0.35
Pyr	$Y = 7.560 \times 10^7 X - 1.651 \times 10^6$	0.9980	0.35–100	0.10	0.35
BaA	$Y = 5.501 \times 10^3 X - 1.299 \times 10^7$	0.9995	0.35–100	0.10	0.35
Chr	$Y = 5.360 \times 10^3 X - 3.304 \times 10^7$	0.9993	0.35–100	0.10	0.35
5-Mer	$Y = 6.422 \times 10^3 X - 1.383 \times 10^7$	0.9973	0.35–100	0.10	0.35
BbFlu	$Y = 3.057 \times 10^3 X - 2.642 \times 10^6$	0.9982	0.35–100	0.10	0.35
BkFlu	$Y = 5.564 \times 10^3 X - 1.284 \times 10^7$	0.9983	0.35–100	0.10	0.35
BeP	$Y = 4.652 \times 10^3 X - 5.661 \times 10^6$	0.9991	0.70–100	0.20	0.70
BaP	$Y = 3.472 \times 10^3 X - 1.561 \times 10^7$	0.9961	0.70–100	0.20	0.70
BghiP	$Y = 3.064 \times 10^3 X - 2.157 \times 10^5$	0.9992	1.00–100	0.30	1.00
IP	$Y = 6.064 \times 10^3 X - 1.553 \times 10^7$	0.9984	1.00–100	0.30	1.00
DBahA	$Y = 5.064 \times 10^3 X - 1.258 \times 10^7$	0.9991	1.00–100	0.30	1.00
DBaiP	$Y = 4.064 \times 10^3 X - 6.069 \times 10^6$	0.9990	1.60–100	0.50	1.60
DBaeP	$Y = 3.074 \times 10^3 X - 5.235 \times 10^7$	0.9951	1.60–100	0.50	1.60
DBaiP	$Y = 5.054 \times 10^3 X - 3.456 \times 10^7$	0.9952	2.00–100	0.60	2.00
DBahP	$Y = 3.729 \times 10^3 X - 4.176 \times 10^7$	0.9961	2.00–100	0.60	2.00

found to be within in the ranges 1.7–6.4% and 2.3–9.2% in both matrices, respectively.

Recovery and Precision

In this experiment, soybean oil, sesame oil, sunflower seed oil, peanut oil, olive oil, and rapeseed oil were selected for standard addition and determination so as to investigate the precision and recovery rate of the method. The sensitivity of the proposed method was significantly improved because the matrix interference was reduced. Recovery and repeatability experiments were performed at three levels (5, 50, and 100 μg/kg) with six replicates at each level to evaluate the accuracy and precision of the methods. The accuracy was estimated by recoveries (%) and the precision was evaluated by RSDs (%) of the spiked samples. The results were shown in **Table 4**, which showed that the mean recoveries of 22 PAHs were 85.1–115.4% except that the recoveries of DBaiP and DBahP ranged from 79.2 to 82.2% and 76.4 to 80.4% respectively at three levels. Additionally, the average RSDs were 1.8–10.8%. It shows that the method has good recovery and repeatability, and can meet the requirements of daily monitoring of 22 PAHs in vegetable oil samples, and the data are accurate and reliable.

Determination of Actual Samples

A total of 90 samples of 6 edible vegetable oils collected from the Chinese market were analyzed in this study, including rapeseed oil (*n* = 10), soybean oil (*n* = 12), olive oil (*n* = 12), peanut oil

(*n* = 20), sunflower seed oil (*n* = 18) and sesame oil (*n* = 18). The method established in this experiment can determine low levels of PAHs, and has the advantages of accurate qualitative and quantitative characteristics. It can fully meets the needs of actual sample screening.

The detection range of individual PAHs and the concentration range of LPAHs, HPAHs, PAH4, and PAH22 were determined by the type of edible oil studied. Twenty-two analytes were detected in all oil samples. The content of PAH22 in 90 oil samples ranged from 7.38 to 143.25 μg/kg, with an average concentration of 42.03 μg/kg. The BaP concentration ranged from 0.15 to 8.43 μg/kg, with an average concentration of 1.52 μg/kg. The variation range of PAH4 content was 1.24–25.34 μg/kg, and the average concentration was 2.03 μg/kg. The results showed that Phe, Fluo, and Pyr were the three compounds that has the highest concentrations. DbA had the relatively lowest concentrations, with an average concentration of 0.35 μg/kg. The concentrations of BaP of tested oils (0.15–8.43 μg/kg) were all conformed to the upper limit, 10 mg/kg, set by China. However, in the 90 edible oils tested, a total of 12 oil samples (2 canola oil, 4 peanut oil and 6 sesame oil) exceeded the EU Commission’s maximum limit of Bap, 2 μg/kg, and 10 samples (7 peanut oil and 2 sesame oil) exceeded the EU Commission’s limit of PAH4, 10 μg/kg.

In order to assess the individual contributions of the 22 PAHs more reasonably, the entire PAHs group was divided into two parts, LPAHs and HPAHs. The total concentration of LPAHs and HPAHs were calculated. LPAHs were the major contaminants in

TABLE 3 | Precision of the method in soybean oil and sesame oil at levels of 5 and 50 $\mu\text{g/kg}$.

PAE	Intra-day variability (RSDs/%)				Inter-day variability (RSDs/%)			
	5 $\mu\text{g/kg}$		50 $\mu\text{g/kg}$		5 $\mu\text{g/kg}$		50 $\mu\text{g/kg}$	
	Soybean oil	Sesame oil	Soybean oil	Sesame oil	Soybean oil	Sesame oil	Soybean oil	Sesame oil
Nap	3.2	3.6	1.7	5.8	8.2	5.6	7.6	6.5
Acy	1.7	1.9	1.9	1.9	6.4	8.7	4.6	9.1
Ace	5.5	6.4	2.7	3.7	7.6	6.5	9.0	4.5
Fl	2.6	2.9	2.5	2.9	5.2	6.4	4.5	8.3
Phe	1.9	3.5	2.8	2.6	5.5	8.1	6.6	4.5
Ant	3.5	1.8	2.6	1.8	4.9	8.4	7.4	4.6
Flu	1.8	1.7	1.9	2.6	3.7	5.4	9.6	5.3
Pyr	1.9	2.8	3.7	2.8	9.2	6.7	6.6	2.8
BaA	3.5	2.9	2.8	2.5	6.5	6.4	8.5	6.5
Chr	2.8	2.4	2.5	2.8	7.5	3.5	5.4	4.6
5-Mer	4.4	4.7	1.8	1.9	6.4	7.5	6.5	7.6
BbFlu	1.8	1.8	1.9	1.8	9.0	6.4	5.6	6.4
BkFlu	1.9	2.4	1.7	3.8	6.4	6.6	8.4	8.1
BeP	1.7	1.8	4.8	3.5	5.3	5.8	7.5	4.8
BaP	6.7	5.6	3.9	6.3	8.3	5.5	3.3	5.7
BghiP	4.5	1.9	2.7	6.0	2.3	9.1	8.2	6.4
IP	2.7	2.7	2.5	3.5	10	3.4	7.3	5.5
DBahA	1.8	3.9	2.8	1.9	4.4	7.4	6.4	4.5
DBaIP	3.4	1.8	3.4	4.4	7.5	8.5	7.5	5.7
DBaEP	2.6	5.6	2.9	5.7	8.3	4.5	4.6	6.7
DBaIP	3.7	3.7	1.8	4.8	5.4	3.5	3.4	3.4
DBaHP	4.8	3.5	3.6	1.8	6.8	3.5	4.3	5.4

all tested oil samples, and as mentioned above, Phe, Flu, and Pyr were the major contaminants in edible oils. Since the abundance of LPAHs in vegetable oil samples was higher than that of HPAHs, the relative contribution of LPAHs to total PAHs was higher. The concentration of LPAHs in the 90 oil samples ranged from 5.42 to 132.34 $\mu\text{g/kg}$, with an average concentration of 38.78 $\mu\text{g/kg}$. The concentration of HPAHs ranged from 0.85 to 27.03 $\mu\text{g/kg}$, with an average concentration of 6.58 $\mu\text{g/kg}$. Since ~90% of the PAH content comes from the contribution of LPAHs, the distribution of total PAHs observed in our study is similar to that of LPAHs, while the contribution of HPAHs is much smaller (about 10%). However, most carcinogens (BaP and DBaH) were included in HPAHs and their relative carcinogenicity is extremely high. In consequence, the presence of HPAHs in edible oil still needs special attention. Therefore, measuring LPAHs or HPAHs alone cannot fully evaluate the characteristics of PAHs content in edible vegetable oils, and an overall evaluation of both is required.

In this study, PAHs in the 90 vegetable oils tested of different types were different. Peanut oil and sesame oil were the two most polluted oils, and soybean oil and sunflower seed oil were the two least polluted species. The average concentration of PAH22 in the tested oil samples was as follows: peanut oil > sesame oil > olive oil > rapeseed oil > soybean oil > sunflower seed oil. The contents of BaP, PAH4, and PAH22 in peanut oil were 0.34–6.21, 2.45–30.25, and 39.42–162.43 $\mu\text{g/kg}$, respectively. The contents

of BaP, PAH4, and PAH22 in sesame oil were 0.21–2.31, 2.08–8.56, and 11.32–38.08 $\mu\text{g/kg}$, respectively. Peanut oil and sesame oil showed higher levels of PAHs than other edible vegetable oils. It can be seen that there is great variability in the levels of PAHs among different kinds of vegetable oils. Reasonable explanations for the higher PAHs contamination levels in peanut oil and sesame oil are as follows: in order to maintain the flavor of peanut oil and sesame oil, only a cold filtration process was used in the refining process to remove colloidal impurities such as phospholipids, therefore, the PAHs contamination in peanut oil and sesame was not eliminated during roasting, and these compounds would still remain in the final oil.

CONCLUSION

In this experiment, a method for the analysis of 22 kinds of PAHs in vegetable oils was established by the combination of defatting purification with Orbitrap GC-MS. Retrospective analyses (post-target and non-target screenings) was performed by taking advantage of the high sensitivity of the Orbitrap analyzer when operating in full scan mode, and the valuable accurate mass information provided. This method has the advantages of simple pretreatment, high purification efficiency, high throughput, and accurate analysis. The validated data showed the suitability of the

TABLE 4 | Recoveries and RSDs of soybean oil, sesame oil, sunflower seed oil, peanut oil, olive oil, and rapeseed oil samples at three spiked levels of the 22 PAHs.

PAH	Spiked/ ($\mu\text{g/kg}$)	Soybean oil Recoveries/ % (RSDs/%)	Sesame oil Recoveries/ % (RSDs/%)	Sunflower seed oil Recoveries/ % (RSDs/%)	Peanut oil Recoveries/ % (RSDs/%)	Olive oil Recoveries/ % (RSDs/%)	Rapeseed oil Recoveries/ % (RSDs/%)
Nap	5	88.5 (9.8)	88.5 (10.8)	102.4 (9.6)	87.5 (7.2)	86.5 (6.8)	108.5 (5.6)
	50	85.3 (9.1)	94.2 (4.5)	96.5 (7.4)	85.3 (8.2)	85.9 (5.1)	86.3 (7.2)
	100	86.6 (7.1)	95.6 (9.7)	98.4 (7.2)	85.6 (5.5)	86.4 (5.6)	98.6 (3.4)
Acy	5	90.2 (8.2)	87.4 (8.2)	88.4 (9.1)	89.2 (8.6)	88.2 (7.4)	85.2 (5.7)
	50	89.4 (6.1)	92.7 (4.8)	94.2 (9.5)	85.4 (5.9)	86.4 (3.8)	86.4 (8.2)
	100	91.8 (7.2)	85.1 (9.7)	92.8 (9.2)	85.1 (6.5)	88.8 (2.8)	97.8 (6.6)
Ace	5	95.2 (6.1)	94.4 (6.3)	90.4 (9.5)	91.2 (2.3)	92.2 (6.4)	85.2 (4.3)
	50	92.2 (7.2)	88.5 (8.1)	101.3 (4.2)	93.2 (3.4)	91.2 (5.2)	89.2 (2.8)
	100	93.3 (9.2)	97.1 (4.4)	92.3 (8.7)	88.3 (4.4)	90.3 (6.2)	91.3 (4.3)
Fl	5	97.1 (8.2)	93.5 (5.3)	93.5 (8.9)	92.1 (2.9)	97.1 (8.7)	87.1 (2.2)
	50	94.2 (7.1)	102.4 (9.4)	97.2 (7.7)	93.2 (3.6)	95.2 (7.6)	90.2 (6.5)
	100	91.2 (6.2)	96.5 (7.1)	108.4 (6.5)	89.2 (5.4)	93.2 (6.2)	91.2 (4.9)
Phe	5	101.1 (7.1)	98.4 (7.2)	103.4 (8.2)	102.1 (6.1)	99.1 (8.1)	108.1 (8.5)
	50	107.3 (1.2)	103.4 (9.1)	89.3 (2.4)	104.3 (7.4)	97.3 (4.2)	105.3 (7.6)
	100	103.1 (7.1)	97.2 (9.4)	88.3 (9.5)	102.1 (5.2)	102.1 (5.1)	104.1 (5.9)
Ant	5	86.1 (7.1)	102.8 (9.2)	93.5 (5.2)	87.1 (5.9)	85.1 (6.1)	87.1 (4.6)
	50	86.2 (5.2)	90.4 (9.5)	105.2 (4.4)	85.2 (4.7)	89.2 (4.2)	85.2 (5.6)
	100	85.9 (5.1)	80.3 (4.3)	95.6 (4.5)	88.5 (1.9)	88.9 (5.8)	86.9 (7.7)
Flu	5	89 (9.1)	92.3 (8.5)	91.2 (9.5)	91.2 (7.7)	91.2 (5.1)	91.2 (4.3)
	50	93.2 (8.1)	93.5 (8.6)	90.4 (4.2)	88.2 (5.9)	93.2 (6.1)	96.2 (5.2)
	100	89.3 (8.2)	97.2 (7.4)	94.2 (4.5)	88.9 (4.5)	89.3 (8.9)	88.3 (6.6)
Pyr	5	92.2 (6.1)	108.4 (6.3)	105.6 (9.7)	92.2 (6.3)	93.2 (4.1)	90.2 (7.2)
	50	92.8 (7.2)	93.4 (8.9)	92.1 (4.2)	94.8 (2.9)	94.8 (7.9)	91.8 (4.5)
	100	95.2 (6.1)	89.3 (2.2)	104.1 (4.0)	93.2 (7.2)	96.2 (6.5)	93.2 (3.8)
BaA	5	102.2 (7.2)	89.3 (9.3)	95.3 (6.5)	104.2 (4.3)	99.2 (7.4)	104.2 (4.9)
	50	103.3 (7.2)	93.5 (5.4)	88.3 (4.4)	102.3 (6.6)	100.3 (5.2)	115.4 (6.7)
	100	104.1 (8.2)	105.2 (4.4)	95.4 (6.2)	103.1 (7.8)	102.1 (6.8)	102.1 (5.6)
Chr	5	85.9 (7.1)	95.6 (4.4)	92.2 (7.1)	87.4 (5.9)	94.9 (5.9)	86.9 (4.4)
	50	86.2 (6.2)	87.5 (7.4)	92.3 (7.3)	86.5 (6.9)	89.2 (6.4)	88.2 (5.9)
	100	89.1 (7.1)	87.1 (6.2)	99.3 (8.3)	90.1 (5.9)	87.1 (7.5)	89.1 (5.6)
5-Mer	5	107.3 (8.2)	106.1 (6.4)	107.6 (11.2)	104.3 (4.6)	105.3 (5.2)	97.3 (4.8)
	50	104.1 (7.1)	89.4 (5.2)	109.5 (9.8)	102.5 (3.6)	102.4 (4.1)	104.1 (8.1)
	100	108.1 (7.1)	87.5 (7.2)	95.5 (9.0)	105.1 (5.4)	103.1 (6.1)	98.1 (4.8)
BbFlu	5	86.2 (5.2)	108.3 (9.2)	86.7 (6.8)	86.2 (2.9)	86.2 (3.2)	86.2 (5.6)
	50	85.2 (7.1)	86.8 (9.1)	96.5 (8.3)	97.2 (4.3)	85.2 (7.8)	89.2 (7.2)
	100	88.1 (9.8)	112.6 (8.2)	82.8 (7.4)	86.1 (3.8)	87.1 (5.5)	85.1 (5.6)
BkFlu	5	89.2 (5.3)	87.4 (7.3)	98.1 (8.2)	88.2 (4.3)	86.2 (6.1)	89.5 (7.2)
	50	93.2 (5.1)	109.1 (9.1)	89.2 (5.5)	93.2 (6.1)	98.2 (5.2)	96.2 (5.9)
	100	95.1 (4.0)	93.3 (9.1)	93.2 (6.6)	94.1 (5.3)	94.1 (4.5)	92.1 (4.3)
BeP	5	99.2 (7.3)	98.0 (6.2)	95.3 (4.2)	97.2 (2.3)	94.2 (3.3)	99.1 (5.6)
	50	105.2 (7.3)	104.2 (9.3)	98.5 (7.7)	104.2 (6.3)	98.2 (9.8)	104.2 (4.8)
	100	103.2 (8.2)	98.3 (8.2)	88.5 (7.5)	107.2 (6.2)	103.2 (6.2)	102.2 (5.5)
BaP	5	90.3 (7.2)	89.1 (9.3)	106.5 (7.4)	106.3 (7.8)	91.5 (8.2)	100.6 (4.8)
	50	101.2 (9.3)	102.4 (9.4)	94.5 (5.3)	92.2 (9.4)	102.2 (6.3)	92.2 (7.4)
	100	100.2 (8.3)	96.5 (7.1)	96.9 (1.8)	101.2 (8.2)	93.4 (4.3)	103.1 (5.9)
BghiP	5	91.2 (8.3)	98.4 (7.2)	104.2 (8.3)	101.2 (5.3)	94.2 (7.3)	103.2 (6.8)
	50	86.2 (5.3)	88.4 (9.1)	95.5 (4.0)	86.5 (4.3)	87.2 (6.3)	86.2 (5.8)
	100	88.1 (2.2)	97.2 (9.4)	97.2 (6.3)	89.1 (6.2)	91.1 (4.1)	89.1 (4.6)

(Continued)

TABLE 4 | Continued

PAH	Spiked/ ($\mu\text{g/kg}$)	Soybean oil Recoveries/ % (RSDs/%)	Sesame oil Recoveries/ % (RSDs/%)	Sunflower seed oil Recoveries/ % (RSDs/%)	Peanut oil Recoveries/ % (RSDs/%)	Olive oil Recoveries/ % (RSDs/%)	Rapeseed oil Recoveries/ % (RSDs/%)
IP	5	91.3 (5.3)	92.8 (9.2)	90.3 (8.1)	90.3 (4.3)	92.3 (5.8)	91.5 (5.7)
	50	89.4 (8.1)	90.4 (9.5)	107.5 (9.2)	89.4 (5.1)	89.4 (6.4)	92.4 (5.9)
	100	92.1 (8.2)	100.3 (4.3)	92.3 (7.5)	90.1 (3.2)	93.1 (7.2)	97.1 (4.9)
DBahA	5	87.3 (7.4)	102.3 (8.5)	103.5 (9.3)	94.5 (9.2)	92.5 (8.4)	101.3 (4.4)
	50	89.2 (9.1)	93.5 (8.6)	110.3 (8.5)	102.6 (8.1)	103.3 (8.5)	88.2 (4.5)
	100	93.4 (9.2)	97.2 (7.4)	90.2 (9.1)	104.2 (7.3)	96.3 (7.1)	94.2 (8.2)
DBaP	5	90.5 (9.6)	98.4 (6.3)	95.2 (6.5)	115.1 (6.4)	113.5 (9.1)	100.2 (7.4)
	50	85.5 (9.3)	103.4 (8.9)	92.5 (5.5)	92.9 (9.2)	113.1 (8.2)	99.3 (6.4)
	100	93.2 (9.1)	91.2 (9.4)	95.5 (8.7)	102.3 (4.2)	121.3 (9.2)	92.1 (9.1)
DBaP	5	94.3 (9.4)	90.4 (4.5)	87.4 (4.3)	87.8 (4.4)	97.9 (6.3)	88.6 (8.2)
	50	95.6 (9.7)	94.2 (4.6)	95.1 (6.4)	95.4 (6.7)	108.5 (9.6)	102.4 (8.2)
	100	107.2 (9.3)	105.6 (9.3)	108.8 (9.2)	89.6 (7.5)	111.4 (6.3)	100.5 (5.2)
DBaP	5	80.2 (9.4)	80.4 (8.2)	79.2 (9.8)	80.4 (6.2)	80.3 (4.6)	80.4 (9.8)
	50	79.5 (9.6)	82.1 (4.1)	82.2 (5.4)	79.4 (7.8)	79.1 (6.3)	79.3 (9.1)
	100	78.8 (9.2)	81.6 (9.7)	79.2 (8.2)	81.6 (6.7)	81.5 (8.2)	78.5 (6.4)
DBaP	5	79.5 (9.1)	76.4 (6.4)	79.5 (6.3)	76.5 (7.4)	78.5 (8.2)	76.4 (7.5)
	50	80.2 (9.5)	78.5 (8.1)	77.5 (7.4)	79.3 (3.1)	78.4 (5.2)	78.3 (6.2)
	100	80.4 (4.2)	77.1 (4.8)	76.4 (6.3)	80.1 (9.6)	76.4 (7.2)	79.1 (4.2)

applied method for the determination of 22 PAHs in vegetable oils. It provides an important technology for the determination of trace PAHs in vegetable oil samples.

Twenty-two PAHs in 6 types of edible vegetable oils from the Chinese market were determined. The abundance of LPAHs is higher than that of HPAHs, and the relative contribution rate of LPAHs to the total PAHs is higher. The determined levels of BaP met the upper level, 10 mg/kg, set in China national standard. However, 13.3 and 11.1% of the samples exceeded the EU-regulated maximum limits for BaP and PAH4, 2 and 10 $\mu\text{g/kg}$, respectively. The content of PAH22 varies greatly among different oil species, and the average PAH22 content is listed in descending order as follows: peanut oil > sesame oil > olive oil > rapeseed oil > soybean oil > sunflower seed oil. Findings of this study will help us to better understand the risk characteristics of PAHs in vegetable oil. Moreover, its application will provide regulators a useful guide to update the information in the context of risk evaluation.

REFERENCES

- Juhasz AL, Naidu R. Bioremediation of high molecular weight polycyclic aromatic hydrocarbons: a review of the microbial degradation of benzo [a] pyrene. *Int Biodeteriorat Biodegrad.* (2000) 45:57–88. doi: 10.1016/S0964-8305(00)00052-4
- Singh L, Agarwal T. PAHs in Indian diet: assessing the cancer risk. *Chemosphere.* (2018) 202:366–76. doi: 10.1016/j.chemosphere.2018.03.100
- Armstrong B, Hutchinson E, Unwin J, Fletcher T. Lung cancer risk after exposure to polycyclic aromatic hydrocarbons: a review and meta-analysis. *Environ Health Perspect.* (2004) 112:970–8. doi: 10.1289/ehp.6895
- Stofyho A, Sikorski ZE. Polycyclic aromatic hydrocarbons in smoked fish a critical review. *Food Chem.* (2005) 91:303–11. doi: 10.1016/j.foodchem.2004.06.012
- Zhang YX, Chen HY, Liu C, Chen RH, Wang YY, Teng YG. Developing an integrated framework for source apportionment and source-specific health risk assessment of PAHs in soils: application to a typical cold region in China. *J Hazard Mater.* (2021) 415:125730. doi: 10.1016/j.jhazmat.2021.125730
- Anderson KE, Kadlubar FF, Kulldorff M, Harnac L, Gross M, Lang NP, et al. Dietary intake of heterocyclic amines and benzo(a)pyrene: associations with pancreatic cancer. *Cancer Epidemiol Biomark Prevent.* (2005) 14:2261–5. doi: 10.1158/1055-9965.EPI-04-0514

DATA AVAILABILITY STATEMENT

The original contributions presented in the study are included in the article/supplementary material, further inquiries can be directed to the corresponding authors.

AUTHOR CONTRIBUTIONS

GS and YZ conceived and designed the experiments. ZM, SF, YH, and LN performed the experiments. QL analyzed the data. XY wrote the original draft. All authors have read and approved the manuscript.

FUNDING

This work was supported by National Key Research and Development Program of China (Project No. 2019YFC1606400).

7. Drabova L, Tomaniova M, Kalachova K, Kocourek V, Hajslova J, Pulkrabova J et al. Application of solid phase extraction and two-dimensional gas chromatography coupled with time-of-flight mass spectrometry for fast analysis of polycyclic aromatic hydrocarbons in vegetable oils. *Food Control*. (2013) 33:489–97. doi: 10.1016/j.foodcont.2013.03.018
8. Sun, JY, Feng, XN, Lyu CM, Zhou S, Liu Z. Effects of different processing methods on the lipid composition of hazelnut oil: a lipidomics analysis. *Food Sci Hum Wellness*. (2022) 11:427–35. doi: 10.1016/j.fshw.2021.11.024
9. Hossain MA, Salehuddin SM. Polycyclic aromatic hydrocarbons (PAHs) in edible oils by gas chromatography coupled with mass spectroscopy. *Arab J Chem*. (2012) 5:391–6. doi: 10.1016/j.arabjc.2010.09.012
10. Moret S, Dudine A, Conte LS. Processing effects on the polyaromatic hydrocarbon content of grapeseed oil. *J Am Oil Chem Soc*. (2000) 77:1289–92. doi: 10.1007/s11746-000-0203-5
11. Rojo Camargo MC, Antoniolli PR, Vicente E. Evaluation of polycyclic aromatic hydrocarbons content in different stages of soybean oils processing. *Food Chem*. (2012) 135:937–42. doi: 10.1016/j.foodchem.2012.06.031
12. *National Food Safety Standard Limits Contaminants in Food: GB 2762-2017*. Beijing: China Standard Press (2012). p. 8–9.
13. Official Journal of the European Union. Commission Regulation (EU) No 835/2011 of 19 August 2011 amending Regulation (EC) No 1881/2006 as regards maximum levels for polycyclic aromatic hydrocarbons in food stuffs. *Off. J. Eur. Union*. (2011) L215:4–8. Available online at: <http://data.europa.eu/eli/reg/2011/835/oj>
14. Ministry of Health. *National Food Safety Standard Determination of Polycyclic Aromatic Hydrocarbons in Food: GB5009.265-2021*. Beijing: China Standard Press (2021). p. 3–19.
15. Farhadian, A, Jinap, S, Abas, F, et al. Determination of polycyclic aromatic hydrocarbons in grilled meat. *Food Control*. (2010) 21:606–10. doi: 10.1016/j.foodcont.2009.09.002
16. Yousefi M, Shemshadi G, Khorshidian N, Ghasemzadeh-Mohammadi V, Fakhri Y, Hosseini H, et al. Polycyclic aromatic hydrocarbons (PAHs) content of edible vegetable oils in Iran: a risk assessment study. *Food Chem Toxicol*. (2018) 118:480–9. doi: 10.1016/j.fct.2018.05.063
17. Wang JH, Guo C. Ultrasonication extraction and gel permeation chromatography clean-up for the determination of polycyclic aromatic hydrocarbons in edible oil by an isotope dilution gas chromatography mass spectrometry. *J Chromatogr A*. (2010) 1217:4732–7. doi: 10.1016/j.chroma.2010.05.008
18. Fromberg A, Hojgard A, Duedahl OL. Analysis of polycyclic aromatic hydrocarbons in vegetable oils combining gel permeation chromatography with solid-phase extraction cleanup. *Food Addit Contamin*. (2007) 24:758–67. doi: 10.1080/02652030601150505
19. Jiang DF, Xin CL, Li W, Chen JD, Li FH, Chu ZH, et al. Quantitative analysis and health risk assessment of polycyclic aromatic hydrocarbons in edible vegetable oils marketed in Shandong of China. *Food Chem Toxicol*. (2015) 83:61–7. doi: 10.1016/j.fct.2015.06.001
20. Cai Y, Yan ZH, Nguyenvan M, Wang LJ, Cai QY. Magnetic solid phase extraction and gas chromatography-mass spectrometric analysis of sixteen polycyclic aromatic hydrocarbons. *J Chromatogr A*. (2015) 1406:40–7. doi: 10.1016/j.chroma.2015.06.024
21. Huertas-Pérez JF, Bordajandi LR, Sejerøe-Olsen B, Emteborg H, Baù A, Schimmel H, et al. PAHs in baby food: assessment of three different processing techniques for the preparation of reference materials. *Anal Bioanal Chem*. (2015) 407:3069–81. doi: 10.1007/s00216-015-8490-z
22. Purcaro G, Picardo M, Barp L, Moret S, Conte LS. Direct-immersion solid-phase microextraction coupled to fast gas chromatography mass spectrometry as a purification step for polycyclic aromatic hydrocarbons determination in olive oil. *J Chromatogr A*. (2013) 1307:166–71. doi: 10.1016/j.chroma.2013.07.068
23. Silva SA, Sampaio GR, Silva Torres EAF. Optimization and validation of a method using UHPLC-fluorescence for the analysis of polycyclic aromatic hydrocarbons in cold-pressed vegetable oils. *Food Chem*. (2017) 221:809–14. doi: 10.1016/j.foodchem.2016.11.098
24. Olsson P, Sadiktsis I, Holmbäck J, Westerholm R. Class separation of lipids and polycyclic aromatic hydrocarbons in normal phase high performance liquid chromatography—a prospect for analysis of aromatics in edible vegetable oils and biodiesel exhaust particulates. *J Chromatogr A*. (2014) 1360:39–46. doi: 10.1016/j.chroma.2014.07.064
25. Wu SM, Yu WJ. Liquid-liquid extraction of polycyclic aromatic hydrocarbons in four different edible oils from China. *Food Chem*. (2012) 134:597–601. doi: 10.1016/j.foodchem.2012.02.155
26. Shi LK, Zhang DD, Liu YL. Incidence and survey of polycyclic aromatic hydrocarbons in edible vegetable oils in China. *Food Control*. (2016) 62:165–70. doi: 10.1016/j.foodcont.2015.10.037
27. Zhou RZ, Jiang J, Mao T, Zhao YS, Lu Y. Multiresidue analysis of environmental pollutants in edible vegetable oils by gas chromatography-tandem mass spectrometry. *Food Chem*. (2016) 207:43–50. doi: 10.1016/j.foodchem.2016.03.071
28. Li, J, Ma, JM, Zhang, Y, Zheng L. Determination of 19 polyphenolic compounds in tea by ultra-high performance liquid chromatography combined with quadrupole-time of flight mass spectrometry. *Food Sci Hum Wellness*. (2022) 11:719–26. doi: 10.1016/j.fshw.2021.12.029
29. Baldwin S, Bristow T, Ray A, Rome K, Sanderson N, Sims M, et al. Applicability of gas chromatography/quadrupole-orbitrap mass spectrometry in support of pharmaceutical research and development. *Rapid Commun Mass Spectrom*. (2016) 30:873–80. doi: 10.1002/rcm.7505
30. Postigo C, Cojocariu C I, Richardson S D, Silcock P J, Barcelo D. Characterization of iodinated disinfection by-products in chlorinated and chloraminated waters using Orbitrap based gas chromatography-mass spectrometry. *Anal Bioanal Chem*. (2016) 408:3401–11. doi: 10.1007/s00216-016-9435-x
31. Meng ZJ, Li Q, Cong JH, Huang YX, Wang D, Pan CP, et al. Rapid screening of 350 pesticide residues in vegetable and fruit juices by multi-plug filtration cleanup method combined with gas chromatography-electrostatic field orbitrap high resolution mass spectrometry. *Foods*. (2021) 10:1651–65. doi: 10.3390/foods10071651
32. European Commission Directorate-General for Health and Food Safety. *Guidance Document on Analytical Quality Control and Method Validation Procedures for Pesticides Residues Analysis in Food and Feed: SANTE/11945/2015*. European: the institutions of the EU (2015). p. 1–42.

Conflict of Interest: The authors declare that the research was conducted in the absence of any commercial or financial relationships that could be construed as a potential conflict of interest.

Publisher's Note: All claims expressed in this article are solely those of the authors and do not necessarily represent those of their affiliated organizations, or those of the publisher, the editors and the reviewers. Any product that may be evaluated in this article, or claim that may be made by its manufacturer, is not guaranteed or endorsed by the publisher.

Copyright © 2022 Meng, Fan, Yuan, Li, Huang, Niu, Shi and Zhang. This is an open-access article distributed under the terms of the Creative Commons Attribution License (CC BY). The use, distribution or reproduction in other forums is permitted, provided the original author(s) and the copyright owner(s) are credited and that the original publication in this journal is cited, in accordance with accepted academic practice. No use, distribution or reproduction is permitted which does not comply with these terms.



OPEN ACCESS

EDITED BY

Liguang Xu,
Jiangnan University, China

REVIEWED BY

Guoqiang Li,
Foshan University, China
Yuan Yuan,
Jilin University, China

*CORRESPONDENCE

Jie Zheng
zhengjie@jnu.edu.cn

†These authors have contributed
equally to this work

SPECIALTY SECTION

This article was submitted to
Food Chemistry,
a section of the journal
Frontiers in Nutrition

RECEIVED 19 June 2022

ACCEPTED 12 July 2022

PUBLISHED 02 August 2022

CITATION

Chen M, Liu P, Zhou H, Huang C,
Zhai W, Xiao Y, Ou J, He J,
El-Nezami H and Zheng J (2022)
Formation and metabolism of
6-(1-acetol)-8-(1-acetol)-rutin in
foods and *in vivo*, and their
cytotoxicity. *Front. Nutr.* 9:973048.
doi: 10.3389/fnut.2022.973048

COPYRIGHT

© 2022 Chen, Liu, Zhou, Huang, Zhai,
Xiao, Ou, He, El-Nezami and Zheng.
This is an open-access article
distributed under the terms of the
Creative Commons Attribution License
(CC BY). The use, distribution or
reproduction in other forums is
permitted, provided the original
author(s) and the copyright owner(s)
are credited and that the original
publication in this journal is cited, in
accordance with accepted academic
practice. No use, distribution or
reproduction is permitted which does
not comply with these terms.

Formation and metabolism of 6-(1-acetol)-8-(1-acetol)-rutin in foods and *in vivo*, and their cytotoxicity

Min Chen^{1†}, Pengzhan Liu^{2†}, Hua Zhou¹, Caihuan Huang¹,
Weiye Zhai³, Yuantao Xiao³, Juanying Ou⁴, Jun He⁵,
Hani El-Nezami^{6,7} and Jie Zheng^{1,8*}

¹Department of Food Science and Engineering, Jinan University, Guangzhou, China, ²School of Food Science and Engineering, South China University of Technology, Guangzhou, China, ³Dongguan Silang Foods Co., Ltd., Dongguan, China, ⁴Institute of Food Safety and Nutrition, Jinan University, Guangzhou, China, ⁵Institute of Laboratory Animal Science, Jinan University, Guangzhou, China, ⁶School of Biological Sciences, University of Hong Kong, Pok Fu Lam, Hong Kong SAR, China, ⁷School of Medicine, Institute of Public Health and Clinical Nutrition, University of Eastern Finland, Kuopio, Finland, ⁸Guangdong-Hong Kong Joint Innovation Platform for the Safety of Bakery Products, Guangzhou, China

Methylglyoxal (MGO) is a highly reactive precursor which forms advanced glycation end-products (AGEs) *in vivo*, which lead to metabolic syndrome and chronic diseases. It is also a precursor of various carcinogens, including acrylamide and methylimidazole, in thermally processed foods. Rutin could efficiently scavenge MGO by the formation of various adducts. However, the metabolism and safety concerns of the derived adducts were paid less attention to. In this study, the optical isomers of di-MGO adducts of rutin, namely 6-(1-acetol)-8-(1-acetol)-rutin, were identified in foods and *in vivo*. After oral administration of rutin (100 mg/kg BW), these compounds reached the maximum level of 15.80 $\mu\text{g/L}$ in plasma at 15 min, and decreased sharply under the quantitative level in 30 min. They were detected only in trace levels in kidney and fecal samples, while their corresponding oxidized adducts with dione structures presented as the predominant adducts in kidney, heart, and brain tissues, as well as in urine and feces. These results indicated that the unoxidized rutin-MGO adducts formed immediately after rutin ingestion might easily underwent oxidation, and finally deposited in tissues and excreted from the body in the oxidized forms. The formation of 6-(1-acetol)-8-(1-acetol)-rutin significantly mitigated the cytotoxicity of MGO against human gastric epithelial (GES-1), human colon carcinoma (Caco-2), and human umbilical vein endothelial (HUVEC) cells, which indicated that rutin has the potential to be applied as a safe and effective MGO scavenger and detoxifier, and AGEs inhibitor.

KEYWORDS

rutin, methylglyoxal (MGO), adducts, food, absorption, accumulation, *in vivo*

Introduction

Methylglyoxal (MGO) is a typical reactive α -oxoaldehydes which can react very fast with proteins and nucleic acids to form advanced glycation end-products (AGEs) in the body. AGEs formation causes the dysfunction of functional proteins, ligates the receptor for advanced glycation end-products (RAGE), increases the production of reactive oxygen species (ROS), and triggers cellular apoptosis (1). Thus, the carbonyl stress caused by the excessive accumulation of MGO is always implicated in tissue damage in aging and various diseases, such as diabetic complications and cancer (2). Other than its reactions with body components *in vivo*, the appearance of MGO in foods also provides reactive precursors for the formation of AGEs, as well as the generation of potent carcinogens like acrylamide and methylimidazole (3, 4).

Nevertheless, MGO is ubiquitously present in all kinds of foods, especially in those containing high amounts of carbohydrates and lipids and underwent thermal processing. It is generated dominantly through the Maillard reaction in thermally processed foods when hexoses initially react with amino acids to generate Schiff bases, and convert to Amadori products, which undergo a serial of reaction steps to yield MGO (5). In foods containing high amounts of hexoses, such as honey, MGO is produced by the autoxidation of hexoses, which involves retro-aldol condensation, isomerisation and consequent fragmentation of sugars (6). In honey, another pathway to generate MGO is the dehydration of dihydroxyacetone (7). This is the main explanation of the high detection levels of MGO in the commercial Manuka honey since the precursor dihydroxyacetone present highly in this kind of honey (8). However, dihydroxyacetone do not contribute to the formation of MGO in other foods because of its absence. Oxidation of unsaturated fatty acids is another important pathway for the generation of MGO in fatty foods (5, 9). Moreover, MGO could also be generated through the microbial metabolism of dihydroxyacetone phosphate by the catalysis of methylglyoxal synthase, which explains its occurrence in some fermented beverages and foods (10). Therefore, given its ubiquitously appearance in foods, people are inevitably exposed to MGO through the consumption of foods. In fact, the deposit of MGO in human body is not only come exogenously from food ingestion, but also from the endogenous production through the glycolysis metabolism in animals (11). MGO is primarily produced in organisms by the degradation of triosephosphate intermediates during glycolysis (12). The plasma concentration of MGO in human samples varied from 96 to 652 nmol/L between different studies (13). It was further reported that MGO concentration elevated significantly under conditions of high glucose load (1). Scheijen and Schalkwijk reported a 31% increase in plasma concentration of MGO in patients with type 2 diabetes compared to the non-diabetic controls (13). Moreover,

a maximum 6-fold elevation in MGO concentration could be reached in patients with renal disease (12).

Given the deleterious effects of MGO *in vivo* and the inevitable exposure of human being toward the exogenous and endogenous derived MGO, mitigation of MGO in both foods and *vivo* is highly demanded in these decades. As a result, various strategies have been investigated and applied to address this problem. They include the selection of raw materials, adjustment of processing parameters during food processing (14), and the addition of harmful substances inhibitors (15). Among these strategies, the use of natural compounds as MGO scavengers was considered the most applicable. They can be applied both for the control of hazardous compound generation in food, and disease protection or intervention *in vivo*.

Phenolic compounds are among the most applied natural compounds owing to their effective scavenging capacity of carbonyl compounds and other hazardous derivatives (16–18), in accompany with their distinguished physiological benefits (19–21). The flavonoids with typical *meta*-phenol structures possess efficient scavenging capacity for MGO. For example, epicatechin, (–)-epigallocatechin gallate and phloretin showed the highest elimination rate on MGO by 99% when incubated with MGO at 37°C for 24 h, and others like hesperetin, resveratrol and apigenin could also scavenge MGO by 63, 61, and 40%, respectively (16). Recent studies elucidated that these flavonoids eliminated MGO by means of reactions between the aromatic substitution and the electrophilic carbonyl group, which consequently brought various new products discovered (15, 17).

In our recent study, we found quercetin-3-O-rutinoside, usually called rutin, could eliminate 50% of MGO when incubated for 24 h under physiological conditions (22). Rutin is an important dietary flavonoid widely distributed in plant-derived food raw materials, such as vegetables, fruits, and grains (23). It has also been extensively used in food production and pharmaceutical development due to its health promoting properties, and the potential to prevent and treat various chronic diseases (24, 25). As a result, the Dietary Supplement Label Database have listed more than 860 commercial products containing rutin in the USA (24). This means humans are unavoidably exposed to rutin, and the reaction products of rutin and MGO formed both in food and *in vivo*.

However, although numerous flavonoid–MGO adducts have yet been reported as a consequent result of MGO elimination by flavonoids (15), few study focus on their generation levels in foods and *in vivo*, and much less attention has been paid to their metabolism and distribution *in vivo*, and the subsequent safety concerns. Some researchers found that myricetin (26), genistein (27, 28), and epicatechin (29) trapped MGO *in vivo* and produced mono- and di-MGO adducts. The formation levels of the flavonoid-MGO adducts in foods were, on the other hand, less investigated. We found that incorporation

of quercetin and rutin-rich materials during food preparation yielded different adducts in the thermally processed foods (22, 30). Moreover, in contrast to the discovery of adducts in food and *in vivo*, the safety concerns of these neo-formed adducts were paid less attention and lack of evaluation, which might bring potential threaten to food safety and human health. In the last study (22), we identified three oxidized rutin-MGO adducts with novel dione structures in foods and *in vivo*, and found them to be less toxic than MGO in different cell lines. But in another study, we found that the unoxidized mono- and di-MGO adducts of quercetin formed during the preparation of biscuits displayed higher cytotoxicity than MGO in PC-12 cell line (30). This study aims to investigate the unoxidized rutin-MGO adducts formed between rutin and MGO, compare the differences in their generation and distribution in food and *in vivo* with those of the oxidized adducts, explain their metabolism *in vivo*, and evaluate their cytotoxicity against different cell lines related to their potential appearance *in vivo*.

Materials and methods

Materials and reagents

The commercial food products analyzed in this study were randomly purchased from the local market in Guangzhou, China. 40% aqueous solution of MGO was obtained from Macklin Biochemical Co., Ltd. (Shanghai, China). Standard compound of rutin was obtained from Ark Pharm, Inc. (IL, USA). Formic acid (HPLC grade) was obtained from Kermel Chemical Reagent Co., Ltd. (Tianjin, China). Methanol (HPLC grade) was purchased from Mallinckrodt Baker, Inc. (NJ, USA). CD₃OD were purchased from Cambridge Isotope Laboratories, Inc. (MA, USA). Human gastric epithelial cell line (GES-1) and human colon carcinoma cell line (Caco-2) were bought from the American Type Culture Collection (ATCC, Rockville, MD, USA). Human umbilical vein endothelial (HUVEC) cell was bought from Shanghai iCell Bioscience Inc. (Shanghai, China). PBS was purchased from Boster Biological Technology Co., Ltd. (CA, USA). Trypsin-EDTA and MTT assay were obtained from Biosharp Co., Ltd. (Hefei, China). Fetal bovine serum (FBS), penicillin and streptomycin were purchased from Thermo Fisher Scientific Inc. (MA, USA).

Reactions between rutin and MGO under simulated physiological condition

To investigate the unoxidized adducts formed between rutin and MGO, the simulated physiological reactions between rutin and MGO were established as described by Chen et al. (22). Briefly, 0.5 mM MGO and 0.5 mM rutin were reacted at 37°C for 24 h in PBS buffer (pH 7.4, 0.2 M). The reaction media

were taken at 0.25, 0.5, 1, 2, 4, 8, 12, and 24 h, respectively for analyses. The formation of rutin-MGO adducts were detected at 360 nm by a high-performance liquid chromatography (HPLC) coupled with a diode array detector (DAD), and the yields were quantified through the external standard curves established with the standards prepared in Section 2.3 Preparation and purification of rutin-MGO adducts. The HPLC-DAD system consists of a Shimadzu LC-20AT HPLC system and an SPD-M20AVP diode array detector (Shimadzu Corporation, Kyoto, Japan). A Phenomenex Aeris Peptide XB-C18 column (4.60 mm × 250 mm, 5 μm; Torrance, CA) was applied for separation of rutin-MGO adducts. The chromatographic parameters and the eluting gradients were the same as described by Chen et al. (22).

Preparation and purification of rutin-MGO adducts

In order to prepare enough unoxidized rutin-MGO adducts for latter the structural elucidation and quantification of adducts in foods and *in vivo*, the effects of pH, temperature, molar ratio, and reaction time on the formation of the adducts were investigated to obtain the optimal conditions for the preparation procedure. Firstly, the pH was set as 3, 5, 7.4, 9, and 11 when incubating 10 mM rutin with 50 mM MGO at 70°C for 9 h. Secondly, the temperature was set at 30, 50, and 70 °C when 10 mM rutin and 50 mM MGO were incubated at pH 7.4 for 9 h. Thirdly, the molar ratio of 1: 1, 1: 5, and 1: 10 were selected for rutin: MGO to be incubated at 70°C, pH 7.4 for 9 h, where the concentration of rutin was kept constantly at 10 mM. Finally, the reaction times of 4, 7, 10, 13, and 16 h was tested when 10 mM rutin reacted with 100 mM MGO at pH 7.4 under 70°C. At each point, the reaction solution was taken, filtered through 0.45 μm membrane, and analyzed by HPLC-DAD to calculate the yield of the adducts under different conditions. Finally, the standards of rutin-MGO adducts were prepared under the optimal conditions obtained.

The target adducts in the current study was hard to be separated by column chromatography applied in our previous study (22). Thus, these unoxidized adducts were separated using a LC-100 preparative medium-pressure liquid chromatograph equipped with a DAD (Shanghai Wufeng Scientific Instrument Co., Ltd., Shanghai, China). The column of Pntulips QC-C18 (10 mm × 250, 5 μm; Shanghai Puning Analysis Technology Co., Ltd., Shanghai, China) was applied for compound separation. A binary eluting gradient program was applied as follows using 0.1% aqueous formic acid as solvent A and methanol as solvent B: 0–8 min, 10–70% B; 8–11 min, 70–90% B; 11–13 min, 90% B; 13–14 min, 90–10% B; 14–22 min, 10% B. The flow rate was set at 3.0 mL/min, and the inject volume was 100 μL. The peaks of the adducts were monitored at 360 nm, and the corresponding adducts were collected. The

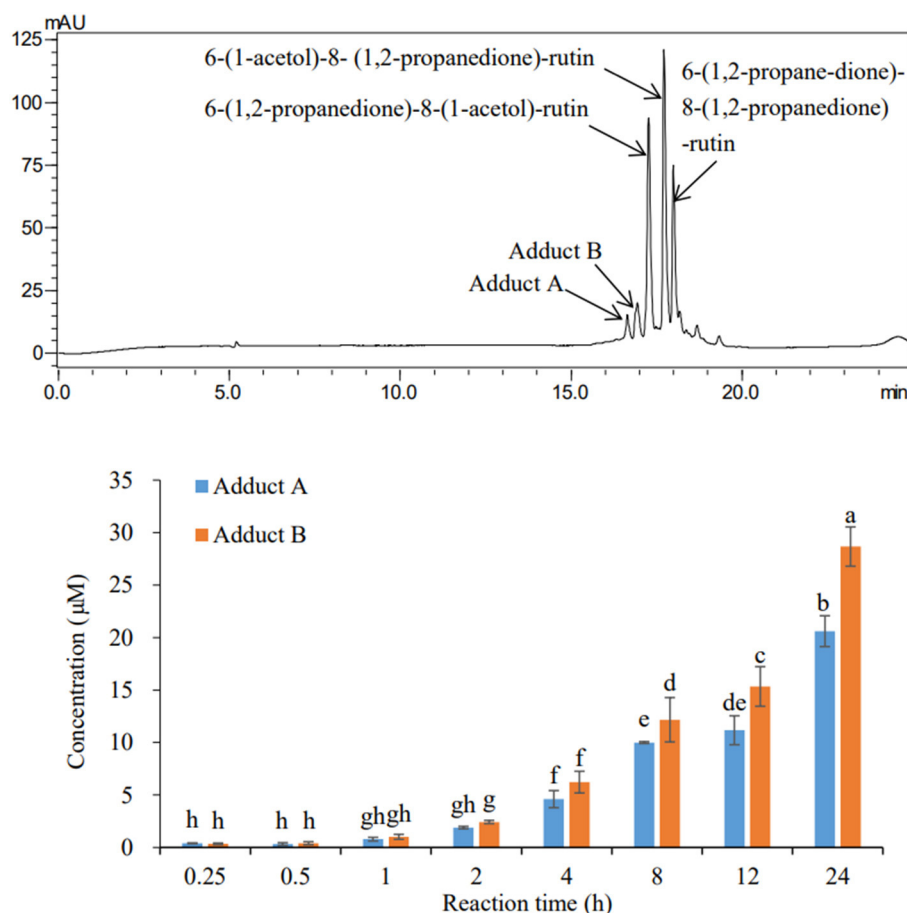


FIGURE 1
HPLC chromatogram (upper) of the adducts and their formation levels (bottom) during 24 h incubation of rutin and MGO under simulated physiological condition.

adduct fractions with purity over $\geq 95\%$ were combined, and the organic solvents were removed with a rotary evaporator. The pure adducts were then freeze-dried and stored at -20°C prior to NMR analysis and further analyses.

Structural characterization of rutin–MGO adducts

To elucidate the structures of the rutin–MGO adducts formed, both HPLC-MS/MS analysis and nuclear magnetic resonance (NMR) analysis were conducted. The freeze-dried adduct was dissolved in methanol and analyzed with a Shimadzu Nexera X2 UHPLC coupled with a LCMS-8045 mass spectrometer (Shimadzu Corporation, Kyoto, Japan). The eluting solvents and the flow rate were the same as described in Section 2.2 Reactions between rutin and MGO under simulated physiological condition. The eluting program was modified as: 0–12 min, 10–70% B; 12–15 min, 70–90% B; 15–17 min, 90% B;

17–18 min, 90–10% B; 18–25 min, 10% B. The injection volume was $1\ \mu\text{L}$. The operating conditions of mass spectrometer were as follows: negative ion mode; scanning range, m/z 100–1,000; pressure of drying gas and nebulizer gas, 50 psi; capillary voltage, 4 kV; declustering potential, 50 V; collision voltage, 25 eV; desolvation temperature, 300°C .

After the molecular structure were revealed by HPLC-MS/MS analysis, adducts A and B were further dissolved in CD_3OD , and analyzed with a Bruker Avance III 600 MHz NMR spectrometer (Fällanden, Switzerland) to obtain ^1H , ^{13}C , HMQC, HMBC, and ROESY spectra for structure elucidation.

Determination of rutin–MGO adducts in food samples

In the current study, multiple reaction monitoring (MRM) mode of HPLC-MS/MS analysis was applied to measure the formation levels of rutin–MGO adducts in 15 food samples

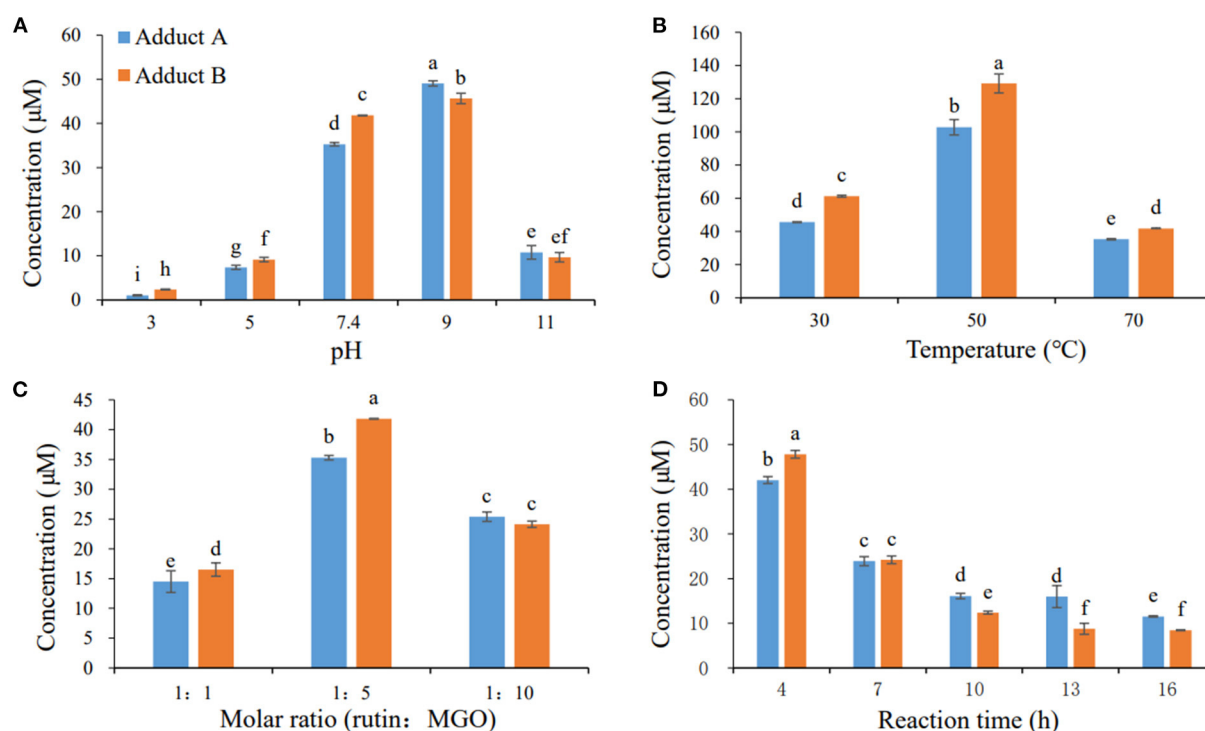


FIGURE 2

Effects of pH (A), temperature (B), molar ratio (C), and reaction time (D) on the formation of adducts A and B. Different letters represent significant differences ($P < 0.05$).

brought randomly from the local market. The samples were prepared and analyzed as the same way as described by Chen et al. (22). The qualification and quantification fragmentation transitions for each adduct are as follows: Adduct A, $m/z = 753 \rightarrow 373$ and $751 \rightarrow 426$ (collision energy, 48 eV and 43 eV, respectively) for qualification, and $m/z = 753 \rightarrow 401$ (47 eV) for quantification; Adduct B, $m/z = 753 \rightarrow 426$ and $751 \rightarrow 444$ (43 and 38 eV, respectively) for qualification, and $m/z = 753 \rightarrow 401$ (48 eV) for quantification. The external calibration curve ($r > 0.99$) of each standard adduct prepared by our laboratory was used for quantification. The LOD ($S/N > 3$) and LOQ ($S/N > 10$) were 0.60 and 0.81 $\mu\text{g/L}$ for adducts A, and 0.50 and 0.76 $\mu\text{g/L}$ for adduct B, respectively.

Determination of rutin–MGO adducts in plasma, urine, feces, and tissues of rats

The animals were treated as described in the study by Chen et al. (22). In brief, five 7 weeks old male Sprague–Dawley rats (190–220 g) were exposed to rutin (100 mg/kg BW) by oral gavage after fasting for 16 h. The plasma samples were collected at 0.25, 0.5, 1, 2, 4, 6, 8, 10, and 24 h after the administration, and stored under -80°C until analysis. The feces and urine were

collected with the metabolic cages throughout the 24 h period. At 24 h, the rats were sacrificed after anesthetization, and the tissues including stomach, intestine (divided into duodenum, jejunum, ileum, caecum, and colon), heart, liver, kidney, and brain were taken and frozen immediately in liquid nitrogen and transferred to a deep freezer (-80°C) for storage before analysis. The procedures of the animal study followed the protocol by the Institutional Animal Care and Use Committee of the Laboratory Animal Center of Jinan University.

The plasma samples were treated as described by Chen et al. (22). About half gram of feces and tissue samples were weight accurately, and homogenized with 2 mL saline on an ice-bath. The homogenates were transferred to a centrifuge tube, added with 1 mL PBS (pH 5.0, 0.05 M) and 100 μL ascorbic acid (150 mg/mL), and extracted with 3 mL of methanol twice. The supernatants were combined after centrifugation at $13,000 \times g$ under 4°C for 10 min, evaporated to dryness, re-dissolved in 500 μL of 50% aqueous methanol containing 0.1% formic acid (v/v), and filtered through a 0.22 μm membrane for HPLC-MS/MS analysis. The adducts in 200 μL of urine were extracted twice with 1 mL methanol. The supernatants were collected after centrifugation at $13,000 \times g$ under 4°C for 10 min, and evaporated to dryness. The residues were dissolved in 200 μL of 50% aqueous methanol containing 0.1% formic

acid (v/v), and filtered through a 0.22 μm membrane for HPLC-MS/MS analysis. A sample of 1 μL was injected into an Agilent Technologies 1,260 Infinity HPLC (Agilent Technologies, CA, USA) interfaced to an AB 4500 Q-Trap mass spectrometer (AB Sciex, MA, USA) in the negative mode for quantification of adducts A and B, respectively. The eluting programs for HPLC analysis, and the operation conditions of mass spectrometer refers to those established by Chen et al. (22). The qualification and quantification fragmentation transitions for each adduct are the same as provided in Section 2.5 Determination of rutin-MGO adducts in food samples. Moreover, as the information on the occurrence levels of 6-(1,2-propanedione)-8-(1-acetol)-rutin, 6-(1-acetol)-8-(1,2-propanedione)-rutin, and 6-(1,2-propanedione)-8-(1,2-propanedione)-rutin discovered in the last study was still missing, the concentration of these oxidized rutin-MGO adducts in various tissues and urine and feces were also determined in this study. The qualification and quantification fragmentation transitions of these adducts refers to those provided previously (22).

Cytotoxicity evaluation of rutin-MGO adducts in four different cell lines

The cytotoxicity of the unoxidized rutin-MGO adducts were tested against the GES-1, Caco-2, and HUVEC cell lines representing gastrointestinal and circulation systems. The cells were cultivated as described by Chen et al. (22), and treated with 0, 200, 400, 600, 800, 1,000 μM of rutin, MGO, adduct A, and adduct B for 24 h, after which the viability of the cells was evaluated by MTT assay (22).

Statistical analysis

All the experiments were performed in triplicate, and the results were expressed as mean \pm standard deviation. Statistical analyses were conducted with SPSS Statistics 25.0 (SPSS, Inc., Chicago, IL, USA). One-way analysis of variance (ANOVA) was applied to investigate the differences between samples or treatments ($P < 0.05$). Furthermore, multiple comparisons between different samples were carry out by the Duncan's test at significant level of 0.05.

Results and discussions

Formation of rutin-MGO adducts under simulated physiological condition

In our previous study, we found that rutin displayed considerable scavenging capacity for MGO under simulated physiological condition. 50% of MGO was eliminated

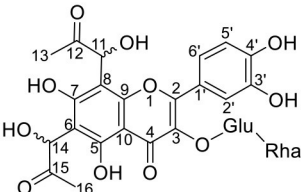
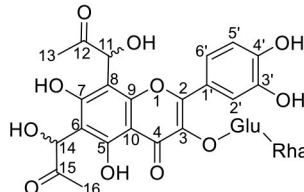
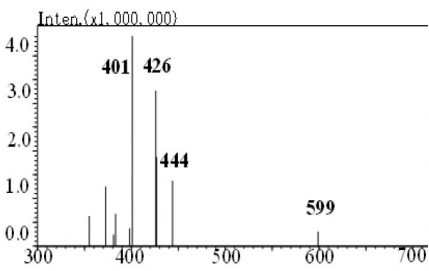
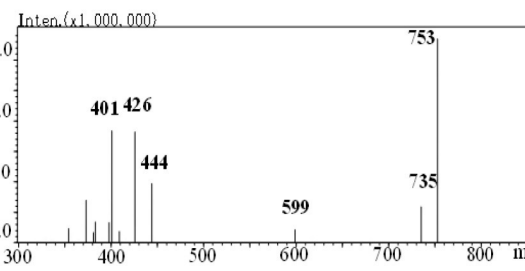
when rutin (0.5 mM) was incubated with MGO (0.5 mM) under 37 $^{\circ}\text{C}$ for 24 h (22). Moreover, three major adducts were detected as a consequence of the elimination reaction. They were unambiguously identified to be 6-(1,2-propanedione)-8-(1-acetol)-rutin ($\text{C}_{33}\text{H}_{36}\text{O}_{20}$), 6-(1-acetol)-8-(1,2-propanedione)-rutin ($\text{C}_{33}\text{H}_{36}\text{O}_{20}$), and 6-(1,2-propanedione)-8-(1,2-propanedione)-rutin ($\text{C}_{33}\text{H}_{34}\text{O}_{20}$), all of which were oxidized adducts of rutin and MGO with dione structures. This was the first report of polyphenol-MGO adducts with oxidized dione structures. However, the majority of investigations on the scavenging mechanism of polyphenols on MGO reported the formation of unoxidized adducts between polyphenols and MGO. Yoon and Shim (31) reported that non-oxidized rutin-di-MGO adducts were formed when incubating rutin and MGO for 24 h, and speculated it contributed to the highly inhibitory effects (more than 90%) of rutin on the formation of AGEs in glycation reaction (31).

From the HPLC chromatogram obtained after incubation of rutin and MGO under simulated physiological condition (Figure 1), two peaks, hereby named adduct A and B, were also formed at detectable levels other than the three oxidized adducts with dione structures reported (22). The formation of these two adducts also showed a time-dependent manner. Through the quantification of adducts with external standard curves obtained by the adduct standards prepared in the next sections, the yields of these adducts at different periods under the simulated physiological condition were determined. At the first 15 min, the contents of adducts A and B were only 0.74 μM in total, accounting for 6% of the total adducts (the sum of three oxidized adducts and adducts A and B). As the incubation time prolonged, the yield of the adducts hardly increased within 1 h, but started to increase significantly after 4 h and reached finally a total of 49.27 μM at 24 h. Adducts A and B were generated at levels of 20.61 and 28.67 μM , respectively, at the reaction time of 24 h. While by that time, the adducts 6-(1,2-propanedione)-8-(1-acetol)-rutin, 6-(1-acetol)-8-(1,2-propanedione)-rutin, and 6-(1,2-propanedione)-8-(1,2-propanedione)-rutin identified in the last study (22) were produced at levels of 20.49, 21.18, and 53.35 μM , respectively.

Preparation and structural elucidation of rutin-MGO adducts

In our previous study, adducts A and B could not be successfully separated and purified by the column chromatograph with all kinds of absorbents tried (22). Thus, the preparative medium-pressure liquid chromatograph was applied to obtain the standard adducts. Firstly, the effects of different reaction parameters on the yield of these two adducts were investigated to optimize the preparation conditions for the adducts. As shown in Figure 2A, the formation of

TABLE 1 Structure, mass spectra, ¹H (600 MHz), and ¹³C (126 MHz) NMR data of Adduct A and B.

Adduct A			Adduct B		
					
					
No.	δ_{H} (ppm)	δ_{C} (ppm)	δ_{H} (ppm)	δ_{C} (ppm)	
2	-	146.08	-	146.07	
3	-	135.47	-	135.43	
4	-	179.98	-	179.85	
5-OH	-	165.81	-	165.15	
6	-	103.97	-	103.81	
7-OH	-	162.86	-	162.83	
8	-	103.54	-	103.49	
9	-	159.50	-	159.38	
10	-	102.49	-	102.51	
11	5.58 (s, 1H)	70.23	5.47 (s, 1H)	71.83	
12	-	209.32	-	209.68	
13	2.15 (s, 3H)	25.93	2.17 (s, 3H)	25.81	
14	5.44 (s, 1H)	68.66	5.34 (s, 1H)	69.72	
15	-	209.32	-	209.16	
16	1.71 (s, 3H)	23.13	1.69 (s, 3H)	21.41	
1'	-	123.80	-	123.85	
2'	7.69 (s, 1H)	116.11	7.63 (s, 1H)	116.10	
3'-OH	-	145.93	-	145.94	
4'-OH	-	150.05	-	150.06	
5'	6.90 (d, $J = 8.5$ Hz, 1H)	117.69	6.88 (d, $J = 8.5$ Hz, 1H)	117.68	
6'	7.69 (d, $J = 8.5$ Hz, 1H)	122.78	7.63 (d, $J = 8.5$ Hz, 1H)	122.80	
3-O-glu					
1''	5.23 (d, $J = 7.8$ Hz, 1H)	107.23	5.27 (d, $J = 7.8$ Hz, 1H)	106.32	
2''	3.16-3.82 (m, 10H, H-2''-H-6'', H-2'''-5''')	75.66	3.18-3.87 (m, 10H, H-2''-H-6'', H-2'''-5''')	75.66	
3''		78.11		78.10	
4''		71.77		72.00	
5''		77.28		77.37	
6''		68.91		68.79	

(Continued)

TABLE 1 Continued

No.	δ_H (ppm)	δ_C (ppm)	δ_H (ppm)	δ_C (ppm)
6"-O-rha				
1"	4.49 (s, 1H)	108.77	4.48 (s, 1H)	107.17
2"	3.16–3.82 (m, 10H, H-2"-H-6", H-2"-5")	72.05	3.18–3.87 (m, 10H, H-2"-H-6", H-2"-5")	72.05
3"		72.19		72.19
4"		73.86		73.85
5"		69.68		69.68
6"	1.13 (d, $J = 6.2$ Hz, 3H)	17.90	1.12 (d, $J = 6.0$ Hz, 3H)	17.91

TABLE 2 Contents (mg/kg) of adducts A and B in commercial food samples.

Code	Product	Grain ingredients	Adduct A	Adduct B
1	Coarse multi-grain biscuit 1	Oat flour, barley flour, buckwheat flour, quinoa flour	N.D. ^a	N.D.
2	Coarse multi-grain biscuit 2	Coarse rice flour, tapioca starch	N.D.	N.D.
3	Multi-grain bar 1	Buckwheat, wheat, barley, oat	N.D.	N.D.
4	Multi-grain bar 2	Buckwheat, wheat, barley, oat	0.27±0.02	0.89±0.05
5	Oat biscuit	Wheat, oat	N.D.	N.D.
6	Biscuit	Wheat	N.D.	N.D.
7	Cracker	Wheat	N.D.	N.D.
8	Potato chip 1	Potato	N.D.	N.D.
9	Potato chip 2	Potato	N.D.	N.D.
10	Shortbread	Wheat flour, sesame	N.D.	N.D.
11	Quinoa cracker	Wheat flour, oat, sesame, quinoa	N.D.	N.D.
12	Quinoa rolls	Wheat flour, quinoa flour	N.D.	N.D.
13	Nut bar	Rice, coarse rice, cashew, almond	N.D.	N.D.
14	Coarse grain cracker	Corn, black rice	N.D.	N.D.
15	Buckwheat noodle	Rye flour, buckwheat flour	N.D.	N.D.

^aN.D., not detected.

adducts A and B increased as the pH of the medium elevated from 3 to 9, and decreased dramatically when the pH further increased. The yields of these two adducts increased as the reaction temperature increased from 30 to 50°C, and decreased when the temperature further elevated to 70°C (Figure 2B). The adducts reached maximum yields at the substrate molar ratio of 1:5 for rutin:MGO, while higher or lower substrate molar ratio all decreased the formation of these two adducts (Figure 2C). Figure 2D showed that the formation of both adducts A and B decreased as the reaction time prolonged. In contrast, a highly oxidized adduct of rutin and MGO, 6-(1,2-propanedione)-8-(1,2-propanedione)-rutin, was formed moderately (42.53 μM compared to 42.04 and 47.81 μM for adducts A and B, respectively) under the same condition at 4 h, and increased dramatically as the reaction proceeded until 16 h, which reached maximum of 122.20 μM. While at 16 h, the yields of adducts A and B decreased to minimum of 11.53 and 8.42 μM, respectively. As the adducts A and B

were latter identified to be unoxidized di-MGO adducts of rutin, this indicated that the unoxidized adducts might undergo oxidation reactions and be predominantly converted to the highly oxidized products as the reaction proceeded. As a result, the optimal reaction condition chosen for the preparation of the target adducts A and B was as follows: 10 mM rutin and 50 mM MGO were combined and reacted at 50 °C and pH 9 for 4 h. When the reaction ends, the reactants were separated by preparative medium-pressure liquid chromatograph to obtain the highly purified (≥ 95%) standards of the adducts for structural elucidation.

The mass spectra displayed in Table 1 showed that adducts A and B were isomers with the same molecular ion [M-H]⁻ detected at m/z 753 and fragment ions at m/z 444, 425 and 401. The m/z 753 [M-H]⁻ is 144 mass units greater than the m/z 609 [M-H]⁻ of rutin. Thus, they were preliminarily identified as conjugates of the rutin molecule with two moieties of MGO attached, whose molecular formula were

both C₃₃H₃₈O₂₀. Abundant investigations pointed the trapping of α -dicarbonyl compounds dominantly happened at C-6 and C-8 positions of the flavonoids with *meta*-phenol structures. Yoon and Shim (31) detected previously a di-MGO-rutin adduct after incubation of rutin and MGO for 24 h. However, only mass spectrometric analysis was conducted for the structural elucidation, which was hard to provide unambiguous information on the adduct structure (31). Therefore, we isolated the two adducts by the preparative medium-pressure liquid chromatograph for NMR analysis. The ¹H and ¹³C NMR data were listed in Table 1, and the spectra of heteronuclear multiple bond correlation (HMBC), heteronuclear multiple quantum correlation (HMQC) and Rotating Frame Nuclear Overhauser Effect Spectroscopy (ROESY) analyses were provided in Supplementary Figures S1, S2, for adducts A and B, respectively. According to all the NMR data obtained, adducts A and B were assigned to be both as 6-(1-acetol)-8-(1-acetol)-rutin, in which MGO attacked the *ortho*-position at C-6 and C-8 in the aromatic A ring. The chemical shifts in adducts A and B were very close to each other, the main difference between the two compounds in the NMR spectra is that the chemical shifts of the corresponding carbons at C-11 and C-14 are more than 1.10 ppm, and the corresponding chemical shifts of hydrogen are more than 0.10 ppm, indicating that C-11 and C-14 in the two compounds possess different chiral centers. Therefore, adducts A and B were supposed to be optical isomers, which possess identical planar molecular structures.

Determination of 6-(1-acetol)-8-(1-acetol)-rutin in commercial foods

Flavonoids could efficiently trap MGO generated during thermal processing of carbohydrate and lipid rich food materials by the formation of corresponding adducts (15). Rutin is widely distributed in various grains. Its content was announced to be the highest in buckwheat, which ranges from 0.17 to 17.95 g/kg (32). Other grains, such as wheat, barley, quinoa, oat, and potato also contained rutin in moderate levels up to 38.3 mg/kg (33), 20.6 mg/kg (34), 5.8 mg/kg (35), 3.2 mg/kg (36), and 36 mg/kg (37), respectively. Therefore, the occurrence of rutin-MGO adducts in thermally processed foods were expected. To determine whether the unoxidized adducts of rutin and MGO exist in foods, 15 different food products randomly collected from the local market were analyzed. However, only one sample (code 4 listed in Table 2) contained detectable amount of unoxidized rutin-MGO adducts, with the values of 0.27 mg/kg and 0.89 mg/kg for adducts A and B, respectively. The contents of the oxidized adducts were also determined, which were 0.41 ± 0.07, 2.85 ± 0.17, and

TABLE 3 Plasma concentration of adducts A and B in rats administrated with 100 mg/kg BW rutin.

Time point (h)	Adduct A (μg/L)	Adduct B (μg/L)
0.00	N.D. ^a	N.D.
0.25	9.40 ± 6.37	6.40 ± 3.90
0.50	N.D.	N.D.
1.00	trace	trace
2.00	trace	trace
4.00	N.D.	N.D.
6.00	N.D.	N.D.
8.00	N.D.	trace
10.00	trace	N.D.
24.00	N.D.	trace

^aN.D., not detected.

0.29 ± 0.09 mg/kg, respectively, for 6-(1,2-propanedione)-8-(1-acetol)-rutin, 6-(1-acetol)-8-(1,2-propanedione)-rutin, and 6-(1,2-propanedione)-8-(1,2-propanedione)-rutin. The sum of oxidized adducts were 3-folds higher than that of the unoxidized ones. Furthermore, samples with codes of 1, 3, and 5-9 were investigated in our previous study (22) and also showed considerable amount of oxidized adducts in ranges of 0.15–1.43, 0–2.43, and 0.29–2.79 mg/kg for 6-(1,2-propanedione)-8-(1-acetol)-rutin, 6-(1-acetol)-8-(1,2-propanedione)-rutin, and 6-(1,2-propanedione)-8-(1,2-propanedione)-rutin, respectively. All of these might indicate that the unoxidized rutin-MGO adducts would undergo oxidation during processing and storage of the foods after their formation, and predominantly exist in oxidized forms in the commercial products.

Plasma concentration variation of 6-(1-acetol)-8-(1-acetol)-rutin after rutin administration

To satisfy the need of pharmacokinetics investigation of exogenous substances such as those in foods and drugs, various methods have been developed and applied including radiography, fluorescent analysis, liquid chromatography, and LC-MS/MS. Among them, LC-MS/MS analysis was the most promised with much better specificity, less limitation and wider application range (38, 39). MRM mode of HPLC-MS/MS analysis has shown advantages for the identification and determination of exogenous substances and their metabolites in complex biological samples especially when the compounds were at extremely low-abundance levels (39, 40), and therefore, was applied herein to measure the concentration levels of rutin-MGO adducts in plasma and organs to reveal the formation, metabolism and distribution of adducts *in vivo*. As shown in Table 3, 9.40 and 6.40 μg/L of adducts A and

TABLE 4 Concentrations of rutin-MGO adducts in tissues, urine, and feces of rats after 24 h of rutin administration (100 mg/kg BW).

Tissue	Concentration ($\mu\text{g/kg}$ for tissues and feces; $\mu\text{g/L}$ for urine)				
	6-(1,2-propanedione)-8-(1-acetol)-rutin	6-(1-acetol)-8-(1,2-propanedione)-rutin	6-(1,2-propanedione)-8-(1,2-propanedione)-rutin	Adduct A	Adduct B
Stomach	N.D. ^a	trace	0.10 ± 0.01	N.D.	N.D.
Duodenum	N.D.	N.D.	N.D.	N.D.	N.D.
Jejunum	N.D.	N.D.	N.D.	N.D.	N.D.
Ileum	trace	trace	trace	N.D.	N.D.
Caecum	N.D.	N.D.	trace	N.D.	N.D.
Colon	N.D.	trace	N.D.	N.D.	N.D.
Liver	trace	trace	0.09 ± 0.01	N.D.	N.D.
Kidney	0.07 ± 0.01	0.12 ± 0.02	0.16 ± 0.04	trace	trace
Heart	0.09 ± 0.03	trace	0.14 ± 0.09	N.D.	N.D.
Brain	0.11 ± 0.02	0.45 ± 0.28	0.12 ± 0.02	N.D.	N.D.
Urine	trace	0.09 ± 0.00	0.10 ± 0.01	N.D.	N.D.
Feces	1.54 ± 0.49	2.23 ± 0.54	0.26 ± 0.18	Trace	Trace

^aN.D., not detected.

B, respectively, were detected in the plasma 15 min after the administration of rutin. At that time, the formation of oxidized rutin-MGO adducts, 6-(1,2-propanedione)-8-(1-acetol)-rutin, 6-(1-acetol)-8-(1,2-propanedione)-rutin, and 6-(1,2-propanedione)-8-(1,2-propanedione)-rutin were 2.38, 1.61, and 1.02 $\mu\text{g/L}$, respectively (22). These results indicated that rutin reacts with endogenous MGO after ingestion, and form mainly unoxidized adducts initially. But these unoxidized adducts remained in the plasma only for a very short period, with none or only trace levels of these adducts detected after 30 min of rutin administration. Compared to the sharp concentration decline of unoxidized adducts, the oxidized adducts decreased gradually to 0.39–0.67 $\mu\text{g/L}$ after 4 h, and remained constantly at these levels until 24 h. This indicated that the unoxidized adducts are easily metabolized or excreted through circulation, whereas the oxidized ones are much more stable and retained longer in blood circulation. In an anesthetized, mesenteric lymphatic/duodenum-cannulated rat model, the plasma concentration of rutin reached maximum at 60 min, and declined afterwards (41). Therefore, the structural differences of these compounds should determine to a large extent to their metabolic and pharmacokinetic properties *in vivo*.

Distribution of different rutin-MGO adducts in tissues of rats

Furthermore, we investigated all of the unoxidized and oxidized adducts formed between rutin and MGO after 24 h of rutin administration. This was not conducted in the previous study (22). We found that the unoxidized adducts A and B were

hardly remained in all the tissues after 24 h. Only trace amount of unoxidized adducts were detected in the kidney. The highly oxidized adduct, 6-(1,2-propanedione)-8-(1,2-propanedione)-rutin, was detected at the level of 0.10 $\mu\text{g/kg}$ in stomach, but was not detected over LOQ level in the intestine. The two moderately oxidized adducts, 6-(1,2-propanedione)-8-(1-acetol)-rutin and 6-(1-acetol)-8-(1,2-propanedione)-rutin, were hardly detected at quantitative levels in the gastrointestinal tract. Interestingly, although these oxidized adducts hardly existed in the digestive tract, their occurrence in organs of kidney, heart and brain were detected. In liver, only 6-(1,2-propanedione)-8-(1,2-propanedione)-rutin existed in dosable level (0.09 $\mu\text{g/kg}$). These data indicated that the unoxidized rutin-MGO adducts, which displayed higher pharmacokinetic rate, could hardly accumulate in tissues. While the oxidized rutin-MGO adducts were the predominant deposit forms of the adducts between rutin and MGO, and lasting in tissues for long periods after oral administration. Rutin has been reported to possess various biological activities and present clinically relevant functions, but is of poor bioavailability which is mainly owing to its low solubility. Studies indicated that changes of the solubility of rutin, not only in the aqueous phase but also in lipid phase, might influence greatly the bioavailability of rutin (24). For example, the rutin concentration in brain of rats intranasally administrated with rutin loaded chitosan nanoparticles was significantly 7-folds higher than that in rats treated with rutin solution (42). Thus, it was speculated that the oxidized structures of rutin-MGO adducts might change the solubility properties and the bioavailability of the compounds, and facilitate them to pass the blood-brain barrier in rats.

Excretion of different rutin-MGO adducts via urine and feces

In the current study, the urine and fecal samples were collected within 24 h after the rats were orally administrated with rutin (100 mg/kg BW). Different unoxidized and oxidized adducts were detected and quantified with the HPLC-MS/MS method developed and the corresponding synthetic adduct prepared by our laboratory as the authentic standard. As shown in Table 4, the unoxidized adducts were not detected in any urine samples. They appeared in the feces only at detectable levels. In contrast, the three oxidized adducts were all detected at quantitative levels in feces. Moreover, the adducts oxidized at one moiety of MGO substitute were the major forms of the adducts excreted in feces. The content of the highly oxidized 6-(1,2-propanedione)-8-(1,2-propanedione)-rutin was 6–9-folds <6-(1,2-propanedione)-8-(1-acetol)-rutin and 6-(1-acetol)-8-(1,2-propanedione)-rutin. In urine samples, only 6-(1-acetol)-8-(1,2-propanedione)-rutin and 6-(1,2-propanedione)-8-(1,2-propanedione)-rutin were detected at levels of 0.09 and 0.10 µg/L, respectively. The other adducts were not found or only observed in trace amount over the LOD level. The excretion of unoxidized flavonoid-MGO adducts from urine and feces has been reported by other researchers in acute and chronic studies of mice. Zhang et al. treated mice with 100–400 mg/kg BW of myricetin by oral gavage, and detected two mono-MGO-myricetin adducts in the urine and fecal samples collected afterwards (26). Huang et al. observed there were three isomers of mono-MGO adducts of epicatechin and seven isomers of di-MGO adducts in urine samples collected from the mice fed with 200 mg/kg BW of epicatechin and 1.0 g/kg BW of MGO (29). In contrast to our findings, Wang et al. (27) observed both the mono- and di-MGO adducts of genistein in the *in vitro* study, but only found two peaks corresponding to the mono-MGO adducts *in vivo* by selected ion monitoring (SIM) in HPLC-MS analysis. This indicated that different flavonoid structures would derive totally different adducts *in vivo* after trapping of MGO. Moreover, this was the first time that the oxidized flavonoid-MGO adducts were found *in vivo*, and displayed to be the predominant forms excreted and accumulated in certain tissues, which might indicate that the unoxidized flavonoid-MGO adducts would undergo further oxidation to yield oxidized adducts during digestion and metabolism.

Cytotoxicity of 6-(1-acetol)-8-(1-acetol)-rutin in different cell lines

Although the flavonoid-MGO adducts were proven to be formed both in foods and *in vivo* in the current and the other studies (22, 26–30), their safety concerns were hardly evaluated.

Gastric and intestinal mucosae form the barrier between the body and the ingested substances in the lumens (43). Endothelial cells are involved in the exchanges of metabolites between blood and tissues (44). Thus, both the gastrointestinal epithelial cells and the endothelial cells could be target of numerous xenobiotics. Given the discovery of unoxidized rutin-MGO adducts in both the commercial foods and in animal plasma, evaluation of the toxicity of these adducts are very important for the sake of food safety concerns. Cell proliferation was thought to be the primary point of control in the regulation of normal tissue kinetic homeostasis, and has been the major focus of the etiology of diseases (45). Therefore, in order to get a first insight and assessment on the safety of the formation of flavonoid-MGO adducts, we evaluated the cytotoxicity of the rutin-MGO adducts toward the GES-1, Caco-2 and HUVEC cell lines representing gastrointestinal epithelial cells and vascular endothelial cells by determination of the cell viability under different treatment levels of the adducts in comparison to those of MGO and rutin (43, 44, 46). As shown in Figure 3, MGO displayed remarkable cytotoxicity toward GES-1 in a clear dose-dependent manner. The growth of the cells was inhibited by 18–19% when treated with 200–400 µM MGO, while more than 50% was inhibited when treated with 600 µM MGO. When the treatment level of MGO further increased to 1 mM, only 17% of the cells left alive. In comparison, the viability of HUVEC cells was not impacted by 200 µM MGO treatment, while decreased significantly to 47% when treated with 400 µM MGO, then became resistant and kept within the range of 44–49% at treatment levels of 600–1,000 µM. The Caco-2 cells were more resistant toward MGO treatment than both GES-1 and HUVEC cells as observed previously in our other studies (22, 47). The viability of Caco-2 cells was between 83 and 100% when treated with 200–800 µM of MGO. It decreased further to 56% when treated with 1.0 mM MGO. In comparison to MGO, rutin displayed much less toxicity toward all the cells tested. Only 16, 15, and 12% of the cells were dead under the highest treatment level (1 mM) of rutin in GES-1, Caco-2, and HUVEC cell lines, respectively. Adducts A and B also displayed comparable low cytotoxicity toward the three cell lines. As shown in Figure 3, treatment with 1 mM of adducts A and B reduced the cell viability by 27 and 25% in GES-1 cell line; by 19 and 18% in Caco-2 cell line; and by 19 and 16% in HUVEC cell line, respectively. Through the comparison of cell proliferation under different treatments with MGO, rutin and the adducts, it was indicated that the formation of unoxidized rutin-MGO adducts significantly mitigated the cytotoxicity of MGO to a level comparable to that of rutin. Since the oxidized adducts formed between rutin and MGO also displayed much lower toxicity toward these gastrointestinal epithelial cell lines and vascular endothelial cell line compared to that of MGO (22), the scavenging of MGO by rutin and the consequent formation of various rutin-MGO adducts were suggested not to only inhibit the formation of AGEs, but also to lower the toxicity of MGO.

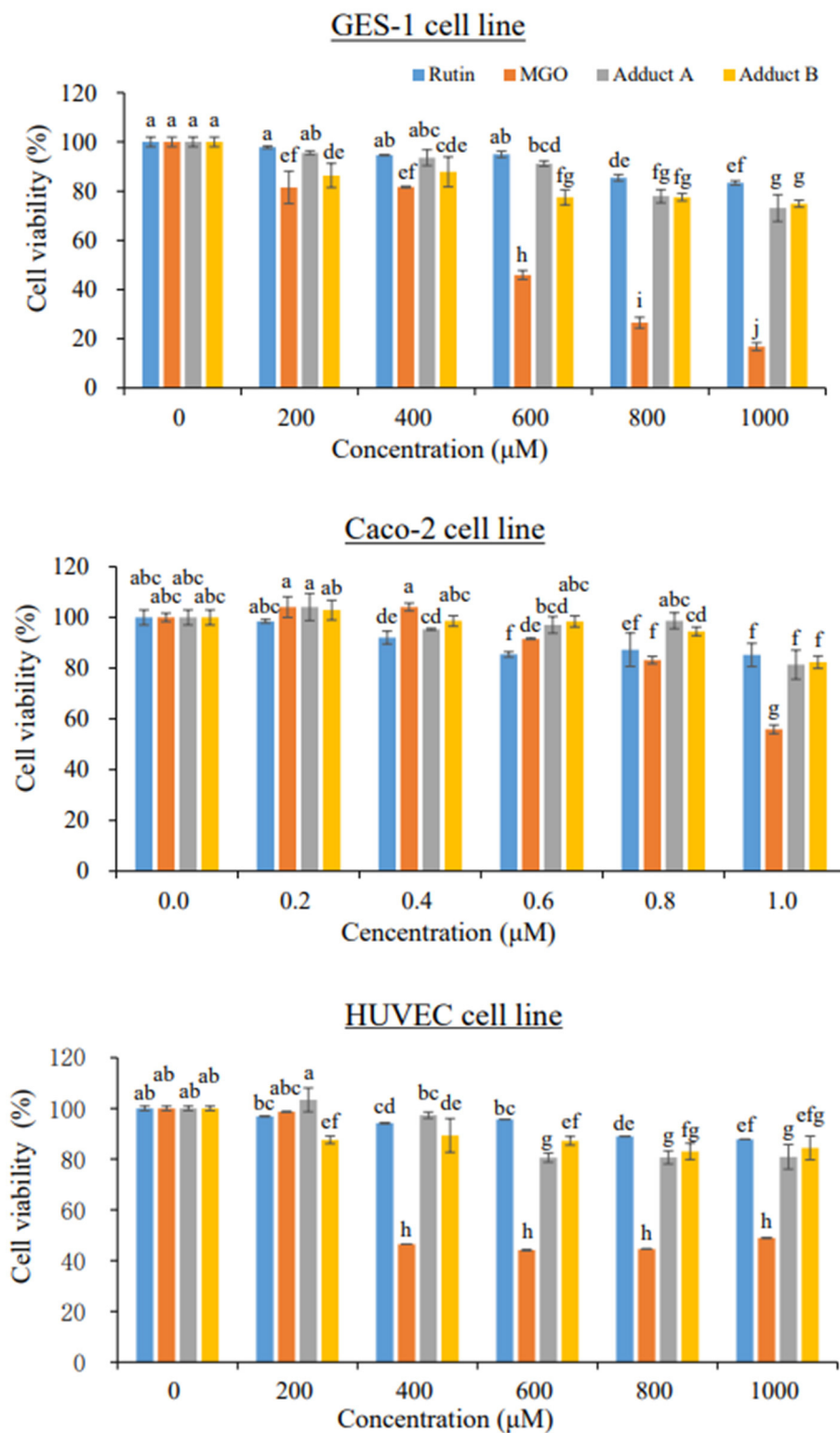


FIGURE 3

Cell viability of GES-1 (upper), Caco-2 (middle), and HUVEC cells (bottom) under 24 h treatments by different concentrations of rutin, MGO, adduct A, and adduct B. Different letters represent significant differences ($P < 0.05$).

Conclusion

In our previous study, we identified for the first time three oxidized rutin-MGO adducts with dione structures formed in foods and *in vivo*. This study focused on the unoxidized rutin-MGO adducts. Through separation and purification, the di-MGO adducts of rutin obtained were identified by HPLC-MS/MS and NMR analysis to be optical isomers of 6-(1-acetol)-8-(1-acetol)-rutin. They were detected in commercial thermal processed foods, although in much less amounts than the oxidized rutin-MGO adducts detected previously (22). The animal study showed that 6-(1-acetol)-8-(1-acetol)-rutin were first formed in larger amount than the oxidized rutin-MGO *in vivo*, and appeared in the blood circulation at a total level of 15.80 $\mu\text{g/L}$ after 15 min of oral gavage of rutin. But they were detected only in trace levels in the blood circulation after 30 min of rutin administration, which indicated that they might be quickly metabolized (including oxidation to oxidized adducts) or excreted. In the 24 h urine and fecal samples collected, the oxidized adducts again presented as the predominant adducts excreted. Moreover, the unoxidized rutin-MGO adducts were hardly detected in all the tissues investigated, while the oxidized adducts still deposited in detectable amount in kidney, heart and brain after 24 h of oral intake of rutin. Considering their appearance in foods and *in vivo*, the cytotoxicity of the adducts were evaluated in gastrointestinal epithelial cells and vascular endothelial cells, and were proven to be much lower than their precursors of MGO. The results of this study further promised the application of rutin as an effective MGO scavenger and AGEs inhibitor both in food production and for health intervention.

Data availability statement

The original contributions presented in the study are included in the article/Supplementary material, further inquiries can be directed to the corresponding author/s.

Ethics statement

The animal study was reviewed and approved by Institutional Animal Care and Use Committee of the Laboratory Animal Center of Jinan University.

Author contributions

Conceptualization: JZ, WZ, and YX. Methodology: JZ, CH, and JO. Data curation, funding acquisition, and supervision: JZ. Investigation: MC, HZ, YX, and PL. Formal analysis: JH

and JO. Validation: JH and YX. Writing—original draft: PL and JZ. Writing—review & editing: JZ, HZ, CH, and HE-N. Project administration: JZ and WZ. All authors contributed to the article and approved the submitted version.

Funding

This work was financed by the National Natural Science Foundation of China (grant number 31972180); the Basic and Applied Basic Research Fund of Guangdong Province (grant numbers 2019A1515011967, 2021A1515010822, and 2019A1515011994); the Fundamental Research Funds for the Central Universities of Jinan University (grant number 21620107); the Pearl River Talent Program (grant number 20170096) by Guangdong Science and Technology Department, Guangdong, China.

Acknowledgments

We acknowledge the Analytical and Testing Center in Jinan University for providing the instruments for the HPLC-MS/MS and NMR analyses in this study. We also appreciate the technical assistance by Ms. Aihua Hong in the HPLC-MS/MS analyses.

Conflict of interest

Authors WZ and YX were employed by the company “Dongguan Silang Foods Co., Ltd.”

The remaining authors declare that the research was conducted in the absence of any commercial or financial relationships that could be construed as a potential conflict of interest.

Publisher's note

All claims expressed in this article are solely those of the authors and do not necessarily represent those of their affiliated organizations, or those of the publisher, the editors and the reviewers. Any product that may be evaluated in this article, or claim that may be made by its manufacturer, is not guaranteed or endorsed by the publisher.

Supplementary material

The Supplementary Material for this article can be found online at: <https://www.frontiersin.org/articles/10.3389/fnut.2022.973048/full#supplementary-material>

References

- Distler MG, Palmer AA. Role of glyoxalase 1 (Glo1) and methylglyoxal (MG) in behavior: recent advances and mechanistic insights. *Front Genet.* (2012) 3:250. doi: 10.3389/fgene.2012.00250
- Rabbani N, Thornalley PJ. Measurement of methylglyoxal by stable isotopic dilution analysis LC-MS/MS with corroborative prediction in physiological samples. *Nat Protoc.* (2014) 9:1969–79. doi: 10.1038/nprot.2014.129
- Jang HW, Jiang YP, Hengel M, Shibamoto T. Formation of 4(5)-methylimidazole and its precursors, α -dicarbonyl compounds, in Maillard model systems. *J Agric Food Chem.* (2013) 61: 6865–72. doi: 10.1021/jf401958w
- Ni MT, Song X, Pan JH, Gong DM, Zhang GW. Vitexin inhibits protein glycation through structural protection, methylglyoxal trapping, and alteration of glycation site. *J Agric Food Chem.* (2021) 69:2462–76. doi: 10.1021/acs.jafc.0c08052
- Zheng J, Ou J, Ou S. Alpha-dicarbonyl compounds. In: *Chemical Hazards in Thermally-Processed Foods*. Singapore: Springer Nature (2019). p. 19–46. doi: 10.1007/978-981-13-8118-8_2
- Wang Y, Ho CT. Flavour chemistry of methylglyoxal and glyoxal. *Chem Soc Rev.* (2012) 41:4140–9. doi: 10.1039/c2cs35025d
- Atrott J, Haberlau S, Henle T. Studies on the formation of methylglyoxal from dihydroxyacetone in Manuka (*Leptospermum scoparium*) honey. *Carbohydr Res.* (2012) 361:7–11. doi: 10.1016/j.carres.2012.07.025
- Adams CJ, Manley-Harris M, Molan PC. The origin of methylglyoxal in New Zealand manuka (*Leptospermum scoparium*) honey. *Carbohydr Res.* (2009) 344:1050–3. doi: 10.1016/j.carres.2009.03.020
- Nemet I, Varga-Defterdarović L, Turk Z. Methylglyoxal in food and living organisms. *Mol Nutr Food Res.* (2006) 50:1105–17. doi: 10.1002/mnfr.200600065
- Saxena RK, Anand P, Saran S, Isar J, Agarwal L. Microbial production and applications of 1, 2-propanediol. *Indian J Microbiol.* (2010) 50:2–11. doi: 10.1007/s12088-010-0017-x
- Matafome P, Sena C, Seica R. Methylglyoxal, obesity, and diabetes. *Endocrine.* (2013) 43:472–84. doi: 10.1007/s12020-012-9795-8
- Schalkwijk CG, Stehouwer CDA. Methylglyoxal, a highly reactive dicarbonyl compound, in diabetes, its vascular complications, and other age-related diseases. *Physiol Rev.* (2020) 100:407–61. doi: 10.1152/physrev.00001.2019
- Scheijen J, Schalkwijk CG. Quantification of glyoxal, methylglyoxal and 3-deoxyglucosone in blood and plasma by ultra performance liquid chromatography tandem mass spectrometry: evaluation of blood specimen. *Clin Chem Lab Med.* (2014) 52:85–91. doi: 10.1515/cclm-2012-0878
- Dong L, Qiu C, Wei F, Yu Z, Zhang Y, Wang S. The effect of microwave-baking conditions on the quality of biscuits and the control of thermal processing hazards of Maillard reaction. *Front Nutr.* (2022) 9:825365. doi: 10.3389/fnut.2022.825365
- Zheng J, Guo H, Ou J, Liu P, Huang C, Wang M, et al. Benefits, deleterious effects and mitigation of methylglyoxal in foods: a critical review. *Trends Food Sci Tech.* (2021) 107:201–12. doi: 10.1016/j.tifs.2020.10.031
- Cömert ED, Gökmen V. Kinetic evaluation of the reaction between methylglyoxal and certain scavenging compounds and determination of their in vitro dicarbonyl scavenging activity. *Food Res Int.* (2019) 121:257–68. doi: 10.1016/j.foodres.2019.03.046
- Ou J, Wang M, Zheng J, Ou S. Positive and negative effects of polyphenol incorporation in baked foods. *Food Chem.* (2019) 284:90–9. doi: 10.1016/j.foodchem.2019.01.096
- Cao H, Chen BH, Inbaraj BS, Chen L, Alvarez-Rivera G, Cifuentes A, et al. Preventive potential and mechanism of dietary polyphenols on the formation of heterocyclic aromatic amines. *Food Front.* (2020) 1:134–51. doi: 10.1002/fft2.30
- Higbee J, Solverson P, Zhu M, Carbonero F. The emerging role of dark berry polyphenols in human health and nutrition. *Food Front.* (2022) 3:3–27. doi: 10.1002/fft2.128
- Catalkaya G, Venema K, Lucini L, Rocchetti G, Delmas D, Daglia M, et al. Interaction of dietary polyphenols and gut microbiota: Microbial metabolism of polyphenols, influence on the gut microbiota, and implications on host health. *Food Front.* (2020) 1:109–33. doi: 10.1002/fft2.25
- Zhao C, Wan X, Zhou S, Cao H. Natural polyphenols: A potential therapeutic approach to hypoglycemia. *eFood.* (2020) 1:107–18. doi: 10.2991/efood.k.200302.001
- Chen M, Zhou H, Huang C, Liu P, Fei J, Ou J, et al. Identification and cytotoxic evaluation of the novel rutin–methylglyoxal adducts with dione structures in vivo and in foods. *Food Chem.* (2022) 377:132008. doi: 10.1016/j.foodchem.2021.132008
- Hosseinzadeh H, Nassiri-Asl M. Review of the protective effects of rutin on the metabolic function as an important dietary flavonoid. *J Endocrinol Invest.* (2014) 37:783–8. doi: 10.1007/s40618-014-0096-3
- Gullón B, Lú-Chau TA, Moreira MT, Lema JM, Eibes G. Rutin: A review on extraction, identification and purification methods, biological activities and approaches to enhance its bioavailability. *Trends Food Sci Tech.* (2017) 67:220–35. doi: 10.1016/j.tifs.2017.07.008
- Lapa FD, Soares KC, Rattmann YD, Crestani S, Missau FC, Pizzolatti MG, et al. Vasorelaxant and hypotensive effects of the extract and the isolated flavonoid rutin obtained from *Polygala paniculata* L. *J Pharm Pharmacol.* (2011) 63:875–81. doi: 10.1111/j.2042-7158.2010.01240.x
- Zhang SW, Xiao LB, Lv LS, Sang SM. Trapping methylglyoxal by myricetin and its metabolites in mice. *J Agric Food Chem.* (2020) 68:9408–14. doi: 10.1021/acs.jafc.0c03471
- Wang P, Chen HD, Sang SM. Trapping methylglyoxal by genistein and its metabolites in mice. *Chem Res Toxicol.* (2016) 29:406–14. doi: 10.1021/acs.chemrestox.5b00516
- Zhao YT, Wang P, Sang SM. Dietary genistein inhibits methylglyoxal-induced advanced glycation end product formation in mice fed a high-fat diet. *J Nutr.* (2019) 149:776–87. doi: 10.1093/jn/nxz017
- Huang QJ, Wang P, Zhu YD, Lv LS, Sang SM. Additive capacity of [6]-shogaol and epicatechin to trap methylglyoxal. *J Agric Food Chem.* (2017) 65:8356–62. doi: 10.1021/acs.jafc.7b02917
- Liu PZ, Yin Z, Chen M, Huang CH, Wu ZH, Huang JQ, et al. Cytotoxicity of adducts formed between quercetin and methylglyoxal in PC-12 cells. *Food Chem.* (2021) 352:129424. doi: 10.1016/j.foodchem.2021.129424
- Yoon SR, Shim SM. Inhibitory effect of polyphenols in *Houttuynia cordata* on advanced glycation end-products (AGEs) by trapping methylglyoxal. *LWT-Food Sci Technol.* (2015) 61:158–63. doi: 10.1016/j.lwt.2014.11.014
- Jiang P, Burczynski F, Campbell C, Pierce G, Austria JA, Briggs CJ. Rutin and flavonoid contents in three buckwheat species *Fagopyrum esculentum*, *F-tataricum*, and *F-homotropicum* and their protective effects against lipid peroxidation. *Food Res Int.* (2007) 40:356–64. doi: 10.1016/j.foodres.2006.10.009
- Suchowilska E, Bienkowska T, Stuper-Szablewska K, Wiwart M. Concentrations of phenolic acids, flavonoids and carotenoids and the antioxidant activity of the grain, flour and bran of *Triticum polonicum* as compared with three cultivated wheat species. *Agriculture.* (2020) 10:591. doi: 10.3390/agriculture10120591
- Yang XJ, Dang B, Fan MT. Free and bound phenolic compound content and antioxidant activity of different cultivated blue highland barley varieties from the Qinghai-Tibet Plateau. *Molecules.* (2018) 23:879. doi: 10.3390/molecules23040879
- Starzyńska-Janiszewska A, Stodolak B, Gómez-Caravaca AM, Mickowska B, Martín-García B, Byczyński Ł. Mould starter selection for extended solid-state fermentation of quinoa. *LWT-Food Sci Technol.* (2019) 99:231–7. doi: 10.1016/j.lwt.2018.09.055
- Bei Q, Liu Y, Wang L, Chen G, Wu Z. Improving free, conjugated, and bound phenolic fractions in fermented oats (*Avena sativa* L) with *Monascus anka* and their antioxidant activity. *J Funct Foods.* (2017) 32:185–94. doi: 10.1016/j.jff.2017.02.028
- Tudela JA, Cantos E, Espín JC, Tomás-Barberán FA, Gil MI. Induction of antioxidant flavonol biosynthesis in fresh-cut potatoes. Effect of domestic cooking. *J Agric Food Chem.* (2002) 50:5925–31. doi: 10.1021/jf020330y
- Liu M, Li N, Zhang Y, Zheng Z, Zhuo Y, Sun B, et al. Characterization of covalent protein modification by triclosan in vivo and in vitro via three-dimensional liquid chromatography-mass spectrometry: New insight into its adverse effects. *Environ Int.* (2020) 136:105423. doi: 10.1016/j.envint.2019.105423
- Gong S, Zhuo Y, Chen S, Hu X, Fan XX, Wu JL, Li N. Quantification of osimertinib and metabolite–protein modification reveals its high potency and long duration of effects on target organs. *Chem Res Toxicol.* (2021) 34:2309–18. doi: 10.1021/acs.chemrestox.1c00195
- Hu X, Wu JL, Miao W, Long F, Pan H, Peng T, et al. Covalent protein modification: An ignorable factor for bisphenol A-induced hepatotoxicity. *Environ Sci Technol.* (2022) 56: 9536–45. doi: 10.1021/acs.est.2c01307
- Chen IL, Tsai YJ, Huang CM, Tsai TH. Lymphatic absorption of quercetin and rutin in rat and their pharmacokinetics in systemic plasma. *J Agric Food Chem.* (2010) 58:546–51. doi: 10.1021/jf9026124
- Ahmad N, Ahmad R, Naqvi AA, Alam MA, Samim M, Iqbal Z, et al. Quantification of rutin in rat's brain by UHPLC/ESI-Q-TOF-MS/MS

after intranasal administration of rutin loaded chitosan nanoparticles. *EXCLI J.* (2016) 15:518. doi: 10.17179/excli2016-361

43. Cui J, Xing L, Li Z, Wu S, Wang J, Liu J, et al. Ochratoxin A induces G2 phase arrest in human gastric epithelium GES-1 cells *in vitro*. *Toxicol Lett.* (2010) 193:152–8. doi: 10.1016/j.toxlet.2009.12.019

44. Gutiérrez-Praena D, Pichardo S, Jos Á, Moreno FJ, Cameán AM. Alterations observed in the endothelial HUVEC cell line exposed to pure Cylindrospermopsin. *Chemosphere.* (2012) 89:1151–60. doi: 10.1016/j.chemosphere.2012.06.023

45. Haake AR, Polakowska RR. Cell death by apoptosis in epidermal biology. *J Invest Dermatol.* (1993) 101:107–12. doi: 10.1111/1523-1747.ep12363594

46. Moyes SM, Morris JF, Carr KE. Culture conditions and treatments affect Caco-2 characteristics and particle uptake. *Int J Pharmaceut.* (2010) 387:7–18. doi: 10.1016/j.ijpharm.2009.11.027

47. Wang G, Liu P, He J, Yin Z, Yang S, Zhang G, et al. Identification of a 5-hydroxymethylfurfural-lysine Schiff base and its cytotoxicity in three cell lines. *J Agric Food Chem.* (2019) 67:10214–21. doi: 10.1021/acs.jafc.9b04539



OPEN ACCESS

EDITED BY

Jie Zheng,
Jinan University, China

REVIEWED BY

Chunqing Guo,
School of Medicine, Virginia
Commonwealth University,
United States
Hou-Zao Chen,
Chinese Academy of Medical Sciences
and Peking Union Medical
College, China

*CORRESPONDENCE

Pin Lv
lvpin@hebmu.edu.cn
Yan Zhang
snowwinglv@126.com

[†]These authors have contributed
equally to this work

SPECIALTY SECTION

This article was submitted to
Food Chemistry,
a section of the journal
Frontiers in Nutrition

RECEIVED 26 June 2022

ACCEPTED 14 July 2022

PUBLISHED 04 August 2022

CITATION

Fu C, Li Y, Xi H, Niu Z, Chen N, Wang R,
Yan Y, Gan X, Wang M, Zhang W,
Zhang Y and Lv P (2022)
Benzo(a)pyrene and cardiovascular
diseases: An overview of pre-clinical
studies focused on the underlying
molecular mechanism.
Front. Nutr. 9:978475.
doi: 10.3389/fnut.2022.978475

COPYRIGHT

© 2022 Fu, Li, Xi, Niu, Chen, Wang, Yan,
Gan, Wang, Zhang, Zhang and Lv. This
is an open-access article distributed
under the terms of the [Creative
Commons Attribution License \(CC BY\)](#).
The use, distribution or reproduction
in other forums is permitted, provided
the original author(s) and the copyright
owner(s) are credited and that the
original publication in this journal is
cited, in accordance with accepted
academic practice. No use, distribution
or reproduction is permitted which
does not comply with these terms.

Benzo(a)pyrene and cardiovascular diseases: An overview of pre-clinical studies focused on the underlying molecular mechanism

Chenghao Fu^{1†}, Yuemin Li^{1†}, Hao Xi¹, Zemiao Niu¹,
Ning Chen¹, Rong Wang¹, Yonghuan Yan², Xiaoruo Gan¹,
Mengtian Wang², Wei Zhang³, Yan Zhang^{2,4*} and Pin Lv^{1*}

¹Department of Cell Biology, Cardiovascular Medical Science Center, Key Laboratory of Neural and Vascular Biology of Ministry of Education, Hebei Medical University, Shijiazhuang, China, ²Hebei Key Laboratory of Forensic Medicine, College of Forensic Medicine, Hebei Medical University, Shijiazhuang, China, ³Eco-Environmental Monitoring Center of Hebei Province, Shijiazhuang, China, ⁴Hebei Food Safety Key Laboratory, Hebei Food Inspection and Research Institute, Shijiazhuang, China

Benzo(a)pyrene (BaP) is a highly toxic and carcinogenic polycyclic aromatic hydrocarbon (PAH) whose toxicological effects in the vessel-wall cells have been recognized. Many lines of evidence suggest that tobacco smoking and foodborne BaP exposure play a pivotal role in the dysfunctions of vessel-wall cells, such as vascular endothelial cell and vascular smooth muscle cells, which contribute to the formation and worsening of cardiovascular diseases (CVDs). To clarify the underlying molecular mechanism of BaP-evoked CVDs, the present study mainly focused on both cellular and animal reports whose keywords include BaP and atherosclerosis, abdominal aortic aneurysm, hypertension, or myocardial injury. This review demonstrated the aryl hydrocarbon receptor (AhR) and its relative signal transduction pathway exert a dominant role in the oxidative stress, inflammation response, and genetic toxicity of vessel-wall cells. Furthermore, antagonists and synergists of BaP are also discussed to better understand its mechanism of action on toxic pathways.

KEYWORDS

Benzo(a)pyrene, cardiovascular diseases, AhR, oxidative stress, inflammation, genotoxicity

Introduction

BaP is a crystalline, aromatic hydrocarbon consisting of five fused benzene rings found in coal tar with the formula $C_{20}H_{12}$ in the nineteenth century (1). The main sources of BaP in food are from pollution materials in the environment or produced by the pyrolysis of amino acids, fatty acids, and carbohydrates (2). The BaP is formed during the incomplete combustion of organic matter at temperatures between 300 and 600°C,

and is primarily found in automobile emissions, cigarette smoke, coal tar and charcoal-broiled foods (3, 4). Due to their lipophilic and hydrophobic characteristics, polycyclic aromatic hydrocarbon (PAH) finally accumulates in the food chain. Dietary exposure accounts for more than 90% of the total exposure to PAHs in the general population in various countries (5). Nowadays, BaP is the first pollution indicator of PAHs in food designated by the scientific community (6).

Cardiovascular diseases (CVDs) are associated with DNA damage, including DNA adduct and oxidative DNA damage, in both circulating and vessel-wall cells. And environmental chemical carcinogens have been identified to be as a risk factor for CVDs (7–10). In addition, collective evidence from these studies revealed that the cardiovascular toxicity of foodborne contaminants is mainly attributed to PAHs, especially BaP. However, no literature review focuses on the association between BaP and CVDs. In this review, we aimed to provide a comprehensive understanding of the mechanism of cell toxicity effects of BaP in CVDs, mainly focusing on atherosclerosis (AS), hypertension (HTN), and abdominal aortic aneurysm (AAA).

Sources, metabolism and tissue toxicity of BaP

The primary sources of PAH contamination can be divided into two groups: anthropogenic pollution and natural pollution. Natural sources of PAHs are negligible or less important. The significant determinants of PAH pollution are anthropogenic pollution sources, classified into four groups, i.e., industrial, mobile, domestic, and agricultural pollution sources (11). In fact, the main source of exposure to PAHs for non-smokers and non-occupationally exposed adults are food. Diet contributes to more than 90% of total PAHs exposures in the general population in various countries (2, 5). PAHs can generate during the food preparation procession (contaminated by environmental PAH that are present in air, soil, or water by deposition and transfer), or during processing and cooking (12). BaP is the first pollution indicator of PAHs in food. Therefore, foodborne BaP contaminants are a primary source of BaP uptake by humans.

After entering the body, except for a small part of BaP excreted in the feces in its original form, most of the BaP accumulated in the gastrointestinal tract, epididymal fat, lung, liver, brain, and kidney (13). BaP is highly lipophilic and can be easily absorbed into cells through the plasma membrane. BaP can be metabolized into dozens of metabolites through AhR and aromatic hydrocarbon metabolizing enzymes (14–16), such as 1, 2-dihydroxy-1, 2-dihydrobenzopyrene, benzopyrene diketone, and BPDE. The conversion to hydroxyl compounds or ketones is a detoxification reaction, while the conversion to epoxide is an activation reaction. About 10% of BaP is converted to BPDE in the organism (17). BPDE has a strong oxidizing capacity, which

can cause oxidative damage to DNA, affect DNA replication, and induce apoptosis and gene mutation.

BaP is well known for its carcinogenic activity early in 1930, and numerous studies since the 1970s have documented links between BaP intake and cancers (1, 18, 19). It has been classified as class I carcinogen by the International Agency for Research on Cancer (www.iarc.who.int). The exposure of BaP results in extensive and selective formation of BPDE, which has high interaction activity with DNA and forms a DNA adduct, the major mutagen in tobacco smoke (7, 20). Properly speaking, BaP is a procarcinogen. Its carcinogenic effects depend on the activity of the detoxification enzymes cytochrome P450 1A1 (CYP1A1) and CYP1B1, which enzymatic metabolism BaP to BPDE (21, 22). Furthermore, BaP induces the CYP1A1 gene expression by activating the AhR nuclear translocation signal pathway (23, 24). Furthermore, most of the BPDE-DNA adducts can be removed from DNA by nucleotide excision repair mechanism within the cell. Therefore, continuous or high doses of BaP intake will inevitably cause errors during DNA replication leading to carcinogenic mutations (23–25). Besides, there is growing evidence that BaP has strong toxic effects on the nervous system (26), immune system (27, 28), and reproductive system (29).

AhR is a ligand-activated transcription factor best known for mediating carcinogen toxicity and tumor-promoting properties, including dioxin and BaP (30). AhR belongs to the basic helix-loop-helix transcription factors family. And numerous studies have revealed that the toxicity of BaP has been linked to activation of the AhR (31–33). In the absence of ligands, AhR exists predominantly in the cytosolic compartment in association with a chaperone complex (Hsp90/XAP/p23) (30). Upon BaP binding to AhR, dimerization of AhR and the aryl hydrocarbon receptor nuclear translocator (ARNT) occurs. The AhR/ARNT heterodimer then binds to xenobiotic responsive elements (XREs) (core sequence: GCGTG) in the promoters of BaP-regulated genes, such as cytochrome P450s (CYPs), intercellular cell adhesion molecule 1 (ICAM1), vascular cell adhesion molecule 1 (VCAM1), and prostaglandin endoperoxide synthase 2 (PTGS2) (33–35).

CYPs are membrane-associated proteins that use molecular oxygen and reduce the equivalents of NADPH to catalyze oxidative, peroxidative, and reductive metabolism of endogenous and exogenous substrates (36). More than 400 genes encoding CYP-associated activities have been cloned, but their relative expression exhibits remarkable tissue, gender, and developmental specificity (37). Kerzee and Ramos investigated constitutive and inducible expression of these two CYPs from AhR knockout mice. Their results show that the expression of CYP1A1 was inducible in BaP-treated AhR^{+/+} mice, and CYP1B1 was expressed under constitutive and inducible conditions irrespective of AhR phenotype or growth status (36). In mouse aortic smooth muscle cells, BaP increased the aryl hydrocarbon hydroxylase activity. The specific inhibitor of CYP1B1, but not CYP1A1, could reverse the BaP-induced

DNA adducts formation, which may contribute to atherogenesis by PAHs (38). Furthermore, CYP1A1^{-/-} and AhR^{-/-} mice formed smaller atherosclerotic lesions size and oxidative stress when suffering over 10 weeks of 10 mg/kg/body weight(bw) BaP treatment (39, 40).

Vascular toxicity effects and underlying mechanism of BaP

As early as 1977, it was reported that the aorta was the target organ of BaP (41). However, it is only in recent years, the cardiovascular toxicity of BaP attracted considerable attention. Currently, as an independent risk factor for CVDs, BaP has been found to be closely related to CVDs, including AS, HTN and AAA, and shows multiple kinds of vascular toxicity (10, 11, 13, 42). Preclinical studies have found that BaP exposure is correlated with oxidative stress and vascular toxicity. In addition, investigations have discovered a relationship between BaP exposure and the occurrence and development of CVDs (11).

Atherogenic effect of BaP

Atherosclerosis (AS) is a chronic pathological process in the large artery wall and is characterized by the accumulation of oxidized lipid, fibrous elements, and calcification. This process is initiated by endothelium injury, followed by a cascade of events, which causes the vessel narrowing and activation of inflammatory responses leading to atheroma plaque formation (43–45). As a result, these processes result in multiple cardiovascular complications, including myocardial infarction, heart failure, stroke, and claudication, which remain the leading cause of death globally (46). Moreover, this complex disease is caused by the interaction of multiple genetic and environmental risk factors, which include western pattern diet, tobacco smoking, and air pollution (45).

In ApoE^{-/-} background atherosclerotic animal models, 4 days of 5–8 mg/kg/bw BaP grave treatment can increase the serum epsilon A and high-density lipoprotein (HDL) level (47). Moreover, the BPDE-DNA adduct could also be observed in the aorta tissues (47), while compared to the control groups, 12–24 weeks of treatment increased the expression of monocyte chemoattractant protein 1 (MCP1), and promoted the release of transforming growth factor beta (TGFβ) and tumor necrosis factor α (TNFα) in vascular wall cells (48–50). In response to the inflammatory mediator, the atherosclerosis lesion may be heavily infiltrated with pro-inflammation cells, including macrophages, T cells and neutrophils (49), and the lesion size began to enlarge (13, 50).

Exposure to BaP plays a vital role in the etiology of atherosclerosis (Table 1). The endothelium represents the inner

cell layer of blood vessels and is supported by smooth muscle cells and pericytes, which form the vessel structure (51). Due to direct blood contact, the blood vessel endothelium is inevitably exposed to genotoxic substances that are systemically taken up by the body, including BaP (17). One key step in the development of atherosclerosis is vascular endothelial dysfunction, followed by cell death and a local inflammatory response (48, 53, 67). Besides, there is strong evidence to suggest oxidative stress is one of the most potent inducers of vascular inflammation in atherogenesis. nuclear factor-κB (NF-κB) may respond directly to BaP-induced oxidative stress, and the activation of NF-κB is a key redox-sensitive event associated with vascular dysfunction (54).

Caveolae are non-clathrin-coated plasma membrane microdomains enriched in cholesterol and glycosphingolipids. They are particularly abundant in endothelial cells and play an important role in membrane traffic and cellular signal transduction (52, 68). Oesterling and his collage observed that caveolin-1 mediated the BaP-induced ICAM1 expression in primary human endothelial cells. They also illustrated that β-naphthoflavone/BaP induced ICAM1 expression by signaling through MEK, MAPK, and AP-1 leading to increased adhesion of monocytes to the activated endothelium (52, 68).

Besides, BaP-induced bulky DNA adducts and the consequent DNA mutations in vascular cells are considered to be involved in AS (31). BaP forms BPDE through a three-step activation process catalyzed by human cytochrome P450 enzymes, notably CYP1A1 and CYP1B1, and by epoxide hydrolase (17). A screening for DNA repair factors in BPDE treated human umbilical vein endothelial cells (HUVECs) revealed that the nucleotide excision repair (NER) proteins excision repair cross-complementation (ERCC) 1, ERCC 4 and ligase I were expressed at lower levels in HUVECs compared with human umbilical artery smooth muscle cells (HUASMCs) and haemopoietic progenitor cell (HPCs), which corresponds with the impaired NER-mediated removal of BPDE adducts from DNA (17). These data revealed that HUVECs is more sensitive to BPDE than HPCs and HUASMCs and displays an unexpected DNA repair-impaired phenotype.

Vascular smooth muscle cells (VSMCs) are located in the mid-membrane of the vascular wall and are responsible for the structural characteristics of the vessel wall. Abnormal proliferation, migration, and invasion of VSMCs have been suggested to be the major contributor to the development of atherosclerotic lesions (57, 58, 69). Evidence shows that BaP could activate interleukin 6 (IL6) production and suppress nitric oxide-induced apoptosis in VSMCs. A significant role of IL6 in the pathophysiology of atherosclerosis has also been suggested, and atherosclerosis even has been suggested to be an inflammatory disease (69, 70). Furthermore, BaP was capable of inducing the activation of NF-κB and MAPK in VSMCs. Both NF-κB inhibitor and MAPK inhibitor significantly reversed

TABLE 1 Effects of BaP on AS.

	Models	Treatment	Effects	Reference
Cell model	HUVECs	1 $\mu\text{mol/L}$ BaP for 2 h	pro-inflammation and enhance COX2, CYP1A1 and cPLA2 activity; \uparrow CYP1A1, ICAM1, VCAM1, \downarrow PTGS2, PLA2G4A, NOS3 gene expression	(51)
		10–25 $\mu\text{mol/L}$ for 24 h	\uparrow monocyte adhesion and ICAM-1 depend on AhR activation, \uparrow MEK, p38-MAPK, c-Jun phosphorylation; \uparrow AP-1 DNA binding	(52)
		0.5–1.5 $\mu\text{mol/L}$ BPDE for 96 h	\uparrow apoptosis, necrosis, \downarrow ERCC1, ERCC4 and ligase I, \uparrow BPDE-DNA adducts	(17)
		0–10 $\mu\text{mol/L}$ for 4 or 24 h	\uparrow MCP1, CYP1A1, \downarrow cell viability	(48)
		10 $\mu\text{mol/L}$ for 1–5 d	\uparrow VEGF, and can be reversed by ERK inhibitor	(53)
		10 μM for 24h	\uparrow CCL1, CYP1A1 in an AhR- and calcium-dependent manner	(32)
	Human endothelial progenitor cells	10–50 $\mu\text{mol/L}$ for 24 h	\downarrow proliferation, migration, adhesion, and angiogenesis, \uparrow IL1 β , TNF α , ROS, \uparrow NF- κ B activation	(54)
		0.1–10 $\mu\text{mol/L}$ for 5–7 d	\downarrow adherent and proliferation, \uparrow CYP1A1, and reversed by AhR antagonist, \uparrow PAH-related adducts	(55)
	Human fetoplacental ECs	0.01–1 $\mu\text{mol/L}$ for 6–24 h	\downarrow angiogenesis, \uparrow COX2, PTGS2 mediated by AhR activation	(33)
	Human coronary artery ECs	30 $\mu\text{mol/L}$ for 0–140 min	\uparrow 3H-arachidonate release and apoptosis, \uparrow phospholipase A2 activation	(56)
Animal models	Mouse aortic endothelial cells	1 $\mu\text{mol/L}$	\uparrow Cu/Zn- SOD and catalase, \uparrow AhR, CYP1A1/1B1 protein level; \uparrow GST activity and BaP detoxification;	(31)
	Rat VSMCs	10 $\mu\text{mol/L}$ for 24 h	\downarrow NO-induced apoptosis, \uparrow NF- κ B and MAPK, \uparrow IL6 production	(57)
		0.1–2 $\mu\text{mol/L}$ for 24 h	\uparrow cell migration and invasion, \uparrow MMPs, and inhibited by MMPs inhibitor or AhR antagonist	(58)
		0–10 $\mu\text{mol/L}$ for 0–30 h	\downarrow T-cadherin, and reversed by AhR antagonist a-naphthoflavone	(59)
		0.1–5 $\mu\text{mol/L}$ for 24 h	\uparrow COX2, prostaglandin, ERK phosphorylation, and NF- κ B activation; reversed by MAPK or NF- κ B inhibitor	(60)
		3 $\mu\text{mol/L}$ for 24 h	\uparrow C/EBP- α/β , ARE/EpRE repressed, whereas AhR enhanced, GST-Ya gene expression	(61)
	Mouse VSMCs	3 $\mu\text{mol/L}$ for 24 h	\uparrow DNA adducts, \uparrow aryl hydrocarbon hydroxylase and CYP1B1 activity	(38)
		3 $\mu\text{mol/L}$ for 1–5 h	\uparrow CYP1A1, CYP1B1 and reversed by AhR knockout	(36)
		0.03–3 $\mu\text{mol/L}$ for 24 h	\uparrow ROS, ARE/EpRE, \downarrow c-Ha-ras transcription	(62)
		0.3–2 $\mu\text{mol/L}$ for 1–5 h	\uparrow c-Ha-ras and oxidative stress; inhibited by P450 or AhR inhibitor ellipticine	(63)
		10 μM for 24 h	TGF β 2 and IGF1 are potential candidates signaling pathways of AhR	(64)
	HAECs, HCSMCs	3 $\mu\text{mol/L}$ for 24 h	\downarrow prolyl-4-hydroxylase, \downarrow cellular collagen levels, atherosclerotic cap thickness	(65)
	ApoE ^{-/-} mice	5 mg/kg/bw daily for 4 d	\uparrow aorta BPDE-DNA adduct, epsilon A, and HDL level	(47)
		5 mg/kg/bw, weekly for 2 w	\uparrow aortic tissue MCP1 gene expression	(48)
		5 mg/kg/bw, weekly for 12–24 w	\uparrow plaques and lipid core size; \uparrow T cells and macrophages infiltration;	(49)

(Continued)

TABLE 1 Continued

Models	Treatment	Effects	Reference
	5 mg/kg/bw, weekly for 24 w	↑ PAH-DNA adducts in lung, ↑ TGFβ and TNFα release, ↑ atherosclerotic plaque size	(50)
	8.5 mg/kg/bw daily for 24 w	↑ inflammatory response, ↑ atherosclerosis lesion size	(13)
ApoE ^{-/-} mice; CYP1A1 ^{-/-} mice	12.5 mg/kg/day	↑ atherosclerotic lesions, ↑ ROS level, ↑ inflammatory markers, ↑ VEGF gene expression, ↑ DNA adduct formation	(39)
ApoE ^{-/-} ; AhR ^{bi/bi} and ApoE ^{-/-} ; AhR ^{d/d}	10 mg/kg/bw, 5 days/week for 10–23 w	↑(↓) plaque size and initial time, ↑(↓) AhR affinity, ↑(↓) immune response genes	(40)
ApoE ^{-/-} ; hSod1 ^{-/-} mice	2.5 mg/kg/bw weekly for 24 w	↑ oxidized lipids, ↑ atherosclerotic lesions; and ↓ cell adhesion molecules, monocyte adhesion, ↓ oxidized lipids, ↓ atherosclerotic lesions	(66)

“↑” means up-regulation and “↓” means down-regulation; human aortic endothelial cells (HAECs); human coronary artery smooth muscle cells (HCSMCs); unless noted the treatment agent is BaP in all Tables.

the anti-apoptotic effect of BaP on NO-induced VSMCs apoptosis (57).

Matrix metalloproteinases (MMPs) are a family of over 20 different endopeptidases that each degrades several extracellular matrix proteins and non-matrix substrates. MMPs play a major role in cell migration, differentiation, angiogenesis, and host defense (71). Expression of various MMPs was found to increase in BaP-induced transcriptional activation of MMPs, especially MMP3, is not through activator protein 1 (AP-1) or NF-κB, and the expression of MMPs increased the migration and invasion ability of VSMCs in rats (58). Besides, when treated with BaP, the expression level of T-cadherin, an atypical glycosylphosphatidylinositol-anchored member of the cadherin superfamily of adhesion molecules, is significantly repressed (59). However, further investigation of the relationship between the upregulation of MMPs and T-cadherin degradation still needs further exploration.

Cyclooxygenase (COX2), also known as prostaglandin-endoperoxide synthase (PTGS2), is a rate-limiting enzyme responsible for prostaglandins forming and plays both physiologic and pathologic roles in vascular function. In BaP-treated VSMCs, ERK and NF-κB signal pathways are involved in the expression of COX2, which may participate in the genesis of AS (60).

Miller and his colleagues observed that treatment of VSMC with BaP induced reactive oxygen species (ROS) accumulation which leads to a variety of different outcomes, including activation of nuclear proteins to bind antioxidant response element/electrophilic response element (ARE/EpRE), activation of cytosolic proteins that translocate and bind ARE/EpRE, or redox sensor that interacts with cellular proteins to activate binding to ARE/EpRE. As a result, oxidative intermediates of BaP mediate activation of nuclear protein binding to ARE/EpRE and contribute to transcriptional de-regulation of c-Ha-ras (62). Kerzee et al. (63) found the upregulation of oxidative stress and c-Ha-ras in VSMCs could be reserved by CYPs and AhR inhibitor ellipticine. Chen et al. (61) observed another nuclear protein CCAAT/enhancer-binding protein alpha and beta (C/EBP-α, β) which was activated by AhR signal pathway and lead to the inhibition of glutathione S-transferase (GST)-Ya subunit gene expression. In addition, overexpression of antioxidant enzymes suppressed BaP-accelerated atherosclerosis in ApoE-deficient mice (66, 72).

BaP and hypertension

Hypertension (HTN), also known as high blood pressure, is a long-term medical condition in which the blood pressure in the arteries is persistently elevated (7). HTN usually does not cause noticeable symptoms. However, long-term untreated HTN is a major risk factor for heart attacks, stroke, atrial fibrillation, heart failure, and peripheral arterial disease. HTN is a major cause

of premature death worldwide (73, 74). Over 90% of HTN is classified as a primary type and is usually caused by unhealthy lifestyles such as a high salt diet, overweight, alcohol drinking, and smoking. The remaining cases are categorized as secondary types due to identifiable causes, including chronic kidney disease, narrowing of the kidney arteries, and an endocrine disorder (73).

Studies have shown that systolic blood pressure is significantly increased, and aortic responsiveness to phenylephrine is enhanced in rats exposed to BaP (Table 2). Inhibitors of protein kinase C (PKC), MAPK, myosin light-chain kinase (MLCK) and Rho kinases significantly inhibit BaP-enhanced vasoconstriction (Table 2). BaP induces ROS production in vascular smooth muscle cells in a time-dependent manner (7). Heart rate was not affected in BaP-treated sprague-dawley rats, however, weight loss, markedly elevated blood pressure (14). BaP exposure may affect cardiovascular development and increased systolic blood pressure. Jules et al. (76) show that exposure to BaP results in functional deficits in offspring during cardiovascular development, which may lead to cardiovascular dysfunction later in life. BaP exposure altered the circadian pattern of blood pressure, with a reduction in the normal dipping pattern during sleep. This was associated with increased neutrophil recruitment in the lungs of BaP-exposed rats (75). Intraperitoneal injection of BaP up regulated the expression of CYP1A, CYP1B1, CYP1C1, CYP1C2, and COX1 in zebrafish mesenteric arteries suggesting that BaP is associated with changes in cardiovascular function (77).

BaP and abdominal aortic aneurysm

Abdominal aortic aneurysm (AAA) is defined as a localized enlargement of the abdominal aorta more than 50% of its diameter. The aortic wall continues to weaken and becomes unable to hold the forces of the luminal blood pressure, resulting in progressive dilatation and rupture. They usually cause no symptoms, except during rupture. Smoking and advanced age are the primary risk factors for AAA; if ruptured, the mortality is 85–90% (42, 92).

Co-stimulation of male C57BL/6J mice with angiotensin (Ang) II and BaP induced AAA significantly increased rates of formation and mean aortic diameter. The samples were subjected to circRNA expression analysis, and a circRNA-miRNA co-expression network was established based on six apoptosis-related circRNAs. Genes regulated by this network map to multiple pathways, including apoptosis, IL-17 signaling, and vascular endothelial growth factor signaling, all of which are involved in AAA formation (78). BaP increases macrophage infiltration, activates NF- κ B, upregulates MMP2, MMP9, and MMP12 expression, elastic lamina disorder, and VSMCs loss (79), which increased AAA formation and rupture in C57/B6J mice (80). Furthermore, the metabolites of BaP such as

7,8-dihydrodiol, 3,6-, and 6,12-dione metabolites are reported involvement in BaP induced abdominal aortic toxicity *via* elevating plasma ROS levels and increased protein expression of TNF α , CYP1A1, and MMP9 (42).

BaP and myocardial injury

In BaP-treated offspring rats, microarray and quantitative real-time PCR analysis revealed that the up-regulated gene expression of AngII, angiotensinogen and, eNOS, which are associated with the dysregulate cardiovascular development (76). BaP increased heart-to-body weight ratios, as well as hypertrophy markers, atrial natriuretic peptide and brain natriuretic peptide. BaP treatment increased the gene expression of CYP1A1, CYP1B1, CYP2E1, CYP4F4, CYP4F5 and soluble epoxide hydrolase. BaP treatment increased the ratios of dihydroxyecosatrienoic acid and 20-hydroxyecosatetraenoic acid in total epoxyecosatrienoic acid. Benzo(e)pyrene, an isomer of BaP and a poor ligand for AhR, did not cause cardiac hypertrophy in rats, confirming the role of AhR in the development of cardiac hypertrophy (82). Zebrafish exposed to solutions containing 5 μ mol/L BaP treatment exhibit cardiovascular malformations. Microarray analysis was performed to identify heart-specific transcriptomic changes in BaP/fluoranthene (FL) during early development, with Ca²⁺ cycling and muscle contraction genes being the most differentially expressed class of transcripts (Table 2). BaP/FL may affect cellular Ca²⁺ levels, which subsequently affect myocardial function and may underlie BaP/FL cardiotoxicity (84). Exposure of zebrafish embryos to BaP for 72 h resulted in defective cardiac development in zebrafish embryos (85). BaP co-exposure with alpha-naphthoflavone or resveratrol resulted in the most dramatic changes in heart and vessel morphology, with decreased ventricular length and width, increased ventricular wall thickness, and increased vessel lumen diameter. In addition, decreased expression of COX2, which is inversely associated with cardiac malformations and vasodilation (86). Moreover, BaP-induced NCF1/p47(phox) expression enhances superoxide anion production in an AhR-dependent manner in PMA-treated human macrophages; regulation of NCF1/NADPH oxidase by such PAHs may be involved in atherosclerotic heart disease associated with vascular disease such as sclerosis (81).

BaP and angiogenesis

BaP exposure is also associated with angiogenesis both *in vivo* and *in vitro* (Table 2). Evidence shows that BaP reduced corpus luteum number, disrupted steroid secretion, affected the corpus luteum vascular network in pregnant female mice, and significantly decreased angiogenic factors (VEGFR, Ang-1, and

TABLE 2 Effects of BaP on HTN and AAA.

	Models	Treatment	Effects	Reference
Hypertension	Rat aortas and VSMCs Sprague-Dawley rats	1–10 μ mol/L BaP	\uparrow vasoconstriction and reversed by AhR, PKC, MAPK, MLCK, and Rho-kinase inhibitor; \uparrow ROS	(7)
		20 mg/kg/bw for 8 w	\uparrow systolic blood pressure, \uparrow aortic hyperreactivity to phenylephrine	(7)
		0.01 mg/kg, Intranasal	altered rhythm of blood pressure, \uparrow lung neutrophil recruitment	(75)
		0.15–1.2 mg/kg/ bw at E14–17	\uparrow blood pressure relative genes NOS, eNOS, NADP oxidoreductase (BH4/BH2) and AngII	(76)
		10 mg/kg/bw, weekly for 4 w	\uparrow blood pressure	(14)
	Zebrafish	1 mg/kg/bw for 24 h	\uparrow CYP1A, CYP1B1, CYP1C1, CYP1C2, and COX-1 in mesenteric artery	(77)
Abdominal Aortic Aneurysm	WT mouse + Ang II	10 mg/kg/bw, weekly for 6 w	\uparrow AAA pathogenesis, \uparrow VSMC apoptosis	(78)
		10 mg/kg/bw, weekly for 5 w	\uparrow AAA incidence, \uparrow macrophage infiltration, elastic lamella degeneration	(79)
		10 mg/kg/bw, weekly for 5 w	\uparrow AAA pathogenesis, \uparrow macrophage infiltration, \uparrow MMP2, MMP9, MMP12, NF- κ B expression	(80)
	ApoE ^{-/-} mouse+Ang II	5 mg/kg/bw, weekly for 7 w	\uparrow AAA pathogenesis, \uparrow TNF α , Cyp1 A, MMP9	(42)
Myocardial injury	Sprague-Dawley rats	0–10 μ mol/L BaP for 0–48 h	\uparrow ROS, \uparrow NCF1/p47(phox) in macrophages, and reversed by AhR knock down	(81)
		20 mg/kg/bw for 7 d	\uparrow cardiac hypertrophy, \uparrow CYP1A1, CYP1B1, CYP2E1, CYP4F4, CYP4F5 and soluble epoxide hydrolase	(82)
	Zebrafish embryos	5 μ mol/L	\uparrow cardiac abnormalities, \uparrow CYP1A1,	(83)
		100 μ g/L for 2–18 h	\uparrow cardiac deformities, Ca ²⁺ -cycling gene alteration	(84)
		0.02–2 μ mol/L for 72 h	\uparrow cardiotoxicity, \uparrow AhR1B, CYP1C1, CYP1A1, MMP9, \downarrow prox1, tbx5, pak2a	(85)
		5,000 ng/L for 5 d	\uparrow cardiac deformities, \uparrow CYP1A, \downarrow COX2b	(86)
Angiogenesis	HUVECs	0.5 μ mol/L (BPDE)	\downarrow angiogenesis, \downarrow Notch1, \uparrow Dll4, Jag1, and \downarrow Hey2	(10)
		0–10 μ mol/L for 24 h	\downarrow angiogenesis, \downarrow integrin α v/ β 3, AhR, MAPK phosphorylation, \uparrow CYP1A1	(87)
	Zebrafish embryos	1 μ mol/L for 24–96 h	\uparrow cardiovascular toxicity, \downarrow AhR2, myh6, \uparrow CYP1A, atp2a2	(88)
	Japanese medaka	0.1–1 μ g/L for 6 d	\uparrow heart hypertrophy, \uparrow CYP2J23, Coro2A	(89)
	WT and AhR-null mice	125 mg/kg/bw weekly for 4 w	\uparrow ischemia-induced angiogenesis, \uparrow IL6, VEGF in AhR-null mice	(90)
	Kunming mice	0.2–20 mg/kg/ bw for 1–8 d	\downarrow decidual angiogenesis, \downarrow CD34, ER, FOXO1, HoxA10, and BMP2	(91)
	Sprague-Dawley rats	0.2 mg/kg/bw for 9 d	\downarrow luteal angiogenesis and vascular maturation, \downarrow VEGFR, Ang-1 and Tie2, \uparrow THBS1	(10)

“ \uparrow ” means up-regulation and “ \downarrow ” means down-regulation.

TABLE 3 Antagonist and synergistic agents of BaP.

	Models	Treatment	Effects	Reference
Antagonist agent	Resolvin D1	HUVECs	↓ BaP-induced CYP1A1, PTGS2, COX2, cPGES, ↑ GSTM1 level; and ↑ cPLA2, ↓ CYP1A1 activity	(97)
	Flavonoids	HUVECs	↓ BaP-induced ICAM1 expression in HUVEC	(98)
	Hesperidin	Human EAhy-926 cells	↓ BaP-induced AhR activation, ↑ ABCA1, ↓ IL-1β and TNFα, ↓ LDL accumulation	(99)
	Ostreococcus tauri and Phaeodactylum tricornutum Extracts	Human micro-vascular endothelial cell	↓ cell apoptosis and extracellular vesicles, ↓ CYP1A1, IL-8 and IL1-β	(100)
	Budesonide-poly(lactide-co- glycolide)	A/J mice	↓ BaP-induced oxidative stress, and vascular leakage, ↓ VEGF and c-myc expression	(101)
	Soluble epoxide hydrolase inhibitor	Sprague-Dawley rats	reversed the BaP-induced CYP1A1, CYP1B1, CYP4F4, and CYP4F5 ↑	(102)
	Ginkgo biloba extract	Stomach Neoplasms mice	↓ ameliorating cardiotoxic effects of doxorubicin, ↓ serum NO, ↓ liver cytosolic glutathione S-transferase, G6PDH activity	(103)
Synergistic agent	1,25(OH)2D3	THP-1 and U937 cells	↑ BaP-DNA adduct formation	(104)
	Carbon black particles	Human EAhy-926 cells	↑ cell proliferation, migration and invasion, and metabolism, ↓ PPARγ activity	(105)
	SiNPs	HUVECs	↑ ROS, DNA damage, cell cycle arrest, ↑ bax, caspase-3, and caspase-9, ↓ Cdc25C, cyclin B1, bcl-2	(106)
		Zebrafish embryos	↑ inflammation and coagulation, ↑ pAP-1/c-Jun, CD142	(107)
		Zebrafish embryos	signaling pathway alteration such as MAPK, PI3K-Akt, JAK/STAT	(108)

“↑” means up-regulation and “↓” means down-regulation.

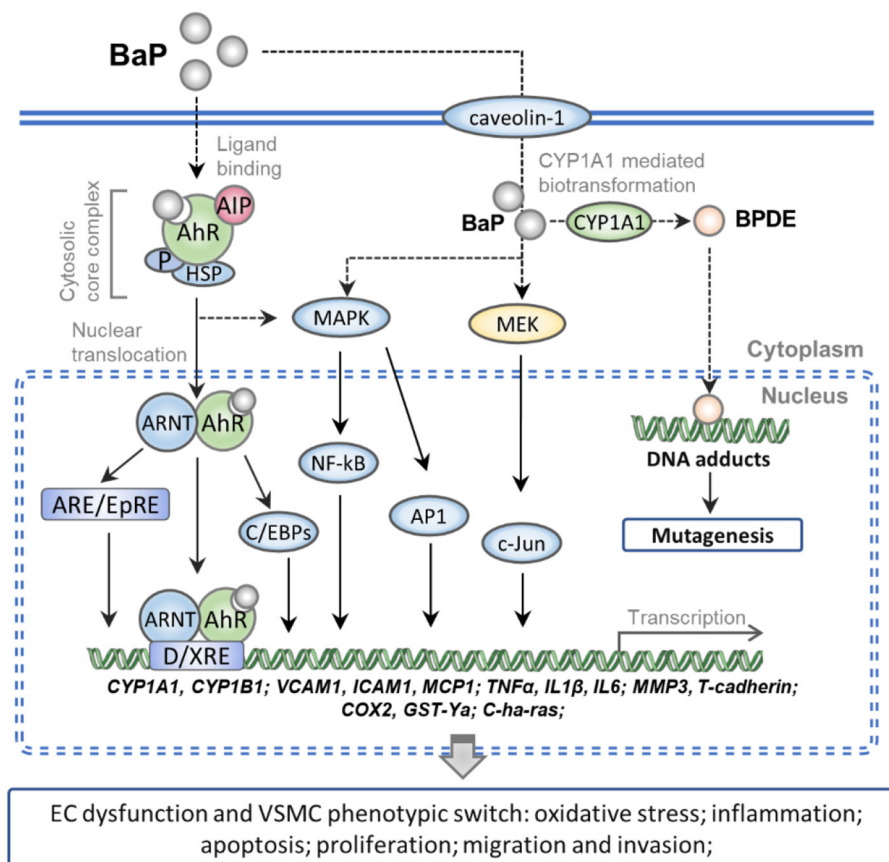


FIGURE 1

Schematic representation of the molecular mechanism of BaP exposure-induced CVDs. Numerous pieces of evidence show that the caveolin-1 can facilitate entry of the BaP into vessel-wall cells. The AhR complex is translocated into nuclear after binding with intracellular BaP. And then the BaP-AhR complex could activate the AhR/ARNT/XRE, MEK/c-Jun, and MAPK/NF-kB/AP-1 signaling pathway which can up-regulate the gene of CYPs, cell adhesion molecules, pro-inflammatory factors, and peroxidase. Besides, the activated CYP1A1 actually increased the metabolism of BaP into BPDE, which can form DNA adducts and induce mutation. As a result, BaP exposure increases the ECs dysfunction and VSMC phenotypic switch which accelerates the pathological progress of CVDs.

Tie2), and increased the anti-angiogenic factor THBS1. The BaP metabolite BPDE also interfered with the expression levels of angiogenesis-related factors, such as Notch signaling molecules in HUVECs *in vitro* (10). The expression of several decidua-related factors was altered, including FOXO1, HoxA10, and BMP2 (Table 2). BaP reduced CD34 expression, suggesting that BaP treatment inhibited decidual angiogenesis. Furthermore, BaP induced the downregulation of vascular endothelial growth factors suggesting that oral administration of BaP impairs decidualization and decidual angiogenesis (91).

After exposure to BaP, the expression of metallothionein was upregulated in the ischemic hindlimb of wild-type mice and markedly inhibited ischemia-induced angiogenesis. The mRNA amount of IL6 and VEGF was reduced in the ischemic hindlimb of wild-type mice (90). BaP-treated HUVECs reduced endothelial capillary formation, cell migration, MAPK phosphorylation, and integrin expression when stimulated by angiogenic factors. Angiogenesis was also inhibited in the chorionic villus assay (87).

Using zebrafish embryos model, 6H-benzo[cd]pyren-6-one induced developmental and cardiovascular toxicity at lower doses, including reduced heart rate and blood flow. The mixture of PAHs and oxy-PAHs may lead to increased developmental and cardiovascular toxicity of zebrafish embryos through an AhR-dependent mechanism (88). Embryonic teratogenicity and developmental toxicity of BaP in Japanese medaka, BaP was efficiently incorporated into embryos by nanosecond pulsed electric field treatment. Embryos containing BaP exhibited typical teratogenic and developmental effects, such as cardiovascular abnormalities, dysplasia, and spinal curvature (89).

BaP and other CVDs

Two blood-testis barrier proteins, Claudin-11 and Connexin 43, were impaired by treatment with a mixture of 1 µg/L streptozotocin and 1 µg/L BaP (93). The function of blood brain

barrier was assessed by measuring the transendothelial electrical resistance of mouse brain microvascular endothelial cells, and the viability of cells was altered in the presence of BaP (94). Besides, BaP elicited mouse testicular sertoli cells apoptosis and blood-testis barrier disruption, which involves mitochondrial dysfunction and oxidative stress (95). These evidence imply that BaP can damage vascular barrier which in turn cause other injury includes neurotoxicity and reproductive toxicity.

Chronic BaP exposure did not alter hepatocellular carcinoma cell (HCC) growth, but promoted cell migration and invasion both *in vitro* and *in vivo*. There was a negative correlation between BaP exposure and survival in tumor-bearing mice. In addition, BaP-treated HCC cells recruited vascular endothelial cells and promoted tumor angiogenesis, possibly by increasing the secretion of vascular endothelial growth factor. The NF- κ B pathway may be an adverse outcome pathway related to the cumulative effect of BaP on HCC metastasis (96).

Antagonist and synergistic agents of BaP

Numerous reports examined different types of agents in interfering BaP metabolism and molecular signing alteration, which have potential therapeutic implications in BaP induced CVDs (Table 3). Gdula-Argasińska et al. observed that resolvin D1, a product of transcellular biosynthesis with leukocytes and endothelial cells from docosa-hexaenoic acid, reversed the overexpression of COX2, cPGES and repression of GSTM1 protein after co-cultured with BaP incubated HUVEC. Besides, an increase of cPLA2 and a decrease of CYP1A1 activity were also noted in RvD1 and BaP co-treatment (97). These data suggested that resolvin D1 could contribute to vascular function and alleviate the harmful effects caused by BaP, which might potentially aid in repairing the injured endothelium. In addition, flavonoids that contain a 40 B-ring hydroxyl substitution and a 2-3 C-ring double bond can decrease proinflammatory molecular ICAM1 expression in endothelial cells (98). Two latest reports show that bioactive compounds, hesperidin, and phaeodactylum tricornutum extracts can also inhibit the pro-inflammation mediators, including IL1 β , TNF α , and IL8 (99, 100). Moreover, Budesonide-poly(lactide-co-glycolide), Soluble epoxide hydrolase inhibitor, and Ginkgo biloba extract have been proved to have anti-oxidative effects. In BaP-treated animals, the repression of ROS, NO, and CYP1A1 level and multiple cell protection effects were observed (100, 102, 103). Collectively, the above observations indicate that the anti-oxidative and anti-inflammation natural extract or inhibitors have potential protective effects on BaP-induced damage on vascular wall cells.

Using the zebrafish model, Duan and Asweto et al. found that co-exposure of silica nanoparticles and BaP activate the

AP-1/c-Jun and MAPK/PI3K signaling pathway, upregulate the expression of proinflammatory and procoagulant genes. As a result, silica nanoparticles help trigger the inflammation response and ROS generation, which could cause cardiac toxicity and erythrocyte aggregation (106–108). Interestingly, the protective effects of vitamin D on cardiovascular disease are principally mediated by the conversion of vitamin D to the active form, 1 α ,25-dihydroxy vitamin D3 [1,25(OH)2D3]. However, combined treatment with BaP and 1,25(OH)2D3 enhances BaP toxicity, including BaP-DNA adduct formation and ROS production (104).

Conclusions

The present review summarizes the molecular mechanisms underlying the vascular cell toxicity effects of BaP in CVDs as follows: (1) numerous studies have demonstrated that BaP can accelerate the pathological progress of AS, and many lines of evidence show that excessive daily BaP intake is a potent risk factor which accompanied by AAA, HTN, and MI. (2) BaP binds to the ligand-activated transcription factor AhR, which evokes oxidative stress and inflammation response molecules in ECs *via* activating the AhR/ARNT/XRE, MEK/c-Jun, and MAPK/NF- κ B/AP-1 signaling pathway. (3) BaP exposures increase the cell proliferation, migration, and invasion ability of VSMC by a similar signaling pathway in BaP-treated ECs. (4) The activation of CYP1A1 actually increased the genetic toxicity on vessel-wall cells through the metabolism of BaP into BPDE, which can form DNA adducts and induce mutation (Figure 1). Furthermore, compounds with AhR activation activity probability exert synergism effects on BaP vascular toxicity. In contrast, this toxicity might be alleviated by bioactive materials which process anti-oxidative and anti-inflammation action.

Author contributions

PL and YZ: ideas, conceptualization, supervision, and funding acquisition. CF and YL: resources, literature collection, and writing-review and editing. HX, ZN, NC, RW, YY, XG, MW, and WZ: literature collection and initial draft writing. All authors contributed to the article and approved the submitted version.

Funding

This work was supported by the National Key Research Project of China (2019YFC1606400), Major Public Welfare Projects in Henan Province (201300110200), National Key Research Project of Hebei Province (20375502D), Fund of National R&D Center for Edible Fungus Processing Technology, Henan University (20200109), Postdoctoral

Research Funds of Hebei Medical University (30705010016-3759), and University Science and Technology Research Project of Hebei Province (QN2017107).

Conflict of interest

The authors declare that the research was conducted in the absence of any commercial or financial relationships that could be construed as a potential conflict of interest.

References

- Phillips DH. Fifty years of benzo(a)pyrene. *Nature*. (1983) 303:468–72. doi: 10.1038/303468a0
- Domingo JL, Nadal M. Human dietary exposure to polycyclic aromatic hydrocarbons: a review of the scientific literature. *Food Chem Toxicol*. (2015) 86:144–53. doi: 10.1016/j.fct.2015.10.002
- Hu G, Cai K, Li Y, Hui T, Wang Z, Chen C, et al. Significant inhibition of garlic essential oil on benzo(a)pyrene formation in charcoal-grilled pork sausages relates to sulfide compounds. *Food Res Int*. (2021) 141:110127. doi: 10.1016/j.foodres.2021.110127
- Liao K, Yu JZ. Abundance and sources of benzo(a)pyrene and other PAHs in ambient air in Hong Kong: a review of 20-year measurements (1997–2016). *Chemosphere*. (2020) 259:127518. doi: 10.1016/j.chemosphere.2020.127518
- Alomirah H, Al-Zenki S, Al-Hooti S, Zaghoul S, Sawaya W, Ahmed N, et al. Concentrations and dietary exposure to polycyclic aromatic hydrocarbons (PAHs) from grilled and smoked foods. *Food Control*. (2011) 22:2028–35. doi: 10.1016/j.foodcont.2011.05.024
- Zhang Y, Chen X, Zhang Y. Analytical chemistry, formation, mitigation, and risk assessment of polycyclic aromatic hydrocarbons: from food processing to in vivo metabolic transformation. *Compr Rev Food Sci Food Saf*. (2021) 20:1422–56. doi: 10.1111/1541-4337.12705
- Tzeng H-P, Yang T-H, Wu C-T, Chiu H-C, Liu S-H, Lan K-C. Benzo(a)pyrene alters vascular function in rat aorta ex vivo and in vivo. *Vascul Pharmacol*. (2019) 121:106578. doi: 10.1016/j.vph.2019.106578
- Pulliero A, Godschalk R, Andreassi MG, Curfs D, Van Schooten FJ, Izzotti A. Environmental carcinogens and mutational pathways in atherosclerosis. *Int J Hyg Environ Health*. (2015) 218:293–312. doi: 10.1016/j.ijheh.2015.01.007
- Vayssier-Taussat M, Camilli T, Aron Y, Meplan C, Hainaut P, Polla BS, et al. Effects of tobacco smoke and benzo(a)pyrene on human endothelial cell and monocyte stress responses. *Am J Physiol Heart Circ Physiol*. (2001) 280:H1293–300. doi: 10.1152/ajpheart.2001.280.3.H1293
- Liu M, Deng T, He J, Ding Y, Liu X, Xu H, et al. Exposure to Benzo(a)pyrene impairs the corpus luteum vascular network in rats during early pregnancy. *Environ Pollut*. (2020) 259:113915. doi: 10.1016/j.envpol.2020.113915
- Mallah MA, Changxing L, Mallah MA, Noreen S, Liu Y, Saeed M, et al. Polycyclic aromatic hydrocarbon and its effects on human health: an overview. *Chemosphere*. (2022) 296:133948. doi: 10.1016/j.chemosphere.2022.133948
- Singh L, Varshney JG, Agarwal T. Polycyclic aromatic hydrocarbons' formation and occurrence in processed food. *Food Chem*. (2016) 199:768–81. doi: 10.1016/j.foodchem.2015.12.074
- Jin X, Hua Q, Liu Y, Wu Z, Xu D, Ren Q, et al. Organ and tissue-specific distribution of selected polycyclic aromatic hydrocarbons (PAHs) in ApoE-KO mouse. *Environ Pollut*. (2021) 286:117219. doi: 10.1016/j.envpol.2021.117219
- Gan TE, Xiao SP, Jiang Y, Hu H, Wu YH, Duerksen-Hughes PJ, et al. Effects of benzo(a)pyrene on the contractile function of the thoracic aorta of Sprague-Dawley rats. *Biomed Environ Sci*. (2012) 25:549–56. doi: 10.3967/0895-3988.2012.05.008
- Bolton JL, Trush MA, Penning TM, Dryhurst G, Monks TJ. Role of quinones in toxicology. *Chem Res Toxicol*. (2000) 13:135–60. doi: 10.1021/tx9902082
- Shimada T, Guengerich FP. Inhibition of human cytochrome P450 1A1-, 1A2-, and 1B1-mediated activation of procarcinogens to genotoxic metabolites by polycyclic aromatic hydrocarbons. *Chem Res Toxicol*. (2006) 19:288–94. doi: 10.1021/tx050291v
- Kress JM, Dio LD, Heck L, Pulliero A, Izzotti A, Laarmann K, et al. Human primary endothelial cells are impaired in nucleotide excision repair and sensitive to

Publisher's note

All claims expressed in this article are solely those of the authors and do not necessarily represent those of their affiliated organizations, or those of the publisher, the editors and the reviewers. Any product that may be evaluated in this article, or claim that may be made by its manufacturer, is not guaranteed or endorsed by the publisher.

benzo(a)pyrene compared with smooth muscle cells and pericytes. *Sci Rep*. (2019) 9:13800. doi: 10.1038/s41598-019-49953-w

18. Myers JN, Harris KL, Rekhadevi PV, Pratap S, Ramesh A. Benzo(a)pyrene-induced cytotoxicity, cell proliferation, DNA damage, and altered gene expression profiles in HT-29 human colon cancer cells. *Cell Biol Toxicol*. (2021) 37:891–913. doi: 10.1007/s10565-020-09579-5

19. Xue J, Zhao Q, Sharma V, Nguyen LP, Lee YN, Pham KL, et al. Aryl hydrocarbon receptor ligands in cigarette smoke induce production of interleukin-22 to promote pancreatic fibrosis in models of chronic pancreatitis. *Gastroenterology*. (2016) 151:1206–17. doi: 10.1053/j.gastro.2016.09.064

20. Weng MW, Lee HW, Park SH, Hu Y, Wang HT, Chen LC, et al. Aldehydes are the predominant forces inducing DNA damage and inhibiting DNA repair in tobacco smoke carcinogenesis. *Proc Natl Acad Sci U S A*. (2018) 115:E6152–e6161. doi: 10.1073/pnas.1804869115

21. Abbass M, Chen Y, Arlt VM, Stürzenbaum SR. Benzo(a)pyrene and *Caenorhabditis elegans*: defining the genotoxic potential in an organism lacking the classical CYP1A1 pathway. *Arch Toxicol*. (2021) 95:1055–69. doi: 10.1007/s00204-020-02968-z

22. Jee SC, Kim M, Kim KS, Kim HS, Sung JS. Protective effects of myricetin on benzo(a)pyrene-induced 8-hydroxy-2'-deoxyguanosine and BPDE-DNA adduct. *Antioxidants*. (2020) 9:446. doi: 10.3390/antiox9050446

23. Ghosh J, Chowdhury AR, Srinivasan S, Chattopadhyay M, Bose M, Bhattacharya S, et al. Cigarette smoke toxins-induced mitochondrial dysfunction and pancreatitis involves aryl hydrocarbon receptor mediated cyp1 gene expression: protective effects of resveratrol. *Toxicol Sci*. (2018) 166:428–40. doi: 10.1093/toxsci/kfy206

24. Vázquez-Gómez G, Rocha-Zavaleta L, Rodríguez-Sosa M, Petrosyan P, Rubio-Lightbourn J. Benzo(a)pyrene activates an AhR/Src/ERK axis that contributes to CYP1A1 induction and stable DNA adducts formation in lung cells. *Toxicol Lett*. (2018) 289:54–62. doi: 10.1016/j.toxlet.2018.03.012

25. Mescher M, Haarmann-Stemmann T. Modulation of CYP1A1 metabolism: From adverse health effects to chemoprevention and therapeutic options. *Pharmacol Ther*. (2018) 187:71–87. doi: 10.1016/j.pharmthera.2018.02.012

26. Liu D, Zhao Y, Qi Y, Gao Y, Tu D, Wang Y, et al. Benzo(a)pyrene exposure induced neuronal loss, plaque deposition, and cognitive decline in APP/PS1 mice. *J Neuroinflammation*. (2020) 17:258. doi: 10.1186/s12974-020-01925-y

27. Ma J, Liu X, Yang Y, Qiu J, Dong Z, Ren Q, et al. Binding of benzo(a)pyrene alters the bioreactivity of fine biochar particles toward macrophages leading to deregulated macrophagic defense and autophagy. *ACS Nano*. (2021) 15:9717–31. doi: 10.1021/acsnano.1c00324

28. Cella M, Colonna M. Aryl hydrocarbon receptor: linking environment to immunity. *Semin Immunol*. (2015) 27:310–4. doi: 10.1016/j.smim.2015.10.002

29. Rahmani Z, Karimpour Malekshah A, Zargari M, Talebpour Amiri F. Effect of prenatal exposure to Benzo(a)pyrene on ovarian toxicity and reproductive dysfunction: protective effect of atorvastatin in the embryonic period. *Environ Toxicol*. (2021) 36:1683–93. doi: 10.1002/tox.23164

30. Murray IA, Patterson AD, Perdew GH. Aryl hydrocarbon receptor ligands in cancer: friend and foe. *Nat Rev Cancer*. (2014) 14:801–14. doi: 10.1038/nrc3846

31. Wang Z, Yang H, Ramesh A, Roberts LJ, Zhou L, Lin X, et al. Overexpression of Cu/Zn-superoxide dismutase and/or catalase accelerates benzo(a)pyrene detoxification by upregulation of the aryl hydrocarbon receptor in mouse endothelial cells. *Free Radic Biol Med*. (2009) 47:1221–9. doi: 10.1016/j.freeradbiomed.2009.08.001

32. N'Diaye M, Le Ferrec E, Lagadic-Gossman D, Corre S, Gilot D, Lecureur V, et al. Aryl hydrocarbon receptor- and calcium-dependent induction of the chemokine CCL1 by the environmental contaminant benzo[a]pyrene. *J Biol Chem.* (2006) 281:19906–15. doi: 10.1074/jbc.M601192200
33. Palatnik A, Xin H, Su EJ. Dichotomous effects of aryl hydrocarbon receptor (AHR) activation on human fetoplacental endothelial cell function. *Placenta.* (2016) 44:61–8. doi: 10.1016/j.placenta.2016.06.004
34. Chavan H, Krishnamurthy P. Polycyclic aromatic hydrocarbons (PAHs) mediate transcriptional activation of the ATP binding cassette transporter ABCB6 gene via the aryl hydrocarbon receptor (AhR). *J Biol Chem.* (2012) 287:32054–68. doi: 10.1074/jbc.M112.371476
35. Dolwick KM, Swanson HI, Bradfield CA. In vitro analysis of Ah receptor domains involved in ligand-activated DNA recognition. *Proc Natl Acad Sci U S A.* (1993) 90:8566–70. doi: 10.1073/pnas.90.18.8566
36. Kerzee JK, Ramos KS. Constitutive and inducible expression of Cyp1a1 and Cyp1b1 in vascular smooth muscle cells: role of the Ahr bHLH/PAS transcription factor. *Circ Res.* (2001) 89:573–82. doi: 10.1161/hh1901.097083
37. Zanger UM, Schwab M. Cytochrome P450 enzymes in drug metabolism: regulation of gene expression, enzyme activities, and impact of genetic variation. *Pharmacol Ther.* (2013) 138:103–41. doi: 10.1016/j.pharmthera.2012.12.007
38. Moorthy B, Miller KP, Jiang W, Williams ES, Kondraganti SR, Ramos KS. Role of cytochrome P4501B1 in benzo[a]pyrene bioactivation to DNA-binding metabolites in mouse vascular smooth muscle cells: evidence from 32P-postlabeling for formation of 3-hydroxybenzo[a]pyrene and benzo[a]pyrene-3,6-quinone as major proximate genotoxic intermediates. *J Pharmacol Exp Ther.* (2003) 305:394–401. doi: 10.1124/jpet.102.044271
39. Uno S, Sakurai K, Nebert DW, Makishima M. Protective role of cytochrome P450 1A1 (CYP1A1) against benzo[a]pyrene-induced toxicity in mouse aorta. *Toxicology.* (2014) 316:34–42. doi: 10.1016/j.tox.2013.12.005
40. Kerley-Hamilton JS, Trask HW, Ridley CJ, Dufour E, Lesseur C, Ringelberg CS, et al. Inherent and benzo[a]pyrene-induced differential aryl hydrocarbon receptor signaling greatly affects life span, atherosclerosis, cardiac gene expression, and body and heart growth in mice. *Toxicol Sci.* (2012) 126:391–404. doi: 10.1093/toxsci/kfs002
41. Bond JA, Kocan RM, Benditt EP, Juchau MR. Metabolism of benzo[a]pyrene and 7,12-dimethylbenz[a]anthracene in cultured human fetal aortic smooth muscle cells. *Life Sci.* (1979) 25:425–30. doi: 10.1016/0024-3205(79)90574-5
42. Ramesh A, Prins PA, Perati PR, Rekadevi PV, Sampson UK. Metabolism of benzo(a)pyrene by aortic subcellular fractions in the setting of abdominal aortic aneurysms. *Mol Cell Biochem.* (2016) 411:383–91. doi: 10.1007/s11010-015-2600-2
43. Borén J, Chapman MJ, Krauss RM, Packard CJ, Bentzon JF, Binder CJ, et al. Low-density lipoproteins cause atherosclerotic cardiovascular disease: pathophysiological, genetic, and therapeutic insights: a consensus statement from the European atherosclerosis society consensus panel. *Eur Heart J.* (2020) 41:2313–30. doi: 10.1093/eurheartj/ehz962
44. Jebari-Benslaiman S, Galicia-García U, Larrea-Sebal A, Olaetxea JR, Alloza I, Vandenbroeck K, et al. Pathophysiology of Atherosclerosis. *Int J Mol Sci.* (2022) 23:3346. doi: 10.3390/ijms23063346
45. Falk E. Pathogenesis of atherosclerosis. *J Am Coll Cardiol.* (2006) 47:C7–12. doi: 10.1016/j.jacc.2005.09.068
46. Frostegård J. Immunity, atherosclerosis and cardiovascular disease. *BMC Med.* (2013) 11:117. doi: 10.1186/1741-7015-11-117
47. Godschalk R, Curfs D, Bartsch H, Van Schooten FJ, Nair J. Benzo[a]pyrene enhances lipid peroxidation induced DNA damage in aorta of apolipoprotein E knockout mice. *Free Radic Res.* (2003) 37:1299–305. doi: 10.1080/10715760310001621333
48. Knaapen AM, Curfs DM, Pachen DM, Gottschalk RW, Winther MP, de Daemen MJ, et al. The environmental carcinogen benzo[a]pyrene induces expression of monocyte-chemoattractant protein-1 in vascular tissue: a possible role in atherogenesis. *Mutat Res.* (2007) 621:31–41. doi: 10.1016/j.mrfmmm.2006.12.010
49. Curfs DM, Lutgens E, Gijbels MJ, Kockx MM, Daemen MJ, van Schooten FJ. Chronic exposure to the carcinogenic compound benzo[a]pyrene induces larger and phenotypically different atherosclerotic plaques in ApoE-knockout mice. *Am J Pathol.* (2004) 164:101–8. doi: 10.1016/S0002-9440(10)63101-X
50. Curfs DM, Knaapen AM, Pachen DM, Gijbels MJ, Lutgens E, Smook ML, et al. Polycyclic aromatic hydrocarbons induce an inflammatory atherosclerotic plaque phenotype irrespective of their DNA binding properties. *FASEB J.* (2005) 19:1290–2. doi: 10.1096/fj.04-2269fje
51. Sroczynska K, Toton-Zurańska J, Czepiel J, Zajac-Grabiec A, Jurczyszyn A, Wolkow P, et al. Therapeutic role of eicosapentaenoic and arachidonic acid in benzo(a) pyrene-induced toxicity in HUVEC endothelial cells. *Life Sci.* (2022) 293:120345. doi: 10.1016/j.lfs.2022.120345
52. Oesterling E, Toborek M, Hennig B. Benzo[a]pyrene induces intercellular adhesion molecule-1 through a caveolae and aryl hydrocarbon receptor mediated pathway. *Toxicol Appl Pharmacol.* (2008) 232:309–16. doi: 10.1016/j.taap.2008.07.001
53. Gu J, Chan LS, Wong CK, Wong NS, Wong CK, Leung KN, et al. Effect of benzo[a]pyrene on the production of vascular endothelial growth factor by human eosinophilic leukemia EoL-1 cells. *J Environ Pathol Toxicol Oncol.* (2011) 30:241–9. doi: 10.1615/JEnvironPatholToxicolOncol.v30.i3.70
54. Ji K, Xing C, Jiang F, Wang X, Guo H, Nan J, et al. Benzo[a]pyrene induces oxidative stress and endothelial progenitor cell dysfunction via the activation of the NF-κB pathway. *Int J Mol Med.* (2013) 31:922–30. doi: 10.3892/ijmm.2013.1288
55. van Grevenynghe J, Monteiro P, Gilot D, Fest T, Fardel O. Human endothelial progenitors constitute targets for environmental atherogenic polycyclic aromatic hydrocarbons. *Biochem Biophys Res Commun.* (2006) 341:763–9. doi: 10.1016/j.bbrc.2006.01.028
56. Tithof PK, Elgayyar M, Cho Y, Guan W, Fisher AB, Peters-Golden M. Polycyclic aromatic hydrocarbons present in cigarette smoke cause endothelial cell apoptosis by a phospholipase A2-dependent mechanism. *FASEB J.* (2002) 16:1463–4. doi: 10.1096/fj.02-0092fje
57. Tzeng HP, Lan KC, Yang TH, Chung MN, Liu SH. Benzo[a]pyrene activates interleukin-6 induction and suppresses nitric oxide-induced apoptosis in rat vascular smooth muscle cells. *PLoS ONE.* (2017) 12:e0178063. doi: 10.1371/journal.pone.0178063
58. Meng D, Lv DD, Zhuang X, Sun H, Fan L, Shi XL, et al. Benzo[a]pyrene induces expression of matrix metalloproteinases and cell migration and invasion of vascular smooth muscle cells. *Toxicol Lett.* (2009) 184:44–9. doi: 10.1016/j.toxlet.2008.10.016
59. Niermann T, Schmutz S, Erne P, Resink T. Aryl hydrocarbon receptor ligands repress T-cadherin expression in vascular smooth muscle cells. *Biochem Biophys Res Commun.* (2003) 300:943–9. doi: 10.1016/S0006-291X(02)02970-4
60. Yan Z, Subbaramaiah K, Camilli T, Zhang F, Tanabe T, McCaffrey TA, et al. Benzo[a]pyrene induces the transcription of cyclooxygenase-2 in vascular smooth muscle cells. Evidence for the involvement of extracellular signal-regulated kinase and NF-κappaB. *J Biol Chem.* (2000) 275:4949–55. doi: 10.1074/jbc.275.7.4949
61. Chen YH, Ramos KS. A CCAAT/enhancer-binding protein site within antioxidant/electrophile response element along with CREB-binding protein participate in the negative regulation of rat GST-Ya gene in vascular smooth muscle cells. *J Biol Chem.* (2000) 275:27366–76. doi: 10.1016/S0021-9258(19)61520-6
62. Miller KP, Chen YH, Hastings VL, Bral CM, Ramos KS. Profiles of antioxidant/electrophile response element (ARE/EpRE) nuclear protein binding and c-Ha-ras transactivation in vascular smooth muscle cells treated with oxidative metabolites of benzo[a]pyrene. *Biochem Pharmacol.* (2000) 60:1285–96. doi: 10.1016/S0006-2952(00)00439-1
63. Kerzee JK, Ramos KS. Activation of c-Ha-ras by benzo(a)pyrene in vascular smooth muscle cells involves redox stress and aryl hydrocarbon receptor. *Mol Pharmacol.* (2000) 58:152–8. doi: 10.1124/mol.58.1.152
64. Karyala S, Guo J, Sartor M, Medvedovic M, Kann S, Puga A, et al. Different global gene expression profiles in benzo[a]pyrene- and dioxin-treated vascular smooth muscle cells of AHR-knockout and wild-type mice. *Cardiovasc Toxicol.* (2004) 4:47–73. doi: 10.1385/CT:4:1:47
65. Raveendran M, Senthil D, Utama B, Shen Y, Dudley D, Wang J, et al. Cigarette suppresses the expression of P4Halpa and vascular collagen production. *Biochem Biophys Res Commun.* (2004) 323:592–8. doi: 10.1016/j.bbrc.2004.08.129
66. Yang H, Zhou L, Wang Z, Roberts LJ, Lin X, Zhao Y, et al. Overexpression of antioxidant enzymes in ApoE-deficient mice suppresses benzo(a)pyrene-accelerated atherosclerosis. *Atherosclerosis.* (2009) 207:51–8. doi: 10.1016/j.atherosclerosis.2009.03.052
67. Wang JC, Bennett M. Aging and atherosclerosis: mechanisms, functional consequences, and potential therapeutics for cellular senescence. *Circ Res.* (2012) 111:245–59. doi: 10.1161/CIRCRESAHA.111.261388
68. Luchetti F, Crinelli R, Nasoni MG, Benedetti S, Palma F, Fraternali A, et al. LDL receptors, caveolae and cholesterol in endothelial dysfunction: oxLDLs accomplices or victims? *Br J Pharmacol.* (2021) 178:3104–14. doi: 10.1111/bph.15272
69. Bennett MR, Sinha S, Owens GK. Vascular Smooth Muscle Cells in Atherosclerosis. *Circ Res.* (2016) 118:692–702. doi: 10.1161/CIRCRESAHA.115.306361
70. Hartman J, Frishman WH. Inflammation and atherosclerosis: a review of the role of interleukin-6 in the development of atherosclerosis

and the potential for targeted drug therapy. *Cardiol Rev.* (2014) 22:147–51. doi: 10.1097/CRD.000000000000021

71. Visse R, Nagase H. Matrix metalloproteinases and tissue inhibitors of metalloproteinases: structure, function, and biochemistry. *Circ Res.* (2003) 92:827–39. doi: 10.1161/01.RES.0000070112.80711.3D

72. Holme JA, Brinckmann BC, Refsnes M, Låg M, Øvrevik J. Potential role of polycyclic aromatic hydrocarbons as mediators of cardiovascular effects from combustion particles. *Environ Health.* (2019) 18:74. doi: 10.1186/s12940-019-0514-2

73. Lackland DT, Weber MA. Global burden of cardiovascular disease and stroke: hypertension at the core. *Can J Cardiol.* (2015) 31:569–71. doi: 10.1016/j.cjca.2015.01.009

74. Lau DH, Nattel S, Kalman JM, Sanders P. Modifiable Risk Factors and Atrial Fibrillation. *Circulation.* (2017) 136:583–96. doi: 10.1161/CIRCULATIONAHA.116.023163

75. Gentner NJ, Weber LP. Intranasal benzo[a]pyrene alters circadian blood pressure patterns and causes lung inflammation in rats. *Arch Toxicol.* (2011) 85:337–46. doi: 10.1007/s00204-010-0589-6

76. Jules GE, Pratap S, Ramesh A, Hood DB. In utero exposure to benzo(a)pyrene predisposes offspring to cardiovascular dysfunction in later-life. *Toxicology.* (2012) 295:56–67. doi: 10.1016/j.tox.2012.01.017

77. Bugiak B, Weber LP. Hepatic and vascular mRNA expression in adult zebrafish (Danio rerio) following exposure to benzo-a-pyrene and 2,3,7,8-tetrachlorodibenzo-p-dioxin. *Aquat Toxicol.* (2009) 95:299–306. doi: 10.1016/j.aquatox.2009.03.009

78. Wang J, Sun H, Zhou Y, Huang K, Que J, Peng Y, et al. RNA microarray expression profile in 3,4-benzopyrene/angiotensin II-induced abdominal aortic aneurysm in mice. *J Cell Biochem.* (2019) 120:10484–94. doi: 10.1002/jcb.28333

79. Zhang Y, Ramos KS. The development of abdominal aortic aneurysms in mice is enhanced by benzo(a)pyrene. *Vasc Health Risk Manag.* (2008) 4:1095–102. doi: 10.2147/VHRM.S3038

80. Ji K, Zhang Y, Jiang F, Qian L, Guo H, Hu J, et al. Exploration of the mechanisms by which 3,4-benzopyrene promotes angiotensin II-induced abdominal aortic aneurysm formation in mice. *J Vasc Surg.* (2014) 59:492–9. doi: 10.1016/j.jvs.2013.03.022

81. Pinel-Marie ML, Sparfel L, Desmots S, Fardel O. Aryl hydrocarbon receptor-dependent induction of the NADPH oxidase subunit NCF1/p47 phox expression leading to priming of human macrophage oxidative burst. *Free Radic Biol Med.* (2009) 47:825–34. doi: 10.1016/j.freeradbiomed.2009.06.025

82. Aboutabl ME, Zordoky BN, El-Kadi AO. 3-methylcholanthrene and benzo(a)pyrene modulate cardiac cytochrome P450 gene expression and arachidonic acid metabolism in male sprague dawley rats. *Br J Pharmacol.* (2009) 158:1808–19. doi: 10.1111/j.1476-5381.2009.00461.x

83. Greer JB, Magnuson JT, McGruer V, Qian L, Dasgupta S, Volz DC, et al. miR133b microinjection during early development targets transcripts of cardiomyocyte ion channels and induces oil-like cardiotoxicity in zebrafish (Danio rerio) embryos. *Chem Res Toxicol.* (2021) 34:2209–15. doi: 10.1021/acs.chemrestox.1c00238

84. Jayasundara N, Van Tiem Garner L, Meyer JN, Erwin KN, Di Giulio RT. AHR2-Mediated transcriptomic responses underlying the synergistic cardiac developmental toxicity of PAHs. *Toxicol Sci.* (2015) 143:469–81. doi: 10.1093/toxsci/kfu245

85. Huang L, Wang C, Zhang Y, Li J, Zhong Y, Zhou Y, et al. Benzo[a]pyrene exposure influences the cardiac development and the expression of cardiovascular relative genes in zebrafish (Danio rerio) embryos. *Chemosphere.* (2012) 87:369–75. doi: 10.1016/j.chemosphere.2011.12.026

86. Bugiak BJ, Weber LP. Phenotypic anchoring of gene expression after developmental exposure to aryl hydrocarbon receptor ligands in zebrafish. *Aquat Toxicol.* (2010) 99:423–37. doi: 10.1016/j.aquatox.2010.06.003

87. Li CH, Cheng YW, Hsu YT, Hsu YJ, Liao PL, Kang JJ, et al. Benzo[a]pyrene inhibits angiogenic factors-induced alphavbeta3 integrin expression, neovasclogenesis, and angiogenesis in human umbilical vein endothelial cells. *Toxicol Sci.* (2010) 118:544–53. doi: 10.1093/toxsci/kfq279

88. Cunha V, Vogs C, Le Bihanic F, Dreij K. Mixture effects of oxygenated PAHs and benzo[a]pyrene on cardiovascular development and function in zebrafish embryos. *Environ Int.* (2020) 143:105913. doi: 10.1016/j.envint.2020.105913

89. Yamaguchi A, Uchida M, Ishibashi H, Hirano M, Ichikawa N, Arizono K, et al. Potential mechanisms underlying embryonic developmental toxicity caused by benzo[a]pyrene in Japanese medaka (Oryzias latipes). *Chemosphere.* (2020) 242:125243. doi: 10.1016/j.chemosphere.2019.125243

90. Ichihara S, Yamada Y, Gonzalez FJ, Nakajima T, Murohara T, Ichihara G, et al. Inhibition of ischemia-induced angiogenesis by benzo[a]pyrene in a manner

dependent on the aryl hydrocarbon receptor. *Biochem Biophys Res Commun.* (2009) 381:44–9. doi: 10.1016/j.bbrc.2009.01.187

91. Li X, Shen C, Liu X, He J, Ding Y, Gao R, et al. Exposure to benzo[a]pyrene impairs decidualization and decidual angiogenesis in mice during early pregnancy. *Environ Pollut.* (2017) 222:523–31. doi: 10.1016/j.envpol.2016.11.029

92. Kent KC. Clinical practice. abdominal aortic aneurysms. *N Engl J Med.* (2014) 371:2101–8. doi: 10.1056/NEJMcp1401430

93. Durand P, Blondet A, Martin G, Carette D, Pointis G, Perrard MH. Effects of a mixture of low doses of atrazine and benzo[a]pyrene on the rat seminiferous epithelium either during or after the establishment of the blood-testis barrier in the rat seminiferous tubule culture model. *Toxicol In Vitro.* (2020) 62:104699. doi: 10.1016/j.tiv.2019.104699

94. Ho DH, Burggren WW. Blood-brain barrier function, cell viability, and gene expression of tight junction-associated proteins in the mouse are disrupted by crude oil, benzo[a]pyrene, and the dispersant COREXIT. *Comp Biochem Physiol C Toxicol Pharmacol.* (2019) 223:96–105. doi: 10.1016/j.cbpc.2019.05.011

95. Zhang L, Ji X, Ding F, Wu X, Tang N, Wu Q, et al. Apoptosis and blood-testis barrier disruption during male reproductive dysfunction induced by PAHs of different molecular weights. *Environ Pollut.* (2022) 300:118959. doi: 10.1016/j.envpol.2022.118959

96. Ba Q, Li J, Huang C, Qiu H, Li J, Chu R. Effects of benzo[a]pyrene exposure on human hepatocellular carcinoma cell angiogenesis, metastasis, and NF-κB signaling. *Environ Health Perspect.* (2015) 123:246–54. doi: 10.1289/ehp.1408524

97. Gdula-Argasińska J, Czepiel J, Totoń-Zurańska J, Jurczynski A, Wolkow P, Librowski T, et al. Resolvin D1 down-regulates CYP1A1 and PTGS2 gene in the HUVEC cells treated with benzo(a)pyrene. *Pharmacol Rep.* (2016) 68:939–44. doi: 10.1016/j.pharep.2016.05.005

98. Owens EO, Toborek M, Hennig B. Flavonoids protect against intercellular adhesion molecule-1 induction by benzo[a]pyrene. *Bull Environ Contam Toxicol.* (2009) 83:4–7. doi: 10.1007/s00128-009-9664-1

99. Duan J, Chen C, Li H, Ju G, Gao A, Sun Y, et al. Multifaceted protective effects of hesperidin by aromatic hydrocarbon receptor in endothelial cell injury induced by Benzo[a]Pyrene. *Nutrients.* (2022) 14:574. doi: 10.3390/nu14030574

100. Goff ML, Delbrut A, Quinton M, Pradelles R, Bescher M, Burel A, et al. Protective action of ostreococcus tauri and phaodactylum tricornutum extracts towards benzo[a]pyrene-induced cytotoxicity in endothelial cells. *Mar Drugs.* (2019) 18. doi: 10.3390/md18010003

101. Bandi N, Ayalamayajula SP, Dhanda DS, Iwakawa J, Cheng PW, Kompella UB, et al. Intratracheal budesonide-poly(lactide-co-glycolide) microparticles reduce oxidative stress, VEGF expression, and vascular leakage in a benzo(a)pyrene-fed mouse model. *J Pharm Pharmacol.* (2005) 57:851–60. doi: 10.1211/0022357056334

102. Aboutabl ME, Zordoky BN, Hammock BD, El-Kadi AO. Inhibition of soluble epoxide hydrolase confers cardioprotection and prevents cardiac cytochrome P450 induction by benzo(a)pyrene. *J Cardiovasc Pharmacol.* (2011) 57:273–81. doi: 10.1097/FJC.0b013e3182055baf

103. Agha AM, El-Fattah AA, Al-Zuhair HH, Al-Rikabi AC. Chemopreventive effect of Ginkgo biloba extract against benzo(a)pyrene-induced forestomach carcinogenesis in mice: amelioration of doxorubicin cardiotoxicity. *J Exp Clin Cancer Res.* (2001) 20:39–50.

104. Nakagawa M, Uno S, Iriyama N, Matsunawa M, Makishima M, Takeuchi J, et al. Combined treatment with benzo[a]pyrene and 1α,25-dihydroxyvitamin D(3) induces expression of plasminogen activator inhibitor 1 in monocyte/macrophage-derived cells. *Toxicol Appl Pharmacol.* (2018) 345:48–56. doi: 10.1016/j.taap.2018.03.003

105. Pink M, Verma N, Rettenmeier AW, Schmitz-Spanke S. Integrated proteomic and metabolomic analysis to assess the effects of pure and benzo[a]pyrene-loaded carbon black particles on energy metabolism and motility in the human endothelial cell line EA.hy926. *Arch Toxicol.* (2014) 88:913–34. doi: 10.1007/s00204-014-1200-3

106. Asweto CO, Wu J, Hu H, Feng L, Yang X, Duan J, et al. Combined effect of silica nanoparticles and benzo[a]pyrene on cell cycle arrest induction and apoptosis in human umbilical vein endothelial cells. *Int J Environ Res Public Health.* (2017) 14:289. doi: 10.3390/ijerph14030289

107. Duan J, Yu Y, Li Y, Wang Y, Sun Z. Inflammatory response and blood hypercoagulable state induced by low level co-exposure with silica nanoparticles and benzo[a]pyrene in zebrafish (Danio rerio) embryos. *Chemosphere.* (2016) 151:152–62. doi: 10.1016/j.chemosphere.2016.02.079

108. Asweto CO, Hu H, Liang S, Wang L, Liu M, Yang H, et al. Gene profiles to characterize the combined toxicity induced by low level co-exposure of silica nanoparticles and benzo[a]pyrene using whole genome microarrays in zebrafish embryos. *Ecotoxicol Environ Saf.* (2018) 163:47–55. doi: 10.1016/j.ecoenv.2018.07.059



OPEN ACCESS

EDITED BY

Hongshun Yang,
National University of
Singapore, Singapore

REVIEWED BY

Lishuang Lv,
Nanjing Normal University, China
Maomao Zeng,
Jiangnan University, China

*CORRESPONDENCE

Guoqiang Li
liguoqiang@fosu.edu.cn
Shiyi Ou
tosy@jnu.edu.cn

[†]These authors have contributed
equally to this work and share first
authorship

SPECIALTY SECTION

This article was submitted to
Food Chemistry,
a section of the journal
Frontiers in Nutrition

RECEIVED 23 June 2022

ACCEPTED 18 July 2022

PUBLISHED 16 August 2022

CITATION

Chen P, Liu S, Yin Z, Liang P, Wang C,
Zhu H, Liu Y, Ou S and Li G (2022)
Rutin alleviated acrolein-induced
cytotoxicity in Caco-2 and GES-1 cells
by forming a cyclic hemiacetal
product. *Front. Nutr.* 9:976400.
doi: 10.3389/fnut.2022.976400

COPYRIGHT

© 2022 Chen, Liu, Yin, Liang, Wang,
Zhu, Liu, Ou and Li. This is an
open-access article distributed under
the terms of the [Creative Commons
Attribution License \(CC BY\)](#). The use,
distribution or reproduction in other
forums is permitted, provided the
original author(s) and the copyright
owner(s) are credited and that the
original publication in this journal is
cited, in accordance with accepted
academic practice. No use, distribution
or reproduction is permitted which
does not comply with these terms.

Rutin alleviated acrolein-induced cytotoxicity in Caco-2 and GES-1 cells by forming a cyclic hemiacetal product

Peifang Chen^{1†}, Shuang Liu^{2†}, Zhao Yin², Pengjie Liang¹,
Chunhua Wang¹, Hanyue Zhu¹, Yang Liu¹, Shiyi Ou^{3*} and
Guoqiang Li^{1,4,5*}

¹Department of Food Science, Foshan University, Foshan, China, ²Department of Hematology, Guangdong Second Provincial General Hospital, Guangzhou, China, ³Department of Food Science and Engineering, Jinan University, Guangzhou, China, ⁴Guangdong Provincial Key Laboratory of Intelligent Food Manufacturing, Foshan University, Foshan, China, ⁵South China National Center for Food Safety Research and Development, Foshan University, Foshan, China

Acrolein (ACR), an α , β -unsaturated aldehyde, is a toxic compound formed during food processing, and the use of phenolics derived from dietary materials to scavenge ACR is a hot spot. In this study, rutin, a polyphenol widely present in various dietary materials, was used to investigate its capacity to scavenge ACR. It was shown that more than 98% of ACR was eliminated under the conditions of reaction time of 2 h, temperature of 80 °C, and molar ratio of rutin/ACR of 2/1. Further structural characterization of the formed adduct revealed that the adduct of rutin to ACR to form a cyclic hemiacetal compound (RAC) was the main scavenging mechanism. Besides, the stability of RAC during simulated *in vitro* digestion was evaluated, which showed that more than 83.61% of RAC was remained. Furthermore, the cytotoxicity of RAC against Caco-2 and GES-1 cells was significantly reduced compared with ACR, where the IC₅₀ values of ACR were both below 20 μ M while that of RAC were both above 140 μ M. And the improvement of the loss of mitochondrial membrane potential (MMP) by RAC might be one of the detoxification pathways. The present study indicated that rutin was one of the potential ACR scavengers among natural polyphenols.

KEYWORDS

acrolein, rutin, hemiacetal adduct, simulated *in vitro* digestion, cytotoxicity

Introduction

Acrolein (ACR), an α , β -unsaturated aldehyde, is one of the typical active carbonyl compounds (1). ACR could be produced endogenously by enzyme-mediated metabolism of threonine and polyamines, metabolism of the anticancer drug cyclophosphamide, and oxidation of unsaturated fatty acids on the cell membrane (2–5). Due to the presence of the olefinic double bond and carbonyl group, ACR could react with biological nucleophiles such as DNA and proteins, resulting in dysfunction of biomacromolecules

(6). Besides, ACR mediated cytotoxicity and genotoxicity through mitochondrial dysfunction, oxidative stress, endoplasmic reticulum stress and so on (7–9). It was also reported that ACR was associated with several diseases, including chronic kidney disease, cardiovascular disease, and Alzheimer's disease (AD) (10–12). However, ACR could be metabolized into S-(hydroxypropyl)-mercapturic acid (3-HPMA) *in vivo* as an elimination pathway (13). And the deregulated ACR metabolism to generate 3-HPMA was found in AD patients (14, 15). On the other side, ACR was formed exogenously. The combustion of organic stuff, for instance, gasoline, plastics, and cigarettes, resulted in the presence of ACR in the environment (16, 17). Notably, ACR was even found in foodstuffs, such as cheese, donuts, beer, and wine, ranging from 10 to 600 $\mu\text{g/kg}$ (12, 13, 18). And vegetable oil rich in polyunsaturated fatty acids was another important source of ACR, which could generate ACR through oxidative degradation under high-temperature treatment. It was reported that after heating at 180°C for 24 h the content of ACR reached 29.3 mg/kg in olive oil, 156.4 mg/kg in rapeseed oil, and 207.4 mg/kg in linseed oil (19). Though endogenous ACR could be scavenged by enzymatic metabolism, a large amount of exogenous ACR poses a serious threat to human health.

In recent years, searching for naturally occurring polyphenols to effectively capture ACR has received extensive attention (20). A study performed by Zhu et al. (21) investigated the capacity of 21 natural polyphenols to trap ACR under simulated physiological conditions and found that phloretin exhibited an outstanding ability to scavenge ACR, with more than 99% of ACR being quenched. After that, other polyphenols, such as myricetin, curcumin, and tea catechins, were also shown to remove this detrimental compound (22–25). In fact, it was the *meta*-phenol structure of polyphenols that played an essential role in their reaction with ACR (26). Inspired by previous literature, we paid more attention to potential ACR scavengers derived from dietary materials.

Previously, a study by Zamora et al. (27) showed that ACR was trapped by quercetin to form an equimolar adduct that was detected not only in an experimental model of frying onions with fresh rapeseed oil but also in the commercial crispy fried onions. While quercetin is the dominant flavonol in onions, it usually exists in the form of glycosides, such as rutin (quercetin 3-O-rhamnosylglucoside) (28, 29). Literature also reported that rutin was the second most abundant flavonoid in dry red onion skins after quercetin (30). Besides, rutin is also widely present in asparagus, buckwheat, and peppers, being an important dietary constituent (31–33). In addition to culinary virtues, substantial evidence suggested that rutin was involved in a variety of biological activities, including antioxidant, antiallergic, anti-inflammatory, and cardioprotective effects (34, 35). Chemically, rutin also possesses the typical *meta*-phenol structure as a reaction site for ACR, but the scavenging effect of rutin on ACR was lack of discussion.

In this work, a simulated system was established to investigate the effect of three factors on the scavenging of ACR by rutin. Subsequently, the adduct between ACR and rutin was identified, which also helped to elucidate the reaction mechanism. Considering that the adduct might be formed and ingested after cooking, a three-stage simulated *in vitro* digestion of the adduct was conducted. Furthermore, the cytotoxicity of RAC against the human intestinal epithelial cells (Caco-2) and gastric epithelial cells (GES-1) was determined with ACR as the control, followed by the measurement of mitochondrial membrane potential (MMP).

Materials and methods

Materials and chemicals

Acrolein (95%) was acquired from Energy Chemical Co., Ltd. Rutin (98%), 2,4-dinitrophenylhydrazine (DNPH), and ACR-DNPH standard were from Shanghai Macklin Biochemical Co., Ltd. Dulbecco's Modified Eagle Medium (DMEM), Fetal Bovine Serum (FBS), non-essential amino acids (NEAA), penicillin, streptomycin, trypsin-EDTA, and phosphate buffered saline (PBS, pH = 7.4) were bought from Thermo Fisher Scientific Inc. (MA, USA). Simulated saliva (SSF), gastric (SGF), and intestinal (SIF) fluids were from Phygene Biotechnology Co., Ltd. (Fuzhou, China). Cell counting kit-8 (CCK-8), apoptosis detection kit (including Annexin-V fluorescein isothiocyanate, Annexin-V FITC, and propidium iodide, PI), and JC-1 mitochondrial membrane potential assay kit were from Shanghai BestBio Co., Ltd. All the analytical and high-performance liquid chromatography (HPLC) grade reagents were obtained from Sigma-Aldrich (St. Louis, MO, USA). SephadexTM LH-20 column fillers were obtained from GE Healthcare Bio-Sciences AB (Uppsala, Sweden).

The influence of temperature, reaction time, and molar ratio on the elimination of ACR by rutin

In the present study, three variables were taken into consideration, namely temperature (40–100°C), reaction duration (0.5–8 h), and molar ratio of rutin to ACR (from 1/2 to 4/1), and the remaining level of ACR was determined. A mixture of rutin, ACR, and 20 mL of PBS was prepared in a 50 mL three-necked flask and reacted under light-proof conditions. The different variables were studied separately while keeping other conditions constant as follows: temperature of 80°C, reaction time of 2 h, and the molar ratio of rutin/ACR of 1/1. At the end of each reaction, ACR was derivatized with DNPH, and its content was determined as below.

Qualitative and quantitative determination of ACR

The stock solution equivalent to ACR concentration of 100 mg/mL was prepared by dissolving 10.7 mg of ACR-DNPH standard with 25 mL of acetonitrile (ACN). And the ACR-DNPH standard curve (2 to 100 μ g/mL) was established by serial dilutions of the stock solution. The HPLC conditions were as below. An Agilent 1,260 Infinity II HPLC system (Agilent Technologies, Palo Alto, CA) equipped with a DAD and a Zorbax SB-C18 column (250 \times 4.6 mm; 5 μ m; Agilent Technologies) was utilized for the determination of ACR-DNPH. The separation was conducted under isocratic conditions by introducing 50% A (water) and 50% B (ACN) at a flow rate of 1.0 mL/min for 15 min. The temperature was 35°C, the injection volume was 20 μ L, and the detection wavelength was set at 365 nm. According to the retention time as well as the peak area, the standard curve of ACR-DNPH derivatives was obtained.

DNPH was recrystallized as the followings before use: excess DNPH was added into 200 mL of methanol (MeOH) heating for 1 h, and the supernatant was collected and further heated at 60°C to remove 95% of the solvent; the crystals were then washed twice with 100 mL of MeOH, transferred to another clean beaker, and co-heated with 200 mL of MeOH; and the resulting crystal was stored under seal. The 0.1 M DNPH solution was prepared by dissolving 5.0548 g of the purified DNPH in 250 mL of ACN containing 5 mL of 10% phosphoric acid solution.

Derivatization of ACR with DNPH was conducted in accordance with Reilly et al. (36). In short, one milliliter of each sample was incubated with 1 mL of diluted DNPH solution (0.01 M) for 40 min at 40°C, followed by extraction with 10 mL of MeOH/water (75: 25, v/v). After centrifugation (6,000 rpm, 10 min), the supernatant was collected and was further extracted with 10 mL of dichloromethane to obtain the DNPH derivatives. Prior to HPLC analysis as above, the DNPH derivatives were re-dissolved in 1 mL of HPLC grade ACN and passed through a 0.45 μ m filter (Bie & Berntsen, Rødovre, Denmark).

Preparation and purification of the rutin-acrolein adduct (RAC)

Based on the above results, rutin (2 mmol) and ACR (1 mmol) dissolved in 25 mL of PBS were mixed in a three-necked flask and reacted at 80°C for 2 h in the dark. After cooling to room temperature, the supernatant was obtained by vacuum filtration and concentrated to 2 mL in a rotary evaporator at 45°C before loading onto a Sephadex LH-20 column (105 \times 2.2 cm) for purification. MeOH was applied as the eluent and the

flow rate was set at 0.6 mL/min. As a result, the purified adduct of rutin and ACR, namely RAC, was obtained.

Structural characterization of the adduct

The reaction progress was tracked and determined by the Shimadzu LC-20 system (Tokyo, Japan) equipped with a diode array detector (DAD). The HPLC conditions were as follows: the mobile phase was composed of MeOH (A) and 0.1% acetic acid water (B) with gradient elution from 10% A to 100% A within 30 min at a flow rate of 1.0 mL/min. With an injection volume of 10 μ L, a Zorbax SB-C18 column (150 \times 4.6 mm; 5 μ m; Agilent Technologies) was used and the UV spectra were recorded in the range of 190–400 nm.

The mass spectrum (MS) data was obtained in the negative mode by direct injection into an LCMS-8045 triple quadrupole mass spectrometer (Shimadzu Corporation, Tokyo, Japan) equipped with electrospray as the ionization source. The scan range was from m/z 50 to m/z 1000. Other parameters for MS and MS/MS measurements were set in refer to the method of Qi et al. (37).

Additionally, 0.5 mL of DMSO- d_6 and 15 mg of the sample were added into a 5-mm nuclear magnetic resonance (NMR) tube, and the spectra, including ^1H NMR, ^{13}C NMR, distortionless enhancement by polarization transfer 135 (DEPT 135), ^1H - ^1H correlation spectroscopy (COSY), heteronuclear single-quantum correlation (HSQC) and heteronuclear multiple-bond correlation (HMBC), were recorded on a Bruker 600 MHz NMR apparatus (Bruker Corp, Fallanden, Switzerland). Rutin was applied as the reference.

Rutin. ^1H NMR (600 MHz, DMSO- d_6): δ 12.60 (s, 1H, 5-OH), 10.84 (s, 1H, 7-OH), 9.67 (s, 1H, 4'-OH), 9.18 (s, 1H, 3'-OH), 7.55 (m, 1H, H-6'), 7.53 (s, 1H, H-5'), 6.84 (d, J = 8.3 Hz, 1H, H-2'), 6.39 (d, J = 2.0 Hz, 1H, H-8), 6.19 (d, J = 2.0 Hz, 1H, H-6), 5.34 (d, J = 7.1 Hz, 1H, H-1 Glc), 4.38 (s, 1H, H-1 Rha), 3.05–3.72 (m, protons for glycoside region), 0.99 (d, J = 6.2 Hz, 3H, H-6 Rha). ^{13}C NMR (150 MHz, DMSO- d_6): δ 177.4 (C-4), 164.0 (C-7), 161.2 (C-5), 156.6 (C-2), 156.4 (C-9), 148.4 (C-4'), 144.7 (C-3'), 133.3 (C-3), 121.6 (C-6'), 121.2 (C-1'), 116.3 (C-5'), 115.2 (C-2'), 104.0 (C-10), 101.2 (Glc, C-1"), 100.7 (Rha, C-1"), 98.7 (C-6), 93.6 (C-8), 76.5 (Glc, C-3"), 75.9 (Glc, C-5"), 74.1 (Glc, C-2"), 71.8 (Rha, C-4"), 70.6 (Rha, C-3"), 70.4 (Rha, C-2"), 70.0 (Glc, C-4"), 68.2 (Rha, C-5"), 67.0 (Glc, C-6"), 17.7 (Rha, C-6"). The obtained NMR data showed consistence with those in the literature (38).

In vitro simulated digestion

The simulated oral, gastric, and intestinal digestion experiments of RAC were carried out according to Mamone et al. (39) with minor adjustments. One milliliter of RAC (1

mg/mL) was mixed with 4 mL SSF and stirred at 170 rpm for 2 min in lightproof condition to mimic the oral phase digestion. Based on the oral stage, 10 mL of SGF was added and reacted for another 2 h under the same condition to imitate the gastric phase digestion. To investigate the intestinal phase digestion, 20 mL of SIF was further added, and the mixture was stirred for another 2 h after simulated gastric digestion. For each stage, the same volume of deionized water was used in place of the corresponding digestive fluid as the control. At the end of each stage, 0.8 mL of the mixture was withdrawn and diluted with MeOH to 1.0 mL for HPLC analysis.

The standard curve of RAC was prepared as follows: one milligram of RAC was dissolved with MeOH to a final concentration of 1 mg/mL. The above solution was further used to prepare a series of RAC concentrations at 0.02, 0.04, 0.08, 0.2, and 1.0 mg/mL, respectively. The HPLC conditions for the determination of the content of RAC in the digestion mixture and the preparation of the standard curve of RAC were the same as those for the analysis of RAC, except that the detection wavelength was at 358 nm.

Cell culture

The Caco-2 cell line and GES-1 cell line were obtained from iCell Bioscience (Shanghai, China). As described by Chai et al. (40) with a bit modification, the Caco-2 cells were cultured within a medium composed of DMEM supplemented with 1% (v/v) NEAA, 10% (v/v) FBS, and penicillin and streptomycin (100 U/mL). GES-1 cells were cultivated according to Xu et al. (41) with slight modifications as follows: DMEM medium including 1% (v/v) NEAA, 10% (v/v) FBS, and penicillin and streptomycin (100 U/mL). Cells were all maintained in a humidified incubator containing 5% CO₂ and 95% air at 37°C.

Cell survival

The effects of ACR and RAC on cell survival (both Caco-2 and GES-1 cells) were measured by the CCK-8 assay (41). Briefly, cells (1×10^4 cells/well) were seeded into a 96-well plate and cultivated overnight. Then 100 μ L of sample solutions at different concentrations were added into the wells, followed by incubation at 37°C for another 48 h. After cells were rinsed twice with PBS and resuspended in 100 μ L of DMEM supplemented with 10% FBS, 10 μ L of CCK-8 solution was added into each well and the plate was maintained for 1 h in the incubator. The plate was read at 450 nm on a microplate reader (BioTek, Epoch 2, USA), and all experiments were performed thrice. Cell viability was expressed as a percentage of the control group as shown below:

$$\text{Cell viability (\%)} = A_{\text{sample}}/A_{\text{control}} \times 100\%$$

Where A_{sample} was the absorbance (Abs) of the cells incubated with different concentrations of sample solutions, and A_{control} was the Abs of the cells incubated without sample solution.

Apoptosis assay

Cell apoptosis assay was conducted in refer to Abas et al. (42) with modifications. In short, cells at a density of 1×10^4 cells/well were seeded in 96-well plates and incubated overnight, followed by exposure to different concentrations of ACR and RAC for another 24 h. After that, cells were rinsed twice with PBS, resuspended in 200 μ L of Annexin-binding buffer, and finally stained with Annexin-V FITC and PI (5 μ L each) for 10 min at 37°C in darkness. After adding 400 μ L of Annexin-binding buffer, the signal intensity was measured using a FACSCalibur (Becton Dickinson, CA, USA) flow cytometry within 1 h, and data was analyzed with FlowJo software (Ashland, OR, USA).

JC-1 staining

After incubation with different concentrations of samples, the changes of MMP in Caco-2 and GES-1 cells were measured in accordance with Liu et al., with slight modifications (43). In brief, cells (1×10^4 cells/well) were exposed to different concentrations of ACR and RAC for 24 h, respectively. Then 500 μ L of JC-1 staining solution was added into each well and the plate was further incubated at 37°C for 15 min. Cells were then rinsed twice with 1 mL of staining buffer and resuspended with 500 μ L of staining buffer prior to MMP determination in the flow cytometry.

Statistical analysis

All experiments were carried out in triplicate, and the data was expressed as mean \pm standard deviation. As for statistical analysis, analysis of variance (ANOVA) was performed with GraphPad Prism version 9.0.0 (GraphPad Software Inc., San Diego, CA). Differences were considered significant if $p < 0.05$.

Results and discussion

Effects of different parameters on the elimination of ACR

Based on the calibration curve ($y = 326781x - 183802$; $r^2 = 0.9999$; x was the concentration of each sample and y was the corresponding peak area), the residual content of ACR was depicted in Figure 1. After incubation at 40, 60, 80, 90, and

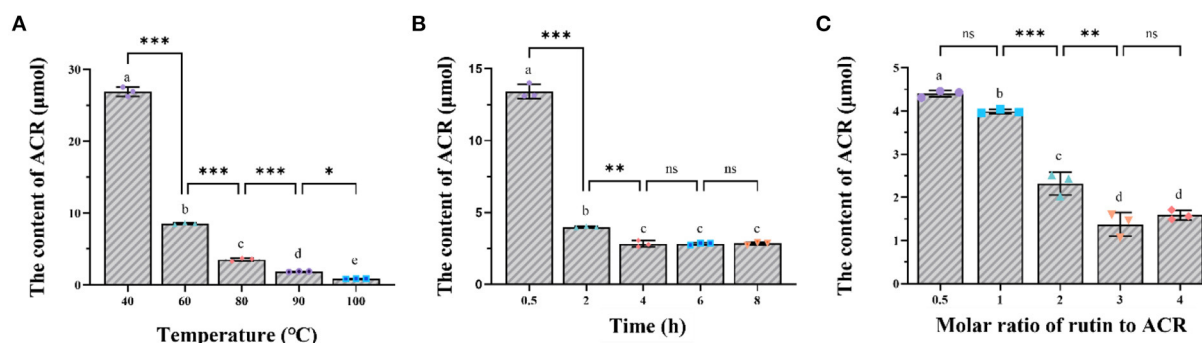


FIGURE 1

The impact of (A) temperature, (B) reaction time, and (C) molar ratio of rutin to ACR on the elimination of ACR by rutin. *: $p < 0.05$; **: $p < 0.01$; ***: $p < 0.001$; ns, not significant.

100°C for 2 h, the content of ACR was determined to be 113.28, 35.9, 14.88, 7.83, and 3.60 μmol, respectively (Figure 1A). In other words, compared with the initial content (200 μmol), the amount of ACR was reduced by 43.36, 82.05, 92.56, 96.09, and 98.20%, respectively. A sharp decline of the content of ACR could be observed with the increase of temperature, especially from 40 to 80°C ($p < 0.001$), which indicated that temperature had a significant effect on the elimination of ACR ($p < 0.05$). Similar phenomena could be seen in regard to the effect of reaction time on the capture of ACR. As displayed in Figure 1B, ACR was eliminated by rutin in a time-dependent manner, with more than 94% being removed after 8 h of reaction. However, the content of ACR did not decrease significantly after 4 h of reaction ($p > 0.05$). Figure 1C showed the effect of molar ratio of rutin to ACR on the elimination of ACR. With the rise of molar ratio of rutin/ACR, the content of residual ACR exhibited an overall downward trend, from 18.54 μmol of 1/2 to 6.69 μmol of 4/1. Additionally, it could be observed that the content of ACR reduced significantly between the molar ratios of 1/1 and 2/1 ($p < 0.001$).

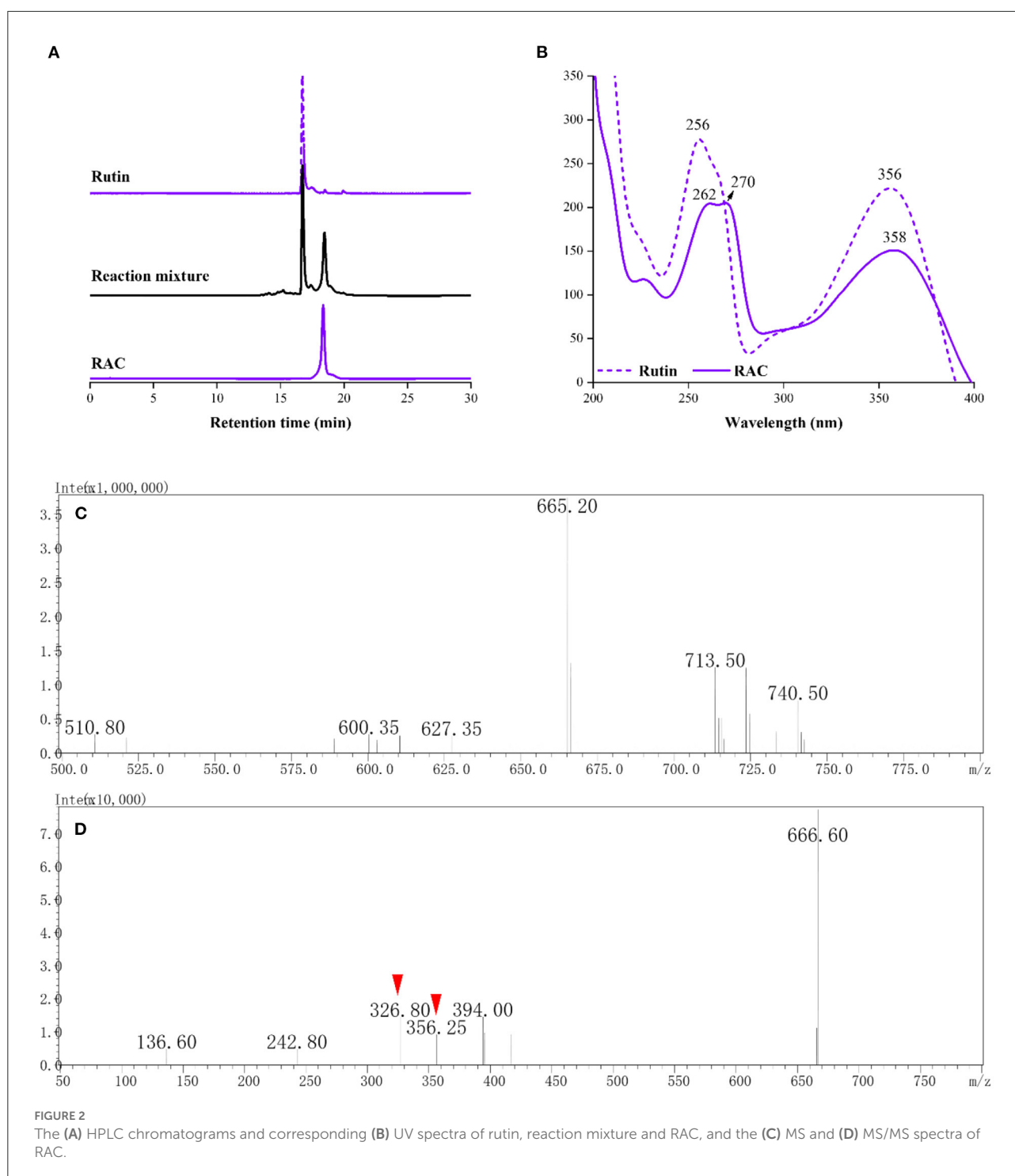
In addition to rutin, other phenolic compounds with a *meta*-phenol configuration in A ring were also found to capture ACR. According to Zhu et al. (21), after polyphenols (1.0 mM) incubating with ACR (0.5 mM) for 1.5 h at 37°C, the ability of them to remove ACR in a decrease sequence was phloretin, epigallocatechin-3-gallate, epicatechin-3-gallate, epicatechin, epigallocatechin, theaflavin-3,3'-digallate, theaflavin, cyanomacurin, and phloridzin. Additionally, in the study by Wang et al. (25), resveratrol and hesperetin could eliminate 93.6 and 94.87% of ACR, respectively, after incubating with equal concentrations of ACR for 12 h at 37°C. Combined the above results, it was found that not only the specific structure of polyphenols but also the elevated temperature contributed to the higher scavenging efficiency of ACR. As a result, more RAC were prepared under the reaction conditions of temperature at 80°C,

reaction time of 2 h, and molar ratio of rutin/ACR of 2/1 for subsequent experiments.

Structural characterization of RAC

Compared with rutin [retention time (R_t), 16.73 min], a newly occurred chromatographic peak ($R_t = 18.46$ min) could be seen after 0.5 h of reaction (Figure 2A). This compound was obtained after purification with a chromatographic purity of 99%, and given RAC. As displayed in Figure 2B, it had absorption peaks at 262, 270, and 358 nm, redshifted relative to rutin (absorption peaks at 256 and 356 nm). The molecular weight of RAC was collected prior to the NMR experiment. In the MS of RAC (Figure 2C), a major ion peak [$M - H$][−] at m/z 665 was observed, which was 56 mass units (the molecular weight of ACR) higher than rutin [($M - H$)[−]: 609]. This deprotonated precursor ion was further subjected to MS/MS analysis (Figure 2D), and the product ion at m/z 356 suggested the loss of the rutinoside moiety, whereas the product ion at m/z 326 indicated the further loss of [−CO-2H][−] moiety.

The exact structure of RAC was determined by its NMR data. Compared with rutin, the ¹H NMR spectrum (Supplementary Figure S1) of RAC displayed part of the same resonances, including one methyl at δ_H 0.96 (3H, dd, $J = 15.5$, 6.2 Hz), two methines at δ_H 4.37 (1H, d, $J = 1.9$ Hz) and 5.35 (1H, d, $J = 7.6$ Hz), and four aromatic protons at δ_H 6.17 (1H, d, $J = 3.7$ Hz), 6.90 (1H, d, $J = 8.5$ Hz), 7.62 (1H, d, $J = 8.5$ Hz), and 7.65 (1H, d, $J = 2.1$ Hz). However, the signal at δ_H 6.38 was absent, indicating the replacement of proton happened to C-8. In addition, three additional groups of signals, interpreted with the aid of an HSQC experiment (Supplementary Figure S4), suggested the existence of one methine [δ_H 5.56 (1H, s)] and two methylene groups [δ_H 1.92 (2H, m), 2.85 (2H, m)]. The ¹³C and DEPT 135 data of RAC (Supplementary Figures S2, S3) revealed thirty carbon resonances, including one carbonyl, ten



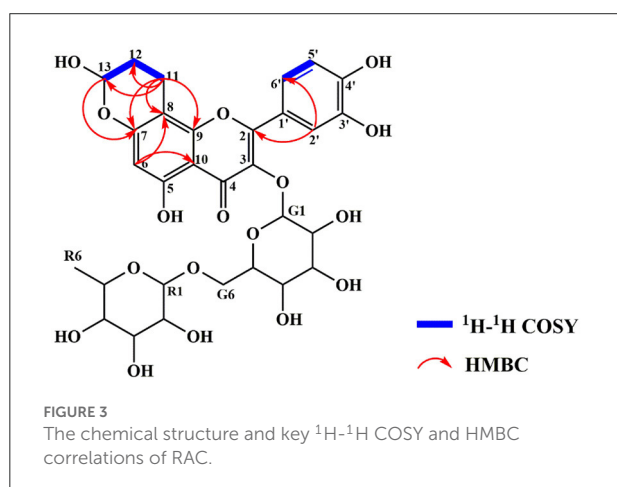
quaternary carbons, fifteen methine groups, three methylene groups, and one methyl. Further comparing with the carbon resonances of rutin, changes in the chemical shift of C-7 and C-8 as well as the appearance of three new signals (δ_C 92.9, 26.4 and 14.5) could be observed. The detailed assignments of ^1H and ^{13}C signals of RAC were present in [Table 1](#).

Since the 1D NMR data of rutin and RAC exhibited high similarity, comprehensive interpretation of the 2D NMR data of RAC mainly focused on the newly occurred signals. Its ^1H - ^1H COSY spectrum ([Supplementary Figure S5](#)) showed the correlations from δ_H 5.56 (H-13) to δ_H 1.92 (H-12) and from δ_H 1.92 (H-12) to δ_H 2.85 (H-11), together with the HMBC

TABLE 1 The ^1H and ^{13}C assignments of RAC^a.

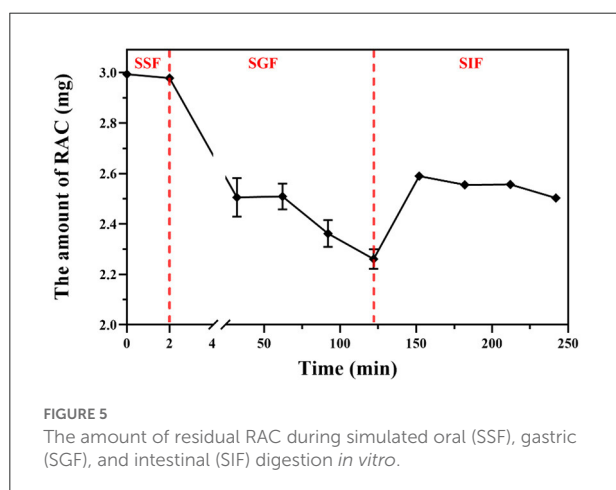
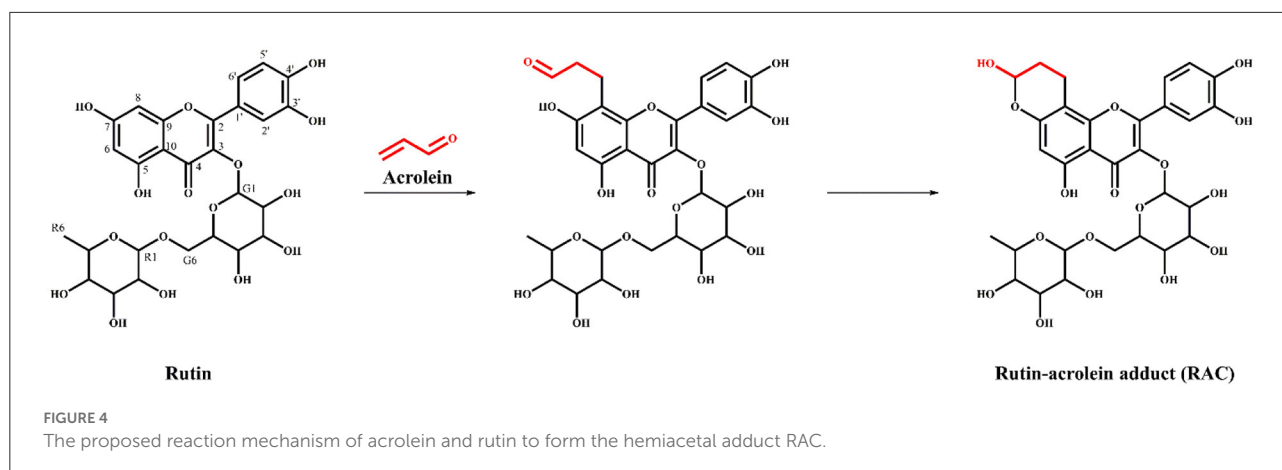
No.	^1H	^{13}C	^1H - ^1H COSY	HMBC
2	-	156.5		
3	-	133.5		
4	-	177.6		
5	-	158.6		
6	6.17 (d, $J = 3.7$ Hz, 1H)	99.0		C-5, 7, 8, 10
7	-	158.5		
8	-	101.0		
9	-	152.9		
10	-	104.7		
11	2.85, m, 2H	14.5	H-12	C-7, 8, 9, 12, 13
12	1.92, m, 2H	26.4		C-13
13	5.56, s, 1H	92.9	H-12	C-7
1'	-	121.3		
2'	7.65 (d, $J = 2.1$ Hz, 1H)	115.5		C-2, 3', 4', 6'
3'	-	144.9		
4'	-	148.6		
5'	6.90 (d, $J = 8.5$ Hz, 1H)	116.2		C-3', 4', 6'
6'	7.62 (d, $J = 8.5$ Hz, 1H)	121.6	H-5'	C-2, 2', 4', 5'
G1 ^b	5.35 (d, $J = 7.6$ Hz, 1H)	101.1		
G2		74.1		
G3		76.5		
G4	3.06–3.69	70.0		
G5		75.9		
G6		66.9		
R1 ^b	4.37 (d, $J = 1.9$ Hz, 1H)	100.6		
R2		70.4		
R3		70.6		
R4	3.06–3.69	71.8		
R5		68.2		
R6	0.95 (dd, $J = 15.5, 6.2$ Hz, 2H)	17.7		

^a Measured at 600 (^1H) and 150 (^{13}C) MHz in DMSO- d_6 for RAC, and chemical shifts were expressed in parts per million (ppm). ^b "G" is the abbreviation of "glucose" and "R" of "rhamnose".



(Supplementary Figure S6) correlations from H-11 to C-12/C-13, indicating the fragment of C(13)–C(12)–C(11). Additionally, HMBC correlations from H-11 to C-8/C-9/C-7 indicated the linkage of C-11 to C-8, and from H-13 to C-7 indicated the fragment of C(13)–O–C(7). Therefore, the chemical structure of RAC was established, as shown in Figure 3, which was a novel compound.

The reaction mechanism of ACR and polyphenols with *meta*-phenol structures to form the corresponding hemiacetals had been put forward previously (20, 26). Therefore, the chemical rationale for the interaction between ACR and rutin was proposed as followed (Figure 4) the C=C of ACR adducted to C-8 of rutin through electrophilic addition, followed by intramolecular nucleophilic addition between the contiguous hydroxyl at



C-7 and the -CHO of ACR to form a more stable cyclic hemiacetal structure.

Simulated *in vitro* digestion

The content of RAC was calculated based on its calibration curve ($y = 34274493x - 100977$; $r^2 = 0.9998$; x was the concentration of each sample and y was the corresponding peak area). As depicted in Figure 5 and Supplementary Table S1, after mimic oral digestion, the content of RAC was 0.595 ± 0.0018 mg/mL, and a decrease of 0.33% indicated that RAC remained unchanged at this stage ($p > 0.05$). When the adduct was further subjected to simulated gastric digestion for 120 min, a reduction of 24.41% was observed, from 0.167 ± 0.0042 mg/mL to 0.151 ± 0.0021 mg/mL. Surprisingly, a significant increase in the amount of RAC after 30 min of mimic intestinal digestion was observed, compared with that of RAC after 120 min of mimic gastric digestion ($p < 0.001$). In addition, the amount of RAC after 120 min of mimic intestinal digestion (2.50 ± 0.01 mg) and that

of RAC after 30 min of mimic gastric digestion (2.50 ± 0.06 mg) were almost at the same level ($p > 0.05$). In a whole, 83.61% of RAC was remained after *in vitro* simulated oral, gastric, and intestinal digestion.

It was reported that hemiacetals were stable under alkaline conditions, but could be reversibly hydrolyzed back to the starting aldehyde and alcohol in acidic aqueous solution (44, 45). Therefore, the negligible hydrolysis of RAC during simulated oral and intestinal digestion was attributed to the weakly acidic environment (pH 6.8) ($p > 0.05$), while the low pH condition (pH 1.5) during simulated gastric digestion led to the sharp decline of RAC. Furthermore, after 30 min of simulated gastric digestion (Supplementary Figure S7), new peaks could be observed by HPLC analysis, and the peak areas increased with time. However, owing to the low content of the newly occurred peaks, their detailed information was hard to obtain in this study. But based on their UV spectra, it was tentatively presumed that they had a similar structure to RAC, with absorbances at 260, 270, and 359 nm.

Cytotoxicity of the adduct against Caco-2 and GES-1 cells with acrolein as the control

Given that ingested ACR mainly affected the gastrointestinal system (46), the cytotoxicity of ACR and RAC against GES-1 and Caco-2 cell lines was examined. The CCK-8 assay was one of the effective methods to quantify viable cells, as the formation of orange and water-soluble formazan was positively correlated with the number of living cells (47). As demonstrated in Figures 6A,B, ACR inhibited the cell viability of both Caco-2 and GES-1 cells in a concentration-dependent manner. Specifically, after incubation with ACR for 24 h, the viable cell number of Caco-2 cells decreased by 93.06%, from 31.83% (20 μ M) to 6.97% (140 μ M), and that of GES-1 cells decreased by 88.78%,

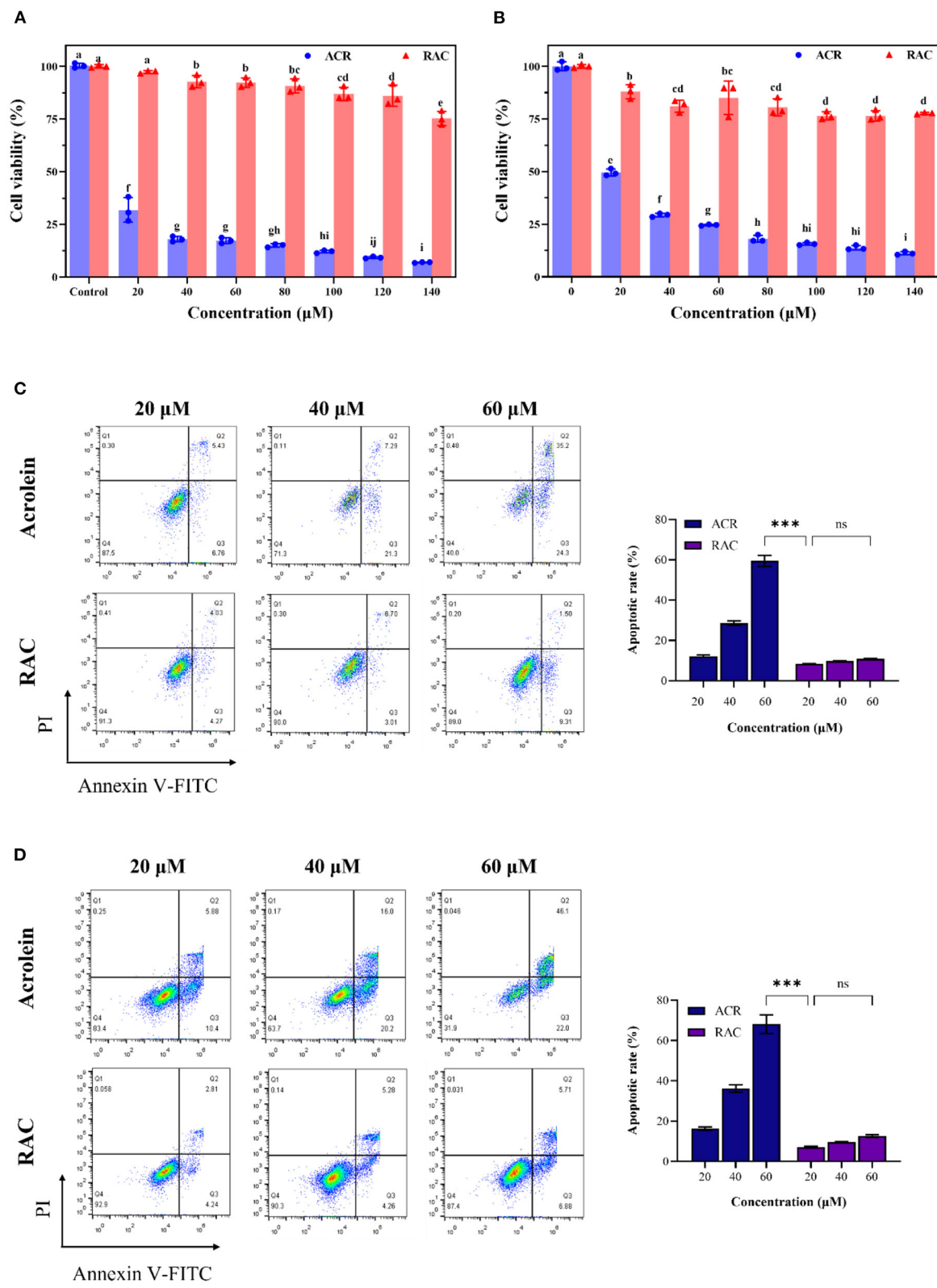


FIGURE 6
The cell viability of (A) Caco-2 and (B) GES-1 cells after incubation with ACR (acrolein) and RAC at the concentrations of 20–140 μ M for 48 h, and the apoptosis induced by ACR and RAC at the concentrations of 20–60 μ M in (C) Caco-2 and (D) GES-1 cells. Different letters indicated significant differences ($p < 0.05$). ***: $p < 0.001$; ns: not significant.

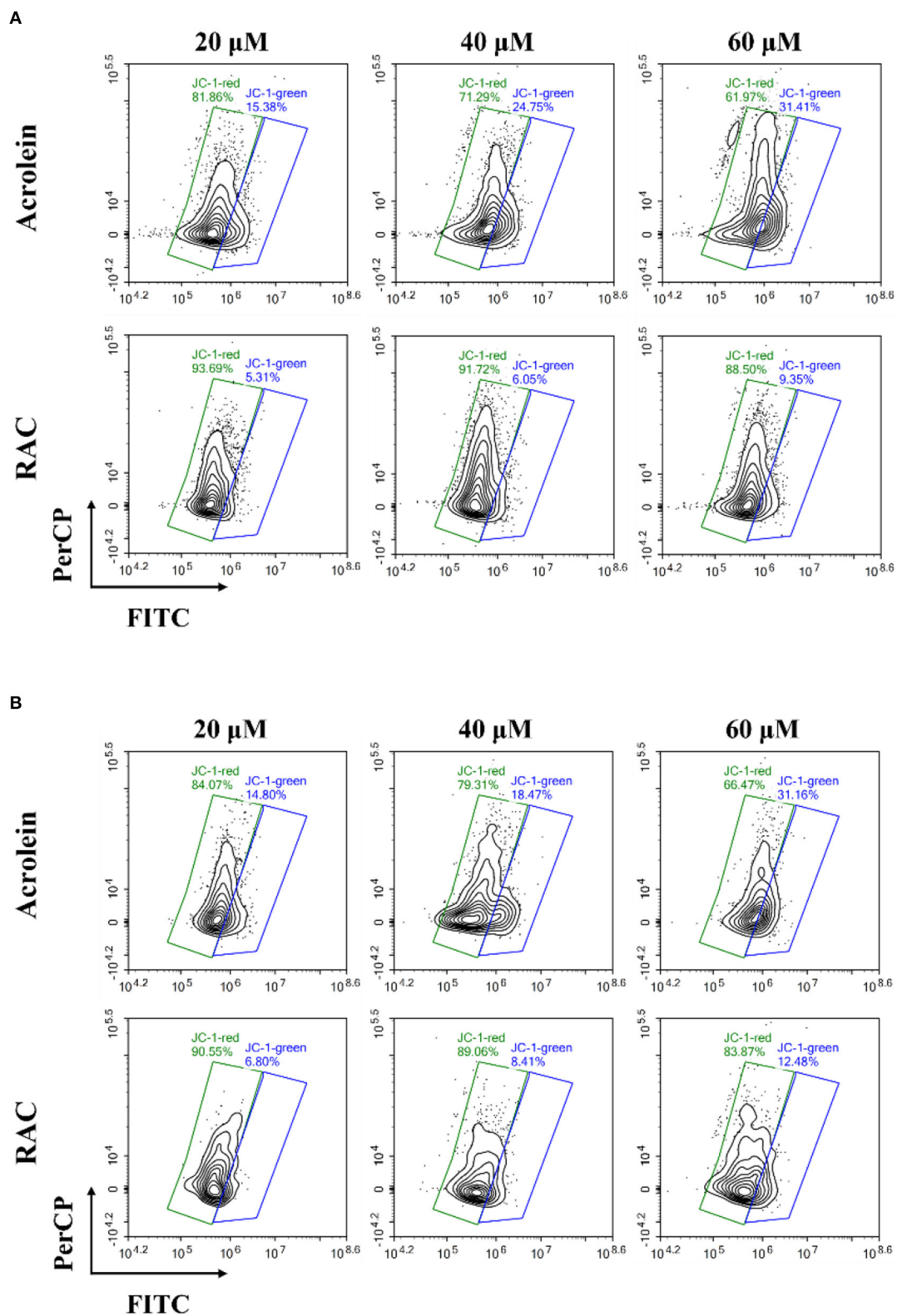


FIGURE 7
The changes of the mitochondrial membrane potential (MMP) in **(A)** Caco-2 and **(B)** GES-1 cells after incubation with acrolein and RAC at the concentrations of 20, 40, and 60 μ M respectively.

from 49.57% (20 μ M) to 11.22% (140 μ M). In comparison, RAC-induced cell death was relatively modest. More than 75% of both Caco-2 and GES-1 cells survived after exposure to 140 μ M of RAC for the same duration. It was also observed that the viability of Caco-2 and GES-1 cells treated with RAC was 10- and 6.5-fold higher than that of ACR-treated Caco-2 and GES-1 cells respectively. Furthermore, the IC₅₀ values of ACR for Caco-2 and GES-1 cells were both below 20 μ M, while that of RAC for both cells were above 140 μ M.

Annexin V had high affinity and specificity for phosphatidylserine, which could appear on the outer side of plasma membrane as a signal of apoptosis, while PI was capable of permeating incomplete membrane and binding to DNA (48). Therefore, Annexin V and PI double staining was further introduced to determine apoptosis. It could be seen that ACR concentration-dependently induced apoptosis in Caco-2 and GES-1 cells as well (Figures 6C,D). After Caco-2 cells were treated with 20, 40, and 60 μ M ACR for 24 h, the number of viable cells declined to 87.5, 71.3, and 40.0%, respectively, while that of apoptotic cells increased to 12.19, 28.59, and 59.50%, respectively. In contrast, Caco-2 cells treated with different concentrations of RAC exhibited a negligible increase in apoptosis ($p > 0.05$), from 8.3% (20 μ M) to 10.81% (60 μ M). Furthermore, the apoptotic rate of cells exposed to 60 μ M of ACR was 5.5 times higher than that of the same concentration of RAC. The above data demonstrated that ACR-induced apoptosis was significantly alleviated after ACR was captured by rutin to form RAC. Similar results could be seen in GES-1 cells. To be specific, the apoptotic rate of ACR-treated GES-1 cells increased from 16.28% (20 μ M) to 68.10% (60 μ M). However, even exposure to 60 μ M of RAC caused only 12.59% of GES-1 cells undergoing apoptosis, 5.4-fold <60 μ M ACR-treated group. Consequently, it could be concluded that the formation of RAC attenuated ACR-induced cytotoxicity against Caco-2 and GES-1 cells.

Determination of MMP in Caco-2 and GES-1 cells

The cytotoxic effects of ACR against Caco-2 and GES-1 cells were also studied in other literature, and there was accumulating evidence suggesting the link between mitochondrial dysfunction and apoptosis (9, 49). Hence, changes of MMP in cells were further measured by JC-1, as the decrease of MMP in cells was an iconic issue found in early apoptotic cells (50). JC-1 was a lipophilic fluorescent probe and was capable of entering the mitochondrial matrix, where it aggregated to form polymers with red fluorescence under high membrane potential while existed as monomers with green fluorescence under low membrane potential. In addition, the enhancement of green

fluorescence along with the reduction of red fluorescence was correlated with the loss of MMP (51).

As depicted in Figure 7A, ACR induced the loss of MMP in Caco-2 cells dose-dependently, with the increase of green fluorescence and the decrease of red fluorescence. And the ratio of red/green fluorescence intensity in ACR-treated group significantly decreased from 26.54 (control, data not shown) to 1.97 (60 μ M) (Supplementary Table S2) ($p < 0.001$), highly suggesting depolarization of the MMP in Caco-2 cells. However, RAC attenuated the transformation from red to green fluorescence (Figure 7A), and the ratio of red/green fluorescence intensity of the 60 μ M RAC-treated group (9.47) was even higher than that of the 20 μ M ACR-treated group (5.32) (Supplementary Table S2). Similar phenomenon was also observed in GES-1 cells incubated with ACR and RAC (Figure 7B). With the increased concentrations of ACR, the red fluorescence was reduced while the green fluorescence was increased. Besides, the ratio of red/green fluorescence intensity in ACR-treated group significantly reduced from 17.71 (control, data not shown) to 2.13 (60 μ M) ($p < 0.001$), further indicating the disruption of MMP in GES-1 cells (Supplementary Table S3). However, the reduction of MMP in GES-1 cells was alleviated when incubated with RAC (Figure 7B), where the ratio of red/green fluorescence intensity of 60 μ M RAC-treated group (6.72) was also higher than that of 20 μ M ACR-treated group (5.68) (Supplementary Table S3). As a result, it could be tentatively concluded that RAC attenuated ACR-induced cytotoxicity in Caco-2 and GES-1 cells by ameliorating the loss of MMP in mitochondria.

Conclusion

ACR was not only a foodborne pollutant but also a trigger of several serious diseases. In this study, the capacity of rutin, a nutrient polyphenol found in several frequently consumed ingredients like onions and peppers, to scavenge ACR was investigated. It was shown that rutin could scavenge more than 98% of ACR under the set conditions (temperature, 80°C; reaction time, 2 h; and the molar ratio of rutin/ACR, 2/1). Besides, the results indicated that rutin scavenged ACR through the formation of a hemiacetal adduct (RAC), of which the structure was identified for the first time, and C-8 and the hydroxyl at C-7 of rutin were the reaction sites for ACR. Due to the presence of the hemiacetal structure that was pH-sensitive, RAC was partially degraded after the three-stage simulated digestion, with 83.61% remained. Furthermore, the results revealed that RAC ameliorated ACR-induced cytotoxicity against Caco-2 and GES-1 cells through improvement of the loss of MMP. Overall, the above observations suggested that rutin could also be one of the potential ACR scavengers, and rutin-enriched dietary materials might contribute to limit ACR released during domestic cooking.

Data availability statement

The original contributions presented in the study are included in the article/Supplementary materials, further inquiries can be directed to the corresponding authors.

Author contributions

PC: methodology and writing-original draft. SL: methodology and investigation. ZY and PL: data curation. CW: supervision. HZ: resources. YL: visualization. SO: conceptualization. GL: conceptualization, review, and funding acquisition. All authors contributed to the article and approved the submitted version.

Funding

This work was supported by grants from Guangdong Basic and Applied Basic Research Foundation (2019A1515011967 and 2021A1515110430), Doctoral Workstation Foundation of Guangdong Second Provincial General Hospital (2021BSGZ017), Science and Technology Planning Project of Guangdong Province (202002030404 and 2021B1212030008),

Foundation of Guangdong Second Provincial General Hospital (3DB2020014 and TJGC-2021011).

Conflict of interest

The authors declare that the research was conducted in the absence of any commercial or financial relationships that could be construed as a potential conflict of interest.

Publisher's note

All claims expressed in this article are solely those of the authors and do not necessarily represent those of their affiliated organizations, or those of the publisher, the editors and the reviewers. Any product that may be evaluated in this article, or claim that may be made by its manufacturer, is not guaranteed or endorsed by the publisher.

Supplementary material

The Supplementary Material for this article can be found online at: <https://www.frontiersin.org/articles/10.3389/fnut.2022.976400/full#supplementary-material>

References

- Zhang H, Troise AD, Qi Y, Wu G, Zhang H, Fogliano V. Insoluble dietary fibre scavenges reactive carbonyl species under simulated physiological conditions: the key role of fibre-bound polyphenols. *Food Chem.* (2021) 349:129018. doi: 10.1016/j.foodchem.2021.129018
- Aizenbud D, Aizenbud I, Reznick AZ, Avezov K. Acrolein-an α,β -unsaturated aldehyde: A review of oral cavity exposure and oral pathology effects. *Rambam Maimonides Med J.* (2016) 7:e0024. doi: 10.5041/RMMJ.10251
- Alarcon RA. Formation of acrolein from various amino-acids and polyamines under degradation at 100 °C. *Environ Res.* (1976) 12:317–26. doi: 10.1016/0013-9351(76)90041-4
- Voulgaridou G-P, Anestopoulos I, Franco R, Panayiotidis MI, Pappa A. DNA damage induced by endogenous aldehydes: current state of knowledge. *Mutat Res Fund Mol M.* (2011) 711:13–27. doi: 10.1016/j.mrfmmm.2011.03.006
- Cox PJ. Cyclophosphamide cystitis-identification of acrolein as the causative agent. *Biochem Pharmacol.* (1979) 28:2045–9. doi: 10.1016/0006-2952(79)90222-3
- Tang M, Wang H, Hu Y, Chen W, Akao M, Feng Z, et al. Acrolein induced DNA damage, mutagenicity and effect on DNA repair. *Mol Nutr Food Res.* (2011) 55:1291–300. doi: 10.1002/mnfr.201100148
- Stevens JF, Maier CS. Acrolein: sources, metabolism, and biomolecular interactions relevant to human health and disease. *Mol Nutr Food Res.* (2008) 52:7–25. doi: 10.1002/mnfr.200700412
- Sun L, Luo C, Long J, Wei D, Liu J. Acrolein is a mitochondrial toxin: effects on respiratory function and enzyme activities in isolated rat liver mitochondria. *Mitochondrion.* (2006) 6:136–42. doi: 10.1016/j.mito.2006.04.003
- Chen W, Wang M, Zhang J, Barve SS, McClain CJ, Joshi-Barve S. Acrolein disrupts tight junction proteins and causes endoplasmic reticulum stress-mediated epithelial cell death leading to intestinal barrier dysfunction and permeability. *Am J Pathol.* (2017) 187:2686–97. doi: 10.1016/j.ajpath.2017.08.015
- Lovell MA, Xie C, Markesbery WR. Acrolein is increased in Alzheimer's disease brain and is toxic to primary hippocampal cultures. *Neurobiol Aging.* (2001) 22:187–94. doi: 10.1016/S0197-4580(00)00235-9
- Hong J, Lee P, Lu Y, Huang C, Chen C, Chiang C, et al. Acrolein contributes to urothelial carcinomas in patients with chronic kidney disease. *Urol Oncol-Semin Ori.* (2020) 38:465–75. doi: 10.1016/j.urolonc.2020.02.017
- Henning RJ, Johnson GT, Coyle JP, Harbison RD. Acrolein can cause cardiovascular disease: A review. *Cardiovasc Toxicol.* (2017) 17:227–36. doi: 10.1007/s12012-016-9396-5
- Abraham K, Andres S, Palavinskas R, Berg K, Appel KE, Lampen A. Toxicology and risk assessment of acrolein in food. *Mol Nutr Food Res.* (2011) 55:1277–90. doi: 10.1002/mnfr.201100481
- Calingasan NY, Uchida K, Gibson GE. Protein-bound acrolein: a novel marker of oxidative stress in Alzheimer's disease. *J Neurochem.* (1999) 72:751–6. doi: 10.1046/j.1471-4159.1999.0720751.x
- Tsou HH, Hsu WC, Fuh JL, Chen S, Liu T, Wang H. Alterations in acrolein metabolism contribute to Alzheimer's disease. *J Alzheimers Dis.* (2018) 61:571–80. doi: 10.3233/JAD-170736
- Faroon O, Roney N, Taylor J, Ashizawa A, Lumpkin M, Plewak D. Acrolein environmental levels and potential for human exposure. *Toxicol Ind Health.* (2008) 24:543–64. doi: 10.1177/0748233708098124
- Chen L, Wu X, Zeb F, Huang Y, An J, Jiang P, et al. Acrolein-induced apoptosis of smooth muscle cells through NEAT1-Bmal1/clock pathway and a protection from asparagus extract. *Environ Pollut.* (2020) 258:113735. doi: 10.1016/j.envpol.2019.113735
- Chadwick AC, Holme RL, Chen Y, Thomas MJ, Sorci-Thomas MG, Silverstein RL, et al. Acrolein impairs the cholesterol transport functions of high density lipoproteins. *PLoS ONE.* (2015) 10:e0123138. doi: 10.1371/journal.pone.0123138

19. Ewert A, Granvogl M, Schieberle P. Development of two stable isotope dilution assays for the quantitation of acrolein in heat-processed fats. *J Agric Food Chem.* (2011) 59:3582–9. doi: 10.1021/jf200467x
20. Zhu Q, Sun Z, Jiang Y, Chen F, Wang M. Acrolein scavengers: reactivity, mechanism and impact on health. *Mol Nutr Food Res.* (2011) 55:1375–90. doi: 10.1002/mnfr.201100149
21. Zhu Q, Zheng Z, Cheng K, Wu J, Zhang S, Tang Y, et al. Natural polyphenols as direct trapping agents of lipid peroxidation-derived acrolein and 4-hydroxy-trans-2-nonenal. *Chem Res Toxicol.* (2009) 22:1721–7. doi: 10.1021/tx900221s
22. Sugimoto K, Matsuoka Y, Sakai K, Fujiya N, Fujii H, Mano J. Catechins in green tea powder (matcha) are heat-stable scavengers of acrolein, a lipid peroxide-derived reactive carbonyl species. *Food Chem.* (2021) 355:129403. doi: 10.1016/j.foodchem.2021.129403
23. Jiang X, Lv H, Lu Y, Lu Y, Lv L. Trapping of acrolein by curcumin and the synergistic inhibition effect of curcumin combined with quercetin. *J Agric Food Chem.* (2020) 69:294–301. doi: 10.1021/acs.jafc.0c06692
24. Zhang D, Jiang X, Xiao L, Lu Y, Sang S, Lv L, et al. Mechanistic studies of inhibition on acrolein by myricetin. *Food Chem.* (2020) 323:126788. doi: 10.1016/j.foodchem.2020.126788
25. Wang W, Qi Y, Rocca JR, Sarnoski PJ, Jia A, Gu L. Scavenging of toxic acrolein by resveratrol and hesperetin and identification of adducts. *J Agric Food Chem.* (2015) 63:9488–95. doi: 10.1021/acs.jafc.5b03949
26. Hidalgo FJ, Zamora R. 2-Alkenal-scavenging ability of *m*-diphenols. *Food Chem.* (2014) 160:118–26. doi: 10.1016/j.foodchem.2014.03.071
27. Zamora R, Aguilar I, Granvogl M, Hidalgo FJ. Toxicologically relevant aldehydes produced during the frying process are trapped by food phenolics. *J Agric Food Chem.* (2016) 64:5583–9. doi: 10.1021/acs.jafc.6b02165
28. Bystrická J, Musilová J, Vollmannová A, Timoracká M, Kavalcová P. Bioactive components of onion (*Allium cepa* L.) - a review. *Acta Aliment.* (2013) 42:11–22. doi: 10.1556/AAlim.42.2013.1.2
29. Shimoi K, Yoshizumi K, Kido T, Usui Y, Yumoto T. Absorption and urinary excretion of quercetin, rutin, and α -G-rutin, a water soluble flavonoid, in rats. *J Agric Food Chem.* (2003) 51:2785–9. doi: 10.1021/jf026108a
30. Liu Y, Zhao W, Song H, Liu S, Liu J, Yang J, et al. Isolation of flavonoids from onion skins and their effects on K562 cell viability. *Bangladesh J Pharmacol.* (2016) 11:S18–25. doi: 10.3329/bjp.v11iS1.26419
31. Hosseinzadeh H, Nassiri-Asl M. Review of the protective effects of rutin on the metabolic function as an important dietary flavonoid. *J Endocrinol Invest.* (2014) 37:783–8. doi: 10.1007/s40618-014-0096-3
32. Özcan MM, Uslu N, Efe NS, Erdem AN, Degerli Z, Kulluk DA, et al. Effect of thermal processing on the bioactive compounds and color parameters of types of three sweet pepper. *J Food Process Preserv.* (2021) 45:e15661. doi: 10.1111/jfpp.15661
33. Yi T, Yeoung Y, Choi I, Park N. Transcriptome analysis of *Asparagus officinalis* reveals genes involved in the biosynthesis of rutin and protodioscin. *PLoS ONE.* (2019) 14:e0219973. doi: 10.1371/journal.pone.0219973
34. Gao L, Schafer C, O'Reardon K, Gorgus E, Schulte-Hubbert R, Schrenk D. The mutagenic potency of onion juice vs. its contents of quercetin and rutin. *Food Chem Toxicol.* (2021) 148:111923. doi: 10.1016/j.fct.2020.111923
35. Yang J, Guo J, Yuan J. *In vitro* antioxidant properties of rutin. *LWT.* (2008) 41:1060–6. doi: 10.1016/j.lwt.2007.06.010
36. Reilly SM, Goel R, Bitzer Z, Elias RJ, Foulds J, Muscat J, et al. Effects of topography-related puff parameters on carbonyl delivery in mainstream cigarette smoke. *Chem Res Toxicol.* (2017) 30:1463–9. doi: 10.1021/acs.chemrestox.7b00104
37. Qi Y, Zhang H, Zhang H, Wu G, Wang L, Qian H, et al. Epicatechin adducting with 5-hydroxymethylfurfural as an inhibitory mechanism against acrylamide formation in maillard reactions. *J Agric Food Chem.* (2018) 66:12536–43. doi: 10.1021/acs.jafc.8b03952
38. Ganbaatar C, Gruner M, Mishig D, Duger R, Schmidt AW, Knölker H-J. Flavonoid glycosides from the aerial parts of *Polygonatum odoratum* (Mill.) druce growing in Mongolia. *Open Nat Prod J.* (2015) 8:1–7. doi: 10.2174/1874848101508010001
39. Mamone G, Nitride C, Picariello G, Addeo F, Ferranti P, Mackie A. Tracking the fate of pasta (*T. Durum semolina*) immunogenic proteins by *in vitro* simulated digestion. *J Agric Food Chem.* (2015) 63:2660–7. doi: 10.1021/jf505461x
40. Chai G, Xu Y, Chen S, Cheng B, Hu F, You J, et al. Transport mechanisms of solid lipid nanoparticles across Caco-2 cell monolayers and their related cytotoxicology. *ACS Appl Mater Interfaces.* (2016) 8:5929–40. doi: 10.1021/acsami.6b00821
41. Xu Z, Lan J, Jin J, Dong P, Jiang F, Liu Y. Highly photoluminescent nitrogen-doped carbon nanodots and their protective effects against oxidative stress on cells. *ACS Appl Mater Interfaces.* (2015) 7:28346–52. doi: 10.1021/acsami.5b08945
42. Abas E, Espallargas N, Burbello G, Mesonero JE, Rodriguez-Dieguez A, Grasa L, et al. Anticancer activity of alkynylgold(I) with P(NMe₂)[[sb]]2[[/s]][[sb]]3[[/s]] phosphane in mouse colon tumors and human colon carcinoma Caco-2 cell Line. *Inorg Chem.* (2019) 58:15536–51. doi: 10.1021/acs.inorgchem.9b02528
43. Liu P, Yin Z, Chen M, Huang C, Wu Z, Huang J, et al. Cytotoxicity of adducts formed between quercetin and methylglyoxal in PC-12 cells. *Food Chem.* (2021) 352:129424. doi: 10.1016/j.foodchem.2021.129424
44. Ouellette RJ, Rawn JDX. *Organic Chemistry Study Guide: Key Concepts, Problems, and Solutions.* Elsevier (2015).
45. Chiang Y, Kresge AJ. Kinetics of hydrolysis of acetaldehyde ethyl hemiacetal in aqueous solution. *J Org Chem.* (1985) 50:5038–40. doi: 10.1021/jo00225a007
46. Moghe A, Ghare S, Lamoreau B, Mohammad M, Barve S, McClain C, et al. Molecular mechanisms of acrolein toxicity: relevance to human disease. *Toxicol Sci.* (2015) 143:242–55. doi: 10.1093/toxsci/kfu233
47. Cai L, Qin X, Xu Z, Song Y, Jiang H, Wu Y, et al. Comparison of cytotoxicity evaluation of anticancer drugs between real-time cell analysis and CCK-8 method. *ACS Omega.* (2019) 4:12036–42. doi: 10.1021/acsomega.9b01142
48. Yan C, Zhang J, Liang T, Li Q. Diorganotin (IV) complexes with 4-nitro-*N*-phthaloyl-glycine: Synthesis, characterization, antitumor activity and DNA-binding studies. *Biomed Pharmacother.* (2015) 71:119–27. doi: 10.1016/j.biopha.2015.02.027
49. Zou Z, Yin Z, Ou J, Zheng J, Liu F, Huang C, et al. Identification of adducts formed between acrolein and alanine or serine in fried potato crisps and the cytotoxicity-lowering effect of acrolein in three cell lines. *Food Chem.* (2021) 361:130164. doi: 10.1016/j.foodchem.2021.130164
50. Zhai K, Duan H, Cui C, Cao Y, Si J, Yang H, et al. Liquiritin from *Glycyrrhiza uralensis* attenuating rheumatoid arthritis via reducing inflammation, suppressing angiogenesis, and inhibiting MAPK signaling pathway. *J Agric Food Chem.* (2019) 67:2856–64. doi: 10.1021/acs.jafc.9b00185
51. Nowak A, Zaklos-Szyda M, Zyzelewicz D, Koszucka A, Motyl I. Acrylamide decreases cell viability, and provides oxidative stress, DNA damage, and apoptosis in human colon adenocarcinoma cell line Caco-2. *Molecules.* (2020) 25:368. doi: 10.3390/molecules25020368

Frontiers in Nutrition

Explores what and how we eat in the context of health, sustainability and 21st century food science

A multidisciplinary journal that integrates research on dietary behavior, agronomy and 21st century food science with a focus on human health.

Discover the latest Research Topics

[See more →](#)

Frontiers

Avenue du Tribunal-Fédéral 34
1005 Lausanne, Switzerland
frontiersin.org

Contact us

+41 (0)21 510 17 00
frontiersin.org/about/contact

